PAPER

Electron swarm parameters in C_2H_2, C_2H_4 and C_2H_6: measurements and kinetic calculations

View the article online for updates and enhancements.

Electron swarm parameters in C_2H_2, C_2H_4 and C_2H_6: measurements and kinetic calculations

N R Pinhão[1] ⓘ, D Loffhagen[2] ⓘ, M Vass[3,4] ⓘ, P Hartmann[3] ⓘ, I Korolov[4] ⓘ, S Dujko[5] ⓘ, D Bošnjaković[5] ⓘ and Z Donkó[3] ⓘ

[1] Instituto de Plasmas e Fusão Nuclear, Instituto Superior Técnico, Universidade de Lisboa, Av. Rovisco Pais, 1049-001 Lisboa, Portugal
[2] Leibniz Institute for Plasma Science and Technology, Felix-Hausdorff-Str. 2, D-17489 Greifswald, Germany
[3] Institute for Solid State Physics and Optics, Wigner Research Centre for Physics, 1121 Budapest, Konkoly Thege Miklós str. 29-33, Hungary
[4] Department of Electrical Engineering and Information Science, Ruhr-University Bochum, D-44780, Bochum, Germany
[5] Institute of Physics, University of Belgrade, Pregrevica 118, 11080 Belgrade, Serbia

E-mail: npinhao@ctn.tecnico.ulisboa.pt

CrossMark

Abstract

This work presents swarm parameters of electrons (the bulk drift velocity, the bulk longitudinal component of the diffusion tensor, and the effective ionization frequency) in C_2H_n, with $n = 2, 4$, and 6, measured in a scanning drift tube apparatus under time-of-flight conditions over a wide range of the reduced electric field, $1\,\mathrm{Td} \leqslant E/N \leqslant 1790\,\mathrm{Td}$ ($1\,\mathrm{Td} = 10^{-21}\,\mathrm{V\,m^2}$). The effective steady-state Townsend ionization coefficient is also derived from the experimental data. A kinetic simulation of the experimental drift cell allows estimating the uncertainties introduced in the data acquisition procedure and provides a correction factor to each of the measured swarm parameters. These parameters are compared to results of previous experimental studies, as well as to results of various kinetic swarm calculations: solutions of the electron Boltzmann equation under different approximations (multiterm and density gradient expansions) and Monte Carlo simulations. The experimental data are consistent with most of the swarm parameters obtained in earlier studies. In the case of C_2H_2, the swarm calculations show that the thermally excited vibrational population should not be neglected, in particular, in the fitting of cross sections to swarm results.

Supplementary material for this article is available online

1. Introduction

Acetylene (C_2H_2), ethylene (C_2H_4) and ethane (C_2H_6) are relatively simple hydrocarbons useful in specialized applications such as plasma-assisted combustion [1–6], the fabrication of diamond-like films [7], graphene and carbon nanostructures [8], and particle detectors [9]. They are also involved in various chemical reactions in fusion plasmas [10], the Earth's atmosphere [11] and in planetary atmospheric chemistry [12].

Knowledge on both electron collision cross sections and electron swarm parameters is needed for the quantitative modeling of plasmas. However, with the exception of the drift velocity, which was measured e.g. in [13–17] for C_2H_2, in [13, 16–23] for C_2H_4, and in [13, 15–17, 19, 24, 25] for C_2H_6, further experimental transport and ionization coefficients have less frequently been reported for these hydrocarbon gases. Measurements of the longitudinal component of the diffusion tensor under time-of-flight (TOF) conditions were additionally reported in [14] for C_2H_2, [18–20] for
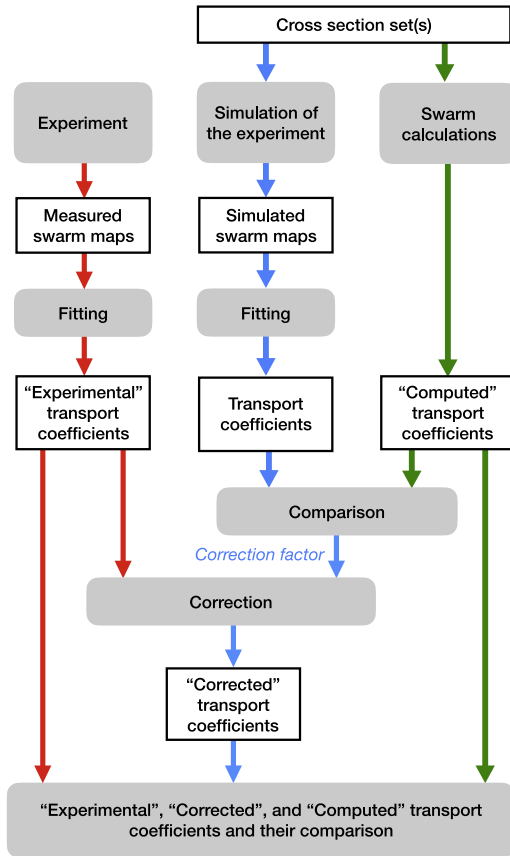
Figure 1. Graphical representation of the work reported in this article. The red arrows indicate the path from the measurements to the 'Experimental' transport coefficients and ionization frequencies via fitting of the measured 'swarm maps'. Another 'Corrected' set of experimental data is also derived based on a correction procedure which is aided by simulations of the experimental setup and related data acquisition (indicated by blue arrows) and by kinetic computations of the swarm parameters. The results of these calculations ('Computed' transport coefficients) are also compared to the experimental data (green arrows).

C_2H_4, and [19, 24] for C_2H_6. Hasegawa and Date [13] also determined the effective ionization coefficient by the steady-state Townsend (SST) method for seven organic gases including acetylene, ethylene, and ethane. In addition to the drift velocity for C_2H_6, Kersten [25] measured the effective ionization coefficient under TOF conditions for a narrow range of the reduced electric field, E/N. Furthermore, measured data for the effective SST ionization coefficient have been reported e.g. in [26] for C_2H_2, in [26, 27] for C_2H_4, and in [28–30] for C_2H_6.

The aim of this work is (i) to determine the electron transport and ionization coefficients in C_2H_2, C_2H_4 and C_2H_6 gases in a wide range of E/N, (ii) to compare these results with those obtained in earlier investigations of these gases, and (iii) to compare the experimental data with those obtained from kinetic calculations and simulations using up-to-date electron collision cross section sets.

The workflow of our studies can be followed with the aid of figure 1. The red arrows show the path to the 'Experimental transport coefficients' including the effective ionization frequencies. The first step along this path consists of the

measurements carried out with our scanning drift tube apparatus. This is a pulsed system, which is described in section 2. It records current traces generated by electrons collected from clouds that arrive after having flown over the drift region. The results of the experiments are the so-called 'swarm maps' which are collections of these current traces for a number of drift gap length values. The swarm parameters are derived from the measured swarm maps via a fitting procedure that assumes that the current measured in the experiment is proportional to the electron density. For the fitting we use the theoretical form of the electron density in the presence of an electric field pointing in the $-z$ direction and under TOF conditions:

$$n_e(z, t) = \frac{n_0}{(4\pi D_L t)^{1/2}} \exp\left[\nu_{\text{eff}} t - \frac{(z - Wt)^2}{4D_L t}\right]. \qquad (1)$$

This is the solution of the spatially one-dimensional continuity equation and represents a Gaussian pulse drifting along the z direction with the bulk drift velocity, W, and diffuses along the center-of-mass according to the bulk longitudinal component of the diffusion tensor D_L. Here n_0 is the electron density at $z = 0$ at time $t = 0$, and ν_{eff} is the effective ionization frequency. From the fitting procedure we obtain W, D_L, and ν_{eff}. The application of the relation [31]

$$\frac{1}{\alpha_{\text{eff}}} = \frac{W}{2\nu_{\text{eff}}} + \sqrt{\left(\frac{W}{2\nu_{\text{eff}}}\right)^2 - \frac{D_L}{\nu_{\text{eff}}}} \qquad (2)$$

allows us to derive the effective SST ionization coefficient, α_{eff}, as well.

The assumption that the measured current is proportional to the electron density is, in fact, an approximation, due to two reasons. First, the measured current is generated by moving charges in the detector of the system (see later). In our previous work [32] we have found that the detection sensitivity depends on the gas pressure and the collision cross sections, which both influence the free path of the electrons. This means that any variation of the energy distribution along the z direction in the electron cloud may results in a distortion of the detected pulse and a deviation from the analytical fitting function (1) assumed. Second, the measured current is proportional to the electron flux consisting of the advective and diffusive component. The advective component is proportional to the electron density, where the coefficient of proportionality is the flux drift velocity, and the diffusive component is proportional to the gradient of the electron density. Using Ramo's theorem [33], it can be shown that for the experimental conditions considered in the present work, the contribution of the diffusive component to the current is negligible compared to the contribution of the advective component, except in the early stage of the swarm development when the spatial gradients of the electron density are more significant.

The errors introduced by the first effect mentioned above can be quantified by a procedure, which is marked by blue arrows in figure 1. We carry out a (Monte Carlo (MC)) simulation of the electrons' motion in the experimental system. This simulation generates the *same* type of swarm maps,

which are obtained in the experiments, and a set of swarm parameters is derived via the *same* fitting procedure as in the case of experimental swarm maps. The transport coefficients and ionization frequencies obtained in this way are compared with the 'Computed' ones, originating from kinetic swarm calculations. We note that (i) this comparison does not include any experimental data, (ii) the system's simulations use the *same* cross section set as in the kinetic swarm calculations, and (iii) uncertainties of the collision cross sections used have little influence on the outcome of the comparison of the parameter sets obtained by swarm calculations and simulations of the experimental system. The result of this comparison is gas- and E/N-dependent correction factors that are applied to the experimental data, providing sets of 'Corrected' experimental transport and ionization coefficients. Details are given below in section 4.

The two (raw and corrected) sets of experimental results are compared with swarm parameters derived from kinetic calculations based on solutions of the electron Boltzmann equation (BE) and on MC simulations as described in detail in section 3. The application of these different approaches allows us to mutually verify the accuracy of the different methods and test the assumptions used by each method. The 'flow' of this process is indicated by the green arrows in figure 1.

The manuscript is organized as follows: in section 2 we give a concise description of our experimental setup. A discussion of the various computational methods and the resulting swarm parameters is presented in section 3, and section 4 describes the correction procedure applied to the experimental data. It is followed by the discussion of the results in section 5. This section comprises the presentation of the present experimental results for each gas and their comparison with previously available measured data as well as the comparison between transport parameters and ionization coefficients computed using the various numerical methods and the present experimental data. Section 6 gives our concluding remarks.

2. Experimental system

The experiments are based on a 'scanning' drift tube apparatus, of which the details have been presented in [34]. This apparatus has already been applied for the measurements of transport and ionization coefficients of electrons in various gases: argon, synthetic air, methane, deuterium [35] and carbon dioxide [36]. In contrast to previously developed drift tubes, our system allows for recording of 'swarm maps' that show the spatio-temporal development of electron clouds under TOF conditions. The simplified scheme of our experimental apparatus is shown in figure 2.

The drift cell is situated within a vacuum chamber made of stainless steel. The chamber can be evacuated by a turbomolecular pump backed with a rotary pump to a level of about 1×10^{-7} mbar. The pressure of the working gases inside the chamber is measured by a Pfeiffer CMR 362 capacitive gauge.

Ultraviolet light pulses (1.7 μJ, 5 ns) of a frequency-quadrupled diode-pumped YAG laser enter the chamber via a feedthrough with a quartz window and fall on the surface of a Mg disk used as photoemitter. This disk is placed at the center of a stainless steel electrode with 105 mm diameter that serves as the cathode of the drift cell. The detector that faces the cathode at a distance L_1 consists of a grounded nickel mesh (with $T = 88\%$ 'geometric' transmission and 45 lines/inch density) and a stainless steel collector electrode that is situated at a distance of $L_2 = 1$ mm behind the mesh.

Electrons emitted from the Mg disk fly towards the collector under the influence of an accelerating voltage that is applied to the cathode. This voltage is established by a BK Precision 9185B power supply. Its value is adjusted according to the required E/N for the given experiment and the actual value of the gap (L_1) during the scanning process, where E/N is ensured to be fixed. The current of the detector system is generated by the moving charges within the mesh-collector gap: according to the Shockley–Ramo theorem [33, 37, 38] the current induced by an electron moving in a gap between two plane-parallel electrodes with a velocity v_z perpendicular to the electrodes is $I = -e_0 v_z / L$, where $-e_0$ is the charge of the electron and L is the distance between the electrodes ($L = L_2$ in our case). Accordingly, in our setting the measured current at a given time t is

$$I(t) = c \sum_k v_{z,k}(t), \qquad (3)$$

where c is a constant. The summation goes over all electrons being present in the volume bounded by the mesh and the collector at time t, and $v_{z,k}$ is the velocity component of the kth electron in z direction.

Electrons entering the detector region (the gap between the nickel mesh and the collector) contribute to the measured current until their first collisions with the gas molecules, as these collisions randomize the angular distribution of their velocities. Therefore, the free path of the electrons plays a central role in the magnitude of the current. For conditions when this free path is longer than the detector gap, the electron sticking property of the collector surface plays a crucial role too, as reflected electrons generate a current contribution with an opposite sign with respect to that generated by the 'incoming' electrons. According to the above effects, which have been explored to some details in [32], the sensitivity of the detector changes with the nature of the gas (magnitudes and energy dependence of the electron collision cross sections), the pressure, as well as the energy distribution of the electrons. This dependence is the primary reason which calls for a correction of the measured transport and ionization coefficients as discussed in more details in section 4.

The collector current is amplified by a high speed current amplifier (type Femto HCA-400M) connected to the collector, with a virtually grounded input, and is recorded by a digital oscilloscope (type Picoscope 6403B) with sub-ns time resolution. Data collection is triggered by a photodiode that senses the laser light pulses. The low light pulse energy necessitates averaging over typically 20 000–150 000 pulses. The
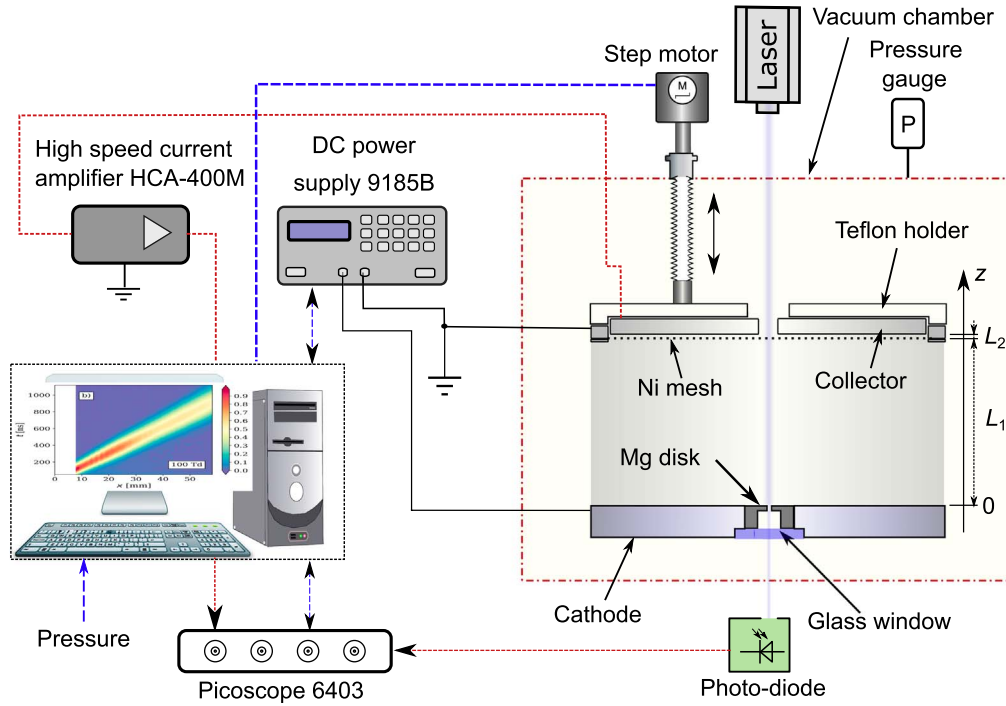
Figure 2. Simplified schematic of the scanning drift tube apparatus.
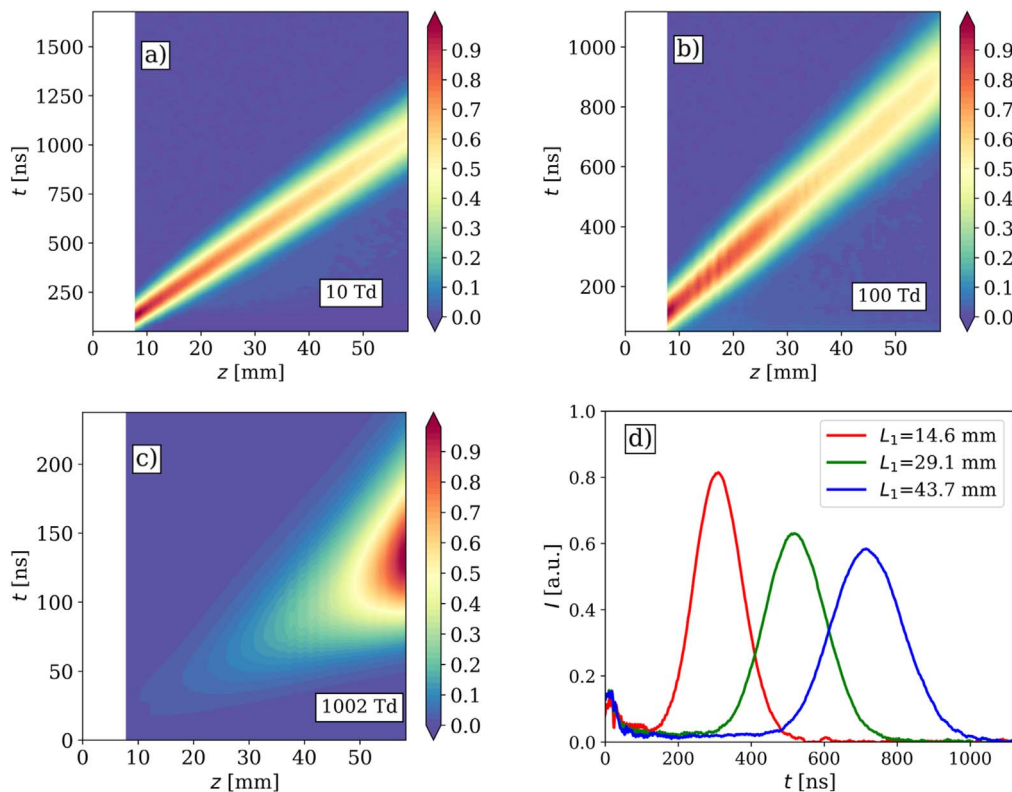
Figure 3. (a)–(c) Swarm maps recorded in C_2H_6 for different values of E/N, as indicated. (d) Vertical cuts of the swarm map of (b), which are the measured current traces at the drift length values given in the legend. The pulses have nearly Gaussian shapes. The 'shift' of the pulses with increasing drift length (L_1) is the manifestation of the drift, while their widening is due to (longitudinal) diffusion. As ionization in C_2H_6 is weak at $E/N = 100$ Td, the amplitude of the pulses decreases with increasing L_1 due to the widening of the pulse.

experiment is fully controlled by a computer using LabView software.

During the course of the measurements current traces are recorded for several values of the gap length. The grid and the collector are moved together by a step motor connected to a micrometer screw mounted via a vacuum feedthrough to the vacuum chamber. The distance between the cathode and the mesh, i.e. the 'drift length', can be set within a range of $L_1 = (7.8–58.3)$ mm. Here, we use 53 positions within this domain.

Sequences of the measured current traces are subsequently merged to form 'swarm maps', which provide information about the spatio-temporal development of the electron cloud. Figures 3(a)–(c) illustrates such swarm maps, obtained in experiments on C_2H_6, for different values of the reduced electric field. The qualitative behavior of the swarm is directly seen in these pictures: the slope of the region with appreciable current indicates the drift of the cloud, the widening of this region is related to (longitudinal) diffusion, while an increasing amplitude (as seen in panel (c)) is an indication of ionization. Figure 3(d) displays vertical 'cuts' of the map shown in panel (b), for $E/N = 100$ Td. These cuts are, actually, the current traces recorded in the measurements at different gap length values.

3. Simulation of the electron swarm

The experimental studies of the electron transport are supplemented by numerical modeling and simulation. In addition to MC simulations, three different methods are applied to solve the BE for electron swarms in a background gas with density N and acted upon by a constant electric field, $\vec{E}$: a multiterm method for the solution of the time-independent BE under spatially homogeneous and SST conditions, respectively, and the S_n method applied to a density gradient expansion of the electron velocity distribution function (EVDF). They differ in their initial physical assumptions and in the numerical algorithms used and provide different properties of the electron swarms

Details of the different BE methods, as well as main aspects of the MC simulation have been discussed in [36], and we just provide a brief discussion below.

In the following, the electric field is parallel to the z axis and points in the negative direction, $\vec{E} = -E\vec{e}_z$, and θ is the angle between $\vec{v}$ and $\vec{E}$. Moreover, we assume that the spatial and time scales, respectively, exceed the energy relaxation length and time, such that the transport properties of the electrons do not change with time t and distance z any longer. That is, the electrons have reached a hydrodynamic regime characterizing a state of equilibrium of the system where the effects of collisions and forces are dominant and the EVDF, $f(\vec{r}, \vec{v}, t)$, has lost any memory of the initial state.

We base our studies on the electron collision cross section sets from Song *et al* [39] for acetylene, Fresnet *et al* [40] for ethylene and Shishikura *et al* [24] for ethane. The cross sections for acetylene and ethane were extended to

electron kinetic energies, ϵ, of 1000 eV by fitting a function with a $\log(\epsilon)/\epsilon$ dependence, according to the Born-Bethe high-energy approximation, to the tail of the original cross sections.

The C_2H_2 data set includes the momentum transfer cross section for elastic collisions, three vibrational cross sections for single quanta excitation of modes v_1/v_3, v_4/v_5 and v_2 (the first two unresolved) and one vibrational cross section for two quanta excitation of v_4+v_5, three electronic excitation cross sections, the total electron-impact ionization cross section and the total dissociative electron attachment cross section for C_2H_2 leading to the formation of C_2H^-, H^- and C_2^-, respectively.

The C_2H_4 data set includes the momentum transfer cross section, two lumped vibrational cross sections with thresholds at 0.118 and 0.365 eV, three electronic excitation cross sections, the total electron ionization cross section and a collision cross section for electron attachment.

Finally, the C_2H_6 set of collision cross sections includes the momentum transfer cross section, three lumped vibrational cross sections with thresholds at 0.112, 0.167 and 0.36 eV, two electronic excitation cross sections, the total electron ionization cross section and an electron attachment cross section.

All of the above cross section sets were developed neglecting the population of thermally excited vibrational states and superelastic processes. The implications of this approximation are discussed in section 5.4.

3.1. BE methods

3.1.1. Multiterm method for spatially homogeneous conditions. In this approach, to describe $f(\vec{r}, \vec{v}, t)$ (abbreviated by BE 0D in the figures shown in section 5), we consider that the EVDF is spatially homogeneous (0D) and the electron density changes exponentially in time according to $n_e(t) \propto \exp(\nu_{\text{eff}} t)$ at the scale of the swarm. Here, the effective ionization frequency $\nu_{\text{eff}} = \nu_i - \nu_a$ is the difference of the ionization (ν_i) and attachment (ν_a) frequencies. In this case we can neglect the dependence of f on the space coordinates and write the EVDF under hydrodynamic conditions as

$$f(\vec{v}, t) = \hat{F}(\vec{v})n_e(t). \tag{4}$$

The corresponding microscopic and macroscopic properties of the electrons are determined by the time-independent, spatially homogeneous BE for $\hat{F}(\vec{v})$. As this distribution is symmetric around the field direction, it can be expanded with respect to the angle θ in Legendre polynomials $P_n(\cos\theta)$ with $n \geqslant 0$. Substituting this expansion in the BE leads to a hierarchy of partial differential equations for the coefficients $\hat{f}_n(v)$ of this expansion. The resulting set of equations with typically eight expansion coefficients is solved employing a generalized version of the multiterm solution technique for weakly ionized steady-state plasmas [41] adapted to take into

account the ionizing and attaching electron collision processes.

Using the computed expansion coefficients $\hat{f}_n(v)$, we obtain the effective ionization frequency, ν_{eff}, and the *flux* drift velocity

$$w = -\mu E, \qquad (5)$$

where μ is the *flux* mobility. Explicit formulas of these transport parameters obtained by the BE 0D method can be found in [36].

3.1.2. Multiterm method for SST conditions. This approach to describe the EVDF (abbreviated by BE SST in the figures shown in section 5) takes into account that $f(\vec{r}, \vec{v}, t)$ has reached SST conditions so that the mean transport properties of the electrons are time-independent, do not vary with position any longer, and the electron density assumes an exponential dependence on the distance according to $n_{\text{e}}(z) \propto \exp(\alpha_{\text{eff}} z)$. Thus, we can neglect the dependence of f on time and write the EVDF under SST conditions as

$$f(z, \vec{v}) = \tilde{F}^{(\text{S})}(\vec{v}) n_{\text{e}}(z), \qquad (6)$$

where the upper index (S) denotes SST conditions. In accordance with the procedure described in section 3.1.1, the corresponding microscopic and macroscopic properties of the electrons are determined by the steady-state, spatially homogeneous BE for $\tilde{F}^{(\text{S})}(\vec{v})$. Since this distribution is again symmetric around the direction of the field, it can be expanded in Legendre polynomials $P_n(\cos\theta)$ with $n \geqslant 0$. The substitution of this expansion into the BE leads to a set of partial differential equations for the expansion coefficients $\tilde{f}_n^{(\text{S})}(v)$, which is solved efficiently by a modified version of the multiterm method [41] adapted to treat SST conditions [36].

In this approach, the effective SST ionization coefficient is directly given by

$$\alpha_{\text{eff}} = \frac{\nu_{\text{eff}}^{(\text{S})}}{v_{\text{m}}^{(\text{S})}}. \qquad (7)$$

Here, $\nu_{\text{eff}}^{(\text{S})}$ and $v_{\text{m}}^{(\text{S})}$ are the effective ionization frequency and mean velocity at SST conditions, respectively, which are calculated by means of the computed expansion coefficients $\tilde{f}_n^{(\text{S})}(v)$ [36].

3.1.3. Density gradient representation. When ionization or attachment processes become important in TOF experiments, the electron swarm can no longer be considered homogeneous and the electron density gradients become significant.

This approach to describe the electron swarm at hydrodynamic conditions (labeled as BE DG below) is based on an expansion of the EVDF with respect to space gradients of the electron density n_{e}, of consecutive order. In this case, f depends on $(\vec{r}, t)$ only via the density $n_{\text{e}}(\vec{r}, t)$ and can be written as an expansion on the gradient operator ∇ according

to

$$f(\vec{r}, \vec{v}, t) = \sum_{j=0} F^{(j)}(\vec{v}) \overset{j}{\odot} (-\nabla)^j n_{\text{e}}(\vec{r}, t), \qquad (8)$$

where the expansion coefficients $F^{(j)}(\vec{v})$ are tensors of order j depending only on $\vec{v}$, and $\odot^j$ indicates a j-fold scalar product [42]. Note that the first coefficient $F^{(0)}(\vec{v})$ corresponds to the function $\hat{F}(\vec{v})$ above, for spatially homogeneous conditions (see section 3.1.1).

The expansion coefficients $F^{(j)}$ of order j are obtained from a hierarchy of equations for each component, which all have the same structure and depend on the previous orders. In particular, to obtain the transport coefficients measured in TOF experiments, a total of five equations are required, namely for the expansion coefficients $F^{(0)}$, $F_z^{(1)}$, $F_T^{(1)}$, $F_{zz}^{(2)}$ and $F_{TT}^{(2)}$. In the present study, these equations are solved using a variant of the finite element method given in [43] in a $(v, \cos\theta)$ grid.

From the above expansion coefficients we obtain two sets of transport coefficients: the *flux* coefficients, neglecting the contribution of non-conservative processes and equivalent to those obtained by the BE 0D approach described in section 3.1.1, and the *bulk* coefficients including a contribution from ionization and attachment. The latter are, the *bulk* drift velocity

$$W = w + \int \tilde{\nu}_{\text{eff}}(v) F_z^{(1)}(\vec{v}) \mathrm{d}\vec{v} \qquad (9)$$

with $\tilde{\nu}_{\text{eff}}(v) = vN[\sigma^{\text{i}}(v) - \sigma^{\text{a}}(v)]$ where σ^{i} and σ^{a} are, respectively, the ionization and attachment cross sections; and the longitudinal and transverse components of the diffusion tensor

$$D_{\text{L}} = \int v_z F_z^{(1)}(\vec{v}) \mathrm{d}\vec{v} + \int \tilde{\nu}_{\text{eff}}(v) F_{zz}^{(2)}(\vec{v}) \mathrm{d}\vec{v}, \qquad (10)$$

$$D_{\text{T}} = \frac{1}{2} \left\{ \int v_T F_T^{(1)}(\vec{v}) \mathrm{d}\vec{v} + \int \tilde{\nu}_{\text{eff}}(v) F_{TT}^{(2)}(\vec{v}) \mathrm{d}\vec{v} \right\}. \qquad (11)$$

Note that the first terms of the right-hand side of equations (9)–(11) are the *flux* component. Further details can be found in [36].

The effective or apparent Townsend ionization coefficient α_{eff}, as determined in SST experiments, can be computed from the TOF parameters using equation (2).

3.2. MC technique

In the MC simulation technique, we trace the trajectories of the electrons in the external electric field and under the influence of collisions. As the degree of ionization under the swarm conditions considered here is low, only electron-background gas molecule collisions are taken into account. The motion of the electrons with mass m_{e} between collisions is described by their equation of motion

$$m_{\text{e}} \frac{\mathrm{d}^2\vec{r}}{\mathrm{d}t^2} = -e_0 \vec{E}. \qquad (12)$$

The electron trajectories between collisions are determined by integrating this equation numerically over time steps of

duration Δt ranging between 0.5 and 2.5 ps for the various conditions. While this procedure is totally deterministic, the collisions are handled in a stochastic manner. The probability of the occurrence of a collision is computed after each time step, for each of the electrons, as

$$P(\Delta t) = 1 - \exp[-N\nu\sigma^{\mathrm{T}}(v)\Delta t]. \qquad (13)$$

The occurrence of a collision is determined by comparing $P(\Delta t)$ with a random number with a uniform distribution over the (0, 1) interval. The type of collision is also selected in a random manner taking into account the values of the cross sections of all possible processes at the energy of the colliding electron. For a more detailed description see [36].

The transport parameters (labeled as MC below) are determined as

$$W = \frac{\mathrm{d}}{\mathrm{d}t}\left[\frac{\sum_{j=1}^{N_e(t)} z_j(t)}{N_e(t)}\right] \qquad (14)$$

and

$$w = \frac{1}{N_e(t)}\sum_{j=1}^{N_e(t)} \frac{\mathrm{d}z_j(t)}{\mathrm{d}t}, \qquad (15)$$

respectively, for the *bulk* and *flux* drift velocities, where $N_e(t)$ is the number of electrons in the swarm at time t. The bulk longitudinal and transverse components of the diffusion tensor are

$$D_{\mathrm{L}} = \frac{1}{2}\frac{\mathrm{d}}{\mathrm{d}t}[\langle z^2(t)\rangle - \langle z(t)\rangle^2], \qquad (16)$$

$$D_{\mathrm{T}} = \frac{1}{4}\frac{\mathrm{d}}{\mathrm{d}t}[\langle x^2(t) + y^2(t)\rangle], \qquad (17)$$

and the effective ionization frequency is given by

$$\nu_{\mathrm{eff}} = \frac{\mathrm{d}\ln(N_e(t))}{\mathrm{d}t}. \qquad (18)$$

Furthermore, the effective SST ionization coefficient α_{eff} is also calculated according to relation (2) using (14), (16) and (18).

All results of calculated electron swarm parameters presented in this work were additionally verified by independent MC simulations and calculations based on multi-term solutions of the electron BE developed by the Belgrade group [44, 45]. For clarity, these results are not included in the figures shown in the next sections, but are available from the authors on request.

As it was already mentioned in the Introduction and is discussed in somewhat more detail in the next section, MC simulations are also applied in the simulation of the electrons' motion in the experimental system, assisting a correction procedure of the experimental data.

4. Correction of the experimental results

To quantify the effect caused by the variations of the electron energy distribution along the swarm, that in turn makes the detection sensitivity time-dependent, MC simulations of the experimental system have been carried out for most of the sets of conditions $(p, E/N)$ in the experiments. These simulations generate swarm maps, similarly to those measured, and a set of swarm parameters is derived from these maps via exactly the same fitting procedure as in the case of the experimental data. The transport parameters and ionization frequencies obtained from the simulations of the setup are compared with those obtained from kinetic swarm calculations based on the solution of the electron BE, where the same electron collision cross section sets are used. Good agreement between the two sets of swarm parameters implies that the assumption made in the fitting of the experimental data, i.e. the use of the theoretical form (1) of $n_e(z, t)$ as a fit to the measured data, is acceptable. In contrast, strong deviations indicate that this assumption is not applicable for the given condition. We note that no experimental data are involved in this procedure.

In these MC simulations the electrons leaving the cathode had an initial energy of 1 eV, which is a realistic value considering the photon energy and the work function of the cathode material. These electrons were started with a uniform angular distribution over the positive half sphere. The sensitivity of the computed swarm maps on this latter assumption is not expected to be strong because the collisions quickly randomize the initial directions of the electrons. As in these simulations the motion of the electrons in the whole experimental system is described, the dependence of the detector's sensitivity on the energy of the electrons entering the mesh-collector gap is 'automatically' included as the detector current generated by these electrons is computed directly.

Results of this procedure for each of the gases and for the whole domain of E/N are presented in figure 4. The panels correspond to the swarm parameters W, D_{L}, ν_{eff}, and α_{eff}, respectively, and show the differences of each parameter derived by the simulation of the experimental system with respect to its theoretical value obtained from the BE solution. That is, if we denote the values obtained from the simulation of the experimental system by S, and those obtained from the BE solution by T, the quantity depicted in figure 4 is $(S - T)/T$. The set of 'Corrected' transport coefficients can thus be obtained from the experimentally measured values (X_{corr} and X_{exp}, respectively) as $X_{\mathrm{corr}} = \frac{X_{\mathrm{exp}}}{1 + \frac{S-T}{T}} = \frac{T}{S}X_{\mathrm{exp}}$.

In the case of the bulk drift velocity (figure 4(a), the error is in the few % range for most of the conditions, and it approaches $\approx 10\%$ at the highest E/N values. This indicates that the determination of the bulk drift velocity values from the experimental data is quite reliable.

The situation turns out to be much worse for the longitudinal component of the diffusion tensor (figure 4(b)). Here, the error ranges from $\approx -40\%$ to $\approx +80\%$, depending on E/N. The D_{L} data can be considered to be acceptably accurate at intermediate E/N values only. The much larger error of D_{L} with respect to that of W can be explained by the fact that the distribution of the average electron energy along the swarm is inhomogeneous. In the close vicinity of the maximum of the spatial distribution of the electron density, the variation of the average energy along the swarm is comparatively small. However, by moving away from this maximum, the spatial
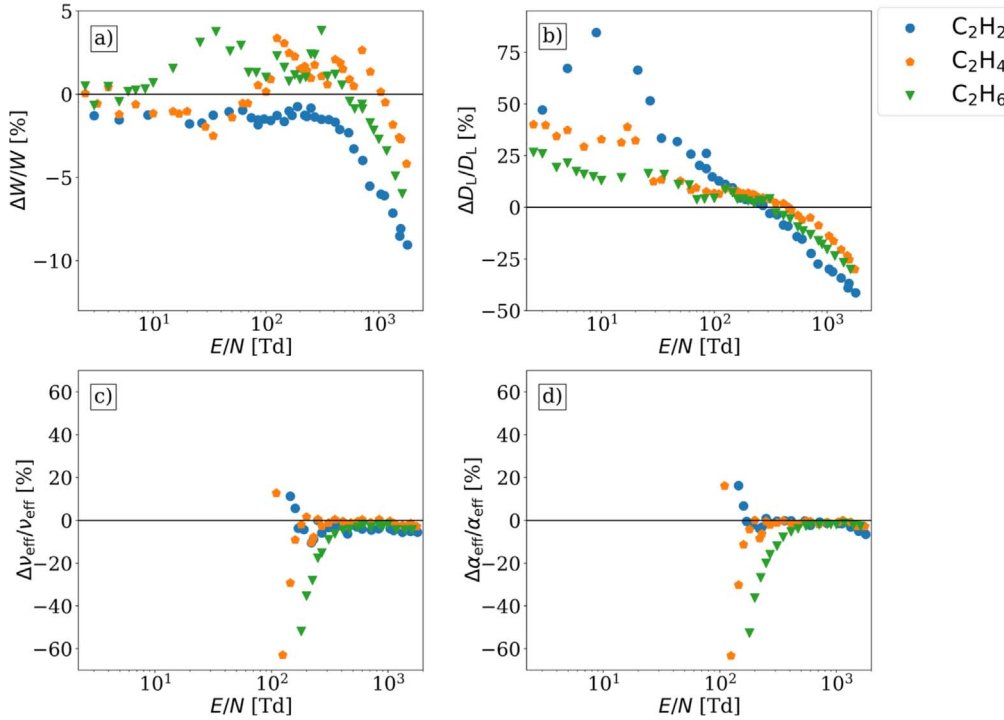
Figure 4. Deviations of the results between the swarm parameters obtained from the simulations of the experimental system (S) versus the theoretical values (T), i.e. $(S - T)/T$ for the bulk drift velocity (a), the longitudinal component of the diffusion tensor (b), the effective ionization frequency (c) and the effective SST ionization coefficient (d). Applying these correction factors to the experimental results (X_{exp}) leads to the set of 'Corrected' transport coefficients (X_{corr}) as $X_{\text{corr}} = \dfrac{X_{\text{exp}}}{1 + \frac{S-T}{T}} = \dfrac{T}{S} X_{\text{exp}}$.

variations of the average energy along the swarm increase. As the drift velocity is primarily determined by the position of the maximum of the spatial profile of the electron density while the diffusion is predominantly determined by the width of this distribution, it is clear that the width of the distribution is more affected by non-uniform sensitivity of the detector with respect to the average electron energy than the position of the maximum.

Regarding the effective ionization frequency (figure 4(c)) and the strongly related SST ionization coefficient (figure 4(d)), we observe small errors at high E/N values, where ionization is appreciable. The error, on the other hand, grows high when E/N approaches $\approx$100 Td, where both ν_{eff} and α_{eff} drop rapidly.

5. Results and discussion

The electron swarm parameters have been measured in a wide range of the reduced electric field, between 1 and 1790 Td at a gas temperature T of 293 K. The pressure of the gases ranged between 5 and 1000 Pa in the measurements. The actual value for any given E/N was set to optimize the measured current of the drift cell, while paying attention that the corresponding voltage remains below the breakdown threshold over the whole range of the electrode distances covered during the scanning process.

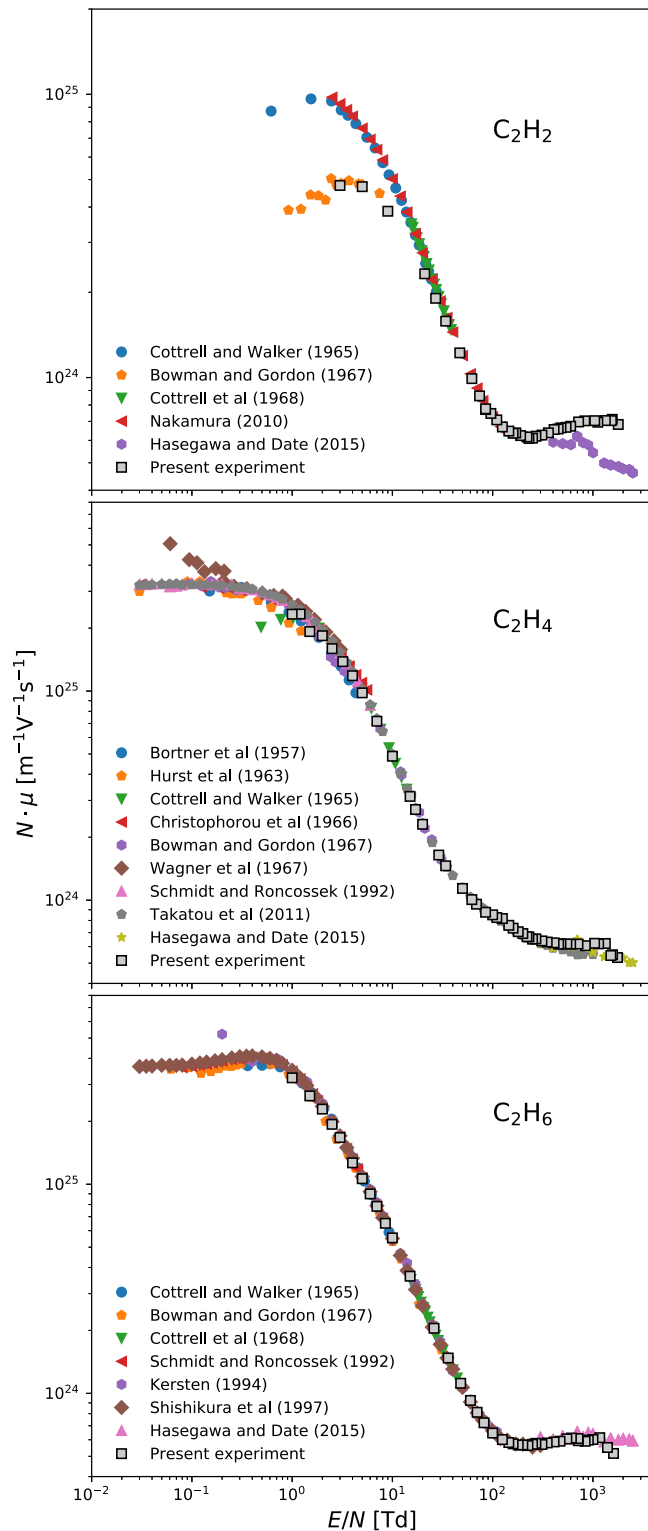In the following, results of our measurements are presented for the three hydrocarbon gases C_2H_2, C_2H_4, and

C_2H_6. Besides the transport parameters and ionization coefficients resulting from the experiments via the fitting procedure described in section 1, we also present the corrected values of these data resulting from the procedure introduced in section 4. For each swarm parameter, we compare the present measured data with previous experimental results and with the results of the kinetic computations based on the solution of the electron BE or on MC simulations, obtained with the selected electron collision cross sections. The results for the *flux* parameters obtained by methods BE 0D, BE DG and MC overlap, and so do the *bulk* parameters obtained from the BE DG and MC methods. Our experimental results for each transport parameter and gas (uncorrected and corrected values) are available in the supplementary data file (online at stacks.iop.org/PSST/29/045009/mmedia) Furthermore, the present measured data as well as results of the kinetic computations are available online at [46–48].
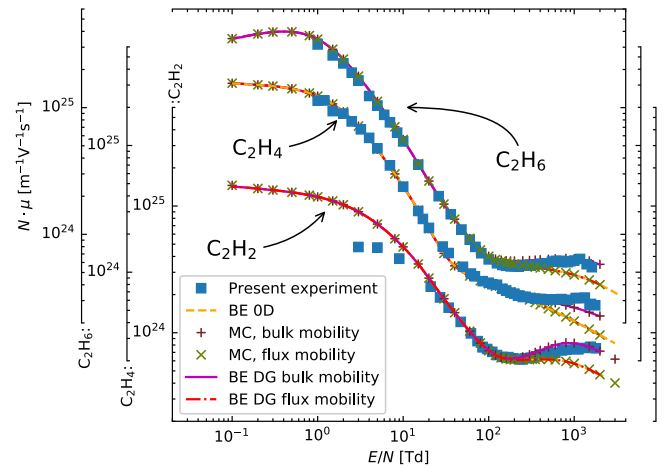
5.1. Electron mobility

We start by comparing the values of the gas number density times mobility, $N\mu$, derived from the bulk drift velocity, with previous experimental data for the three hydrocarbon gases in figure 5. We estimate the maximum experimental error of these values to be around 6%.

Except for the high values of E/N, our measured *bulk* drift velocity and mobility results are in excellent agreement with all previous results. In C_2H_2, however, at low E/N we find two distinct sets of results: the present results are

Figure 6. Mobility in C_2H_2, C_2H_4 and C_2H_6: present experiment and modeling results. The results and $N\mu$ scale for C_2H_4 and C_2H_6 have been shifted. 'Present experiment' corresponds to the uncorrected experimental data. The corrected data are not shown here because of the small correction factors for the bulk drift velocity/mobility.

consistent with the measurements of Bowman and Gordon [16], while the results of Cottrell and Walker [17] are in accordance with those of Nakamura [14]. Note that the latter results were used to obtain the recommended electron collision cross sections for C_2H_2 [39] used in the present modeling and simulation. At high E/N the present results deviate from those of Hasegawa and Date [13] in C_2H_2 and C_2H_4. However the latter results are obtained from the mean arrival-time velocity defined in [49] and are not easily comparable with the present TOF results in the presence of reaction processes.

In figure 6 we compare the results of the present measurements with the kinetic computation results. In this figure the E/N scale is common to the three gases but the $N\mu$ scale and data for C_2H_4 and C_2H_6 have been shifted upwards to avoid overlapping of the curves. Above 200 Td the contribution of non-conservative processes becomes visible and the mobility results are split into a *bulk* branch (for MC and BE DG *bulk* mobilities and the present measurements) and *flux* values (respectively for BE 0D, MC and BE DG *flux* mobilities). Here our measured data show some differences to the MC and BE DG bulk results for all three gases. In case of C_2H_2, as the electron collision cross sections used are based on the swarm results of Nakamura [14], the modeling results deviate from the present experimental results below 10 Td. Note that below 3 Td the modeling results also deviate from the measurements of Bowman and Gordon [16] as well as of Cottrell and Walker [17] in figure 5.

5.2. Diffusion tensor

The present experimental results for the gas number density times the longitudinal component of the diffusion tensor, $N D_L$, for C_2H_2, C_2H_4 and C_2H_6 are shown in figure 7 together with previously measured data as well as with the kinetic computation values for the *bulk* longitudinal and

Figure 5. Mobility in C_2H_2, C_2H_4 and C_2H_6 obtained from drift velocity results: Bortner *et al* [23], Hurst *et al* [22], Cottrell and Walker [17], Christophorou *et al* [21], Bowman and Gordon [16], Wagner *et al* [20], Cottrell *et al* [15], Schmidt and Roncossek [19], Kersten [25], Shishikura *et al* [24], Nakamura [14], Takatou *et al* [18], Hasegawa and Date [13] and present measurements. The figures share the same E/N scale. 'Present experiment' corresponds to the uncorrected experimental data. The corrected data are not shown here because of the small correction factors for the bulk drift velocity and the mobility.
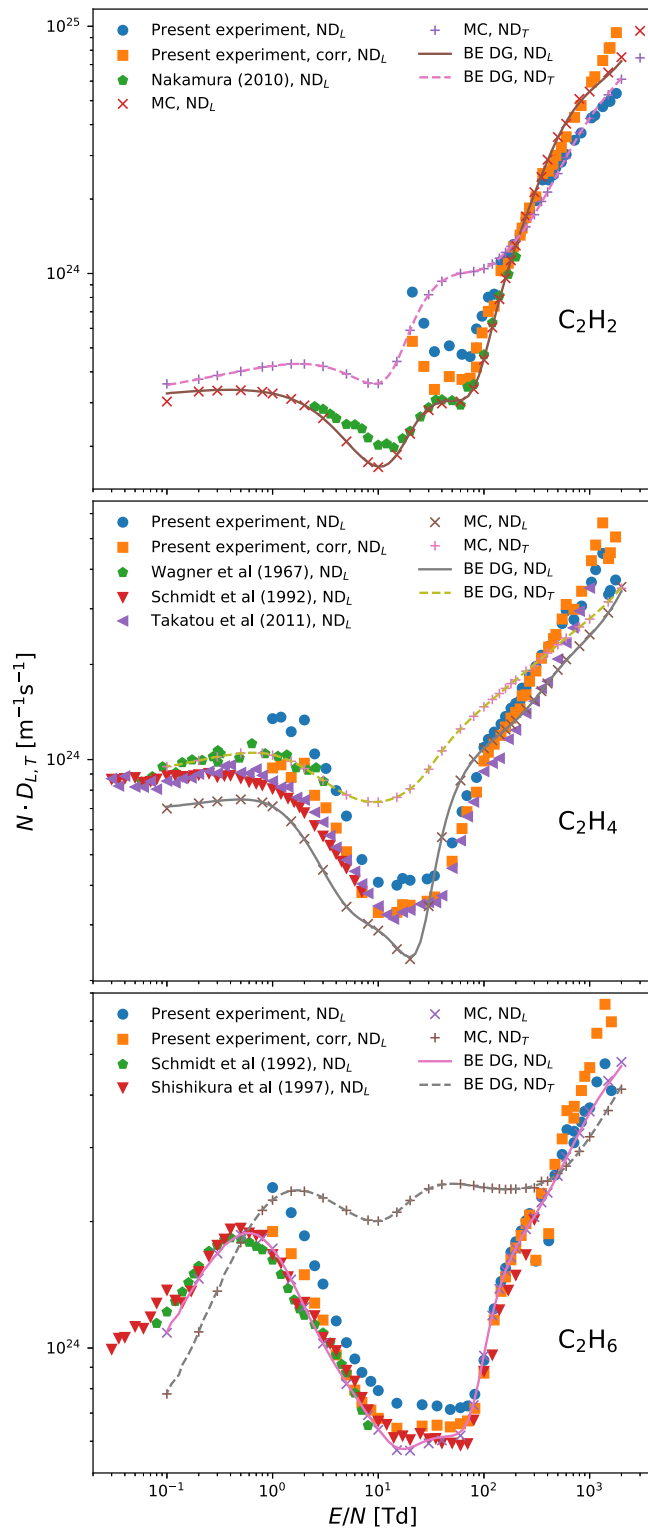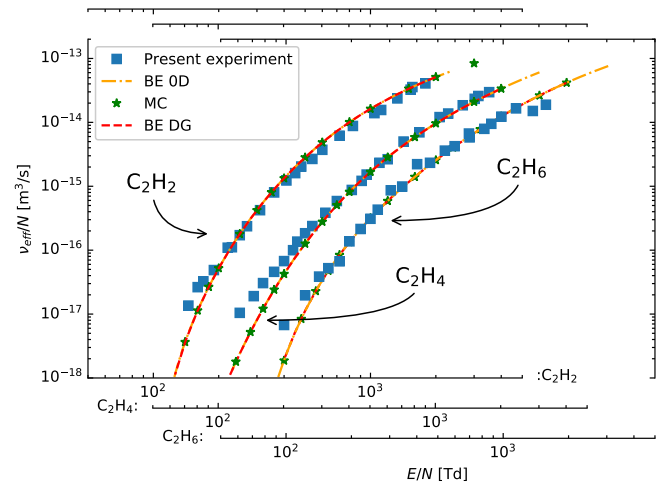
Figure 8. Reduced effective ionization frequency in C_2H_2, C_2H_4 and C_2H_6: present experiment and modeling results. The results and E/N scale for C_2H_4 and C_2H_6 are shifted horizontally. 'Present experiment' corresponds to the uncorrected data.

transverse components of the diffusion tensor for each gas. The present measured values of $N\,D_L$ exhibit larger scattering, which is explained by the higher uncertainty of the determination of D_L in the experiments ($\approx 10\%$) compared to that of the drift velocity.

Above 100 Td there is reasonable agreement of the present measurements with previous experimental data and the modeling results for the three gases. Below 100 Td however, the present measurements evidence the same qualitative behavior but are systematically above previous measurements. Note that the application of the correction procedure, detailed in section 4, to our experimental results leads to much better agreement with previously measured data, in particular for C_2H_4 and C_2H_6. In case of C_2H_2, we observe a qualitative difference between our measurements and those performed by Nakamura [14]. These differences can be attributed to the non-uniform sensitivity of the detector in our experimental setup, which has been already discussed in section 4.

The modeling results for D_L in C_2H_2 and C_2H_4 below 2 Td and 5 Td, respectively, also deviate from all experimental results indicating that the corresponding cross section sets require improvement. In each of the three gases, the values of the transverse component of the diffusion tensor, D_T, obtained by the kinetic computations, are very different from the longitudinal component, D_L. The measurement of data of this component can provide additional tests for the fitting of the electron collision cross sections.

5.3. Effective ionization frequency and SST ionization coefficient

The experimental and modeling results for the reduced effective ionization frequency, ν_{eff}/N, for the three gases

Figure 7. Longitudinal and transverse *bulk* components of the diffusion tensor in C_2H_2, C_2H_4 and C_2H_6. Experimental results: present experiment, Wagner *et al* [20], Schmidt and Roncossek [19], Shishikura *et al* [24], Nakamura [14], Takatou *et al* [18]. Modeling results: MC and BE DG (ND_L and ND_T). The figures share the same E/N scale. The panels show both the uncorrected and corrected experimental results of this study.

studied are displayed in figure 8. To our best knowledge this is the first report of ν_{eff} in these three gases for an extended range of 100 Td $\leqslant E/N \leqslant$ 1790 Td, for which the estimated experimental error of the data is $\leqslant 8\%$. In order to accommodate the results on the same figure, all gases share the same ν_{eff}/N axis but the E/N scales for C_2H_4 and C_2H_6 have been shifted to the right.

Good agreement between our measured and calculated results is generally found for E/N values larger than about 200 Td, indicating that the electron collision cross section sets for the three gases are reasonably well adapted to allow for an appropriate determination of the rate coefficients for ground state ionization. Certain differences are obvious for lower E/N values. These differences seem to result from the measurement and/or, more likely, from the fitting procedure (see figure 4).

Our experimental data for the reduced effective SST ionization coefficient, α_{eff}/N, obtained using equation (2), are compared with previous measurements and the kinetic computation results in figure 9. As α_{eff} is derived from the set of parameters $\{W, D_L, \nu_{\text{eff}}\}$, these results have a higher uncertainty than ν_{eff} with an estimated experimental error of $\leqslant 10\%$. Notice that the kinetic computation results using method BE SST do not include the approximations involved in equation (2), but are directly obtained by solving the electron BE at SST conditions according to (7). In this respect, their comparison with the BE DG and MC results can indicate the range of validity of equation (2).

Except for the low values of E/N, our results for the effective SST ionization coefficient are in excellent agreement with all previous results and the kinetic computations. At values close to the threshold, however, the present results are higher than previous measurements. Notice that Kersten's effective Townsend ionization coefficient was measured under TOF conditions and corresponds to ν_{eff}/W [25]. Thus, it represents the effective SST ionization coefficient α_{eff} according to (2) only in the absence of diffusion, i.e. $D_L = 0$.

5.4. Effect of the vibrationally excited population

The cross sections sets used above were obtained considering only electron collisions with the ground state of the molecules. However, the correct description of the characteristics of electrons in molecular gases at low reduced electric fields, requires to take into account superelastic collisions of electrons with thermally excited molecules. For example, this is discussed in [50] for the case of molecular hydrogen and nitrogen. For diatomic molecules superelastic collisions with rotationally excited molecules have to be taken into account in calculations for low reduced electric fields (see, for example [51]).

As polyatomic molecules have multiple vibrational modes and these modes can be degenerate, in these gases we can find a significant fraction of molecules in thermally excited vibrational states at room temperature. In addition to their contribution to energy losses due to elastic, exciting, ionizing and attaching collision processes, these excited states contribute to electron energy gains due to superelastic
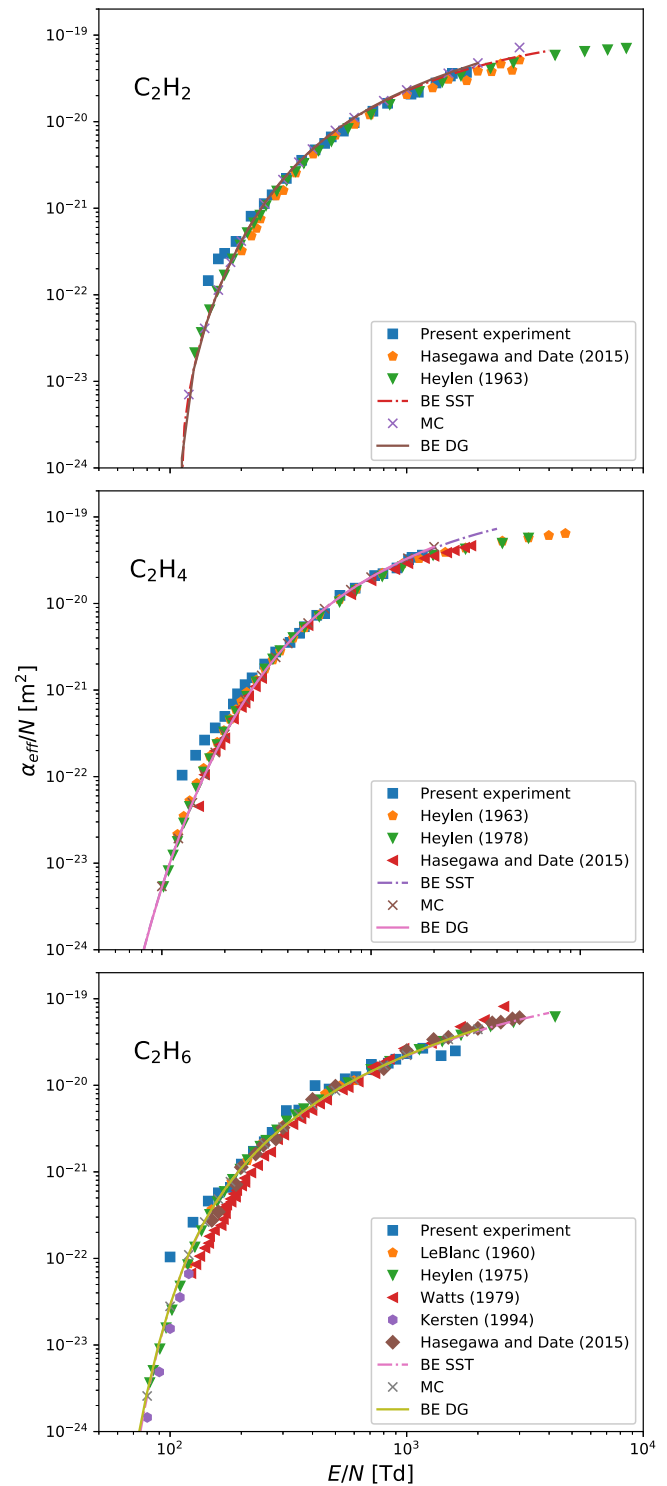
Figure 9. Reduced effective Townsend ionization coefficient in C_2H_2, C_2H_4 and C_2H_6. Experimental results: present experiment, Heylen [26, 29], Watts and Heylen [28], Kersten [25] and Hasegawa and Date [13]. Modeling results: BE SST, MC and BE DG. 'Present experiment' corresponds to the uncorrected data.

collisions and influence the EVDF and transport parameters, mainly at low to medium E/N field values. The importance of their effect increases with the energy associated with the collision and the fractional population of thermally excited states with that energy. This population, however, decreases

Table 1. Fractional population of the first vibrational levels of C_2H_2 at 293.15 K.

Vibr. state	Short notation	g	Energy (eV)	Frac pop. (%)
(00000)	v_0	1	0.0	85.37
(10000)	v_1	1	0.421	5.5×10^{-6}
(01000)	v_2	1	0.245	5.3×10^{-3}
(00100)	v_3	1	0.411	8.3×10^{-6}
(00010)	v_4	2	0.075	8.47
(00020)		3	0.150	0.63
(00001)	v_5	2	0.0905	4.75
(00002)		3	0.180	0.20
(00011)	$v_4 + v_5$	4	0.165	0.47

exponentially with energy. From the combination of these two factors, the effect on the EVDF should be maximum for a given energy value.

Taking into account the equations for the fractional populations and statistical weights of polyatomic molecules in the appendix, we can estimate the populations of the different states of these gases.

- *Acetylene* has five vibrational modes, with the two bending modes (v_4 and v_5) double degenerate and with energies of, respectively, 0.075 eV and 0.0905 eV [52]. At a gas temperature of 293.15 K, the vibrational states with fractional population above 0.1% are indicated in table 1. At this temperature only around 85% of the acetylene molecules are in the ground state and the vibrational population in excited states of modes v_4 and v_5 is significant.
- *Ethylene*: In contrast to C_2H_2, none of the twelve ethylene vibrational modes [52] is degenerate, where the lowest threshold energy for vibrational excitation to v_{10} is 0.102 eV and, at the same temperature, more than 95% of the molecules are in the ground state.
- *Ethane*: All the degenerate vibrational modes of ethane [52] have energies above 0.15 eV and at room temperature their fractional population is small. Overall, however, only 73% of ethane molecules are in the ground state as mode v_4 has an excitation energy of only 0.036 eV. Molecules in the two first excited vibrational states of this mode represent 22% of the total. On the other hand, as the excitation energy of the v_4 mode transitions is very small, the effect on the EVDF and transport parameters is also small.

Of the three gases analyzed, the impact of the thermally excited vibrational population on the EVDF should be largest in C_2H_2. The vibrational excitation cross section set for C_2H_2 [39] is also more complete than the vibrational cross section sets for C_2H_4 and C_2H_6 used in this study. For these reasons we study the effect of the thermally excited vibrational states only for acetylene.

Our goal is to single out the contribution of the vibrationally excited molecules due to superelastic collisions and we will change the electron collision cross sections in such a way that, if we neglect these collisions, we obtain the same
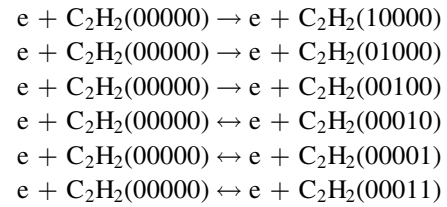
results as before. Starting from the recommended cross section set for ethylene [39], we introduce the following modifications:

(a) We split the lumped cross sections for the vibrational excitation of modes v_1/v_3 and v_4/v_5 into individual cross sections for each modes, with a value of half of the original cross section. That is $\sigma_{v_1} = \sigma_{v_3} = \frac{1}{2}\sigma_{v_1/v_3}$ and $\sigma_{v_4} = \sigma_{v_5} = \frac{1}{2}\sigma_{v_4/v_5}$.

(b) The threshold for the excitation of modes v_1 and v_3 and of modes v_4 and v_5 is set at the same value as before of, respectively, 0.411 eV and 0.0905 eV.
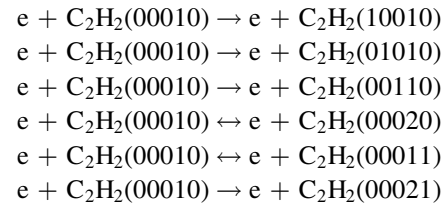
(c) We assume that all molecules are in one of the three states (00000), (00010) and (00001), with the fractional population, δ, of the last two states in thermal equilibrium with the gas and the ground state fraction given by $\delta_{00000} = (1 - \delta_{00010} - \delta_{00001})$.

(d) We consider the following vibrational excitation processes for electron collisions with the ground state (00000):

$$e + C_2H_2(00000) \rightarrow e + C_2H_2(10000)$$
$$e + C_2H_2(00000) \rightarrow e + C_2H_2(01000)$$
$$e + C_2H_2(00000) \rightarrow e + C_2H_2(00100)$$
$$e + C_2H_2(00000) \leftrightarrow e + C_2H_2(00010)$$
$$e + C_2H_2(00000) \leftrightarrow e + C_2H_2(00001)$$
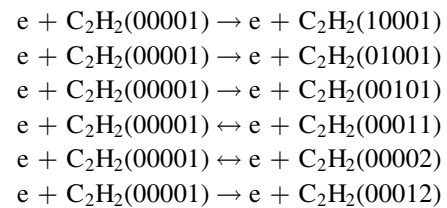$$e + C_2H_2(00000) \leftrightarrow e + C_2H_2(00011)$$

where reactions with double-arrows include superelastic collisions.

(e) We additionally include the following vibrational excitation processes on collisions with states (00010) and (00001):

$$e + C_2H_2(00010) \rightarrow e + C_2H_2(10010)$$
$$e + C_2H_2(00010) \rightarrow e + C_2H_2(01010)$$
$$e + C_2H_2(00010) \rightarrow e + C_2H_2(00110)$$
$$e + C_2H_2(00010) \leftrightarrow e + C_2H_2(00020)$$
$$e + C_2H_2(00010) \leftrightarrow e + C_2H_2(00011)$$
$$e + C_2H_2(00010) \rightarrow e + C_2H_2(00021)$$

and

$$e + C_2H_2(00001) \rightarrow e + C_2H_2(10001)$$
$$e + C_2H_2(00001) \rightarrow e + C_2H_2(01001)$$
$$e + C_2H_2(00001) \rightarrow e + C_2H_2(00101)$$
$$e + C_2H_2(00001) \leftrightarrow e + C_2H_2(00011)$$
$$e + C_2H_2(00001) \leftrightarrow e + C_2H_2(00002)$$
$$e + C_2H_2(00001) \rightarrow e + C_2H_2(00012)$$

adopting for these processes the same cross sections as the corresponding excitations from the ground state.

(f) We further assume that the electron collision cross sections for momentum transfer, electronic excitation, ionization and attachment with the vibrational states (00010) and (00001) are the same as for state (00000).

(g) We obtain the superelastic vibrational cross sections from the corresponding direct processes assuming that the detailed balance principle is valid.

Note that if we neglect superelastic collisions, the EVDF and swarm parameters obtained with these modified cross sections and electron collision reactions are exactly the same
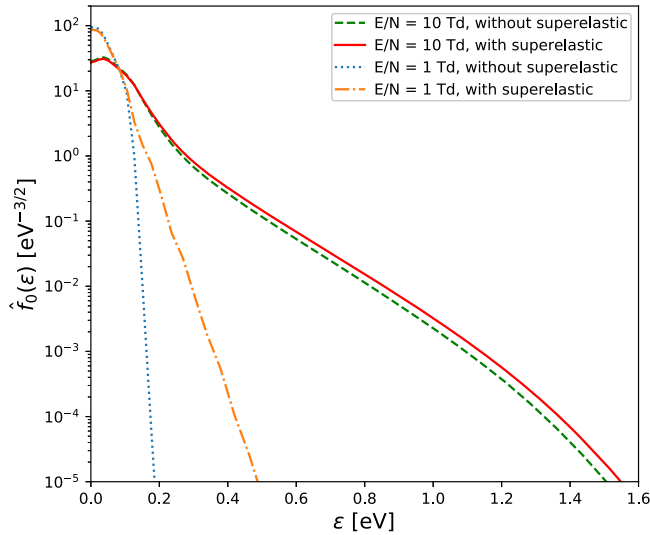
Figure 10. Isotropic component of the EVDF in C_2H_2 at 293.15 K for 1 and 10 Td, with and without superelastic collision processes included.

as with the original set [39] and are independent of the fractional population of levels (00010) and (00001).

The influence of superelastic collisions is illustrated in figure 10 which shows the isotropic component $\hat{f}_0(\epsilon)$ of the EVDF as a function of the electron kinetic energy, $\epsilon = m_e v^2/2$, calculated at E/N values of 1 Td and 10 Td, respectively, with and without the inclusion of superelastic processes. Pronounced differences between the corresponding isotropic distributions $\hat{f}_0(\epsilon)$ are found at $E/N = 1$ Td, while the impact of superelastic electron collision processes is comparatively small at 10 Td. This finding is not only reflected by the isotropic distribution but also by different macroscopic properties.

The influence of superelastic collisions is mostly visible in the drift velocity and mobility as shown in figure 11. This figure compares the values of mobility and the longitudinal and transverse *bulk* components of the diffusion tensor obtained with the original cross sections set with the results obtained using the modified set with and without the inclusion of superelastic processes. As predicted, the results of the modified set neglecting superelastic collisions are the same as those obtained with the original set. Superelastic collisions are responsible for a reduction of the electron mobility in the range of low reduced field, visible up to approximately 20 Td. The influence on the components of the diffusion tensor is overall smaller than that on the mobility with the largest differences in the longitudinal component around 10 Td.

As the impact of superelastic collisions decreases remarkably above about 20 Td, their influence on the effective ionization frequency and Townsend ionization coefficient is negligible.

6. Concluding remarks

We have investigated electron swarm parameters in C_2H_2, C_2H_4 and C_2H_6 experimentally using a scanning drift tube, as
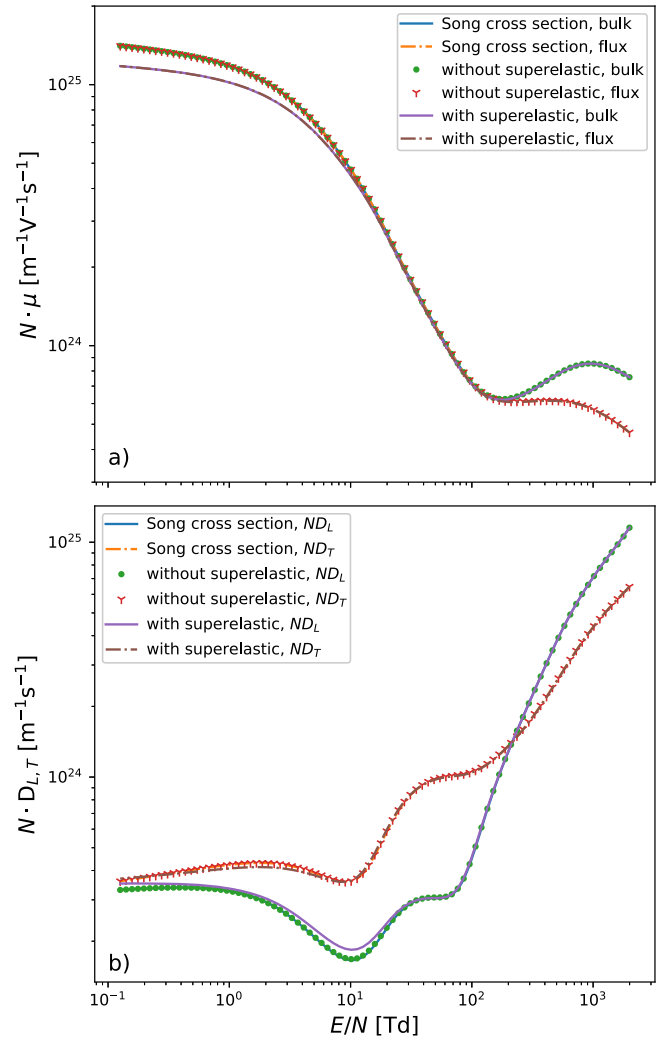
Figure 11. (a) Mobility and (b) longitudinal and transverse *bulk* components of the diffusion tensor in C_2H_2 at 293.15 K: modeling results obtained with the electron collision cross sections from [39] without considering superelastic processes and with a modified set with and without superelastic processes.

well as computationally by solutions of the electron BE and via MC simulation, corresponding to both TOF and SST conditions. The measured data made it possible to derive the bulk drift velocity, the bulk longitudinal component of the diffusion tensor and the effective ionization frequency of the electrons, for the wide range of the reduced electric field from 1 to 1790 Td. The measured TOF transport parameters as well as the effective SST ionization coefficient, deduced from the TOF swarm parameters, have been compared to experimental data obtained in previous studies. Here, generally good agreement with most of the transport parameters and the effective SST ionization coefficients obtained in these earlier studies was found. In the case of the drift velocity or the mobility, respectively, and the longitudinal component of the diffusion tensor we found disagreements at low or high values of E/N.

The experimental data have undergone a correction procedure, which was supposed to quantify the errors caused by the dependence of the sensitivity of the detector of the drift

cell on the energy distribution of the electrons in the swarm that may have a spatial dependence.

In particular, in case of C_2H_2 our measured drift velocities at low E/N agree well with previous data of Bowman and Gordon [16] but not with the results of Cottrell and Walker [17] as well as of Nakamura [14]. Further measurements in this range are required to clarify this contradiction.

The comparison of the experimental data was also carried out with swarm parameters resulting from various kinetic computations, which used the most recently recommended cross section sets [24, 39, 40]. Here, excellent agreement between electron BE and MC simulation results verifies the computational approaches and data for the three gases. The agreement of the computed data with the present and previously measured values of the reduced effective ionization frequency and SST ionization coefficient was generally good. However, certain differences between kinetic computational and measured results found for the drift velocities and, especially, for the longitudinal component of the diffusion tensor illustrate the need for an improvement of the existing collision cross section sets for the three hydrocarbon gases considered.

We have also studied the influence of the thermally excited vibrational populations on the transport parameters. In the case of C_2H_2 we have found that this population has a significant value and superelastic collisions influence the drift velocity and the components of the diffusion tensor up to 20 Td. The fitting of electron collision cross sections for this gas using swarm experiments should include these processes.

Acknowledgments

Appendix. Statistical weights and statistical sums

The fractional populations for the levels of a polyatomic molecule with n_v modes and vibrational quantum numbers $(v_1 v_2 v_3 \ldots)$ are given by

$$\delta_{(v_1 v_2 v_3 \ldots)} = \frac{g_{(v_1 v_2 v_3 \ldots)}}{Q_v} \exp\left(-\frac{\epsilon_{(v_1 v_2 v_3 \ldots)}}{k_B T}\right), \quad (A.1)$$

where $\epsilon_{(v_1 v_2 v_3 \ldots)}$ is the level energy and g the total statistical weight

$$g_{(v_1 v_2 v_3 \ldots)} = \prod_{n=1}^{n=n_v} \frac{(v_n + d_n - 1)!}{v_n!(d_n - 1)!}, \quad (A.2)$$

where d_n is the degeneracy multiplicity for mode n, and Q_v the vibrational statistical sum which, in the harmonic oscillator approximation for the vibrational states, is

$$Q_v = \prod_{n=1}^{n=n_v} (1 - Z_n)^{-d_n}, \quad Z_n = \exp\{-h\nu_n/k_B T\}, \quad (A.3)$$

where h is the Planck constant and ν_n are the vibrational frequencies.

ORCID iDs

N R Pinhão ● https://orcid.org/0000-0002-4185-2619
D Loffhagen ● https://orcid.org/0000-0002-3798-0773
M Vass ● https://orcid.org/0000-0001-9865-4982
P Hartmann ● https://orcid.org/0000-0003-3572-1310
I Korolov ● https://orcid.org/0000-0003-2384-1243
S Dujko ● https://orcid.org/0000-0002-4544-9106
D Bošnjaković ● https://orcid.org/0000-0002-2725-5287
Z Donkó ● https://orcid.org/0000-0003-1369-6150

References

[1] Adamovich I V and Lempert W R 2014 *Plasma Phys. Control. Fusion* **57** 014001
[2] Starikovskiy A and Aleksandrov N 2013 *Prog. Energy Combust. Sci.* **39** 61–110
[3] Kosarev I, Aleksandrov N, Kindysheva S, Starikovskaia L S and Starikovskii A Y 2009 *Combust. Flame* **156** 221–33
[4] Kosarev I, Pakhomov A, Kindysheva S, Anokhin E and Aleksandrov N 2013 *Plasma Sources Sci. Technol.* **22** 045018
[5] Kosarev I, Kindysheva S, Aleksandrov N and Starikovskiy A Y 2015 *Combust. Flame* **162** 50–9
[6] Kosarev I, Kindysheva S, Momot R, Plastinin E, Aleksandrov N and Starikovskiy A Y 2016 *Combust. Flame* **165** 259–71
[7] Robertson J 2002 *Mater. Sci. Eng.* R **37** 129–281
[8] Kumar M and Ando Y 2010 *J. Nanosci. Nanotechnol.* **10** 3739–58
[9] Fonte P and Peskov V 2010 *Plasma Sources Sci. Technol.* **19** 034021
[10] von Keudell A, Schwarz-Selinger T, Jacob W and Stevens A 2001 *14th Int. Conf. on Plasma-Surface Interactions in Controlled Fusion Devices; J. Nucl. Mater.* **290-293** 231–7
[11] Varanasi P, Giver L and Valero F 1983 *J. Quant. Spectrosc. Radiat. Transfer* **30** 497–504
[12] Courtin R, Gautier D, Marten A, Bezard B and Hanel R 1984 *Astrophys. J.* **287** 899–916
[13] Hasegawa H and Date H 2015 *J. Appl. Phys.* **117** 133302
[14] Nakamura Y 2010 *J. Phys. D: Appl. Phys.* **43** 365201
[15] Cottrell T L, Pollock W J and Walker I C 1968 *Trans. Faraday Soc.* **64** 2260–6
[16] Bowman C R and Gordon D E 1967 *J. Chem. Phys.* **46** 1878–83

[17] Cottrell T L and Walker I C 1965 *Trans. Faraday Soc.* **61** 1585–93

[18] Takatou J, Sato H and Nakamura Y 2011 *J. Phys. D: Appl. Phys.* **44** 315201

[19] Schmidt B and Roncossek M 1992 *Aust. J. Phys.* **45** 351–64

[20] Wagner E B, Davis F J and Hurst G S 1967 *J. Chem. Phys.* **47** 3138–47

[21] Christophorou L G, Hurst G S and Hadjiantoniou A 1966 *J. Chem. Phys.* **44** 3506–13

[22] Hurst G S, O'Kelly L B, Wagner E B and Stockdale J A 1963 *J. Chem. Phys.* **39** 1341–5

[23] Bortner T E, Hurst G S and Stone W G 1957 *Rev. Sci. Instrum.* **28** 103–8

[24] Shishikura Y, Asano K and Nakamura Y 1997 *J. Phys. D: Appl. Phys.* **30** 1610–5

[25] Kersten H J 1994 *Messung der Driftgeschwindigkeit Und Des Effektiven Townsendkoeffizienten Von Elektronen Bei Hohen Elektrischen Feldstärken* (Heidelberg: Diploma thesis Ruprecht-Karls-Universität) (https://www.lxcat.net/Heidelberg)

[26] Heylen A E D 1963 *J. Chem. Phys.* **38** 765–71

[27] Heylen A E D 1978 *Int. J. Electron.* **44** 367–74

[28] Watts M P and Heylen A E D 1979 *J. Phys. D: Appl. Phys.* **12** 695–702

[29] Heylen A E D 1975 *Int. J. Electron.* **39** 653–60

[30] LeBlanc O H and Devins J C 1960 *Nature* **188** 219–20

[31] Blevin H A and Fletcher J 1984 *Aust. J. Phys.* **37** 593–600

[32] Donkó Z, Hartmann P, Korolov I, Jeges V, Bošnjaković D and Dujko S 2019 *Plasma Sources Sci. Technol.* **28** 095007

[33] Ramo S 1939 *Proc. IRE* **27** 584

[34] Korolov I, Vass M, Bastykova N K and Donkó Z 2016 *Rev. Sci. Instrum.* **87** 063102

[35] Korolov I, Vass M and Donkó Z 2016 *J. Phys. D: Appl. Phys.* **49** 415203

[36] Vass M, Korolov I, Loffhagen D, Pinhão N and Donkó Z 2017 *Plasma Sources Sci. Technol.* **26** 065007

[37] Shockley W 1938 *J. Appl. Phys.* **9** 635

[38] Sirkis M and Holonyak N 1966 *Am. J. Phys.* **34** 943

[39] Song M Y, Yoon J S, Cho H, Karwasz G P, Kokoouline V, Nakamura Y and Tennyson J 2017 *J. Phys. Chem. Ref. Data* **46** 013106

[40] Fresnet F, Pasquiers S, Postel C and Puech V 2002 *J. Phys. D: Appl. Phys.* **35** 882–90

[41] Leyh H, Loffhagen D and Winkler R 1998 *Comput. Phys. Commun.* **113** 33–48

[42] Kumar K, Skullerud H and Robson R 1980 *Aust. J. Phys.* **33** 343–448

[43] Segur P, Bordage M C, Balaguer J P and Yousfi M 1983 *J. Comput. Phys.* **50** 116–37

[44] Dujko S, White R D, Petrović Z L and Robson R E 2010 *Phys. Rev.* E **81** 046403

[45] Dujko S, White R D, Petrović Z L and Robson R E 2011 *Plasma Sources Sci. Technol.* **20** 024013

[46] Loffhagen D, Pinhão N R, Vass M, Hartmann P, Korolov I, Dujko S, Bošnjaković D and Donkó Z 2020 Electron Swarm Parameters in C_2H_2—Measurements and Kinetic Calculations (https://doi.org/10.34711/inptdat.112)

[47] Loffhagen D, Pinhão N R, Vass M, Hartmann P, Korolov I, Dujko S, Bošnjaković D and Donkó Z 2020 Electron Swarm Parameters in C_2H_4—Measurements and Kinetic Calculations (https://doi.org/10.34711/inptdat.122)

[48] Loffhagen D, Pinhão N R, Vass M, Hartmann P, Korolov I, Dujko S, Bošnjaković D and Donkó Z 2020 Electron Swarm Parameters in C_2H_6—Measurements and Kinetic Calculations (https://doi.org/10.34711/inptdat.124)

[49] Kondo K and Tagashira H 1990 *J. Phys. D: Appl. Phys.* **23** 1175–83

[50] Frost L S and Phelps A V 1962 *Phys. Rev.* **127** 1621–33

[51] Ridenti M A, Alves L L, Guerra V and Amorim J 2015 *Plasma Sources Sci. Technol.* **24** 035002

[52] Shimanouchi T 1972 *Tables of Molecular Vibrational Frequencies Consolidated Volume I Report* NSRDS-NBS 39 National Bureau of Standards, Washington

PAPER

Experimental observation and simulation of the equilibration of electron swarms in a scanning drift tube

To cite this article: Z Donkó *et al* 2019 *Plasma Sources Sci. Technol.* **28** 095007

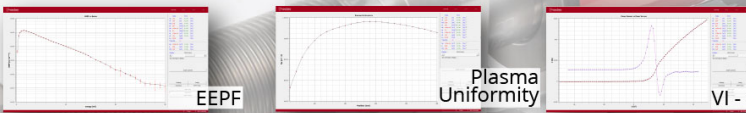View the article online for updates and enhancements.

You may also like

- Electron swarm properties under the influence of a very strong attachment in SF_6 and CF_3I obtained by Monte Carlo rescaling procedures
  J Miri, D Bošnjakovi, I Simonovi et al.

- Electron transport parameters in CO_2: scanning drift tube measurements and kinetic computations
  M Vass, I Korolov, D Loffhagen et al.

- Scanning drift tube measurements of electron transport parameters in different gases: argon, synthetic air, methane and deuterium
  I Korolov, M Vass and Z Donkó

Experimental observation and simulation of the equilibration of electron swarms in a scanning drift tube

Z Donkó[1] ⦿, **P Hartmann**[1], **I Korolov**[2] ⦿, **V Jeges**[1], **D Bošnjaković**[3] ⦿ **and S Dujko**[3] ⦿

[1] Institute for Solid State Physics and Optics, Wigner Research Centre for Physics, Hungarian Academy of Sciences, 1121 Budapest, Konkoly Thege Miklós str. 29-33, Hungary
[2] Department of Electrical Engineering and Information Science, Ruhr-University Bochum, D-44780, Bochum, Germany
[3] Institute of Physics, University of Belgrade, Pregrevica 118, 11080 Belgrade, Serbia

E-mail: donko.zoltan@wigner.mta.hu

CrossMark

Abstract

We investigate the spatially and temporally resolved electron kinetics in a homogeneous electric field in argon gas, in the vicinity of an emitting boundary. This (transient) region, where the electron swarm exhibits non-equilibrium character with energy gain and loss processes taking place at separate positions (in space and time), is monitored experimentally in a scanning drift tube apparatus. Depending on the strength of the reduced electric field we observe the equilibration of the swarm over different length scales, beyond which the energy gain and loss mechanism becomes locally balanced and transport properties become spatially invariant. The evolution of the electron swarm in the experimental apparatus is also described by Monte Carlo simulations, of which the results are in good agreement with the experimental observations, over the domains of the reduced electric field and the gas pressure covered.

Keywords: electron swarm, drift tube measurement, Monte Carlo simulation

1. Introduction

The description of charged particle transport in plasma modelling is often based on *transport coefficients* (e.g. mobility and diffusion coefficients) that are functions of the reduced electric field (electric field to gas density ratio, E/N). These coefficients can be determined experimentally in *swarm experiments* in which a cloud of charged particles (e.g. electrons) moves under the influence of a homogeneous electric field. The basic tools for measurements of these coefficients have been *drift tubes*, e.g. [1–5], which can operate in different modes (steady-state or pulsed) and give various transport coefficients [6]. Obtaining precise transport coefficients experimentally also aids the optimisation of cross section sets [7–9].

Swarm experiments aimed at the determination of transport coefficients have to be conducted under the conditions of *equilibrium transport*, where the effects of boundaries are negligible, gradients are weak and the electron velocity distribution function (VDF, $f(\mathbf{v})$) is uniquely defined by E/N. As the VDF of the 'initial' electrons (created, e.g. by ultraviolet radiation) in any experimental system is different from the equilibrium VDF, the swarm needs a certain length to equilibrate, during which length the energy (momentum) gain and loss mechanisms get balanced (see, e.g. [10, 11]). This equilibration domain (within which the transport has 'non-hydrodynamic' or 'non-local' character) should ideally be excluded from the region from which data for the determination of transport coefficients is collected as here the characteristics of the swarm vary spatially despite the fact that the electric field that drives the transport, is homogeneous. Excluding the equilibration region from the measurements is, however, normally not possible, but one has to ensure that the effects of swarm equilibration in the drift region are minimal, e.g. by setting the drift length significantly longer than the

equilibration length. Simulations of the electron transport are indispensable tools for checking this condition.

The *equilibration length* of any swarm depends on the type of its constituents (electrons/ions), the electric field, the gas pressure, and the types of collision processes between the charged particles and the atoms/molecules of the buffer gas. In the following we focus only on electron swarms. In the case of atomic gases, at very low E/N values, where the electron energy cannot reach the threshold for inelastic processes (which is typically several eV), only elastic collisions take place. At very high E/N values, where several inelastic channels are open, the electrons can lose several discrete values of energy in various excitation events, and, in ionisation processes their energy loss can vary continuously. Under these conditions the equilibration of the swarms proceeds quickly, over a short spatial domain. There exist, however, a 'window' of E/N values, typically in the range of several tens of Td-s (1 Td = 10^{-21} V m^2), where the equilibration takes place over an extended spatial scale [12–15]. The reason for this is that the electrons gain energy slowly (due to the relatively low electric field) and predominantly excite only the lowest excited state(s). In these conditions, the energy-gain—energy-loss cycle may repeat many times, the local swarm characteristics exhibit a periodic spatial dependence, before stationary state forms. In the case of molecular gases, the equilibration of the electron swarms proceeds more quickly due to the existence of various types of excitations processes (rotational, vibrational and electronic excitation), some of them having low threshold energies [16, 17]. It should be noted that additional control of the spatial relaxation of electrons under the steady-state conditions can be achieved using a magnetic field [17, 18].

The aim of this work is to examine the equilibration of electron swarms experimentally, in a drift tube apparatus that allows the observation of the spatio-temporal development of the particle cloud [19]. We do not target here the determination of transport coefficients. Parallel to the experimental studies we also carry out simulations at the particle level, to illustrate the phenomenon of swarm equilibration and to describe particle motion in the actual experimental system. Our studies are conducted using argon as a buffer gas.

In section 2 we give a brief description of the experimental system and outline the basics of the Monte Carlo simulation method that we use as a computational tool for our studies of swarm equilibration. In order to illustrate the phenomenon of swarm equilibration, in general, we first present a set of simulation results for a simple setting with a plane-parallel electrode configuration, for steady-state and time-dependent conditions, in section 3.1. Subsequently, in section 3.2, we turn to the presentation of experimental results and we compare these results with those obtained from simulations of the experimental system. Subsequently, in section 3.3, we also present additional simulation results that aid the understanding the operation of the detector of the drift tube. Section 4 summarises our findings.

2. Methods

We investigate the equilibration of electron swarms both experimentally, in a scanning drift tube apparatus [20] and via particle level simulations based on the Monte Carlo technique. The latter provides a description of particle transport at the level of kinetic theory, thus it is expected to account fully for the behaviour of the swarms under the specific (usually non-hydrodynamic) conditions considered here.

Full description of the experimental apparatus has been given in [20], thus only the main features of the setup are presented below, in section 2.1. The basics of the simulation method are outlined in section 2.2.

2.1. Experimental system

The simplified scheme of the experimental setup is shown in figure 1. The drift tube is situated within a stainless steel vacuum chamber that is evacuated by a turbomolecular pump backed with a rotary pump, down to a level of $\sim 10^{-7}$ mbar. A feedthrough with a quartz window allows the 1.7 μJ energy, 5 ns long pulses of a frequency-quadrupled diode-pumped YAG laser (MPL-F-266) to fall on the surface of a Mg disk used as photoemitter. This disk is mounted at the centre of a stainless steel electrode (having a diameter of 105 mm) serving as the cathode of the drift tube, which is connected to a BK Precision 9185B power supply to establish the accelerating voltage for the swarm that moves towards the detector, situated at a distance L_1 from the emitter. The detector consists of a grounded nickel mesh (with $T = 88\%$ 'geometric' transmission and 45 lines/inch density) and a stainless steel collector electrode that is situated at 1 mm distance behind the mesh. The mesh and the collector are moved together by a step motor connected to a micrometre screw mounted via a vacuum feedthrough to the vacuum chamber. The distance between the cathode and the mesh can be set within a range of $L_1 = 7.8$–58.3 mm. The electric field is kept constant during the scanning process by automatically adjusting the cathode-mesh voltage, according to their actual distance. In the experiments presented here, we used 53 equidistant positions within the accessible range of L_1 given above.

The data collection is triggered with a photodiode, using a part of the laser light that passes through a hole in the magnesium disk and leaves the chamber via a window mounted on its bottom. The current of the detector system is generated by the moving charges within the mesh-collector gap (see below). This current is amplified by a high speed current amplifier (type Femto HCA-400M) connected to the collector, with a virtually grounded input and is recorded by a digital oscilloscope (type Picoscope 6403B) with sub-ns time resolution. During the experiments a slow ($\sim$sccm) flow of (6.0 purity) argon gas is established by a flow controller, the gas pressure inside the chamber is measured by a Pfeiffer CMR 362 capacitive gauge. The low light pulse energy necessitates averaging over a high number typically 20 000–150 000) of pulses. The experiment is fully controlled by a computer using LabView software.
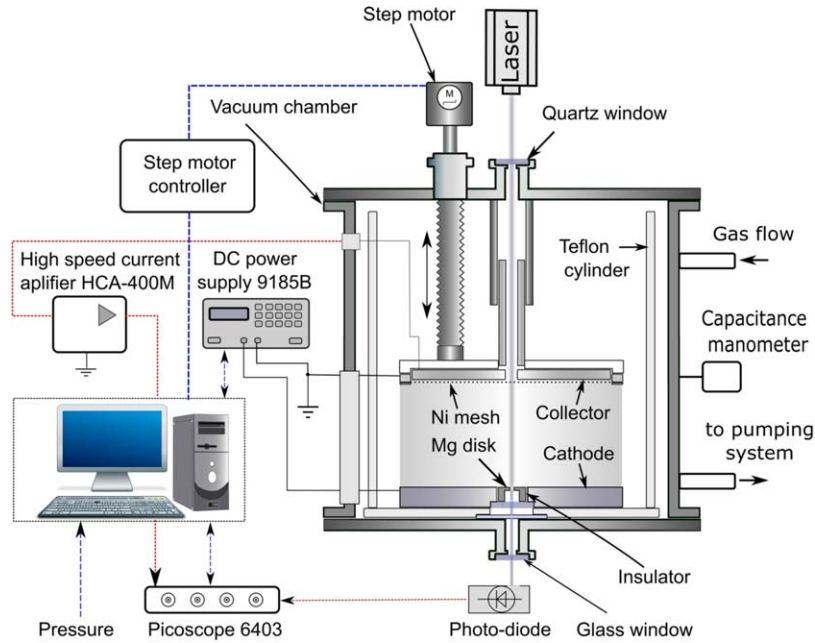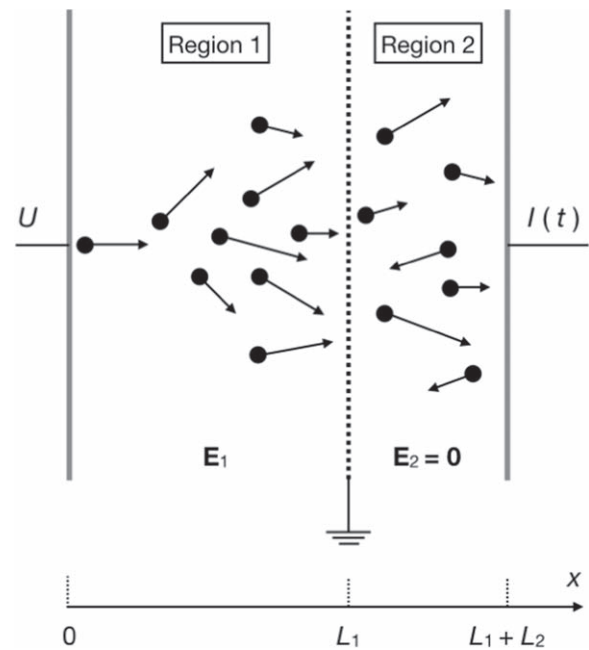
Figure 1. Simplified scheme of the experimental setup.

The operation of the drift tube described above can be understood by the simplified configuration shown in figure 2. The system consists of two regions, in Region 1 a homogeneous electric field $E_1 = U/L_1$ (where U is the voltage applied to the cathode (emitter)) is present, while, as both the mesh and the collector reside at ground potential, the electric field in Region 2, E_2, is zero. Electrons from the cathode (situated at $x = 0$) are emitted by short laser pulses (see above) and are accelerated by the electric field E_1 towards the mesh. During their flight, they undergo collisions with the background gas, the frequency of these collisions depends on their energy and the gas pressure. When the electrons arrive at the mesh, most of them are transmitted due to the high geometric transmission of the mesh, while a smaller portion is absorbed by/reflected from the mesh. The electrons, which enter Region 2 with some kinetic energy through the mesh, move in the field free Region 2. The measured current at the collector is generated by these moving electrons.

According to the Shockley–Ramo theorem [21–23] the current induced by an electron moving in a gap between two plane-parallel electrodes with a velocity v perpendicular to the electrodes is $I = ev/L$, where e is the charge of the electron and L is the distance between the electrodes. Accordingly, in our setting the measured current at a given time t is:

$$I(t) = c \sum_k v_{x,k}(t), \tag{1}$$

where c is a constant, the summation goes over all the electrons being present in Region 2 at time t, and $v_{x,k}$ is the velocity component of the kth electron in the x direction. The actual value of c is not important as the current is being measured as well as computed in arbitrary units. In the experiments, this current is measured at a sequence of spatial positions of the detector, L_1, as explained above. Examples of


Figure 2. Scheme of the two regions in the drift tube. A negative voltage U is applied at the cathode. In the experimental system L_1 can be changed between 7.8 and 58.3 mm, the distance L_2 is fixed at 1 mm. As the current $I(t)$ is measured with an amplifier that has a virtually grounded input, Region 2 is field-free. The measured current is generated by the moving electrons within this region.

$I(t)$ for $p = 200$ Pa and $E/N = 30$ Td are shown in figure 3 for few cathode-mesh separations.

2.2. Simulation method

We use simulations of electron swarms for three different purposes:
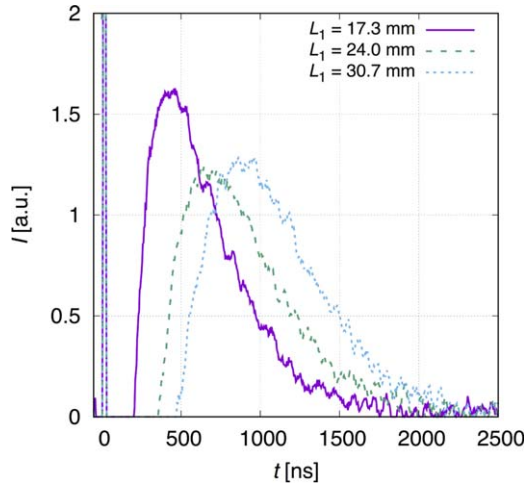
Figure 3. Time dependence of the measured current in the drift tube for $E/N = 30$ Td and $p = 200$ Pa, at different values of L_1. The sharp peak at $t = 0$ originates from an interference from the laser pulse, it is not taken into account in the data acquisition.

- *To illustrate the general features of swarm equilibration within a plane-parallel electrode gap:* in these simulations electrons are emitted from the negatively biased cathode at $x = 0$ and their tracing continues until the electrons are absorbed at the grounded anode at $x = L$, that has a reflectance R for the electrons. We investigate both steady-state and time-dependent cases. In the steady-state case we illustrate the behaviour of the swarm by presenting the average velocity and the mean electron energy as a function of position. In the time-dependent case we show the spatio-temporal evolution of the density of the swarm, for different E/N values.

- *To describe the experimental system:* in this case we adopt the model geometry shown in figure 2. An electric field is applied only in Region 1, between the cathode and the mesh. The electrons can pass through the mesh with a probability that equals its geometric transmission ($T = 88\%$). Electrons interacting with the mesh can be absorbed/elastically reflected with given probabilities. Electrons reaching the collector can as well be absorbed/elastically reflected with given probabilities.

- *To study the sensitivity of the detector as a function of electron energy and gas pressure:* in this study we inject electrons with given energies into Region 2 (the 'detector gap', see figure 2) and analyse the response of the detector as a function of these parameters.

Our simulations are based on the conventional Monte Carlo approach. Electrons are emitted from the cathode (situated at $x = 0$) at $t = 0$, with an initial energy of 1 eV. The typical number of initial electrons is in the order of 10^5–10^6. The electrons move under the influence of a homogeneous electric field, or in a field-free region, while interacting with the background gas via collision processes: elastic and inelastic (excitation and ionisation) collisions. Between collisions the electrons move on trajectories defined by their equations of motion that are discretised and solved

with a time step Δt:

$$x(t + \Delta t) = x(t) + v_x(t)\Delta t + \frac{1}{2}a\Delta t^2, \qquad (2)$$

$$v_x(t + \Delta t) = v_x(t) + a\Delta t, \qquad (3)$$

with $a = -\frac{eE}{m}$, where e is the elementary charge and m is the electron mass. The directions (y and z) perpendicular to the direction of the electric field are not resolved.

The probability of a collision to take place after Δt is given as

$$P(\Delta t) = 1 - \exp[-N\sigma_{\mathrm{T}}(v)v\Delta t], \qquad (4)$$

where N is the gas density, σ_{T} is the total scattering cross section, and v is the velocity of the electron (i.e. we use the cold-gas approximation, where target atoms are at rest). The simulation time step is in the order of 10^{-12} s.

Comparison of $P(\Delta t)$ with a random number r_{01} (having a uniform distribution over the [0, 1] interval) allows deciding about the occurrence of a collision: if $r_{01} \leqslant P(\Delta t)$ a collision is simulated. The type of collision is determined in a random manner. The probability of a process s at a given energy ε is given by:

$$P_s = \frac{\sigma_s(\varepsilon)}{\sigma_{\mathrm{T}}(\varepsilon)}, \qquad (5)$$

where $\sigma_s(\varepsilon)$ is the cross section of the sth process. In our simulations the cross sections are adopted from [24]. Collisions are assumed to result in isotropic scattering. Accordingly, we use the elastic momentum transfer cross section. For a given gas pressure, the background gas number density is calculated assuming the temperature of 300 K.

3. Results

3.1. Swarm equilibration under steady-state and time-dependent conditions

The relaxation of electron swarms is first illustrated for steady-state systems (termed as 'Steady State Townsend' (SST) scenario [13, 25–27] in swarm physics). In these simulations we assume a simple plane-parallel electrode configuration and consider a continuous source of electrons at the cathode. The electrode gap is chosen to be the largest distance of the cathode and the mesh in the experiment, $L = 58.3$ mm.

Figure 4 shows the average velocity and the mean energy of the electrons as a function of position in the electrode gap, for steady-state conditions. Panel (a) shows the results for $E/N = 300$ Td. The equilibrium transport, with transport properties specific to a given E/N, is established beyond a certain distance. Within the 'transient region' the local transport coefficients (like $\langle v \rangle$ and $\langle \varepsilon \rangle$) and the VDF, $f(\mathbf{v})$, change with position. Here, the swarm relaxes over a length of ≈ 20 mm, beyond this distance from the cathode the transport acquires equilibrium character, the transport parameters reach constant values and $f(\mathbf{v})$ takes a steady shape (while its magnitude grows according to the increase of the
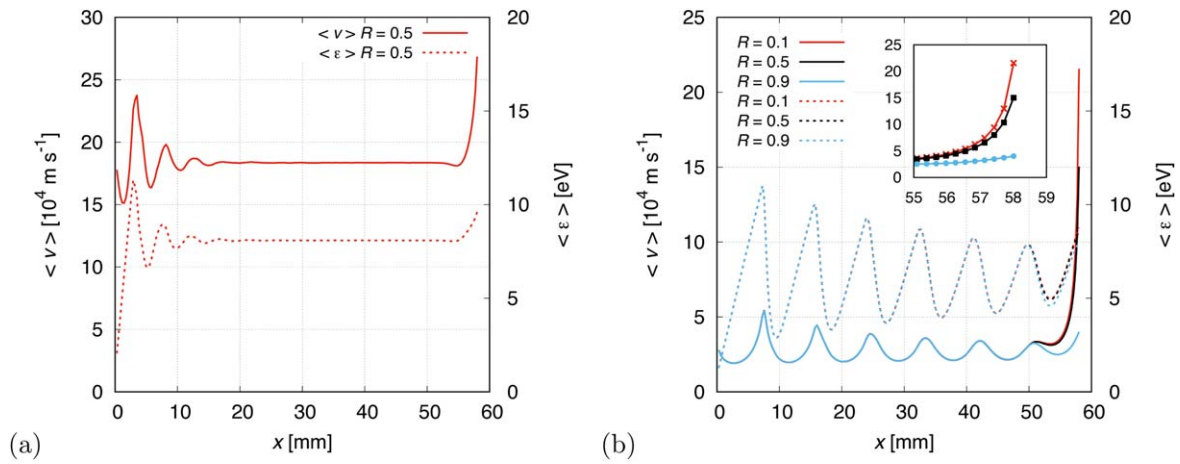
Figure 4. Average velocity (solid lines, left scale) and mean energy (dashed lines, right scale) of the electrons at (a) 300 Td ($p = 50$ Pa) and (b) 30 Td ($p = 200$ Pa), in the steady-state case. The cathode is situated at $x = 0$ mm, while the anode is at $L = 58.3$ mm. R denotes the electron reflection coefficient of the anode. The inset in (b) shows the effect of R on the average velocity in the near-anode region.
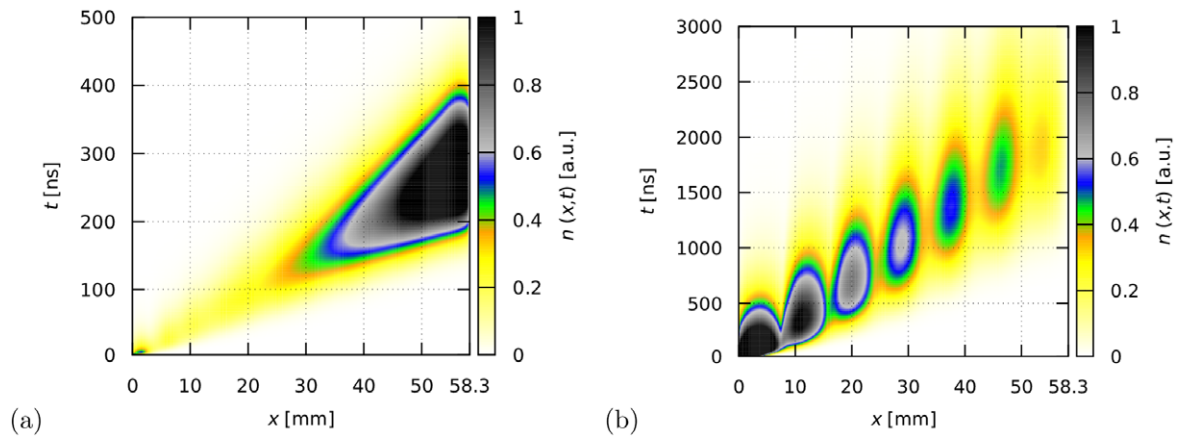

Figure 5. The evolution of the electron density in space and time for time-dependent conditions (swarm initiated at $x = 0$ mm and $t = 0$ ns) at (a) 300 Td ($p = 50$ Pa) and (b) 30 Td ($p = 200$ Pa). The cathode is situated at $x = 0$ mm, while the anode is at $L = 58.3$ mm.

electron density, due to ionising collisions). These characteristics become, however, perturbed again near the anode that is normally partially reflecting/absorbing for the electrons. The data shown here were obtained with a reflection coefficient of $R = 0.5$ (that we assume to be independent of the electron energy and angle of incidence at the surface). As part of the electrons is absorbed by the anode, in its vicinity the $f(\mathbf{v})$ distribution function is depleted in the $v_x < 0$ domain. This results in a significant increase of the average velocity and a moderate increase of the mean electron energy within a distance of a few mm-s from the anode.

At a lower E/N value of 30 Td, the relaxation of the swarm requires a notably longer distance, as indicated in figure 4(b). In this case even the full length, L, is too short for the swarm to acquire the equilibrium character, $\langle v \rangle$ and $\langle \varepsilon \rangle$ exhibit oscillations over the whole electrode gap. For this E/N value, simulations were carried out with different reflection coefficients. As expected, the mean velocity becomes more perturbed (increased) near the anode when R is decreased. As in the experiments the measured current

originates from the motion of the electrons in the x direction near the collector (in Region 2), the above observations have consequences on the performance of the experimental system.

Next, we turn to time-dependent conditions: figure 5 shows the spatio-temporal evolution of the electron density for two different values of E/N, same as above. In this case electrons are emitted in the MC simulations from the cathode (situated at $x = 0$) at time $t = 0$. Panel (a) displays the case of 300 Td ($p = 50$ Pa). For this E/N we observe a smooth development of the (density of the) particle cloud. Three basic effects are visible in this plot: (i) the centre of mass of the cloud *drifts* to higher x values with increasing time, (ii) with increasing time we observe an increasing width of the cloud due to *diffusion*, and (iii) the density increases with position as a consequence of *ionising collisions*. Except from the vicinity of the cathode no structures can be seen in the density distribution, unlike in the case of 30 Td ($p = 200$ Pa), shown in panel (b) of figure 5. Here, similar to the steady-state case, a significant spatial variation of the swarm evolution is found. The 'lobes' in figure 5(b) represent local density peaks, where
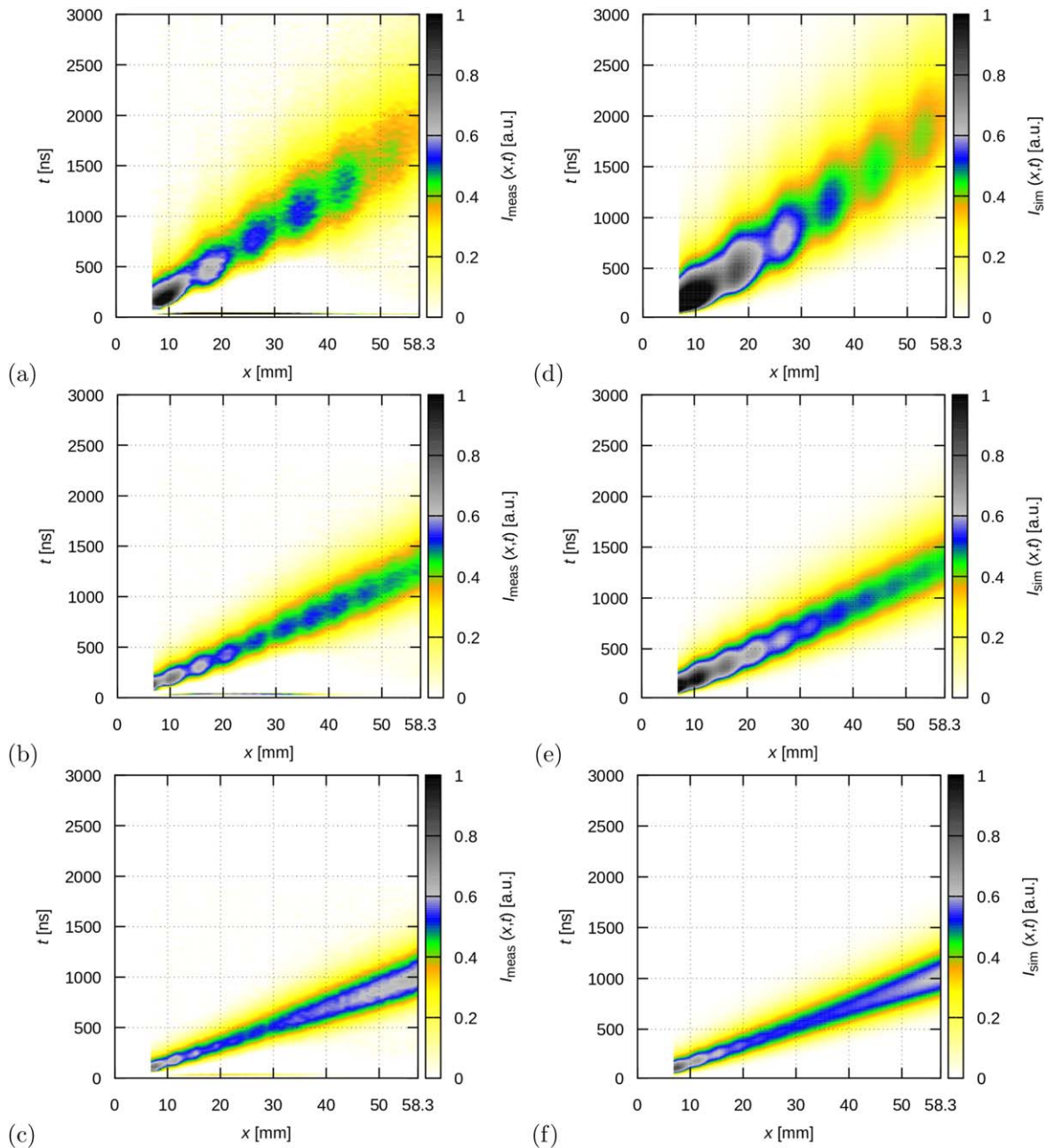
Figure 6. Experimentally recorded detector current (a)–(c), at E/N values of 30 Td, 50 Td and 70 Td, respectively, and (d)–(f) corresponding MC simulation results. $p = 200$ Pa for all results.

electrons accumulate. These localised maxima in space and time are created as a consequence of the repeating energy-gain—energy-loss cycles. For the given conditions the voltage over the gap is 84.5 V, that gives an electric field of 1.45 V mm^{-1}. For the distance of the peaks, $\Delta x \approx 9$ mm, a potential drop of ≈ 13 V over the length scale of Δx is obtained, which corresponds closely to lowest excitation energies of argon atoms. As the electrons can excite a number of energy levels with different threshold energies, their energy gain/loss cycles are not completely synchronised and therefore the density modulation decreases while the swarm moves, and after a certain distance the modulation disappears, and the swarm takes the equilibrium character.

3.2. Swarm equilibration in the drift tube—experiment versus simulation

Following the brief introduction to the equilibration phenomenon, now we turn to the presentation of experimental results confirming this behaviour by direct measurements on electron swarms in argon, and to the comparison of the experimental results with simulation data obtained at identical conditions. This comparison is carried out in terms of the measured/computed currents.

We start with the presentation of the experimentally recorded 'swarm maps' and the corresponding simulation results. Figure 6 displays the experimental data in the left
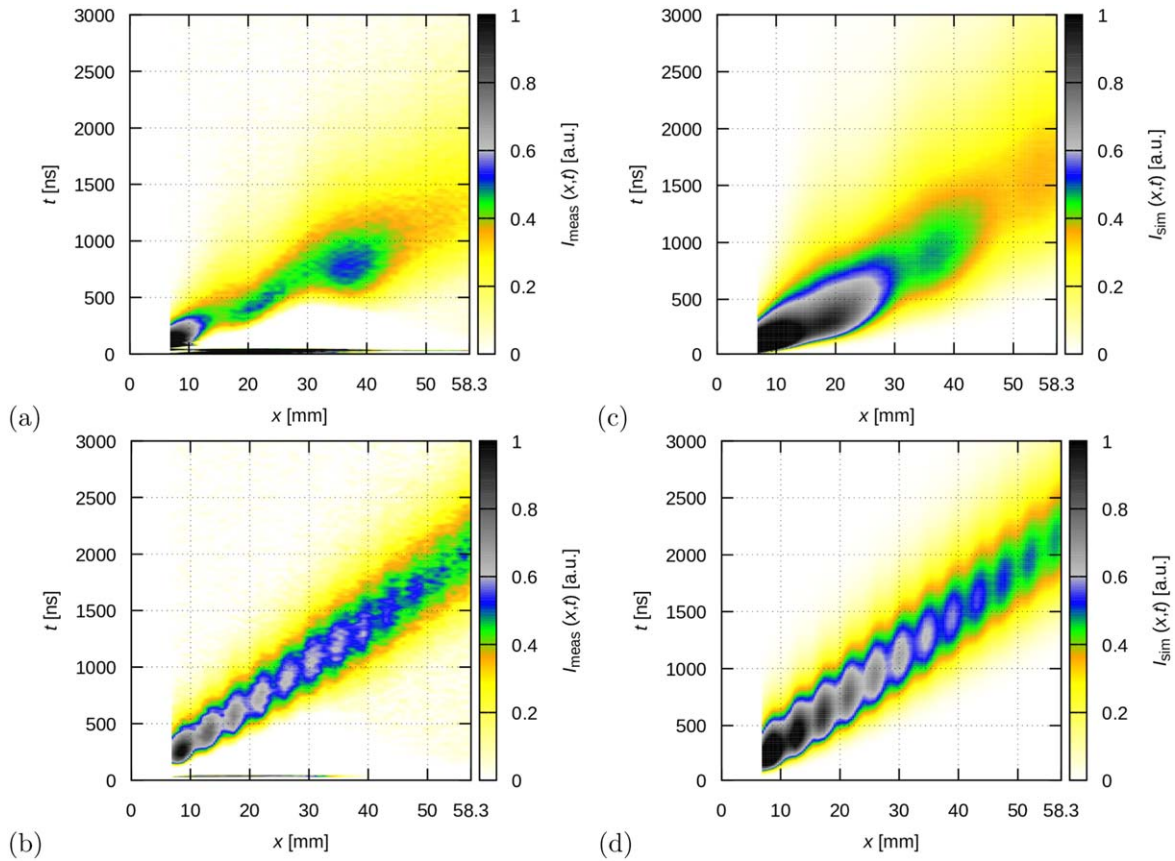
Figure 7. Experimentally recorded detector current (a), (b), at pressure values of 100 Pa and 400 Pa, respectively, and (c), (d) corresponding simulation results, at $E/N = 30$ Td.

column (panels (a)–(c)) obtained at 30 Td, 50 Td, and 70 Td values of the reduced electric field, respectively, at a fixed Ar pressure of $p = 200$ Pa. These swarm maps have been generated by measuring the $I(t)$ current of the detector at 53 equidistant values within the $L_1 = 7.8$–58.3 mm range of drift distances, and by merging these sets of data.

At the lower E/N values the maps clearly show sequences of 'lobes' that correspond to maxima of the measured currents, localised in both space and time. Taking the $E/N = 30$ Td case as an example, the distance of the lobes in space is again approximately $\Delta x = 9$ mm, as in the case of the theoretical results for the swarm density, shown in figure 5(b). Note, however, that while in the density distribution maxima occur e.g. at about 29 and 38 mm, the measured current peaks at approximately 27 and 35 mm, i.e. the peaks are shifted by about 2 mm. The reason for this shift will be discussed later, based on an analysis of the electron trajectories in the detector region. When, however, the experimentally obtained map (of the detector current) is compared with that obtained from the simulation of the experimental configuration, a very good agreement is obtained both in terms of the structure of the map as well as in the precise positions of the maxima. This confirms the validity of the model and the correct description of the system by the simulation.

With increasing E/N, the distance of the lobes decreases as dictated by the above condition (at a fixed pressure). At

$E/N = 50$ Td a clear sequence of lobes can still be resolved (figures 6(b) and (e)), while at 70 Td signatures of periodic structures can still be seen within the first half of the drift distance, while the second half of the gap shows a smooth distribution (figures 6(c) and (f)).

Figure 7 presents the results of the variation of the pressure at fixed $E/N = 30$ Td. As expected, when a lower pressure of 100 Pa is used in the measurements (and in the corresponding simulations) compared to the 200 Pa case, for which the results were presented in figures 6(a) and (d), the density maxima are separated by a higher distance. Oppositely, at $p = 400$ Pa, the periodicity of the maxima becomes two times more dense, as compared to the 200 Pa case.

The experimental results presented above provide a direct way to observe the equilibration of electron swarms at moderate E/N values, which was mostly studied only theoretically so far. The good agreement with the corresponding simulation results confirms the correctness of the data.

3.3. Characterisation of the detector

Now we turn to the analysis of the electrons' motion in the detector to answer the question: 'What property of the swarm is measured by the detector?' To answer this question we need to pay attention to the electron trajectories in the detector region ('Region 2' in figure 2).
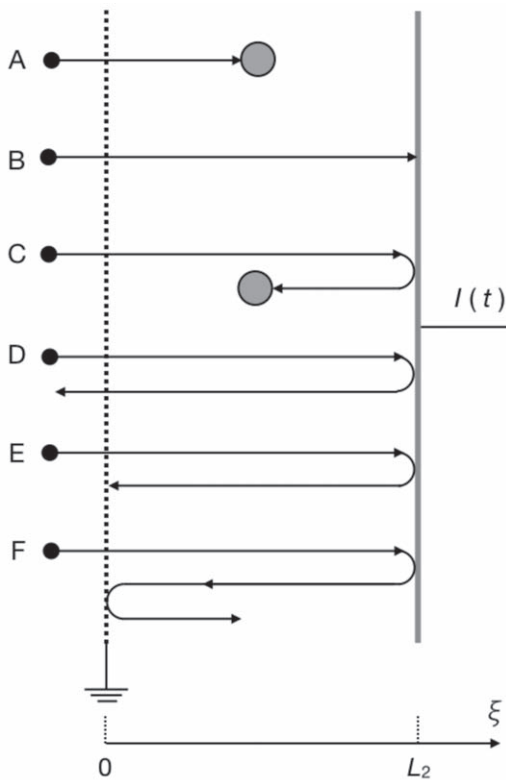
Figure 8. Basic types of electron trajectories (assuming that electrons enter the detector region have a velocity vector parallel to the *x* direction. The small black circles represent incoming electrons, the big circles represent gas atoms with which the electrons collide.

Figure 8 shows basic types of electron trajectories and their contributions to the detector current. In this analysis, we assume that (i) electrons pass through the mesh with a velocity vector that points in the *x* direction, (ii) all collision events results in isotropic scattering (as above), and (iii) electrons reaching the collector are reflected elastically with a given probability (taken to be $P = 0.5$, as above). Whenever we discuss a certain type of trajectory, we have in mind a large number of electrons (with similar energy and thus a similar collision free path length) that cross the mesh over some time interval that is (i) longer than the flight time of the electrons in the detector region, but (ii) much shorter than the period during which the whole electron cloud arrives at the detector.

If the collision free path is much shorter than the width of the detector region ($\lambda \ll L_2$) predominantly type A trajectories (see figure 8) will occur. The free flight length of the electrons within the detector is in the order of λ. It is important to recognise that, as collisions result in isotropic scattering, these electrons give a detector current contribution only up to the first collision events, because after the collisions the direction of their velocities is randomised. Accordingly, the further transport of these electrons towards the two electrodes does not give a contribution to the measured current.

With an increasing free path the electrons may reach the collector, where they may be absorbed (type B trajectories) or

reflected (C–F-type trajectories). Note that reflected electrons give a negative contribution to the measured current as they move in the negative *x* direction. The occurrence of type C trajectories is likely only when $\lambda \sim L_2$, as otherwise reflected electrons are again expected to have a long free path, that gives preference to the D-, E-, and F-type trajectories, which represent electron groups crossing the mesh (type D trajectories), being absorbed by the mesh (type E trajectories), or being reflected by the mesh (type F). Type F trajectories could be divided into further sub-types, however, this type of trajectory is not expected to occur frequently, as it requires reflection of electrons on the collector ($P = R = 0.5$), interaction with the mesh ($P = 0.12$, i.e. one minus the geometric transmission) and reflection there (assumed to have $P = R = 0.5$), giving an overall probability of $P = 0.03$. Thus F type trajectories may be excluded as major sources of the detector current. Returning to the D- and E-types of trajectories, these will give zero contribution on time average, for a large group of electrons.

Thus in summary,

- Whenever $\lambda \ll L_2$, the measured current will be proportional to the number of electrons entering the detector per unit time, i.e. their flux, the value of their v_x velocity component (according to equation (1)) and to their flight time up to the first collision. As the product of the latter two is actually the path length, the current can be approximated as being proportional to λ;
- Whenever $\lambda \gg L_2$, the measured current will be proportional again to the flux of electrons entering the detector, the value of their v_x velocity component and the probability of their absorption by the collector. Thus, a strongly reflecting collector will decrease the level of the measured signal for electrons with a long free path.

These arguments are indeed confirmed by simulation results obtained with different values of electron reflectivity of the collector, presented in figure 9. These data have been obtained at $E/N = 30$ Td and 200 Pa argon pressure. The reflectivity values are $R = 0.99$ for (a) and $R = 0.01$ for (b). The conditions are the same in figure 6(b), for which $R = 0.5$ was assumed.

As it can be seen in figure 9(a), the high reflectivity of the collector has a detriment effect on the detector signal, while a low reflectivity (figure 9(b)) further increases the quality of the detector signal, beyond that shown in figure 6(b) for the realistic choice of $R = 0.5$. These observations confirm the reasoning presented above and the good agreement between the experimental and simulation results shown in figure 6 also confirms that the $R = 0.5$ value, assumed for the reflectivity, is indeed realistic.

We have conducted additional simulations to determine the sensitivity of the detector, S_{det}, as a function of electron energy and background gas pressure. The pressure and the energy were scanned over the domains 3 Pa–240 Pa and 0.4 eV–40 eV, respectively. For each pair of these parameters 10^5 initial electrons were injected into the detector gap (at
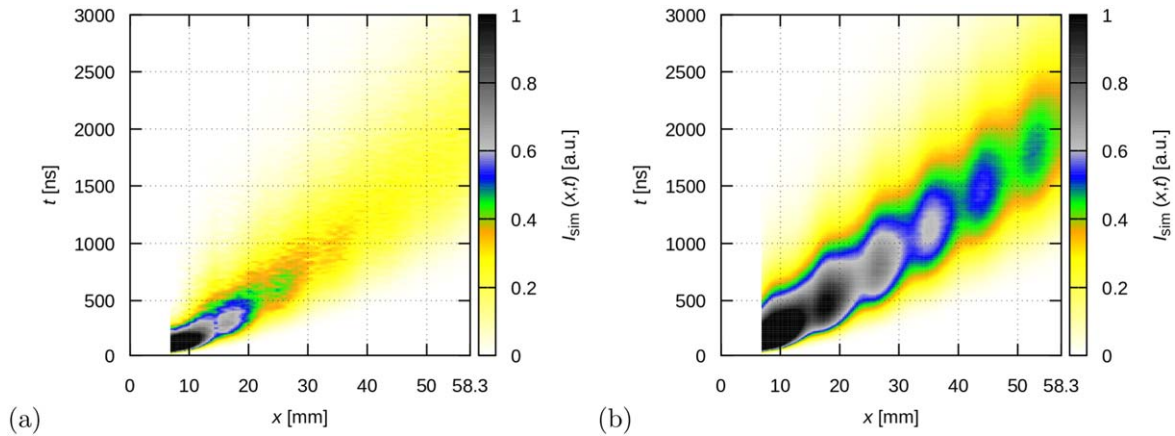
Figure 9. (a) Simulation results with (a) a highly reflecting ($R = 0.99$) collector and (b) a low-reflection ($R = 0.01$) collector, at $E/N = 30$ Td and $p = 200$ Pa.

$t = 0$), with isotropic angular distribution of their initial velocity directions over the positive half sphere. (This latter choice is justified by the fact that the VDF of electrons is nearly isotropic at low to moderate E/N values, as the average velocity is much smaller than the thermal velocity.) The motion of these electrons was traced up to their first collision only, as the collisions randomise the direction of velocities resulting in a vanishing subsequent contribution to the current. The sensitivity was determined as the time integral of the induced current, given by equation (1), for this 'pulse' of electrons:

$$S_{\text{det}} = \int I(t)\,\mathrm{d}t, \qquad (6)$$

where integration was carried out over times when the pulse of electrons creates a current. The results of these simulations are presented in figure 10.

Panel (a) shows the results for the case of a collector with $R = 0.5$ reflection coefficient, a value that has been assumed in the simulations of the experimental system, while panel (b) shows the case of a highly reflecting collector, with $R = 0.99$. We find that the sensitivity of the detector depends in a complicated manner on both the gas pressure and the energy of the incoming electrons.

For the $R = 0.5$ case we find a high sensitivity at low pressures. Up to about 5 Pa, the response of the detector is strong for all electron energies. At these low pressures, the majority of the electrons reaches the collector. Half of these electrons are absorbed, i.e. their trajectories are of type B (see figure 8). The other half of the electrons will have trajectories of types C–F, which may decrease the response by ∼50%. With an increasing pressure the detector sensitivity decreases, except for the electrons with very low energies. The electrons with energies ∼1 eV, or lower, still have a long free path (due to the Ramsauer minimum in the momentum transfer cross section) and many of them reach the collector and the above arguments apply to the types of their trajectories. For electrons with higher energies, however, the sensitivity drops and shows a minimum around 12 eV, where, actually the mean free path is the shortest (see later, in figure 11). This drop of

sensitivity is attributed to the A-type trajectories, which have gradually lower contributions to the detector current when the electron free flight becomes shorter at higher pressures.

The reflectivity of the collector plays a central role in the sensitivity as the comparison of the panels of figure 10 reveals. The differences are concentrated, however, to the low-pressure domain, as at higher pressures, as discussed above, A-type trajectories form and the electrons do not reach the collector without collisions. Therefore, above ≈50 Pa, the panels of figure 10 look identical. At low pressures, however, the sensitivity of the detector decreases drastically (by about a factor of 10 at the lowest pressures covered) when the reflectivity of the collector is increased to 0.99. This is due to the fact that the B-type trajectories will be replaced by mostly D–F type trajectories, which result in a cancellation of the current created by the electrons moving into opposite directions.

We note that the results shown here are specific for argon gas, for any other gases the results for S_{det} may differ significantly because of the different cross sections. The existence of the Ramsauer minimum for argon, e.g. plays an important role in the behaviour of slow electrons in the detector region and influences the sensitivity considerably.

The dependence of the sensitivity of the detector on the gas pressure and electron energy contributes to the slight shift of the structures seen in the density of the swarm in a plane-parallel configuration (figure 5(b)) versus the measured current in the experimental system and its computed counterpart (figures 6(a) and (d)). Figure 11 displays, at two different positions, the energy resolved fluxes of electrons (i) entering Region 2 via the mesh (labelled as 'positive'), (ii) being absorbed by the collector (labelled as 'collected') and (iii) leaving the detector (Region 2) via the mesh, in the negative direction (labelled as 'negative'). Panel (a) corresponds to a position, $L_1 = 30.6$ mm, where the measured current is minimum (see figure 6(a)), while panel (b) corresponds to a position, $L_1 = 34.8$ mm, where the current is maximum. In both cases $E/N = 30$ Td, $p = 200$ Pa, and the reflectivity of the detector is $R = 0.5$. The mean free path of the electrons is
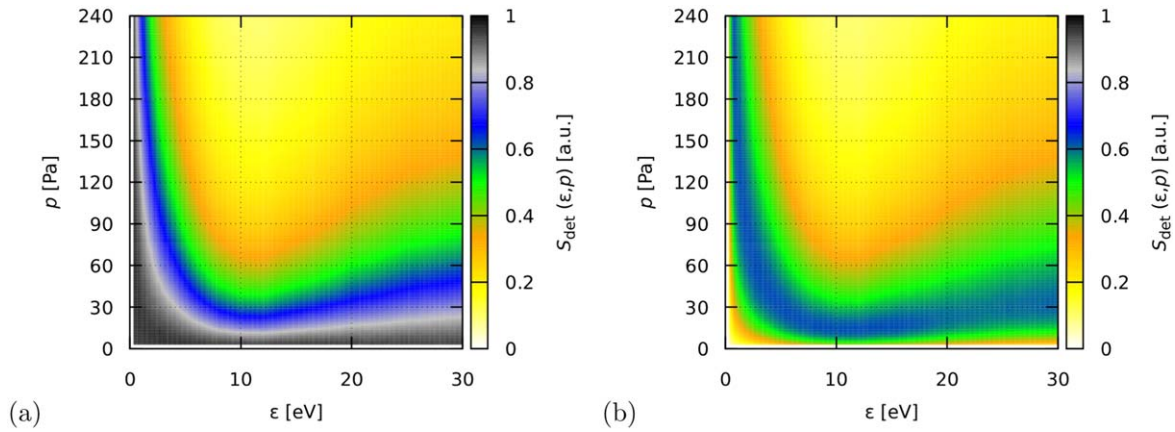
Figure 10. Sensitivity of the detector, S_{det}, (in arbitrary units) as a function of the energy of incoming electrons and the buffer gas pressure, for $R = 0.5$ (a) and for a highly reflecting collector with $R = 0.99$ (b). An isotropic angular distribution of the incoming electrons is assumed.
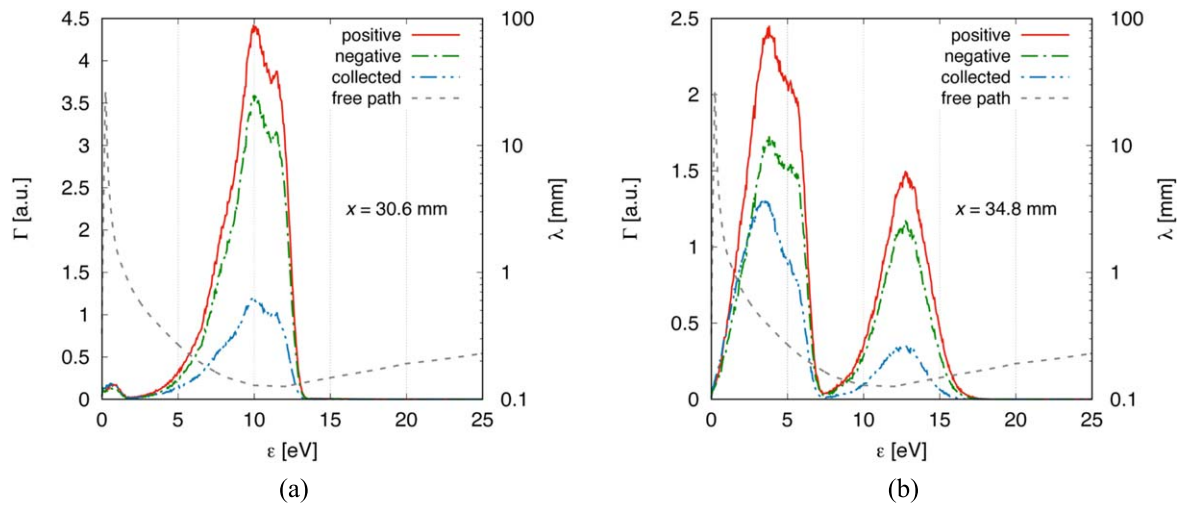
Figure 11. The distribution (flux) of the electrons according to their energy crossing the mesh in the positive and negative directions (labelled as 'positive' and 'negative', respectively), and absorbed at the collector (labelled as 'collected'). $E/N = 30$ Td, $p = 200$ Pa, $R = 0.5$. (a) $x = 30.6$ mm and (b) $x = 34.8$ mm. The free path (λ) of the electrons at the given gas pressure is shown on the right axis.

also shown in figure 11 (as curves labelled 'free path'). At $L_1 = 30.6$ mm one major electron group enters the detector with energies between 5 and 13 eV. In this case (figure 11(a)) the free path is much smaller than $L_2 = 1$ mm, therefore only about a quarter of these electrons, is collected. Compared to this, at $L_1 = 34.8$ mm, two electron groups reach the detector. While for the high energy group the collection efficiency is also small, for the low energy group, as the free path is longer (see figure 11(b)) about the half of the electrons are collected. This shows a drastic change of the sensitivity of the detector, S_{det}, as a function of spatial position under the actual conditions of the experiment, where swarm equilibration is studied.

4. Summary

We have investigated the equilibration of electron swarms in argon gas. Following the illustration of the general behaviour of electron swarm equilibration via numerical simulations of steady-state (SST) and time-dependent systems, we presented experimental investigations of the equilibration phenomenon by using a scanning drift tube apparatus that allows observation of the spatio-temporal development of electron swarms The experimental studies have been complemented with numerical simulations of the experimental system. A very good agreement has been found between the measured and computed detector currents.

We have also presented a detailed study of the operation of the detector by analysing types of possible electron trajectories and by carrying out simulations for the detector sensitivity as a function of electron energy and the gas pressures. This analysis has indicated a strong variation of the sensitivity on these two parameters, which explains the slight differences between the spatio-temporal distributions of electron density in the swarm and that of the measured detector current. These differences, thus, do not originate from uncertainties in the measurements and/or in the computations, but have well-defined reasons.

Our studies provided an insight into the equilibration effects from the experimental side, complementing a number of previous theoretical/simulation studies. The robustness of the

phenomena investigated allowed us to use simplifications in our modelling studies, in which we have neglected, e.g. the penetration of the electric field via the mesh, as well as the energy and angular dependence of the reflection/sticking coefficient of electrons at the different metal surfaces (mesh and collector). These, and other possible fine details of the experiment would be quite difficult to consider (partly because precise data for the electron-surface interaction are not available), nonetheless, these seem to be attractive topics for further investigations.

Acknowledgments

ORCID iDs

Z Donkó ⓘ https://orcid.org/0000-0003-1369-6150
I Korolov ⓘ https://orcid.org/0000-0003-2384-1243
D Bošnjaković ⓘ https://orcid.org/0000-0002-2725-5287
S Dujko ⓘ https://orcid.org/0000-0002-4544-9106

References

[1] Crompton R W, Elford M T and Jory R L 1967 *Aust. J. Phys.* **20** 369
[2] Crompton R W 1972 *Aust. J. Phys.* **25** 409
[3] Nakamura Y 1987 *J. Phys. D: Appl. Phys.* **20** 933
[4] De Urquijo J, Arriaga C A, Cisneros C and Alvarez I 1999 *J. Phys. D: Appl. Phys.* **32** 41
[5] Dahl D A, Teich T H and Franck C M 2012 *J. Phys. D: Appl. Phys.* **45** 485201
[6] Petrović Z L, Dujko S, Marić D, Malović G, Nikitović Ž, Šašić O, Jovanović J, Stojanović V and Radmilović-Radenović M 2009 *J. Phys. D: Appl. Phys.* **42** 194002
[7] Tagashira H 1992 *Aust. J. Phys.* **45** 365
[8] Petrović Z L, Šuvakov M, Nikitović Ž, Dujko S, Šašić O, Jovanović J, Malović G and Stojanović V 2007 *Plasma Sources Sci. Technol.* **16** S1
[9] Morgan W L 1991 *Phys. Rev.* A **44** 1677
[10] Malović G, Strinić A, Živanov A, Marić D and Petrović Z 2003 *Plasma Sources Sci. Technol.* **12** S1
[11] Donkó Z 2011 *Plasma Sources Sci. Technol.* **20** 024001
[12] Kolobov V I and Arslanbekov R R 2006 *IEEE Trans. Plasma. Sci.* **34** 895
[13] Dujko S, White R D and Petrović Z 2008 *J. Phys. D: Appl. Phys.* **41** 245205
[14] White R D, Robson R E, Dujko S, Nicoletopoulos P and Li B 2009 *J. Phys. D: Appl. Phys.* **42** 194001
[15] Nicoletopoulos P and Robson R E 2008 *Phys. Rev. Lett.* **100** 124502
[16] Li B, White R D and Robson R E 2002 *J. Phys. D: Appl. Phys.* **35** 2914
[17] Dujko S, White R D, Petrović Z L and Robson R E 2011 *Plasma Source Sci. Technol.* **20** 024013
[18] Li B, Robson R E and White R D 2006 *Phys. Rev.* E **74** 026405
[19] Vass M, Korolov I, Loffhagen D, Pinhão N and Donkó Z 2017 *Plasma Sources Sci. Technol.* **26** 065007
[20] Korolov I, Vass M, Bastykova N K and Donkó Z 2016 *Rev. Sci. Instrum.* **87** 063102
[21] Ramo S 1939 *Proc. IRE* **27** 584
[22] Shockley W 1938 *J. Appl. Phys.* **9** 635
[23] Sirkis M D and Holonyak N Jr 1966 *Am. J. Phys.* **34** 943
[24] Hayashi M 1981 *Recommended values of transport cross sections for elastic collision and total collision cross section for electrons in atomic and molecular gases* Report IPPJ-AM-19 (unpublished) Nagoya Institute of Technology
[25] Robson R E 1991 *Aust. J. Phys.* **44** 685
[26] Sakai Y, Tagashira H and Sakamoto S 1977 *J. Phys. D: Appl. Phys.* **10** 1035
[27] Stojanović V D and Petrović Z L 1998 *J. Phys. D: Appl. Phys.* **31** 834

PAPER

Electron transport and negative streamers in liquid xenon

View the article online for updates and enhancements.

Electron transport and negative streamers in liquid xenon

I Simonović[1] ⬤, **N A Garland**[2] ⬤, **D Bošnjaković**[1] ⬤, **Z Lj Petrović**[1,3] ⬤,
R D White[2] ⬤ and **S Dujko**[1] ⬤

[1] Institute of Physics, University of Belgrade, Pregrevica 118, 11080 Belgrade, Serbia
[2] College of Science and Engineering, James Cook University, Townsville, QLD 4811, Australia
[3] Serbian Academy of Sciences and Arts, Knez Mihailova 35, 11000 Belgrade, Serbia

E-mail: sasa.dujko@ipb.ac.rs

CrossMark

Abstract

In this work we investigate electron transport, transition from an electron avalanche into a
negative streamer, and propagation of negative streamers in liquid xenon. Our standard Monte
Carlo code, initially developed for dilute neutral gases, is generalized and extended to consider
the transport processes of electrons in liquids by accounting for the coherent and other liquid
scattering effects. The code is validated through a series of benchmark calculations for the
Percus–Yevick model, and the results of the simulations agree very well with those predicted by
a multi term solution of Boltzmann's equation and other Monte Carlo simulations. Electron
transport coefficients, including mean energy, drift velocity, diffusion tensor, and the first
Townsend coefficient, are calculated for liquid xenon and compared to the available
measurements. It is found that our Monte Carlo method reproduces both the experimental and
theoretical drift velocities and characteristic energies very well. In particular, we discuss the
occurrence of negative differential conductivity in the E/n_0 profile of the drift velocity by
considering the spatially-resolved swarm data and energy distribution functions. Calculated
transport coefficients are then used as an input in fluid simulations of negative streamers, which
are realized in a 1.5 dimensional setup. Various scenarios of representing the inelastic energy
losses in liquid xenon, ranging from the case where the energy losses to electronic excitations are
neglected, to the case where some particular excitations are taken into account, and to the case
where all electronic excitations are included, are discussed in light of the available spectroscopy
and photoconductivity experiments. We focus on the way in which electron transport coefficients
and streamer properties are influenced by representation of the inelastic energy losses,
highlighting the need for the correct representation of the elementary scattering processes in the
modeling of liquid discharges.

Keywords: liquid xenon, electron transport, Monte Carlo, inelastic collisions, negative streamers

1. Introduction

Transport of charged particles in liquids, plasma-liquid
interactions and streamer discharges in the liquid phase con-
stitute a growing field of research, which has many important
applications [1, 2]. These applications include plasma medi-
cine [3, 4], plasma water purification [5–9], transformer oils
[10, 11] and particle detectors [12, 13]. In particular, there is a
rich variety of liquid xenon particle detectors [14]. The wide
range of existing and potential applications of these detectors

includes gamma ray astrophysics [13], particle physics [15]
and medical imaging [16], as well as direct dark matter
detection [17, 18]. Liquid xenon is a very good detection
medium, due to its physical properties [14]. Its high values of
density and atomic number make liquid xenon very efficient
in stopping penetrating radiation, while a significant abun-
dance of many isotopes, with different values of nuclear spin,
enables the study of both spin dependent and spin indepen-
dent interactions [14]. Further optimization and understanding
of such applications is dependent on an accurate knowledge

of the charged particle transport coefficients, streamer properties and the physical processes involved.

In addition to many useful applications, further theoretical and experimental investigation of transport phenomena in liquids would help in the development of insight into various effects, which are relevant for the interaction of charged particles with dense and disordered media [19]. These effects include multiple scattering effects and structure effects, trapping of charged particles in density fluctuations and the solvation of charged particles in polar liquids [19, 20]. As liquid rare gases are the simplest liquids, they are a good starting point for the development of theoretical models of transport and breakdown phenomena in the liquid phase [19].

1.1. A brief overview of electron transport in liquid rare gases

In recent years the modeling of charged particle transport processes in neutral gases has matured and a number of methods to treat this problem have been developed, e.g. various techniques for solving the Boltzmann equation [21], the Monte Carlo method [22] and semi-quantitative momentum transfer theory [21, 23]. For the more general case of the dense gases and liquids, there has been comparatively less investigation. Most investigations in liquid phase have been performed for electron transport in the sub-excitation energy region [19]. Lekner developed an *ab initio* method for determining the effective potential and the corresponding effective cross section for electron scattering on a focus atom in the liquid phase [24]. This effective potential is determined by using the potential of a single atom and the pair correlation function of the liquid. In addition, Cohen and Lekner have shown that the coherent elastic scattering can be represented in the Boltzmann equation by combining the effective cross section for the liquid phase and the static structure factor [25]. By simplifying the arguments of Lekner, Atrazhev and co-workers have shown that the effective cross section for elastic scattering in liquid argon, krypton and xenon are constant in the limit of lower electron energies [26, 27]. This work was extended by using the partial wave method for determining the effective cross sections for electron scattering in liquid argon and liquid xenon [28–31]. Based on these results, they have calculated mobility, mean energy, and characteristic energy of electrons in liquid argon and liquid xenon, in the framework of the Cohen–Lekner theory [30, 31]. The Cohen–Lekner theory was also used in the study of Sakai and co-workers, who have investigated the electron transport in liquid argon, krypton and xenon [32, 33]. In order to improve the agreement between the calculated and measured drift velocities, they have modified the cross section for elastic scattering empirically. In addition, they have demonstrated that the saturation of drift velocity at higher electric fields, which was previously observed in experiments, can be adequately described by including an effective inelastic cross section for vibrational modes. It was argued that these vibrational modes correspond to the change of the translational states of the clusters of atoms. More recently, Boyle *et al* [19, 34] have evaluated the differential cross sections for electron scattering in liquid argon and liquid xenon by solving

the Dirac–Fock scattering equations. In these works, Boyle *et al* [19, 34] extended Lekner's theory by considering multipole polarizabilities and non-local treatment of exchange [19, 34]. Transport coefficients have been calculated for electrons using these cross sections as an input into the multi term Boltzmann equation solution, for the lower values of the reduced electric field. It is also worth noting that in order to thermalize electrons to low energies in rare gases (especially those with Ramsauer–Townsend minimum) in the most efficient way and with a small experimental error, it was necessary to perform swarm experiments at higher pressures, where high density effects became observable [35–37]. One of the alternatives to avoid such effects and obtain low-energy cross sections and scattering lengths was to use molecular hydrogen in the mixture at low reduced electric fields, where the unique solution for the rotational energy loss cross sections for hydrogen exists [38].

Theoretical studies of electron transport processes in liquid rare gases, at higher electric fields, have been performed by several authors. In 1976, Atrazhev and co-workers studied the influence of density dependent scattering effects on the Townsend ionization coefficient [39]. The results of this work are two estimates of the first Townsend ionization coefficient, which have been made by considering the two distinctively different representations of energy losses in the electronic excitations. Jones and Kunhardt also studied electron transport in liquid xenon by using Monte Carlo simulations [40]. The semiclassical model used, was previously applied by Kunhardt for studying electron transport in liquid argon [41]. In this work, the interaction of electrons with the liquid is described in the framework of Van Hove's theory [42]. The group at Hokkaido University has also studied ionization in liquid xenon, as well as the electron attachment in the mixtures of liquid argon and electronegative impurities, including O_2, SF_6 and N_2O, using previously developed cross sections [32]. Considerable contributions in this field have been made by Boyle and co-workers who developed the fluid equation based model for electrons and positrons in liquids by utilizing dilute gas phase cross sections together with a structure factor for the medium [43–46].

1.2. Streamers in liquid rare gases

In comparison to gas phase modeling, there are only a few modeling studies of streamer propagation in liquids. Simulations of positive streamers in hydrocarbon liquids using 1.5D classical streamer model have been performed by Naidis and co-workers [10, 47]. Simulations are performed both without formation of expanding gaseous filaments and in conditions when such filaments due to vaporization are formed. Contemporary studies include both the experimental and numerical studies of propagating streamers inside bubbles elongated along the external electric field and compressed bubbles immersed in water [48, 49]. The salient feature of these studies is that transport coefficients of electrons in liquids required for streamer simulations are evaluated approximately, e.g. without taking into account more serious

perturbations to the transport due to the formation of bubbles and clusters.

Numerical modeling of streamer dynamics, in liquid argon and liquid xenon, has been performed by Babaeva and Naidis [50–52]. They have investigated the formation of a positive streamer in a strong non-uniform field and its subsequent propagation in a weak uniform field, by employing a two dimensional fluid model [50, 51]. Among many important points in these papers, it has been shown that the nature of the streamer propagation in the liquid phase is significantly influenced by the electron-ion recombination [50, 51]. In addition, they found that the calculated streamer velocities are of the same order of magnitude as the measured velocity of the breakdown wave in liquid argon [50, 51].

1.3. Motivational factors for this study

One of the most important conclusions from the previous studies of electron transport in atomic liquids is the fact that still there is no consensus on the importance of excitations in the liquid phase. For example, Atrazhev *et al* [39] have shown that if the portion of energy losses due to excitations is assumed to be just the same as in the gas phase, the first Townsend coefficient is underestimated. On the other hand, if the inelastic energy losses are completely neglected then the first Townsend coefficient is overestimated [39]. Along similar lines, Nakamura and co-workers also disregarded the explicit influence of energy losses associated with the electronic excitations in their calculations of transport properties of electrons in the liquid phase [20, 53]. Instead, they have represented the inelastic energy losses by using an effective inelastic cross section, which corresponds to vibrational modes [20, 32, 53]. In 1993, Jones and Kunhardt carried out Monte Carlo simulations in which the inelastic energy losses due to electronic excitations were included [40]. However, in this work it has not been specified which electronic excitations are included in the set of cross sections [40]. Atrazhev *et al* [39] have shown that a different representation of the inelastic energy losses leads to a significant difference in the calculated values of the ionization rate in liquid xenon. Thus, it is clear that a rigorous analysis of the inelastic energy losses in studies of electron transport in liquid rare gases is long overdue and the present study takes the first steps in this direction. We believe that this is of key importance for numerical studies of streamer propagation, since ionization controls the development of a discharge and occurs in both the streamer head and in the streamer channel.

In this work, we investigate how various representations of the inelastic energy losses affect transport properties of electrons and streamer dynamics in liquid xenon. Cross sections for electronic excitations are taken from the set for electron scattering in the gas phase compiled by Hayashi [54]. This set of cross sections yields swarm parameters in good agreement with the available measurements [55]. We identify and consider the following three global scenarios: (i) no electronic excitations, (ii) some electronic excitations are included and some of them are neglected, and (iii) all

electronic excitations are included in the modeling. Various representations of inelastic energy losses are first discussed in light of previous spectroscopy and photoconductivity experiments and then are used in Monte Carlo simulations. The calculated values of the first Townsend coefficient in these various cases are compared with respect to the experimental results of Derenzo *et al* [56]. These calculations are augmented by those in which gaseous xenon is scaled up to the liquid density. In addition to the study of transport processes, in this work we investigate the propagation of negative streamers in liquid xenon. The axial profiles of electric field and number density of electrons are calculated in the absence of vaporization and the occurrence of bubbles.

1.4. Organization of the paper

In section 2 we give the details of cross sections for elastic and inelastic scattering of electrons in liquid xenon. We identify and review the four different cases in three global scenarios for representing the inelastic energy losses. In section 3.1 we briefly outline the Monte Carlo method used in the present work and present the results of benchmark calculations for the Percus–Yevick model in section 3.2. In section 3.3 we present the basic elements of a fluid theory used to simulate negative streamers in liquid xenon. In section 4 we present the electron transport coefficients in liquid xenon with particular emphasis on the structure induced negative differential conductivity (NDC). In the same section, we discuss the transition from an avalanche into a streamer and propagation of negative streamers. In section 5 we present our conclusions and recommendations for future work.

2. Cross sections for electron scattering in liquid xenon

In the gas phase, the electron transport can be represented as a series of individual collisions, which are separated by free flights [19]. However, this picture is no longer valid in the liquid phase. Since no particular volume is owned by a single atom, due to small interparticle spacings in liquids, as compared to the range of interaction between electrons and the targets, the potential in which an excess electron is scattered is determined by many surrounding atoms [19, 24]. Namely, it has been shown that the polarization potential of a single atom is significantly screened by polarization potentials of neighboring atoms [19, 24]. Due to this effect, at low energies, the effective potential changes from an attractive long range potential, which corresponds to scattering on an isolated xenon atom, to a repulsive short range potential, which corresponds to scattering in the liquid phase [24, 28]. In addition, electron scattering on a focus atom will be influenced by electrostatic terms and non-local exchange terms of all neighboring atoms [19]. Moreover, the de Broglie wavelengths of excess electrons at thermal energies are larger than the interatomic spacing by several orders of magnitude [19].

This leads to significant coherent scattering effects, for low energy electrons, which make the electron scattering structure dependent and strongly anisotropic [19, 24]. The anisotropy of coherent scattering leads to a difference between the effective mean free paths for the transfer of energy and momentum [24, 57]. It has been shown that the effective mean free path for the transfer of energy is independent of the liquid structure, while the effective mean free path for the transfer of momentum is structure dependent [24, 57]. The coherent scattering effects and the modification of the scattering potential strongly influence the elastic scattering of the lower energy electrons. However, these effects are reduced with an increasing energy becoming negligible for electron energies higher than approximately 10 eV [39, 57]. This is demonstrated by the density independence of the measured drift velocity for swarms of electrons in compressed gases under high electric fields [58, 59].

Excitations in liquid xenon have been investigated in spectroscopy experiments [60–65]. It has been shown that the reflection spectrum of liquid xenon is very similar to the reflection spectrum of solid xenon [60, 61]. In this spectrum, intermediate $n = 1 \left[\Gamma\left(\frac{3}{2}\right)\right]$ and $n' = 1 \left[\Gamma\left(\frac{1}{2}\right)\right]$ excitons have been observed at 8.2 eV and 9.45 eV, respectively [61–63]. The former has parentage in the excited atomic $6s[3/2]_1$ state, while the latter has parentage in the $6s'[1/2]_1$ state [63]. In addition, a spectral line, which has developed from the two neighboring $5d[3/2]_1$ and $7s[3/2]_1$ states, has been observed at about 10.32 eV [63, 66]. Another spectral line has been observed at 9 eV [61–63]. This line belongs to the $n = 2$ $\left[\Gamma\left(\frac{3}{2}\right)\right]$ Wannier exciton, which does not originate from the states of an isolated atom [61–63]. Since excitons are closely related to the electron band structure, the presence of excitonic lines in the reflection spectrum indicates the existence of the valence band and the conduction band in liquid xenon [66]. In addition, the value of $\Gamma\left(\frac{3}{2}\right)$ band gap has been determined from the corresponding Wannier series [67]. The obtained value of the band gap is 9.22 eV, and it is in excellent agreement with the prediction on the change of the corresponding band gap in the solid phase [66, 67]. This value has been further verified by using the measured photoconductivity threshold in liquid xenon (9.202 eV) and the known difference between the photoconductivity threshold and the $\Gamma\left(\frac{3}{2}\right)$ band gap in the solid xenon (0.013 eV) [67].

Thus, a cross section set for electron scattering in liquid xenon has to include the cross sections for elastic scattering, inelastic energy losses and the interband transitions [40, 41]. We employ four different cases for representing the inelastic energy losses in order to study the influence of the inelastic collisions on the transport properties of electron swarms and the dynamics of negative streamers in liquid xenon. Each of these cases is discussed in light of previous spectroscopy and photoconductivity experiments. Elastic scattering and the interband transitions are represented in the same way in all cases considered.

2.1. Elastic scattering and interband transitions

The elastic scattering of low energy electrons is strongly influenced by the changes in the scattering potential and the coherent scattering effects [19, 24, 26, 34]. Moreover, the effective mean free paths for the transfer of momentum and energy in liquids are different due to a strong anisotropy of coherent scattering [24, 57]. These mean free paths are given by

$$\Lambda_0 = (n_0 \sigma_m)^{-1}$$
$$= \left(n_0 2\pi \int_0^\pi d\chi \sin\chi (1 - \cos\chi) \sigma_{sp}(\epsilon, \chi)\right)^{-1}, \quad (1)$$

$$\Lambda_l = (n_0 \tilde{\sigma}_m)^{-1}$$
$$= \left(n_0 2\pi \int_0^\pi d\chi \sin\chi (1 - \cos\chi) \sigma_{sp}(\epsilon, \chi) S(\Delta k)\right)^{-1}, \quad (2)$$

where n_0 is the liquid number density, $\sigma_{sp}(\epsilon, \chi)$ is the differential cross section for elastic scattering of an electron on a focus atom in the liquid phase, ϵ is the relative energy in the center of mass frame, χ is the angle through which the relative velocity is changed and $S(\Delta k)$ is the static structure factor, as a function of the transferred momentum. In these equations $\tilde{\sigma}_m$ and σ_m represent the momentum transfer cross sections with and without the structure modification, respectively [57].

As proposed by Tattersall and co-workers, the ratio $\gamma(\epsilon) = \frac{\Lambda_0}{\Lambda_l}$ represents the measure of the anisotropy of coherent scattering [57]. The coherent scattering is modeled as a combination of three distinct effective scattering processes, which give a good representation of the average transfer of momentum and energy [57]. In the first of these processes, represented by the σ_{both} cross section, both energy and momentum are transferred as in an ordinary binary collision [57]. In the second process, represented by the $\sigma_{momentum}$ cross section, the electron is scattered in a random direction, but the speed of the electron remains unchanged. This leads to a transfer of momentum, without a concomitant transfer of energy [57]. In the third process represented by the σ_{energy} cross section the energy of the electron is reduced as in an ordinary binary collision, but the electron does not change the direction of its motion. This leads to a transfer of energy, which is accompanied by a minimal transfer of momentum [57]. It is important to emphasize that these effective scattering processes do not represent individual microscopic collisions, but rather provide a good representation of the average rates of momentum transfer and energy transfer in structured media [57].

The cross sections for the corresponding effective processes are determined from $\gamma(\epsilon)$ and the momentum transfer cross section, for electron scattering on a focus atom in the liquid phase, $\sigma_m(\epsilon)$ [57]. The values of $\sigma_m(\epsilon)$ and $\gamma(\epsilon)$, which are used in the present work, have been determined by Boyle *et al* [34].

For $\gamma(\epsilon) < 1$ these cross sections are calculated as [57]:

$$\sigma_{\text{both}}^{\gamma < 1} = \gamma(\epsilon) \cdot \sigma_m(\epsilon)$$
$$\sigma_{\text{energy}}^{\gamma < 1} = (1 - \gamma(\epsilon)) \cdot \sigma_m(\epsilon)$$
$$\sigma_{\text{momentum}}^{\gamma < 1} = 0. \qquad (3)$$

For $\gamma(\epsilon) > 1$, these cross sections are given by [57]

$$\sigma_{\text{both}}^{\gamma > 1} = \sigma_m(\epsilon)$$
$$\sigma_{\text{energy}}^{\gamma > 1} = 0$$
$$\sigma_{\text{momentum}}^{\gamma > 1} = (\gamma(\epsilon) - 1) \cdot \sigma_m(\epsilon). \qquad (4)$$

We model the elastic scattering by using these effective cross sections, for energies up to approximately 10 eV. At higher energies both σ_{momentum} and σ_{energy} are taken to be negligible, while σ_{both} is approximated by the elastic cross section for electron scattering in the gas phase [68]. This is a good approximation, since both modifications of the scattering potential and the coherent scattering effects are small for high energy electrons [39, 57].

The cross section for interband transitions is approximated by the cross section for the electron impact ionization, from the Hayashi's cross section set, which is shifted towards lower energies. Specifically, the cross section for ionization is shifted by 2.91 eV, so that its threshold is moved to 9.22 eV. This value corresponds to the $\Gamma\left(\frac{3}{2}\right)$ band gap in liquid xenon, which is the energy difference between the uppermost valence band and the bottom of the conduction band [67]. The use of this cross section gives a good energy balance for the interband transitions, since the energy levels of excess electrons in the conduction band can be represented by a continuous energy spectrum, due to a high density of states in the conduction band [41].

We should note that the energy of the bottom of the conduction band in liquid xenon $V_0 = -(0.66 \pm 0.05)$ eV [69, 70] is not explicitly included in our calculations. This is justified since the system is homogeneous and the inclusion of V_0 would be equivalent to introducing a constant electric potential of the entire system, which would not influence the electron dynamics due to the constant value of this potential. It should also be noted that V_0 is implicitly included in the formula for the difference between the value of the ionization potential of an isolated atom and the value of the band gap in the liquid phase [40]. The inclusion of V_0 in calculations is necessary in the case of the gas-liquid interface (and other situations in which the number density of the background atoms is inhomogeneous) since the change of V_0 across the interface produces an effective electric field as shown in the recent study of Garland and co-workers [71]. Thus, in our calculations we can effectively represent discrete energy levels of quasi free electrons in the conduction band which have a minimum of V_0 with a continuous energy spectrum of free electrons which have a minimum of 0 eV.

2.2. Case 1: No electronic excitations

In the first case, the inelastic energy losses are completely neglected. It was shown by Atrazhev *et al* that this approach overestimates the first Townsend coefficient in liquid xenon [39]. However, this case is considered in our study with the aim of establishing the influence of electronic excitations on the first Townsend coefficient. This case will be referred to as case 1.

2.3. Case 2: Only excitations $6s[3/2]_2$ and $6s[3/2]_1$ are included

In our remaining cases inelastic energy losses are taken into account, since it has been shown in experiments that both excitons and perturbed atomic excitations exits in liquid xenon [62, 63]. Moreover, it has been determined that the excitation of these electronic states is the main channel of energy loss of excess electrons in liquid argon, krypton and xenon under the moderate electric fields [72–74]. However, no cross sections for the excitation of these discrete states can be found in the literature. Since intermediate excitons have unique parentage in the excited states of the atom [62, 63, 75], we approximate the cross sections for both intermediate excitons and the perturbed atomic excitations by the cross sections for the corresponding excitations of an isolated atom. The cross sections for excitations, which are used in our work, are those from the Hayashi cross section set for electrons in gaseous xenon [54, 68].

We do not change the values of the thresholds for excitations, since only thresholds for optically allowed excitons are present in the literature [75], while the optically forbidden states have to be included in our model as well. Therefore, it would be somewhat inconsistent to modify the thresholds for the optically allowed transitions, while leaving the thresholds for the optically forbidden transitions unchanged. Moreover, it has been shown that in the reflection spectrum of liquid xenon, there exists an additional line, next to the $n = 1$ $\left[\Gamma\left(\frac{3}{2}\right)\right]$ exciton line [62, 63]. This line corresponds to the perturbed atomic $6s[3/2]_1$ state [62, 63]. It was determined by Laporte *et al* that about 10% of atomic clusters in liquid xenon, near the triple point, will give rise to the perturbed atomic line, instead of the corresponding exciton line [62]. This is caused by the fact that these clusters do not have a sufficient number of atoms for the formation of the exciton inside a volume which corresponds to the exciton radius [62, 63]. Therefore, if one was to construct a model which distinguishes intermediate excitons from the corresponding perturbed atomic states, one would have to know which percentage of atomic clusters give rise to the perturbed atomic lines, instead of the corresponding excitonic lines, for each atomic excitation. In addition, one would have to know the thresholds for all excitons and all perturbed atomic excitations, including the optically forbidden states. This is beyond the scope of our paper, and we model both the intermediate excitons and the perturbed atomic excitations with the corresponding excitations of an isolated atom. However, the difference between these thresholds is less than 5% for all observed excitons [62, 63, 75]. Thus, we anticipate a small error is made by using the thresholds from the gas phase.

We neglect the observed $n = 2\,\Gamma\!\left(\frac{3}{2}\right)$ Wannier exciton, in all of our cases, since it does not correspond to any individual atomic state. No other Wannier exciton, for $n > 1$, has been identified in the reflection spectra of liquid xenon [61–63, 75]. For simplicity, in the rest of this work the interband transition and the inelastic collisions will be sometimes referred to as ionization and excitations, respectively. Comparing to binary inelastic collisions, these processes are not the same, as every xenon atom is located in a cluster of the surrounding atoms. Thus, atomic excitations are replaced either by excitons or by perturbed atomic excitations, depending on the size of the atomic cluster [62, 63]. Likewise, binary ionization is replaced by the excitation of an electron from the valence band to a quasi free state in the conduction band [66, 67].

In the second case, only excitations with thresholds, which are lower than the threshold of the interband transition, are included in the cross section set. This includes $6s\,[3/2]_2$ and $6s\,[3/2]_1$ atomic states. These two excitations correspond to the first two inelastic collisions in the Hayashi's cross section set [54]. The former of this state is optically forbidden, while the latter is optically allowed. Both the $n = 1$ $\left[\Gamma\!\left(\frac{3}{2}\right)\right]$ exciton, and the corresponding perturbed atomic state, which have been observed in experiment [61–63], have parentage in the second of these excitations.

2.4. Case 3: The first four excitations from the Hayashi's set of cross sections are included

In the previous experimental investigation of photo-conductivity in liquid xenon it has been shown that other discrete states should also be included in the set of cross sections. Specifically, a dip has been observed in the photo-conductivity spectra of liquid xenon at 9.45 eV [67]. This dip is induced by the competition between continuous band to band transitions and the discrete $n' = 1\left[\Gamma\!\left(\frac{1}{2}\right)\right]$ exciton [67]. The observed dip in the photoconductivity spectra of liquid xenon indicates that the corresponding discrete state has decay channels alternative to dissociation like luminescence [66]. This indicates that the inelastic energy losses due to this discrete state should be included in the modeling of electron transport in liquid xenon. The $n' = 1\,\Gamma(\frac{1}{2})$ exciton has parentage in the $6s'[1/2]_1$ atomic state [62, 63]. Another atomic excitation exists between $6s\,[3/2]_1$ and $6s'[1/2]_1$ states [54]. This is the optically forbidden $6s'[1/2]_0$ state. In this case it is important to take into account both $6s'[1/2]_0$ and $6s'[1/2]_1$ states, in addition to the excitations which are included in the second case. The $6s'[1/2]_0$ state corresponds to the third electronic excitation in the set of cross sections developed by Hayashi [54]. The fourth electronic excitation in the Hayashi's cross section set corresponds to a combination of $6s'[1/2]_1$ and $6p\,[1/2]_1$ states [54]. Thus, we include the first four excitations from the Hayashi's cross section set in our third case. This case will be referred to as case 3.

2.5. Case 4: All electronic excitations from Hayashi's cross section set are included

In the experimental investigation of the photoconductivity spectra of liquid xenon near the triple point, no further structure could be ascertained above 9.45 eV [67], and the photoconductivity spectra has only been shown for energies lower than 10 eV [67]. However, in a latter experimental investigation of the density dependence of the photo-conductivity spectra in fluid xenon by Reininger *et al*, two more dips have been observed for densities up to 77.86% of the triple point density [66]. This is the highest density for which results are reported in their study. The first of these dips is at 10.32 eV corresponding to the discrete transition, which is formed from the two neighboring $5d\,[3/2]_1$ and $7s\,[3/2]_1$ states [66]. The second dip is caused by the perturbed $5d'[3/2]_1$ atomic state and it is observed at 11.6 eV [66].

Thus, it is clear that the discrete states with energies above 10 eV exist in liquid xenon, since a line at 10.32 eV has been observed in the reflectivity spectra [60, 62, 63]. It is also clear that they cause dips in the photoconductivity in fluid xenon up to densities close to the triple point density [66]. This indicates that these states should be included in the calculation of inelastic energy losses of electrons in fluid xenon. However, we are not certain if these discrete states should be included in the representation of the inelastic energy losses in liquid xenon, or if they dissociate into a quasi-free electron in the conduction band and a quasi-free positive hole in the valence band. The presence of the line at 10.32 eV in the reflection spectrum of liquid xenon [60, 63] seems to indicate that these states have alternative decay channels to dissociation due to luminescence. This means that they also contribute to inelastic energy losses of excess electrons. We are not certain which percentage of these discrete states dissociates into a quasi-free electron and a quasi-free positive hole. This case for representing the inelastic energy losses in liquid xenon is based on the assumption that these discrete states always decay through luminescence, or some other non-dissociative process. Thus, the corresponding excitations fully contribute to the inelastic energy losses of excess electrons.

The atomic $5d\,[3/2]_1$ state corresponds to the 11th excitation of Hayashi's cross section set, while the $7s\,[3/2]_1$ state is included in the 12th Hayashi's excitation [54]. The $5d'[3/2]_1$ atomic excitation, which causes a dip in the photoconductivity at 11.6 eV, is not included in Hayashi's cross section set. However, the 14th Hayashi's excitation, which corresponds to $9s\,[3/2]_2$ state, has a threshold of 11.58 eV, and it gives the effective energy loss for all excitations in this energy range in the gas phase. All other effective excitations, from the Hayashi's set, include contributions from the optically forbidden states. Therefore, we should include these excitations in our model, since the absence of the optically forbidden states in the reflection spectrum does not mean that these states do not contribute to the energy losses of excess electrons. Thus, our fourth case for representing the inelastic
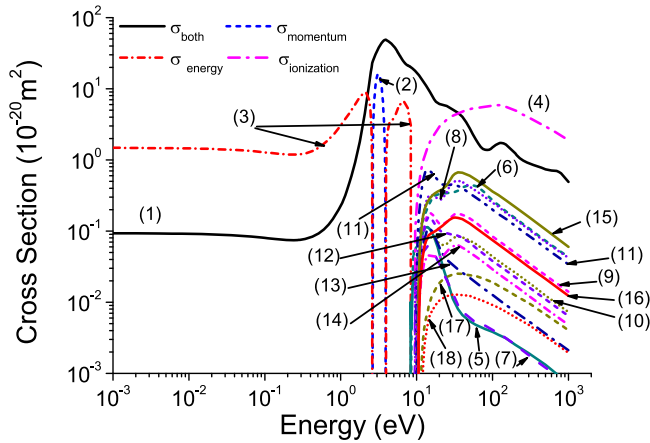
Figure 1. Cross sections for electron scattering in liquid xenon:
(1) σ_{both}, (2) $\sigma_{momentum}$, (3) σ_{energy}, (4) ionization (the interband
transition), effective electronic excitations: (5) $6s[3/2]_2$, (6)
$6s[3/2]_1$, (7) $6s'[1/2]_0$, (8) $6s'[1/2]_1$ and $6p[1/2]_1$, (9) $6p[5/2]_2$ and
$6p[5/2]_3$, (10) $6p[3/2]_1$ and $6p[3/2]_2$, (11) $5d[1/2]_0$, $5d[1/2]_1$,
$6p[1/2]_0$, $5d[7/2]_4$ and $5d[3/2]_2$, (12) $5d[7/2]_3$, (13) $5d[5/2]_2$,
(14) $5d[5/2]_3$, (15) $5d[3/2]_1$, (16) $7s[3/2]_2$, $7s[3/2]_1$, $7p[1/2]_1$,
$7p[5/2]_2$, $6p'[3/2]_1$, $7p[5/2]_3$, $6d[1/2]_0$, $6d[1/2]_1$, $7p[3/2]_2$
$6d[3/2]_2$, $7p[3/2]_1$, $7p[1/2]_0$, $6d[7/2]_4$, $6d[7/2]_3$, $6p'[3/2]_2$,
$6d[5/2]_2$, $6p[1/2]_1$, $6d[5/2]_3$, $6p'[1/2]_0$ and $6d[3/2]_1$, (17)
$8s[3/2]_2$ and (18) $9s[3/2]_2$.

energy losses in liquid xenon includes all excitations from
Hayashi's cross section set. This case will be referred to as
case 4. The cross sections for electron scattering in liquid
xenon included in all four cases considered in this work are
shown in figure 1.

3. Methods of calculation

3.1. Monte Carlo method

In this work we use the Monte Carlo method to simulate a
swarm of electrons in an infinite space, which is filled with a
homogeneous background liquid, under the action of a static
and uniform electric field. For this purpose, we have modified
our existing Monte Carlo code, which has been developed for
the study of electron transport in the gas phase [76–78]. Since
the dispersion relation for electrons in liquid xenon can be
taken to be parabolic and isotropic [40], the influence of the
liquid on the electron motion is restricted to scattering events.
Thus, the appropriate modification of the scattering dynamics
is sufficient to make our Monte Carlo code applicable to the
study of electron transport in liquid xenon. This modification
has been done by including three effective scattering pro-
cesses, which represent the coherent scattering of low energy
electrons [57]. These scattering processes are described in
section 2.1. Our study of the electron transport is performed
under the assumption that the density of charged particles is
very low (the swarm limit). Thus, we neglect the electron–
electron interactions, the space charge effects and collisions
with the results of previous collisions (holes and excited
states). Therefore, the dynamics of each electron can be fol-
lowed independently.

The dynamics of an individual electron is determined by
the action of the electric field and by collisions between the
electron and the atoms of the background liquid. The integral
equation for the collisional probability is solved numerically
by generating the random numbers from the uniform dis-
tribution on the interval (0,1) [76–78].

The type of the next collision is determined by using an
additional random number, while taking into account the
relative probabilities of all scattering processes for the
corresponding value of the electron energy [76–78]. The
change of direction of the electron motion after a collision is
represented by a pair of angles, i.e. the scattering angle and
the azimuthal angle. Isotropic scattering is assumed for all
scattering processes, except for the effective scattering pro-
cess which corresponds to the σ_{energy} cross section. In this
process the direction of the electron motion is unchanged by
the collision.

After the collision which is represented by the σ_{both} cross
section the electron energy is reduced by the factor
$\frac{2m\epsilon}{M}(1 - \cos\chi)$, where m is the electron mass, M is the mass
of a background atom, ϵ is the initial energy of the electron
and χ is the scattering angle. The same amount of energy is
lost by a low energy electron in the effective scattering pro-
cess, which is represented by σ_{energy} cross section. When an
inelastic collision, or interband transition takes place, the
energy of the incident electron is reduced by the energy loss
(i.e. the threshold energy) of the corresponding process. After
the interband transition, the remaining energy is redistributed
between the primary electron and the secondary electron. The
fraction of the postcollisional energy, which is obtained by
each of these two electrons, is determined by using an addi-
tional random number.

In our Monte Carlo code, monomials of coordinates and
velocity components of each individual electron are sampled
and averaged, over the entire electron ensemble, at discrete
sampling times [76–78]. These expressions are used to cal-
culate both bulk and flux transport coefficients of the swarm,
with explicit formulas given elsewhere [76–78].

As a large number of electrons must be followed, in order
to reduce the statistical fluctuations of the output data, our
Monte Carlo simulations are very time consuming. The
computational time is particularly large for lower values of
reduced electric field, where few inelastic collisions take
place. Under these conditions due to a small rate of energy
transfer in elastic collisions, the relaxation of energy is inef-
ficient. In order to optimize the computational time and speed
of our simulations in the limit of low reduced electric fields,
the simulations are performed with a lower number of elec-
trons until the swarm reaches the steady state. After relaxation
the swarm is multiplied several times, by cloning each elec-
tron, until the desired number of electrons is obtained. When
the multiplication is finished all transport properties are cal-
culated from average monomials of both velocities and
coordinates. For a more detailed description of our Monte
Carlo code, we refer readers to our reviews [76–78].
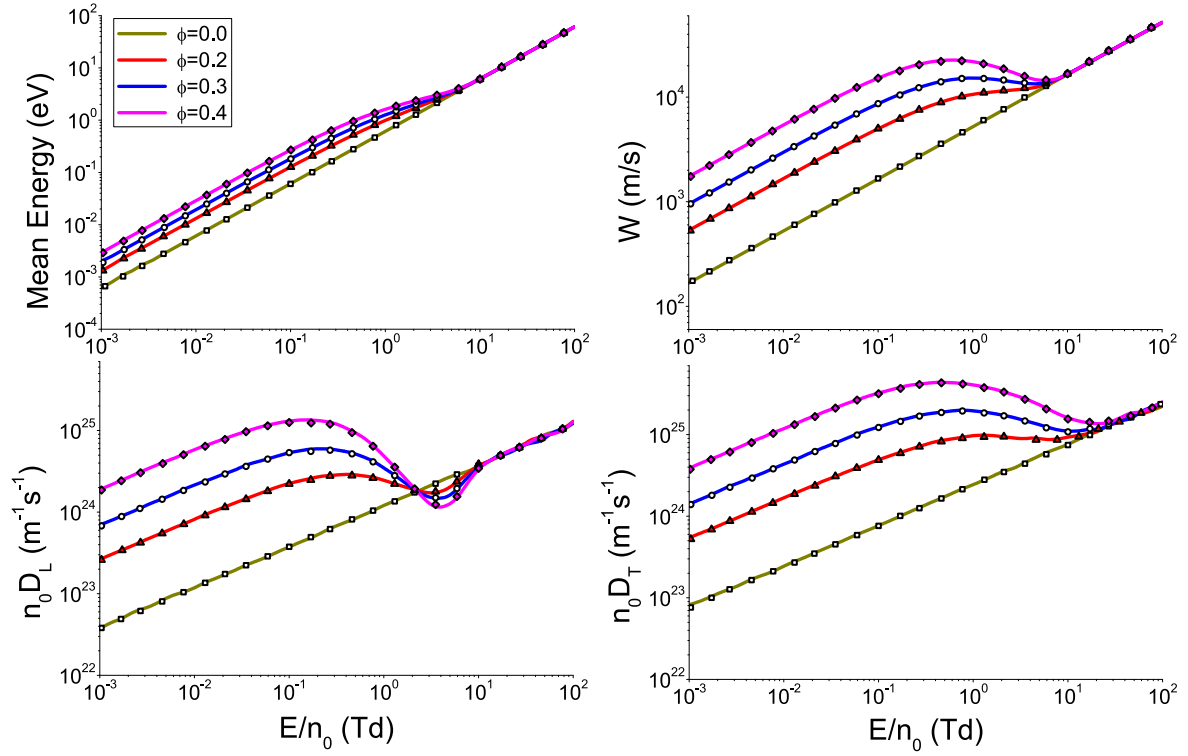
Figure 2. Comparison of our results for mean energy, drift velocity W, longitudinal diffusion coefficient $n_0 D_L$ and transverse diffusion coefficient $n_0 D_T$ of an electron swarm in the Percus–Yevick model liquid, with those of Tattersall *et al* [57]. Transport properties are presented as a function of the reduced electric field E/n_0 and the Percus–Yevick packing ratio ϕ. The present calculations are represented by lines, while the results of Tattersall *et al* [57] are represented by symbols.

3.2. Benchmark calculations

We present our benchmark calculations for the Percus Yevick model liquid, in order to test the implementation of the coherent scattering effects in our Monte Carlo code. The radial pair correlation function, which corresponds to this model, is obtained by applying the Percus Yevick approximation as a closure to the Ornstein–Zernike equation and by representing the interaction between the background molecules by the hard sphere potential [57, 79]. The corresponding static structure factor is obtained as a Fourier transform of this pair correlation function [57]. The modified Verlet and Weis structure factor for the Percus Yevick liquid [80] is used in this work, as in the study of Tattersall *et al* [57]. This structure factor is given by

$$
S(\Delta k) = \left(1 + \frac{24\eta}{\Delta k^2}\left[\frac{2}{\Delta k^2}\left(\frac{12\zeta}{\Delta k^2} - \beta\right)\right.\right.
$$
$$
+ \frac{\sin(\Delta k)}{\Delta k}\left(\psi + 2\beta + 4\zeta - \frac{24\zeta}{\Delta k^2}\right)
$$
$$
\left.\left.+ \cos(\Delta k)\left(\frac{2}{\Delta k^2}\left(\beta + 6\zeta - \frac{12}{\Delta k^2}\right) - \psi - \beta - \zeta\right)\right]\right)^{-1},
$$

$$(5)$$

where $\eta = \phi - \frac{\phi^2}{16}$, $\psi = \frac{(1+2\eta)^2}{(1-\eta)^4}$, $\beta = \frac{-6\eta\left(1+\frac{\eta}{2}\right)^2}{(1-\eta)^4}$, and $\zeta = \frac{\eta\psi}{2}$ [57]. The packing ratio ϕ determines the percentage of space which is occupied by the hard spheres. This ratio can be written as $\phi = \frac{4}{3}\pi r^3 n_0$, where r and n_0 are the hard sphere radius and the neutral number density respectively [57].

In figure 2 we show our benchmark results for mean energy, drift velocity and components of the diffusion tensor for electrons in the Percus Yevick liquid, for several values of the packing ratio ϕ. For comparison, the benchmark results of Tattersall *et al* [57] are included in the same figure. Our results are represented by lines, while the results of Tattersall and co-workers are represented by symbols. From a comparison between our results and those predicted by Tattersall *et al* [57], it is evident that the results are consistent for all E/n_0 and ϕ and for all transport coefficients. This suggests that the representation of the coherent scattering effects has been included properly in our Monte Carlo code [81].

In figure 2 we see that all transport properties are distinctively dependent on ϕ for the lower values of E/n_0. Due to coherent scattering effects, all transport properties increase with the increase of ϕ. At the higher values of E/n_0, however, the strong dependence of transport properties on ϕ is firstly reduced and then entirely removed as the influence of the coherent scattering is negligible for the high energy electrons. On the other hand, the behavior of the longitudinal diffusion coefficient D_L is more complex. We see that D_L increases with the increase of ϕ at low electric fields, but this dependence is inverted for E/n_0 between approximately 2 and 10 Td. The mean energy monotonically increases with the increase of E/n_0 for all values of ϕ. The drift velocity exhibits structure induced NDC, i.e. for E/n_0 approximately between

0.5 and 6 Td and for $\phi \geqslant 0.3$, values of drift velocity decrease as the driving field is increased. The quantitative criterion for the occurrence of the structure induced NDC has been discussed by White and Robson [82]. The decrease of the drift velocity with increasing field can be attributed to the reduction of the coherent scattering effects, which in turn enhance the directional motion of low energy electrons. The reduction of both D_L and D_T with an increasing E/n_0 is also clearly evident. In the limit of the highest E/n_0 considered, all profiles approach to that for $\phi = 0$. It is interesting to note that the values of E/n_0 for this transition decrease with increasing ϕ.

3.3. Fluid model of negative streamers

Our simulations of negative streamers in liquid xenon are performed by using a 1.5 dimensional fluid model [83, 84]. In this model, we assume that the space charge is contained inside a cylinder with radius R_0 and that the charge density varies along the axial direction only. The electron dynamics is described by the continuity equation for the electron number density

$$\frac{\partial n_e(x, t)}{\partial t} = \frac{\partial}{\partial x}\left(D_L \frac{\partial n_e(x, t)}{\partial x} + W n_e(x, t)\mathrm{sgn}(E)\right) + (\nu_i - \beta n_p(x, t))n_e(x, t), \tag{6}$$

where $n_e(x, t)$ and $n_p(x, t)$ are the number densities of electrons and positive holes, respectively, which are functions of the coordinate x and time t. In this equation D_L and W are the longitudinal diffusion and the drift velocity respectively, $\mathrm{sgn}(E)$ is the sign function of the electric field E which is oriented along the x-axis, while ν_i and β are the ionization rate and the recombination coefficient, respectively.

Since the hole mobility in liquid xenon is much smaller than the mobility of electrons [85, 86], the positive holes are assumed to be stationary, on the time scales relevant for this study. Thus, the time evolution of the number density of positive holes is described by the number balance equation

$$\frac{\partial n_p(x, t)}{\partial t} = (\nu_i - \beta n_p(x, t))n_e(x, t). \tag{7}$$

The total electric field in the system is represented as the sum of the uniform external field and the electric field due to space charge effects [83, 84]

$$E(x, t) = E_0 + \frac{e}{2\varepsilon_0 \varepsilon_r} \int_0^l \left(\mathrm{sgn}(x - x') - \frac{x - x'}{\sqrt{(x - x')^2 + R_0^2}} \right)(n_p(x', t) - n_e(x', t))\mathrm{d}x', \tag{8}$$

where E_0 is the external field, e is the elementary charge, ε_0 and ε_r are the vacuum permittivity and the relative permittivity, respectively, and l is the length of the system. The recombination coefficient is given by the scaled Debye

formula [50–52]

$$\beta = \xi\beta_{\mathrm{D}} = \xi \frac{4\pi e \mu_e}{\varepsilon_0 \varepsilon_r}, \tag{9}$$

where β_{D} is the Debye recombination coefficient, μ_e is the electron mobility, while ξ is the scaling factor which is taken to be 0.1 [10, 50, 51].

The above fluid equations are closed assuming the local field approximation—all transport properties of electrons at a given value of the coordinate x and time t are determined by the local instantaneous electric field, $E(x, t)$ and are evaluated from data computed in Monte Carlo simulations. In the numerical implementation of our fluid model, the spatial discretization is performed by using the second order central finite difference, while the fourth order Runge–Kutta method is used for the integration in time. In fluid simulations we follow the transition of an electron avalanche into a negative streamer and its subsequent propagation in liquid medium.
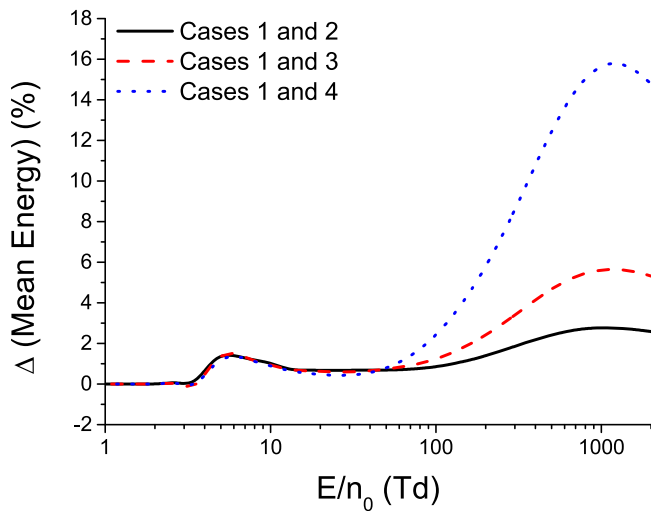
4. Results and discussion

4.1. Transport coefficients for electrons in liquid xenon

In our study of the transport properties of electrons in liquid xenon we cover a range of reduced electric fields between 1×10^{-3} and 2×10^3 Td. The number density of xenon atoms is 1.4×10^{28} m^{-3}, while the temperature of the background liquid is 163 K. For E/n_0 higher than 10 Td, we follow 10^6 electrons during the entire simulation. However, at lower fields our simulations begin with 10^4 electrons and after the relaxation to the steady state the electron swarm is gradually scaled up to 10^6 electrons by cloning each electron at fixed time intervals. The initial velocities of electrons are randomly selected from a Maxwell–Boltzmann velocity distribution which corresponds to a mean energy of 1 eV. All electrons start their trajectories from the same point in space. This point is chosen as the origin of our coordinate system. The cross sections for electron scattering employed in this work are shown in figure 1. The mean energy, drift velocity and diffusion coefficients are shown for cases 1 and 4, as differences between individual cases are too small to be clearly distinguished on logarithmic scale.

4.1.1. Mean swarm energy.
The comparison of the mean energies of electron swarms in liquid and gaseous xenon is shown in figure 3. For the lower values of electric fields up to approximately 0.6 Td, the mean energy is higher in liquid xenon than in gaseous xenon due to a significant reduction of the cross section for elastic scattering of the lower energy electrons in the liquid phase. Such behavior is different at higher fields as the mean energy of electrons approaches 1 eV, owing to the fact that the electron scattering in atomic liquids is similar to the scattering in dilute gases for the electron energies higher than 1 eV [19, 34]. The mean energy is lower in the liquid phase than in the gas phase for E/n_0 between approximately 0.6 and 350 Td. At the lower edge of this field region, the difference between the mean
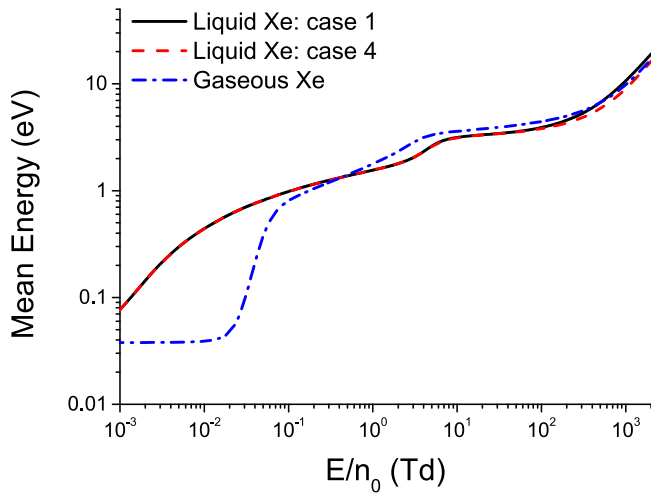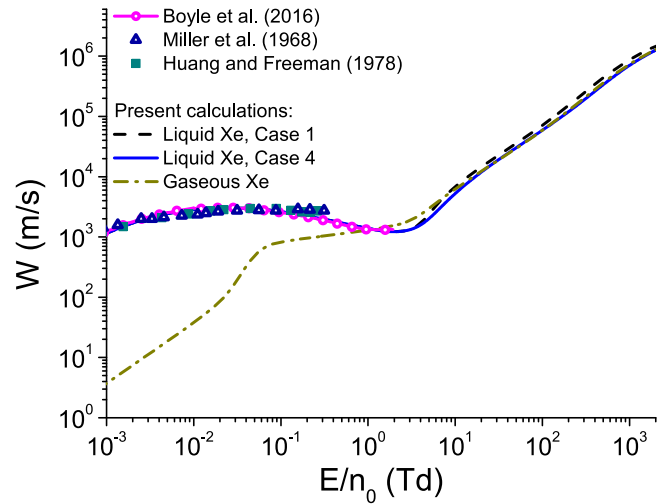
Figure 3. Comparison of the mean energies of electrons in gaseous and liquid xenon. The values of mean energy in liquid xenon, determined by employing two different methods for representing the inelastic energy losses, are shown. In the first case all excitations are neglected, while in the fourth case all excitations from Hayashi's cross section set for electron scattering in gaseous xenon [54, 68] are included.

Figure 5. Comparison of the measured drift velocities in liquid xenon (Miller *et al* [88] and Huang and Freeman [89]) with the theoretical calculations. The theoretically determined drift velocities in liquid xenon include those of Boyle *et al* [34] as well as the bulk drift velocities calculated in this study by employing two different methods for representing the inelastic energy losses. The bulk drift velocity of electrons in gaseous xenon is also shown in this figure for comparison.

Figure 4. Percentage difference between the values of mean energy, for electrons in liquid xenon, which are determined by using different representations of the inelastic energy losses. All excitations are neglected in the first case. In the second and the third cases only the first two ($6s[3/2]_2$ and $6s[3/2]_1$) and the first four ($6s[3/2]_2$, $6s[3/2]_1$, $6s'[1/2]_0$ and an effective excitation which represents both $6s'[1/2]_1$ and $6p[1/2]_1$) excitations from the cross section set of Hayashi [54, 68] are included. All excitations from the cross section set of Hayashi are included in the fourth case.

energies in gaseous and liquid xenon can be attributed to the greater amount of energy losses in elastic collisions in the liquid phase in the energy region between approximately 0.4 and 10 eV [34]. This is represented by the combined effect of the scattering processes which correspond to σ_{both} and σ_{energy} cross sections. For E/n_0 between approximately 3 and 350 Td this energy difference is caused by the intensive ionization cooling in the liquid phase. Ionization

cooling of an electron swarm in gases has been discussed by Robson and Ness [87]. At higher fields the mean energy in the first case for representing excitations in liquid xenon is slightly higher, while the mean energy in the fourth case is slightly lower, than the mean energy in the gas phase.

In figure 4 we show the percentage difference between the calculated mean energy, assuming the first and the remaining three cases. This difference is negligible for E/n_0 less than 2 Td as electrons undergo elastic collisions only. For E/n_0 higher than 2 Td the mean energy reaches the highest value in the first case due to the absence of inelastic energy losses. The percentage differences between the values of mean energy in the first case and the remaining three cases reach two local maximums at about 5 and 1000 Td, and a local minimum around 27 Td. The first local maximum occurs due to the absence of inelastic energy losses, lower than the threshold energy for ionization, in the first case. The local minimum appears in the field region in which the energy losses due to ionization become comparable to the inelastic energy losses. For E/n_0 higher than 50 Td, the mean energy decreases with the increase of the number of excitations which are included in the model. This is a consequence of a significant competition between ionization and excitations with thresholds higher than 9.22 eV in this field region. The percentage difference between the mean energy in the first case and the remaining cases never exceeds 3%, 6% and 16% for the second, third and fourth cases respectively. Even though the percentage difference between the values of mean energy in various cases decreases for E/n_0 greater than 1000 Td, the absolute difference continues to rise monotonically in the entire field region covered in this study. For the values of E/n_0 lower than 50 Td, these differences are
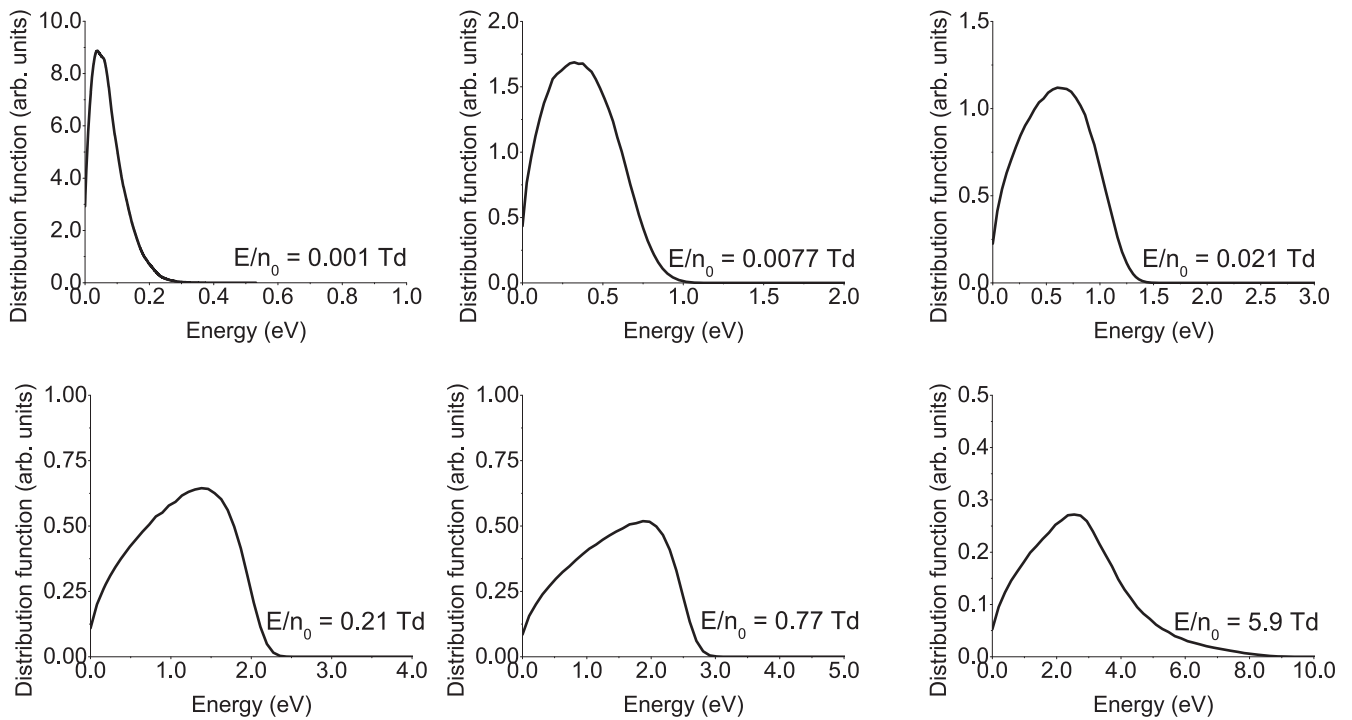
Figure 6. Energy distribution function of the electrons for various E/n_0 as indicated on the graph. Calculations are performed assuming the case 2 where excitations $6s[3/2]_2$ and $6s[3/2]_1$ from the set of cross sections developed by Hayashi are included.

very small and are close to the statistical uncertainty of the Monte Carlo simulations.

4.1.2. Drift velocity and NDC.　In figure 5 we show bulk drift velocities assuming the first and the fourth cases for representing the inelastic energy losses as a function of E/n_0. For comparison, the theoretical [34] and experimental [88, 89] drift velocities in liquid xenon determined by previous authors are displayed in the same figure, along with the bulk velocity in gaseous xenon. For the values of E/n_0 lower than 1 Td, the drift velocity in the liquid phase exceeds the drift velocity in the gas phase. This is a consequence of the significant reduction of the rate for momentum transfer of the lower energy electrons in liquid xenon due to the modifications of the scattering potential and the coherent scattering effects. The lowering of the rate for momentum transfer enables the electric field to accelerate electrons more efficiently in liquid xenon than in the gas phase, which leads to a significant enhancement of the drift velocity compared to the gaseous xenon. However, this effect is reduced at higher fields as the scattering of a high energy electron on a xenon atom is weakly perturbed by the surrounding liquid. Thus, for the values of E/n_0 between approximately 0.02 and 2 Td the drift velocity in liquid xenon decreases with increasing field, until it reaches the values that are close to the drift velocity in gaseous xenon. The reduction of the drift velocity with increasing E/n_0 is a phenomenon that is well known as NDC [90–92]. While this phenomenon is caused by inelastic and non-conservative collisions in various gases [90, 92], the NDC observed in liquid argon and liquid xenon is entirely structure induced phenomenon [19, 34, 82]. The quantitative

criterion for the occurrence of the structure induced NDC has been discussed by White and Robson [82]. At the end of the field region, which corresponds to NDC, the drift velocity in gaseous xenon slightly exceeds the drift velocity in liquid xenon. For the values of E/n_0 higher than 10 Td the bulk drift velocity in the first case exceeds the bulk drift velocities in all other cases as well as the bulk drift velocity in the gas phase due to the strongest explicit effects of ionization in this case.

In order to understand the occurrence of NDC in liquid xenon at low electric fields, in figure 6 we show the energy distribution functions for a few values of E/n_0. Results are presented for the case two only, as the rate coefficients for those inelastic processes excluded in this case are negligible over the range of reduced electric fields considered. At low electric fields, up to approximately 0.008 Td, the majority of electrons have energies below approximately 0.7 eV. The cross section for momentum transfer is very small over the range of energies less than 0.7 eV and hence the drift velocity in liquid xenon is much greater than in the gas phase. However, for E/n_0 greater than approximately 0.02 Td (at this particular value of E/n_0 NDC begins to develop) a large fraction of electrons have energies between approximately 0.7 and 2 eV. There is a rapid rise in both σ_{both} and σ_{energy} with increasing energy in this region. As a consequence, these two cross sections quickly approach the cross section for elastic collisions in the gas phase. For E/n_0 between 0.2 and 1 Td the majority of the high energy electrons have energies between 1.5 and 3 eV where the cross sections σ_{both} and $\sigma_{momentum}$ increase rapidly and approach their maximal values. The rapid rise of both σ_{both} and $\sigma_{momentum}$ leads to a decrease of the drift velocity with increasing E/n_0. For E/n_0 higher than approximately 5 Td a large fraction of electrons have energies
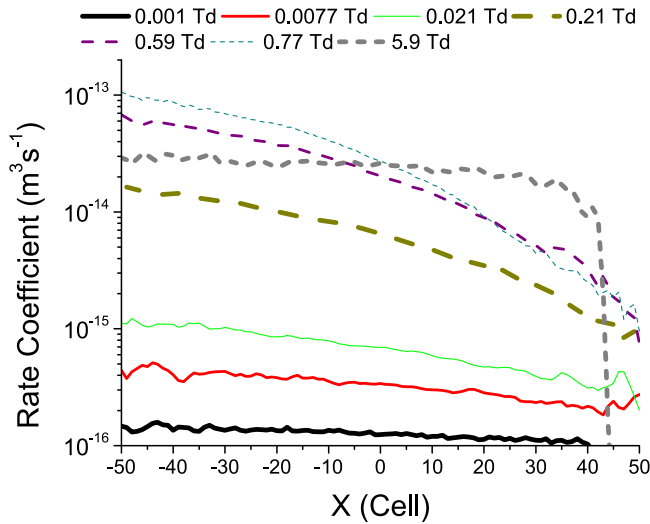
Figure 7. Spatially-resolved rate coefficient for the σ_{both}. Calculations are performed assuming the case 2 where excitations $6s[3/2]_2$ and $6s[3/2]_1$ from the set of cross sections developed by Hayashi are included.


Figure 8. Percentege difference between the values of drift velocities, for electrons in liquid xenon, which are determined by using different methods for representing the inelastic energy losses. These methods are described in the caption of figure 4. Flux and bulk results are represented by solid lines and dashed lines, respectively.

higher than approximately 4 eV, and at these energies the cross section for elastic scattering rapidly drops off with an increase of electron energy. In this range of fields, the drift velocity monotonically increases with E/n_0.

We may also observe that over the range of E/n_0, where the structure induced NDC occurs, the high-energy tail of the distribution function quickly drops off with increasing energy. This is caused due to rapid increase of energy transfer associated with the σ_{both} and σ_{energy}. For E/n_0 lower than approximately 0.008 Td and higher than approximately 4 Td, the high-energy tail of the distribution function drops off more slowly.

In figure 7 we show the spatially-resolved rate coefficient for the σ_{both}. In order to sample spatially-resolved rate coefficients we have divided the real space into cells. The space is divided uniformly into 100 cells in such a way that cells indexed by $(-50, +50)$ correspond to the real coordinates $(x_{cm} \pm 3\sigma)$, where x_{cm} is the coordinate of the center of mass of the swarm, and the σ is the standard deviation of the x-coordinate of the electrons [93]. Comparing the leading and trailing edges of the swarm, this property is higher at the leading edge where the average energy of the electrons is always greater than at the trailing edge. The slope of the spatially-resolved rate coefficient is the largest over the range of E/n_0 where NDC occurs. Moreover, we observe that the maximal values of this property at the leading edge of the swarm are higher for 0.59 and 0.77 Td than for a higher value of 5.9 Td. A similar behavior is observed for the spatially-resolved rate coefficient for the $\sigma_{momentum}$.

The drift velocity calculated in our study is in an excellent agreement with the theoretical results of Boyle *et al* [34]. Our values of the drift velocity are close to those predicted in the experiments of Miller *et al* and Huang and Freeman [88, 89]. However, while most theoretical calculations of the drift velocity predict a structure induced NDC, this effect has not been observed in the experiments. In the
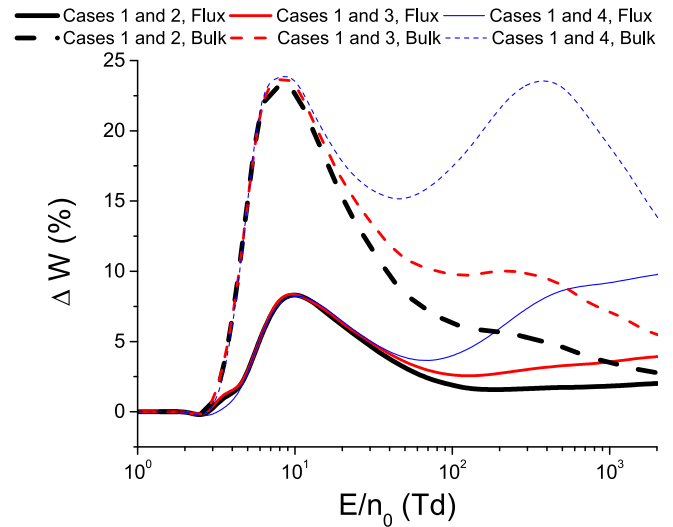
field region which corresponds to the onset of the structure induced NDC of the theoretically determined drift velocity, the experimental drift velocity saturates with increasing field. At higher fields, no experimental results are available.

This discrepancy between theoretical and experimental results has been attributed by Sakai *et al* [32] to the presence of additional channels of energy loss in liquids, which are not included in the existing theoretical models. These energy losses correspond to the changes in the translational states of pairs and triplets of xenon atoms upon the electron impact, and they occur for energies much lower than the first threshold for excitations [20, 32]. Sakai and co-workers have empirically derived the sets of cross sections for electron scattering in liquid argon, krypton and xenon [32] which include effective cross sections for representing these additional energy losses. However, an alternative explanation for this discrepancy between theory and experiment could be the presence of molecular impurities in the liquid rare gases used in the experiments. Indeed, it has been shown by Sakai *et al* [32] that even a small amount of molecular impurities in liquefied rare gases leads to a significant enhancement of the electron drift velocity. It might also be the case that the structure induced NDC would be observed in the profiles of the experimentally determined drift velocity at higher electric fields. Further experimental and theoretical investigations are required for the resolving this discrepancy. Thus, the measurement of the drift velocity of electrons in liquid xenon at higher electric fields is of a great importance. In any case, we do not include the effective cross section developed by Sakai *et al* [32] in our model, as it is not adjusted to our cross section for elastic scattering.

In figure 8 we show the percentage difference between the calculated drift velocity assuming the first and the remaining three cases. The flux drift velocity increases with the decrease of the number of excitations, which are
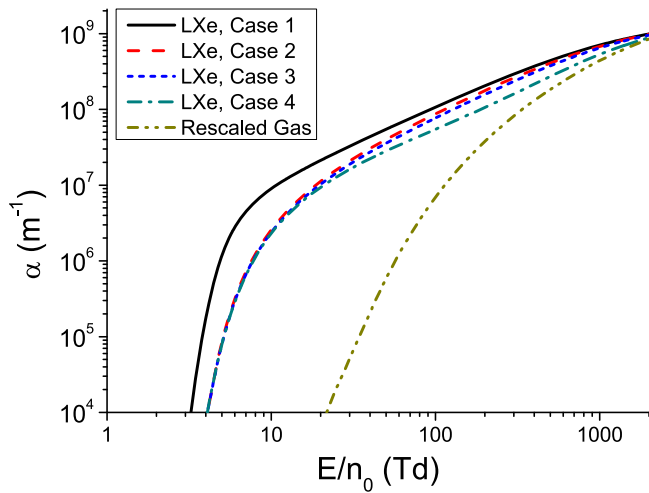
Figure 9. Variation of the first Townsend coefficient with E/n_0 for electrons in liquid xenon. Calculations are performed by assuming all four different methods for representing the inelastic energy losses. These methods are described in the caption of figure 4. The first Townsend coefficient for gaseous xenon, which is scaled up to liquid density is also shown, for comparison.

Figure 10. Comparison between the theoretical calculations of the first Townsend coefficient α determined in this study and the results of previous authors. These results include the measurements of Derenzo *et al* [56] and calculations of Atrazhev *et al* [39], Jones and Kunhardt [40] and Nakamura *et al* [53].

considered in the model. This is caused by the lowering of the chaotic component of the electron velocity due to the increase of the ionization cooling with the reduction of the inelastic energy losses [87]. In the case of the bulk drift velocity, this increase is even more pronounced due to the explicit effects of ionization. The percentage difference between drift velocities determined in the first case and the remaining three cases has a local maximum at about 8 Td, as the relative difference between rates for ionization has the highest values at low electric fields. This local maximum has a value of about 8% and 24% for flux and bulk drift velocity, respectively. For E/n_0 higher than 100 Td, the percentage difference between flux drift velocities in the first case and the last two cases rises due to increasing rates for inelastic collisions with thresholds higher than 9.22 eV in this field region. The percentage difference between the corresponding bulk drift velocities reaches another local maximum at about 200 Td and 400 Td for the third and the fourth cases respectively. Although the percentage difference between bulk drift velocities in different cases decreases after the last local maximum, the absolute difference monotonically increases in the entire field region below 2000 Td.

4.1.3. First Townsend coefficient. The first Townsend coefficient expresses the number of ion pairs generated by an electron per unit length. It is equal to the ionization collision frequency divided by the electron drift velocity. Our calculations of the first Townsend coefficient α determined by using different representations of the inelastic energy losses in liquid xenon are shown in figure 9. The first Townsend coefficient in gaseous xenon is scaled up to the liquid density and displayed in the same figure for comparison. It can be seen that α monotonically increases with increasing field in all four cases for representing the inelastic energy losses. We also observe that α is reduced with increasing number of
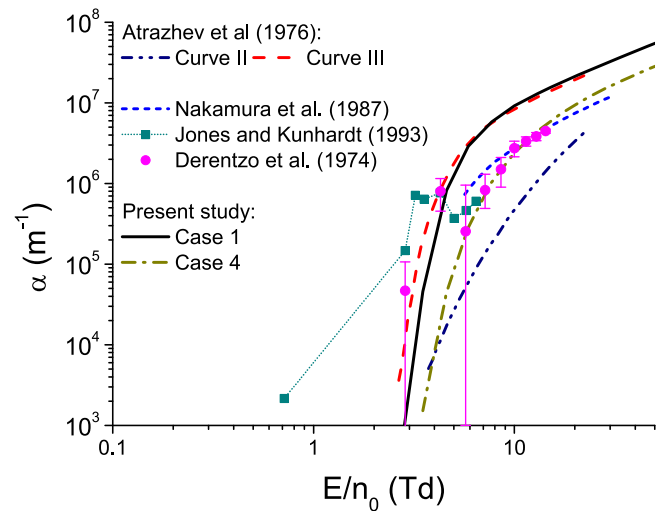
included excitations. In the first case, where all excitations are neglected, the coefficient α overestimates those calculated in the remaining three cases over the range of E/n_0 considered. While the absolute difference between the first Townsend coefficient in the first case and the remaining cases increases over the entire E/n_0 range covered in this study, the relative difference has the highest values at E/n_0 lower than approximately 20 Td. For E/n_0 greater than 20 Td the ionization rate coefficient in the fourth case, where all excitations are included, becomes significantly lower than the corresponding rate coefficients in the other three cases. This is a consequence of the increasing inelastic energy losses which have thresholds higher than 9.22 eV in this case.

The first Townsend coefficient in liquid xenon is much higher than the rescaled coefficient in gaseous xenon for E/n_0 lower than 100 Td. In the limit of the highest E/n_0 considered in the present work, however, we observe that the deviations between the ionization coefficients in liquid and rescaled gas are significantly reduced. One of the main reasons for the significant difference between the rate coefficients for ionization in the scaled gaseous xenon and liquid xenon is the reduction of the threshold for ionization in the liquid phase. An electron in gaseous xenon can undergo ionization only at energies higher than 12.13 eV. Moreover, it can lose a significant amount of energy in a wide range of inelastic scattering processes at energies lower than the threshold energy for ionization. However, in liquid xenon any electron with the energy higher than 9.22 eV can excite an electron from the valence band to the conduction band. Furthermore, there is a far lower number of inelastic scattering processes with thresholds which are lower than the threshold for ionization in the liquid phase compared to the gas phase.

In figure 10 we show the first Townsend coefficient measured by Derenzo *et al* [56] along with the theoretical results obtained by previous authors [39, 40, 53]. The values

of the first Townsend coefficient determined in this study by assuming the first and the fourth cases for representing the inelastic collisions are displayed in the same figure for comparison. The experimental results of Derenzo *et al* [56] are significantly higher than the values of α for electrons in gaseous xenon which are scaled to liquid density. An unusual feature of the first Townsend coefficient measured by Derenzo and co-workers is a non-monotonous behavior with the increase of the reduced electric field. However, this non-monotonicity is not outside the range of experimental uncertainty.

The two sets of results determined by Atrazhev *et al* [39] are calculated by assuming two different methods for representing the inelastic energy losses. The values of α represented by curve II are determined under the assumption that the percentage of inelastic energy losses in the liquid phase are just the same as in the gas phase [39]. This curve is significantly below all other curves presented in this figure. The underestimation of α in curve II demonstrates the significant reduction of the inelastic energy losses in liquid xenon compared to gaseous xenon as discussed by Atrazhev *et al* [39]. The values of α represented by curve III are determined by completely neglecting the inelastic energy losses in liquid xenon. This curve is in the best agreement with the first two experimental points of Derenzo *et al* [56] and with our case 1. The first Townsend coefficient determined by Jones and Kunhardt [40] is the only present theoretical result which predicts the non-monotonic behavior of α and it is in a good agreement with the first four experimental points of Derenzo *et al* [56]. However the values of α at higher fields are not shown in their work. The results of Nakamura *et al* [53] agree very well with the last segment of experimental points of Derenzo *et al* [56], while the values at lower fields are not displayed in their paper.

While our case 1 for representing the inelastic energy losses is in the best agreement with the first two experimental points of Derenzo *et al* [56], all other experimental points are in an excellent agreement with our remaining three cases. No experimental data are present in the field range in which there is a significant difference between our last three cases for representing the inelastic collisions in liquid xenon. However, the last two experimental points of Derenzo *et al* [56] are in a slightly better agreement with our fourth case than with the remaining cases.

A possible explanation for the high values of the first two experimental points determined by Derenzo *et al* [56] is the presence of another mechanism for populating the conduction band in liquid xenon, which is more significant than electron impact ionization at low electric fields. One example of such a mechanism is the dissociation of high order Wannier excitons ($n > 1$) due to scattering on the walls of the system, or under the influence of some other perturbation. Another possible explanation is the reduction of the inelastic energy losses at energies lower than 9.22 eV due to some other effects, which are not included in our model.
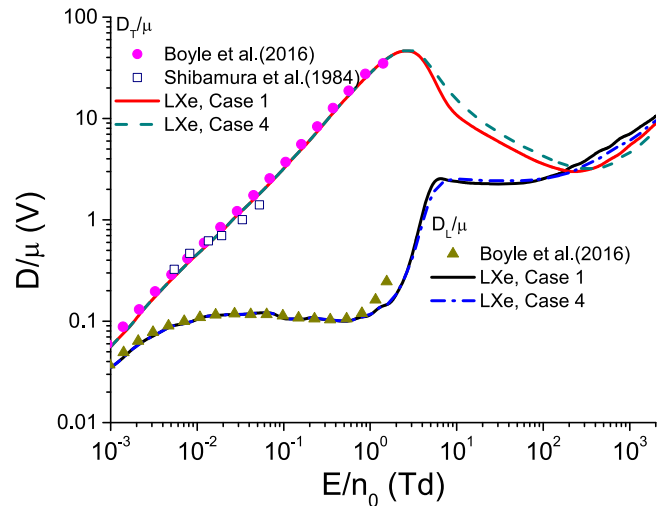
Figure 11. Comparison between the present calculations and those predicted by a multi term solution of the Boltzmann equation (Boyle *et al* [34]) and experimental measurements (Shibamura *et al* [94]) for the bulk values of D_L/μ and D_T/μ. Our results are evaluated by assuming the cases 1 and 4.

4.1.4. Longitudinal and transverse diffusion coefficients. In figure 11 we show the variation of D_L/μ and D_T/μ with E/n_0 assuming the first and the fourth cases for representing the inelastic collisions in liquid xenon. The calculated values of these quantities obtained by Boyle *et al* [34] are also displayed in the same figure for comparison, along with the characteristic energy measured by Shibamura *et al* [94]. Here D_L and D_T denote the longitudinal and the transverse components of the bulk diffusion tensor, while μ is the bulk mobility of electrons. The characteristic energy D_T/μ initially increases with increasing E/n_0, reaching a local peak around 2 Td, and then starts to decrease with E/n_0. For E/n_0 higher than approximately 300 Td, we see that D_T/μ again increases with E/n_0. The E/n_0 dependence of D_L/μ is more complicated. First, there is a region of slow rise of D_L/μ with increasing E/n_0 due to a reduction of the momentum transfer of the lower energy electrons in liquid xenon. Second, there is a region of slow decrease for E/n_0 between approximately 0.05 and 0.4 Td, and then for E/n_0 up to approximately 6 Td there is again a region of rapid rise. Between approximately 6 and 30 Td D_L/μ is reduced as the inelastic collisions start to exert their influence on the swarm. Finally, D_L/μ rises again as the electrons start to rapidly gain energy from the electric field. The complex behavior of D_L/μ in liquid xenon reflects the high sensitivity of this property with respect to the details of cross sections.

We also observe that D_L/μ agree very well with the results of Boyle *et al* [34] for E/n_0 lower than 0.7 Td. However, our results are lower than those of Boyle and co-workers at higher electric fields. The discrepancy can be attributed to the difference in the employed cross sections for the electron scattering, as Boyle and coworkers have neglected the inelastic collisions in their study. As the mean energy of electrons is around 1.8 eV at 1 Td, the most energetic electrons have enough energy to undergo inelastic collisions. The present calculations
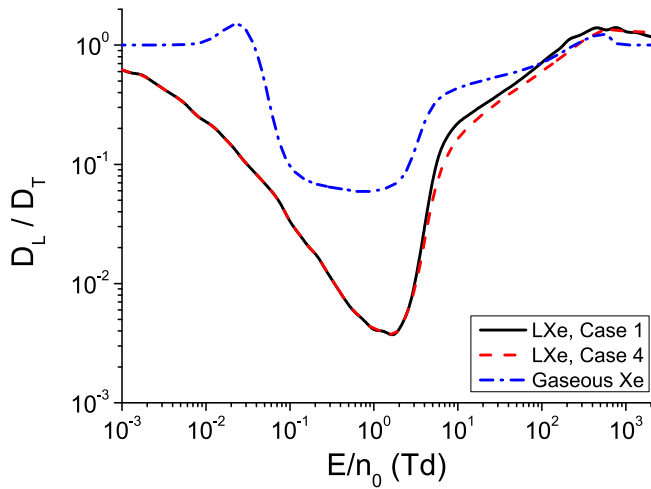
Figure 12. Comparison of the ratios between the bulk longitudinal diffusion and the bulk transversal diffusion in liquid xenon assuming cases 1 and 4 and the same ratio in gaseous xenon. These cases are described in the caption of figure 3.

of D_T/μ are in a good agreement with those predicted by Boyle *et al* [34] and Shibamura *et al* [94].

In figure 12 we show the ratio D_L/D_T for electrons in liquid xenon assuming the first and the fourth cases for representing the inelastic energy losses. The values of D_L/D_T for electrons in gaseous xenon are shown in the same figure for comparison. For electrons in liquid xenon this ratio is decreasing with increasing field up to approximately 1 Td, due to the rising rates for elastic scattering in this field region. However, this ratio is increasing at higher fields due to the reduction of the rate for elastic scattering of high energy electrons. The E/n_0 dependence of this ratio is different for electrons in gases at low electric fields. For the values of E/n_0 lower than 10^{-2} Td this ratio is constant in the gas phase as the mean energy of electrons is very close to the thermal values. There is a narrow range of the reduced electric field between approximately 10^{-2} and 2×10^{-2} Td in which this ratio is rising with increasing field, due to the influence of the Ramsauer–Townsend minimum. At higher fields the qualitative trend of behavior of D_L/D_T is the same for electrons in liquid and gaseous xenon though the minimum is more pronounced in the liquid phase.

4.2. Streamer calculations

In our fluid simulations, we follow the transition of an electron avalanche into a negative streamer as well as the subsequent propagation of this streamer. The initial condition for both electrons and positive holes is a Gaussian distribution which is given by

$$n_e(x, 0) = \frac{300}{0.05\pi R_0^2 \frac{l}{3}\sqrt{2\pi}} \exp\left(-\frac{(x - 0.95l)^2}{2\left(0.05\frac{l}{3}\right)^2}\right). \quad (10)$$

This Gaussian is positioned near the cathode. It should be noted that the initial number densities of electrons and positive holes are selected so that the space charge effects are

negligible. The values of l and R_0 are set to 5×10^{-5} m and 1×10^{-5} m respectively. The particular value of R_0 is chosen as an educated guess taking into account the initial distribution width and the spreading due to transverse diffusion. This value is in a good agreement with the values evaluated by the other authors [50, 51]. The length of the system l is determined by the requirement that the streamer velocity relaxes to a stationary value. The number of spatial cells used in our fluid simulations is 25000.

In figures 13 and 14 we show the formation and propagation of a negative streamer, assuming cases 1 and 4 for representing the inelastic energy losses, under the influence of the externally applied electric fields of 59 Td and 100 Td, respectively. For $E/n_0 = 59$ Td the difference between the ionization coefficients for liquid phase and rescaled gas is much higher than for $E/n_0 = 100$ Td. The simulations in the liquid phase are augmented by the simulation in which the transport data for electrons in the gas phase are for the gas phase scaled to the liquid density. The general features of the streamer profiles in the liquid xenon are the same as those of the streamers in gases [95, 96]. However, the space and time scales of the streamer formation are reduced by about three orders of magnitude due to a much greater number density of the background atoms in the liquid phase. The electron number density has a sharp peak in the streamer head where the electric field is significantly enhanced by the space charge effects. However, the number density is greatly reduced in the streamer channel where the external electric field is significantly screened. The further reduction of the number density of electrons in the streamer channel with increasing distance from the streamer head is clearly evident in the streamer profiles. This reduction can be attributed to the recombination of electrons and positive holes [50, 51]. A similar decrease of the electron number density in the streamer channel is observed for streamers in electronegative gases [50, 51].

We observe that the streamer formation as well as streamer propagation are greatly reduced with an increase of the number of excitations which are included in the model. The number density of electrons in both the streamer head and the streamer channel is also reduced. It can also be seen that the transition from an electron avalanche into a streamer is much slower in the case of the rescaled gas than in the first and the fourth cases of the liquid phase. Comparing figures 13 and 14, we see that this difference is much more pronounced at 59 Td than at 100 Td. To be specific, at 59 Td the distribution of electrons modeled in the case of the rescaled gas is still in the avalanche phase at the time instant when the streamer in the liquid phase, assuming the first case of representing inelastic energy losses, crosses the entire length l. On the other hand, at 100 Td the streamer modeled in the case of the rescaled gas is almost completely formed by the time when the streamer modeled in the first case reaches the boundary of the system. However, the streamer velocity and the number density of electrons calculated in the rescaled gas case are well below those in the liquid phase, assuming both cases 1 and 4, even at 100 Td. The observed streamer properties may be understood by considering the differences
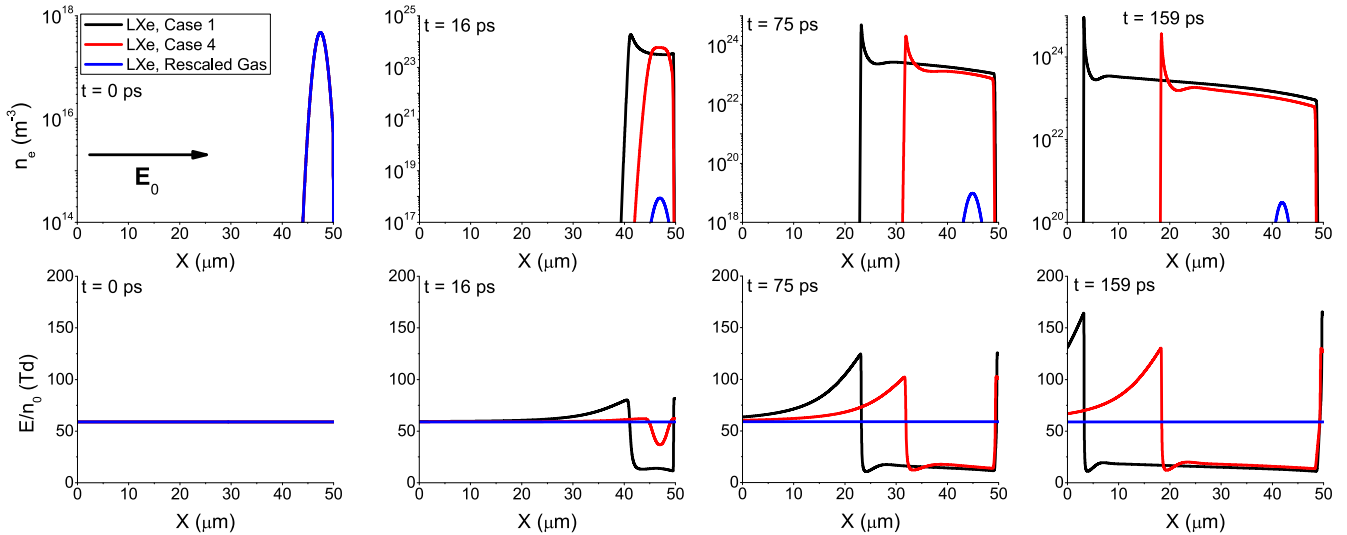
Figure 13. The formation and propagation of a negative streamer in liquid xenon for $E_0/n_0 = 59$ Td. The presented results are determined by assuming the first and the fourth cases for representing the inelastic energy losses. The results of streamer simulations obtained by using the gas phase transport properties which are scaled to liquid density are shown in the same figure for comparison. Here n_e refers to the electron number density, while E/n_0 refers to the reduced resultant electric field. The direction of the external electric field $\vec{E}_0$ is also shown in this figure.
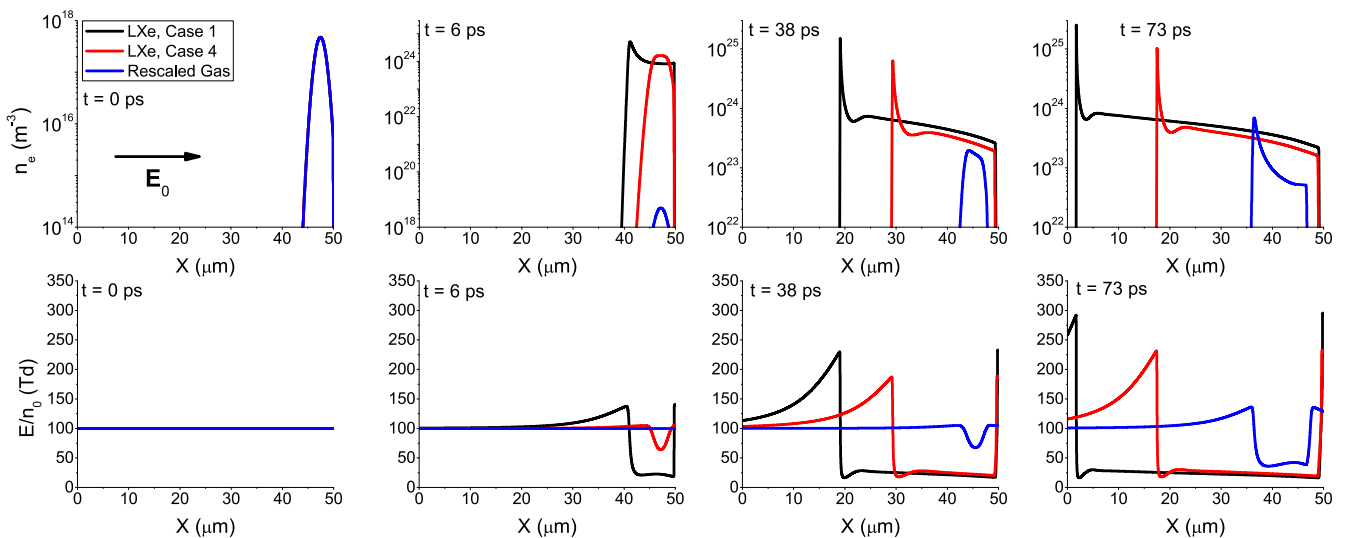
Figure 14. The formation and propagation of a negative streamer in liquid xenon for $E_0/n_0 = 100$ Td.

between the ionization coefficients in liquid and gaseous xenon. These differences are the most dominant at lower electric fields and gradually decrease with increasing field.

In figure 15 we show the profiles of negative streamers in liquid xenon for the applied reduced electric fields of 35 Td, 59 Td and 100 Td, respectively, at time 73 ps. The time instant of 73 ps has been carefully chosen since the fastest streamer in our simulations reaches the boundary of the system exactly at this time. The results are evaluated by considering all four cases for representing the inelastic energy losses. We observe that the number density of electrons in the streamer head and behind the ionization front in the streamer channel are decreased with the increase of the number of excitations in the model, independently of the applied electric

field. It can also be seen that the number density of electrons and the streamer velocity increase with increasing E_0/n_0.

The streamer velocities determined by employing all four cases for representing the inelastic energy losses, are shown in figure 16 along with the streamer velocity calculated by using the gas phase transport properties which are scaled to liquid density. For comparison, the bulk drift velocity obtained in the first case, is shown in the same figure. It can be seen that the streamer velocity greatly exceeds the bulk drift velocity. This is expected, as the velocity of a negative streamer is determined by the combination of the electron velocity and the rate of the electron impact ionization in the streamer head, where the electric field is significantly enhanced, as well as by the strong diffusive fluxes in the streamer front. It can also be
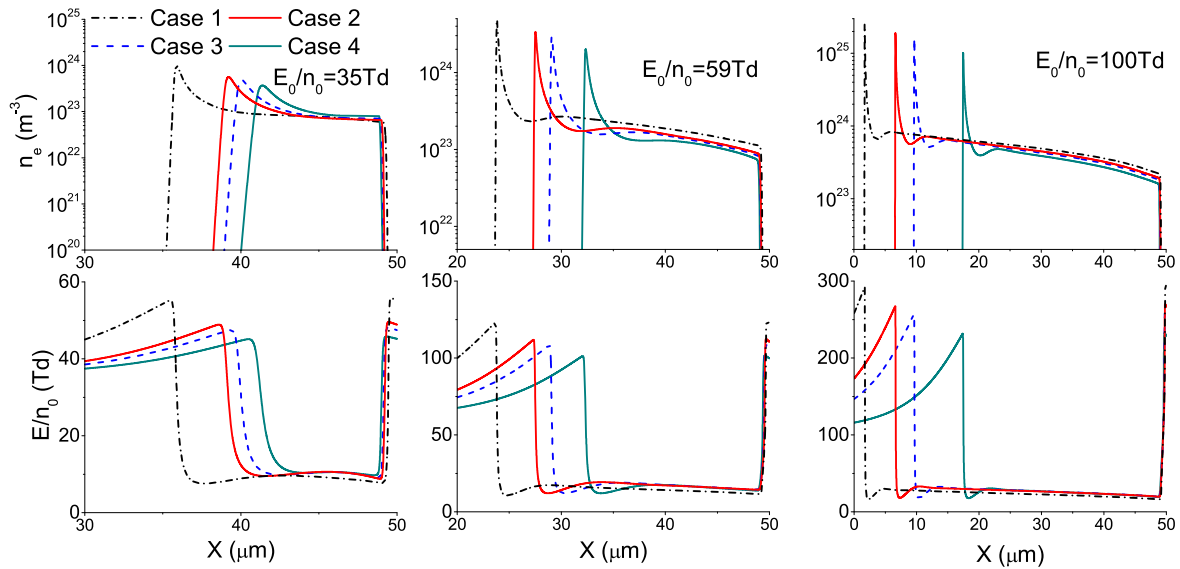
Figure 15. The spatial profiles of the electron number density n_e and the reduced electric field E/n_0 for three different values of the external electric field E_0. The displayed spatial profiles are determined by assuming all representations of the inelastic energy losses considered in the present work. All profiles are shown at 73 ps.
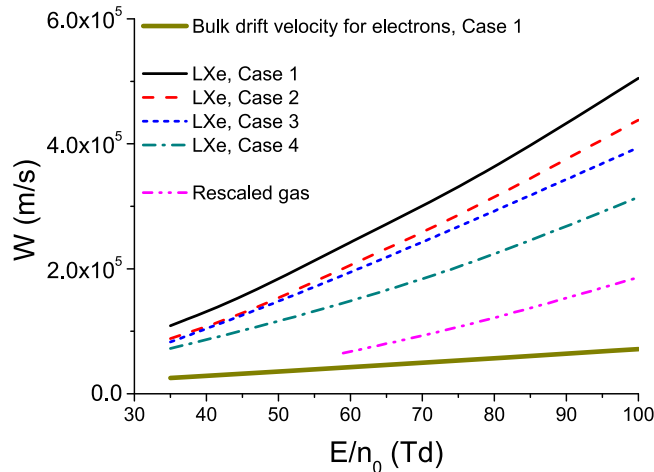
Figure 16. The streamer velocities calculated by assuming all representations of the inelastic energy losses considered in the present work. The streamer velocity obtained by using the gas phase transport data which is scaled to liquid density is displayed for comparison, as well as the bulk drift velocity of electrons, which is determined for the first case of representing the inelastic energy losses.

seen that the intensity of the streamer velocity determined in our fluid simulations strongly depends on the employed case for representing the inelastic energy losses in the liquid phase. The difference between the values of streamer velocities, which are obtained by assuming the first and the fourth cases, is about 40% at high electric fields. In addition, for the values of E_0/n_0 around 100 Td the streamer velocity determined by using the gas phase transport properties, which are scaled to liquid density, is about 2.5 times lower than the streamer velocity obtained in the first case for representing the inelastic energy losses. This difference is even more pronounced at lower electric fields. The differences between the calculated velocities of negative streamers are reflections of the

corresponding differences between the first Townsend coefficient (see figure 9).

5. Conclusion

We have investigated the influence of the inelastic energy losses in liquid xenon on the transport properties of electrons and the dynamics of negative streamers, by using Monte Carlo simulations and the 1.5 dimensional fluid model. Four cases for representing the inelastic energy losses in liquid xenon are discussed in light of previous spectroscopy and photoconductivity experiments. These cases are employed for determining the transport properties of electrons by using Monte Carlo simulations. Our Monte Carlo code has been modified by including three effective scattering processes, which give a good representation of the coherent scattering of low energy electrons in non-polar liquids. The validity of our Monte Carlo code has been tested by calculating the mean energy, the drift velocity and the components of the diffusion tensor for electrons in the Percus Yevick model liquid. Our benchmark results for the Percus Yevick model are in an excellent agreement with those calculated by Tattersall *et al* [57]. We have determined the values of mean energy, drift velocity, diffusion tensor and the first Townsend coefficient for electrons in liquid xenon. Our results are in a good agreement with those of Boyle *et al* [34], as well as with the available experiments [56, 88, 89, 94]. However, since our calculations of transport properties span a range of the reduced electric field much wider than that investigated in experiments, one should be cautious to trust the calculated data outside the range covered in the experiments. This should be noted since we have approximated the cross sections for inelastic scattering and interband transitions of electrons in liquid xenon by using the cross sections for

electron scattering on an isolated xenon atom. In addition, we have neglected the electron phonon scattering, and we did not take into account the structure of the conduction band since we have approximated each electron by a free particle moving between individual collisions. It has been shown that there is a significant difference between the values of the first Townsend coefficient determined by employing different representations of the inelastic energy losses. The transport properties of electrons obtained in our Monte Carlo simulations, are used as input data in our simulations of the streamer dynamics. These simulations are based on the first order fluid model, and they follow the transition of an electron avalanche into a negative streamer and the subsequent streamer propagation. The results of these simulations strongly depend on the number of excitations which are included in the model. The intensity of the streamer velocity in the case in which all excitations are neglected exceeds the corresponding intensity in the case in which all excitations are included by about 40%, at high electric fields. This difference is in agreement with the difference in rates for ionization in these cases. Moreover, the value of the streamer velocity determined by using the transport properties from the gas phase, which are scaled to liquid density, is over 2.5 times lower than the streamer velocity calculated in the case in which all excitations are neglected. Furthermore, the speed of transition of an electron avalanche into a streamer in the rescaled gas phase is significantly lower than in the other cases investigated in our study. This difference is especially pronounced for the reduced electric fields lower than 100 Td. These results indicate that the correct representation of the elementary scattering processes in liquids is of crucial importance for the modeling of the electron transport and the electrical discharges in the liquid phase.

Our work concerning the modeling of electron transport in liquid xenon can be extended by employing *ab initio* cross sections for inelastic scattering and interband transitions in the liquid phase after these cross sections are determined. Further improvement of the model would be achieved by taking into account electron phonon scattering and trapping of electrons in density fluctuations as well as by going beyond the free electron approximation by considering the structure of the conduction band.

The extension of our streamer calculations by investigating the propagation of positive and negative streamers in a point to plane geometry and by taking into account non-locality of the electron mean energy will be covered in future work. These calculations can be further generalized by considering the formation of gaseous filaments due to heating of the liquid, which is important on the nanosecond time scale.

Acknowledgments

ORCID iDs

I Simonović https://orcid.org/0000-0001-6704-9042
N A Garland https://orcid.org/0000-0003-0343-0199
D Bošnjaković https://orcid.org/0000-0002-2725-5287
Z Lj Petrović https://orcid.org/0000-0001-6569-9447
R D White https://orcid.org/0000-0001-5353-7440
S Dujko https://orcid.org/0000-0002-4544-9106

References

[1] Bruggeman P and Leys C 2009 *J. Phys. D: Appl. Phys.* **42** 053001
[2] Bruggeman P J *et al* 2016 *Plasma Sources Sci. Technol.* **25** 053002
[3] Fridman A and Friedman G 2012 *Plasma Medicine* (New York: Wiley)
[4] Kong M G, Kroesen G, Morfill G, Nosenko T, Shimizu T, van Djik J and Zimmermann J L 2009 *New J. Phys.* **11** 115012
[5] Jiang B, Zheng J, Qiu S, Wu M, Zhang Q, Yan Z and Xue Q 2014 *Chem. Eng. J.* **236** 348–68
[6] Malik M A, Ghaffar A and Malik S A 2001 *Plasma Sources Sci. Technol.* **10** 82
[7] Škoro N, Puač N, Živković S, Krstić-Milosević D, Cvelbar U, Malović G and Petrović Z L 2018 *Eur. Phys. J.* D **72** 2
[8] Puač N, Škoro N, Spasić K, Živković S, Milutinović M, Malović G and Petrović Z L 2017 *Plasma Process. Polym.* **15** e1700082
[9] Rond C, Desse J M, Fagnon J M, Aubert X, Er M, Vega A and Duten X 2018 *J. Phys. D: Appl. Phys.* **51** 335201
[10] Naidis G V 2015 *J. Phys. D: Appl. Phys.* **48** 195203
[11] Ushakov V Y, Klimkin V F and Korobeynikov S M 2007 *Impulse Breakdown of Liquids* (Berlin: Springer)
[12] Regenfus C and (The ArDM Collaboration) 2010 *J. Phys.: Conf. Ser.* **203** 012024
[13] Aprile E, Mukherjee R and Suzuki M 1990 *IEEE Trans. Nucl. Sci.* **37** 553
[14] Aprile E and Doke T 2010 *Rev. Mod. Phys.* **82** 2053
[15] Okada H, Doke T, Kashiwagi T, Kikuchi J, Kobayashi M, Masuda K, Shibamura E, Suzuki S, Takashima T and Terasawa K 2000 *Nucl. Instrum. Methods Phys. Res.* A **451** 427
[16] Egorov V V, Miroshnichenko V P, Rodionov B U, Bolozdinja A I, Kalashnikov S D and Krivoshein V L 1983 *Nucl. Instrum. Methods Phys. Res.* A **205** 373
[17] Aprile E and Baudis L 2008 *Proc. Sci.* **IDM2008** 018
[18] Gaitskell R 2008 *Proc. Sci.* **IDM2008** 018
[19] Boyle G J, McEachran R P, Cocks D G and White R D 2015 *J. Chem. Phys.* **142** 154507
[20] Sakai Y 2007 *J. Phys. D: Appl. Phys.* **40** R441
[21] White R D, Robson R E, Dujko S, Nicoletopoulos P and Li B 2009 *J. Phys. D: Appl. Phys.* **42** 194001
[22] Petrović Z L, Dujko S, Marić D, Malović G, Nikitović Ž, Šašić O, Jovanović J, Stojanović V and Radmilović-Radjenović M 2009 *J. Phys. D: Appl. Phys.* **42** 194002
[23] Robson R E, White R D and Petrović Z L 2005 *Rev. Mod. Phys.* **77** 1303
[24] Lekner J 1967 *Phys. Rev.* **158** 130

[25] Cohen M H and Lekner J 1967 *Phys. Rev.* **158** 305
[26] Atrazhev V M and Iakubov I T 1981 *J. Phys. C* **14** 5139
[27] Atrazhev V M and Dmitriev E G 1985 *J. Phys. C* **18** 1205
[28] Atrazhev V M, Iakubov I T and Pogosov V V 1995 *Phys. Lett. A* **204** 393
[29] Atrazhev V M and Timoshkin I V 1996 *Phys. Rev. B* **54** 252
[30] Atrazhev V M and Timoshkin I V 1998 *IEEE Trans. Dielectr. Electr. Insul.* **5** 450
[31] Atrazhev V M, Berezhnov A V, Dunikov D O, Chernysheva I V, Dmitrenko V V and Kapralova G 2005 *Proc. IEEE Int. Conf. on Dielectric Liquids (ICDL 2005)* p 329
[32] Sakai Y, Nakamura S and Tagashira H 1985 *IEEE Trans. Electr. Insul.* **EI-20** 133
[33] Nakamura S, Sakai Y and Tagashira H 1986 *Chem. Phys. Lett.* **130** 551
[34] Boyle G J, McEachran R P, Cocks D G, Brunger M J, Buckman S J, Dujko S and White R D 2016 *J. Phys. D: Appl. Phys.* **49** 355201
[35] Milloy H B and Crompton R W 1977 *Aust. J. Phys.* **30** 51
[36] Borghesani A F and Lamp P 2011 *Plasma Sources Sci. Technol.* **20** 034001
[37] Borghesani A F 2014 *Eur. Phys. J. D* **68** 62
[38] Petrović Z L, O'Malley T F and Crompton R W 1995 *J. Phys. B* **28** 3309
[39] Atrazhev V M, Iakubov I T and Roldughin V I 1976 *J. Phys. D: Appl. Phys.* **9** 1735
[40] Jones H M and Kunhardt E E 1993 *Phys. Rev. B* **48** 9382
[41] Kunhardt E E 1991 *Phys. Rev. B* **44** 4235
[42] Hove L V 1954 *Phys. Rev.* **95** 249
[43] Boyle G J, White R D, Robson R E, Dujko S and Petrović Z L 2012 *New. J. Phys.* **14** 045011
[44] Garland N A, Cocks D G, Boyle G J, Dujko S and White R D 2017 *Plasma Sources Sci. Technol.* **26** 075003
[45] White R D *et al* 2018 *Plasma Sources Sci. Technol.* **27** 053001
[46] Garland N A, Boyle G J, Cocks D G and White R D 2018 *Plasma Sources Sci. Technol.* **27** 024002
[47] Naidis G V 2016 *J. Phys. D: Appl. Phys.* **49** 235208
[48] Babaeva N Y, Naidis G V, Tereshonok D V and Smirnov B M 2017 *J. Phys. D: Appl. Phys.* **50** 364001
[49] Tereshonok D V, Babaeva N Y, Naidis G V, Panov V A, Smirnov B M and Son E E 2018 *Plasma Sources Sci. Technol.* **27** 045005
[50] Babaeva N Y and Naidis G V 1999 *Proc. 13th Int. Conf. on Dielectric Liquids (ICDL 1999) (Nara, Japan, July 20-25)* p 437
[51] Babaeva N Y and Naidis G V 1999 *Tech. Phys. Lett.* **25** 91
[52] Babaeva N Y and Naidis G V 2001 *J. Electrost.* **53** 123
[53] Nakamura S, Sakai Y and Tagashira H 1987 *JIEE Japan* **A107** 543
[54] Hayashi M 2003 *Bibliography of Electron and Photon Cross sections with Atoms and Molecules Published in the 20th Century—Xenon (NIFS-DATA-79)*
[55] Pitchford L C *et al* 2013 *J. Phys. D: Appl. Phys.* **46** 334001
[56] Derenzo S E, Mast T S and Zaklad B 1974 *Phys. Rev. A* **9** 2582
[57] Tattersall W J, Cocks D G, Boyle G J, Buckman S J and White R D 2015 *Phys. Rev. E* **91** 043304

[58] Bartels A 1973 *Phys. Lett.* **44A** 403
[59] Allen N L and Prew B A 1970 *J. Phys. B* **3** 1113
[60] Beaglehole D 1965 *Phys. Rev. Lett.* **15** 551
[61] Asaf U and Steinberger I T 1971 *Phys. Lett.* **34A** 207
[62] Laporte P and Steinberger I T 1977 *Phys. Rev. A* **15** 2538
[63] Laporte P, Subtil J L, Asaf U, Steinberger I T and Wind S 1980 *Phys. Rev. Lett.* **45** 2138
[64] Raz B and Jortner J 1968 *J. Chem. Phys.* **49** 3318
[65] Raz B and Jortner J 1970 *Proc. R. Soc. A* **317** 113
[66] Reininger R, Asaf U, Steinberger I T, Saile V and Laporte P 1983 *Phys. Rev. B* **28** 3193
[67] Asaf U and Steinberger I T 1974 *Phys. Rev. B* **10** 4464
[68] Hayashi M 2014 Hayashi Database www.lxcat.net
[69] von Zdrojewski W 1980 *Z. Naturforsch.* **35a** 672
[70] Reininger R, Asaf U and Steinberger I T 1982 *Chem. Phys. Lett.* **90** 287
[71] Garland N A, Simonović I, Boyle G J, Cocks D G, Dujko S and White R D 2018 *Plasma Sources Sci. Technol.* **27** 105004
[72] Gordon E B *et al* 1994 *Chem. Phys. Lett.* **217** 605
[73] Schüssler A S *et al* 2000 *Appl. Phys. Lett.* **77** 2786
[74] Gordon E B and Shestakov A F 2001 *Low Temp. Phys.* **27** 883
[75] Kunhardt E E, Christophorou L G and Luessen L H 1988 *The Liquid State and its Electrical Properties* (New York: Plenum) p 235
[76] Dujko S, Raspopović Z M and Petrović Z L 2005 *J. Phys. D: Appl. Phys.* **38** 2952
[77] Dujko S, White R D, Ness K F, Petrović Z L and Robson R E 2006 *J. Phys. D: Appl. Phys.* **39** 4788
[78] Dujko S, Raspopović Z M and Petrović Z L 2008 *J. Phys. D: Appl. Phys.* **41** 245205
[79] Perram J W 1975 *Mol. Phys.* **30** 1505
[80] Verlet L and Weis J J 1972 *Phys. Rev. A* **5** 939
[81] White R D and Robson R E 2011 *Phys. Rev. E* **84** 031125
[82] White R D and Robson R E 2009 *Phys. Rev. Lett.* **102** 230602
[83] Davies A J, Evans C J and Jones F L 1964 *Proc. R. Soc. A* **281** 164
[84] Bošnjaković D, Petrović Z L and Dujko S 2016 *J. Phys. D: Appl. Phys.* **49** 405201
[85] Hilt O and Schmidt W F 1994 *Chem. Phys.* **183** 147
[86] Hilt O and Schmidt W F 1994 *J. Phys. Condens. Matter* **6** L735
[87] Robson R E and Ness K F 1988 *J. Chem. Phys.* **89** 4815
[88] Miller L S, Howe S and Spear W E 1968 *Phys. Rev.* **166** 871
[89] Huang S S S and Freeman G R 1978 *J. Chem. Phys.* **47** 1355
[90] Petrović Z L, Crompton R W and Haddad G N 1984 *Aust. J. Phys.* **37** 23
[91] Robson R E 1984 *Aust. J. Phys.* **37** 35
[92] Vrhovac S B and Petrović Z L 1996 *Phys. Rev. E* **53** 4012
[93] Dujko S, White R D and Petrović Z L 2008 *J. Phys. D: Appl. Phys.* **41** 245205
[94] Shibamura E, Masuda K and Doke T 1984 *Proc. 8th Workshop on Electron Swarms*
[95] Li C, Brok W J M, Ebert U and Mullen J J A M 2007 *J. Appl. Phys.* **101** 123305
[96] Li C, Ebert U and Hundsdorfer W 2010 *J. Comput. Phys.* **229** 200

PAPER

Third-order transport coefficients for electrons in N_2 and CF_4: effects of non-conservative collisions, concurrence with diffusion coefficients and contribution to the spatial profile of the swarm

View the article online for updates and enhancements.

Third-order transport coefficients for electrons in N_2 and CF_4: effects of non-conservative collisions, concurrence with diffusion coefficients and contribution to the spatial profile of the swarm

I Simonović[1] , **D Bošnjaković**[1] , **Z Lj Petrović**[2,3] , **R D White**[4] and **S Dujko**[1,*]

[1] Institute of Physics Belgrade, University of Belgrade, Pregrevica 118, 11080 Belgrade, Serbia
[2] University of Ulster, Newtownabbey, Antrim, Northern Ireland, United Kingdom
[3] Serbian Academy of Sciences and Arts, Knez Mihailova 35, 11000 Belgrade, Serbia
[4] College of Science and Engineering, James Cook University, Townsville, QLD 4811, Australia

E-mail: sasha@ipb.ac.rs

CrossMark

Abstract

Using a multi-term solution of the Boltzmann equation and Monte Carlo simulation technique we study behaviour of the third-order transport coefficients for electrons in model gases, including the ionisation model of Lucas and Saelee and modified Ness–Robson model of electron attachment, and in real gases, including N_2 and CF_4. We observe negative values in the E/n_0-profiles of the longitudinal and transverse third-order transport coefficients for electrons in CF_4 (where E is the electric field and n_0 is the gas number density). While negative values of the longitudinal third-order transport coefficients are caused by the presence of rapidly increasing cross sections for vibrational excitations of CF_4, the transverse third-order transport coefficient becomes negative over the E/n_0-values after the occurrence of negative differential conductivity. The discrepancy between the two-term approximation and the full multi-term solution of the Boltzmann equation is investigated for electrons in N_2 and CF_4. While the accuracy of the two-term approximation is sufficient to investigate the behaviour of the third-order transport coefficients in N_2, it produces large errors and is not even qualitatively correct for electrons in CF_4. The influence of implicit and explicit effects of electron attachment and ionisation on the third-order transport tensor is investigated. In particular, we discuss the effects of attachment heating and attachment cooling on the third-order transport coefficients for electrons in the modified Ness–Robson model, while the effects of ionisation are studied for electrons in the ionisation model of Lucas and Saelee, N_2 and CF_4. The concurrence between the third-order transport coefficients and the components of the diffusion tensor, and the contribution of the longitudinal component of the third-order transport tensor to the spatial profile of the swarm are also investigated. For electrons in CF_4 and CH_4, we found that the contribution of the component of the third-order transport tensor to the spatial profile of the swarm between approximately 50 Td and 700 Td, is almost identical to the corresponding contribution for electrons in N_2. This suggests that the recent measurements of third-order transport coefficients for electrons in N_2 may be extended and generalised to other gases, such as CF_4 and CH_4.

---

* Author to whom any correspondence should be addressed.

1. Introduction

Non-equilibrium plasmas have a wide range of important applications including micro and nano-electronic device fabrication [1–4], surface etching [5, 6], sputtering [7, 8], chemical processing [9, 10], and plasma medicine [11–13]. The modelling of non-equilibrium plasma is important for further development and optimization of these applications [14–17]. However, this can be quite challenging due to a wide variety of effects that determine the nature of non-equilibrium plasma. These effects include collisions of electrons and ions with neutral particles of the background fluid [18–20], kinetics of excited species [21–23], generation of fast neutrals [24], space charge effects [25, 26], and plasma-surface interaction [27, 28]. Despite their simplicity, charged-particle swarms are at the heart of non-equilibrium plasma modelling [2, 18, 29, 30]. Specifically, transport coefficients that describe the dynamics of a swarm of charged particles are used as input data into the fluid models of non-equilibrium plasma [31–38]. In addition, transport coefficients are required in the swarm procedure for determining the complete and consistent sets of cross-sections for collisions of charged particles with atoms and molecules of the background fluid [39–42]. These sets of cross-sections are employed as input data into the particle models of non-equilibrium plasma [43–49]. Due to the sensitivity of plasma models to transport coefficients and cross-section sets in the case of fluid and particle models, respectively, a great amount of attention has been dedicated to the calculation and measurement of transport coefficients of electrons and ions in numerous atomic and molecular gases. However, this attention has been limited to the lower-order transport coefficients such as rate coefficients for non-conservative processes, drift velocity, and diffusion tensor components [18, 19, 50].

Transport coefficients of third and higher order have been implemented to analyse ion swarm experiments [51–55]. However, they have been almost systematically ignored in the traditional analysis of electron swarm experiments, as they are difficult to measure and difficult to study by employing theoretical methods [56–58]. However, Kawaguchi and co-workers have recently measured third-order transport coefficients for electrons in molecular nitrogen by employing the arrival time spectra experiment [59]. In addition, they have shown that it is necessary to consider the longitudinal component of the third-order transport tensor Q_L in order to correctly determine the longitudinal component of the diffusion tensor D_L from the arrival time spectra data. The difference between the values of D_L, which are estimated after neglecting Q_L, and the corresponding values, which are determined from the expression that includes Q_L, is greater than the sum of their experimental errors at high electric fields. Moreover, it is known that the third-order transport coefficients are required for the conversion of hydrodynamic flux transport coefficients into transport parameters that are determined from the steady state Townsend experiment [60]. Third-order transport coefficients are more sensitive to energy dependence of the cross sections for the scattering of charged particles on the constituents of the background medium than drift velocity and diffusion tensor [56, 61, 62]. For this reason, third-order transport coefficients would be very useful in the swarm procedure for determining the complete sets of cross sections, if these transport coefficients were calculated and measured with a sufficient precision. Kawaguchi *et al* [59] have shown that the third-order transport coefficients are sensitive to the anisotropy of electron scattering. Thus, inclusion of the third-order transport coefficients would help in testing the implementation of anisotropic scattering in transport calculations, if the values of these transport coefficients were known from experiments [63]. This is important as the correct implementation of anisotropic scattering is required for determining the values of the rate coefficient for electron impact ionisation at high electric fields, with high precision [63, 64].

The structure of the third-order transport tensor in the electric field only configuration was determined by Whealton and Mason [65], Vrhovac *et al* [56] and Koutselos [52]. Simonović and co-workers have determined the structure of this tensor in all configurations of electric and magnetic field, and they have investigated the physical interpretation of the individual components of this tensor [58]. Koutselos studied the third-order transport coefficients for ions in atomic gases, by employing molecular dynamics simulations and a three-temperature method for solving the Boltzmann equation [52, 66–68]. Third-order transport coefficients for electrons in noble gases were investigated by Penetrante and Bardsley [61], Vrhovac *et al* [56] and Simonović *et al* [69]. Penetrante and Bardsley used the two-term approximation for solving the Boltzmann equation and Monte Carlo (MC) simulations, Vrhovac *et al* employed the momentum transfer theory and generalized Einstein relations, while Simonović *et al* used a multi-term theory for solving the Boltzmann equation. Stokes and co-workers investigated the effects of localized and delocalized electron states on the third-order transport coefficients [70]. Recently, Kawaguchi *et al* [71] have shown that the third-order transport coefficients can be measured in the arrival time spectra experiment by employing MC simulations, and they have determined the values of these transport coefficients for electrons in CH_4 and SF_6 by using the same method. They have subsequently measured the longitudinal component of the third-order transport tensor for electrons in N_2 by employing the arrival time spectra experiment. Kawaguchi

et al have further verified these results by using MC simulations [59, 63].

Although the lower-order transport coefficients have been carefully investigated in the literature, the third-order transport coefficients are still largely unexplored. For this reason, a number of questions concerning the properties of these transport coefficients and their dependence on elementary scattering processes are still open. How sensitive are these transport coefficients to effects of non-conservative collisions such as ionisation and electron attachment? Are the differences between the flux and bulk values of the third order transport coefficients higher or lower than the corresponding differences in the lower order transport coefficients? Is there any concurrence between these transport coefficients and those of lower-order? If such concurrence exists, how can it be accounted for? Can third-order transport coefficients be negative, and what would the negative values of these transport coefficients mean physically? Some of these issues will be addressed in this work. Implicit and explicit effects of electron attachment and ionisation on the third-order transport tensor are investigated, for electrons in Ness–Robson model and Lucas–Saelee model, respectively, by employing MC simulations and a multi-term method for solving the Boltzmann equation. In addition, explicit effects of ionisation on this transport tensor for electrons in N_2 and CF_4 are studied. Negative values of the third-order transport coefficients for electrons in CF_4 are also investigated. The concurrence between these transport coefficients and diffusion is analysed for electrons in N_2 and CF_4. The values of the longitudinal component of the third-order transport tensor for electrons in N_2, that are determined in this work, are compared with results of Kawaguchi *et al*. The contribution of the third-order transport coefficients to the spatial profile of the swarm is determined for electrons in N_2, CF_4 and CH_4 over a wide range of the reduced electric field. The third-order transport coefficients are defined in section 2. The methods for calculating these transport coefficients by employing a multi-term solution of the Boltzmann equation and MC simulations are discussed in sections 3.1 and 3.2, respectively. The cross sections for model and real gases, that are used as input data in this work, are discussed in section 4.1. The variation of the flux third-order transport tensor with the reduced electric field for electrons in N_2 and CF_4 is analysed in section 4.2. The impact of electron attachment on the third-order transport coefficients for electrons in the modified Ness–Robson model is studied in section 4.3.1, while the influence of electron impact ionisation on these transport coefficients for electrons in Lucas–Saelee model, N_2 and CF_4 is investigated in section 4.3.2. The longitudinal component of the third-order transport tensor, that is determined in this study, is compared with the measurements and calculations of Kawaguchi and co-workers in section 4.4. Concurrence between the third-order transport coefficients and individual components of the diffusion tensor for electrons in N_2 and CF_4 is analysed in this section as well. In the same section the contribution of the third-order transport coefficients to the spatial profile of the swarm is determined for electrons in N_2, CF_4 and CH_4. The concluding remarks are given in section 5.

2. Theory

Transport coefficients are defined for a swarm of charged particles in hydrodynamic conditions. A swarm is an ensemble of charged particles that moves in a neutral background fluid under the influence of an external electric and/or magnetic field. The density of charged particles is considered to be small, so that their mutual interactions, as well as the effects induced by the space-charge, are neglected. The swarm gains energy from the external electric field and it dissipates this energy input into collisions with the particles of the background fluid. However, the probability of having collisions with molecules perturbed/excited by the swarm itself is negligible due to a low swarm particle density.

If the external fields are uniform in space, the swarm relaxes to a stationary state in which the amount of energy that is gained per unit time, is equal to the amount of energy that is dissipated in collisions during this time. The influence of the swarm on the background fluid and fields is neglected, due to the low density of charged particles, and it is considered that this fluid is in a state of thermodynamic equilibrium. Hydrodynamic conditions are fulfiled for a swarm of charged particles if the background fluid and the electric/magnetic fields are spatially homogeneous, and if the swarm is far from the boundaries of the system and far from sources and sinks of charged particles. Under these conditions the phase space distribution function can be expanded into a density gradient series as [72]:

$$f(\mathbf{r}, \mathbf{c}, t) = \sum_{k=0}^{\infty} \mathbf{f}^{(k)}(\mathbf{c}) \odot (-\nabla)^k n(\mathbf{r}, t), \qquad (1)$$

where $\mathbf{r}$, $\mathbf{c}$ and t are radius vector, velocity vector and time, respectively, $\mathbf{f}^{(k)}(\mathbf{c})$ are tensors of rank k, $\odot$ is tensor contraction of order k, while $n(\mathbf{r}, t)$ is number density of charged particles. Under hydrodynamic conditions the flux of velocity of charged particles can be written as [56]:

$$\mathbf{\Gamma}(\mathbf{r}, t) = \mathbf{W}^{(f)} n(\mathbf{r}, t) - \hat{\mathbf{D}}^{(f)} \cdot \nabla n(\mathbf{r}, t)$$
$$+ \hat{\mathbf{Q}}^{(f)} \odot (\nabla \otimes \nabla) n(\mathbf{r}, t) + \cdots, \qquad (2)$$

where $\mathbf{W}^{(f)}$, $\hat{\mathbf{D}}^{(f)}$ and $\hat{\mathbf{Q}}^{(f)}$ are flux drift velocity, flux diffusion tensor and flux third-order transport tensor, respectively, and $\otimes$ is the tensor product. The equation (2) is truncated at the third term, as this is sufficient for defining the flux third-order transport tensor. Explicit expressions for the flux transport coefficients in terms of the phase space distribution function are given in reference [58].

Bulk transport coefficients appear in the generalized diffusion equation [56], which has been truncated at the third-order gradients for our needs:

$$\frac{\partial n(\mathbf{r}, t)}{\partial t} + \mathbf{W}^{(b)} \cdot \nabla n(\mathbf{r}, t) - \hat{\mathbf{D}}^{(b)} : (\nabla \otimes \nabla) n(\mathbf{r}, t)$$
$$+ \hat{\mathbf{Q}}^{(b)} \vdots (\nabla \otimes \nabla \otimes \nabla) n(\mathbf{r}, t) = R_i n(\mathbf{r}, t), \quad (3)$$

where $\mathbf{W}^{(b)}$, $\hat{\mathbf{D}}^{(b)}$, $\hat{\mathbf{Q}}^{(b)}$ and R_i are bulk drift velocity, bulk diffusion tensor, bulk third-order transport tensor and effective

rate coefficient for non-conservative processes, respectively, while : and ⋮ represent tensor contractions of second and third-order, respectively. Bulk transport coefficients can be expressed in terms of flux transport coefficients as [58]:

$$\mathbf{W}^{(b)} = \mathbf{W}^{(f)} + \mathbf{S}^{(1)}, \quad \hat{\mathbf{D}}^{(b)} = \hat{\mathbf{D}}^{(f)} + \mathbf{S}^{(2)}, \quad \hat{\mathbf{Q}}^{(b)} = \hat{\mathbf{Q}}^{(f)} + \mathbf{S}^{(3)}, \quad (4)$$

where $\mathbf{S}^{(k)}$ is the coefficient in the hydrodynamic expansion of the source term, that is contracted with kth derivative of the density gradient. For a swarm of electrons in the presence of electron impact ionisation and/or electron attachment, the source term is defined as:

$$S(\mathbf{r}, t) = \int n_0 c \left(\sigma_i(\epsilon) - \sigma_a(\epsilon) \right) f(\mathbf{r}, \mathbf{c}, t) \mathrm{d}\mathbf{c}, \quad (5)$$

where n_0, ϵ, $\sigma_i(\epsilon)$ and $\sigma_a(\epsilon)$ are number density of the background molecules, electron energy, and cross sections for ionisation and electron attachment, respectively.

Implicit effects of non-conservative collisions arise due to population and depopulation of different parts of the distribution function in velocity space, that are caused by the energy dependence of collision frequencies of non-conservative processes. These effects refer to the influence of non-conservative collisions on tensors $\mathbf{f}^{(k)}(\mathbf{c})$ in equation (1). Explicit effects of non-conservative processes arise due to the spatial dependence of collision frequencies for these processes. This spatial dependence is caused by the energy dependence of the collision frequencies for non-conservative collisions and spatial variation of energy of charged particles. Explicit effects of non-conservative collisions are represented by tensors $\mathbf{S}^{(k)}$ from the equation (4) and they determine the difference between flux and bulk transport coefficients.

The influence of implicit and explicit effects of non-conservative collisions on low order transport coefficients has been thoroughly studied in previous publications [73, 75]. Implicit effects of ionisation on the third-order transport coefficients refer to the influence of ionisation cooling on the asymmetric component of the diffusive flux, which is represented by the flux third-order transport tensor. Due to explicit effects of ionisation more electrons are created at the front of the swarm than at the back of the swarm, which in turn elongate the spatial distribution of electrons along both longitudinal and transverse directions at the leading edge of the swarm. Similarly, the implicit effects of electron attachment relate to the influence of depopulation of low-energy part of the distribution function, in case of attachment heating, and depopulation of high-energy part of the distribution function, in case of attachment cooling, on the asymmetric component of the diffusive flux. Explicit effects of electron attachment on the third-order transport coefficients refer to the influence of the spatial variation of electron losses to the compression of the spatial distribution of the swarm in those regions of space where electron attachment is more frequent.

The studied system is a swarm of electrons which move in a homogeneous background gas under the influence of a homogeneous and constant electric field that is oriented along the z axis. In this field configuration the flux third-order transport tensor has three independent components Q_{zzz}, Q_{xxz} and Q_{zxx}. In this field configuration, the following relations are

imposed on the off-diagonal components of the flux third-order transport tensor: $Q_{xxz} = Q_{xzx} = Q_{yyz} = Q_{yzy}$ and $Q_{zxx} = Q_{zyy}$ [52, 56, 58, 65]. The structure of the third-order transport tensor and physical interpretation of its individual components are extensively discussed in our recent work [58]. In particular, contribution of the third-order transport coefficients to the spatial profile of the swarm is represented by the following approximate expression [58]:

$$n^{(1)}(\mathbf{r}, t) = n^{(0)}(\mathbf{r}, t) \left[1 + \frac{t Q_{\mathrm{L}}^{(b)}}{\sigma_z^3} \chi_z \left(\chi_z^2 - 3 \right) \right.$$
$$\left. + \frac{3 t Q_{\mathrm{T}}^{(b)}}{\sigma_x^2 \sigma_z} \chi_z \left(\chi_x^2 + \chi_y^2 - 2 \right) \right], \quad (6)$$

where $n^{(0)}(\mathbf{r}, t)$ is the solution of the diffusion equation in which third and higher order transport coefficients are neglected, $Q_{\mathrm{L}} = Q_{zzz}$, $Q_{\mathrm{T}} = \frac{1}{3}(Q_{xxz} + Q_{xzx} + Q_{zxx})$, $\sigma_z = \sqrt{2 D_{\mathrm{L}}^{(b)} t}$ and $\sigma_x = \sigma_y = \sqrt{2 D_{\mathrm{T}}^{(b)} t}$, while χ_z, χ_x, χ_y are defined as:

$$\chi_z = \frac{z - W^{(b)} t}{\sigma_z}, \qquad \chi_x = \frac{x}{\sigma_x}, \qquad \chi_y = \frac{y}{\sigma_y}. \quad (7)$$

The equation (6) can be derived from the Fourier transform of the generalized diffusion equation in which third-order transport coefficients are included [58]. It can be seen from equation (6) that contribution of the longitudinal component of the third-order transport tensor to the spatial profile of the swarm is proportional to $Q_{\mathrm{L}}^{(b)}/(D_{\mathrm{L}}^{(b)})^{3/2}$. In statistics the asymmetry of the probability distribution of a random variable about its expected value is represented by skewness [74]. There are several ways to express skewness in statistics including the third central moment and the third standardized moment of a random variable [74]. It can be shown that the bulk third-order transport tensor is proportional to the third central moment of the position vector, while $Q_{\mathrm{L}}^{(b)}/(D_{\mathrm{L}}^{(b)})^{3/2}$ is proportional to the longitudinal component of the third standardized moment of the position vector. Likewise, the $Q_{\mathrm{T}}^{(b)}/(D_{\mathrm{T}}^{(b)}(D_{\mathrm{L}}^{(b)})^{1/2})$ term is proportional to the off-diagonal component of the same standardized moment with the combination of indices π_{xxz}, where π_{abc} represents any permutation of a, b and c.

The flux third-order transport tensor is defined by the flux gradient relation. The last two indices of this tensor are contracted with partial derivatives of the charged-particle number density with respect to spatial coordinates. The third-order bulk transport tensor is however defined by the generalised diffusion equation, in which the three indices of this tensor are contracted with partial derivatives. For this reason, all three indices of the bulk third-order transport tensor commute, as this transport property is symmetrized in the equation in which it is defined. The same reasoning applies to the bulk diffusion tensor and higher order bulk transport tensors. Using these arguments, in the case of bulk third-order transport coefficients and when the swarm of charged-particles is acted on solely by an electric field, we can identify only two independent bulk components $Q_{\mathrm{L}}^{(b)}$ and $Q_{\mathrm{T}}^{(b)}$. In a more general configuration of electric and magnetic fields, we can identify those components

of the bulk third-order transport tensor that are symmetrized along all three indices. These are third-order transport coefficients that can be distinguished in our MC simulations, as we calculate transport coefficients using expressions derived from the generalized diffusion equation [58].

3. Methodology

3.1. Multi-term solution of the Boltzmann equation

The Boltzmann equation describes the evolution of the phase space distribution function $f(\mathbf{r}, \mathbf{c}, t)$. For a swarm of electrons the Boltzmann equation can be written as:

$$\frac{\partial f(\mathbf{r}, \mathbf{c}, t)}{\partial t} + \mathbf{c} \cdot \frac{\partial f(\mathbf{r}, \mathbf{c}, t)}{\partial \mathbf{r}} + \frac{q}{m}\mathbf{E} \cdot \frac{\partial f(\mathbf{r}, \mathbf{c}, t)}{\partial \mathbf{c}} = -J(f, f_0),$$
(8)

where q and m are electron charge and electron mass respectively, $\mathbf{E}$ is electric field and J is collision operator. This operator represents change of the electron distribution function per unit time, due to collisions with particles of the background medium. These particles are described by the distribution function f_0.

In the multi-term method for solving Boltzmann's equation the phase space distribution function is expanded in terms of spherical harmonics and Sonine polynomials in angular and radial parts of the velocity space, respectively. Thus, under hydrodynamic conditions $f(\mathbf{r}, \mathbf{c}, t)$ is expanded as follows [75–79]:

$$f(\mathbf{r}, \mathbf{c}, t) = \omega(\alpha, c) \sum_{s=0}^{\infty} \sum_{\lambda=0}^{s} \sum_{\mu=-\lambda}^{\lambda} \sum_{\nu, l=0}^{\infty} \sum_{m=-l}^{l} F(\nu l m | s \lambda \mu; \alpha)$$
$$\times R_{\nu l}(\alpha, c) Y_m^{[l]}(\hat{\mathbf{c}}) G_\mu^{(s\lambda)} n(\mathbf{r}, t),$$
(9)

where $F(\nu l m | s \lambda \mu; \alpha)$ are moments of the distribution function, $\hat{\mathbf{c}}$ is unit vector in velocity space, $Y_m^{[l]}(\hat{\mathbf{c}})$ are spherical harmonics, $G_\mu^{(s\lambda)}$ is the spherical form of the gradient tensor operator, while α, $\omega(\alpha, c)$ and $R_{\nu l}(\alpha, c)$ are given by:

$$\alpha^2 = \frac{m}{kT_b},$$
(10)

$$\omega(\alpha, c) = \left(\frac{\alpha^2}{2\pi}\right)^{3/2} e^{-\alpha^2 c^2/2},$$
(11)

$$R_{\nu l}(\alpha c) = N_{\nu l} \left(\frac{\alpha c}{\sqrt{2}}\right)^2 S_{l+1/2}^{(\nu)}(\alpha^2 c^2/2),$$
(12)

where k is the Boltzmann constant, T_b is the basis temperature, which is a parameter for optimizing convergence, $S_{l+1/2}^{(\nu)}$ is Sonine polynomial, while $N_{\nu l}$ is given by:

$$N_{\nu l}^2 = \frac{2\pi^{3/2}\nu!}{\Gamma(\nu + l + 3/2)},$$
(13)

where $\Gamma(\nu + l + 3/2)$ is gamma function.

The Boltzmann equation is decomposed into a hierarchy of kinetic equations by applying the relations of orthogonality for spherical harmonics and Sonnine polynomials [76]. The moments of the distribution function $F(\nu l m | s \lambda \mu; \alpha)$ can

be obtained by solving this system of kinetic equations [75, 80]. The resulting hierarchy of kinetic equations is truncated at finite values of $l = l_{\max}$ and $\nu = \nu_{\max}$. Unlike the two-term approximation, in which small anisotropy in velocity space is assumed and $l_{\max}$ is set to 1, in the multi-term method $l_{\max}$ is increased until full convergence of transport coefficients is obtained, after which the obtained hierarchy is solved numerically.

Spherical form of the velocity vector is defined as [76]:

$$c_m^{[1]} = \sqrt{\frac{4\pi}{3}} c Y_m^{[1]}(\hat{\mathbf{c}}).$$
(14)

Cartesian components of a vector can be expressed via spherical form as:

$$c_x = \frac{i}{\sqrt{2}} \left(c_1^{[1]} - c_{-1}^{[1]}\right),$$
(15)

$$c_y = \frac{1}{\sqrt{2}} \left(c_1^{[1]} + c_{-1}^{[1]}\right),$$
(16)

$$c_z = -i c_0^{[1]}.$$
(17)

Spherical form of the flux of velocity of electrons can be written as [80]:

$$\Gamma_m^{(1)}(\mathbf{r}, t) = \frac{1}{\alpha} \sum_{s=0}^{\infty} \sum_{\lambda=0}^{s} \sum_{\mu=-\lambda}^{\lambda} F(01m|s\lambda\mu) G_\mu^{(s\lambda)} n(\mathbf{r}, t).$$
(18)

Explicit expressions for the individual components of the flux third-order transport tensor can be determined from the Cartesian components of the flux of velocity from equation (18) after identifying terms that are contracted with the corresponding partial derivatives [58].

Expressions for three independent components of the flux third-order transport tensor in the electric field only configuration defined to be in the z direction, are given by:

$$Q_{xxz}^{(f)} = \frac{1}{\sqrt{2}\alpha} \left[\text{Im}(F(011|221; \alpha)) - \text{Im}(F(01-1|221; \alpha))\right],$$
(19)

$$Q_{zxx}^{(f)} = -\frac{1}{\alpha} \left[\frac{1}{\sqrt{3}} \text{Im}(F(010|200; \alpha)) \right.$$
$$+ \frac{1}{\sqrt{6}} \text{Im}(F(010|220; \alpha))\bigg]$$
$$+ \frac{1}{\alpha} \text{Im}\left[F(010|222; \alpha)\right],$$
(20)

$$Q_{zzz}^{(f)} = \frac{1}{\alpha} \left[\sqrt{\frac{2}{3}} \text{Im}(F(010|220; \alpha)) \right.$$
$$- \frac{1}{\sqrt{3}} \text{Im}(F(010|200; \alpha))\bigg],$$
(21)

where Im denotes imaginary parts of the moments of the phase space distribution function.

3.2. Monte Carlo simulations

In MC simulations, we track the space and time evolution of a swarm of electrons. The extensive use of random numbers is required in order to determine the exact moment and the type of the individual collisions of electrons with the background molecules, as well as the direction of the post collisional electron velocity. The transport coefficients are computed from the corresponding polynomials of the electron coordinates and velocity components, which are averaged over the entire swarm. The details of our MC code are discussed in our previous publications [75, 81–83]. Bulk third-order transport coefficients are calculated as:

$$\mathbf{Q}^{(b)} = \frac{1}{3!} \frac{d}{dt} \langle \mathbf{r}^\star \mathbf{r}^\star \mathbf{r}^\star \rangle, \tag{22}$$

while the flux third-order transport coefficients are determined from:

$$\mathbf{Q}^{(f)} = \frac{1}{3!} \left\langle \frac{d}{dt} \left(\mathbf{r}^\star \mathbf{r}^\star \mathbf{r}^\star \right) \right\rangle, \tag{23}$$

where $\mathbf{r}^\star = \mathbf{r} - \langle \mathbf{r} \rangle$, and the brackets $\langle \rangle$ represent ensemble averages. Expressions for transport coefficients, that are used in our MC method, are derived from the generalized diffusion equation, in which all tensor indices are contracted with partial derivatives. Thus, in the generalized diffusion equation symmetrization of the third-order transport tensor with respect to all indices is performed. For this reason, we cannot determine individual off-diagonal components of the third-order transport tensor or individual off-diagonal components of the diffusion tensor in our MC simulations [75]. Instead, we can determine individual diagonal components such as $Q_L = Q_{zzz}$ and averages of those off-diagonal components that have the same combination of indices like $Q_T = (Q_{xxz} + Q_{xzx} + Q_{zxx})/3$. It should be noted that Q_{xzx} and Q_{zxx} are equal due to the commutativity of the last two indices of the third-order transport tensor [52, 56, 58, 65]. Explicit expressions for $Q_L^{(b)}$ and $Q_T^{(b)}$ in the electric field only configuration are given by:

$$Q_L^{(b)} = \frac{1}{6} \frac{d}{dt} \left(\langle z^3 \rangle - 3 \langle z \rangle \langle z^2 \rangle + 2 \langle z \rangle^3 \right), \tag{24}$$

$$Q_T^{(b)} = \frac{1}{6} \frac{d}{dt} \left(\langle z x^2 \rangle - \langle z \rangle \langle x^2 \rangle \right), \tag{25}$$

while the corresponding flux components $Q_L^{(f)}$ and $Q_T^{(f)}$ are given in [58].

It is important to note that numerical differentiation in time is not used for the calculation of $Q_L^{(b)}$ and $Q_T^{(b)}$, because of the statistical fluctuations of the corresponding expressions in brackets. Direct numerical differentiation of these expressions would create fluctuations that are much more intense than the fluctuations of the initial expressions. Instead, the expression in brackets is fitted to a linear function. The corresponding time derivative is determined as the slope of this linear function. This is justified because $Q_L^{(b)}$ and $Q_T^{(b)}$ are independent of time after relaxation of the swarm, and the corresponding expressions in brackets in equation (24) and (25) are linear functions in time. This method for calculating $Q_L^{(b)}$ and $Q_T^{(b)}$

has been further verified by comparing values of the bulk third-order transport coefficients, that are obtained by this method, with the corresponding values that are determined by employing numerical differentiation in time. An additional check was obtained by comparing $Q_L^{(b)}$ and $Q_T^{(b)}$ with $Q_L^{(f)}$ and $Q_T^{(f)}$, respectively, under conditions where non-conservative processes are absent.

4. Results and discussion

4.1. Preliminaries

In this paper, we consider the transport of electrons in the Lucas–Saelee model, modified Ness–Robson model, N_2 and CF_4. The Ness–Robson model was developed for testing the multi-term method for solving the Boltzmann equation in the presence of electron attachment [80]. Nolan and co-workers presented a new gas model that is based on the Ness–Robson model and the Lucas–Saelee model [73]. In this model the collision frequency of elastic collisions is independent of energy while the cross section for inelastic collisions is the same as in the Lucas–Saeele model. In modifying the Ness–Robson model, which is introduced by Nolan *et al* [73], both inelastic collisions and ionisation are present. The ratio of the cross section for inelastic collisions to the cross section for ionisation is determined by the F parameter, as in the Lucas–Saelee model. Two different versions of the modified Ness–Robson model [73] with different functional dependences of the cross section for electron attachment are considered in this work. In both considered versions of the modified Ness–Robson model the parameter F is set to zero, implying the absence of ionisation. The details of the modified Ness–Robson model, in the absence of ionisation, are given by the following equations:

$$\sigma_{el}(\epsilon) = 4\epsilon^{-1/2} \ \mathring{A}^2 \quad \text{(elastic collision)}$$

$$\sigma_{ex}(\epsilon) = \begin{cases} 0.1(\epsilon - 15.6) \ \mathring{A}^2, & \epsilon \geqslant 15.6 \text{ eV} \\ & \text{(inelastic collision)} \\ 0, & \epsilon < 15.6 \text{ eV} \end{cases}$$

$$\sigma_a(\epsilon) = a\epsilon^p \quad \text{(electron attachment)}$$

$$m/m_0 = 10^{-3},$$

$$T_0 = 0 \text{ K}, \tag{26}$$

where $\sigma_{el}(\epsilon)$, $\sigma_{ex}(\epsilon)$, $\sigma_a(\epsilon)$ are cross sections for elastic collisions, inelastic collisions and electron attachment, respectively, given as functions of electron energy ϵ, T_0 is the temperature of the background gas, while m and m_0 are masses of electrons and of the molecules of the background gas, respectively. In the above equations, the values of the electron energy are given in eV. Parameters a and p determine the magnitude and the functional dependence of the cross section for electron attachment, respectively. The values of p that are considered in this work include -1.0 and 0.5. These values correspond to attachment heating and attachment cooling, respectively. The percentage differences between the third-order transport

coefficients determined for each of these two models and the corresponding values in the model where $p = -0.5$ are considered in this work. In the third model the collision frequency for electron attachment is independent of energy. The values of parameter a, that are used in this work, include 8×10^{-3} Å^2 and 5×10^{-4} Å^2. The first value is used for the attachment heating model, while the second value is used for the attachment cooling model. In the model with constant collision frequency for electron attachment, this non-conservative process is equally frequent at all values of the electron energy, and it does not affect transport coefficients of any order (excluding the rate coefficient for electron attachment). In this model the values of the third-order transport tensor are the same as in the conservative Lucas–Saelee model, where $F = 0$.

The Lucas–Saelee ionisation model was introduced in order to investigate the influence of electron-impact ionisation on the electron transport by using MC simulations [84]. Ness and Robson investigated the electron transport in this model, in order to test the validity of the theory and associated computer code for solving the Boltzmann equation, in the presence of non-conservative processes [80]. The details of the Lucas–Saelee model are given by the following equations:

$$\sigma_{\mathrm{el}}(\epsilon) = 4\epsilon^{-1/2} \text{ Å}^2 \quad \text{(elastic collision)}$$

$$\sigma_{\mathrm{ex}}(\epsilon) = \begin{cases} 0.1(1 - F)(\epsilon - 15.6) \text{ Å}^2, & \epsilon \geqslant 15.6 \text{ eV} \\ & \text{(inelastic collision)} \\ 0, & \epsilon < 15.6 \text{ eV} \end{cases}$$

$$\sigma_{\mathrm{I}}(\epsilon) = \begin{cases} 0.1F(\epsilon - 15.6) \text{ Å}^2, & \epsilon \geqslant 15.6 \text{ eV} \\ & \text{(ionisation)} \\ 0, & \epsilon < 15.6 \text{ eV} \end{cases}$$

$$P(q, \epsilon') = 1, m/m_0 = 10^{-3},$$
$$T_0 = 0 \text{ K}, \tag{27}$$

where $\sigma_{\mathrm{I}}(\epsilon)$ is the cross section for ionisation, $P(q, \epsilon)$ is the ionisation partition function, and F is the parameter that determines the magnitudes of cross sections for inelastic collisions and ionisation. As the scattering is isotropic in this model $\sigma_{\mathrm{el}}(\epsilon)$, $\sigma_{\mathrm{ex}}(\epsilon)$, and $\sigma_{\mathrm{I}}(\epsilon)$ represent total cross sections. Arguments of the ionisation partition function $P(q, \epsilon')$, q and ϵ', are the ratio of total postcollisional energy, that is given to the ejected electron, and the energy of the initial electron before ionisation, respectively. In this model, ionisation partition function is set to unity, indicating that all values $0 \leqslant q \leqslant 1$ are equally probable.

The set of cross sections for electron scattering in N$_2$, which is used in this work, is detailed in [64]. It includes elastic momentum transfer cross section, as well as the total cross section for rotational excitations, and cross sections for vibrational excitations, electronic excitations and electron-impact ionisation. The set of cross sections for electron scattering in CF$_4$, which is employed in this work, was developed

and discussed by Kurihara and co-workers [85]. It includes elastic momentum transfer cross section, cross sections for vibrational excitations, electronic excitations, electron attachment, and ionisation. For some aspects of this work, it was necessary to consider the electron transport in CH$_4$. These results are obtained by using the cross sections developed by Šašić *et al* [86].

The results for the model and the real gases were obtained from the MC simulations and numerical multi-term solution of the Boltzmann equation. In particular, it was necessary to follow a large number of electrons (at least 10^7) in our MC simulations in order to calculate third-order transport coefficients accurately, due to high statistical fluctuations of individual terms appearing in expressions (24) and (25). It was also necessary to determine the phase space distribution function with a high degree of precision in order to calculate the third-order transport coefficients from the multi-term method. While the number of spherical harmonics indicates the degree of anisotropy of the phase space distribution function in velocity space, the number of Sonine polynomials is indicative of the deviation of the energy dependence of the distribution function from a Maxwellian at a particular temperature T_{b} not necessarily equal to the gas temperature T_0. Third-order transport coefficients are more sensitive to the shape of the phase space distribution function than transport coefficients of lower order. For this reason it was necessary to include a large number of spherical harmonics and Sonine polynomials to achieve the convergence of the third-order transport coefficients, in the presence of strong inelastic and/or non-conservative collisions. For example, the required numbers of $l_{\max}$ and $\nu_{\max}$ were 8 and 90, respectively, for electrons in CF$_4$. This was especially pronounced in the energy region where the cross sections for vibrational excitations are rapidly rising functions of electron energy, while the cross section for elastic collisions is being reduced with increasing electron energy. The solutions of the Boltzmann equation are not determined for $E/n_0 > 300$ Td, as the convergence of the transport coefficients was poor in this field region. For this reason, we have only displayed the MC results in the field range above 300 Td.

4.2. Variation of the flux third-order transport coefficients with E/n_0 for electrons in N$_2$ and CF$_4$

In figures 1(a) and (b) we show the mean energy for an electron swarm in N$_2$, and CF$_4$, respectively, as a function of the reduced electric field, E/n_0. At the lowest fields the mean energy is thermal in both gases, while it is rising with increasing E/n_0 at higher fields. The slope of the mean energy is determined by collisions of electrons with atoms/molecules of the background gas [85]. The profiles of the mean energy are useful for analysing the field dependence of the third-order transport coefficients. From these profiles one can determine which collisional processes dominate electron transport in a given field range.

In this section, we study the behaviour of the components of the flux third-order transport tensor for electrons in N$_2$ and CF$_4$ in the presence of an electric field. It has been previously shown that the rise of E/n_0 under constant collision frequency
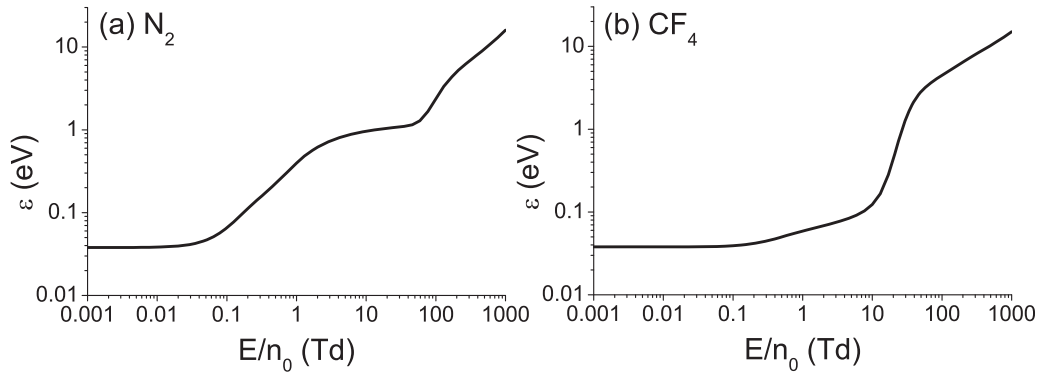
Figure 1. Mean energy of electron swarm in (a) N_2 and (b) CF_4, as a function of the reduced electric field. These results are obtained by using multi term theory for solving the Boltzmann equation up to about 300 Td and by employing MC simulations at higher fields.
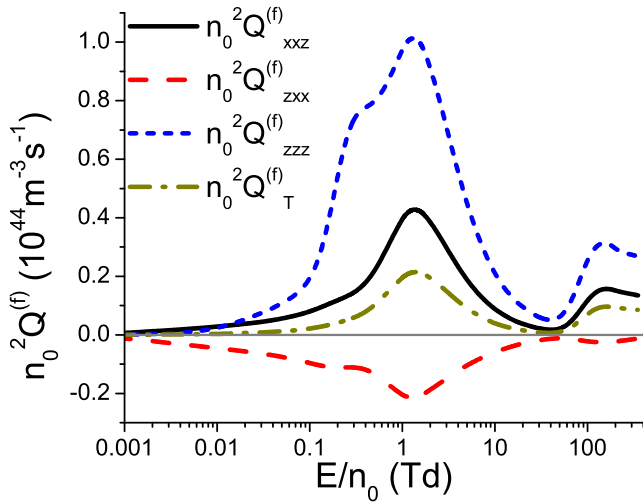

Figure 2. Independent components of the flux third-order transport tensor and $n_0^2 Q_T^{(f)}$ as functions of E/n_0 for electrons in N_2. The results are obtained from numerical multi-term solutions of the Boltzmann equation.
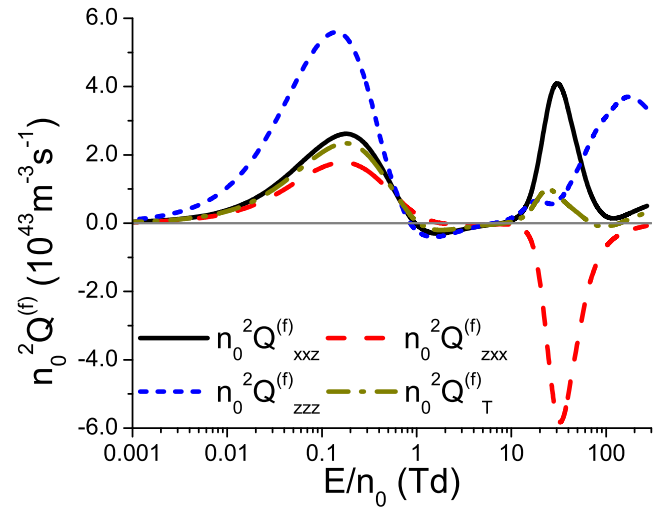
Figure 3. Independent components of the third-order transport tensor and $n_0^2 Q_T^{(f)}$ as functions of E/n_0 for electrons in CF_4. The results are obtained from numerical multi-term solutions of the Boltzmann equation.

conditions leads to an increase of the components of the third-order transport coefficient tensor [58]. It has also been shown that the increase of the collision frequency with increasing energy may lead to a decrease of the components of this tensor, as well as to negative values of these components, if the rise of the collision frequency is steep enough [58, 69]. For this reason, the E/n_0-profile of the third-order transport coefficients is determined by the complex interplay between the electric field, which accelerates electrons and acts to direct their movement along the field lines, and collisions between electrons and atoms/molecules of the background gas, which dissipate electron energy and momentum. Although it is possible to analyse E/n_0 profiles of the third-order transport coefficients directly from the mean energy of electrons and collision frequencies for individual collisional processes, such analysis is often quite complicated and tedious. Therefore, in this section we briefly discuss the general E/n_0-profiles of the third-order transport coefficients for electrons in N_2 and CF_4, while a more detailed analysis is reserved only for the unusual and unexpected aspects of the behaviour of these transport properties.

A more detailed study of the behaviour of $Q_{zzz}^{(f)}$ and $Q_T^{(f)}$ for electrons in N_2 and CF_4 is presented in section 4.4.

In figure 2 we show the independent components of the third-order flux transport tensor for electrons in N_2 as functions of E/n_0. In addition, we also show the variation of $n_0^2 Q_T^{(f)}$ with E/n_0. The $Q_{zxx}^{(f)}$ component is negative, while the remaining quantities are positive over the entire E/n_0 range considered. Negative values of $Q_{zxx}^{(f)}$ can be attributed to the rise of the collision frequency for elastic and inelastic collisions with increasing electron energy. This phenomenon has been observed for electrons in both model and real gases [58, 62, 69]. It can be seen from figure 2 that the absolute values of quantities have a similar qualitative dependence on E/n_0. Specifically, the absolute values of these transport coefficients have two local maximums at about 1.3 Td and 150 Td, and a local minimum at around 46 Td.

In figure 3 we show the three independent components of the flux third-order transport tensor for electrons in CF_4 as functions of E/n_0. In the same figure we show the variation of $n_0^2 Q_T^{(f)}$ with E/n_0. At the lowest fields, all quantities are
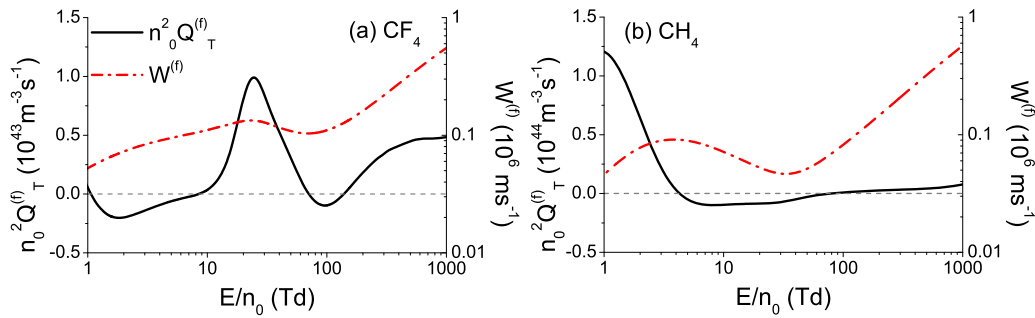
Figure 4. Transverse flux third-order transport coefficients $n_0^2 Q_T^{(f)}$ and the flux drift velocity $W^{(f)}$ as functions of E/n_0 for electrons in (a) CF_4 and (b) CH_4. The results are obtained by employing the multi-term theory for solving the Boltzmann equation up to about 300 Td for electrons in CF_4, and up to 600 Td for electrons in CH_4, and by using MC simulations at higher fields.

positive, and increasing functions E/n_0 up to about 0.14 Td in the case of $Q_{zzz}^{(f)}$, and up to about 0.18 Td in the case of the remaining quantities. At higher fields these quantities are being reduced and they become negative. The $Q_{zxx}^{(f)}$ component becomes negative at about 2 Td. The remaining transport coefficients become negative at about 0.9 Td, and they reach a local minimum at around 1.6 Td. These quantities become positive again at about 7.5 Td. The $Q_{xxz}^{(f)}$ and $Q_{zzz}^{(f)}$ components remain positive until the end of the considered range of E/n_0, while the $Q_{zxx}^{(f)}$ component remains negative. The $Q_{zzz}^{(f)}$ component has two local maximums at about 20 Td and 170 Td and a local minimum at around 27 Td. The $Q_{xxz}^{(f)}$ component and $Q_T^{(f)}$ have a local maximum at about 31 Td and 25 Td, and a local minimum at around 120 Td and 100 Td, respectively. The $Q_{zxx}^{(f)}$ component has a local minimum at about 33 Td. At the lowest E/n_0, all quantities that are displayed in figure 3 are rising functions of E/n_0. This can be attributed to a negligible rise of the mean energy with increasing field in this E/n_0 region, which leads to a small change of the mean collision frequency for elastic and inelastic collisions. At higher fields, the rise of the mean energy and mean collision frequency for vibrational excitations with increasing E/n_0, become more significant, which in turn induces a decrease of the third-order transport coefficients.

We now focus on the negative values of the third-order transport coefficients for electrons in CF_4. As discussed elsewhere [58, 70], the bulk third-order transport tensor represents asymmetric deviation of the spatial distribution of the swarm from an ideal Gaussian. This deviation is caused by different rates of spread of electrons at the swarm front and at the back of the swarm. Due to this difference, different parts of the normalized spatial distribution of electrons may seem elongated or compressed when compared to an ideal Gaussian. Specifically, $Q_{zzz}^{(b)}$ component describes elongation/contraction of the spatial distribution of electrons at the leading edge of the swarm, and the opposite deformation at its trailing edge. A negative value of the $Q_{zzz}^{(b)}$ component implies that the normalized spatial distribution of electrons is compressed (when compared to an ideal Gaussian) along the longitudinal direction at the front of the swarm and expanded along the same direction at the back of the swarm. Similarly, a negative value of $Q_T^{(b)}$ implies that the normalized spatial distribution of electrons is compressed (relative to an ideal Gaussian) along the transverse direction at

the swarm front and expanded along the same direction at the back of the swarm. It is important to emphasize that the spatial distribution of electrons is not being actually compressed in time. Instead, in some regions of space the effective rate of spread of electrons, that is represented by both third-order transport coefficients and diffusion, is smaller than the corresponding rate of spread that would be represented by diffusion alone. In these regions of space, the normalized spatial distribution of electrons seems compressed when compared to an ideal Gaussian. For E/n_0 less than approximately 10 Td, the impact of non-conservative collisions is minimal, and thereby the bulk values of the third-order transport coefficients are equal to the corresponding flux values (see figure 13). In the field region around 0.9 Td, where $Q_{zzz}^{(f)}$, $Q_{xxz}^{(f)}$ and $Q_T^{(f)}$ become negative, electrons with energies that are 3 times higher than the mean energy are in the energy region around 0.2 eV, where the cross sections for two vibrational excitations of the CF_4 molecule reach their global maximums [85]. These cross sections are denoted as Q_{v1} and Q_{v3} in table 1 or reference [85] and their thresholds are 0.108 eV and 0.168 eV, respectively. Moreover, Q_{v1} becomes greater than the elastic momentum transfer cross section in the energy range between approximately 0.12 eV and 0.58 eV. The same holds for Q_{v3} in the energy range between approximately 0.17 eV and 2.6 eV. Thus, in the field region around 0.9 Td where $Q_{xxz}^{(f)}$, $Q_{zzz}^{(f)}$ and $Q_T^{(f)}$ become negative, the high energy tail of the distribution function is in the energy range where the electron transport is dominated by vibrational excitations. As the mean energy of electrons is increasing in the positive direction (direction of the force acting upon electrons), the intense energy losses due to the vibration excitations create a strong resistance to the spreading of the swarm at its front in the longitudinal and transverse directions. This resistance leads to the compression of the spatial distribution of electrons at the front of the swarm along both longitudinal and transverse directions, while this spatial distribution is more expanded along both these directions at the back of the swarm. Such deviation of the spatial profile of electrons from an ideal Gaussian is manifested through negative values of Q_{zzz} and Q_T (in both flux and bulk case).

In figures 4(a) and (b), we show the variation of $n_0^2 Q_T^{(f)}$ and $W^{(f)}$ with E/n_0 for electrons in CF_4 and CH_4, respectively. It should be noted that some general aspects of the behaviour of

third-order transport coefficients for electrons in CH_4 were discussed in our previous publication [62]. CH_4 was introduced here in order to observe relationship of negative values of the higher order transport coefficients with the negative differential conductivity (NDC) for drift velocity. We observe from figures 4(a) and (b) that the drift velocity of electrons in both CF_4 and CH_4 exhibits NDC. NDC refers to the decrease in drift velocity with an increase in the reduced electric field E/n_0. To understand NDC, it is necessary to consider the rates of momentum and energy transfer in elastic and inelastic collisions [87]. Interestingly, Q_T has negative values between approximately 70 Td and 140 Td in CF_4. This approximately corresponds to the field region beyond the end of the NDC where drift velocity begins to rise rapidly (almost reaching its maximum value before the NDC). A similar relationship exists in the E/n_0-profile of the electron drift velocity in CH_4. However, in CH_4, Q_T becomes negative at the beginning of the NDC much earlier than in CF_4.

The qualitative behaviour of the individual off-diagonal components of the third-order transport tensor over the range of E/n_0, where NDC occurs, is different for electrons in CF_4 and CH_4. For electrons in CF_4 the $Q_{xxz}^{(f)}$ component is positive, while the $Q_{zxx}^{(f)}$ component is negative, over the entire range of E/n_0, corresponding to the NDC. For the electrons in CH_4, however, the $Q_{xxz}^{(f)}$ component becomes negative shortly after the start of the NDC, while $Q_{zxx}^{(f)}$ becomes positive at a slightly larger field. The $Q_{xxz}^{(f)}$ component becomes positive again for electrons in CH_4, for the value of E/n_0 where $Q_T^{(f)}$ becomes positive. Thus, it is difficult to find out more about the behaviour of individual off-diagonal components of the third-order transport tensor, from the presence of NDC in the E/n_0-profile of drift velocity in a given field region, due to the complexity of various factors that determine the behaviour of the third-order transport coefficients. However, it is evident that negative values of $Q_T^{(f)}$ can arise in the vicinity of the field region where NDC occurs. Negative values of $Q_T^{(f)}$ imply the compression of the spatial profile of the swarm along the transverse direction at the front of the swarm, and the expansion of this profile along the same direction at the back of the swarm [58]. This implies that the rapid increase of collision frequency for elastic collisions, which leads to a greater randomization of velocity vectors of the individual electrons and the occurrence of NDC, can also hinder transverse spreading of electrons at the swarm front, where the mean energy of electrons is higher than that at the back of the swarm. This is manifested through negative values of $Q_T^{(f)}$. However, this does not lead to negative values of $Q_L^{(f)}$, as they occur only when the spatial profile of the swarm is skewed in the direction opposite to the direction of drift velocity. This kind of deformation requires a strong resistance to the motion of electrons in the direction of drift velocity, which is more easily achieved with inelastic and non-conservative collisions, when the corresponding cross sections are large enough. It can be seen that $Q_T^{(f)}$ is negative in the majority of region where $Q_L^{(f)}$ is negative for electrons in CF_4, as it is easier to achieve negative values of $Q_T^{(f)}$ than negative values of $Q_L^{(f)}$. Thus, one may conclude that the concurrence

between drift velocity and $Q_T^{(f)}$ can be attributed to the corresponding collisions which lead to the occurrence of NDC and to the compression of the spatial distribution of the swarm along the transverse direction at the front of the swarm. However, we observe that for the electrons in CF_4 negative values of $Q_T^{(f)}$ occur only in a small field range after the NDC. Therefore, the presence of NDC at a certain value of E/n_0 does not necessarily result in a negative value of $Q_T^{(f)}$ for these electric fields, but again the conditions in the momentum and energy balances that lead to NDC also favour negative values of Q_T depending on the balance of different competing processes. The concurrence between the transport coefficients of the third-order and the drift velocity is therefore much less pronounced than the concurrence between the transport coefficients of the third-order and diffusion. It would be interesting to investigate the behaviour of $Q_T^{(f)}$ and $Q_T^{(b)}$ in strongly attaching gases under conditions in which NDC occurs only for bulk drift velocity, due to electron attachment [88, 89]. This will be considered in the near future.

It is striking that although similar in the shape of the cross sections the two gases exhibit very different dependences of the NDC. For CF_4 the NDC minimum is much shallower and occurs at higher E/n_0. The depth of the NDC is normally promoted by the separate control of the mean energy and momentum transfer by cross sections that control the energy exchange and momentum transfer. Positioning of vibrational excitation cross sections and overlap of their influences will at the same time affect the magnitude of the peak in drift velocity induced by the inelastic processes and also the onset and overall effect of the NDC.

In figures 5 and 6, we show comparison between the two-term and converged multi-term solutions of the Boltzmann equation for electrons in N_2 and CF_4, respectively. The E/n_0 profiles of the independent components of the flux third-order transport tensor, including $n_0^2 Q_{xxz}^{(f)}$, $n_0^2 Q_{zxx}^{(f)}$ and $n_0^2 Q_{zzz}^{(f)}$ are shown. In addition, the variation of $n_0^2 Q_T^{(f)}$ with E/n_0 is also shown. Comparing two-term and multi-term results for electrons in N_2, it is evident that for the low values of E/n_0 the agreement is good while the maximum error in the two-term approximation occurs at the highest fields. For electrons in CF_4, however, there is a significant difference between the two-term and multi-term solutions of the Boltzmann equation over the entire range of E/n_0 considered in this work, except in the limit of the lowest E/n_0. In contrast to N_2, the two-term and multi-term results are qualitatively different in CF_4, indicating that sometimes the two-term theory predicts physics that is not entirely correct. The maximum errors of the two-term approximation occur over the range of E/n_0 values where $n_0^2 Q_{zzz}^{(f)}$ is negative. This happens at electron energies where elastic momentum transfer is approximately at a minimum while inelastic collisions which lead to the vibrational excitations of CF_4 molecule became significant and are approximately at their maximum. This induces a large asymmetry of the distribution function in velocity space which makes the two-term approximation inadequate for studying the third-order transport coefficients. Thus, it is important to note that neglecting higher terms in the spherical harmonic expansion of the phase
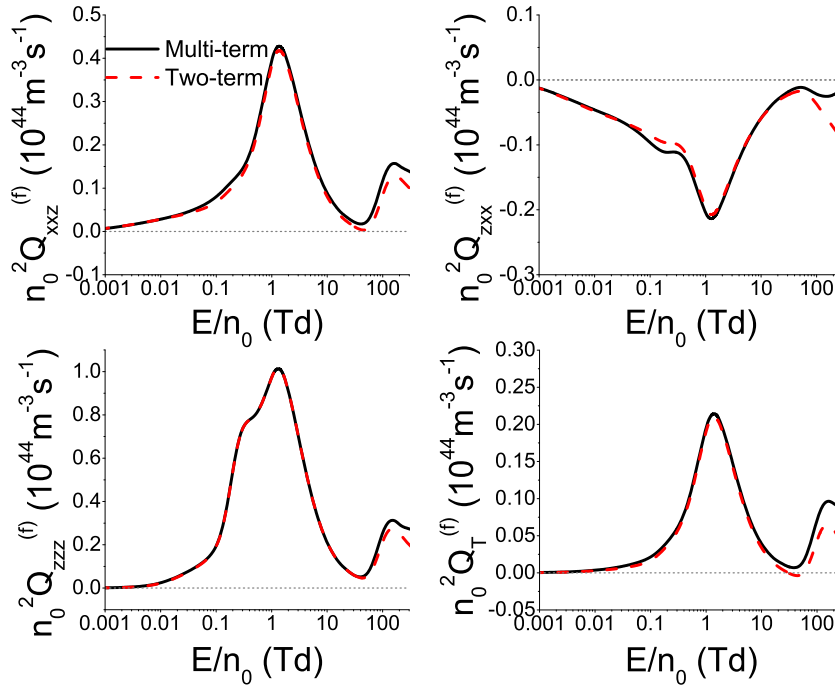
Figure 5. Comparison between the flux third-order transport coefficients obtained by the two-term approximation and multi-term theory for solving the Boltzmann equation. Calculations are performed for electrons in N_2.

space distribution function has a much more pronounced effect for third order transport coefficients than for lower order transport coefficients. For electrons in CF_4 the third-order transport coefficients determined by using the two-term approximation are not even qualitatively correct.

4.3. The influence of non-conservative processes on the third-order transport coefficients

4.3.1. The influence of electron attachment on the third-order transport coefficients for electrons in the modified Ness–Robson model. The bulk and flux values of the longitudinal and transverse components of the third-order transport tensor for electrons in the Ness–Robson attachment heating model, are shown in figures 7(a) and (b), respectively. In this model the slower electrons at the back of the swarm are preferentially attached. As a consequence, the bulk values of Q_L and Q_T exceed the corresponding flux values for lower values of E/n_0, e.g. up to about 3.8 Td for Q_L and 5 Td for Q_T.

For higher values of E/n_0, up to about 8 Td for Q_L and 17 Td for Q_T, the flux values are greater than the corresponding bulk values, although this effect is in the limit of statistical error of MC simulations in the case of Q_T. This can be attributed to a combination of two factors. The first factor is the decreased number of low-energy electrons at the back of the swarm, due to the rise of the mean energy with increasing field. The second factor is the increased number of low-energy electrons at the front of the swarm, due to the influence of inelastic collisions, which are more frequent at the front of the swarm. In the limit of the highest fields, higher than 8 Td for Q_L and 17 Td for Q_T, the difference between flux and bulk values of the third-order transport coefficients is negligible for electrons in this model gas.

The bulk and flux values of the longitudinal and transverse components of the third-order transport tensor for electrons in the Ness–Robson attachment cooling model, are shown in figures 8(a) and (b), respectively. In this model the faster electrons at the front of the swarm, where the mean energy is higher, are preferentially attached. As a consequence, for lower values of E/n_0 bulk values are lower than the corresponding flux values. We observe that this effect is within the statistical uncertainty of MC simulations for Q_T. However, for higher values of E/n_0 (from approximately 5 Td) bulk values are larger than the corresponding flux values in case of Q_L, although this difference is lower than the statistical error of MC simulations. For $E/n_0 \geqslant 10$ Td $Q_L^{(f)}$ and $Q_L^{(b)}$ are practically equal. Similar behaviour is observed for Q_T, because for $E/n_0 \geqslant 7$ Td $Q_T^{(f)}$ and $Q_T^{(b)}$ coincide. Between 5 Td and 10 Td, $Q_L^{(b)}$ exceeds $Q_L^{(f)}$ due to the interplay of inelastic collisions and the increase of the mean electron energy with increasing E/n_0, as in the case of the attachment heating model.

In figure 9 the percentage difference in the longitudinal component of the third-order transport tensor calculated using the modified Ness–Robson models with the attachment heating and with a constant collision frequency for electron attachment, are shown. Panel (a) shows the difference between the flux values, while the panel (b) displays the difference between the bulk values. The percentage differences are calculated using the expression: $Q_L^{heating}/Q_L^{constant} - 1$. The difference between flux values of Q_L in these two models is caused by the implicit effects of electron attachment, while the difference between the corresponding bulk values is induced by a combined effect of implicit and explicit effects of electron attachment. Comparing panels (a) and (b) in the limit of the
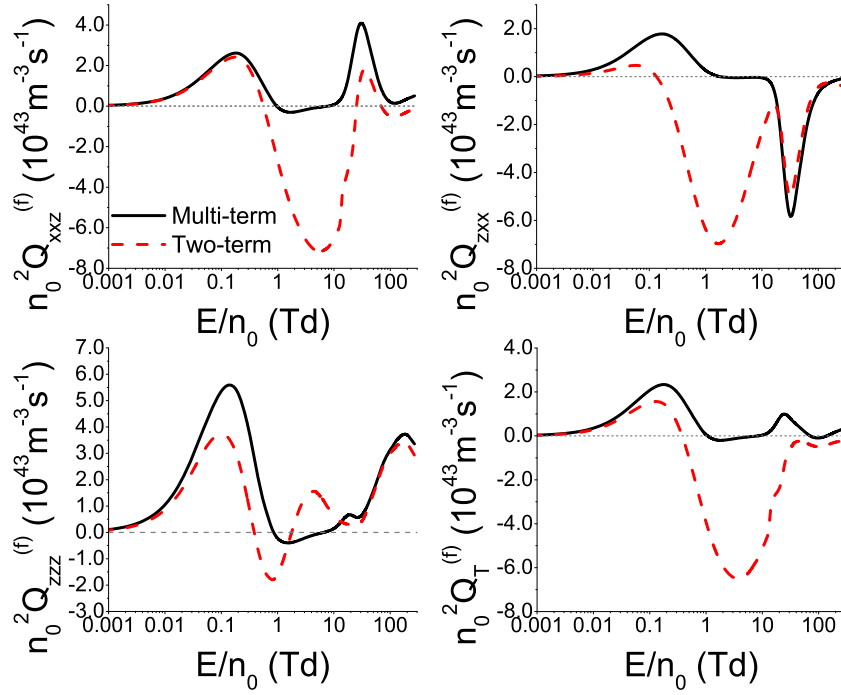
Figure 6. Comparison between the flux third-order transport coefficients obtained by the two-term approximation and multi-term theory for solving the Boltzmann equation. Calculations are performed for electrons in CF_4.
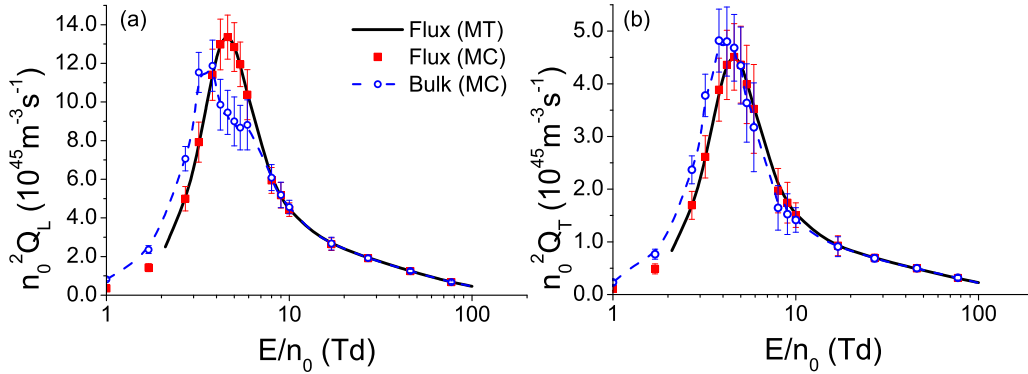
Figure 7. Comparison of the bulk and flux values of (a) $n_0^2 Q_L$ and (b) $n_0^2 Q_T$ for electrons in the modified Ness–Robson attachment heating model. The results are obtained from numerical multi-term solutions of the Boltzmann equation (MT) and MC simulations.

lowest E/n_0, we observe that Q_L is much higher in the attachment heating model than in the model with a constant collision frequency for electron attachment, for both bulk and flux values. It is also evident that these differences are much more pronounced in the case of bulk third-order transport coefficients. These differences decrease with increasing E/n_0 and become even negative over a limited range of E/n_0. As E/n_0 further increases, the differences tend to zero. It should be noted that negative values of these quantities can be attributed to the influence of inelastic collisions, although these values are within the statistical uncertainty of MC simulations.

Similarly, figure 10 shows the difference in Q_L calculated using the modified Ness–Robson models with the attachment cooling and with a constant collision frequency for electron attachment. Results for $Q_L^{(f)}$ and $Q_L^{(b)}$ are shown in panels (a) and (b), respectively. In this case, the following

expression is used for calculating the percentage difference: $Q_L^{cooling}/Q_L^{constant} - 1$. The values of this expression for the longitudinal components of both flux and bulk third-order transport tensor are decreasing functions of E/n_0 up to about 4 Td where they reach a local minimum, which is equal to around -20% and about -50% for $Q_L^{(f)}$ and $Q_L^{(b)}$, respectively. For higher values of E/n_0 these differences are being increased and they reach a local maximum at around 10 Td in the case of $Q_L^{(f)}$ and at about 8 Td in the case of $Q_L^{(b)}$. This local maximum has a positive value, although this value is within the statistical uncertainty of MC simulations. As E/n_0 further increases, these differences converge to zero.

4.3.2. The influence of ionisation on the third-order transport coefficients for electrons in Lucas–Saelee model, N_2 *and* CF_4*.* The variation of the flux and bulk Q_L with E/n_0 of electrons
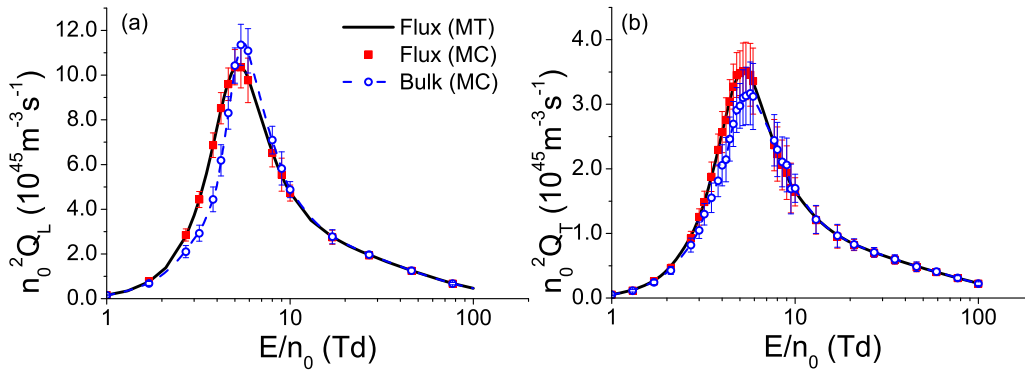
Figure 8. Comparison of the bulk and flux values of (a) $n_0^2 Q_L$ and (b) $n_0^2 Q_T$ for electrons in the modified Ness–Robson attachment cooling model. The results are obtained from numerical multi-term solutions of the Boltzmann equation (MT) and MC simulations.
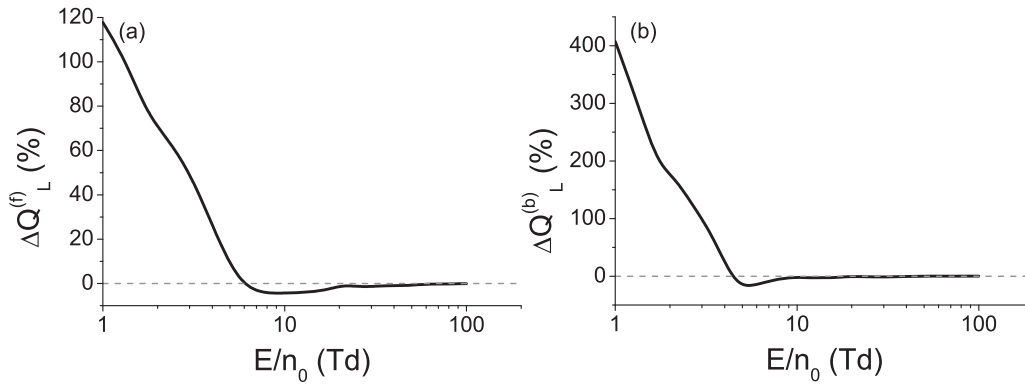
Figure 9. Percentage differences between the values of (a) $Q_L^{(f)}$ and (b) $Q_L^{(b)}$ for electrons in two different versions of the modified Ness–Robson model. Calculations are performed by the MC method in the modified Ness–Robson attachment heating model and in the modified Ness–Robson model with a constant collision frequency for electron attachment.
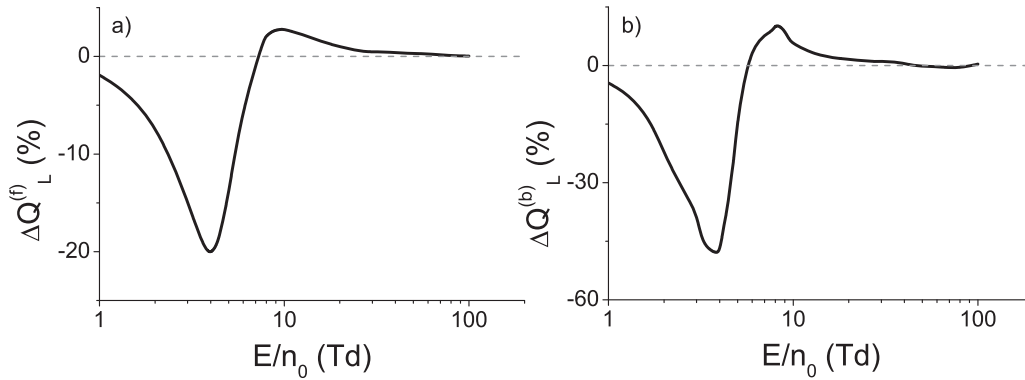
Figure 10. Percentage differences between the values of (a) $Q_L^{(f)}$ and (b) $Q_L^{(b)}$ for electrons in two different versions of the modified Ness–Robson model. Calculations are performed by the MC method in the modified Ness–Robson attachment cooling model and in the modified Ness–Robson model with a constant collision frequency for electron attachment.

in the Lucas–Saelee model for three values of the parameter F is displayed in figure 11(a). Likewise, figure 11(b) shows the flux and bulk Q_T as a function of E/n_0. We observe that bulk values are larger than the corresponding flux values for $F = 0.5$ and $F = 1$, due to explicit effects of ionisation on the third-order transport coefficients. Comparing Q_L and Q_T, we see that the difference between bulk and flux values in this model is much higher for Q_T. This can be attributed to strong

inelastic and non-conservative collisions that provide strong resistance to the spread of the swarm in the direction of the drift velocity. This significantly inhibits the elongation of the spatial distribution of the swarm in the longitudinal direction under the influence of ionisation.

We observe from figure 11 that the flux values of Q_L and Q_T are reduced with increasing parameter F due to ionisation cooling of the swarm. This illustrates the implicit effects
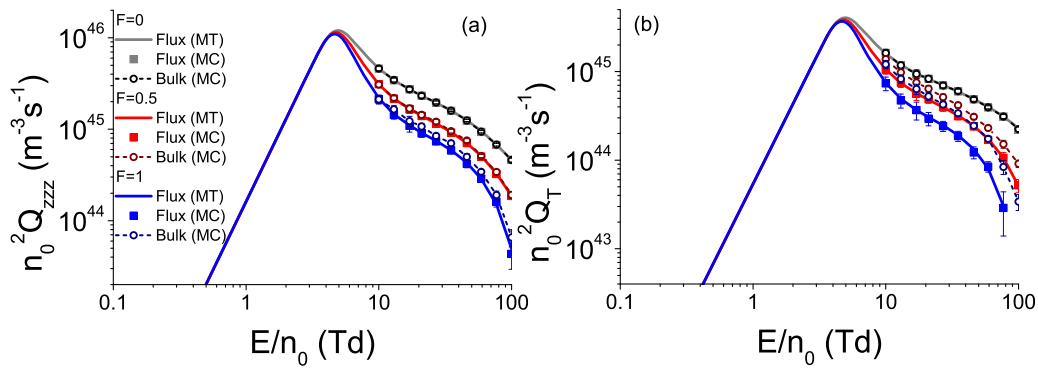
Figure 11. Comparison of the bulk and flux values of (a) $n_0^2 Q_{zzz}$ and (b) $n_0^2 Q_T$ for electrons in the ionisation model of Lucas and Saelee. The results are obtained from numerical multi-term solutions of the Boltzmann equation (MT) and MC simulations.
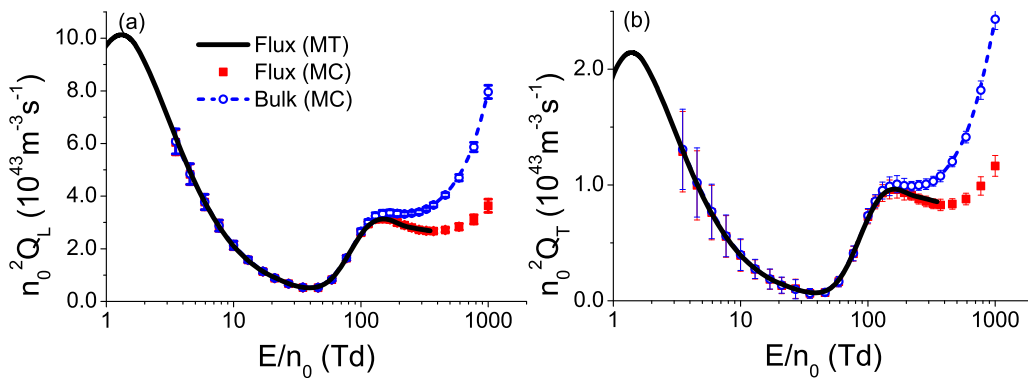
Figure 12. Comparison of the bulk and flux values of (a) $n_0^2 Q_L$ and (b) $n_0^2 Q_T$ for electrons in N$_2$. The results are obtained from numerical multi-term solutions of the Boltzmann equation (MT) and MC simulations.

of ionisation on the third-order transport coefficients. We also note that bulk values of Q_L and Q_T are being reduced with increasing F. This indicates that the influence of the implicit effects of ionisation on the third-order transport tensor is stronger than the corresponding influence of the explicit effects.

　　Figures 12(a) and (b) display the differences between flux and bulk values of Q_L and Q_T respectively, for electrons in N$_2$. The differences between the flux and bulk values of Q_L and Q_T for electrons in CF$_4$ are shown in figures 13(a) and (b), respectively. We observe that bulk values of Q_L and Q_T are larger than the corresponding flux values in both gasses at high electric fields, where electrons undergo many ionisation collisions. Comparing N$_2$ and CF$_4$ on one side, and the Lucas–Saelee ionisation model on the other side, we observe that the impact of the explicit effects on the longitudinal component of the third-order transport tensor is much stronger for real gases. This follows from the fact that the minimal impact of the explicit effects of ionisation on Q_L for electrons in the ionisation model of Lucas and Saelee can be attributed to the specific energy dependence of cross sections for inelastic collisions and ionisation. Generally speaking, the qualitative behaviour of the third-order transport coefficients with increasing E/n_0 is the same in the case of flux and bulk values. However, for electrons in N$_2$, we observe that the bulk values of Q_L and Q_T

reach their last local minimum at the lower E/n_0 than the corresponding flux values. Specifically, $Q_L^{(b)}$ and $Q_T^{(b)}$ reach their last local minimum at about 220 Td, while $Q_L^{(f)}$ and $Q_T^{(f)}$ reach their last local minimum at around 370 Td. We also observe from figures 12 and 13 that the results evaluated by multi term solution to the Boltzmann equation and those obtained in MC simulations agree very well.

4.4. Concurrence of the third-order transport coefficients and diffusion, the contribution of $Q_L^{(b)}$ to the spatial profile of the swarm and the comparison of $Q_L^{(b)}$ values obtained in this work with results of previous authors

The concurrence between third-order transport coefficients and diffusion coefficients for electrons in N$_2$ and CF$_4$ is illustrated by figures 14(a) and (b). Preliminary results in the study of this concurrence for electrons in CH$_4$ and noble gases have already been discussed [62, 69].

　　Specifically, for higher values of E/n_0 we observe that $Q_L^{(f)}$ is a rising function of E/n_0 when $D_L^{(f)}$ increases as a convex (or linear) function of E/n_0 in the log–log scale. One may also observe that $Q_L^{(f)}$ is reduced when $D_L^{(f)}$ decreases, or when $D_L^{(f)}$ rises as a concave function of the field in the log–log scale. This concurrence is absent in the limit of the lowest E/n_0 because the third-order transport coefficients
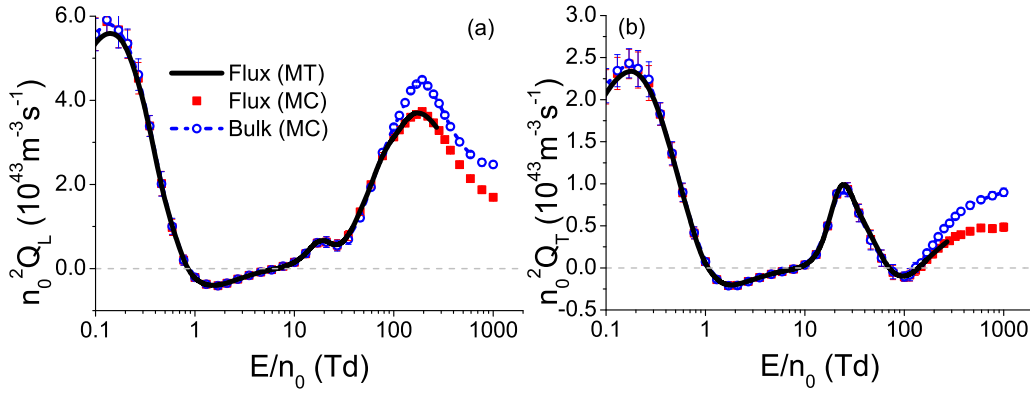
Figure 13. Comparison of the bulk and flux values of (a) $n_0^2 Q_L$ and (b) $n_0^2 Q_T$ for electrons in CF$_4$. The results are obtained from numerical multi-term solutions of the Boltzmann equation (MT) and MC simulations.
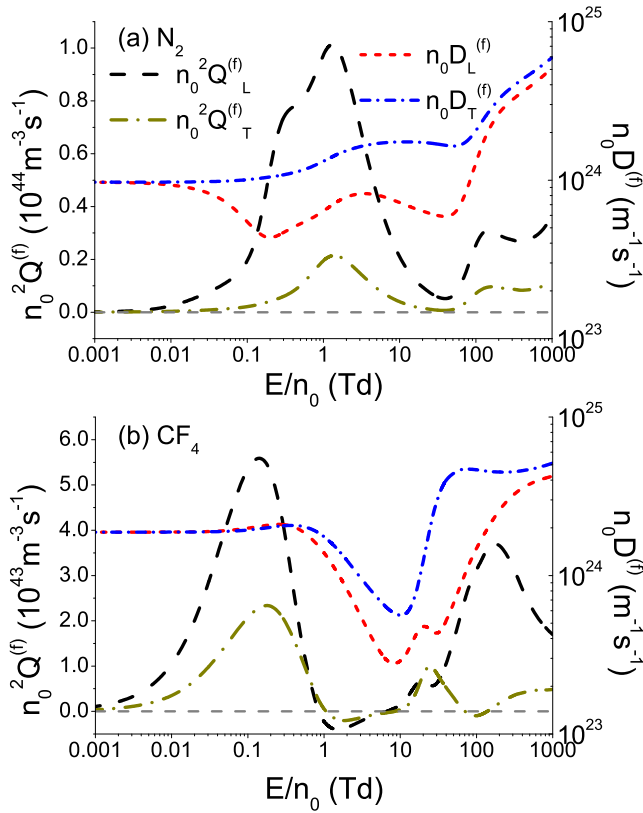
Figure 14. Concurrence of the third-order transport coefficients and diffusion coefficients for electrons in (a) N$_2$ and (b) CF$_4$. For $E/n_0 \leqslant 300$ Td, the results are calculated from numerical multi-term solutions of the Boltzmann equation, while for $E/n_0 > 300$ Td the results are obtained from MC simulations.

vanish in this range of fields unlike diffusion coefficients which have non-zero thermal values.

As can be seen in figure 14(a) the concurrence between $Q_L^{(f)}$ and $D_L^{(f)}$ for electrons in N$_2$ is present in the entire field region above 0.21 Td. For electrons in CF$_4$, we observe that the concurrence between $Q_L^{(f)}$ and $D_L^{(f)}$ is present in the subset of the field range above 0.02 Td, where $Q_L^{(f)}$ is positive (see figure 14(b)). However, this concurrence is absent in the field range between 1.6 Td and 8.5 Td, as $Q_L^{(f)}$ rises with increasing

E/n_0 although $D_L^{(f)}$ is being reduced in this field range. It is important to note that $Q_L^{(f)}$ has negative values over the range of E/n_0 in this field region. Further increase of the absolute value of $Q_L^{(f)}$, while this component is negative, would imply a further skewing of the spatial profile of the swarm in the negative direction (opposite to the drift velocity) along the longitudinal axis. Although the rise of the collision frequency for vibrational excitations with increasing E/n_0 is strong enough to cause a decrease of $D_L^{(f)}$, it is not strong enough to induce further skewing of the spatial profile of the swarm in the negative direction. It is interesting to note that the concurrence between $Q_L^{(f)}$ and $D_L^{(f)}$ is again present at about 8.5 Td, which is slightly above the field where $Q_L^{(f)}$ becomes positive again (at around 7 Td).

For electrons in N$_2$, the qualitative trends of $D_L^{(f)}$ and $D_T^{(f)}$ are the same in the field range above 0.21 Td, where the concurrence between $Q_L^{(f)}$ and $D_L^{(f)}$ is clearly evident. Thus, it is difficult to determine if the E/n_0 profile of $Q_T^{(f)}$ is more related to the corresponding profile of $D_L^{(f)}$ or $D_T^{(f)}$ in the case of N$_2$. For electrons in CF$_4$, E/n_0 profile of $Q_T^{(f)}$ is related to the corresponding profile of $D_T^{(f)}$ in most of the field range where $Q_T^{(f)}$ is positive. The concurrence between these two transport coefficients in CF$_4$ is equivalent to the concurrence between $Q_L^{(f)}$ and $D_L^{(f)}$, which is already discussed in this paper. This concurrence is absent in the field region between approximately 100 Td and 170 Td. However, $Q_T^{(f)}$ is negative up to around 140 Td. Thus, the field dependence of $Q_T^{(f)}$ is not related to the field dependence of diffusion in the field range where it is negative, and in the vicinity of the field where it becomes positive, similarly to $Q_L^{(f)}$.

The physical reasons for the observed concurrence between the third-order transport coefficients and diffusion coefficients have been discussed in our previous paper [69] for the example of atomic gases with considerably simpler sets of cross sections. The third-order transport coefficients represent a small asymmetric correction to diffusive motion, that is represented by the components of the diffusion tensor. As discussed previously [58], the rise of the reduced electric field leads to an increase of the directional component of electron velocity (in the absence of NDC) and to an increase of

15
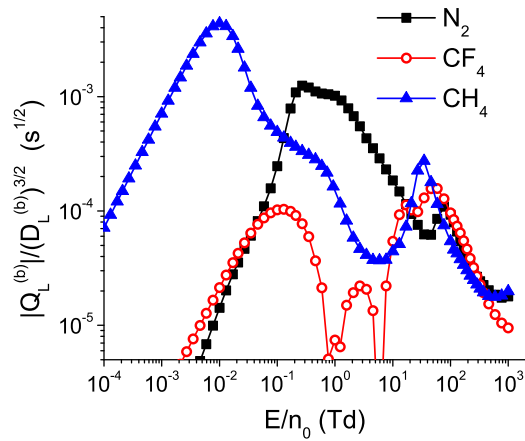
Figure 15. The values of the ratio $|Q_L^{(b)}|/(D_L^{(b)})^{3/2}$ for electrons in N_2, CF_4 and CH_4 as functions of E/n_0. For $E/n_0 \leqslant 100$ Td, where the differences between the bulk and flux values are negligible, the results are obtained from numerical multi-term solutions of the Boltzmann equation, while for higher values of E/n_0 the results are obtained in MC simulations.
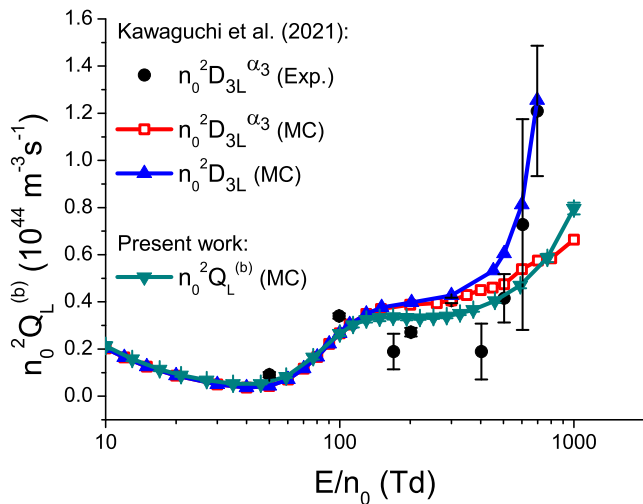
Figure 16. Comparison of the values of $n_0^2 Q_L^{(b)}$, that are determined in this work, with the results of Kawaguchi *et al* [59]. In this figure $n_0^2 D_{3L}$ represents simulation results from the reference [59] that are determined from equation (24) by employing MC simulations, while $n_0^2 D_{3L}^{\alpha_3}$ represents $n_0^2 Q_L^{(b)}$ that are determined in reference [59] form alpha parameters, after neglecting alpha parameters of fourth and higher order. Experimental results of Kawaguchi *et al* are represented by black circles, while results that are obtained from MC simulations are represented by a combination of symbols and continuous lines.

the electron energy. These two effects favour the increase of the third-order transport coefficients if the frequency of electron collisions with atoms/molecules of the background gas is not rising with increasing energy. However, if the collision frequency is rising steeply enough with increasing electron energy, this leads to a reduction of the third-order transport coefficients. The same holds for the components of the diffusion tensor, which are also quenched by elastic and inelastic collisions. Comparing these two sets of transport coefficients, third-order transport coefficients represent a form of motion

that 'carries' a smaller amount of energy and momentum, and as such they are much more sensitive to collisions with the background gas, than the components of the diffusion tensor. This suggests that for a sufficiently high E/n_0, the third-order transport coefficients are reduced with increasing E/n_0, if the diffusion is being reduced, and even if the slope of diffusion in the log–log scale decreases with increasing E/n_0. However, this concurrence is absent at the lowest fields and under conditions in which third-order transport coefficients are negative, due to reasons that are already discussed in this manuscript.

In figure 15 we show the values of the ratio $|Q_L^{(b)}|/(D_L^{(b)})^{3/2}$ for electrons in N_2, CF_4 and CH_4, as functions of E/n_0. Calculations are performed assuming the concentration of background molecules $n_0 = 3.54 \times 10^{22}$ m^{-3}. This ratio determines the contribution of the longitudinal component of the third-order transport tensor to the spatial profile of the swarm, as can be seen from equation (6). From this figure, we observe that the contribution of $Q_L^{(b)}$ to the spatial profile of the swarm is larger in CH_4 than in the remaining two gases for E/n_0 lower than 0.1 Td and for E/n_0 between 21 Td and 46 Td. For E/n_0 between 0.13 Td and 17 Td the quantity $|Q_L^{(b)}|/(D_L^{(b)})^{3/2}$ is larger in N_2 than in CH_4 and CF_4. For E/n_0 between 70 Td and 300 Td this ratio is slightly lower in CH_4 than in the remaining two gases. For E/n_0 between 400 Td and 1000 Td this ratio is lower in CF_4 than in N_2 and CH_4. It is interesting to note that differences between the values of $|Q_L^{(b)}|/(D_L^{(b)})^{3/2}$ in N_2, CH_4 and CF_4 do not exceed the factor of three in the field range between 50 Td and 700 Td. In most of this region, these differences do not exceed the factor of two. Moreover, the values of this ratio are very close to each other for electrons in these three gases in the field range between 200 Td and 450 Td. This indicates that $n_0^2 Q_L^{(b)}$ can be measured in CH_4 and CF_4, in the field range between 50 Td and 700 Td, under similar experimental conditions that were applied for measurements in N_2. Recently Kawaguchi and co-workers using a MC simulation technique have shown that $n_0^2 Q_L^{(b)}$ can be measured in CH_4 and SF_6 in the arrival time spectra experiment [71].

In figure 16 we show the comparison of the longitudinal component of the third-order transport tensor $n_0^2 Q_L^{(b)}$ for electrons in N_2 with the corresponding values that are determined by Kawaguchi *et al* [59]. In this figure, $n_0^2 D_{3L}$ is determined from MC simulations by using equation (24), while $n_0^2 D_{3L}^{\alpha_3}$ is evaluated from the alpha parameters based on equation (25) from reference [59] by neglecting the alpha parameters of fourth and higher order. Kawaguchi and co-workers determined alpha parameters from the arrival time spectra experiment and the MC simulations. All results are in an excellent agreement up to about 130 Td, while differences between these sets of results become noticeable at higher values of E/n_0. Our calculated values of $n_0^2 Q_L^{(b)}$ are somewhat lower than the theoretical results of Kawaguchi *et al* for E/n_0 between 130 Td and 460 Td. For higher values of E/n_0 our results are significantly lower than $n_0^2 D_{3L}$ and somewhat below $n_0^2 D_{3L}^{\alpha_3}$ until approximately 770 Td. At around 1000 Td the value of $n_0^2 Q_L^{(b)}$ in the present calculations, is somewhat above the theoretical values of $n_0^2 D_{3L}^{\alpha_3}$ that are determined by Kawaguchi *et al*. The difference between our calculations of $n_0^2 Q_L^{(b)}$ and those of Kawaguchi and co-workers for $n_0^2 D_{3L}$ is a clear

indication of different sets of cross sections used as input data in MC simulations. The sensitivity of the third-order transport coefficients to the cross sections used in the transport calculations was demonstrated by Kawaguchi and co-workers [63]. The deviation of $n_0^2 D_{3L}^{\alpha_3}$ from $n_0^2 D_{3L}$ for higher values of E/n_0 can be attributed to neglecting alpha parameters of fourth and higher order in equation from which the values of $n_0^2 D_{3L}^{\alpha_3}$ are determined, as discussed by Kawaguchi *et al* [59]. Our calculations of $n_0^2 Q_L^{(b)}$ and experimental values of $n_0^2 D_{3L}^{\alpha_3}$ agree very well up to about 600 Td. If we take a careful look, we observe that our calculations are somewhat below experimental values up to about 100 Td and somewhat above experimental results until approximately 500 Td. For higher values of E/n_0, however, our results are significantly below experimental points. For $E/n_0 = 600$ Td our calculations of $n_0^2 Q_L^{(b)}$ are within the experimental error, while at 700 Td they are significantly below the lower boundary of experimental results at 700 Td. Strictly speaking, $n_0^2 Q_L^{(b)}$ and $n_0^2 D_{3L}^{\alpha_3}$ cannot be directly equated, because $n_0^2 D_{3L}^{\alpha_3}$ represents an approximation of $n_0^2 Q_L^{(b)}$ when the fourth and higher order alpha parameters are negligible. Strict comparison with experimental results obtained by Kawaguchi and co-workers [59] would be possible if $n_0^2 D_{3L}^{\alpha_3}$ was determined using measured or calculated alpha parameters.

5. Conclusion

In this paper, we have investigated the behaviour of the third-order transport coefficients for electrons in N_2 and CF_4. Calculations have been performed using a multi-term theory for solving the Boltzmann equation and MC simulation technique. The initial MC code has been extended to allow the calculations of third-order transport coefficients in the presence of non-conservative collisions. We found that the moment method for solving the Boltzmann equation works very well for the third-order transport coefficients, and is particularly fast and accurate for model gases.

One of the most striking phenomena observed in the present work is the occurrence of negative values in the E/n_0-profiles of $n_0^2 Q_{xxz}^{(f)}$ and $n_0^2 Q_{zzz}^{(f)}$ for electrons in CF_4. After the relaxation of the swarm to the steady-state, transport coefficients of the third-order attain negative values over the range of electron energies where the most energetic electrons may undergo many collisions leading to the vibrational excitation of CF_4 molecule. We have also noticed that the occurrence of negative values in the E/n_0-profiles of $n_0^2 Q_{xxz}^{(f)}$ and $n_0^2 Q_{zzz}^{(f)}$ in CF_4 takes place in the energy region where the cross sections for vibrational excitations exceed the cross section for momentum transfer in elastic collisions. Likewise, we have also observed that $n_0^2 Q_T^{(f)}$ has negative values in the field region between the end of the occurrence of NDC and the field where the drift velocity reaches 90% of its initial value before the onset of NDC. Based on the results presented in this work, it may be assumed that there is a slight concurrence between $n_0^2 Q_T^{(f)}$ and drift velocity. This concurrence refers to the occurrence of negative values of $n_0^2 Q_T^{(f)}$ that are essentially controlled by the collision processes, which promote the development of NDC.

As the two-term approximation has become a commonplace in the calculation of electron transport properties in gases and as it forms the foundations of many publicly available codes for solving the Boltzmann equations, we have been motivated to investigate its limitations in the context of the present research. Comparisons between the two-term and multi-term calculations were performed for E/n_0 less than 300 Td. For electrons in N_2, the accuracy of the two-term approximation is sufficient to investigate the behaviour of the third-order transport coefficients in the presence of the electric field. In contrast, for electrons in CF_4 the two-term approximation produces large errors and it is not even qualitatively correct, particularly over the range of electron energies where the cross section for transfer of momentum in elastic collisions is at minimum, while the cross sections of vibrational excitations become significant. This favours a large asymmetry in the distribution function in the velocity space which in turn renders the two-term approximation quite inappropriate for the analysis of third-order transport coefficients.

In the present work, we have studied the implicit and explicit effects of non-conservative collisions on the third-order transport coefficients. While implicit effects of non-conservative collisions are induced by direct population and depopulation of the distribution function in velocity space, the explicit effects are caused by the combined effects of the energy dependence of non-conservative collisions and spatial variation of the average energy along the swarm. Using the modified Ness–Robson model with the attachment heating, we have observed that the bulk values of $n_0^2 Q_L$ and $n_0^2 Q_T$ are larger than the corresponding flux values at low electric fields. At intermediate fields the opposite situation holds: the flux values are larger than the corresponding bulk values. This behaviour and relationship between the bulk and flux values of both $n_0^2 Q_L$ and $n_0^2 Q_T$, are inverted for the attachment cooling model.

The effects of electron-impact ionisation on the third-order transport coefficients are analysed for electrons in the ionisation model of Lucas and Saelee, N_2 and CF_4. For all gases we considered, bulk values of $n_0^2 Q_L$ and $n_0^2 Q_T$ are larger than the corresponding flux values for the higher electric fields. In particular, comparing the explicit influence of ionisation on $n_0^2 Q_L^{(b)}$ and $n_0^2 Q_T^{(b)}$ in the ionisation model of Lucas and Saelee, effects are more pronounced for $n_0^2 Q_T^{(b)}$.

In this work the concurrence between $n_0^2 Q_L^{(f)}$ and $n_0 D_L^{(f)}$ is analysed. For electrons in N_2 the concurrence is effective over the entire range of the considered E/n_0. This concurrence is also present for electrons in CF_4 over the range of E/n_0 where $n_0^2 Q_L^{(f)}$ is positive. However, in the field region where $n_0^2 Q_L^{(f)}$ is negative, there is a range of E/n_0 values, where $n_0^2 Q_L^{(f)}$ is rising although $n_0 D_L^{(f)}$ is being reduced. This effect is analysed using the physical interpretation of the negative values of $n_0^2 Q_L^{(f)}$. The concurrence between $n_0^2 Q_T^{(f)}$ and the components of the diffusion tensor is also investigated. In particular, for electrons in CF_4 we found that the E/n_0 profile of $n_0^2 Q_T^{(f)}$ is more related to the corresponding profile of $n_0 D_T^{(f)}$ than to the corresponding profile of $n_0 D_L^{(f)}$.

Contribution of the longitudinal component of the third-order transport tensor to the spatial profile of the swarm was

studied for electrons in N_2, CF_4 and CH_4. This contribution is proportional to the ratio $|Q_L^{(b)}|/(D_L^{(b)})^{3/2}$. Between 50 Td to 700 Td differences between the values of this ratio for electrons in N_2, CF_4 and CH_4 do not exceed the factor of 3. More precisely, we have observed that these differences do not differ from each other by a factor of 2 over the majority of E/n_0 values in the above-mentioned field region. Even though this result of the study seems modest, it is very important because it shows that the existing experimental infrastructure used to measure third-order transport coefficients in N_2 can be used equally successfully for measurements of these quantities in other gases.

The present calculations of $n_0^2 Q_L^{(b)}$ for electrons in N_2 are compared with the arrival time spectra measurements and MC simulations of Kawaguchi and co-workers [59]. The present calculations and results of Kawaguchi and co-workers agree very well up to approximately 500 Td. For higher values of E/n_0, the discrepancy between our calculations and those obtained by Kawaguchi and co-workers in MC simulations, may be directly attributed to the details of the cross sections for electron scattering in N_2 used as input data in numerical codes.

It is hoped that the present study will provide an incentive for further theoretical and experimental studies of the third-order transport coefficients for electrons in gases. Particular attention has recently been focussed on extracting cross-sections from swarm data [90, 91]. The inclusion of these sensitive higher order transport coefficients, may result in improved cross-section sets, particularly given the new machine learning algorithms implemented [92–94]. Our plans for future research include the study of third-order transport coefficients in the presence of pressure dependent effects and third-order transport coefficients for positrons in gases of interest for further development and optimization of positron traps.

Acknowledgments

Data availability statement

All data that support the findings of this study are included within the article (and any supplementary files).

ORCID iDs

I Simonović https://orcid.org/0000-0001-6704-9042
D Bošnjaković https://orcid.org/0000-0002-2725-5287
Z Lj Petrović https://orcid.org/0000-0001-6569-9447
R D White https://orcid.org/0000-0001-5353-7440
S Dujko https://orcid.org/0000-0002-4544-9106

References

[1] Lieberman M A and Lichtenberg A J 2005 *Principles of Plasma Discharges and Materials Processing* (New York: Interscience (Wiley-Interscience))
[2] Makabe T and Petrović Z Lj 2014 *Plasma Electronics: Applications in Microelectronic Device Fabrication* (Boca Raton, FL: CRC Press)
[3] Rudenko K V 2009 *High Energy Chem.* **43** 196
[4] Shustin E G 2017 *J. Commun. Technol. Electron.* **62** 454
[5] Shamiryan D, Paraschiv V, Boullart W and Baklanov M R 2009 *High Energy Chem.* **43** 204
[6] Donnelly V M and Kornblit A 2013 *J. Vac. Sci. Technol.* A **31** 050825
[7] Shahidi S and Ghoranneviss M 2015 *Cloth. Text. Res. J.* **34** 37
[8] Xie L, Brault P, Bauchire J-M, Thomann A-L and Bedra L 2014 *J. Phys. D: Appl. Phys.* **47** 224004
[9] Friedrich J F, Wettmarshausen S, Hanelt S, Mach R, Mix R, Zeynalov E B and Meyer-Plath A 2010 *Carbon* **48** 3884
[10] Takai O 2008 *Pure Appl. Chem.* **80** 2003
[11] Weltmann K-D and von Woedtke T 2017 *Plasma Phys. Control. Fusion* **59** 014031
[12] Laroussi M 2018 *Plasma* **1** 47
[13] Griseti E, Kolosnjaj-Tabi J, Gibot L, Fourquaux I, Rols M-P, Yousfi M, Merbahi N and Golzio M 2019 *Sci. Rep.* **9** 7583
[14] Alves L L, Bogaerts A, Guerra V and Turner M M 2018 *Plasma Sources Sci. Technol.* **27** 023002
[15] Colonna G *et al* 2021 *Eur. Phys. J.* D **75** 183
[16] Makabe T 2018 *Plasma Sources Sci. Technol.* **27** 033001
[17] Madshaven I, Hestad O L and Åstrand P-O 2021 *Comput. Phys. Commun.* **265** 107987
[18] Petrović Z Lj, Dujko S, Marić D, Malović G, Nikitović Ž, Šašić O, Jovanović J, Stojanović V and Radmilović-Radjenović M 2009 *J. Phys. D: Appl. Phys.* **42** 194002
[19] Ruiz-Vargas G, Yousfi M and de Urquijo J 2010 *J. Phys. D: Appl. Phys.* **43** 455201
[20] Makabe T 2019 *Japan. J. Appl. Phys.* **58** 110101
[21] Silva T, Grofulović M, Klarenaar B L M, Morillo-Candas A S, Guaitella O, Engeln R, Pintassilgo C D and Guerra V 2018 *Plasma Sources Sci. Technol.* **27** 015019
[22] Minesi N, Mariotto P, Pannier E, Stancu G D and Laux C O 2021 *Plasma Sources Sci. Technol.* **30** 035008
[23] Ribire M, Eichwald O and Yousfi M 2020 *J. Appl. Phys.* **128** 093304
[24] Upadhyay R R, Suzuki K, Raja L L, Ventzek P L G and Ranjan A 2020 *J. Phys. D: Appl. Phys.* **53** 435209
[25] Nijdam S, Teunissen J and Ebert U 2020 *Plasma Sources Sci. Technol.* **29** 103001
[26] Arslanbekov R R and Kolobov V I 2021 *Plasma Sources Sci. Technol.* **30** 045013
[27] Marinov D, Teixeira C and Guerra V 2017 *Plasma Process. Polym.* **14** 1600175
[28] Derzsi A, Horváth B, Donkó Z and Schulze J 2020 *Plasma Sources Sci. Technol.* **29** 074001
[29] Huxley L G H and Crompton R W 1974 *The Diffusion and Drift of Electrons in Gases* (New York: Wiley)
[30] Dyatko N A, Kochetov I V and Ochkin V N 2020 *Plasma Sources Sci. Technol.* **29** 125007
[31] Babaeva N Y and Naidis G V 2016 *Phys. Plasmas* **23** 083527
[32] Babaeva N Y and Naidis G V 2018 *Plasma Sources Sci. Technol.* **27** 075018
[33] Li X, Sun A, Zhang G and Teunissen J 2020 *Plasma Sources Sci. Technol.* **29** 065004
[34] Bagheri B *et al* 2018 *Plasma Sources Sci. Technol.* **27** 095002
[35] Arcese E, Rogier F and Boeuf J-P 2017 *Phys. Plasmas* **24** 113517
[36] Dujko S, Markosyan A H, White R D and Ebert U 2013 *J. Phys. D: Appl. Phys.* **46** 475202

[37] Taran M D, Dyatko N A, Kochetov I V, Napartovich A P and Akishev Y S 2018 *Plasma Sources Sci. Technol.* **27** 055004

[38] Peng Y, Chen X, Lan L, Zhan H, Liu Y, He W and Wen X 2021 *Plasma Sci. Technol.* **23** 064013

[39] Petrović Z Lj, Šuvakov M, Nikitović Ž, Dujko S, Šašić O, Jovanović J, Malović G and Stojanović V 2007 *Plasma Sources Sci. Technol.* **16** S1–S12

[40] Pitchford L C *et al* 2013 *J. Phys. D: Appl. Phys.* **46** 334001

[41] Rabie M, Haefliger P, Chachereau A and Franck C M 2015 *J. Phys. D: Appl. Phys.* **48** 075201

[42] Grofulović M, Alves L L and Guerra V 2016 *J. Phys. D: Appl. Phys.* **49** 395207

[43] Li C, Brok W J M, Ebert U and van der Mullen J J A M 2007 *J. Appl. Phys.* **101** 123305

[44] Li C, Teunissen J, Nool M, Hundsdorfer W and Ebert U 2012 *Plasma Sources Sci. Technol.* **21** 055019

[45] Higginson D P, Holod I and Link A 2020 *J. Comput. Phys.* **413** 109450

[46] Wilczek S *et al* 2016 *Phys. Plasmas* **23** 063514

[47] Hartmann P *et al* 2020 *Plasma Sources Sci. Technol.* **29** 075014

[48] Takahashi H and Sugawara H 2020 *Japan. J. Appl. Phys.* **59** 036001

[49] Nakashima K, Takahashi H and Sugawara H 2019 *Japan. J. Appl. Phys.* **58** 116001

[50] Pitchford L C *et al* 2017 *Plasma Process. Polym.* **14** 1600098

[51] Lovaas T H, Skullerud H R, Kristensen O-H and Linhjell D 1987 *J. Phys. D: Appl. Phys.* **20** 1465

[52] Koutselos A D 2001 *Chem. Phys.* **270** 165

[53] Viehland L A and Johnsen R 2019 *J. Geophys. Res. Atmos.* **124** 13593–600

[54] Viehland L A 2018 *Gaseous Ion Mobility, Diffusion, and Reaction* (Berlin: Springer)

[55] Viehland L A, Ducasse E, Cordier M, Trout A and Dashdorj J 2021 *J. Chem. Phys.* **155** 204301

[56] Vrhovac S B, Petrović Z Lj, Viehland L A and Santhanam T S 1999 *J. Chem. Phys.* **110** 2423

[57] Sugawara H and Sakai Y 2006 *Japan. J. Appl. Phys.* **45** 5189

[58] Simonović I, Bošnjaković D, Petrović Z Lj, Stokes P, White R D and Dujko S 2020 *Phys. Rev.* E **101** 023203

[59] Kawaguchi S, Nakata N, Satoh K, Takahashi K and Satoh K 2021 *Plasma Sources Sci. Technol.* **30** 035006

[60] Dujko S, White R D and Petrović Z Lj 2008 *J. Phys. D: Appl. Phys.* **41** 245205

[61] Penetrante B M and Bardsley J N 1990 *Non-Equilibrium Effects in Ion and Electron Transport* ed J W Gallagher, D F Hudson, E E Kunhardt and R J Van Brunt (New York: Plenum) p 49

[62] Petrović Z Lj, Simonović I, Marjanović S, Bošnjaković D, Marić D, Malović G and Dujko S 2017 *Plasma Phys. Control. Fusion* **59** 014026

[63] Kawaguchi S, Takahashi K and Satoh K 2021 *Plasma Sources Sci. Technol.* **30** 035010

[64] Stojanovic V D and Petrovic Z L 1998 *J. Phys. D: Appl. Phys.* **31** 834

[65] Whealton J H and Mason E A 1974 *Ann. Phys., NY* **84** 8

[66] Koutselos A D 1996 *J. Chem. Phys.* **104** 8442

[67] Koutselos A D 1997 *J. Chem. Phys.* **106** 7117

[68] Koutselos A D 2001 *Chem. Phys.* **315** 193

[69] Simonović I, Bošnjaković D, Petrović Z Lj, White R D and Dujko S 2020 *Eur. Phys. J.* D **74** 63

[70] Stokes P W, Simonović I, Philippa B, Cocks D, Dujko S and White R D 2018 *Sci. Rep.* **8** 2226

[71] Kawaguchi S, Takahashi K and Satoh K 2018 *Plasma Sources Sci. Technol.* **27** 085006

[72] Kumar K, Skullerud H and Robson R 1980 *Aust. J. Phys.* **33** 343

[73] Nolan A M, Brennan M J, Ness K F and Wedding A B 1997 *J. Phys. D: Appl. Phys.* **30** 2865

[74] Franceschini C and Loperfido N 2019 *Symmetry* **11** 970

[75] Dujko S, White R D, Petrović Z Lj and Robson R E 2010 *Phys. Rev.* E **81** 046403

[76] Robson R E and Ness K F 1986 *Phys. Rev.* A **33** 2068

[77] White R D, Ness K F, Robson R E and Li B 1999 *Phys. Rev.* E **60** 2231

[78] White R D, Robson R E, Dujko S, Nicoletopoulos P and Li B 2009 *J. Phys. D: Appl. Phys.* **42** 194001

[79] Dujko S, White R D, Petrović Z Lj and Robson R E 2011 *Plasma Sources Sci. Technol.* **20** 024013

[80] Ness K F and Robson R E 1986 *Phys. Rev.* A **34** 2185

[81] Raspopovic Z M, Sakadzic S, Bzenic S A and Petrovic Z Lj 1999 *IEEE Trans. Plasma Sci.* **27** 1241

[82] Petrović Z Lj, Raspopović Z M, Dujko S and Makabe T 2002 *Appl. Surf. Sci.* **192** 1–25

[83] Dujko S, Raspopović Z M and Petrović Z Lj 2005 *J. Phys. D: Appl. Phys.* **38** 2952

[84] Lucas J and Salee H T 1975 *J. Phys. D: Appl. Phys.* **8** 64

[85] Kurihara M, Petrovic Z Lj and Makabe T 2000 *J. Phys. D: Appl. Phys.* **33** 2146

[86] Sasic O, Malovic G, Strinic A, Nikitovic Z and Petrovic Z L 2004 *New J. Phys.* **6** 74

[87] Petrovic Z Lj, Crompton R and Haddad G 1984 *Aust. J. Phys.* **37** 23

[88] Vrhovac S B and Petrović Z Lj 1996 *Phys. Rev.* E **53** 4012

[89] Mirić J, Bošnjaković D, Simonović I, Petrović Z Lj and Dujko S 2016 *Plasma Sources Sci. Technol.* **25** 065010

[90] White R D *et al* 2018 *Plasma Sources Sci. Technol.* **27** 053001

[91] Casey M J E, de Urquijo J, Serkovic Loli L N, Cocks D G, Boyle G J, Jones D B, Brunger M J and White R D 2017 *J. Chem. Phys.* **147** 195103

[92] Stokes P W, Cocks D G, Brunger M J and White R D 2020 *Plasma Sources Sci. Technol.* **29** 055009

[93] Stokes P W, Casey M J E, Cocks D G, de Urquijo J, Garcia G, Brunger M J and White R D 2020 *Plasma Sources Sci. Technol.* **29** 105008

[94] Stokes P W, Foster S P, Casey M J E, Cocks D G, González-Magaña O, de Urquijo J, Garcia G, Brunger M J and White R D 2021 *J. Chem. Phys.* **154** 084306

PAPER

Transport of electrons and propagation of the negative ionisation fronts in indium vapour

View the article online for updates and enhancements.

Transport of electrons and propagation of the negative ionisation fronts in indium vapour

S Dujko[1,*] , **J Atić**[1] , **D Bošnjaković**[1] , **R D White**[2] , **P Stokes**[2] ,
K R Hamilton[3] , **O Zatsarinny**[3,10] , **K Bartschat**[3] , **M S Rabasović**[1] ,
D Šević[1] , **B P Marinković**[1] , **D V Fursa**[4] , **I Bray**[4] , **R P McEachran**[5] ,
F Blanco[6] , **G García**[7] , **D B Jones**[8,11] , **L Campbell**[8] and
M J Brunger[8,9]

[1] Institute of Physics Belgrade, University of Belgrade, Pregrevica 118, 11080 Belgrade, Serbia
[2] College of Science and Engineering, James Cook University, Townsville, Queensland 4810, Australia
[3] Department of Physics and Astronomy, Drake University, Des Moines, IA 50311, United States of America
[4] Curtin Institute for Computation and Department of Physics and Astronomy, Perth 6102, WA, Australia
[5] Laser Physics Centre, RSP, Australian National University, Canberra, ACT 0200, Australia
[6] Departamento de Estructura de La Materia, Física Térmica y Electrónica e IPARCOS, Universidad Complutense de Madrid, Avenida Complutense, E-28040 Madrid, Spain
[7] Instituto de Física Fundamental, CSIC, Serrano 113-bis, E-28006 Madrid, Spain
[8] College of Science and Engineering, Flinders University, GPO Box 2100, Adelaide, SA 5001, Australia
[9] Department of Actuarial Science and Applied Statistics, Faculty of Business and Management, UCSI University, Kuala Lumpur 56000, Malaysia

E-mail: sasha@ipb.ac.rs

CrossMark

Abstract

We study the transport of electrons and propagation of the negative ionisation fronts in indium vapour. Electron swarm transport properties are calculated using a Monte Carlo simulation technique over a wide range of reduced electric fields E/N (where E is the electric field and N is the gas number density) and indium vapour temperatures in hydrodynamic conditions, and under non-hydrodynamic conditions in an idealised steady-state Townsend (SST) setup. As many indium atoms are in the first $(5s^2 5p)^2 P_{3/2}$ metastable state at vapour temperatures of a few thousand Kelvin, the initial Monte Carlo code was extended and generalized to consider the spatial relaxation and the transport of electrons in an idealised SST experiment, in the presence of thermal motion of the host-gas atoms and superelastic collisions. We observe a significant sensitivity of the spatial relaxation of the electrons on the indium vapour temperature and the initial conditions used to release electrons from the cathode into the space between the electrodes. The calculated electron transport coefficients are used as input for the classical fluid model, to investigate the inception and propagation of negative ionisation fronts in indium vapour at various E/N and vapour temperatures. We calculate the electron density, electric field, and velocity of ionisation fronts as a function of E/N and indium vapour

* Author to whom any correspondence should be addressed.
[11] Present address: Flinders Microscopy and Microanalysis, College of Science and Engineering, Flinders University, GPO Box 2100, Adelaide, SA 5001, Australia.
[10] Dr Oleg Zatsarinny passed away during the preparation of this manuscript.

1

temperature. The presence of indium atoms in the first $(5s^25p)^2P_{3/2}$ metastable state significantly affects the characteristics of the negative ionisation fronts. The transition from an avalanche into a negative ionisation front occurs faster with increasing indium vapour temperature, due to enhanced ionisation and more efficient production of electrons at higher vapour temperatures. For lower values of E/N, the electron density behind the streamer front, where the electric field is screened, does not decay as one might expect for atomic gases, but it could be increased due to the accumulation of low-energy electrons that are capable of initiating ionisation in the streamer interior.

(Some figures may appear in colour only in the online journal)

1. Introduction

Studies of electron swarm transport processes in metal vapours go back many years, for example to the Franck–Hertz experiment and the genesis of quantum physics [1]. Yet much remains to be understood from a fundamental point of view [2–5]. Early studies of electron transport in metal vapours were limited to the vapours of mercury, caesium, and other alkali metals, due to the many technical difficulties associated with the control of high temperatures in swarm experiments. In addition to decades of studying the transport of electrons in mercury vapour [6–11], swarm studies were performed in the vapours of sodium, potassium, and caesium [12] while the experimental results of breakdown voltages and $V–I$ characteristics were measured for sodium, potassium, cadmium, and zinc [13]. The primary driving force behind these early studies was the modelling and optimization of light sources containing mercury [8, 14, 15], sodium [16, 17], and zinc [18, 19]. Other applications include the modelling of a gas laser [20], the magnetohydrodynamics of arcs [21], and a post-arc breakdown plasma [22].

Recently, a new wave of studies on electron scattering in metal vapours has triggered the modelling and analysis of electron transport and different types of plasma discharges in those vapours. The B-spline R-matrix (close-coupling) with pseudo-states method was employed to calculate the cross sections for electron collisions with caesium atoms [23, 24], and those calculated cross sections were then used to model an excimer-pumped alkali laser with caesium as one of the constituent species [24]. The cross sections for the scattering of electrons from zinc [25] and magnesium [26] vapours were recently calculated, using both non-relativistic and relativistic optical-potential methods. The computed cross-sections were subsequently used as input to solve the Boltzmann equation to calculate the electron swarm transport coefficients. The publicly available two-term Boltzmann equation solver BOLSIG+ [27], as well as the Monte Carlo code METHES [28], were recently used to investigate the electron transport and breakdown in a copper vapour post-arc plasma [22]. The relativistic complex optical potential method has also been used to study electron–beryllium scattering [29].

As part of our ongoing investigations of electron scattering and transport in metal vapours, we report in this paper on our study of electron transport and propagation of negative ionisation fronts in indium vapour. Indium (In) is a soft, grey metallic element with an atomic number of 49. It belongs to the group-III elements of the periodic table and has two stable isotopes, [115]In and [113]In, with abundances of 95.7% and 4.3%, respectively. With an electronic configuration $4d^{10}5s^25p$ indium is the first in a series of the $5p$ elements in the periodic table, and most commonly donates the three outermost electrons to become In^{3+} [30]. In certain cases, however, the $5s$-electron pair is not donated, resulting in In^+ [31]. Because of its low melting point of 429.75 K, indium has been recognized as a material with great potential for many technological applications. For example, as an indium tin oxide it is used to produce transparent electrodes in liquid-crystal displays [32], and it is also employed as a light filter in low-pressure sodium lamps. Furthermore, indium has numerous semi-conductor-related applications, including the use of InAs and InSb for low-temperature transistors and InP for high-temperature transistors [33]. Furthermore, InGaN and InGaP are found in both light-emitting diodes and laser diodes [34].

Even though the above-mentioned applications of indium are of great importance in fundamental science and modern technology, the basic motivating factors in the study of electron scattering and transport in indium vapour relate to the modelling of plasma discharges. Since the use of toxic mercury in low-pressure and high-pressure light sources is highly limited in both the European Union and many other countries, there is a strong incentive nowadays to find a less toxic material as an alternative to mercury. For low-pressure discharge lamps, one option would be to use mixtures of halogen–indium compounds with argon [35–37]. The collisional-radiative models of such systems require the knowledge of electron swarm transport coefficients, including rate coefficients for various collisional processes such as ionisation and electron-impact excitation. It is clear that further optimization and understanding of indium-based light sources crucially depends on an accurate knowledge of the cross sections for electron–indium scattering, the relevant transport coefficients,

and in appreciating the physical processes involved in indium vapour discharges.

While electron scattering in indium vapour has been thoroughly discussed in our recent publications [38, 39], in the present paper we focus on electron transport processes and the propagation of negative ionisation fronts. To that end, electron swarm transport coefficients are calculated using a Monte Carlo simulation technique under hydrodynamic conditions, and also for non-hydrodynamic conditions in an idealised steady-state Townsend (SST) setup, over a wide range of reduced electric fields (E/N) and indium vapour temperatures. In particular, the initial Monte Carlo code, which was specifically developed to study the spatial relaxation of electrons in an idealised SST experiment [40–42], was extended and generalized for the present work to investigate the effects of gas temperature in the presence of electron-impact ionisation of indium atoms in the ground state and the lowest-lying metastable state. We comprehensively studied the influence of the indium metastable state $(5s^2 5p)^2 P_{3/2}$ at temperatures of several thousand Kelvin on the electron transport and the spatial relaxation of the electrons. To the best of our knowledge, we present the first systematic investigation for the spatial relaxation of electrons in hot metal vapours, where thermal motion of the background atoms and their influence on the electrons are rigorously considered by implementing electron collisions with the indium atoms in the metastable state $(5s^2 5p)^2 P_{3/2}$, including the effects of superelastic collisions.

The second major objective of the present study is to simulate negative ionisation fronts in indium vapour. Due to the high accelerating voltages in high-pressure light sources, the transition from an electron avalanche into a streamer is a rapid process, which has been studied both experimentally and by means of numerical simulations [43, 44]. It has been shown that streamer-like ionising channels can originate from both the anode and the cathode, and that they can propagate through the gas volume as well as along the inner wall of the discharge lamp. In particular, the first phase of the streamer-breakdown is characterized by a constricted streamer process between the electrode tips [43]. In combination with mercury, indium vapour may serve in high-intensity discharge lamps as a radiation-emitting substance due to its high-vapour pressure and because its emitted radiation covers the UV and visible ranges of the spectrum. Therefore, it is clear that studies of the development of an electron avalanche and its transition into a streamer in indium vapour may support investigations to find the optimal discharge conditions and increase the plasma efficiency. In order to simulate the inception and propagation of negative ionisation fronts in indium vapour, we here apply the classical fluid model, which is based on the drift–diffusion approximation, the local field approximation, and Poisson's equation. This model is implemented numerically in 1D and 1.5D configurations. Our calculated electron swarm transport coefficients, including the ionisation coefficient, drift velocity, and longitudinal diffusion coefficient, are used as input data in this model. However, it should be noted that in the present work we are not attempting to model the inception of the cathode-directed streamers, due to the accumulation of

positive space charge near the cathode, nor do we attempt to consider the effects of the breakdown voltage on the parameters of the equivalent circuit. Both remain the subject of future studies. Instead, we isolate and investigate the dynamics of the negative ionisation fronts only, and in particular we study the effects of varying the indium vapour temperature on the formation and development of those negative ionisation fronts under the action of an externally applied electric field.

The remainder of this paper is organized as follows. In section 2 we briefly present a set of cross sections for electron scattering in indium vapour, including those for excitation from the ground state $(5s^2 5p)^2 P_{1/2}$ and the first excited metastable state $(5s^2 5p)^2 P_{3/2}$. In section 3.1 we present the methods of our calculations, including the basic elements of our Monte Carlo approach for simulating the electron swarm transport properties under hydrodynamic and SST conditions. In section 3.2 we present the basic elements of the classical 1.5D fluid model, which is used for studying the development of an electron avalanche, and its transition into a negative ionisation front in indium vapour. The results of this work are then given in section 4. Specifically, in section 4.2 we show the variation of the electron swarm transport coefficients with E/N and indium vapour temperature, while in section 4.3 we present the results of our study under non-hydrodynamic conditions in an idealised SST setup. Results describing the development of an electron avalanche and its transition into a negative ionisation front are presented in section 4.4. Finally, we summarize our conclusions in section 5 and also provide an outlook regarding possible future studies of electron transport and streamer discharges in indium vapour.

2. Cross sections for electron scattering in indium vapour

2.1. Elastic momentum transfer, electronic excitations and total ionisation

In this work, we utilize the cross sections for electron scattering in indium vapour, which have recently been generated and discussed in detail in our previous publications [38, 39] and to which we refer the interested reader. Here we simply note that the elastic momentum transfer cross section, for energies from 0.001 eV to 10 000 eV, and for scattering from the ground $(5s^2 5p)^2 P_{1/2}$ level, is tabulated in reference [39]. Uncertainty estimates of $\sim \pm 20\%$ for electron energies less than 3 eV and $\sim \pm 15\%$ for energies above 3 eV were quoted [39]. The elastic momentum transfer cross section for scattering from the lowest-lying $(5s^2 5p)^2 P_{3/2}$ metastable state is also tabulated in reference [39].

Cross sections for discrete inelastic transitions from the $^2 P_{1/2}$ ground state and the close-lying metastable $^2 P_{3/2}$ level were calculated using a relativistic *B*-spline *R*-matrix (DBSR) method by Hamilton *et al* [39]. In particular, 21 discrete inelastic cross sections for excitation from the ground state and 21 discrete inelastic cross sections for excitation from the lowest metastable state were provided [39]. Among many interesting points, near-threshold structures in the majority of the discrete inelastic cross sections were reported [39].

The total ionisation cross section for indium atoms initially in the electronic ground state was determined for energies from threshold to 10 000 eV in [39]. The quoted uncertainty on those data was $\sim \pm 20\%$ [39]. The total ionisation cross section for indium atoms in the first $(5s^25p)^2P_{3/2}$ metastable state (0.274 eV), was estimated by simply moving its threshold from that of the ground state (5.786 eV) downward by 0.274 eV.

2.2. Superelastic collisions

One of the objectives of the present work is to study the effects of the indium vapour temperatures on electron transport and the propagation of negative ionisation fronts. To do this, we need to take into account superelastic collisions in our Monte Carlo simulations and/or the solutions of the Boltzmann equation. As pointed out in our previous work [39], the thermal energy at $T = 1260$ K is $\frac{3}{2}kT \approx 0.163$ eV, i.e. near the threshold energy of the first $(5s^25p)^2P_{3/2}$ metastable state. It is therefore important to consider the influence of superelastic collisions on electron transport at indium vapour temperatures of a few thousand Kelvin.

Cross sections for superelastic collisions can be evaluated by applying the principle of microscopic reversibility and detailed balance in a thermal equilibrium. According to this fundamental principle, the cross section for superelastic collision σ_s may be calculated from the cross section σ_j for the discrete inelastic transition to the state j, with the threshold energy ϵ_j and statistical weight g_j, as

$$\sigma_s(\epsilon) = \frac{g_0}{g_j} \frac{\epsilon + \epsilon_j}{\epsilon} \sigma_j (\epsilon + \epsilon_j), \qquad (1)$$

where g_0 is the statistical weight of the ground state.

In figure 1 we show the fractional populations of indium atoms in the ground $(5s^25p)^2P_{1/2}$ state, the first excited $(5s^25p)^2P_{3/2}$ metastable state, and the sum of all the upper excited states, as a function of the indium vapour temperature. At $T = 1260$ K, we observe that 86% of indium atoms are in the ground $(5s^25p)^2P_{1/2}$ state while the remaining 14% are in the first $(5s^25p)^2P_{3/2}$ metastable state. Similarly, but now at $T = 3260$ K, 57% of the indium atoms are in the ground $(5s^25p)^2P_{1/2}$ state while the remaining 43% of indium atoms are in the metastable state. The fractional populations of the third and higher excited levels are only larger than 1% at $T = 7260$ K and higher temperatures. Thus, we limit our calculations to an upper limit of $T = 5260$ K.

The cross sections for electron scattering in indium vapour from the ground $(5s^25p)^2P_{1/2}$ level and the close-by metastable $(5s^25p)^2P_{3/2}$ level are displayed in figures 2 and 3, respectively. The total cross section for superelastic collisions is multiplied with the corresponding fractional populations of the first excited metastable state at 1260 K, 3260 K and 5260 K, and these quantities are also included in figures 2 and 3, respectively. Note that the cross sections for elastic momentum transfer, inelastic discrete transitions and ionization should be multiplied with the corresponding weighting factors to account for the appropriate fractional populations
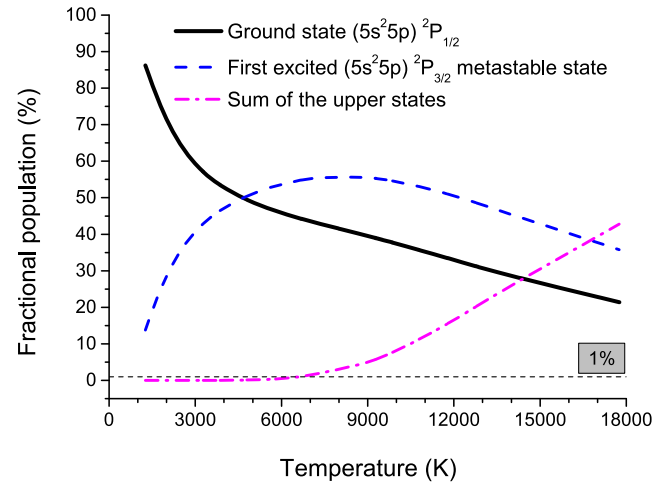
Figure 1. Fractional populations of indium atoms in the $(5s^25p)^2P_{1/2}$ ground state, the first excited $(5s^25p)^2P_{3/2}$ metastable state, and the sum of all higher excited states, as a function of the indium vapour temperature.

of the ground state $(5s^25p)^2P_{1/2}$ and the metastable state $(5s^25p)^2P_{3/2}$ at the temperature being considered.

3. Methods of calculations

3.1. Monte Carlo simulations

In Monte Carlo simulations, we follow the spatial and temporal evolution of a large number of electrons moving under the action of an external electric field in a spatially homogenous indium vapour. Under swarm conditions, the electron density is sufficiently low, so that only electron collisions with indium atoms are taken into account. Electrons gain energy from the externally applied electric field and in superelastic collisions with excited indium atoms. This energy input is released through binary collisions between the electrons and the atoms. Thermal motion of the background indium atoms and their influence on the electrons are taken into account. We implemented an algorithm for calculating the collision frequency in the case when thermal motion of the background indium atoms with a Maxwellian velocity distribution cannot be neglected [45]. We assume isotropic scattering in the electronic excitation and ionisation collisions. The anisotropic nature of elastic collisions is implicitly included through the use of the elastic momentum transfer cross section. The energy available for division after an ionising collision is given by the difference between the incident electron energy and the indium ionisation energy, here modelled as a constant value of 5.786 eV for indium atoms in the ground state and a value of 5.512 eV for indium atoms in the first excited metastable state. To allocate the available energy to the two-post collision electrons, a random fraction of the available energy is awarded to one electron, with the remaining energy being awarded to the second electron. In other words, the available energy is distributed assuming a uniform distribution indicating that all fractions of the available energy post-collision are equally probable.
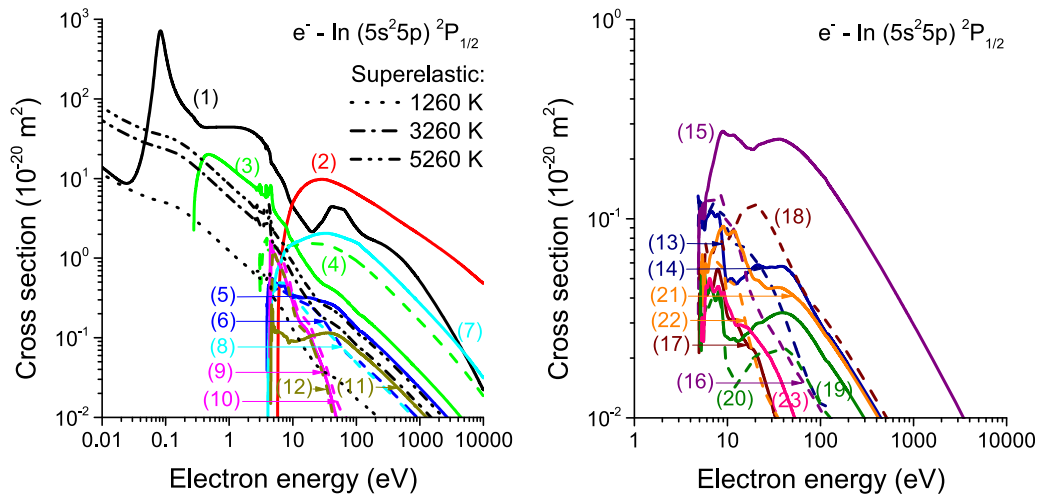
Figure 2. Integral cross sections for electron scattering in indium vapour for atoms in the ground state $(5s^25p)^2P_{1/2}$. The left panel shows the elastic momentum transfer (1), total ionization (2), and quantities that are obtained by multiplying the total cross section for superelastic collisions with the corresponding fractional populations of the first excited metastable state at indium vapour temperatures of 1260 K, 3260 K, and 5260 K. The left panel also includes the following discrete inelastic transitions: $(5s^25p)^2P_{3/2}$ (3), $(5s^26s)^2S_{1/2}$ (4), $(5s^26p)^2P_{1/2}$ (5), $(5s^26p)^2P_{3/2}$ (6), $(5s^25d)^2D_{3/2}$ (7), $(5s^25d)^2D_{5/2}$ (8), $(5s^24p)^2P_{1/2}$ (9), $(5s^24p)^2P_{3/2}$ (10), $(5s^27s)^2S_{1/2}$ (11) and $(5s^24p)^2P_{5/2}$ (12). The right panel includes the following discrete inelastic transitions: $(5s^27s)^2P_{1/2}$ (13), $(5s^27s)^2P_{3/2}$ (14), $(5p^26d)^2D_{3/2}$ (15), $(5p^26d)^2D_{5/2}$ (16), $(5p^24f)^2F_{7/2}$ (17), $(5p^24f)^2F_{5/2}$ (18), $(5p^28s)^2S_{1/2}$ (19), $(5p^28s)^2P_{1/2}$ (20), $(5s^27d)^2D_{3/2}$ (21), $(5s^27d)^2D_{5/2}$ (22) and $(5s^28p)^2P_{3/2}$ (23).
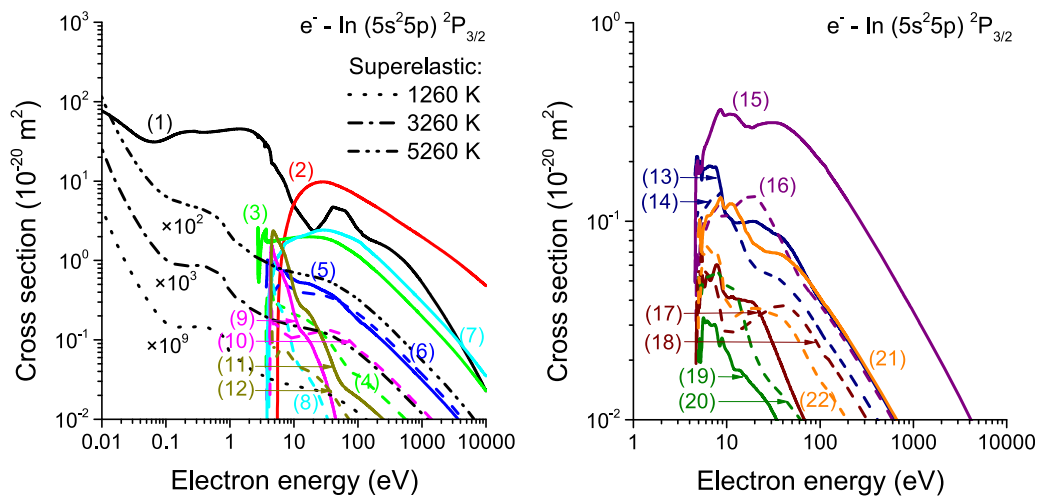
Figure 3. Integral cross sections for electron scattering in indium vapour for atoms in the metastable state $(5s^25p)^2P_{3/2}$. The left panel shows the elastic momentum transfer (1), total ionization (2), and quantities that are obtained by multiplying the total cross section for superelastic collisions with the corresponding fractional populations of the first excited metastable state at indium vapour temperatures of 1260 K, 3260 K, and 5260 K. The quantities obtained as the product of the total cross section for superelastic collisions and the corresponding fractional populations of the first excited metastable state were subsequently multiplied by factors of 10^9, 10^3, and 10^2, at indium vapour temperatures of 1260, 3260 and 5260, respectively. The left panel also includes the following discrete inelastic transitions: $(5s^26s)^2S_{1/2}$ (3), $(5s^26p)^2P_{1/2}$ (4), $(5s^26p)^2P_{3/2}$ (5), $(5s^25d)^2D_{3/2}$ (6), $(5s^25d)^2D_{5/2}$ (7), $(5s^24p)^2P_{1/2}$ (8), $(5s^24p)^2P_{3/2}$ (9), $(5s^27s)^2S_{1/2}$ (10), $(5s^24p)^2P_{5/2}$ (11) and $(5s^27s)^2P_{1/2}$ (12). The right panel includes the following discrete inelastic transitions: $(5s^27s)^2P_{3/2}$ (13), $(5p^26d)^2D_{3/2}$ (14), $(5p^26d)^2D_{5/2}$ (15), $(5p^24f)^2F_{7/2}$ (16), $(5p^24f)^2F_{5/2}$ (17), $(5p^28s)^2S_{1/2}$ (18), $(5p^28s)^2P_{1/2}$ (19), $(5s^27d)^2D_{3/2}$ (20), $(5s^27d)^2D_{5/2}$ (21) and $(5s^28p)^2P_{3/2}$ (22).

We then track a large number of electrons between collisions using finite length time steps. The time step is determined as a fraction of the mean collision time, which is calculated from the total collision frequency. Finite time steps are used to solve the integral equation for the collision probability, in order to determine the exact time of the next collision [46, 47]. If the length of these time steps is too large, then the time of the next collision can be inaccurately computed, which in turn affects the accuracy of the calculation of the electron trajectories. On the other hand, too small time steps lead to an enormous increase of computing time, which is equally unacceptable. For this investigation, the time step was

fixed at one hundredth of the mean time between collisions, regardless of the electron energy. This allows for a precise determination of the time of the next collision and the trajectory of the electrons.

The equation for the collision probability is solved by numerical integration using the above-mentioned time steps. When the moment of the next collision is determined, the next step is to define the nature of the collision. For this purpose, the relative probabilities for each collision process are calculated at the given electron energy. All electron scattering processes are assumed to be isotropic regardless of their specific nature and energy. Therefore, the change in direction of the electron velocity is expressed by a uniformly distributed scattering angle within the interval $[0, \pi]$ and by the azimuthal angle that is uniformly distributed within the interval $[0, 2\pi]$. The change in the electron energy, after elastic and inelastic collisions, is calculated using the laws of elementary collision dynamics. For more details the reader is referred to [40, 47].

3.1.1. Sampling of the bulk and flux transport coefficients. Under hydrodynamic conditions, the electron swarm transport coefficients are calculated after the relaxation of the swarm to the stationary state. The measurable and universal transport coefficients are the bulk transport coefficients [48]. They are calculated in our Monte Carlo simulations from the rate of change of the appropriate averages of the positions of the electrons, in configuration space [40, 47]. The number-changing reaction rate, which for indium vapour is reduced to the ionisation frequency, is defined by

$$\nu_{\text{ION}} = \frac{\mathrm{d}}{\mathrm{d}t} \left(\ln N_{\text{e}} \right), \tag{2}$$

the bulk drift velocity by

$$\boldsymbol{W} = \frac{\mathrm{d}}{\mathrm{d}t} \langle \boldsymbol{r} \rangle, \tag{3}$$

and the bulk diffusion tensor by

$$\boldsymbol{D} = \frac{1}{2} \frac{\mathrm{d}}{\mathrm{d}t} \langle \boldsymbol{r}^\star \boldsymbol{r}^\star \rangle. \tag{4}$$

Here N_{e} is the total number of electrons at any time t, $\langle \boldsymbol{r} \rangle$ is the coordinate of the swarm's centre of mass, and $\boldsymbol{r}^\star = \boldsymbol{r} - \langle \boldsymbol{r} \rangle$. The coordinate of the swarm's centre of mass is given by

$$\langle \boldsymbol{r} \rangle = \frac{1}{N_{\text{e}}} \sum_{k=0}^{N_{\text{e}}} \boldsymbol{r}_k, \tag{5}$$

where $\boldsymbol{r}_k$, $(k = 1, 2, \ldots, N_{\text{e}})$ are the coordinates of all electrons.

The flux transport coefficients are required for some aspects of plasma modelling and elsewhere [49]. The flux drift velocity is given by

$$\boldsymbol{W}^\star = \left\langle \frac{\mathrm{d}\boldsymbol{r}}{\mathrm{d}t} \right\rangle = \langle \boldsymbol{v} \rangle, \tag{6}$$

and the flux diffusion tensor by

$$\boldsymbol{D}^\star = \frac{1}{2} \left\langle \frac{\mathrm{d}}{\mathrm{d}t} \left(\boldsymbol{r}^\star \boldsymbol{r}^\star \right) \right\rangle. \tag{7}$$

The flux drift velocity is in fact the average velocity of the electrons. It is given by

$$\langle \boldsymbol{v} \rangle = \frac{1}{N_{\text{e}}} \sum_{k=0}^{N_{\text{e}}} \boldsymbol{v}_k, \tag{8}$$

where

$$\boldsymbol{v}_k = \frac{\mathrm{d}\boldsymbol{r}_k}{\mathrm{d}t}. \tag{9}$$

Although, at first glance, the expressions (3) and (6) look the same, they are fundamentally different in the presence of non-conservative collisions. Using expressions (5) and (9), the equality of the bulk drift velocity and the flux drift velocity is reduced to

$$\frac{1}{N_{\text{e}}} \frac{\mathrm{d}}{\mathrm{d}t} \sum_{k=0}^{N_{\text{e}}} \boldsymbol{r}_k = \frac{1}{N_{\text{e}}} \sum_{k=0}^{N_{\text{e}}} \frac{\mathrm{d}}{\mathrm{d}t} \boldsymbol{r}_k. \tag{10}$$

In the absence of non-conservative collisions (e.g. ionisation), the total number of the electrons N_{e} remains the same during the simulation, and hence the time derivative commutes with the sum. However, in the presence of non-conservative collisions, the total number of electrons N_{e} is neither a constant nor a continuous function of time and thus the equality (10) no longer holds. In other words, in the presence of non-conservative collisions, the bulk and the flux transport coefficients are not the same. This is no moot point, as the differences between the two families of transport coefficients are often significant, ranging from a few percent to a few orders of magnitude [50].

For electrons in indium vapour, the differences between the bulk and flux transport coefficients are induced by the explicit contribution of ionisation processes. Ionisation is most likely to occur at the leading edge of the swarm, where the higher-energy electrons are located. Thus, in the case of drift, ionisation always acts in such a manner as to push the centre of mass of the swarm forward, which in turn increases the bulk drift velocity. Therefore, for electrons in indium vapour, we may expect that the bulk drift velocity is always larger in magnitude than the flux drift velocity. Similarly, the increase in electron numbers, due to ionisation in the indium vapour, enhances diffusion in both the longitudinal and transverse directions. These observations will be discussed and illustrated later by showing the E/N-profiles of the drift velocity and diffusion coefficients (see section 4.2).

3.1.2. Sampling of spatially-resolved transport data. Under non-hydrodynamic SST conditions, the electrons are released from the cathode into the space between the electrodes. In contrast to our initial Monte Carlo code, where the electrons were released one by one from the cathode [40–42], in this work all electrons are released from the cathode at the same time. In this way, it is possible to use swarm rescaling procedures under SST conditions, which is of great importance for the simulation of electrons at high values of E/N, where a large number of secondary electrons is formed by ionisation processes. Similarly, the code designed in this way permits the

simulation of transport in strongly-attaching molecular gases under SST conditions [50]. The back-diffusion of electrons is not considered, and the electrons are followed until reaching the anode. Note that both electrodes are regarded as perfectly absorbing. Due to the presence of the electrodes, both the implicit and explicit gradients of the electron density exist. Consequently, the hydrodynamic approximation is not valid under SST conditions and the concept of transport coefficients makes no sense, even after reaching the equilibration of the swarm. The spatially-resolved transport data are thus calculated using the so-called box-sampling technique [40, 41]:

$$
\begin{aligned}
\langle \xi \rangle_j &= \left(\frac{1}{\Delta z} \int_{z_j - \Delta z/2}^{z_j + \Delta z/2} f_{\mathrm{SST}} (z, v) \, \mathrm{d}\boldsymbol{r} \, \mathrm{d}\boldsymbol{v} \right)^{-1} \frac{1}{\Delta z} \\
&\quad \times \int_{z_j - \Delta z/2}^{z_j + \Delta z/2} \xi f_{\mathrm{SST}} (z, v) \, \mathrm{d}\boldsymbol{r} \, \mathrm{d}\boldsymbol{v} \\
&\approx \left(\sum_{k=1}^{N_{\mathrm{e}}} \Delta t_k^j \right)^{-1} \sum_{k=1}^{N_{\mathrm{e}}} \xi_k^j \Delta t_k^j.
\end{aligned}
\tag{11}
$$

Here $f_{\mathrm{SST}} (z, v)$ is the steady-state distribution function, ξ_j^k is the value of the quantity to be sampled when the kth electron is contained in the jth box, Δt_k^j is the residence time of the electron in that box, and N_{e} is the number of electrons that appear there.

The spatially-resolved rate coefficients are calculated by determining the number of collisions of type m in the jth spatial box located at z_j [40, 51]:

$$
R^m(z_j) = \frac{N_j^m}{\Delta z \, N_{\mathrm{e}}(z_j)},
\tag{12}
$$

where N_j^m denotes the number of collisions m, Δz is the width of box, and $N_{\mathrm{e}}(z_j)$ is the total number of resident electrons. The expression (12) was tested in nitrogen and other gases, by comparing the calculated ionisation coefficient with the experimental results obtained from the slope of the electron emission, as well as with the results obtained by integrating the distribution function and the corresponding cross section for ionisation [51]. The agreement between these independent techniques was excellent, indicating the accuracy and validity of the methodology used for sampling the spatially-resolved rate coefficients.

3.2. Classical fluid model

The inception and propagation of negative ionisation fronts were studied using a classical fluid model. The classical model involves the first two velocity moments of the Boltzmann equation, i.e. the equation of continuity and the momentum balance equation. The classical drift–diffusion approximation is obtained by assuming a steady state of the momentum balance equation and that the energy of the field-directed motion is much larger than the thermal contribution. For the full and strict derivation of this model the reader is referred to [52]. The generalized one-dimensional continuity equation for the

electron number density is

$$
\frac{\partial n_{\mathrm{e}}}{\partial t} = \frac{\partial}{\partial x} \left(W \, \mathrm{sgn} \, (E) \, n_{\mathrm{e}} + D_{\mathrm{L}} \frac{\partial n_{\mathrm{e}}}{\partial x} \right) + \nu_{\mathrm{ION}} n_{\mathrm{e}},
\tag{13}
$$

where W and D_{L} are the electron drift velocity and longitudinal diffusion coefficient, respectively, E is oriented along the x-axis, while ν_{ION} is the ionisation coefficient. The drift and diffusion of positive ions are neglected here on the basis of the time scales of interest in the present work. Likewise, the discharge model is not coupled to the gas dynamics, even though the indium vapour may be additionally heated by the discharge [53, 54].

The model is realized in a 1.5-dimensional (1.5D) setup, according to which the streamer radius R_0 is fixed. Thus, the total electric field in the system is evaluated as the sum of the uniform external electric field and the electric field due to space charge:

$$
\begin{aligned}
E(x, t) = E_0 &+ \frac{e}{2\varepsilon_0} \int_0^d (n_{\mathrm{p}} - n_{\mathrm{e}}) \left(\mathrm{sgn} \, (x - x') \right. \\
&\left. - \frac{x - x'}{\sqrt{(x - x')^2 + R_0^2}} \right) \mathrm{d}x',
\end{aligned}
\tag{14}
$$

where E_0 and ε_0 are the external (applied) electric field and vacuum permittivity, respectively, and d is the length of the system.

The above fluid equations are closed, assuming the local field approximation. According to this approximation, the input data, including W, D_{L}, and ν_{ION}, are assumed to be functions of the local instantaneous electric field. Equations (13) and (14) are solved numerically, imposing the homogeneous Dirichlet boundary conditions for the electron density n_{e} as

$$
n_{\mathrm{e}} (x = 0, t) = 0, \qquad n_{\mathrm{e}} (x = d, t) = 0,
\tag{15}
$$

and initial conditions

$$
n_{\mathrm{e}} (x, t = 0) = \frac{N_{\mathrm{e}0}}{\pi R_0^2 \sigma_0 \sqrt{2\pi}} \exp \left(-\frac{1}{2} \frac{(x - x_0)^2}{\sigma_0^2} \right).
\tag{16}
$$

Here $N_{\mathrm{e}0}$ is the initial number of electrons with a Gaussian distribution centred at x_0 and a standard deviation σ_0. In the numerical implementation of our fluid model, the spatial discretization is performed by employing the second-order central finite-difference method, while the fourth order Runge–Kutta method is used for the integration in time. For more details, the reader is referred to [52, 55].

4. Results and discussion

4.1. Preliminaries

In Monte Carlo simulations, in which electron transport under hydrodynamic conditions is studied, we cover a range of reduced electric fields E/N between 0.01 Td and 10 000 Td. The pressure of the background gas of indium atoms is fixed at 1 Torr, and our calculations are performed for the indium
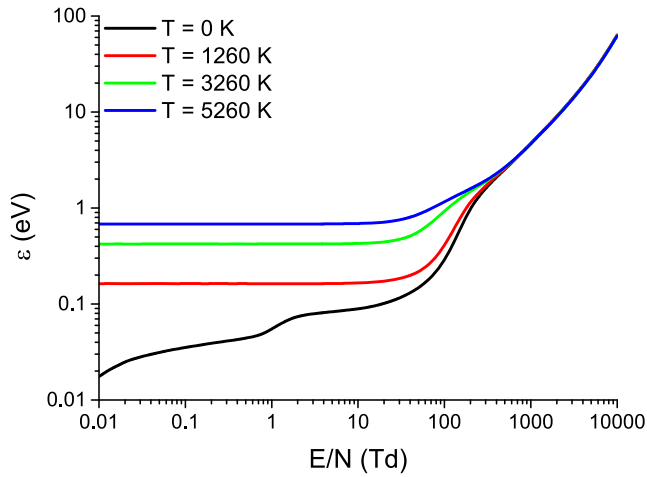
Figure 4. Variation of the mean energy ε of the electron swarm as a function of E/N for various indium vapour temperatures.

vapour temperatures of 1260, 3260, and 5260 K. The cold-gas approximation, according to which the background indium atoms are at rest ($T = 0$ K), is also analysed. The number of electrons in our Monte Carlo simulations, under hydrodynamic conditions was varied between 2.5×10^5 for lower values of E/N to 1×10^6 at higher values of E/N. Under SST conditions, however, the number of electrons is varied between 1×10^5 and 5×10^5, depending on the distance between the electrodes and the applied reduced electric field E/N. In section 4.2 we present the electron swarm transport coefficients as a function of the reduced electric field E/N and indium vapour temperatures, T, while in section 4.3 we present the electron swarm transport properties and spatial relaxation profiles as a function of E/N and T. In the latter case the electrons are released from the cathode under two different sets of initial conditions: (i) the Maxwell–Boltzmann velocity distribution with starting mean energies of 0.1 eV, 1 eV, and 10 eV, and (ii) the beam initial velocity distribution with the same starting mean energies. Finally, in section 4.4 the development of an electron avalanche and its transition into a negative ionisation front is considered.

4.2. Electron transport under hydrodynamic conditions

As noted above, in this section we present results showing the variation of electron swarm transport properties with E/N and indium vapour temperature, T. Figure 4 illustrates the variation of the mean energy with E/N for various temperatures. In the $T = 0$ K profile, we observe that ε is a monotonically increasing function of E/N. The rate of increase of the mean energy varies with E/N, reflecting the energy dependence of the cross sections for electron scattering. For $T = 1260$ K, $T = 3260$ K, and $T = 5260$ K, the profiles of the mean energy also exhibit some generic features. At lower values of E/N, we observe initial plateaus in the profiles, indicating that the electrons are in near thermal equilibrium with the indium vapour. In this range of lower values of E/N, which extends up to approximately 10 Td, the distribution of electrons is of thermal-Maxwellian form, and the mean energy

depends distinctively on the indium vapour temperature. This low E/N regime can be characterized as a vapour-dominated regime, where the electrons are essentially thermalized. As E/N rises, the electrons gain more energy from the electric field and are no longer thermalized. As a result, the velocity distribution deviates from a thermal-Maxwellian, but to a large extent the temperature of the indium vapour still controls the behaviour of the electrons. This is the so-called intermediate regime, which extends from approximately 10 Td to 400 Td. For E/N larger than approximately 400 Td, the mean energies are considerably higher than the corresponding thermal energies. We observe that the influence of indium vapour temperature on the mean energy is minimal in this regime. In what follows, we will refer to this region of electron transport as the field-dominated regime.

Figure 5 shows the variation of the bulk drift velocity with E/N for various T. At first glance, for lower values of E/N, we observe that the drift velocity for $T = 0$ K varies very slowly with increasing E/N. However, looking more closely, we in fact observe that the drift velocity exhibits a region of negative differential conductivity (NDC), i.e. over a range of E/N values the drift velocity decreases as the driving electric field increases [56]. NDC takes place here between approximately 0.03 Td and 0.3 Td, where there is a noticeable transition in the dominant energy loss mechanism from inelastic to elastic processes. In the transition regime, due to numerous elastic collisions, the enhanced randomization of the directed motion decreases the drift velocity even though the mean energy increases. As E/N increases further, NDC is suppressed due to numerous elastic and inelastic collisions. Consequently, for E/N larger than approximately 0.3 Td and at $T = 0$ K, the drift velocity is a monotonically increasing function of E/N. From the E/N-profiles of the bulk drift velocity for $T = 1260$ K, $T = 3260$ K, and $T = 5260$ K, we observe no such NDC and that the drift velocities are increasing functions of E/N. In the vapour-dominated and intermediate regimes, the drift velocity generally decreases with increasing vapour temperature. In this low E/N regime, the drift velocities for $T = 1260$ K is essentially linear, which is a signature of constant mobility. In the field-dominated regime, the impact of the vapour temperature on the drift velocity is minimal.

In figures 6 and 7, respectively, we show the variation of the bulk longitudinal ND_L and bulk transverse ND_T diffusion coefficients with E/N, for various vapour temperatures. In the vapour-dominated and intermediate regimes, at fixed E/N, we observe that ND_L increases with T. On the other hand, in the field-dominated regime, both ND_L and ND_T show no sensitivity with respect to the vapour temperature. We observe a deep minimum in the E/N-profile of ND_L for $T = 0$ K at around 0.45 Td, which can be attributed to the rapid increase of the elastic momentum transfer cross section in the limit of the lowest values of electron energies. For E/N larger than approximately 0.45 Td, ND_L is a generally increasing function of E/N. Similarly, we observe a distinct minimum in the E/N-profile of ND_T for $T = 0$ K at about 30 Td. The fall in ND_T occurs less rapidly in comparison with that of ND_L, but it extends over a wider range of E/N. As for ND_L, the decline in ND_T at $T = 0$ K reflects the rapidly increasing cross section for
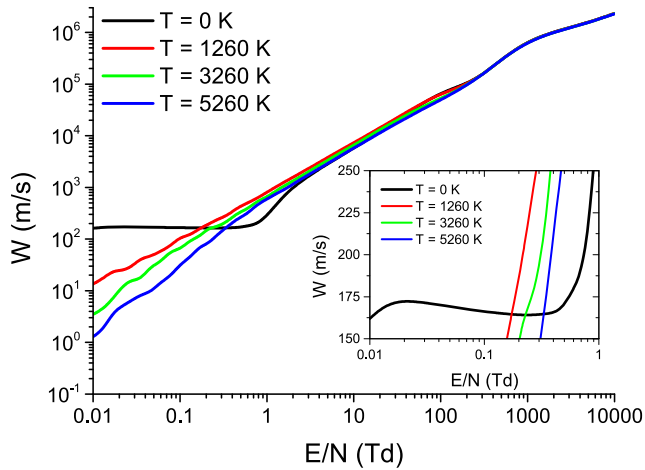
Figure 5. Variation of the bulk drift velocity of the electron swarm as a function of E/N for various indium vapour temperatures.

Figure 6. Variation of the bulk longitudinal diffusion coefficient of the electron swarm as a function of E/N for various indium vapour temperatures.

Figure 7. Variation of the bulk transverse diffusion coefficient of the electron swarm as a function of E/N for various indium vapour temperatures.
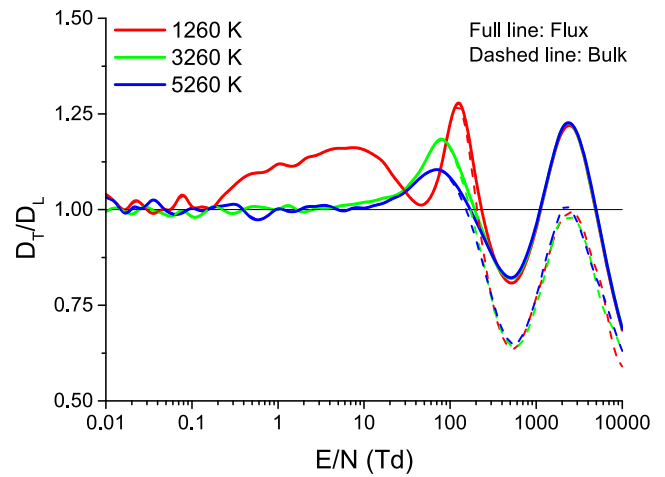
Figure 8. Variation of the ratio of ND_T to ND_L of the electron swarm as a function of E/N for various indium vapour temperatures.

momentum transfer in elastic collisions and the cross section for excitation of the $(5s^2 5p)^2 P_{3/2}$ metastable state. In the vapour-dominated regime, from the E/N-profiles of both ND_L and ND_T for $T = 1260$ K, $T = 3260$ K, and $T = 5260$ K, we observe that the diffusion coefficients have essentially thermal values. These values of the diffusion coefficients are increasing functions of the vapour temperature. As expected, the thermal values of ND_L and ND_T are nearly identical, indicating that the velocity distribution of the electrons is approximately thermal-Maxwellian. As E/N increases further, the intermediate regime is characterized by non-thermal values of the diffusion coefficients, which are still temperature dependent. The temperature dependence of the diffusion coefficients is, however, minimal upon reaching the field-dominated regime.

The anisotropy of the diffusion tensor, i.e. $D_L \neq D_T$, exists over the entire range of E/N for $T = 0$ K. Figure 8 exhibits the ratio of ND_T to ND_L, as a function of E/N, for $T = 1260$ K, $T = 3260$ K, and $T = 5260$ K. As indicated on the graph, both the flux and bulk data are shown. Generally speaking, the anisotropy of the diffusion for electrons in

indium vapour, over the range of vapour temperatures considered in the present work, is relatively low, with the differences between ND_T and ND_L not exceeding approximately 30%. In the limit of the lowest values of E/N, as already emphasized, the diffusion is nearly isotropic. Small fluctuations of the ratio between ND_T and ND_L around unity follow from the statistical uncertainties of the dynamical properties sampled in our Monte Carlo simulations, which are required for the calculation of the diffusion coefficients. As E/N increases further, we observe that the anisotropy of the diffusion tensor is reduced for increasing vapour temperature in the intermediate regime. For higher values of E/N, the sensitivity of the ratio of ND_T to ND_L, with respect to the indium vapour temperature, is minimal in the field-dominated regime. It is also interesting to note that for E/N larger than approximately 200 Td, the bulk values of ND_L are larger than the bulk values of ND_T. This is not the case for the corresponding flux values of the diffusion coefficients.
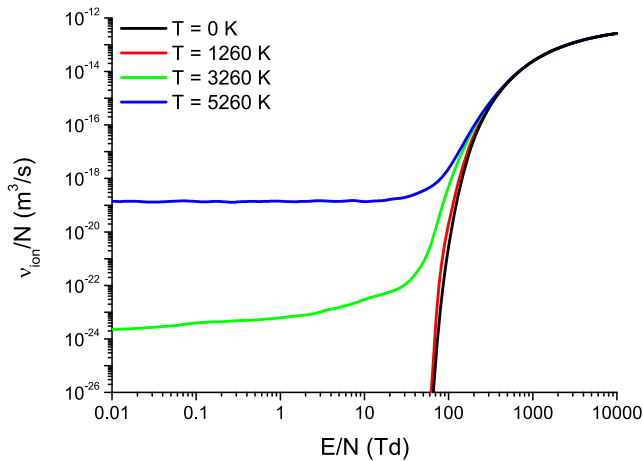
Figure 9. Variation of the ionisation rate of the electron swarm as a function of E/N for various indium vapour temperatures.

In figure 9 we plot the variation of the ionisation rate coefficient as a function of E/N for various vapour temperatures. The ionization rate coefficient corresponds to the density reduced ionization frequency, where the ionization frequency is given by equation (2). As expected, the ionisation rate increases with E/N for all temperatures. The E/N-profiles of ν_{ion}/N, are similar for $T = 0$ K and $T = 1260$ K and resemble the typical behaviour of the ionisation rate in other gases. This follows from the fact that, as in most cases, the E/N-profiles of ν_{ion}/N are essentially featureless, as ionisation only becomes considerable for higher values of E/N when sufficient electrons have enough energy to cause ionisation. However, for higher indium vapour temperatures, e.g. for $T = 3260$ K and $T = 5260$ K, the electrons have enough energy to cause ionisation even in the vapour-dominated regime, i.e. in the limit of the lowest E/N considered in the present work. While at $T = 5260$ K the ionisation rate essentially remains unaltered, at $T = 3260$ K the ionisation rate increases with E/N. Then, as E/N is increased further, the ionisation rates for both $T = 3260$ K and $T = 5260$ K increase rapidly, reaching the field-dominated regime, where the vapour temperature does not affect this property.

Figure 10 displays the variation in the rate coefficients for transfer of momentum in elastic collisions, summed excitation, summed de-excitation, and ionisation as a function of E/N for various vapour temperatures. At $T = 0$ K, the elastic momentum transfer rate increases with E/N up to about 1 Td. Then, as E/N further increases, it starts to decrease slowly in magnitude. For $T = 1260$ K, $T = 3260$ K, and $T = 5260$ K, however, the elastic momentum transfer rate essentially remains constant, before decreasing in the limit of the highest E/N considered in the present work. The summed excitation rate coefficient for $T = 0$ K is a rapidly increasing function of E/N, until ionisation processes start to play a significant role at around 200 Td. For $T = 1260$ K, $T = 3260$ K, and $T = 5260$ K, the summed excitation and de-excitation rates are identical for lower values of E/N, e.g. in the vapour-dominated regime. This follows from detailed balancing and the fact that the electrons are in thermal equilibrium with the

indium vapour. These rate coefficients begin to depart from each other at approximately 20 Td for $T = 1260$ K, 30 Td for 3260 K, and 40 Td for 5260 K, with an increase in excitation events and a decrease in de-excitation events. Comparing the ionisation rates with the rate coefficients for all the other processes considered, we observe that ionisation dominates in the limit of the highest E/N considered in the present study.

In order to illustrate the explicit effects of ionisation collisions on the drift and diffusion of electrons in indium vapour, we show in figure 11 the variation of the percentage difference between the bulk and flux values of the drift velocity (a), and the bulk and flux values of the longitudinal diffusion coefficient (b), as a function of E/N for various vapour temperatures. Figure 11 indicates that the influence of ionisation on the drift and diffusion is not apparent until approximately 200 Td. Even though ionisation is considerable for $T = 3260$ K and $T = 5260$ K in the vapour-dominated regime, the differences between the bulk and flux values of the drift velocity and longitudinal diffusion coefficient are minimal. This could be explained by considering the E/N-dependence of the rate coefficients for the other processes shown in figure 10. There we observe that competitive processes, including electronic excitations and de-excitations, are much more frequent than ionisation processes. As a consequence, the explicit contribution of ionisation to the measurable transport coefficients, e.g. the bulk drift velocity and the bulk diffusion coefficients, are reduced. As E/N increases further, the percentage difference between the bulk and flux values increases, reaching a maximum of around 45% and 80% for the drift velocity and the longitudinal diffusion coefficient, respectively. This indicates that the increase in electron numbers due to ionisation enhances both the drift and diffusion of the electrons in indium vapour. For the highest E/N considered here, the differences between the bulk and flux values are again reduced. Generally speaking, the influence of the vapour temperature on the differences between the bulk and flux values is minimal, reflecting the weak dependence of the drift velocity and longitudinal diffusion coefficient on the temperature in the field-dominated regime. In order to better understand the dual nature of the transport coefficients, and the associated differences between the bulk and flux values of the transport coefficients, the reader is referred to our previous publications [40, 47, 50].

4.3. Electron transport under SST conditions

In this section we present results showing the spatial relaxation of electrons and the variation of electron swarm transport properties with E/N and vapour temperature T under non-hydrodynamic conditions in an idealised SST experiment. Figure 12 shows the exponential growth of the electron number, in the region between the electrodes, as a function of E/N and the temperature. The electrons are released from the cathode into the space between the electrodes, assuming a Maxwell–Boltzmann velocity distribution, with the starting mean energy $\epsilon_0 = 1$ eV. The growth rate in the electron number increases with increasing E/N, indicating that ionisation processes become increasingly important with increasing E/N.
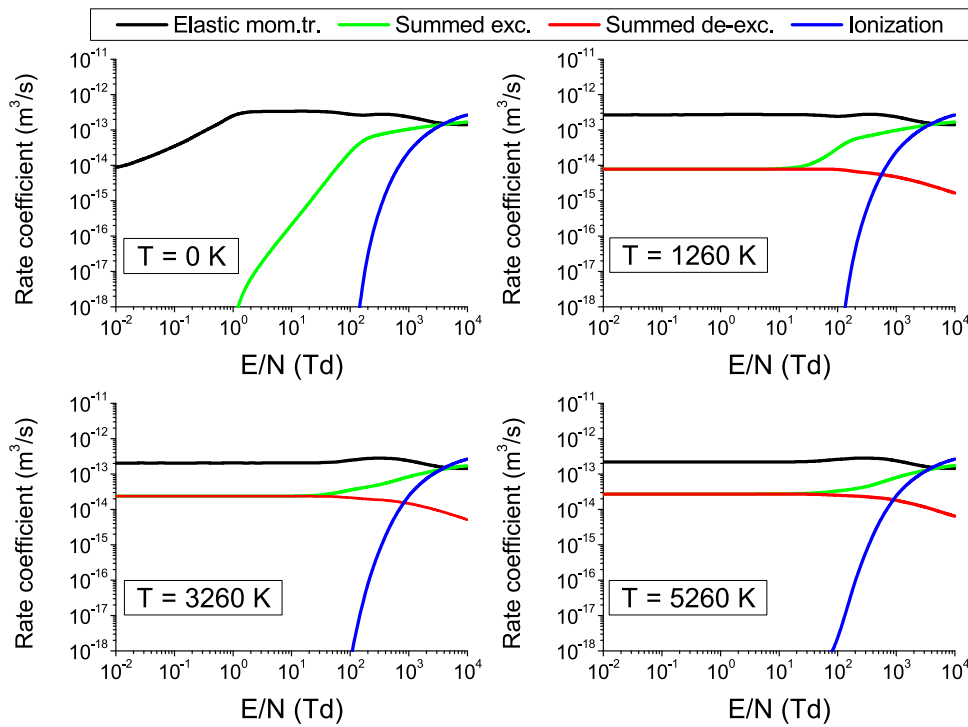
Figure 10. Variation of the rate coefficients for transfer of momentum in elastic collisions, summed excitation, summed de-excitation, and ionisation of the electron swarm, as a function of E/N, for various indium vapour temperatures.
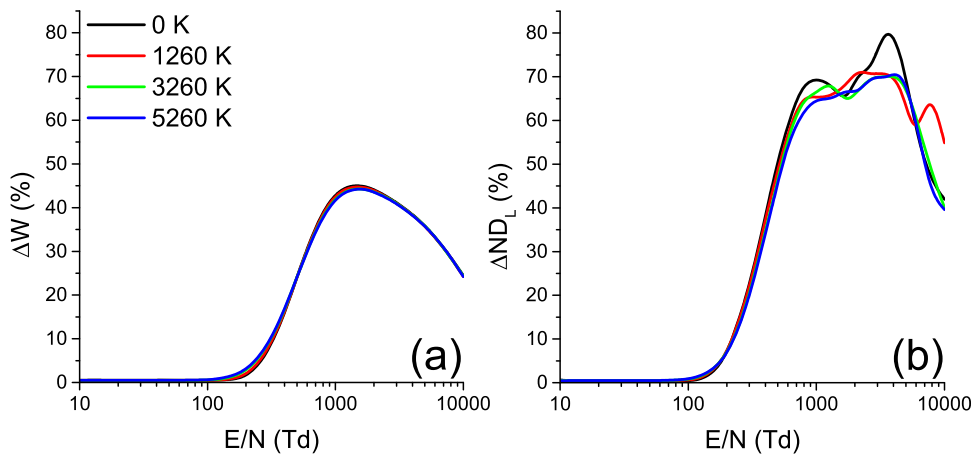
Figure 11. Variation of the percentage difference between the bulk and flux values of the drift velocity (a) and longitudinal diffusion coefficient (b) of the electron swarm, as a function of E/N, for various indium vapour temperatures.

Even though the results are presented on a log–log scale, we observe that the rate of increase in the number of electrons for a fixed E/N increases with the vapour temperature. This is a cumulative effect of the initial spatial relaxation and the following arguments may be used to account for its occurrence. At a fixed reduced electric field, in the initial phase of spatial relaxation, thermal effects play a key role in the multiplication of electrons in ionisation processes. This means that the higher the indium vapour temperature, the more electrons are produced at the beginning of the spatial relaxation. After relaxation, when a steady-state is achieved, these thermal effects are considerably reduced. This is indicative of the field-dominated regime, where swarm behaviour is entirely controlled by the electric field. In this regime, the ionization coefficient is not a function of the indium vapour temperature, which can be clearly seen in figure 9.

Figures 13 and 14 display relaxation profiles of the mean energy and the average velocity for a range of applied reduced electric fields E/N, as indicated on each graph. In both plots the electrons are released from the cathode assuming an initial beam velocity distribution, with a starting mean energy of 1 eV, in indium vapour at $T = 1260$ K. The behaviour of the transport properties is not considered in close vicinity of the anode. The relaxation profiles of the mean energy and the average velocity in indium vapour are consistent with earlier investigations on this topic for other gases [2, 5, 41, 42, 57–59]. First,
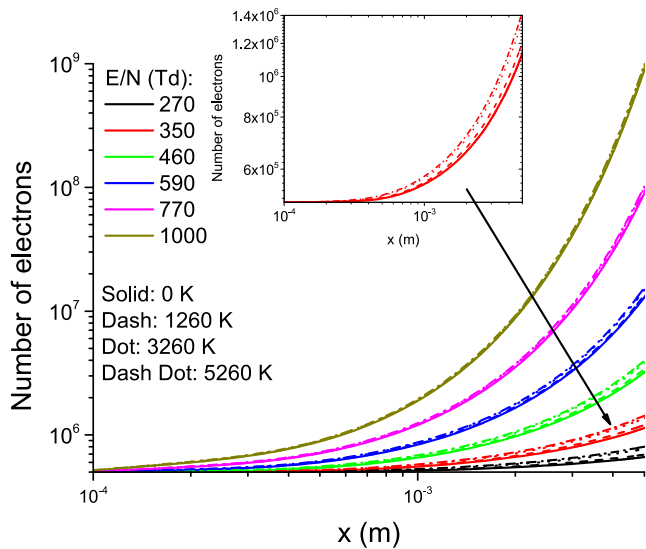
Figure 12. Exponential growth of the number of electrons in an idealized SST experiment as a function of E/N for various indium vapour temperatures.

we observe a limited range of E/N, where the mean energy and average velocity exhibit oscillatory behaviour as they relax towards the stationary state far downstream from the cathode. The spatial relaxation characteristics, including the period and amplitude of the oscillations, and the spatial relaxation length, are distinctively dependent on the applied E/N.

When electrons undergo elastic collisions in indium vapour, the energy transfer is a continuous process occurring in relatively small portions of energy. In inelastic collisions, however, the energy transfer is a discrete process with several orders of magnitude larger portions of energy. In the presence of elastic collisions only, the spatial profiles of the transport quantities would be exclusively monotonic and without oscillations along the relaxation profiles. On the other hand, in the presence of inelastic collisions only, due to the discrete electron energy losses, the spatial profiles would be periodic, with a period inversely proportional to the electric field strength, and an energy threshold that is a composite of several closely-lying inelastic processes that control the relaxation process. For electrons in indium vapour under the conditions considered in the present work, except the zero-temperature case, the electrons undergo both elastic and inelastic collisions with the presence of the elastic collisions always tending to dampen the oscillatory behaviour of the transport properties and broaden the peaks from the profiles. The key quantity in this complex interplay between the elastic and inelastic collisional energy loss processes is the mean energy of the swarm. In the presence of both elastic and inelastic collisions, when the mean swarm energy is much smaller or much larger than the lowest energy threshold of the inelastic processes, the collisional energy loss is controlled by the continuous energy loss processes and, therefore, the spatial relaxation profiles are monotonic or quasi-monotonic on their way to a spatially homogeneous form. Conversely, if the collisional energy loss is primarily controlled by the discrete energy loss processes, then the spatial profiles are periodically decaying.

The occurrence of oscillatory relaxation is particularly stimulated when the threshold energies of the various inelastic processes are concentrated in a relatively narrow energy region. For electrons in indium vapour, the threshold energies span the energy region between approximately 0.3 eV and 6 eV [38, 39]. With the exception of the $T = 0$ K case, for $E/N \leqslant 1$ Td the sensitivity of the relaxation profiles of the mean energy and the average velocity to E/N is minimal. This follows from the fact that the electrons are disturbed only in close vicinity of the cathode, while at longer distances they are essentially in quasi-thermal equilibrium with the indium atoms. As E/N further increases, the oscillatory feature is enhanced, as more and more electrons undergo inelastic collisions. However, the relaxation becomes dramatically slower and the amplitude and period of oscillations are reduced. In particular, when the mean energy is increased to a level that energy losses by inelastic collisions become continuous, the oscillatory feature is reduced. The spatial profiles are then monotonic and the transport properties relax to the spatially uniform states without oscillations.

Figure 15 displays relaxation profiles of the mean energy for a range of applied reduced electric fields E/N and indium vapour temperatures T, as indicated on the graphs. For a fixed value of E/N and for increasing indium vapour temperature T, we observe that significant changes in the spatial relaxation profiles of the mean energy occur. The relaxation proceeds much quicker and, if oscillations are present in the spatial profile, they are quickly dampened. Even though the spatial relaxation of the transport properties is distinctively dependent on E/N, the oscillatory feature is clearly evident for the lower vapour temperatures. As an illustrative example, for $E/N = 4.6$ Td and $T = 0$ K, we observe a sawtooth profile of the mean energy, where the amplitude of oscillations reduces slowly with the distance from the cathode (x). As the temperature T is further increased to 1260 K and 3260 K, the oscillations are first damped and thereafter entirely removed from the spatial profile by $T = 5260$ K. Generally speaking, the spatial relaxation of the mean energy and the other transport properties is monotonic over the entire range of E/N considered in the present work for the indium vapour temperature of 5260 K. For $T = 3260$ K, the relaxation profiles show reduced irregular oscillations, which are quickly dampened with increasing distance from the cathode. Comparing the spatial profiles at $T = 0$ K and $T = 1260$ K over a wide range of E/N (not shown here), we have observed that a window of reduced electric fields, for which the mean energy and transport properties exhibit oscillatory behaviour, is shifted to lower values of E/N. This occurs because of the increase in the mean energy as the indium vapour temperature T rises, enhancing the energy losses due to inelastic collisions, which in turn makes the discrete energy losses more continuous.

Figure 16 displays relaxation profiles of the mean energy for $E/N = 13$ Td and an indium vapour temperature $T = 1260$ K, assuming two different sets of initial conditions, including the beam initial velocity distribution with mean energies of 0.1 eV, 1 eV, and 10 eV (the first row), and a Maxwell velocity distribution with the same starting mean energies (the second row). Generally speaking, for a certain value of E/N,
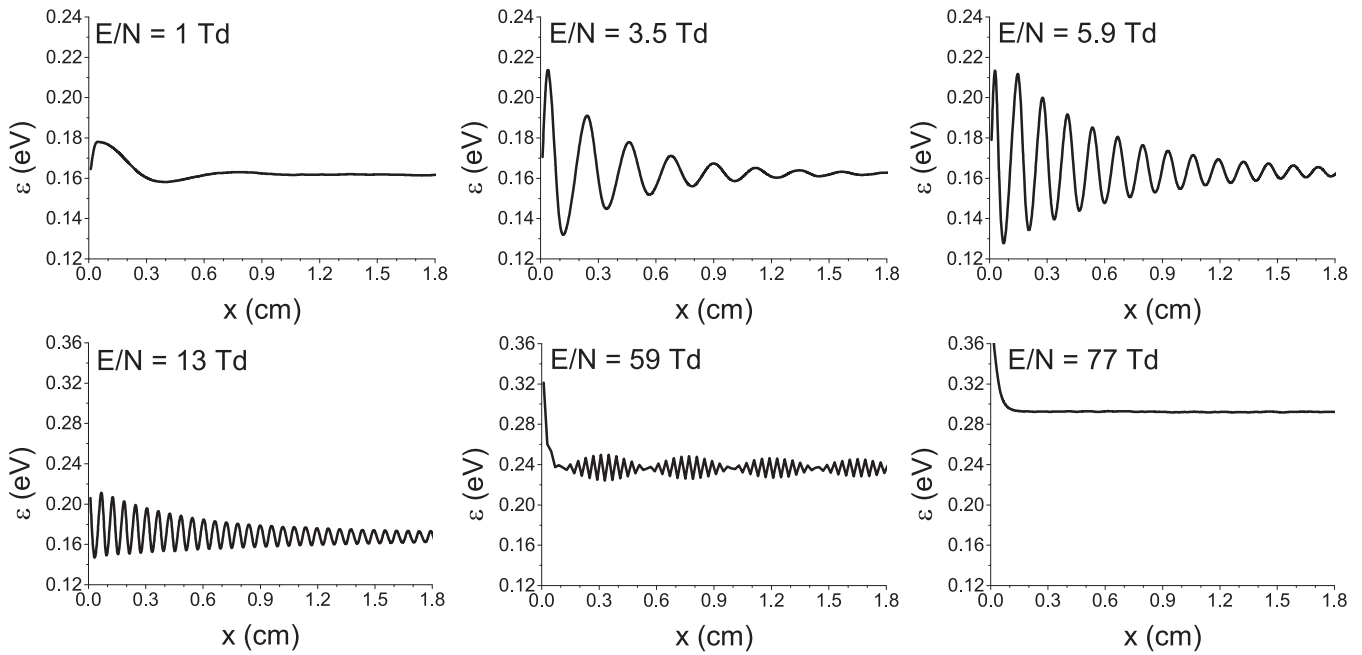
Figure 13. Spatial relaxation of the mean energy for electrons in indium vapour over a range of E/N. The calculations are for a fixed indium vapour temperature of 1260 K. x denotes the distance from the cathode.
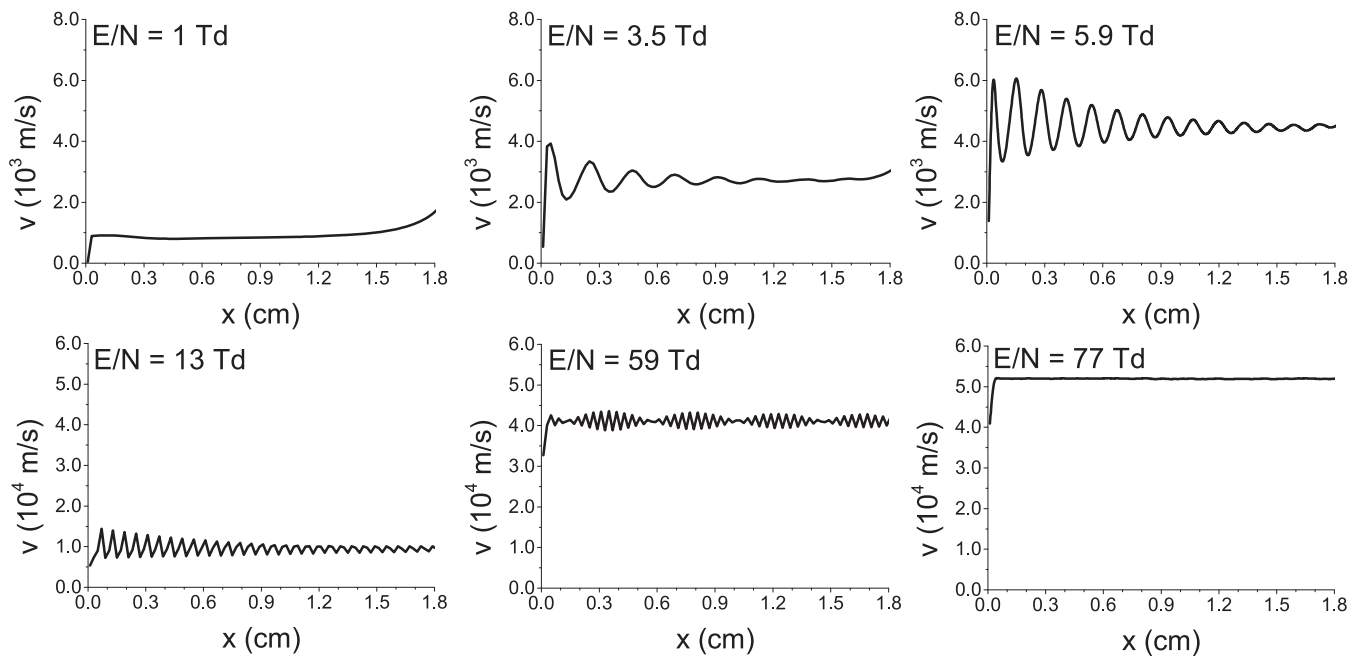
Figure 14. Spatial relaxation of the average velocity for electrons in indium vapour over a range of E/N. The calculations are for a fixed indium vapour temperature of 1260 K. x denotes the distance from the cathode.

the spatial relaxation of the mean energy or any other transport property will be different if the initial conditions for the electrons at the cathode or the disturbing source of electrons are different. On the other hand, the spatially uniform values of the transport properties are independent of the initial values. In the first row of figure 16, where the beam initial velocity distribution is used for the initial conditions, we observe that increasing the mean energy from 0.1 eV to 1 eV does not alter the spatial relaxation significantly. However, when the

initial starting mean energy is further increased to 10 eV, the relaxation is much quicker, i.e. the relaxation length is much less. In addition, we observe that the modulation amplitude and the period of oscillations are also strongly affected. When a Maxwell velocity distribution is used for the initial electrons at the cathode (second row of figure 16), we observe that increasing the starting mean energy from 0.1 eV to 1 eV dampens the oscillations. Then the relaxation proceeds much faster in comparison with the previous case, where the initial beam
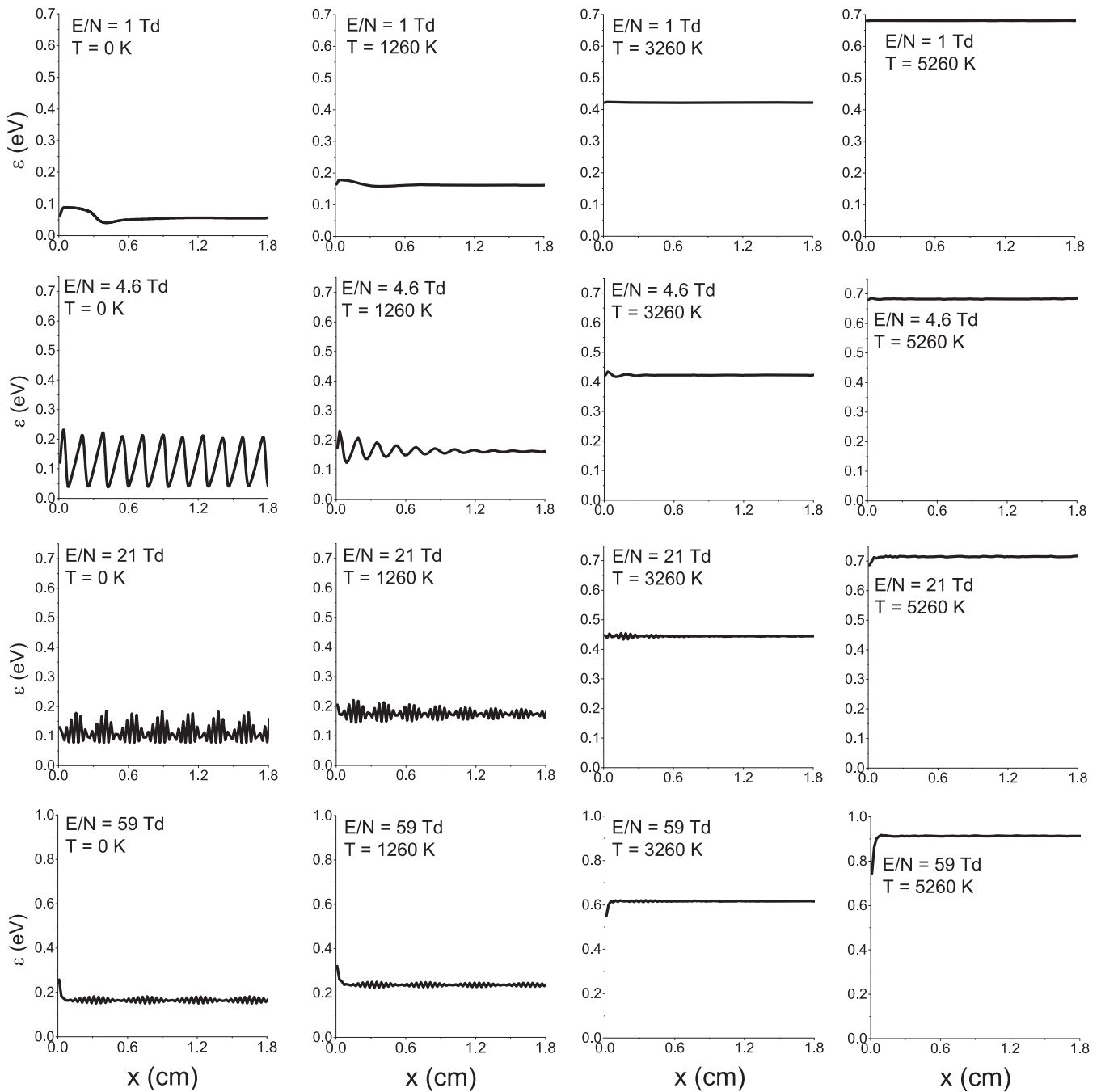
Figure 15. Spatial relaxation of the mean energy for electrons in indium vapour over a range of E/N and indium vapour temperatures T. x denotes the distance from the cathode.

velocity distribution was assumed in the calculations. Regardless of the initial conditions, if the mean electron energy is much higher than the lowest thresholds for inelastic collisions, then the elastic and inelastic collisions are essentially part of the continuous energy loss processes. As a consequence, the oscillatory feature is strongly suppressed and the relaxation towards the spatially uniform state is either monotonic or quasi-monotonic.

Comparing now, in more detail, the spatial profiles in the first and second rows of figure 16, it can be observed that the relaxation proceeds much quicker if a Maxwell initial velocity distribution is employed in the simulations. This is

clearly evident for the starting mean energy of 1 eV. This happens because, according to Maxwell's velocity distribution, the electrons can have a wider range of velocities, so the balance between energy gains from the field and losses in binary collisions with indium atoms is achieved more quickly. In addition to the relaxation length, the modulation amplitude and the period of oscillations are considerably smaller, indicating that the spatial relaxation of electrons in indium vapour may be governed by controlling the initial conditions of the electrons at the cathode.

In the following, we restrict our discussion to the spatially uniform transport properties in an idealised SST setup
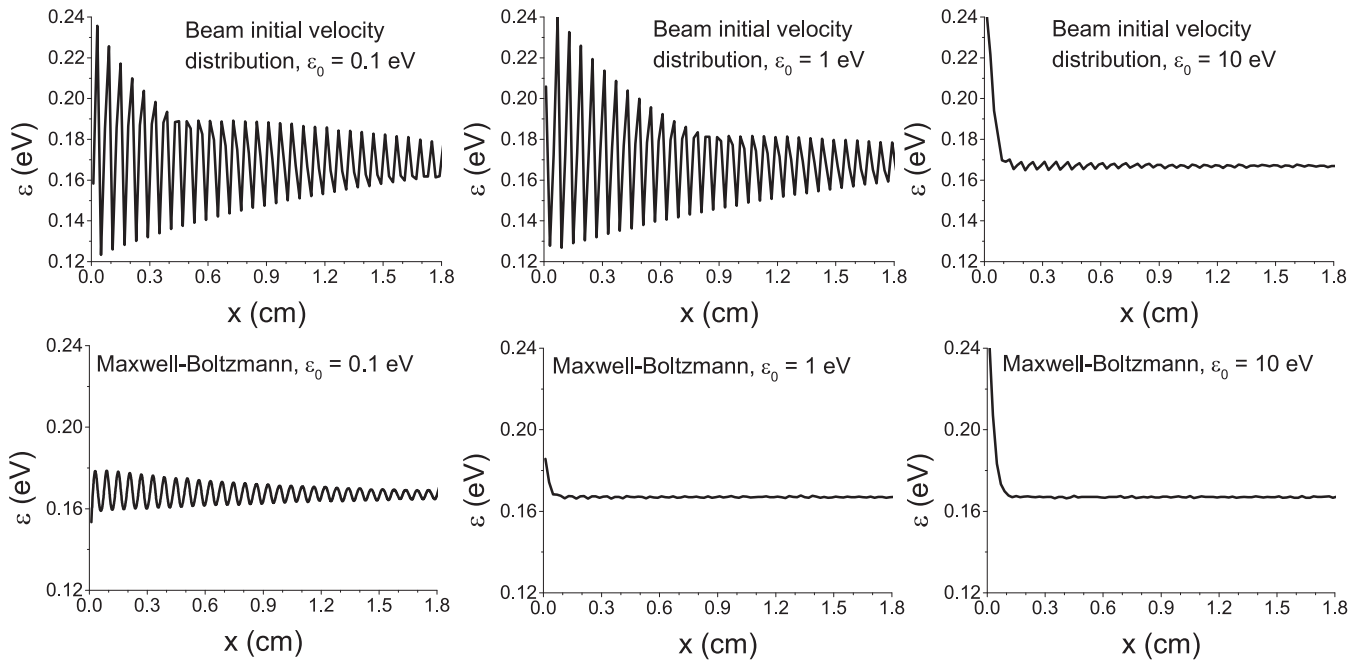
Figure 16. Spatial relaxation of the mean energy for electrons in indium vapour at $E/N = 13$ Td and an indium vapour temperature $T = 1260$ K. The calculations are for two different sets of initial conditions, including the initial beam velocity distribution (first row) and a Maxwell initial velocity distribution (second row), assuming starting mean energies of 0.1 eV, 1 eV, and 10 eV, as indicated on the graph. x again denotes the distance from the cathode.

and their comparison with the hydrodynamic transport coefficients. Using exponential growth curves for the number of electrons under SST conditions, we calculated the density-reduced ionisation coefficient. The SST ionisation coefficient is compared with that derived from our hydrodynamic calculations using the well-known expression [60]

$$\frac{1}{\alpha} = \frac{W}{2\nu_{\text{ION}}} + \sqrt{\left(\frac{W}{2\nu_{\text{ION}}}\right)^2 - \frac{D_{\text{L}}}{\nu_{\text{ION}}}}, \qquad (17)$$

where ν_{ION}, W and D_{L} are the ionisation frequency, bulk drift velocity, and bulk longitudinal diffusion coefficient, respectively. This comparison is shown in figure 17. For all indium vapour temperatures and up to about 3000 Td, we observe that the two sets of results agree very well, indicating the validity of the expression (17). For higher values of E/N, however, we do observe differences between the two sets of results.

The comparison between the mean energies calculated under hydrodynamic and SST conditions is shown in figure 18. Similarly, the comparison between the bulk and flux values of the drift velocity and the SST average velocity is shown in figure 19. The calculations were performed assuming the usual indium vapour temperatures. For higher values of E/N, we observe that the mean energy and flux drift velocity are larger than the corresponding SST average velocity and SST mean energy, respectively. On the other hand, the bulk drift velocity dominates both the flux drift velocity and the SST average velocity. This can be explained using the following physical arguments: when the profile of the electron density increases exponentially, with the distance in the direction of the electric field force (see figure 12), then the diffusive flux induced by this gradient is in opposite direction to the drift

flux. As a result, the diffusive flux acts to reduce the drift flux (or the field flux), and hence the SST average velocity is less than the flux drift velocity. As far as the mean energy is concerned, it is a combination of the spatially homogeneous mean energy and the energy component induced by the diffusive processes. The spatially homogeneous mean energy represents a balance of energy accumulated by electrons moving in the electric field and the losses in binary collisions. Since the diffusive flux is in the opposite direction to the drifted flux, the electrons are forced to move against the field force, and therefore their mean energy is reduced. As a consequence, the SST mean energy is less than the corresponding hydrodynamic mean energy. It should be noted that this behaviour of the mean energy and average velocity in an idealised SST experiment does not depend on the nature of the atomic gas. This can be further generalised to molecular gases, but only for electron energies for which the ionisation contributions are larger than the losses due to electron attachment [40].

4.4. Development of an electron avalanche and its transition into a negative ionisation front

In this section we investigate the development of an electron avalanche and its transition into a negative ionisation front in indium vapour. All simulations were started with the same initial Gaussian-type distribution for the electrons and positive ions

$$n_{\text{e}}(x, 0) = \frac{100}{0.05\pi R_0^2 \frac{l}{3}\sqrt{2\pi}} \exp\left(-\frac{1}{2}\frac{(x - 0.95l)^2}{\left(0.05\frac{l}{3}\right)^2}\right), \quad (18)$$

where l is the distance between the imaginary electrodes and R_0 is the streamer radius, which is calculated to first order by
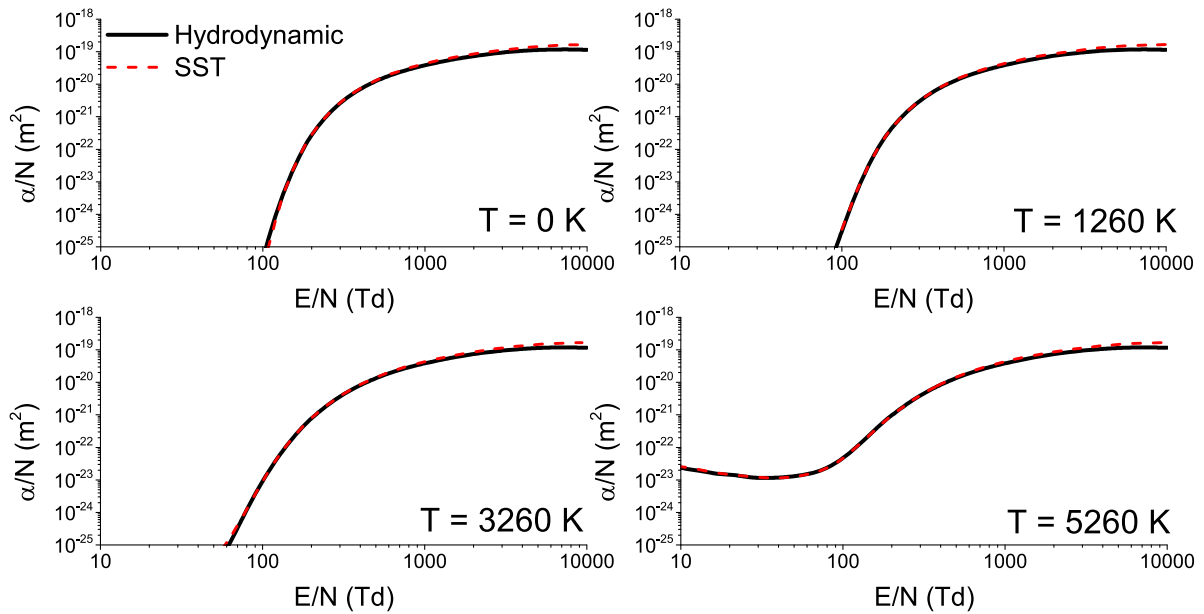
Figure 17. Comparison between the SST reduced ionisation coefficient and the reduced ionisation coefficients calculated using the hydrodynamic values of ionisation frequency, bulk drift velocity, and bulk longitudinal diffusion coefficient. Calculations are performed over a broad range of E/N and indium vapour temperatures T, as indicated on the graph.
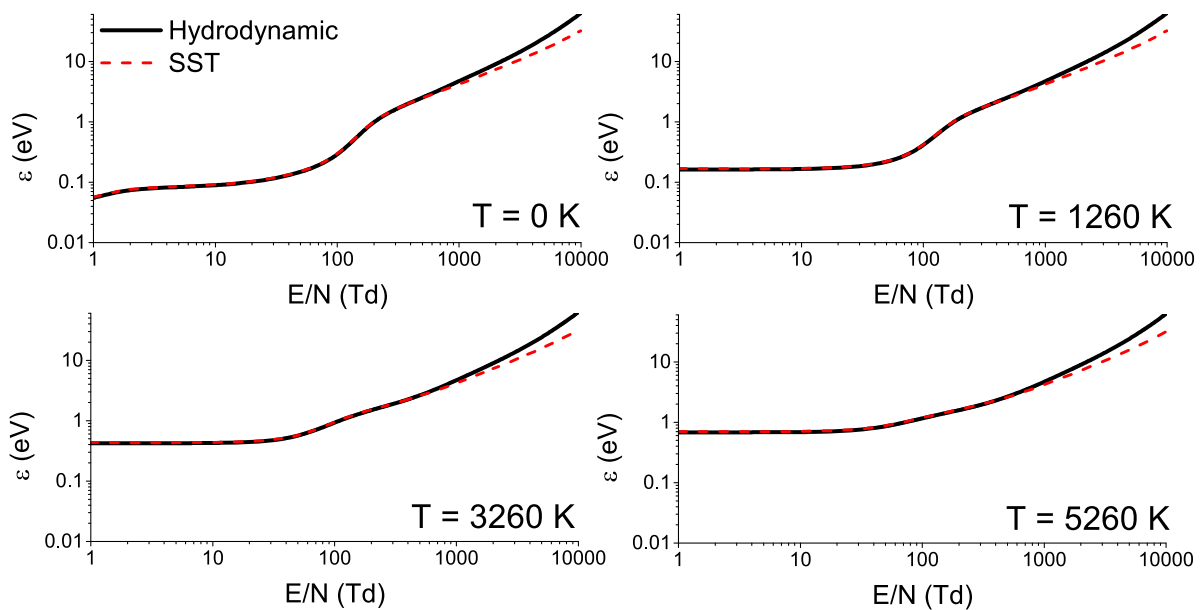
Figure 18. Comparison between the mean energies calculated under hydrodynamic and SST conditions. Calculations are performed over a broad range of E/N and indium vapour temperatures T, as indicated on the graph.

taking into account the initial electron distribution width and the spreading due to diffusion along the transverse direction. The length of the system l is an adjustable parameter, which is determined by the requirement that the streamer velocity relaxes to a stationary value. The externally applied electric field is positive in the x direction, and hence the ionisation fronts propagate to the left. Unless otherwise specified, the simulation results are presented from the 1.5D (axisymmetric) model, in which the radius of the streamer is assumed to be fixed.

Figure 20 exhibits the development of an electron avalanche and its transition into a negative ionisation front for $E/N = 270$ Td and various indium vapour temperatures, as indicated on the graph. The calculations were performed using the bulk transport coefficients as input into the system of fluid equations (13) and (14). The development of an electron avalanche, and its transition to a negative ionisation front, occurs here in the same manner as in other gases [52, 61–64]. In the early stage of development, where there are no space-charge effects, the dynamics of the electron avalanche and
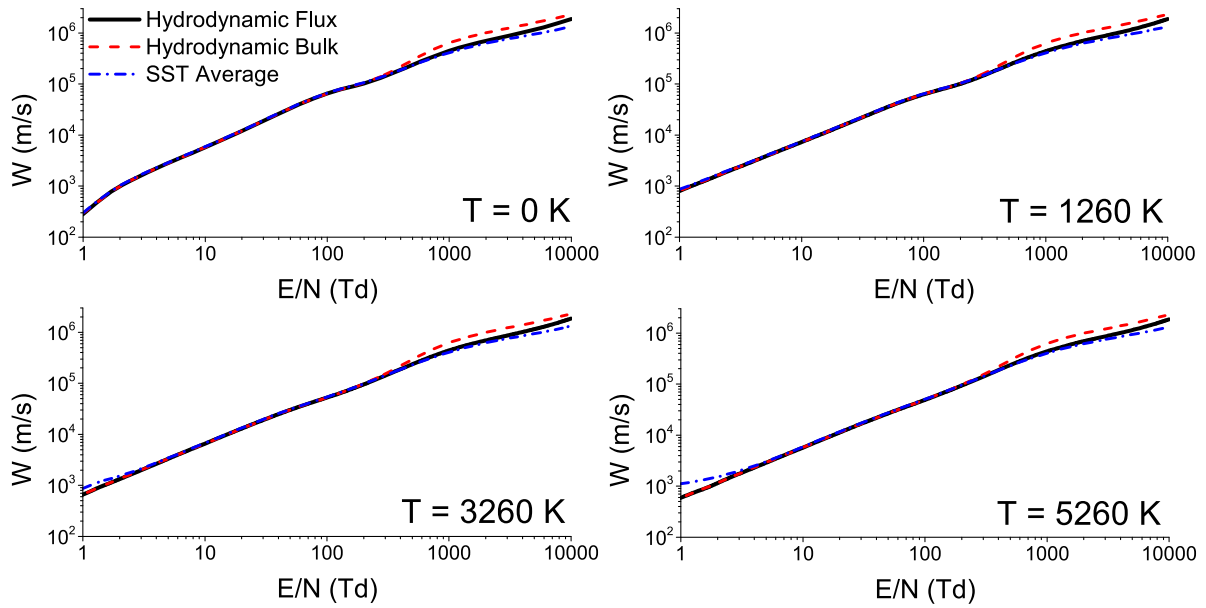
Figure 19. Comparison between the flux and bulk drift velocity, calculated under hydrodynamic conditions, and the SST average velocity. Calculations are performed over a broad range of E/N and indium vapour temperatures T, as indicated on the graph.
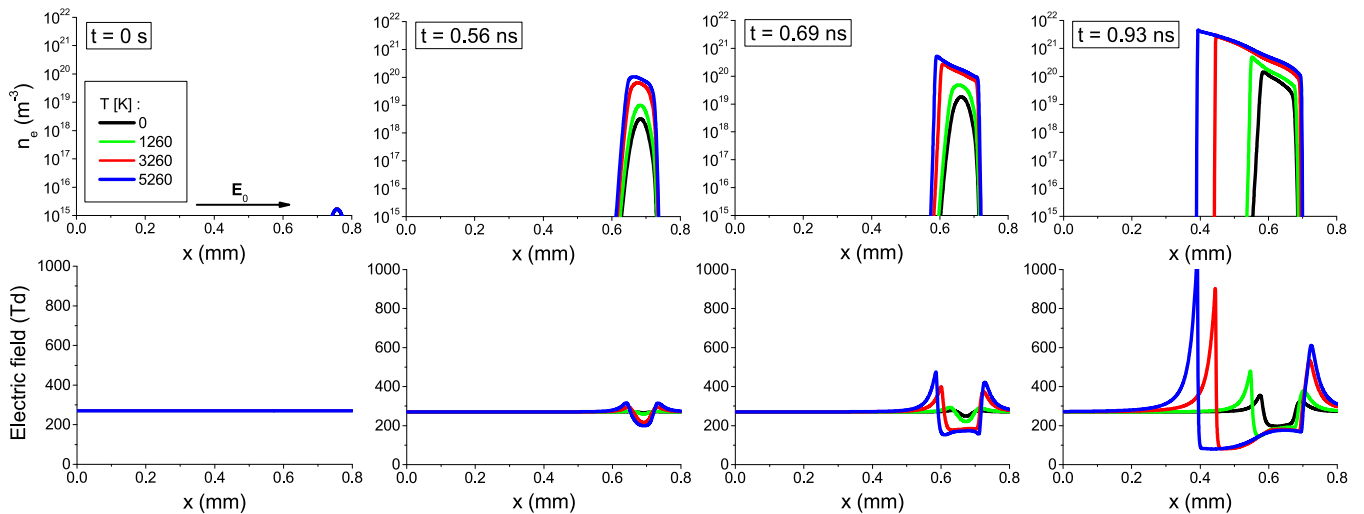
Figure 20. The formation and propagation of a negative ionisation front in indium vapour for $E/N = 270$ Td and various indium vapour temperatures. The calculations are performed using the bulk transport coefficients as input to the classical fluid model.

its spatial and temporal evolution is described by the diffusion equation. The solution of the diffusion equation in free space, and far away from the physical boundaries, is a Gaussian pulse, the peak of which drifts with the bulk drift velocity and diffuses around the centre of mass according to the values of the diffusion coefficient [65]. The electrons drift in the opposite direction to the electric field, while the positive ions are effectively motionless, since the mobility of the electrons is much higher than the mobility of positive ions on the time scales we consider in this work. As a consequence, charge separation occurs and the effects of the space charge develop, which screen the external electric field in the streamer interior. Since the simulations were performed in 1.5D, the space-charge effects do not fully screen the external electric field behind the streamer front. At the same time, at the front of the

streamer, we observe a characteristic field enhancement, which can lead to the appearance of runaway electrons. In any case, as the temperature of the indium vapour rises, the electron density and the streamer velocity increase. This can be explained by the fact that, as the temperature increases, the concentration of metastables and the ionisation coefficient are increased, which in turn accelerate the propagation of the streamer.

In order to better observe the effect of the indium vapour temperature on the spatial and temporal evolution of the electron density in the streamer channel, we show in figure 21 the formation and development of a negative streamer in 1D. The boundary conditions for the numerical solution of the fluid equations are modified: for $x = 0$ we use a homogeneous Neumann boundary condition, to ensure that the electrons that arrive at this boundary may flow out of the system, while for
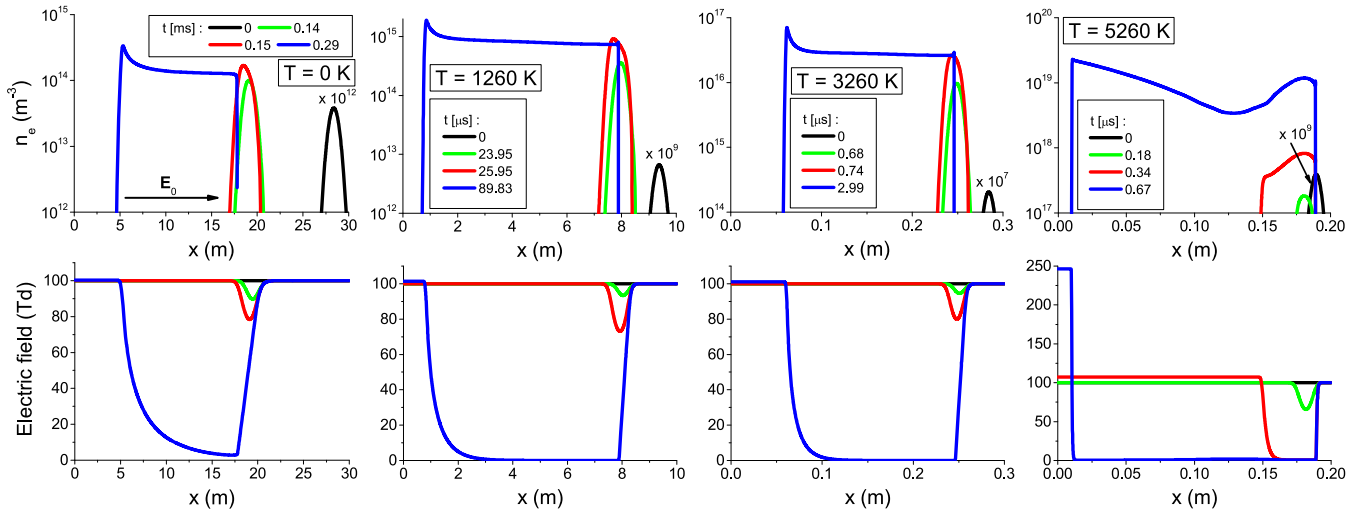
Figure 21. The formation and propagation of a negative ionisation front in indium vapour for $E/N = 100$ Td and various indium vapour temperatures. The calculations are performed using the 1D-set up and the bulk transport coefficients as input to the classical fluid model.
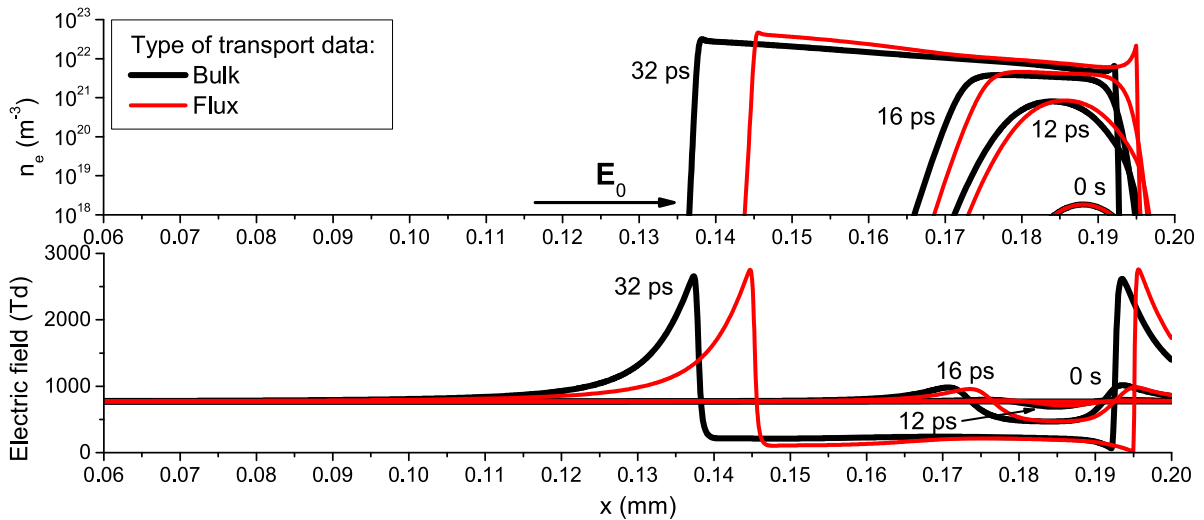
Figure 22. The formation and propagation of a negative ionisation front in indium vapour for $E/N = 770$ Td and $T = 1260$ K. The calculations are performed using the bulk and flux transport coefficients as input to the 1.5D classical fluid model.

$x = d$ we employ a homogeneous Dirichlet boundary condition in order to prevent the outflow of electrons from the system. Bulk transport coefficients were used as input data for the fluid equations. In this case we can observe in figure 21 that streamers at different indium vapour temperatures propagate on completely different time scales. When the full streamer is formed, we may observe a characteristic overshooting effect in the profile of the electron density at the streamer front. Comparing results from the 1D and 1.5D models, the electron density decreases more slowly in the streamer interior behind the front. For an indium vapour temperature $T = 5260$ K, we observe an increase in the electron density at the trailing edge of the negative streamer, where the external electric field is completely screened. This is due to the fact that electrons, even in the limit of thermal energies, where the electric field is entirely screened, may ionize indium atoms in both the ground and metastable states. Similar effects were observed

at lower temperatures, but in this case it was necessary to follow the streamers through space and time much longer. The complete screening of the electric field in the streamer channel is one of the important features distinguishing the results of our simulations in 1D and 1.5D.

Figure 22 illustrates the formation and propagation of a negative ionisation front, under the influence of an externally applied reduced electric field E_0/N of 770 Td. Calculations were performed for an indium vapour temperature of $T = 1260$ K, using the flux and the bulk transport coefficients as input into the system of fluid equations (13) and (14). Figure 22 clearly indicates that the ionisation front at a time of 32 picoseconds, obtained with the bulk drift velocity and the bulk longitudinal diffusion coefficient, is wider while its height is less than with the flux transport coefficients. Similar results were found for ionisation fronts in the 1D configuration and in other gases [52, 61, 64]. As the ionisation rate is the
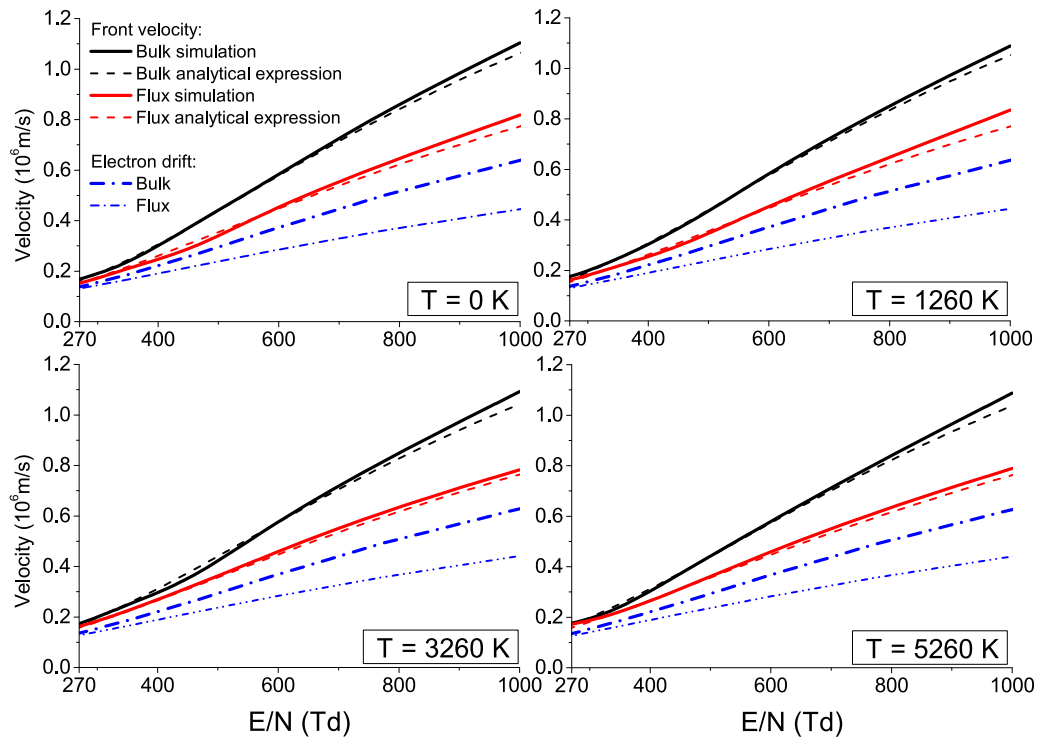
Figure 23. Velocities of planar 1D ionisation fronts as a function of the reduced electric field. The bulk and flux drift velocities of electrons are also included.

same in both cases, figure 22 can be explained by the fact that the bulk drift velocity and the longitudinal diffusion coefficient are larger than the corresponding flux data. Thus, in the early stage of evolution, the motion and diffusion of the centre of mass are faster with the bulk transport coefficients. The same trend continues after completing the transition of an electron avalanche into a negative streamer and during its propagation.

Besides the ionisation level in the streamer interior and the field enhancement at its front, the front velocity is one of the most important streamer properties. It is calculated by following the evolution of a certain level of the electron density at the ionisation front [52, 61, 64]. For ionisation fronts in indium vapour, and for the range of reduced electric fields and vapour temperatures considered in the present work, we observed that after the initial stage of acceleration, deceleration follows towards the quasi-stationary state, where the streamer velocity does not change in time. For planar ionisation fronts in 1D, the velocity of the streamer may be calculated using the following analytical expression [62, 66, 67]:

$$v = \mu(E)E + 2\sqrt{D_{\mathrm{L}}(E)\mu(E)E\alpha(E)}. \tag{19}$$

Here $\mu(E)$ is the electron mobility, E is the electric field strength, D_{L} is the longitudinal diffusion coefficient, and α is the first Townsend ionisation coefficient. Figure 23 shows a comparison between the streamer velocities we obtained in our simulations and those based on the analytic expression (19). The motivation behind using the analytical expression (19) is that, in principle, one may attempt to use swarm data to calculate the streamer velocity. The same figure shows the variation of the bulk and flux drift velocity with E/N. We observe that

the streamer velocity exceeds the bulk and flux drift velocities by more than a factor of two for the largest E/N displayed here. This is one of the common features of streamers in neutral gases [52, 61, 64] and atomic liquids [68]. The velocity of a negative planar ionisation front is determined by the combination of the electron velocity and the ionisation rate in the streamer head. In addition, the ionisation front is pushed further forward due to a strong diffusive flux, which is induced by the strong gradient in the electron density.

The front velocities we obtained in our simulations and those calculated using the analytical expression (19) agree very well. Regardless of the indium vapour temperature, the difference between the two sets of data is most pronounced for the highest E/N value. Finally, we note that the velocities obtained with the bulk data are always larger than those evaluated by the flux data.

5. Conclusions and outlook

We studied the electron transport and propagation of negative ionisation fronts in indium vapour. Among many important points, the key results originating from this work are:

(a) We utilize the available *ab initio* electron impact cross sections for elastic, inelastic, and ionisation processes in indium vapour [39]. Those calculations were performed for indium atoms in the ground state $(5s^2 5p)^2 P_{1/2}$ and the close-by metastable state $(5s^2 5p)^2 P_{3/2}$.

(b) Cross sections for superelastic collisions were calculated by applying the principle of microscopic reversibility and detailed balance in a thermal equilibrium. The fractional

populations of the excited metastable state $(5s^25p)^2P_{3/2}$ were calculated over a range of indium vapour temperatures, and the mixtures of indium atoms in the ground state and the metastable state were made and prepared as input for our Monte Carlo simulations of electron transport.

(c) Using a Monte Carlo simulation technique, the electron swarm transport coefficients were calculated over a range of reduced electric fields E/N and indium vapour temperatures, T, under hydrodynamic conditions. We identified three distinct regimes of electron transport. In the vapour-dominated regime, the velocity distribution function was approximately thermal Maxwellian, while the electron swarm transport coefficients were distinctively dependent on the indium vapour temperature. The intermediate regime was characterized by a non-Maxwellian velocity distribution function, but the electron swarm transport coefficients were to a large extent still found to depend on the indium vapour temperature, T. For higher values of E/N, we noticed that the influence of the indium vapour temperature on the velocity distribution function and transport coefficients was minimal. Under those condition, the velocity distribution function significantly deviated from a thermal Maxwellian.

(d) The initial Monte Carlo code was extended and generalized to consider the spatial relaxation of the electrons and transport under non-hydrodynamic conditions in an idealised SST experiment, when the background gas is heated to high temperatures. It was demonstrated that the spatial relaxation of the mean energy and average velocity was controlled by the nature of the collisional energy loss process in question. It was also shown that the nature of the spatial profiles could be controlled by varying the temperature of the indium vapour, with the oscillations along the decaying profile being suppressed by increasing the indium vapour temperature. Similarly, it was observed that different initial conditions altered the spatial profiles, including the modulation amplitude, relaxation length, and the period of oscillations. The spatially uniform values of the mean energy and average velocity were compared with the corresponding hydrodynamic values. Likewise, the ionisation coefficient evaluated directly from an idealised SST experiment was compared with the value estimated using the hydrodynamic results of the ionisation rate, drift velocity, and longitudinal diffusion coefficient. That two sets of data agreed very well except for the highest E/N. The disagreement between the two sets of data for higher values of E/N was addressed using physical arguments.

(e) Employing the classical fluid model, which was implemented within the 1D and 1.5D setups, we investigated the development of an electron avalanche and its transition into a negative ionisation front. The transition from an electron avalanche into a negative streamer occurred faster with increasing indium vapour temperature. The streamer properties, including the front velocity, the field

enhancement at the streamer front, the ionisation level behind the front, and the overall distribution of the electric field, depend on the indium vapour temperature and the level of presence of metastable indium atoms. This was especially pronounced at lower values of E/N, where the differences in the ionisation coefficient were large at different indium vapour temperatures. Streamers obtained in simulations with bulk transport coefficients were faster than those with flux transport coefficients, indicating that the nature of the transport coefficients in plasma modelling must be carefully considered before their direct application.

Regarding future studies, the cross sections for electron scattering in indium vapour might be gainfully applied to the modelling of electron transport in radio-frequency electric and magnetic fields. It would be interesting to consider, for example, the influence of indium metastable states on the temporal profiles of the transport coefficients, especially under conditions in which resonant absorption of energy in the oscillating radio-frequency electric and magnetic fields takes place [69]. Another logical extension of the current work in indium vapour would be to consider resonances induced by spatial non-locality, as investigated recently for electrons in argon and its mixtures with N_2 [70]. In the context of further streamer studies, it will be challenging to study the occurrence of non-local effects in the profile of the mean energy, in the streamer interior behind the propagating front, and in the branching of the streamers, by carrying out particle-in-cell/Monte Carlo simulations [71] and/or employing a high-order fluid model [52]. Likewise, another remaining step to be taken is to understand the effects of the breakdown voltages on the parameters of the equivalent circuit in high-intensity discharge lamps, where the cathode-directed streamers and the kinetics of the positive indium ions should be carefully considered. All the above applications will remain the focus of our future work.

Acknowledgments

Data availability statement

All data that support the findings of this study are included within the article (and any supplementary files).

ORCID iDs

S Dujko ⬚ https://orcid.org/0000-0002-4544-9106
J Atić ⬚ https://orcid.org/0000-0003-1800-8628
D Bošnjaković ⬚ https://orcid.org/0000-0002-2725-5287
R D White ⬚ https://orcid.org/0000-0001-5353-7440
P Stokes ⬚ https://orcid.org/0000-0002-0956-5927
K R Hamilton ⬚ https://orcid.org/0000-0002-8245-0122
O Zatsarinny ⬚ https://orcid.org/0000-0001-8253-883X
K Bartschat ⬚ https://orcid.org/0000-0001-6215-5014
D Šević ⬚ https://orcid.org/0000-0002-7206-6370
B P Marinković ⬚ https://orcid.org/0000-0002-6904-6360
D V Fursa ⬚ https://orcid.org/0000-0002-3951-9016
I Bray ⬚ https://orcid.org/0000-0001-7554-8044
F Blanco ⬚ https://orcid.org/0000-0003-4332-434X
D B Jones ⬚ https://orcid.org/0000-0001-7425-7157
L Campbell ⬚ https://orcid.org/0000-0003-0728-554X
M J Brunger ⬚ https://orcid.org/0000-0002-7743-2990

References

[1] Franck J and Hertz G 1914 *Verh. Dtsch. Phys. Ges.* **16** 457
[2] Robson R E, Li B and White R D 2000 *J. Phys. B: At. Mol. Opt. Phys.* **33** 507
[3] Sigeneger F, Winkler R and Robson R E 2003 *Contrib. Plasma Phys.* **43** 178
[4] Robson R E, White R D and Hildebrandth M 2014 *Eur. Phys. J. D* **68** 88
[5] Magyar P, Korolov I and Donko Z 2012 *Phys. Rev. E* **85** 056409
[6] Braglia G L, Diligenti M, Wilhelm J and Winkler R 1990 *Il Nuovo Cimento* D **12** 257
[7] Winkler R, Wilhelm J, Braglia G L and Diligenti M 1990 *Il Nuovo Cimento* D **12** 975
[8] Yousfi M, Zissis G, Alkaa A and Damelincourt J J 1990 *Phys. Rev. A* **42** 978
[9] England J and Elford M 1991 *Aust. J. Phys.* **44** 647
[10] McEachran R P and Elford M T 2003 *J. Phys. B: At. Mol. Opt. Phys.* **36** 427
[11] Mirić J, Simonović I, Petrović Z L, White R D and Dujko S 2017 *Eur. Phys. J. D* **71** 289
[12] Al-Amin S A J and Lucas J 1988 *J. Phys. D: Appl. Phys.* **21** 1261
[13] Rajasekaran K and Naidu M S 1991 *J. Appl. Phys.* **70** 4159
[14] Winkler R B, Wilhelm J and Winkler R 1983 *Ann. Phys.* **495** 90
[15] Winkler R B, Wilhelm J and Winkler R 1983 *Ann. Phys.* **495** 119
[16] Lister G, Lawler J, Lapatovich W and Godyak V 2004 *Rev. Mod. Phys.* **76** 541
[17] Flesch P 2006 *Light and Light Sources* (Berlin: Springer)
[18] White R D, McEachran R P, Robson R E, Elford M T and Bartschat K 2004 *J. Phys. D: Appl. Phys.* **37** 3185
[19] Born M 2001 *J. Phys. D: Appl. Phys.* **34** 909
[20] Csel M 2004 *Fundamentals of Light Sources and Lasers* (New York: Wiley)
[21] Schnick M, Füssel U, Hertel M, Rose S, Haessler M, Spille-Kohoff A and Murphy A B 2011 *Weld. World* **55** 114
[22] Yang W, Meng X, Zhou Q and Dong Z 2019 *AIP Adv.* **9** 035041
[23] Zatsarinny O and Bartschat K 2008 *Phys. Rev.* A **77** 062701
[24] Zatsarinny O, Bartschat K, Babaeva N Y and Kushner M J 2014 *Plasma Sources Sci. Technol.* **23** 035011
[25] McEachran R P, Marinković B P, García G, White R D, Stokes P W, Jones D B and Brunger M J 2020 *J. Phys. Chem. Ref. Data* **49** 013102
[26] McEachran R P, Blanco F, García G, Stokes P W, White R D and Brunger M J 2018 *J. Phys. Chem. Ref. Data* **47** 043104
[27] Hagelaar G J M and Pitchford L C 2005 *Plasma Sources Sci. Technol.* **14** 722
[28] Rabie M and Franck C M 2016 *Comput. Phys. Commun.* **203** 268
[29] McEachran R P, Blanco F, García G and Brunger M J 2018 *J. Phys. Chem. Ref. Data* **47** 33103
[30] Aldridge S 2011 The chemistry of the group 13 metals in the +3 oxidation state: simple inorganic compounds *The Group 13 Metals Aluminium, Gallium, Indium and Thallium: Chemical Patterns and Peculiarities* ed S Aldridge and A J Downs (New York: Wiley)
[31] Jones C and Stasch A 2011 The chemistry of the group 13 metals in the +1 oxidation state *The Group 13 Metals Aluminium, Gallium, Indium and Thallium: Chemical Patterns and Peculiarities* ed S Aldridge and A J Downs (New York: Wiley)
[32] Šević D, Rabasović M, Pejčev V and Marinković B P 2013 Experimental study of indium atom using electron and optical spectroscopy *Indium: Properties, Technological Applications and Health Issues* ed H G Woo and H T Choi (New York: Nova Science Publishers)
[33] Azad Malik M and O'Brien P 2011 III—V and related semiconductor materials *The Group 13 Metals Aluminium, Gallium, Indium and Thallium: Chemical Patterns and Peculiarities* ed S Aldridge and A J Downs (New York: Wiley)
[34] Nakamura S 2015 *Rev. Mod. Phys.* **87** 1139
[35] Hayashi D, Hilbig R, Körber A, Schwan S, Scholl R, Boerger M and Huppertz M 2010 *Appl. Phys. Lett.* **96** 061503
[36] Ögün C M, Truong W, Kaiser C, Kling R and Heering W 2014 *J. Phys. D: Appl. Phys.* **47** 285202
[37] Fedorov P P, Popov A I and Simoneaux R L 2017 *Russ. Chem. Rev.* **86** 240
[38] Hamilton K R *et al* 2020 *Phys. Rev. A* **102** 022801
[39] Hamilton K R *et al* 2021 *J. Phys. Chem. Ref. Data* **50** 013101
[40] Dujko S, White R D and Petrović Z L 2008 *J. Phys. D: Appl. Phys.* **41** 245205
[41] Dujko S, White R D, Raspopović Z M and Petrović Z L 2012 *Nucl. Instrum. Methods Phys. Res. B* **279** 84
[42] White R D, Robson R E, Nicoletopoulos P and Dujko S 2012 *Eur. Phys. J. D* **66** 1
[43] Czichy M, Hartmann T, Mentel J and Awakowicz P 2008 *J. Phys. D: Appl. Phys.* **41** 144027
[44] Wendt M, Peters S, Loffhagen D, Kloss A and Kettlitz M 2009 *J. Phys. D: Appl. Phys.* **42** 185208
[45] Ristivojevic Z and Petrović Z L 2012 *Plasma Sources Sci. Technol.* **21** 035001
[46] Raspopovic Z M, Sakadzic S, Bzenic S A and Petrovic Z L 1999 *IEEE Trans. Plasma Sci.* **27** 1241
[47] Dujko S, Raspopović Z M and Petrović Z L 2005 *J. Phys. D: Appl. Phys.* **38** 2952
[48] Robson R 1991 *Aust. J. Phys.* **44** 685
[49] Petrović Z L, Dujko S, Marić D, Malović G, Nikitovi Z, Šašić O, Jovanović J, Stojanović V and Radmilović-Radjenović M 2009 *J. Phys. D: Appl. Phys.* **42** 194002
[50] Mirić J, Bošnjaković D, Simonović I, Petrović Z L and Dujko S 2016 *Plasma Sources Sci. Technol.* **25** 065010
[51] Stojanovic V D and Petrovic Z L 1998 *J. Phys. D: Appl. Phys.* **31** 834
[52] Dujko S, Markosyan A H, White R D and Ebert U 2013 *J. Phys. D: Appl. Phys.* **46** 475202

[53] Agnihotri A, Hundsdorfer W and Ebert U 2016 *Japan. J. Appl. Phys.* **55** 07LD06

[54] Agnihotri A, Hundsdorfer W and Ebert U 2017 *Plasma Sources Sci. Technol.* **26** 095003

[55] Bošnjaković D, Petrović Z L and Dujko S 2016 *J. Phys. D: Appl. Phys.* **49** 405201

[56] Petrovic Z, Crompton R and Haddad G 1984 *Aust. J. Phys.* **37** 23

[57] Donkó Z, Hartmann P, Korolov I, Jeges V, Bošnjaković D and Dujko S 2019 *Plasma Sources Sci. Technol.* **28** 095007

[58] Li B, White R D and Robson R E 2002 *J. Phys. D: Appl. Phys.* **35** 2914

[59] Dyatko N A, Kochetov I V and Ochkin V N 2020 *Plasma Sources Sci. Technol.* **29** 125007

[60] Blevin H and Fletcher J 1984 *Aust. J. Phys.* **37** 593

[61] Markosyan A H, Dujko S and Ebert U 2013 *J. Phys. D: Appl. Phys.* **46** 475203

[62] Li C, Brok W J M, Ebert U and van der Mullen J J A M 2007 *J. Appl. Phys.* **101** 123305

[63] Li C, Ebert U and Hundsdorfer W 2010 *J. Comput. Phys.* **229** 200

[64] Markosyan A H, Teunissen J, Dujko S and Ebert U 2015 *Plasma Sources Sci. Technol.* **24** 065002

[65] Kumar K, Skullerud H and Robson R 1980 *Aust. J. Phys.* **33** 343

[66] Ebert U, van Saarloos W and Caroli C 1997 *Phys. Rev.* E **55** 1530

[67] Lagarkov A N and Rutkevich I M 1994 *Ionisation Waves in Electrical Breakdown of Gases* (Berlin: Springer)

[68] Simonović I, Garland N A, Bošnjaković D, Petrović Z L, White R D and Dujko S 2019 *Plasma Sources Sci. Technol.* **28** 015006

[69] Dujko S, Bošnjaković D, White R D and Petrović Z L 2015 *Plasma Sources Sci. Technol.* **24** 054006

[70] Albert A, Bošnjaković D, Dujko S and Donkó Z 2021 *J. Phys. D: Appl. Phys.* **54** 135202

[71] Nijdam S, Teunissen J and Ebert U 2020 *Plasma Sources Sci. Technol.* **29** 103001

PAPER • OPEN ACCESS

Foundations and interpretations of the pulsed-Townsend experiment

View the article online for updates and enhancements.

Foundations and interpretations of the pulsed-Townsend experiment

M J E Casey[1] , **P W Stokes**[1] , **D G Cocks**[2] , **D Bošnjaković**[3] ,
I Simonović[3] , **M J Brunger**[4,5] , **S Dujko**[3] , **Z Lj Petrović**[6,7] ,
R E Robson[1,8] **and R D White**[1,*]

[1] College of Science and Engineering, James Cook University, Townsville, QLD, Australia
[2] Research School of Physics, The Australian National University, Canberra, ACT, Australia
[3] Institute of Physics, University of Belgrade, Zemun, Belgrade, Serbia
[4] College of Science and Engineering, Flinders University, Adelaide, SA, Australia
[5] Department of Actuarial Science and Applied Statistics, Faculty of Business and Information Science, UCSI University, Kuala Lumpur, Malaysia
[6] School of Engineering, Ulster University, Newtownabbey, Antrim, Northern Ireland, United Kingdom
[7] Serbian Academy of Sciences and Arts, Belgrade, Serbia
[8] Centre for Quantum Dynamics, Griffith University, Nathan, QLD, Australia

E-mail: ronald.white@jcu.edu.au

Abstract

The pulsed-Townsend (PT) experiment is a well known swarm technique used to measure transport properties from a current in an external circuit, the analysis of which is based on the governing equation of continuity. In this paper, the Brambring representation (1964 *Z. Phys.* **179** 532) of the equation of continuity often used to analyse the PT experiment, is shown to be fundamentally flawed when non-conservative processes are operative. The Brambring representation of the continuity equation is not derivable from Boltzmann's equation and consequently transport properties defined within the framework are not clearly representable in terms of the phase-space distribution function. We present a re-analysis of the PT experiment in terms of the standard diffusion equation which has firm kinetic theory foundations, furnishing an expression for the current measured by the PT experiment in terms of the universal bulk transport coefficients (net ionisation rate, bulk drift velocity and bulk longitudinal diffusion coefficient). Furthermore, a relationship between the transport properties previously extracted from the PT experiment using the Brambring representation, and the universal bulk transport coefficients is presented. The validity of the relationship is tested for two gases Ar and SF_6, highlighting also estimates of the differences.

Keywords: pulsed townsend experiment, transport coefficient definition, pulsed townsend governing equation, kinetic theory, Brambring's equation

(Some figures may appear in colour only in the online journal)

1. Introduction

The use of accurate electron swarm transport coefficients in simulations has wide ranging implications for modelling physics, from atmospheric processes through to medical imaging and therapies [2–21]. For the well established swarm experimental techniques, the various experimental parameters (such as temperature, sample purity, uniformity of the applied field, ...) are assumed to be highly accurate (within the reported error bars), and the techniques for extracting the measured quantities are generally considered to be well understood. Within the swarm community itself, consensus on the

extraction of transport parameters/coefficients is essential as this explicitly impacts upon the accuracy of swarm-derived cross-sections [22–43] that may be subsequently used directly for modelling of gas and liquid-phase transport [12, 13], or the direct application of electron swarm transport coefficients in fluid modelling of plasmas [3, 44]. As such, high accuracy is required in both the measurement and definition of the transport coefficients to ensure applications in technology and medicine can be made with confidence.

Transport coefficient definition/measurement was an active area of debate in the 1960–1990s [45–54], and misunderstandings still exist [30]. For example, it is important to understand that different swarm experiments operate in different regimes—time of flight (TOF) and pulsed-Townsend (PT) for example in the hydrodynamic regime, where the space-time dependence of all quantities can be projected onto the number density, $n(\mathbf{r}, t)$ [55], while the steady state Townsend (SST) approach operates in the non-hydrodynamic regime, where one has to treat the space ($\mathbf{r}$) and time (t) dependence more generally [47, 56].

In the hydrodynamic regime, there are two fundamental types of transport coefficients, which we call flux and bulk[10]. The flux coefficients are defined through well-known flux-gradient relationships, such as Fick's law. The bulk coefficients, however, are defined through the diffusion equation, which applies, for example, to the analysis of the various measured currents in both the TOF and PT experiments. Thus we can say quite generally, without reference to the specific form of the solution of the diffusion equation, for any experiment amenable to a hydrodynamic description, that it is the bulk quantities which are extracted and therefore it is these which are tabulated in the literature. On the other hand, the SST experiment is inherently non-hydrodynamic, and measures the microscopic Townsend ionisation coefficient, α, through the particle density relation $n \sim \exp(\alpha z)$. The SST experiment cannot be analysed through the diffusion equation [57], and therefore does not measure any of the hydrodynamic transport coefficients.

In spite of much discussion over the past 30–60 years [45–54], there does, however, remain some residual confusion about what transport coefficients/properties are extracted from the PT experiment, and how they relate to the standard flux and bulk transport coefficients[11]. Currently, the PT experiment is one of the swarm methods in active use, with key groups in Switzerland [58, 63] and México [32, 68], as well as the scanning drift tube experiment in Hungary [69–71] and the double-shutter drift tube experiment in Japan [72], which provide much of the present-day electron swarm data. Consequently, it is essential that the transport properties extracted from the PT

experiments are identified correctly. This represents the focus of the current study.

We begin this paper with a brief review of fundamental swarm transport theory and definitions in section 2, in order to revisit the vexed issue of transport coefficient definition in relation to the PT experiment and their relation to transport coefficients which are derivable from the Boltzmann equation. We demonstrate that the Brambring form of the continuity/diffusion equation [1] generally used to analyse the PT experiment is fundamentally flawed when non-conservative processes are operative. A general solution of the full diffusion equation has long been available in the literature [73, 74], and in section 3 we specifically show how it can be adapted to the PT experiment to extract the standard definitions of the transport coefficients with firm foundations in kinetic theory. With our focus on the PT experiment, in section 3 we demonstrate that the existing transport property measurements extracted from PT experiments using the fundamentally flawed Brambring equation for the current in the external circuit [1], can be transformed to the standard bulk transport coefficient definitions. Transformation of existing measured PT transport properties, for the particular examples of Ar and SF$_6$, are presented in section 4 and compared with the bulk transport coefficients extracted from TOF experiments and calculated using a multi-term solution of Boltzmann's equation. Thereafter, some concluding remarks are drawn in section 5.

2. Theory

2.1. The exact continuity equation, the hydrodynamic regime and the diffusion equation

The exact continuity equation can be derived either from first principles, or from Boltzmann's equation:

$$\frac{\partial \mathrm{f}}{\partial \mathrm{t}} + \boldsymbol{v} \cdot \nabla f + \mathbf{a} \cdot \frac{\partial \mathrm{f}}{\partial \boldsymbol{v}} = -J(f), \tag{1}$$

for the phase-space distribution function, $f(z, \boldsymbol{v}, t)$, a function of velocity $\boldsymbol{v}$ and time t, with spatial gradients taken along the z axis, and acceleration $\mathbf{a}$ due to external forces, with collisional processes represented by Boltzmann's collision integral J. Integrating equation (1) over velocity space yields the continuity equation (here, in one dimension):

$$\frac{\partial n}{\partial t} + \frac{\partial \Gamma}{\partial z} = S(z, t), \tag{2}$$

where $n(z, t)$ is the charged-particle density, $\Gamma(z, t) = \int v_z f(z, \boldsymbol{v}, t) \mathrm{d}\boldsymbol{v}$ is the charged-particle flux in the external field direction and the right-hand side is the rate of production of particles, given by $S(z, t) = \int J_{\mathrm{NC}}(f) \mathrm{d}\boldsymbol{v}$, the integral of the non-conservative collision operator, J_{NC}, for processes such as attachment and ionisation.

Swarm experiments are traditionally designed to operate in the hydrodynamic regime [2, 44, 75]. In this regime, the space-time dependence of $f(z, \boldsymbol{v}, t)$ is a function of the number density (n), and can be expressed in terms of a density gradient expansion:

---

[10] While some associate them with particular experiments, such nomenclature hides their fundamental nature [50].

[11] With regard to the extracted coefficients, we note that while some PT analyses report α_{T}/n_0 (the macroscopic form of Townsend's first ionisation coefficient), the quantity R_{net} has been extracted directly by Franck and co-workers [58–64] and Ridenti *et al* [65], reported for the PT measurements of Aschwanden [66] (along with α_{T}/n_0) when analysis of the current transients was hindered by the strong electron attachment, and in Phelps and Pitchford [67] measurements were transformed to R_{net}, to illustrate a few examples.

$$f(z, \boldsymbol{v}, t) = n(z,t) f^{(0)}(\boldsymbol{v}) - f^{(1)}(\boldsymbol{v}) \frac{\partial n(z,t)}{\partial z}$$

$$+ f^{(2)}(\boldsymbol{v}) \frac{\partial^2 n(z,t)}{\partial z^2} + \cdots, \tag{3}$$

while normalisation requires $\int f^{(j)}(\boldsymbol{v}) d\boldsymbol{v} = \delta_{j0}$. Hence, the flux and source terms in the continuity equation (2) can be identified with:

$$\Gamma(z,t) = nW - D_L \frac{\partial n}{\partial z} + \zeta_L \frac{\partial^2 n}{\partial z^2} - + \cdots, \tag{4}$$

$$S(z,t) = nR_{\text{net}} - S^{(1)} \frac{\partial n}{\partial z} + S^{(2)} \frac{\partial^2 n}{\partial z^2} + \cdots, \tag{5}$$

where ζ_L is the longitudinal component of the third-order transport coefficient tensor (the skewness tensor) [76]. Equation (4) is familiar as a generalisation of Fick's law. The flux drift velocity and the flux longitudinal diffusion coefficient are designated W and D_L respectively, with the net (or effective) production rate given by $R_{\text{net}} = R_{\text{ionis}} - R_{\text{att}}$. The flux transport properties in (4) and non-conservative source terms in (5) can be written in terms of the appropriate integrals of the $f^{(j)}$ appearing in equation (3), or otherwise [51, 56, 77, 78].

Substitution of equations (4) and (5) into equation (2), and grouping coefficients of gradients in the number density, yields the standard diffusion equation, when higher order terms in the hydrodynamic expansion are neglected:

$$\frac{\partial n}{\partial t} + W_B \frac{\partial n}{\partial z} - D_{B,L} \frac{\partial^2 n}{\partial z^2} = nR_{\text{net}}, \tag{6}$$

where we define the bulk (B) transport coefficients in terms of the flux coefficients and the corrections due to the non-conservative source terms:

$$W_B = W + S^{(1)}, \tag{7}$$

$$D_{B,L} = D_L + S^{(2)}. \tag{8}$$

In a drift tube experiment, $S^{(1)}$ and $S^{(2)}$ can be interpreted as modifications to the position of the centre of mass and spread about the centre of mass, respectively, arising from non-conservative processes. In general,

$$S^{(1)} = \int J_{\text{NC}}(f^{(1)}) d\boldsymbol{v}, \tag{9}$$

$$S^{(2)} = \int J_{\text{NC}}(f^{(2)}) d\boldsymbol{v}. \tag{10}$$

Swarm experiments operating in the hydrodynamic regime may be analysed on the basis of the diffusion equation and hence generally sample the bulk transport coefficients. The solution of the diffusion equation for various experimental arrangements, e.g., for sources distributed in space and/or emitting for finite times, can be found by appropriate integration of this fundamental solution over space and/or time respectively, as we highlight below.

2.2. Townsend's first ionisation coefficient(s) and the fundamentally flawed Brambring equation of continuity

The Townsend ionisation coefficient is generally defined under steady state conditions. Confusion over the definition of the Townsend coefficient has however existed for an extended period, with the article by Crompton [45] representing a great overview and attempt to address this issue. In short, there are two definitions of the Townsend ionisation coefficient. The macroscopic version of Townsend's first (net) ionisation coefficient, α_T, (which is the difference of the ionisation and attachment (often referred to as η) coefficients), is defined by the relation to the particle flux (or current):

$$\Gamma \sim \exp(\alpha_T z). \tag{11}$$

The microscopic version of the Townsend (net) ionisation coefficient, α, is defined by the relation to the density:

$$n(z) \sim \exp(\alpha z). \tag{12}$$

The two definitions are quite different, as are their relationships to the other transport coefficients and to each other, as we explore below.

The PT experiment [58, 79–82] may be analysed using the diffusion equation (6). On the other hand, the continuity equation proposed by Brambring [1] is:

$$\frac{\partial n}{\partial t} + \frac{\partial \Gamma}{\partial z} = \alpha_T \Gamma, \tag{13}$$

that is equation (2) with a source term:

$$S = \alpha_T \Gamma. \tag{14}$$

It is unclear from the Brambring paper [1] which form of the Townsend ionisation coefficient was proposed in their continuity equation, and perhaps their equation defines its own form of the Townsend ionisation coefficient. We do highlight, however, that the steady-state solution of equation (13) for the flux is consistent with the macroscopic form of the Townsend coefficient (11) and hence we use that form in the Brambring representation of the equation of continuity. This is a notational issue, however, which does not impact the following arguments.

Most importantly, the Brambring form of the continuity equation (13) is not derivable from the Boltzmann equation (1), except in the trivial case of no ionisation or attachment, where $S = 0$. To illustrate issues associated with the Brambring representation of the equation of continuity (13), let us consider a very simple benchmark system: elastic scattering with an attachment process with a collision frequency, ν_{att}, that is independent of energy. From the Boltzmann equation, the attachment collision operator has the form: $J_{\text{att}}(f) = \nu_{\text{att}} f$. The source term in the exact continuity equation (2) in the hydrodynamic regime takes the form:

$$S(z,t) \equiv \int [J_{\text{elast}}(f) + J_{\text{att}}(f)] d\boldsymbol{v}$$

$$= 0 + \nu_{\text{att}} \int \left[n f^{(0)}(\boldsymbol{v}) - f^{(1)}(\boldsymbol{v}) \frac{\partial n}{\partial z} \right.$$

$$+ f^{(2)}(\boldsymbol{v}) \frac{\partial^2 n}{\partial z^2} + \cdots \right] \mathrm{d}\boldsymbol{v}$$

$$= n\nu_{\mathrm{att}} \int f^{(0)}(\boldsymbol{v}) \mathrm{d}\boldsymbol{v} - \nu_{\mathrm{att}} \int f^{(1)}(\boldsymbol{v}) \mathrm{d}\boldsymbol{v} \frac{\partial n}{\partial z}$$

$$+ \nu_{\mathrm{att}} \int f^{(2)}(\boldsymbol{v}) \mathrm{d}\boldsymbol{v} \frac{\partial^2 n}{\partial z^2} + \cdots$$

$$= n\nu_{\mathrm{att}} + 0 + 0 + \cdots, \tag{15}$$

where the last line follows by virtue of the normalisation condition on the $f^{(j)}$, and J_{elast} denotes the elastic collision operator. In this case, $S(z, t)$ is proportional to the density with no contributions arising from the derivatives of the density. This is inconsistent with the Brambring form for the source term (14), which would have additional first and second order density spatial derivative contributions which are independent of the energy dependence of the non-conservative processes, viz substituting the expression for the flux Γ into equation (14). Physically, if the attachment collision frequency is independent of energy then it cannot modify the position of the centre of mass (first moment of the density) nor the rate of spread/diffusion (second moment of the density) of the pulse. In contrast, the Brambring equation has explicit modifications to both of these moments of the pulse, whenever there are non-conservative processes operative, irrespective of the energy dependence of the non-conservative collision frequency.

While the Brambring representation of the equation of continuity is thus fundamentally flawed from a physical viewpoint, in the following sections, we highlight how to relate the transport properties extracted from the PT experiment via an analysis using the Brambring representation of the continuity equation (and related equation for the measurable current in the external circuit), with the standard definition of the transport coefficients from a Boltzmann equation/kinetic theory perspective. This will have importance for the application of PT transport properties in fluid/moment models of plasmas for example, as well as for the extraction of cross-sections through the swarm inversion process.

3. Interpreting transport coefficients from the measured current in the pulsed-Townsend experiment

3.1. Solution of the standard diffusion equation

Firstly, consider an idealised TOF experiment in a finite geometry $0 \leqslant z \leqslant L$, in which a sharp pulse of n_0 charge carriers is released from a source plane $z = z_0$ at time $t = t_0$, i.e.,

$$n(z, t_0) = n_0 \delta(z - z_0). \tag{16}$$

The solution of the diffusion equation (6) for $z_0 = 0$, $t_0 = 0$ and infinite geometry ($L \rightarrow \infty$) is the well known travelling pulse [2, 53]:

$$n(z, t) = \frac{n_0 \exp(R_{\mathrm{net}} t)}{\sqrt{4\pi D_{B,L} t}} \exp\left[-\frac{(z - W_B t)^2}{4 D_{B,L} t}\right]. \tag{17}$$

In finite geometry, assuming perfectly absorbing boundaries, and

$$n(0, t) = 0 = n(L, t), \tag{18}$$

the solution of the diffusion equation may be obtained using the Poisson summation theorem [73, 74] as,

$$n(z, t; z_0, t_0) = \frac{n_0}{\sqrt{4\pi D_{B,L}(t - t_0)}} \exp$$

$$\times \left\{ R_{\mathrm{net}} t + \frac{W_B}{2 D_{B,L}} \left[z - z_0 - \frac{1}{2} W_B (t - t_0) \right] \right\}$$

$$\times \sum_{j=-\infty}^{\infty} \left\{ \exp\left[-\frac{(z - z_0 - 2jL)^2}{4 D_{B,L}(t - t_0)} \right] \right.$$

$$\left. - \exp\left[-\frac{(z + z_0 - 2jL)^2}{4 D_{B,L}(t - t_0)} \right] \right\}. \tag{19}$$

One can consider more elaborate boundary conditions, however for the current study the simplified boundary conditions (18) are sufficient.

It is convenient for the purposes of the following discussion to consider the situation where the left hand boundary recedes to $-\infty$. This may be achieved mathematically by an appropriate transformation of coordinates, in which L now denotes the distance of the right hand boundary from the source, which is now located at the origin of coordinates. Equation (19) then becomes, with $t_0 = 0$,

$$n(z, t; L) = \frac{n_0 \exp\left(R_{\mathrm{net}} t + \frac{W_B}{2 D_{B,L}} \left(z - \frac{1}{2} W_B t \right) \right)}{\sqrt{4\pi D_{B,L} t}}$$

$$\times \left\{ \exp\left[-\frac{z^2}{4 D_{B,L} t} \right] - \exp\left[-\frac{(z - 2L)^2}{4 D_{B,L} t} \right] \right\}, \tag{20}$$

describing the spatio-temporal variation of $n(z, t)$ in a TOF drift tube.

3.2. Extracting bulk transport coefficients from the pulsed-Townsend experiment

Consider now the PT experiment—a plane parallel swarm system where all spatial variation is confined to the z direction, normal to the electrodes. Under typical measurement conditions, the transit time of the electrons is much less than the RC time constant of the circuit [2] and the current in the external circuit is given by:

$$I = \frac{q}{L} \int_0^L \Gamma(z', t) \mathrm{d}z'. \tag{21}$$

Using Fick's law (4), this can be written in terms of the transport coefficients and is given by:

$$I(t) = \frac{qW}{L} \int_0^L n(z, t) \mathrm{d}z, \tag{22}$$

where the diffusive contribution has been eliminated due to the relation:

$$\int_0^L D_L \frac{\partial n}{\partial z}\, \mathrm{d}z = D_L n(L) - D_L n(0) = 0, \qquad (23)$$

for perfectly absorbing boundary conditions. It follows from (22) that the measurable current in the external circuit is given by:

$$I(t) = \frac{n_0 q W}{2L} \exp\left(R_{\mathrm{net}} t\right) \left\{ \left[1 - \phi\left(\frac{W_B t - L}{\sqrt{4 D_{B,L} t}} \right) \right] \right.$$
$$\left. + \exp\left(\left[\frac{W_B}{D_{B,L}} \right] L \right) \left[\phi\left(\frac{W_B t + L}{\sqrt{4 D_{B,L} t}} \right) - 1 \right] \right\},$$
$$(24)$$

where ϕ represents the error function. Hence, full current transients for the current in the external circuit of the PT experiment fitted to equation (24) can yield the bulk transport coefficients: the net ionisation rate coefficient $R_{\mathrm{net}} = R_{\mathrm{ionis}} - R_{\mathrm{att}}$, the bulk drift velocity W_B, and the bulk diffusion coefficient $D_{B,L}$. Even though the current scales with the flux drift velocity, W, the time-dependence of the measured current is determined by the bulk transport coefficients—R_{net}, W_B and $D_{B,L}$ via (24). This is consistent with the conclusions of Blevin and Fletcher [50] and Robson [53]. If the initial number of electrons is known, then we can also simultaneously extract the flux drift velocity from an analysis of the current in the external circuit. This provides an additional transport coefficient that can be used for cross-section fitting/extraction from swarm experiments.

4. Relating existing PT transport properties to the standard transport coefficient definitions

Given the wealth of experimental work and associated extraction of transport properties and fitting of cross-sections to the PT data, the obvious question remaining is how do we relate the PT experimental transport properties to the transport coefficients which are grounded in the Boltzmann equation/kinetic theory.

Here, we return to the Brambring representation of the equation of continuity (13) and find the equivalent expression for the current in an external circuit[12]. If we substitute Fick's law expression (4) into the Brambring equation (13) (retaining

only first order terms in the density gradient expansion[13]), on re-arranging we obtain the diffusion-type equation:

$$\frac{\partial n}{\partial t} + \left[\tilde{W} + \tilde{\alpha}_{\mathrm{T}} \tilde{D}_L \right] \frac{\partial n}{\partial z} - \tilde{D}_L \frac{\partial^2 n}{\partial z^2} = n \tilde{\alpha}_{\mathrm{T}} \tilde{W}. \qquad (25)$$

The tildes here denote transport properties arising from the Brambring representation of the diffusion equation. Since the Brambring representation of the equation of continuity (13) is not derivable from Boltzmann's equation/kinetic theory, the terms drift velocity, diffusion coefficient and alpha as defined by the Brambring representation do not have a standard kinetic theory definition (i.e. are not representable in terms of an integral of the phase-space distribution function and hence cannot be found directly in terms of a solution of Boltzmann's equation or Monte Carlo simulation) when non-conservative processes are operative and hence may not have the standard meaning of drift velocity, diffusion, etc, under such conditions.

Following the same procedure as above, but using the Brambring representation of the diffusion equation (25) instead of the conventional diffusion equation (6), it follows that the functional form of the current in the external circuit is given by:

$$I(t) = \frac{n_0 q W}{2L} \exp\left(\tilde{\alpha}_{\mathrm{T}} \tilde{W} t \right)$$
$$\times \left\{ \left[1 - \phi\left(\frac{(\tilde{W} + \tilde{\alpha}_{\mathrm{T}} \tilde{D}_L) t - L}{\sqrt{4 \tilde{D}_L t}} \right) \right] \right.$$
$$+ \exp\left(\left[\frac{\tilde{W} + \tilde{\alpha}_{\mathrm{T}} \tilde{D}_L}{\tilde{D}_L} \right] L \right)$$
$$\left. \times \left[\phi\left(\frac{(\tilde{W} + \tilde{\alpha}_{\mathrm{T}} \tilde{D}_L) t + L}{\sqrt{4 \tilde{D}_L t}} \right) - 1 \right] \right\}. \qquad (26)$$

This is the same expression as that from the original Brambring paper (see equation (12) of reference [1]) and used by the experimental groups [58, 79, 83, 84], expressed using the PT transport properties. It is important to note that the W appearing in the first factor on the rhs of equation (26) is the flux drift velocity W, not the bulk drift velocity W_B or the PT transport property $\tilde{W}$.

The key to relating the PT transport properties to the standard transport coefficients is to understand how they are extracted from the fitting of the current in the external circuit in a typical analysis of the PT experiment. The expression for the current in the external circuit, whether it be the expression

---

[12] While the functional form of the current in the external circuit and its relation to the transport coefficients can be a source of uncertainty, these are distinct from the uncertainties that can typically be obtained from approximate analysis of the current in the external circuit. Indeed, some analyses have used quite simplified approaches to extract the various transport properties from the current in the external circuit [58, 65, 79, 83–85], which may lead to further issues.

For example, extracting $\tilde{W}$, through dividing L by the measured electron transit time, T_e, where the transit time is defined as the difference in times between the measured current's rise and fall to the respective half values. This is a measure of a drift velocity, but not one that is consistent with the flux or bulk drift velocities, or equation (24). Using that $\tilde{W}$ to then determine any further parameters (e.g. $\tilde{\alpha}_{\mathrm{T}}$ or $\tilde{D}_L$) will further propagate uncertainties in the other derived coefficients/parameters. Non-linear curve fitting to the full equation (24) should in fact be performed (as in, for example, reference [81]) in all cases.

In addition, extracting $\tilde{\alpha}_{\mathrm{T}}$ from the rising component of the measured current [58] (and $\tilde{W}$ from the earlier step) fails to capture the diffusion contributions to the current in the external circuit.

Using these simplified processes to establish initial estimates of the parameters, to start the non-linear curve fitting of the measured current (as in reference [81], for example) is, however, good practice.

[13] This representation of the current in the external circuit fails to capture the second order contributions to the source term and hence the equation cannot be an accurate representation of the experimentally measured current in the external circuit when the product $\alpha_{\mathrm{T}} \zeta_L$ becomes appreciable relative to D_L. While measurement of the skewness term has not been performed to date, many transient and stationary effects may skew the profile and require consideration [76, 86, 87].

arising from the diffusion equation (24) or the expression arising from the unphysical Brambring equation (26), takes the same general form, i.e. is mathematically equivalent:

$$I(t) = a \exp(bt) \left\{ \left[1 - \phi \left(\frac{ct - L}{\sqrt{4\,dt}} \right) \right] \right.$$
$$\left. + \exp \left(\left[\frac{c}{d} \right] L \right) \left[\phi \left(\frac{ct + L}{\sqrt{4\,dt}} \right) - 1 \right] \right\}, \quad (27)$$

where a, b, c and d can be found from the non-linear curve fitting procedure and are related to the standard bulk transport coefficients/PT transport properties through comparisons with equations (24)/(26), or equivalently through comparison of equations (6)/(25). If in the previous analyses of PT experiments expression (26) has been fitted to the current in the external circuit, it then follows that the PT transport properties $(\tilde{\alpha}_T, \tilde{W}, \tilde{D}_L)$ can be related to the bulk transport coefficients $(R_{net}, W_B, D_{B,L})$ via[14]:

$$R_{net} = \tilde{\alpha}_T \tilde{W} = b, \quad (30)$$

$$W_B = \tilde{W} + \tilde{\alpha}_T \tilde{D}_L = c, \quad (31)$$

$$D_{B,L} = \tilde{D}_L = d. \quad (32)$$

If the initial number of electrons n_0 is measured accurately, the fitting parameter a can provide a technique to measure the flux drift velocity, W—the first experiment able to do so!

We now consider some examples, transforming the PT transport properties extracted from existing PT measurements, through implementation of the theoretical relationships (30)–(32), in order to compare with the bulk transport coefficients which have firm foundations in kinetic theory/Boltzmann's equation. TOF measurements are included as measurements of bulk coefficients since they are analysed according the diffusion equation (6). It is important to note:

- The relationships (e.g. $W_B = \tilde{W} + \tilde{\alpha}_T \tilde{D}_L$) are presented only when all transport properties from the PT experiment $(\tilde{W}, \tilde{\alpha}_T, \tilde{D}_L)$ are available from a single study to do the transformation.

- The intent of this section is purely to highlight the validity of the relationship between the PT transport properties and the bulk transport coefficients. Hence,

  – We do not preference any particular measurement technique over the other, but rather focus on the presentation of coefficients with firm theoretical foundations. Assessment of the quality of any experimental measurements is beyond the scope of the present work.

---

[14] It is important to make the distinction that the relationship (30), $R_{net} = \tilde{\alpha}_T \tilde{W}$, is valid for the PT transport properties $\tilde{\alpha}_T$ and $\tilde{W}$. The relationship between R_{net}, the SST α_T and the bulk transport coefficients, however, is given by [53, 56].

$$R_{net} = \alpha_T W_B - \alpha_T^2 D_{B,L} + \cdots \quad (28)$$

which, in the limit of small diffusion, may be approximated by

$$R_{net} \approx \alpha_T W_B. \quad (29)$$

– Transport coefficient calculations are obviously dependent on the cross-section set used. The calculations presented here are for comparison with the transformed PT results and should not be interpreted as the reference for quality of the experimental results or analysis.

– The error propagation associated with the application of the theoretical relationships (30)–(32) on existing PT transport properties results in large error bars. Ideally, reanalysis of the PT experiment current transients according to equation (24) would be preferred, if available, for appropriate determination of experimental error.

In the following subsections we present the results for Ar and SF$_6$. Ar is considered somewhat of a benchmark gas known for high accuracy measurements and well known cross-sections [33], while SF$_6$ provides a good example of when the differences are quite important due to its strong electron attachment and ionisation.

The numerical methods employed in the solution of Boltzmann's equation (1) for the calculated coefficients have been described in detail previously, and the reader is referred to references [88, 89].

4.1. Argon

Figures 1 and 2 present some of the available experimentally measured bulk drift velocities, W_B, and ionisation rate coefficients, R_{ionis}, for electron swarms in Ar. In the upper panel of figure 1, the W_B transformed via the theoretical relationship (31) from the $\tilde{W}$ extracted from the PT experiment of de Urquijo *et al* [90] and Hernández-Ávila *et al* [91, 92] are shown with the W_B measured from the TOF apparatus of Kücükarpaci and Lucas [93, 94] and Nakamura and Kurachi [37], and the W_B from the scanning drift tube measurements of Korolov *et al* [69]. Measurements of W_B are sparse in the E/n_0 region where the transformation is most pronounced, although the trend of the de Urquijo *et al* W_B lies somewhat above the highest W_B datum of Nakamura and Kurachi [37] at 50 Td, the Kücükarpaci and Lucas [93, 94] W_B at around 150 Td, and the measurements of Korolov *et al* [69]. In contrast, both the $\tilde{W}$ and W_B measurements of Hernández-Ávila *et al* [91, 92] tend to lie below the 50 Td Nakamura and Kurachi [37] value and the measurements of Korolov *et al* [69], with the highest E/n_0 measurement of Kücükarpaci and Lucas [93, 94] in good agreement with the transformed W_B. For Ar, the $\tilde{W}$ and W_B differ by up to 4.2% for the de Urquijo *et al* [90] measurements and up to 8.2% for the Hernández-Ávila *et al* [91, 92] measurements, due to the relative magnitudes of the $D_{B,L}$ and $\tilde{\alpha}$ (as shown in figure 11 of de Urquijo *et al* [90]), the difference increasing with E/n_0. These results highlight the accuracy of the PT measurements and associated analysis in reference [90].

The bulk and flux drift velocity calculated using the cross-section set extracted from Magboltz [95] are also displayed in figure 1 for comparison. While these calculations are dependent on the cross-section set utilised, good agreement is observed between the calculated W_B and the W_B transformed from the PT measurements of de Urquijo *et al* [90].

Figure 2. The ionisation rate coefficient for electron swarms in gaseous argon. The R_{ionis} transformed from the PT measurements of de Urquijo *et al* [90] and Hernández-Ávila *et al* [91, 92], through the theoretical relationship (30) and denoted by the asterisk (*), are compared with the (positive) R_{ionis} values reported in Dahl *et al* [58] and Haefliger and Franck [63, 96] (the representative measurement at 10 kPa has been used). 'Calculated' represents the R_{ionis} calculated from a solution of the Boltzmann equation using the cross-sections extracted from Magboltz [95].

Figure 1. The drift velocity for electron swarms in gaseous argon. For the PT measurements, the bulk drift velocity W_B has been transformed from the PT measurements of $\tilde{W}$ through the theoretical relationship (31), and is denoted by the asterisk (*). (Upper) The W_B transformed from the PT measurements of de Urquijo *et al* [90] (transformed using the $D_{B,L}$ first reported in reference [97] although recorded with the $\tilde{W}$ and $\tilde{\alpha}_T$ reported in reference [90]) and Hernández-Ávila *et al* [91, 92] are compared with the W_B TOF measurements of Kücükarpaci and Lucas [93, 94] and Nakamura and Kurachi [37], and the W_B from the scanning drift tube (SDT) apparatus of Korolov *et al* [69]. (Lower) The ratio of the PT-measured to bulk drift velocities, $\tilde{W}/W_B$, for the measurements of de Urquijo *et al* [90] and Hernández-Ávila *et al* [91, 92]. 'Calculated' represents the flux and bulk drift velocities calculated from a solution of the Boltzmann equation using the cross-sections extracted from Magboltz [95].

The lower panel of figure 1 displays the ratio of the PT drift measurement to the bulk drift velocity, $\tilde{W}/W_B$. The ratio illustrates the difference between the drift velocities, which increases with increasing E/n_0, as expected from the increasing magnitude of the $\tilde{\alpha}_T \tilde{D}_L$ term.

Figure 2 shows a comparison of R_{ionis} in Ar which is, to our knowledge, limited to the transformed PT measurements of de Urquijo *et al* [90] and Hernández-Ávila *et al* [91, 92], through the theoretical relationship (30), and the R_{ionis} extracted directly from the PT measurements of Dahl *et al* [58] and Haefliger and Franck [63, 96]. At the lower E/n_0 of the

de Urquijo *et al* measurements, good agreement is observed with the majority of the Haefliger and Franck coefficients (measured over a range of pressures, although only the 10 kPa measurement is displayed in figure 2), and over intermediate E/n_0 with the Dahl *et al* measurements. Over the full E/n_0 range of the (positive) Dahl *et al* measurements, very good consistency with the transformed Hernández-Ávila *et al* [91, 92] R_{net} is observed.

4.2. SF$_6$

Figures 3 and 4 present the bulk drift velocity, W_B, and net rate coefficient, R_{net}, from some of the available PT and TOF measurements for electron swarms in SF$_6$. The upper panel of figure 3 includes W_B transformed from the $\tilde{W}$ measurements of Aschwanden [66] and Xiao *et al* [98], via the theoretical relationship (31), and the W_B TOF measurements of Nakamura [99] and Naidu and Prasad [100]. The transformation to W_B from the measured $\tilde{W}$ of both Aschwanden and Xiao *et al* results in a *decrease* in magnitude below 361 Td, a consequence of the attachment-dominated $\tilde{\alpha}$, and *increase* in magnitude above this E/n_0 as ionising collisions dominate the $\tilde{\alpha}$ (and similarly, R_{net} in the lower panel of figure 3). The transformation of the Aschwanden [66] drift velocity results in a decrease of up to 4.7% in the attachment-dominated region, and an increase of up to 9.2% in the ionisation-dominated region, at the highest E/n_0, while the transformation of the Xiao *et al* [98] measurements results in a decrease of up to 5.2% in the attachment-dominated region, and an increase of up to 2.3% in the ionisation-dominated region. The results shown in the upper panel of figure 3 highlight, in particular, the accuracy of the PT measurements and associated analysis in the work of Aschwanden [66].

Figure 4. The ionisation coefficient for electron swarms in gaseous SF_6. The absolute value of the R_{net} reported from the PT measurements of Aschwanden [66] are compared with the R_{net} transformed through the theoretical relationship (30) and denoted by the asterisk (*), from the PT measurements of de Urquijo *et al* [103], Xiao *et al* [98] and Xiao *et al* [104]. 'Calculated' represents the R_{net} calculated from a solution of the Boltzmann equation using the cross-section data of Biagi [101] from the LXCat database.

We are thus unable to reconcile the PT measurements of $\tilde{W}$ from Xiao *et al*.

The flux and bulk drift velocity and R_{net} values calculated using the cross-section data of Biagi [101] from the LXCat database, are also shown in figures 3 and 4. These representative calculations are dependent on the cross-section set used, and are included only to indicate the magnitudes of the transport coefficients, in particular highlighting the effect of the non-conservative processes on the calculated W_B compared to the flux drift velocity, W [15]. In both the attachment and ionisation-dominated regions, the transformation of the Aschwanden $\tilde{W}$ changes in the direction consistent with the representative calculations. As a result, the transformed experimental results of Aschwanden are in good agreement with our representative calculations.

The lower panel of figure 3 displays the ratio of the PT drift measurement to the bulk drift velocity, $\tilde{W}/W_B$. The ratio illustrates the contribution of the $\tilde{\alpha}_T \tilde{D}_L$ term in relationship (30), to the transformation to W_B. The change in sign of R_{net} results in a decrease to W_B relative to the measured $\tilde{W}$ for the lower E/n_0, followed by an increase of W_B relative to $\tilde{W}$. The magnitude of the difference increases further from the breakdown E/n_0 value, consistent with the magnitude of R_{net}.

In the absence of any other R_{net} measurements in SF_6, to our knowledge[16], figure 4 only displays the rate coefficient of Aschwanden [66], reported directly in that thesis,

Figure 3. The drift velocity for electron swarms in gaseous SF_6. For the PT measurements, the bulk drift velocity W_B has been transformed from the PT measurements of $\tilde{W}$ through the theoretical relationship (31), and is denoted by the asterisk (*). (Upper) The W_B transformed from the PT measurements of Aschwanden [66] (with the necessary PT transport properties available for $E/n_0 \geqslant 273$ Td) and Xiao *et al* [98] (with the necessary properties available for $E/n_0 = 279$–401 Td), are shown alongside the $\tilde{W}$ measured by the PT apparatus of de Urquijo *et al* [103] (where, in the absence of $D_{B,L}$, W_B could not be determined). Also displayed are the W_B TOF measurements of Nakamura [99] and Naidu and Prasad [100] (digitised from Christophorou and Olthoff [102]). (Lower) The ratio of the PT-measured to bulk drift velocities, $\tilde{W}/W_B$, for the PT measurements of de Urquijo *et al* [103], Xiao *et al* [98] and Xiao *et al* [104]. 'Calculated' represents the flux and bulk drift velocities calculated from a solution of the Boltzmann equation using the cross-section data of Biagi [101] from the LXCat database.

Compared to the other W_B measurements (from the TOF apparatus), the transformation of the Aschwanden data increases the differences when compared to the measurements of Nakamura over all E/n_0, but decreases the differences from the Naidu and Prasad W_B. Similarly, for the four data points of the Xiao *et al* measurements, where all PT transport properties were reported (279–401 Td), the transformation to W_B increases the differences from the other experimental measurements.

---

[15] We make no comment on the validity of that cross-section set here, only to highlight that we are unable to predict accurately the breakdown reduced field as shown in figure 4.

[16] We note that many values of the attachment rate coefficient have been reported for SF_6 in various buffer gases (see the review of Christophorou and Olthoff [102]), but in the absence of any mean energy values for the PT measurements, the comparison of R_{att} at a common mean energy cannot be made.

and the rate coefficients of de Urquijo *et al* [103] and Xiao *et al* [98, 104], transformed through the relationship (30), with good agreement observed between all.

5. Concluding remarks

In this study we have addressed, from a fundamental viewpoint, the issue of the analysis and interpretation of the PT experiment. We have shown that the governing equation traditionally used to analyse the PT experiment—the Brambring representation of the equation of continuity—is fundamentally flawed, and transport properties subsequently defined through that equation do not have a clear representation in terms of the distribution function. We have presented an expression for the current in the external circuit of the PT experiment in terms of the standard diffusion equation and the universal transport coefficients defined through it—the bulk transport coefficients. In addition, we have developed a relationship between the transport properties extracted from the PT experiment using the Brambring representation of the equation of continuity and the bulk transport coefficients, and highlighted the validity of the relationship for various gases. Given the errors that are necessarily propagated through this process, we suggest that all previous transport properties extracted from PT experimental data where non-conservative processes are operative be re-analysed according to the diffusion equation based current expression to enable measurement of standard bulk transport coefficients prior to any subsequent application (e.g. evaluating complete and accurate sets of scattering cross-sections, and further utilisation in modelling of plasmas and ionised gases [3, 12, 13, 44, 105]).

A consequence of the present analysis is the necessary reconciliation between experimental and theoretical studies involving PT measurements.

As a minimum for any swarm study, the *exact* definition of any transport property/coefficient measured or used for further analyses must be identified. Further, the definition of any transport property/coefficient must be consistent with those defined through kinetic theory and representable in terms of the phase-space distribution function.

In addition, the following are recommended for clear identification in experimental studies:

- Primary reference to the exact source equation used for analysis, and any assumptions entailed.
- A description of the method of the analysis of all measurements.
- A detailed estimate of the error associated with the statistical analysis (including systematic errors, reproducibility, etc), alongside the reported experimental uncertainty.
- The applicability of the hydrodynamic or non-hydrodynamic regime, and the methods used to ensure sampling under appropriate conditions. This point is generally well accomplished in the literature.
- Clear uncertainty estimates of all elements (e.g. pressure, mixture ratio, etc) and how they propagate through to the final result [106–109].

Prior to the use of any swarm transport measurements in theoretical models (low temperature plasma models), the effect of non-conservative collisions must be identified, since it is when flux and bulk values start to differ significantly that one needs to pay attention to the nature of the transport data required in their models. A detailed prescription has been presented previously [110].

Using 'wrong' theory yields results that may be up to a factor of 10 different under some circumstances, though often effects are of the order of 10%–30%. However, if one uses a similar theory to implement the cross-sections obtained from incorrectly interpreted data one returns to the original experimental data. Plasma modelling is sufficiently robust that small changes in the transport data are easily compensated by small self consistent adjustments of the local field. Problems occur when one uses more exact models to describe plasmas. PIC codes with a properly implemented and tested Monte Carlo simulation will provide correct calculation of fluxes and thus the effect of the cross-sections obtained from the incorrectly interpreted data may become large, as stated above. Even more so, as the plasma field is calculated self consistently small changes in the local E/n_0 as compared to the properly determined values would originate. Some processes with a high threshold, such as dissociation and ionization, are very strongly affected by the local normalised electric field, even by orders of magnitude (see reference [111], for example).

In this vein, it is recommended that theoretical studies clearly identify the definition of any utilised experimental measurements and any further analysis of those measurements (e.g. transformation from one transport coefficient to another via approximate relationships with associated errors propagated).

In addition to these recommendations to aid reconciliation within the literature, the present work also seeds further investigation, specifically into the analysis and interpretation of the PT experiment. For example, the impact of the boundary conditions, on the electron density at the electrodes, on the expression for the current in the external circuit, and the ability to extract higher order transport coefficients (e.g. skewness) from the current measured from the PT experiment should also be studied.
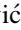
Acknowledgments

Data availability statement

The data that support the findings of this study are available upon reasonable request from the authors.

ORCID iDs

M J E Casey ⬡ https://orcid.org/0000-0003-0193-211X
P W Stokes ⬡ https://orcid.org/0000-0002-0956-5927
D G Cocks ⬡ https://orcid.org/0000-0002-9943-7100
D Bošnjaković ⬡ https://orcid.org/0000-0002-2725-5287
I Simonović ⬡ https://orcid.org/0000-0001-6704-9042
M J Brunger ⬡ https://orcid.org/0000-0002-7743-2990
S Dujko ⬡ https://orcid.org/0000-0002-4544-9106
Z Lj Petrović ⬡ https://orcid.org/0000-0001-6569-9447
R E Robson ⬡ https://orcid.org/0000-0003-2613-4229
R D White ⬡ https://orcid.org/0000-0001-5353-7440

References

[1] Brambring J R 1964 *Z. Phys.* **179** 532
[2] Huxley L G H and Crompton R W 1974 *The Diffusion and Drift of Electrons in Gases* (New York: Wiley)
[3] Adamovich I *et al* 2017 *J. Phys. D: Appl. Phys.* **50** 323001
[4] Brunger M J 2017 *Int. Rev. Phys. Chem.* **36** 333
[5] Campbell L and Brunger M J 2013 *Plasma Sources Sci. Technol.* **22** 013002
[6] Brunetti R *et al* 2005 *New Astron. Rev.* **49** 265
[7] Calvo J *et al* 2017 *J. Cosmol. Astropart. Phys.* JCAP03(2017) 003
[8] Montie T C, Kelly-Wintenberg K and Roth J R 2000 *IEEE Trans. Plasma Sci.* **28** 41
[9] Bekeschus S, Schmidt A, Weltmann K-D and von Woedtke T 2016 *Clin. Plasma Med.* **4** 19
[10] von Woedtke T, Metelmann H-R and Weltmann K-D 2014 *Contrib. Plasma Phys.* **54** 104
[11] Stoffels E, Sakiyama Y and Graves D B 2008 *IEEE Trans. Plasma Sci.* **36** 1441
[12] Muñoz A, Blanco F, Garcia G, Thorn P A, Brunger M J, Sullivan J P and Buckman S J 2008 *Int. J. Mass Spectrom.* **277** 175
[13] Francis Z, Incerti S, Capra R, Mascialino B, Montarou G, Stepan V and Villagrasa C 2011 *Appl. Radiat. Isot.* **69** 220
[14] Rabie M and Franck C M 2018 *Environ. Sci. Technol.* **52** 369
[15] Bartschat K and Kushner M J 2016 *Proc. Natl Acad. Sci. USA* **113** 7026
[16] Kong M G, Kroesen G, Morfill G, Nosenko T, Shimizu T, van Dijk J and Zimmermann J L 2009 *New J. Phys.* **11** 115012
[17] Christophorou L G and Olthoff J K 2001 *Advances in Atomic, Molecular, and Optical Physics* vol 44 (Amsterdam: Elsevier) pp 59–98
[18] Brandenburg R 2017 *Plasma Sources Sci. Technol.* **26** 053001
[19] Roussel-Dupré R, Colman J J, Symbalisty E, Sentman D and Pasko V P 2008 *Space Sci. Rev.* **137** 51
[20] Misra N N, Martynenko A, Chemat F, Paniwnyk L, Barba F J and Jambrak A R 2018 *Crit. Rev. Food Sci. Nutr.* **58** 1832
[21] Marinković B P, Bredehöft J H, Vujčić V, Jevremović D and Mason N J 2017 *Atoms* **5** 46
[22] Frost L S and Phelps A V 1962 *Phys. Rev.* **127** 1621
[23] Engelhardt A G and Phelps A V 1964 *Phys. Rev.* **133** A375
[24] Engelhardt A G, Phelps A V and Risk C G 1964 *Phys. Rev.* **135** A1566
[25] Phelps A V 1968 *Rev. Mod. Phys.* **40** 399
[26] Christophorou L G and Hunter S R 1984 *Electron Molecule Interactions and Their Applications* vol 2 ed L G Christophorou (New York: Academic Press)
[27] Milloy H B and Crompton R W 1977 *Phys. Rev.* A **15** 1847
[28] Crompton R W 1994 *Advances in Atomic, Molecular, and Optical Physics* vol 32 (Amsterdam: Elsevier) pp 97–148

[29] Petrović Z Lj, Šuvakov M, Nikitović Ž, Dujko S, Šašić O, Jovanović J, Malović G and Stojanović V 2007 *Plasma Sources Sci. Technol.* **16** S1
[30] Robson R E, White R D and Ness K F 2011 *J. Chem. Phys.* **134** 064319
[31] Ness K F, Robson R E, Brunger M J and White R D 2012 *J. Chem. Phys.* **136** 024318
[32] de Urquijo J, Basurto E, Juárez A M, Ness K F, Robson R E, Brunger M J and White R D 2014 *J. Chem. Phys.* **141** 014308
[33] Pitchford L C *et al* 2017 *Plasma Proc. Polym.* **14** 1600098
[34] Jovanović J V, Stojanović V, Raspopović Z, de Urquijo J and Petrović Z Lj 2019 *Plasma Sources Sci. Technol.* **28** 045006
[35] Grofulović M, Alves L L and Guerra V 2016 *J. Phys. D: Appl. Phys.* **49** 395207
[36] Schmidt B, Berkhan K, Götz B and Müller M 1994 *Phys. Scr.* **T53** 30
[37] Nakamura Y and Kurachi M 1988 *J. Phys. D: Appl. Phys.* **21** 718
[38] Morgan W L 1992 *Plasma Chem. Plasma Process.* **12** 449
[39] Gibson D K 1970 *Aust. J. Phys.* **23** 683
[40] Davies D K, Kline L E and Bies W E 1989 *J. Appl. Phys.* **65** 3311
[41] Rabie M, Haefliger P, Chachereau A and Franck C M 2015 *J. Phys. D: Appl. Phys.* **48** 075201
[42] Mirić J, Simonović I, Petrović Z Lj, White R D and Dujko S 2017 *Eur. Phys. J. D* **71** 289
[43] Zawadzki M, Chachereau A, Kočíšek J, Franck C M and Fedor J 2018 *J. Chem. Phys.* **149** 204305
[44] Petrović Z Lj, Dujko S, Marić D, Malović G, Nikitović Ž, Šašić O, Jovanović J, Stojanović V and Radmilović-Radenović M 2009 *J. Phys. D: Appl. Phys.* **42** 194002
[45] Crompton R W 1967 *J. Appl. Phys.* **38** 4093
[46] Thomas W R L 1969 *J. Phys. B: At. Mol. Phys.* **2** 551
[47] Tagashira H, Sakai Y and Sakamoto S 1977 *J. Phys. D: Appl. Phys.* **10** 1051
[48] Sakai Y, Tagashira H and Sakamoto S 1977 *J. Phys. D: Appl. Phys.* **10** 1035
[49] Boeuf J P and Marode E 1984 *J. Phys. D: Appl. Phys.* **17** 1133
[50] Blevin H A and Fletcher J 1984 *Aust. J. Phys.* **37** 593
[51] Robson R E 1986 *J. Chem. Phys.* **85** 4486
[52] Kondo K and Tagashira H 1990 *J. Phys. D: Appl. Phys.* **23** 1175
[53] Robson R E 1991 *Aust. J. Phys.* **44** 685
[54] Robson R E 1995 *Aust. J. Phys.* **48** 677
[55] Nakamura Y 2007 *Proc. 28th ICPIG* (Prague) pp 224–6
[56] Dujko S, White R D and Petrović Z Lj 2008 *J. Phys. D: Appl. Phys.* **41** 245205
[57] Robson R E, White R D and Hildebrandt M 2017 *Fundamentals of Charged Particle Transport in Gases and Condensed Matter* (Boca Raton, FL: CRC Press)
[58] Dahl D A, Teich T H and Franck C M 2012 *J. Phys. D: Appl. Phys.* **45** 485201
[59] Dahl D A and Franck C M 2013 *J. Phys. D: Appl. Phys.* **46** 445202
[60] Chachereau A, Rabie M and Franck C M 2016 *Plasma Sources Sci. Technol.* **25** 045005
[61] Chachereau A, Fedor J, Janečková R, Kočíšek J, Rabie M and Franck C M 2016 *J. Phys. D: Appl. Phys.* **49** 375201
[62] Haefliger P, Hösl A and Franck C M 2018 *J. Phys. D: Appl. Phys.* **51** 355201
[63] Haefliger P and Franck C M 2018 *Rev. Sci. Instrum.* **89** 023114
[64] Pachin J, Hösl A and Franck C M 2019 *J. Phys. D: Appl. Phys.* **52** 235204
[65] Ridenti M A, Vivaldini T C, Lima I B and Pascholati P R 2010 *AIP Conf. Proc. (AIP)* vol 1245 pp 92–7
[66] Aschwanden T 1985 Die ermittlung physikalischer entladungsparameter in isoliergasen und isoliergasgemischen

mit einer verbesserten Swarm-methode *PhD Thesis* ETH Zurich

[67] Phelps A V and Pitchford L C 1985 *Phys. Rev.* A **31** 2932

[68] Ruíz-Vargas G, Yousfi M and de Urquijo J 2010 *J. Phys. D: Appl. Phys.* **43** 455201

[69] Korolov I, Vass M, Bastykova N K and Donkó Z 2016 *Rev. Sci. Instrum.* **87** 063102

[70] Donkó Z, Hartmann P, Korolov I, Jeges V, Bošnjaković D and Dujko S 2019 *Plasma Sources Sci. Technol.* **28** 095007

[71] Pinhão N R, Loffhagen D, Vass M, Hartmann P, Korolov I, Dujko S, Bošnjaković D and Donkó Z 2020 *Plasma Sources Sci. Technol.* **29** 045009

[72] Hasegawa H, Date H and Shimozuma M 2007 *J. Phys. D: Appl. Phys.* **40** 2495

[73] Robson R E 1985 *Phys. Rev.* A **31** 3492

[74] Philippa B, White R D and Robson R E 2011 *Phys. Rev.* E **84** 041138

[75] Kumar K, Skullerud H R and Robson R E 1980 *Aust. J. Phys.* **33** 343

[76] Stokes P W, Simonović I, Philippa B, Cocks D G, Dujko S and White R D 2018 *Sci. Rep.* **8** 1

[77] Robson R E and Ness K F 1986 *Phys. Rev.* A **33** 2068

[78] White R D, Ness K F and Robson R E 2002 *Appl. Surf. Sci.* **192** 26

[79] de Urquijo J, Arriaga C A, Cisneros C and Alvarez I 1999 *J. Phys. D: Appl. Phys.* **32** 41

[80] Basurto E, Hernández-Ávila J L, Juárez A M and de Urquijo J 2013 *J. Phys. D: Appl. Phys.* **46** 355207

[81] de Urquijo J, Juarez A M, Rodríguez-Luna J C and Ramos-Salas J S 2007 *IEEE Trans. Plasma Sci.* **35** 1204

[82] Šašić O, de Urquijo J, Juárez A M, Dupljanin S, Jovanović J, Hernández-Ávila J L, Basurto E and Petrović Z Lj 2010 *Plasma Sources Sci. Technol.* **19** 034003

[83] Bekstein A, de Urquijo J, Ducasse O, Rodríguez-Luna J C and Juárez A M 2012 *J. Phys.: Conf. Ser.* **370** 012006

[84] de Urquijo J, Alvarez I, Basurto E and Cisneros C 1999 *J. Phys. D: Appl. Phys.* **32** 1646

[85] Datskos P G, Carter J G and Christophorou L G 1992 *J. Appl. Phys.* **71** 15

[86] Simonović I, Bošnjaković D, Petrović Z Lj, White R D and Dujko S 2020 *Eur. Phys. J.* D **74** 1

[87] Simonović I, Bošnjaković D, Petrović Z Lj, Stokes P W, White R D and Dujko S 2020 *Phys. Rev.* E **101** 023203

[88] Boyle G J, Tattersall W J, Cocks D G, Dujko S and White R D 2015 *Phys. Rev.* A **91** 052710

[89] Boyle G J, McEachran R P, Cocks D G and White R D 2015 *J. Chem. Phys.* **142** 154507

[90] de Urquijo J, Casey M J E, Serkovic-Loli L N, Cocks D G, Boyle G J, Jones D B, Brunger M J and White R D 2019 *J. Chem. Phys.* **151** 054309

[91] Hernández-Ávila J L, Basurto E and de Urquijo J 2004 *J. Phys. D: Appl. Phys.* **37** 3088

[92] Hernández-Ávila J L, Basurto E and de Urquijo J 2004 UNAM database http://lxcat.net accessed 03 January 2018

[93] Kücükarpaci H N and Lucas J 1981 *J. Phys. D: Appl. Phys.* **14** 2001

[94] Kücükarpaci H N and Lucas J 1981 IST-Lisbon database http://lxcat.net accessed 03 January 2019

[95] Biagi S F Magboltz version 8.97 http://magboltz.web.cern.ch/magboltz/ accessed 31 December 2017

[96] Haefliger P and Franck C M 2018 ETHZ (ETH Zurich, high voltage laboratory) database http://lxcat.net accessed 03 January 2019

[97] Foster S 2018 Self-consistency of electron-THFA gaseous cross-sections via Swarm techniques *Undergraduate Honors Thesis* James Cook University

[98] Xiao D M, Zhu L L and Chen Y Z 1999 *J. Phys. D: Appl. Phys.* **32** L18

[99] Nakamura Y 1988 *J. Phys. D: Appl. Phys.* **21** 67

[100] Naidu M S and Prasad A N 1972 *J. Phys. D: Appl. Phys.* **5** 1090

[101] Biagi S F 2014 Biagi database (Magboltz version 10.6) http://lxcat.net/Biagi accessed 03 January 2019

[102] Christophorou L G and Olthoff J K 2000 *J. Phys. Chem. Ref. Data* **29** 267

[103] de Urquijo J, Basurto E and Hernández-Ávila J L 2001 *J. Phys. D: Appl. Phys.* **34** 2151

[104] Xiao D M, Li X G and Xu X 2001 *J. Phys. D: Appl. Phys.* **34** L133

[105] Petrović Z Lj, Marić D, Savić M, Marjanović S, Dujko S and Malović G 2017 *Plasma Proc. Polym.* **14** 1600124

[106] Crompton R W and Jory R L 1962 *Aust. J. Phys.* **15** 451

[107] Crompton R W, Elford M T and Gascoigne J 1965 *Aust. J. Phys.* **18** 409

[108] Elford M T 1971 *Aust. J. Phys.* **24** 705

[109] Crompton R W and Elford M T 1973 *Aust. J. Phys.* **26** 771

[110] Robson R E, White R D and Petrović Z Lj 2005 *Rev. Mod. Phys.* **77** 1303

[111] Mladenović Ž, Gocić S, Marić D and Petrović Z Lj 2018 *Eur. Phys. J. Plus* **133** 344

Monte Carlo simulation of resonance effects of electron transport in a spatially modulated electric field in Ar, N_2 and their mixtures

To cite this article: A Albert *et al* 2021 *J. Phys. D: Appl. Phys.* **54** 135202

View the article online for updates and enhancements.

Monte Carlo simulation of resonance effects of electron transport in a spatially modulated electric field in Ar, N$_2$ and their mixtures

A Albert[1] , **D Bošnjaković**[2] , **S Dujko**[2] and **Z Donkó**[1]

[1] Institute for Solid State Physics and Optics, Wigner Research Centre for Physics, Konkoly Thege Miklós str. 29-33, 1121 Budapest, Hungary
[2] Institute of Physics, University of Belgrade, Pregrevica 118, 11080 Belgrade, Serbia

E-mail: donko.zoltan@wigner.hu

CrossMark

Abstract

The relaxation of the distribution function of the electrons drifting under the influence of a homogeneous electric field in noble gases is known to take place over an extended spatial domain at 'intermediate' values of the reduced electric field, *E/N*. We investigate the transport of electrons in Ar and N$_2$ gases, as well as in their mixtures at such *E/N* values (∼10–40 Td). After discussing briefly the basic scenario of relaxation in a homogeneous electric field, the major part of work concentrates on the properties of transport in an electric field that is spatially modulated within a finite region that obeys periodic boundaries. The spatial distribution of the mean velocity, the mean energy, and the density of the electrons, the importance of the excitation channels, as well as the electron energy distribution function are obtained from Monte Carlo simulations for various lengths of the computational domain, at different mean values and degrees of modulation of the reduced electric field. At low modulations, the spatial profiles of the mean velocity and mean energy are nearly harmonic, however their phases with respect to the electric field perturbation exhibit a complex behaviour as a function of the parameters. With increasing modulation, an increasing higher harmonic content of these profiles is observed and at high modulations where an electric field reversal occurs, we observe trapping of a significant population of the electrons. The effect of mixing a molecular gas, N$_2$, to Ar on the transport characteristics is also examined. Transition to local transport at high N$_2$ admixture concentrations and long spatial domains is observed.

Keywords: electron transport, kinetic simulation, distribution functions

(Some figures may appear in colour only in the online journal)

1. Introduction

Under *hydrodynamic* conditions, the velocity distribution function (VDF) of electrons subjected to a homogeneous and stationary electric field is a unique function of the reduced electric field, *E/N*. Up to moderate values of *E/N* (typically up to few hundred Townsends, $1\,\mathrm{Td} = 10^{-21}\,\mathrm{V\,m^2}$) the VDF of electrons in noble gases generally exhibits only a small anisotropy, i.e. it can be well approximated by an isotropic part and

small anisotropic part. This behaviour, which is the basis of the two-term approximation, stems from the effect of frequent elastic collisions of the electrons with the gas atoms that randomize the directions of velocities and thus their characteristic thermal velocity strongly exceeds the average (directed) velocity. In the hydrodynamic regime, the energy gain and loss of the electrons compensate each other exactly, however, in different ways depending on the strength of the reduced electric field [1, 2].

Considering noble gases, at very low E/N ($\lesssim 10$ Td) the energy loss of electrons is mostly due to elastic collisions. In such events, a fraction of their energy proportional to the electron/atom mass ratio (m/M) is lost. For an electron energy of 1 eV, e.g. such a collision results in a loss of $\approx 10^{-5}$ eV, in the case of argon gas. At somewhat higher E/N values (~tens of Td-s), where the energy of the electrons reaches the threshold for inelastic processes (~10 eV), the main channels of the energy loss become the excitation processes. At such conditions the lowest excited levels can be reached first. With increasing E/N, the number of these channels increases and at some point ionization becomes possible, too. Above ~100 Td, the latter process is usually appreciable. The scenario described above for noble gases changes notably in the case of molecular gases. There, due to the various (rotational and vibrational) excitation processes having low threshold energies the energy dissipation frequency at low energies is much higher as compared to the case of noble gases.

The spatial evolution of the electron VDF in *non-hydrodynamic regimes* is also remarkably different for the E/N rages distinguished above [3–6]. Non-hydrodynamic transport establishes under various conditions: (a) when the electric field varies over a characteristic length that is short compared to the mean free path of the electrons, (b) when the temporal change of the field is quicker than the mean time between electron-neutral collisions, (c) in the presence of sources/sinks of electrons and/or (d) in the presence of boundaries. In the latter case, even in the presence of a homogeneous and stationary electric field, the VDF and the transport parameters (mean velocity, mean energy, etc) of the electrons vary in space. A classical example of this scenario is an electrode that emits electrons with a certain initial velocity distribution that is defined by the emission process (e.g. photoemission). This VDF is clearly different from that acquired by the electrons under hydrodynamic conditions for the given E/N that is present in the volume considered. This implies that a transition region ('equilibration region') must exist within which the VDF transforms from its initial shape to the equilibrium shape, see e.g [7, 8].

The fundamental experiment of Franck and Hertz [9], which provided evidence for the existence of quantised energy levels of the atoms, actually utilised this effect. Specifically, this experiment focused on the early phase of the equilibration, where a prominent periodic structure in the mean energy of the electrons was present. The experiment was operated in the 'window' of E/N values where such behaviour prevails. The electron kinetics in this experiment has been investigated in a number of works, e.g. [10–13].

We note that both at low and high E/N values no, or less prominent periodic structures can be observed, respectively, due to the smooth transition mediated by elastic collisions, and due to the rapid randomisation of the electron energy in the presence of a high number of inelastic energy loss channels and the possibility of ionization that creates additional particles. The extended spatial structures formed at intermediate E/N values have attracted much attention [14–16]. The equilibration of an electron swarm in argon gas at E/N values at few tens of Td-s was as well observed experimentally recently in a scanning drift tube apparatus [17] that makes it possible to follow the spatio-temporal development of electron swarms. Under the conditions, where the electric field is spatially modulated a strong modulation of the electron transport characteristics appears at some E/N values as revealed in studies based on the solution of the Boltzmann equation by Golubovsky *et al* [18, 19]. In the presence of appreciable charge density, the spatial variation of the transport characteristics can itself give rise to a perturbation of the electric field. As this interplay may be self-amplifying, stationary or moving spatial structures can show up in discharge plasmas. Such structures, often termed as 'striations' have thoroughly been investigated for several decades, see, e.g. the review by Kolobov [20]. The early studies of striations based on analytic approaches [21, 22] have later been replaced by kinetic treatment of the electrons [23, 24]. Striations, caused by different mechanisms, are present in a variety of plasma sources, like dc glow discharges [25], plasma display panels [26], and inductively coupled radiofrequency discharges [27]. Despite the extensive work done in this field [28, 29], the complex dynamics of striations is still subject of intensive current research, e.g. [30–33].

Most of the investigations of the electron kinetics have been based on the solution of the Boltzmann equation [1, 34], particle based simulations were used only in a fewer number of cases. As examples for the latter, studies of striations in inductively coupled [35] and capacitively coupled electronegative [36] plasmas, and in ionization waves in barrier discharges [37], as well as the most recent studies of the spatial relaxation of the mean electron energy in inert gases and their mixtures in a uniform electric field [38] may be mentioned.

Due to the rapid development of computing hardware such particle based methods became equally suited as the numerical solutions of the Boltzmann equation, for studies of particle transport in spatially varying fields due to their ability to capture fully the nonlocal kinetic effects appearing in various settings. In this paper, we use Monte Carlo simulation (see e.g. [39, 40]) to investigate certain aspects of the transport of electrons in spatially varying electric fields.

The simulation method is discussed in section 2. In section 3, we briefly introduce some important physical quantities, the characteristic momentum and energy relaxation frequencies and lengths, that help understanding the relaxation and resonance effects to be discussed later on. The presentation of the results in section 4 starts with illustrating the spatial relaxation of electron swarms in Ar and in Ar–N_2 mixtures in a homogeneous electric field. These findings aid choosing the proper parameter range of the reduced electric field for which

J. Phys. D: Appl. Phys. **54** (2021) 135202

A Albert *et al*

the studies of the transport in a periodically modulated electric field are conducted. The results of these simulations for Ar are presented in section 4.2. We analyse the spatial profiles of the mean electron energy, velocity and density for various values of the average E/N and illustrate the effect of the modulation of E/N on these profiles. Additionally, we investigate the spatial distribution of the electron energy distribution function and the distribution of the excitation channels (reaction rates). Fourier analysis of the profiles of the mean velocity and energy (a) reveals the phase between them and the modulated field (at low modulation) and (b) shows how their harmonic content increases at high modulation. In section 4.3 the effect of an N_2 admixture on the electron transport characteristics is addressed. A brief summary is given in section 5.

2. Simulation method

Our studies are based on the Monte Carlo (MC) description of the motion of electrons in (a) homogeneous and (b) spatially modulated electric field $\mathbf{E}(x)$. We use the well-established MC algorithm for charged particle transport (e.g. [8, 41–43]) and solve the discretised version of the equation of the motion of the electrons,

$$m\ddot{\mathbf{r}} = q\mathbf{E}(x),\tag{1}$$

using the Velocity-Verlet method, with constant time steps of $\Delta t = 1$ ps. Here, m and q are the mass and the charge of the electrons. The probability of a collision to occur during the Δt time step is:

$$P_{\text{coll}} = 1 - \exp\left[-N\sigma_{\text{tot}}(v)v\Delta t\right],\tag{2}$$

where the total cross section σ_{tot} is the sum of the cross sections of all possible collision processes. Whenever a collision occurs, its type is chosen randomly, taking into account the values of all cross sections at the actual velocity of the colliding electron.

The electron–Ar atom cross section set is based on [44], includes the elastic momentum transfer cross section, excitation to 25 distinct Ar levels, and the ionisation cross section. The cross section set for electron–N_2 molecule collisions are taken from [45]. The set includes the elastic momentum transfer cross section, excitation to several vibrational and electronic states of N_2, as well as the ionisation cross section. As calculations are performed for $E/N \gg 1$ Td, the cross sections for rotational excitations are not included in the present study. Ionisation is treated here as a number conserving process, i.e. just like an excitation event, to ensure that the number of electrons does not grow in the simulations. This approach is justified at the E/N values considered here, where ionisation has a very small rate (which is confirmed by the results). This simplification could easily be omitted when necessary, e.g. at higher E/N values. All collisions are assumed to result in isotropic scattering, the thermal motion of the background gas atoms is disregarded (i.e. the 'cold gas approximation' is adopted). Collisions are described in the centre-of-mass coordinate
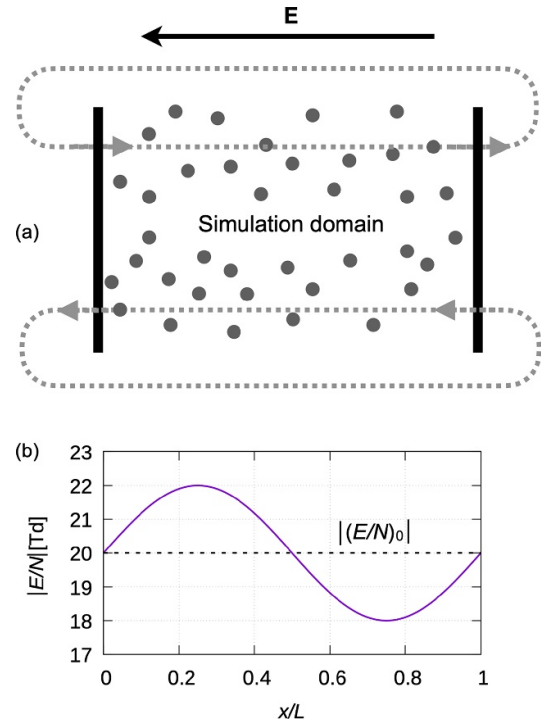
Figure 1. (a) In the case of a modulated electric field, the electrons' motion is followed in a simulation box having a width L, with periodic boundaries. The system is exposed to a sinusoidally spatially modulated electric field as shown in (b) for the case of an average reduced electric field of $(E/N)_0 = 20$ Td (indicated by the dashed horizontal line) and a modulation depth $M = 0.1$.

frame. The velocity of this frame (**w**) and the relative velocity of the collision partners (**g**) are calculated. As known from the classical kinematic treatment of the two-body interaction, elastic collisions change only direction of the relative velocity, while in inelastic collisions its magnitude is decreased as well by an amount that is defined by the excitation energy. The value of the relative velocity vector obtained this way, together with the velocity of the centre-of-mass allows computation of the post-collision velocity of the electrons.

The electrons do not interact with each other, i.e. we study classical swarm conditions at low charged particle density. The simulations are conducted at a pressure of $p = 100$ Pa and at the ambient temperature of $T_g = 300$ K, i.e. at a neutral density of $N \cong 2.42 \times 10^{16}$ cm^{-3}.

Except for the study of swarm relaxation in a homogeneous electric field, the particles are restricted to move within a simulation domain that obeys periodic boundary conditions, as shown in figure 1(a). Particles leaving this domain in the $\pm x$ directions are re-injected into the domain at the opposite sides. The periodic boundaries emulate an infinite system with spatially periodic modulation of E/N.

The electric field points in the $-x$ direction, consequently, the electrons drift in the $+x$ direction. In the following, we omit the negative sign of E. In the case of a modulated electric field, the form

$$E(x) = E_0\left[1 + M\sin(kx)\right],\tag{3}$$

is adopted, where E_0 is spatial average of the electric field, $M \geqslant 0$ is the modulation depth, and $k = 2\pi/L$, with L being the length of the spatial period of modulation (see figure 1(b)). The voltage drop over the length L is $U = (E/N)_0 N L$, i.e.

$$U[\text{V}] = 0.242 \cdot (E/N)_0 (\text{Td}) \times L(\text{cm}). \qquad (4)$$

At a given $(E/N)_0$ this relation connects the length of the computational domain and the voltage drop over this domain. We primarily examine the range of the parameters $(E/N)_0$ and L, where the energy corresponding to the voltage drop over the simulation domain, $q U$, is in the order of the excitation levels of Ar, the lowest being 11.55 eV.

We present results for the spatial profiles of the mean electron velocity $\bar{v}(x)$, the mean energy $\bar{\varepsilon}(x)$, the electron density $n(x)$, the electron energy distribution function (EEDF) $f(x, \varepsilon)$. These characteristics are studied as a function of the reduced electric field and the length of the computation cell (that equals the wavelength of the modulation of $E(x)$.) They are 'measured' within 200 slabs with equal width, covering the simulation domain of length L. A lower spatial resolution is used for the analysis of the excitation rates and of the spatial distribution of the EEDF, to ensure a better statistics.

At low values of modulation, the system is expected to give a linear response for the space-dependent scalar quantities, i.e. the latter are foreseen to exhibit a harmonic spatial profile. With increasing perturbation, a non-linear response is expected to establish. Taking as an example the mean velocity $\bar{v}(x)$, the harmonic content as well as the phase shift of the individual harmonics contributing the spatial profile can be obtained via Fourier analysis, which allows to construct $\bar{v}(x)$ as

$$\bar{v}(x) = \sum_s \bar{v}_s \sin(s k x - \varphi_s), \qquad (5)$$

where $\bar{v}_s$ and φ_s are, respectively, the amplitude and the phase delay of the sth harmonic. This analysis helps, e.g. identifying the conditions when local transport is approached: in the case of low modulation (as long as $\bar{v}$ and $\bar{\varepsilon}$ are monotonically increasing functions of E/N) we expect $\bar{v}_s \to 0, \forall s > 1$ and $\varphi_1 \to 0$, as $E(x)$ contains only a dc component and one (perturbing) harmonic with $s = 1$. Any deviation from this behaviour is the signature of the non-local character of the transport and the non-linear response of the system to the electric field perturbation. We note that this analysis of the phase shifts of the 'macroscopic quantities', like $\bar{v}(x)$ and $\bar{\varepsilon}(x)$ with respect to $E(x)$ does not offer an explanation for the resonance effects, as these are kinetic by nature. We also need to notice that the dependence of $\bar{v}$ on E/N is not necessarily monotonic, this scenario is called Negative Differential Conductivity (NDC) [46], which typically occurs in gas mixtures, including Ar–N$_2$ mixtures that are also studied here [47].

For the case of homogeneous electric field, the EEDF resulting from our simulation code has been cross checked with that obtained from the Bolsig+ Boltzmann solver [48].
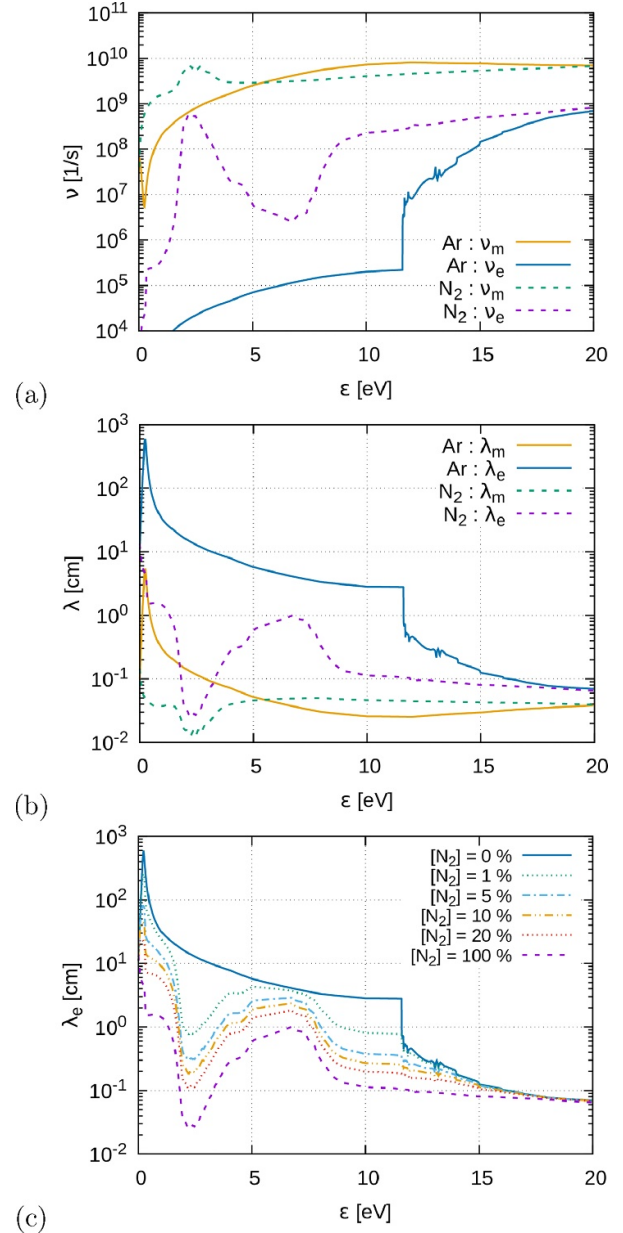
Figure 2. (a) Momentum and energy dissipation frequencies ν_m and ν_e, as well as (b) mean free path λ_m and the energy relaxation length λ_e in Ar (solid lines) and N$_2$ (dashed lines). (c) Dependence of the energy relaxation length on the concentration of N$_2$ in the Ar+N$_2$ mixture. $p = 100$ Pa and $T_\text{g} = 300$ K.

3. Relaxation frequencies and lengths

Before presenting our results it is useful to illustrate the behaviour of few important quantities that have major influence on the relaxation and resonance effects to be discussed. These are the momentum and energy dissipation frequencies, ν_m and ν_e, respectively, as well as the mean free path λ_m and the energy relaxation length λ_e. We have computed these quantities according to the expressions given in [1] and display them in figure 2. Panel (a) shows the energy dissipation frequency (ν_e) and the momentum dissipation frequency (ν_e) for both Ar and N$_2$. We find ν_m to be significantly higher than ν_e over the

whole range of energies considered. ν_e is especially low for Ar below the threshold energy for inelastic loss channels, as in elastic collisions the fractional energy loss of the electrons is in the order of the electron/atom mass ratio, as already mentioned in section 1. Rapid changes of ν_e with ε can be observed for both gases. Whenever the energy distribution of the electrons spans a range that includes such a change, parts of the electron population with different energies will behave dissimilar in terms of energy relaxation, as explained in [1].

The momentum relaxation frequency does not exhibit abrupt changes as a function of the energy, except for Ar at low energies, due to the Ramsauer–Townsend minimum in the elastic collision cross section. Regarding the relaxation lengths in pure gases, figure 2(b) reveals that the energy relaxation length (λ_e) exceeds considerably the mean free path (λ_m). Below the inelastic excitation threshold in Ar, e.g. their ratio amounts about two orders of magnitude. Under such conditions the relaxation of the energy in a swarm is expected to take place over an extended spatial scale, where a high number of collisions is required for equilibration. The difference between λ_e and λ_m for Ar decreases as the energy is increased, at 20 eV the ratio between them drops to a factor of two. As around this energy the sum of inelastic cross sections approaches the value of the elastic momentum transfer cross section energy relaxation becomes efficient. As to N_2, λ_e and λ_m are relatively close to each other, meaning that energy relaxation takes place over a few free flight lengths of the electrons, except at low energies (below 2 eV) and within the $3\,\text{eV} \leqslant \varepsilon \leqslant 8\,\text{eV}$ interval, where the collision cross sections are low.

Due to the large disparity of the relaxation frequencies and lengths in Ar vs. in N_2, even a small amount of the latter causes a significant change of these parameters, as illustrated in figure 2(c) for the case of λ_e. With respect to the case of pure Ar the strongest decrease of λ_e occurs in the $2\,\text{eV} \leqslant \varepsilon \leqslant 3\,\text{eV}$ and $8\,\text{eV} \leqslant \varepsilon \leqslant 11\,\text{eV}$ domains of the electron energy as a result of the addition of N_2 to Ar. This is caused by, respectively, the vibrational and electronic excitation of N_2 molecules. In the first domain, even 1% of N_2 decreases λ_e by a factor of 10 as it can be seen in figure 2(c). At electron energies above $\approx 15\,\text{eV}$ the effect of N_2 on λ_e becomes negligible due to the availability of a high number of inelastic loss channels.

4. Results

4.1. Homogeneous electric field

To illustrate the equilibration of electron swarms in a homogeneous electric field, in figure 3 we depict the mean velocity and the mean energy of the electrons for a steady state scenario when electrons are continuously emitted from an electrode at $x = 0$ and drift in the gas. In this simulation, the electrons are emitted with an initial energy of 1 eV and an initial velocity directed towards the x direction. Such an initial velocity distribution is very clearly far from the equilibrium distribution that is expected to be nearly isotropic with a small drift component. Figures 3(a) and (b) show the case of pure Ar. Here, the ensemble of the electrons requires rather significant 'flight' lengths to acquire a steady-state mean velocity, for the

whole range of E/N covered. The periodic structures seen during this equilibration phase originate from repetitive energy gain—energy loss cycles of the electrons: gain occurs due to acceleration in the electric field, loss occurs primarily due to inelastic collisions. This is especially well seen in the graph of $\overline{\varepsilon}(x)$ for the 20 Td case, for which the x scale is $10\times$ zoomed (red dashed line): here saw-tooth like patterns appear, expressing the slow energy gain and rapid energy loss. While the peaks of this function appear nearly at the same position as those of $\overline{v}(x)$, the functional forms appear to be significantly different. The oscillations of the mean velocity persist for the longest spatial domain for the 20 Td case, both at lower and higher fields we observe equilibration on a shorter length scale.

Figures 3(c) and (d) illustrate the behaviour of the swarm in Ar–N_2 mixtures, as a function of the N_2 concentration, at fixed $E/N = 20$ Td. The equilibration of the transport takes place on a much shorter length scale, as compared to that in pure Ar. Already 1% of N_2 shrinks the equilibration domain by a factor of ~ 10. At higher admixture concentrations equilibrium becomes close to monotonic. This behaviour originates from the wide range of energies (due to processes with low threshold energies, e.g. vibrational channels) of inelastic loss channels in N_2 as compared to Ar. We can note that an increasing N_2 concentration results in a remarkable increase of the steady-state mean velocity and a remarkable decrease of the steady-state mean energy.

Whenever pronounced structures in transport coefficients are seen, it is expected that in a spatially modulated electric field resonances may appear at certain conditions, as it has been recognised in several earlier studies, e.g. [49]. This is indeed the foreseen behaviour in pure Ar, while N_2 is expected to have a converse influence on this effect.

The data presented above help setting the proper range of E/N for the studies of the transport in spatially modulated fields and the timing of the data collection in the simulations (see below).

4.2. Transport in periodically modulated electric field in argon

Below, we present the results for the transport properties in spatially modulated electric field for pure Ar gas. The simulations are initialized by placing $N = 2000$–$20\,000$ electrons (depending on the type of the 'measurement') at random positions within the simulation box (of length L) with a velocity $\mathbf{v}_0 = 0$. First, the electrons are traced for $\Delta T_1 = 900\,\mu\text{s}$, and subsequently for an additional $\Delta T_2 = 100\,\mu\text{s}$, during which the transport data are collected (unless stated otherwise). This timing ensures the decay of the initial transients: at 20 Td, e.g. the relaxation length seen in figure 3 is ~ 1 m and the mean stationary velocity is about $v_0 \approx 1.8 \times 10^4\,\text{m s}^{-1}$, resulting in a characteristic relaxation time of $\approx 55\,\mu\text{s} \ll \Delta T_1$.

First, we analyse the results obtained at $(E/N)_0 = 20$ Td as the longest relaxation length was observed (in figure 3) for this value of the reduced electric field. Figure 4 shows the effect of the length of the simulation domain, L, for this $(E/N)_0$ and for a modulation of $M = 0.2$. Panel (a) shows the mean velocity $\overline{v}(x)$, (b) the normalised electron density n/n_0 (where n_0 is the spatial average of the electron density), and (c) the mean
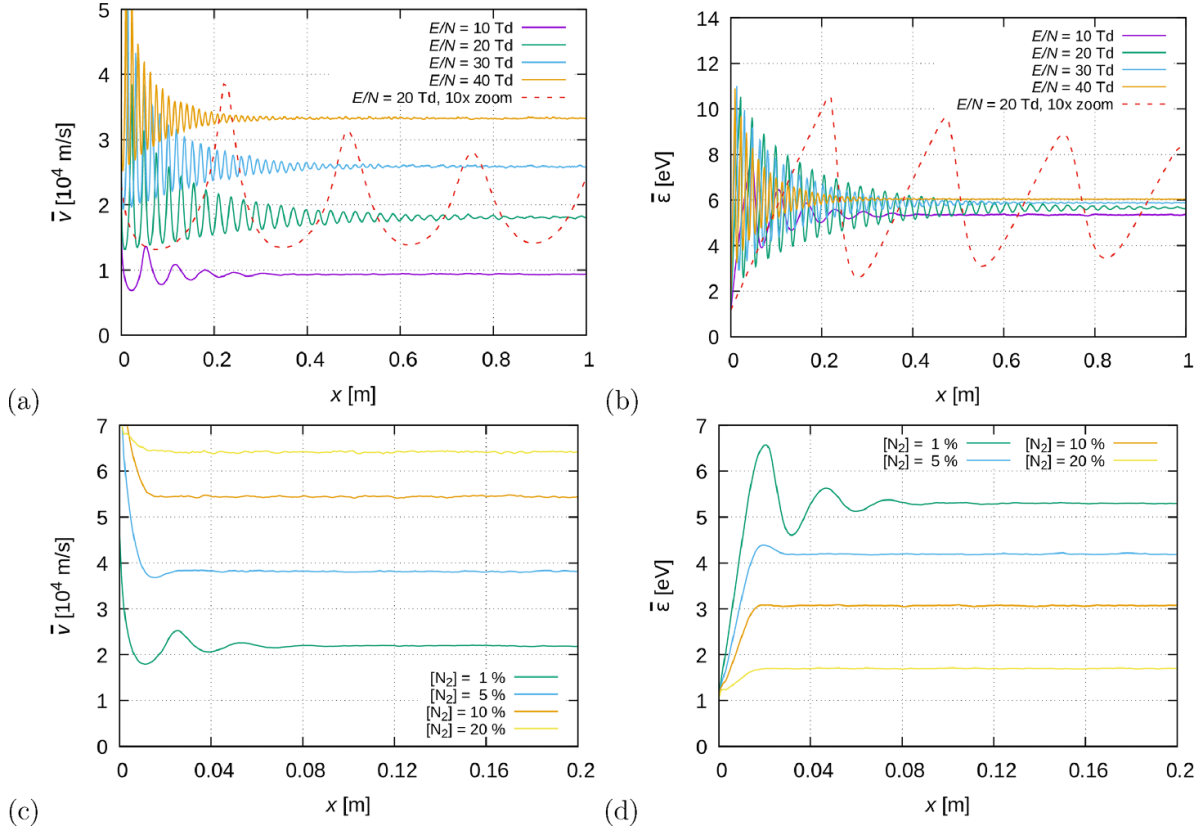
Figure 3. Relaxation of the mean velocity (left column) and the mean energy (right column) of electrons in a homogeneous electric field. The electrons are emitted at $x = 0$ with an initial velocity pointing into the x direction and corresponding to 1 eV initial energy. $p = 100$ Pa and $T_g = 300$ K. (a), (b) Pure Ar at various values of E/N, (c) and (d) Ar–N_2 mixtures at $E/N = 20$ Td and different N_2 concentrations. Note that the domain shown in (c) and (d) is much shorter. The dashed red lines in (a) and (b) correspond to 20 Td, with the x scale $10\times$ zoomed.

energy $\bar{\varepsilon}(x)$. L is varied between 2 and 3 cm, in 0.1 cm steps. Recall that the effect of L translates directly to the effect of the voltage drop over the simulation cell, U, via equation (4), i.e. for the present conditions the voltage is in the $9.68 \text{ V} \leqslant U \leqslant 14.52$ V range.

The characteristics of the spatial profile of the quantities shown in figures 4(a)–(c) (i.e. the amplitude and shape of the curves as well as the positions of their extrema) vary in a complicated manner with L. As regards to $\bar{v}$, in the limit of small L values we observe a weak modulation around the equilibrium value of $v_0 \approx 1.8 \times 10^4$ m s^{-1}, with a peak close to the edge of the cell. A notable increase of the amplitude and a shift of the maximum to higher x/L appear at $L = 2.6$ cm, while the highest modulation is observed at $L = 2.7$ cm, which is, however, accompanied by a 'backward' shift of the profile. At $L > 2.7$ cm we observe a decreasing amplitude of the profile, with maxima approaching $x/L = 0$. For the given strength of modulation, $M = 0.2$, the higher harmonic content of the profiles is limited. Therefore the strength of the 'response' of $\bar{v}$ to the perturbing electric field variation is characterized by the amplitude and the phase of the first Fourier component, $\bar{v}_1$ and φ_1, in figure 4(d). This figure confirms the visual observation of a resonance at $L = 2.7$ cm (corresponding to $U = 13.07$ V), where $\bar{v}_1$ exhibits a sharp peak. The phase of the profile is near $-80°$ both at low and high L and shows a peak at $\varphi_1 \approx 0°$ at $L = 2.6$ cm. As there are no sources and losses in the system, $n\bar{v}$

$= $ const. holds due to flux conservation ($\nabla \cdot (n\bar{v}) = 0$). Therefore, the electron density obtained from the simulation (and shown in figure 4(b) is directly related to the mean velocity. The dependence of the spatial profile of the mean electron energy, $\bar{\varepsilon}(x)$ as a function of L is similar to that of the mean velocity, as it can be seen in figure 4(c). The phases of the $\bar{v}(x)$ and the $\bar{\varepsilon}(x)$ profiles are, however, quite different as revealed quantitatively in figure 4(d). The phase of the latter exhibits a monotonic decrease with the increase of L and passes through $0°$ at $L = 2.6$ cm, near the resonance.

The Electron Energy Distribution Function (EEDF) exhibits marked changes as a function of the position when $M > 0$. An example of this is shown in figure 5 for $(E/N)_0 = 20$ Td and $M = 0.2$, at $L = 2.7$ cm, i.e. for the resonant case. It is remarkable that the strongest high-energy tail of the EEDF develops at the spatial position of $x/L = 0.4$, where, actually the mean energy has a minimum (see figure 4(b)). This is not a contradiction as low-energy part of the EEDF at this position is also highly populated. On the other hand, this observation points out the importance of the whole EEDF in determining the characteristics of the transport. Revoking figure 2(b) we can note that the EEDF-s are populated at energies both below and above the energy where a sudden drop in the energy relaxation length occurs. Therefore, as pointed out in [1] the low- and high-energy parts of the electron population behave in a quite different ways at this resonance. Below the inelastic
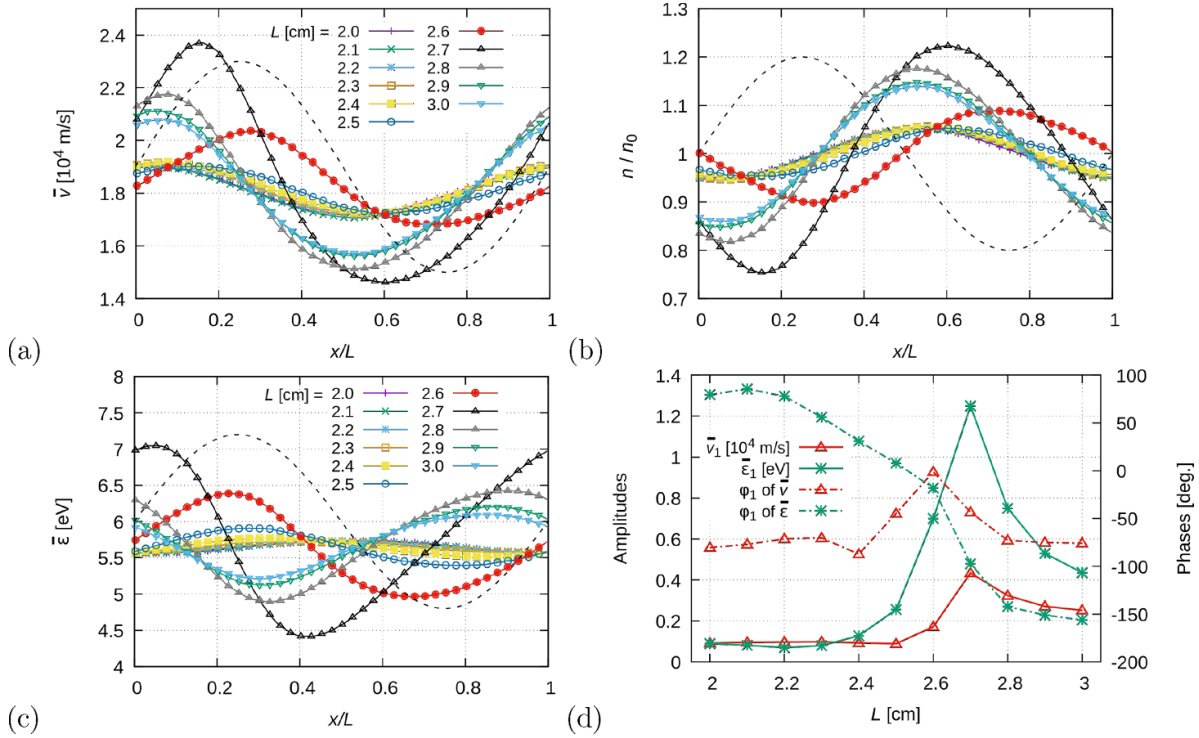
Figure 4. Spatially resolved mean velocity (a), normalized density (b) and mean energy (c) of the electrons at $(E/N)_0 = 20$ Td and $M = 0.2$, as a function of L. (n_0 is the spatial average of the electron density.) The identification of the curves in (c) is the same as in (b). The dashed black lines in each panel show the spatial variation of E/N, these curves are given without units. (d) Amplitudes (left scale, solid lines) and phases (right scale, chain lines) of the first ac component of the profiles of the mean velocity and the mean energy, as a function of L. The amplitudes of $\bar{v}_1$ and $\bar{\varepsilon}_1$ are given in units of 10^4 m s^{-1} and eV, respectively.
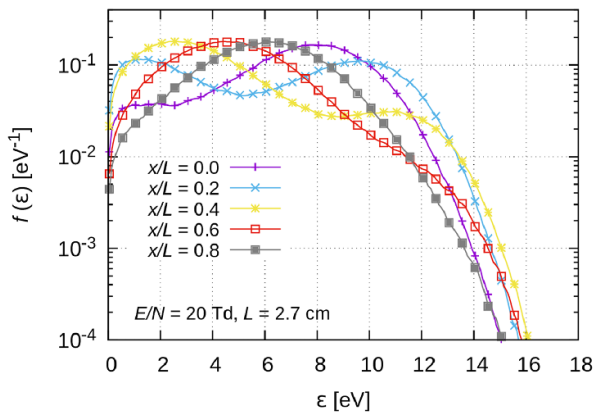
Figure 5. EEDF-s at different spatial locations, at $(E/N)_0 = 20$ Td and $M = 0.2$ and $L = 2.7$ cm.

excitation threshold of Ar (11.55 eV) λ_e is in the order of several cm-s while this drops to several mm-s when the energy is higher than this threshold. The long λ_e at low ε assists the electrons to gain energy from the field, without dissipating it. The short λ_e at $\varepsilon > 11.55$ eV, on the other hand, allows the electrons to dissipate their energy quickly. Actually, at $\varepsilon = 11.55$ eV, $\lambda_e = 2.79$ cm. The energy accumulation for the resonant case ($L = 2.7$ cm) is clearly indicated by the slanted structure in panel (b) of figure 6 that shows the

complete spatial evolution of the EEDF. Remains of this structure are also seen in figures 6(a) and (c), however, these are far less pronounced.

The velocity distribution function of the electrons [50], as a function of the axial and radial components of the velocity, $f(v_x, v_r)$, is plotted in figure 7 at four distinct locations within the simulation cell, for the conditions $L = 2.7$ cm, $M = 0.2$, and $(E/N)_0 = 20$ Td. The VDF at $x/L = 0$ (and at the equivalent position of $x/L = 1$) exhibits a high population of particles with velocities between 1.5×10^6 and 1.8×10^6 m s^{-1}, a small additional peak at low velocities shows that some electrons already suffered a significant energy loss around these positions. At $x/L = 0.25$ (figure 7(b)) most of the electrons have velocities below $\approx 1 \times 10^6$ m s^{-1}, following their inelastic collisions. At the higher x/L values we observe an expanding ring in the velocity distribution, which is caused by the fact that electrons re-gain energy from the electric field (see (figures 7(c) and (d))). Generally, only a quite small anisotropy can be observed at any position, confirming the expected behaviour that at low E/N the drift velocity of the electrons is much smaller compared to their random (thermal) speed. The presence of the modulation of the electric field obviously does not change this general behaviour.

The effect of the modulation depth, M, on the spatial variation of the mean velocity is depicted in figure 8(a). At the lower values of L, the $\bar{v}(x)$ curves are nearly harmonic, an
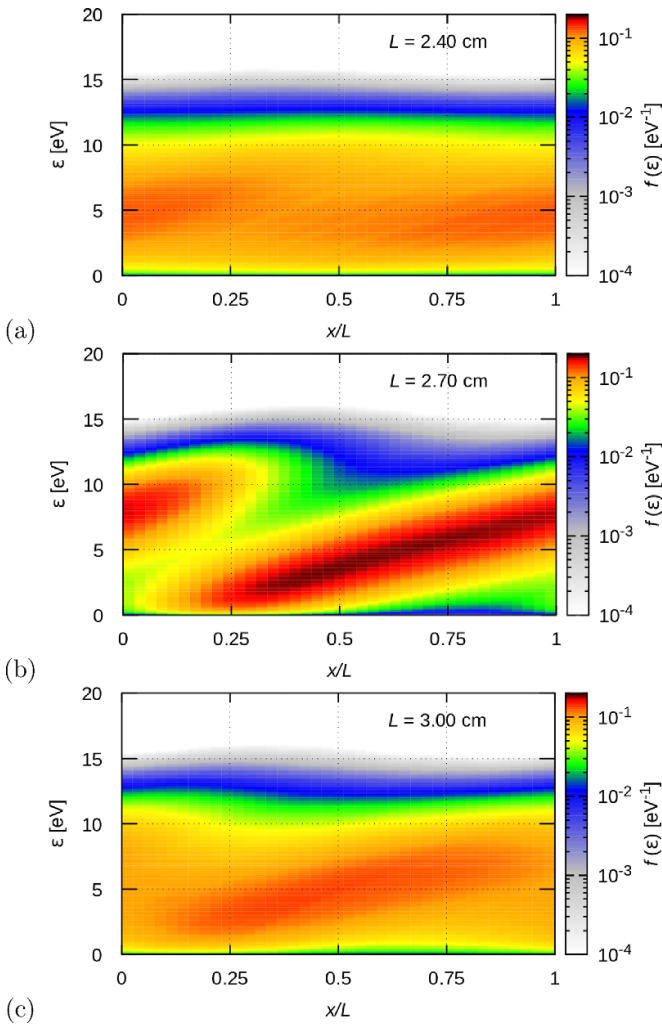
Figure 6. Spatial maps of the EEDF for $(E/N)_0 = 20$ Td and $M = 0.2$, at various values of L.

increasing anharmonicity can be observed with increasing modulation. Figure 8(b) shows the harmonic composition of $\bar{v}(x)$ as a function of M for the case of $L = 2.7$ cm and $(E/N)_0 = 20$ Td. Besides the harmonic amplitudes, $\bar{v}_s$, the phase of the principal component of the 'response', φ_1 is also shown. At low modulation, only $\bar{v}_1$ differs significantly from zero, however, with increasing M the harmonic content increases. The phase is $\varphi_1 \approx -40°$ for all M. We can note that the $s = 0$ component slightly increases with M, i.e. the 'dc component' $\bar{v}_{s=0}$ of $\bar{v}(x)$, which is the spatially averaged velocity of the electrons, increases as an effect of the modulation.

Counting the number of the different electron-Ar atom reactions spatially resolved allows construction of a matrix that shows the collision frequencies associated with the various collision processes. The computational results are shown in figure 9 for the case of $(E/N)_0 = 20$ Td and $L = 2.7$ cm, obtained at $M = 0.0$ (panel a) and $M = 0.2$ (panel b). In these plots, excitation processes are identified by numbers 1...25, ionisation is process 26. The number of elastic collisions is orders of magnitude higher, thus this (process 0) is omitted from the plots. The highest excitation rates are

observed (in both cases) for the four lowest excited levels of Ar, for processes 1–4, corresponding to excitation to the $1s_5$, $1s_4$, $1s_3$, and $1s_2$ levels (Paschen notation), respectively. The energy of these levels is between 11.55 and 11.83 eV. At $M = 0$, significant rates are also observed for the whole domain for processes 5 and 6 ($2p_{10}$ and $2p_9$ levels), 8–10 ($2p_{7,6,5,4}$ levels), and 13–15 ($2p_1$, $3d_{5,6}$ and $3d_3$ levels). The excitation threshold of the latter is 13.90 eV. Ionisation (process 26) is not present with an appreciable rate, justifying our approach of treating this process as a number conserving one, for the rare events of occurrence.

At $M = 0.0$ (figure 9(a)) the spatial distribution of the excitation events is homogeneous, as expected. At $M = 0.2$, however, the modulation of the electric field causes a major perturbation to the excitations [51]. We find that (i) the majority of excitation events is concentrated within the $0.25 \leqslant x/L \leqslant 0.6$ spatial domain with a pronounced maximum near $x/L = 0.4$, where the most notable high energy tail for the EEDF was found for the same conditions (see figure 5) and (ii) the acceleration of the electrons in the modulated field also opens excitation channels with higher thresholds: in figure 9(b) we observe processes with appreciable rates up to #18, which corresponds to levels $3d_1''$ and $2s_5$, with a threshold energy of 14.06 eV [44]. The further increase of the modulation depth, e.g. to $M = 0.5$, results in a slightly increased spatial confinement of the excitation events. While new higher-threshold levels get populated as compared to lower M, it is remarkable that a depletion of the excitation rates of the lowest-threshold $1s_{2,3,4,5}$ levels (processes 1...4) is also observed in the $0.75 \leqslant x/L \leqslant 1$ domain because of the prominent energy deposition of the electrons in the $0.25 \leqslant x/L \leqslant 0.6$ domain.

While in the cases described before, the modulation was kept at moderate levels, here we briefly examine the case of higher modulation, when the electric field changes sign within a certain domain (at $M > 1$). As the presence of a region with a reversed electric field gives rise to a potential well, electrons can accumulate within these regions. For $(E/N)_0 = 20$ Td, $L = 2.7$ cm, and $M = 1.1$, e.g. the depth of this potential well is ≈ 0.1 V. As electrons may undergo such collisions in these regions when their remaining kinetic energy is less than 0.1 eV, such electrons will be trapped as their energy cannot increase anymore to overcome the barrier. Consequently, after a sufficiently long time all electrons are expected to be trapped in our simulation.

While the presence of the reversed field bears some similarity with the case of the negative glow region of dc glow discharges [52–54], in that setting fast electrons arriving from the sheath can interact with the trapped population and can eventually increase the energy of some of the electrons, enabling them this way to get released from the trap. This effect is the result of Coulomb collisions, which are however, not included in the present simulation. Nonetheless, our simulations can follow the time dependence of the trapping phenomenon. This is illustrated in figures 10(a)–(c), where the results (for the mean velocity, mean energy and normalised density) are shown as a function of time. The data were collected in 100 μs wide time windows at different start times, as indicated. The graphs indeed exhibit pronounced structures

J. Phys. D: Appl. Phys. **54** (2021) 135202

A Albert *et al*
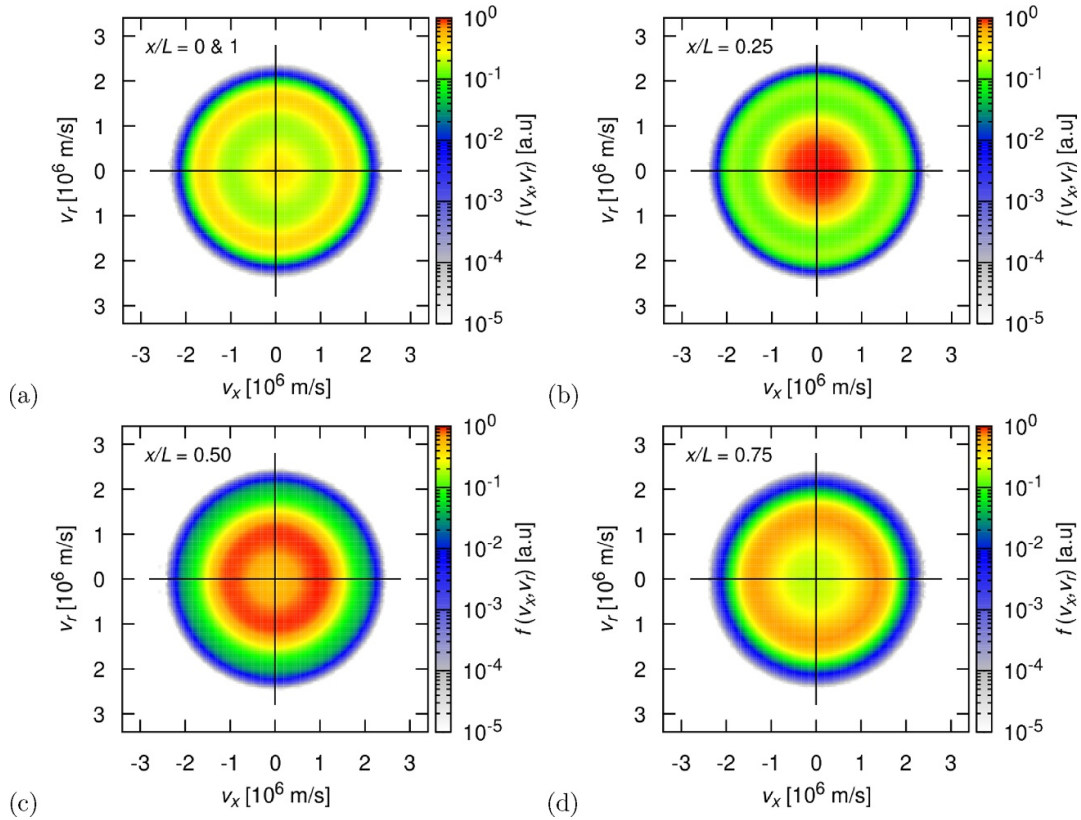
Figure 7. $f(v_x, v_r)$ velocity distribution functions of the electrons at different spatial locations (a) $x/L = 0$ and $x/L = 1$ (which are equivalent positions due to the periodic boundary conditions), (b) $x/L = 0.25$, (c) $x/L = 0.5$, and (d) $x/L = 0.75$. The data have been collected within domains of half width $\Delta(x/L) = 0.025$ around the positions specified. $L = 2.7$ cm, $M = 0.2$, and $(E/N)_0 = 20$ Td.
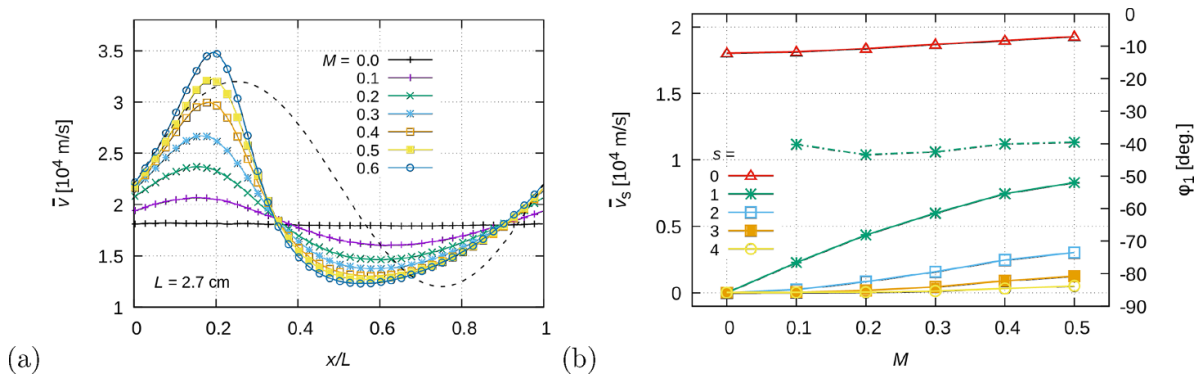
Figure 8. (a) The effect of modulation depth on the spatially resolved mean velocity. The dashed black line shows the spatial variation of E/N, this curve is given without units. (b) Harmonic composition of $\bar{v}(x)$ (solid lines, left scale) and the phase of the first ac component, φ_1 (chain curve, right scale) as a function of the modulation depth of the electric field. $L = 2.7$ cm and $(E/N)_0 = 20$ Td.

around $x/L = 0.75$, where the reversed electric field peaks. They show that a slow change follows after an initial high rate of trapping. From this it follows that the spatial modulation of E actually slows down the trapping process by 'moving' most of the inelastic collisions from a random distribution to spatial positions that exclude the domain of reversed field, as shown in figure 9. In accordance with this it is also interesting to note that the least significant trapping for otherwise same conditions is observed for the resonant case of $L = 2.7$ cm, as revealed in figure 10(d). For other values of

L, we observe a much more significant collection of the electrons within the region of the field reversal and more significant depletion of the density outside this domain. As electrons are less likely to undergo inelastic collisions in the regions with reversed electric field, complete trapping takes place on a time scale much longer than accessible by our simulations. Inclusion of the Coulomb collisions [55] and/or thermal contribution of the background gas are clearly necessary to model correctly the stationary state of our system at such high modulations.

J. Phys. D: Appl. Phys. **54** (2021) 135202

A Albert *et al*
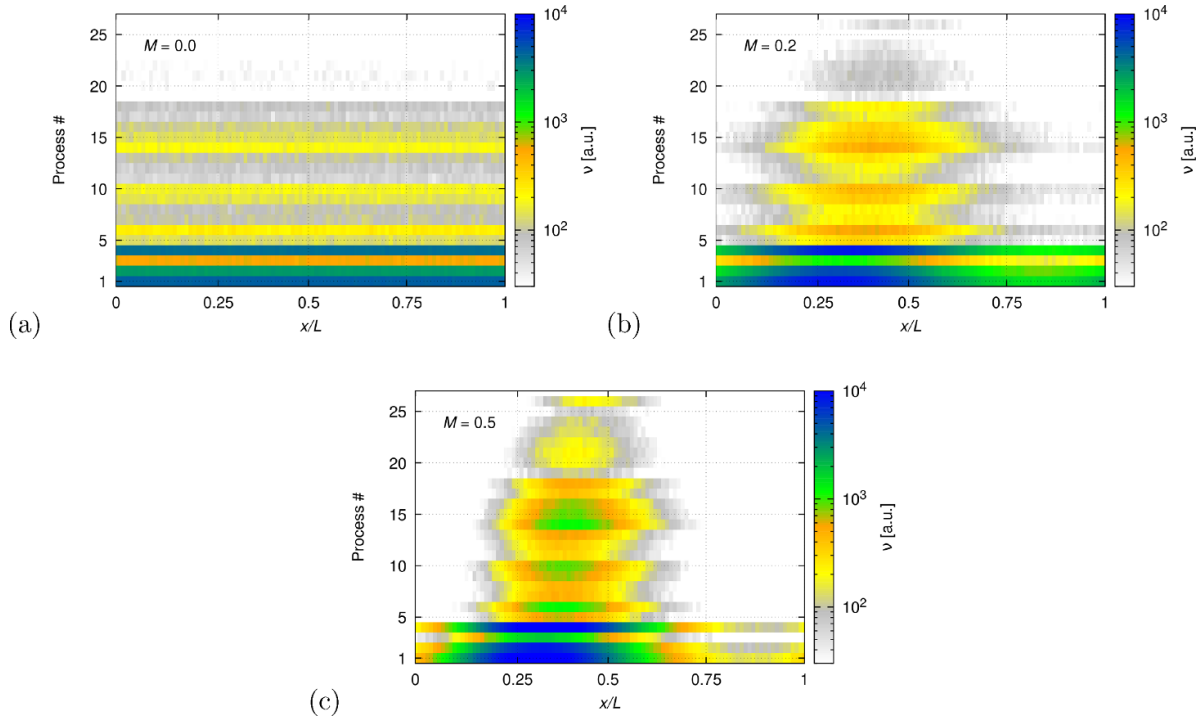
Figure 9. The spatial distribution of collision frequency (in arbitrary units) of individual inelastic collision processes at $(E/N)_0 = 20$ Td and $L = 2.7$ cm ($U = 13.07$ (V), for (a) $M = 0.0$, (b) $M = 0.2$, and (c) $M = 0.5$. (Note, that for these conditions ionisation (process #26) is negligible.)
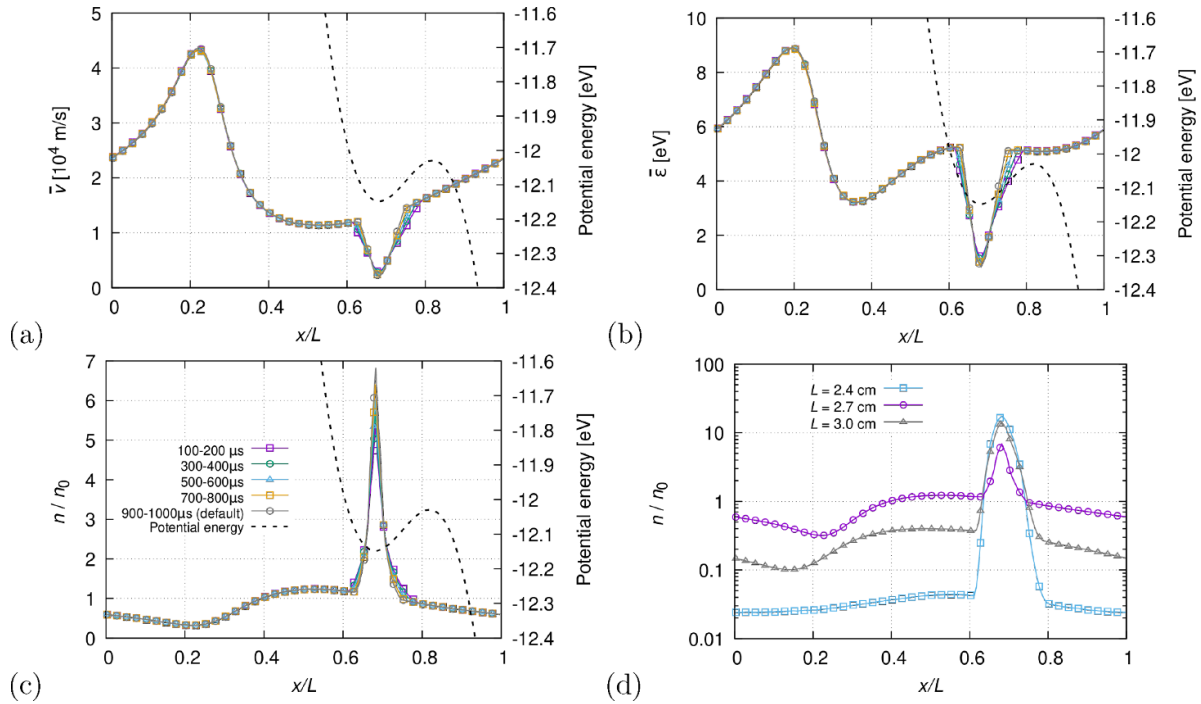
Figure 10. Spatially resolved mean velocity (a), mean energy (b) and normalised density (c) of the electrons at $(E/N)_0 = 20$ Td and $L = 2.7$ cm, for $M = 1.1$. The curves correspond to different data collection time windows, as indicated. The legend shown in (c) is valid for panels (a) and (b), too. Note the slow evolution of the features with time within the domain of the reversed field, centred around $x/L = 0.75$. The dashed black lines show the potential energy of the electrons, with zero value set at $x = 0$. (d) The dependence of the normalised electron density on L at $(E/N)_0 = 20$ Td and $M = 1.1$. These data were collected in the default, 900–1000 μs time window.

After presenting the results obtained for $(E/N)_0 = 20$ Td, we analyse cases with lower and higher values, $(E/N)_0 = 10$ Td and 40 Td. The results for these cases are shown in figures 11(a) and (b), respectively. At $(E/N)_0 = 10$ Td, the profile of the mean velocity changes smoothly with increasing L, without any significant resonance. The phase of the first ac
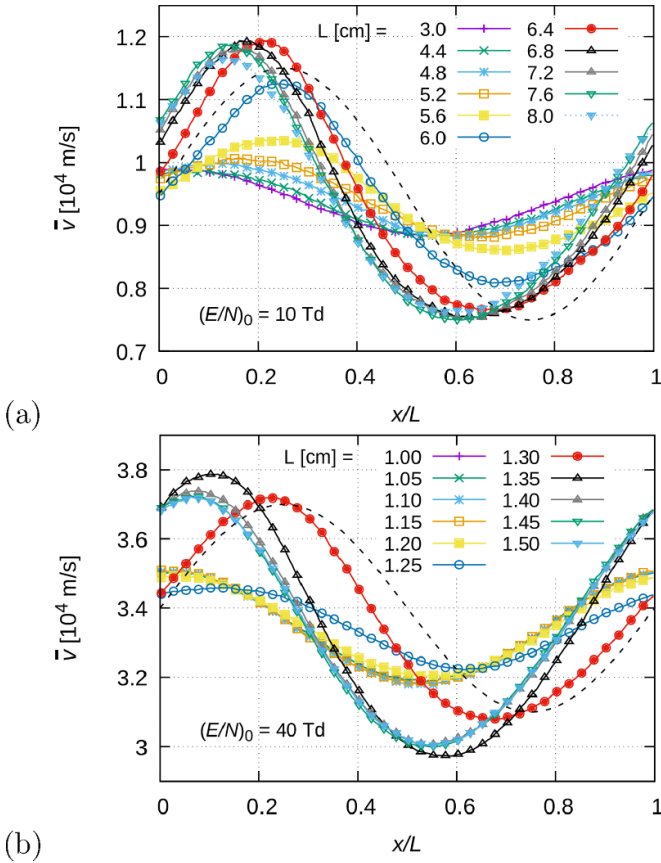
Figure 11. Mean electron velocity at different $(E/N)_0$ values:
(a) 10 Td cm, (b) 40 Td. The dashed black lines in both panels show
the spatial variation of E/N, these curves are given without units.
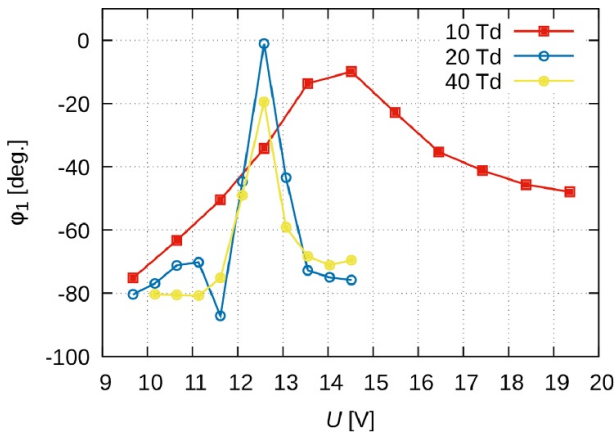
Figure 12. The phase of the first ac component of the mean velocity
at the $(E/N)_0$ values indicated, as a function of the voltage drop
(related to the other parameters via equation (4)) over the
computational cell. $M = 0.2$.

component $\bar{v}_1$, changes however, in the same way as it was
found previously for 20 Td. This is presented in figure 12,
where φ_1 is shown as a function of the voltage drop U (in order
to make the data obtained at different $(E/N)_0$ values compar-
able). The maximum of the phase occurs at a higher voltage
drop (higher L) compared to the higher fields. At $(E/N)_0 = 40$

Td, the behaviour of the phase is very similar to that at 20 Td
(a strong peak at ≈ 12.5 V). The inspection of the amplitude of
$\bar{v}(x)$ in figure 11(b) does not show a strong resonance unlike in
the case of 20 Td. This may be explained by the higher number
of inelastic loss channels at an expanded energy range of the
electrons at the higher accelerating field. Note, that at $E/N =
40$ Td a faster spatial relaxation was found also in the homo-
geneous field, as compared to 20 Td, see section 4.1.

4.3. Transport in periodically modulated electric field in Ar–N$_2$ mixtures and in N$_2$

As discussed above, the pronounced response of the electron
transport parameters on the spatial modulation of the accel-
erating electric field in argon gas is due to the fact that the
number of energy loss channels is limited (excitation predom-
inantly occurs to a few excited states as confirmed by the res-
ults presented in the previous section). As in a molecular gas,
like N$_2$ the possible values of the energy loss in a collision
span a much wider domain as compared to atomic gases, the
response of the system to the modulated electric field is expec-
ted to diminish when even small amounts of molecular gases
are added to Ar.

Figure 13(a) shows $\bar{v}(x)/v_0$ for various percentages of N$_2$
between 0% and 100%, for $(E/N)_0 = 20$ Td, $M = 0.2$, and $L
= 2.7$ cm. The data are normalised by the equilibrium velo-
city v_0, which varies (as shown in figure 13(c)) as a function
of the N$_2$ content in the gas mixture. (In the case of 0% N$_2$ the
data are the same as shown in figure 4). With an increasing N$_2$
percentage the phase of the first harmonic of $\bar{v}(x)$ first slightly
decreases at low nitrogen content, and then increases rapidly to
$\varphi_1 \approx -20°$ above 5% N$_2$ (see figure 13(d)). The velocity pro-
files practically overlap at $\geqslant 40\%$ N$_2$ content indicating that
excitation of Ar is strongly suppressed at these molecular gas
concentrations. Some of the data points belong to the para-
meter range where Negative Differential Conductivity in the
Ar–N$_2$ mixture is present. As revealed from figure 4 of [47],
NDC at $E/N = 20$ Td occurs between N$_2$ concentrations of
approx. 5% and 15%. This effect may have an influence on the
behaviour of φ_1, clarification of this is, however, left for future
work that needs to consider a broader domain of the paramet-
ers especially the spatial wavelength of the modulation. The
addition of N$_2$ efficiently cools the electrons, as the profiles
of the mean energy, shown in figure 13(b) confirm. Besides
the value of ε the modulation of its spatial profile decreases as
well and the phase of the profile changes also significantly as
shown in figure 13(d).

The presence of N$_2$ in the mixture has a dramatic effects on
the EEDF as well, as shown in figure 14. Already at 1% N$_2$
content, the marked spatial modulation of the EEDF observed
in pure Ar (see figure 6(b)) vanishes almost completely. With
the addition of more N$_2$, the low energy part of the EDDF
gets gradually more populated as a result of the low-threshold-
energy processes in N$_2$.

Finally we present results for the case of pure N$_2$.
Figures 15(a) and (b) display spatial profiles of the mean
electron velocity as a function of L, while panel (c) of the
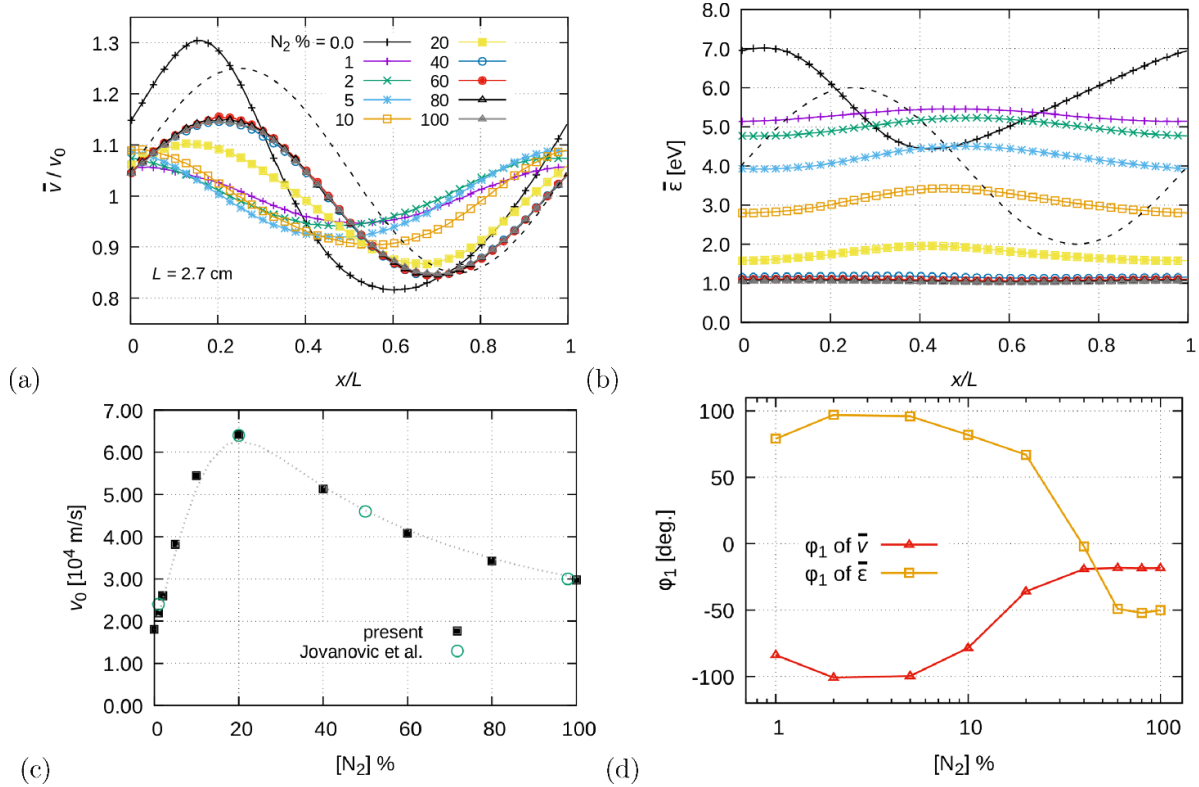
Figure 13. Spatial profiles of the mean electron velocity ($\overline{v}(x)$) (a) and mean electron energy ($\overline{\varepsilon}(x)$) (b) as a function of the N_2 concentration. The legend in (a) also holds for (b). The data in (a) are normalised by the equilibrium velocity of electrons (v_0) that varies as a function of the Ar/N_2 mixing ratio as shown in (c). The results of our calculations are cross checked with the data of [56]. (d) Phase of the first harmonic of $\overline{v}(x)$ and $\overline{\varepsilon}(x)$ as a function of the N_2 content. $(E/N)_0 = 20$ Td, $M = 0.2$, and $L = 2.7$ cm. The dashed black lines in (a) and (b) show the spatial variation of E/N, this curve is given without units.

same figure shows the behaviour of the mean electron energy. At large L (i.e. at $L > 2$ cm), both the $\overline{v}(x)$ and $\overline{\varepsilon}(x)$ profiles approximate the spatial dependence of the electric field. For these conditions, the phases of the first harmonic of both of these profiles approaches zero, as it is revealed from figure 15(d). These are signatures of the local character of the transport. For large L, we indeed find a very slight spatial modulation of the EEDF as well, as it can be seen in figure 16(c) for $L = 4$ cm. The only observable signature there is a small modulation of the high energy cutoff with x/L, around $\varepsilon \approx 2.5$ eV. The vast majority of the electrons have energies less than 2 eV. For such energies, as figure 2(b) reveals, the energy relaxation length is in the order of $\lambda_e \approx 1$–2 cm. For any L exceeding this value we expect that the swarm properties reflect the local value of the electric field, as it is actually confirmed in figure 15(a).

5. Summary

In this work, we have investigated via Monte Carlo simulation the characteristics of electron transport in a stationary, spatially modulated electric field. The computations have been executed for Ar and N_2 gases and their mixtures at (spatially averaged) reduced electric fields in the 10–40 Td

range. Particles have been traced in a finite spatial region subjected to periodic boundary conditions.

Within the range of the reduced electric field considered, a strong response of the transport parameters to the electric field modulation was observed. At low modulation depths, the spatial profiles of the mean electron velocity and energy exhibited a harmonic shape. The phase angle between the electric field and the above quantities, as well as the harmonic content of the latter at higher modulation depths were revealed by Fourier analysis. All the quantities analysed showed highly nonlocal transport, except for the case of pure N_2 at long modulation wavelength, where signatures of local electron transport were observed.

At conditions, where the high modulation depth of E/N resulted in the appearance of a region where the direction of the electric field is reversed, we observed trapping of the electrons. The stationary case, where all electrons are supposed to be trapped was not reached due to the slow accumulation of the electrons. The latter was found to be caused by the fact that the modulation of the electric field favours inelastic collisions (that represent high energy loss) outside the domain of the reversed field. For a realistic description of any experimental setting the inclusion of either Coulomb or thermal collisions is necessary.
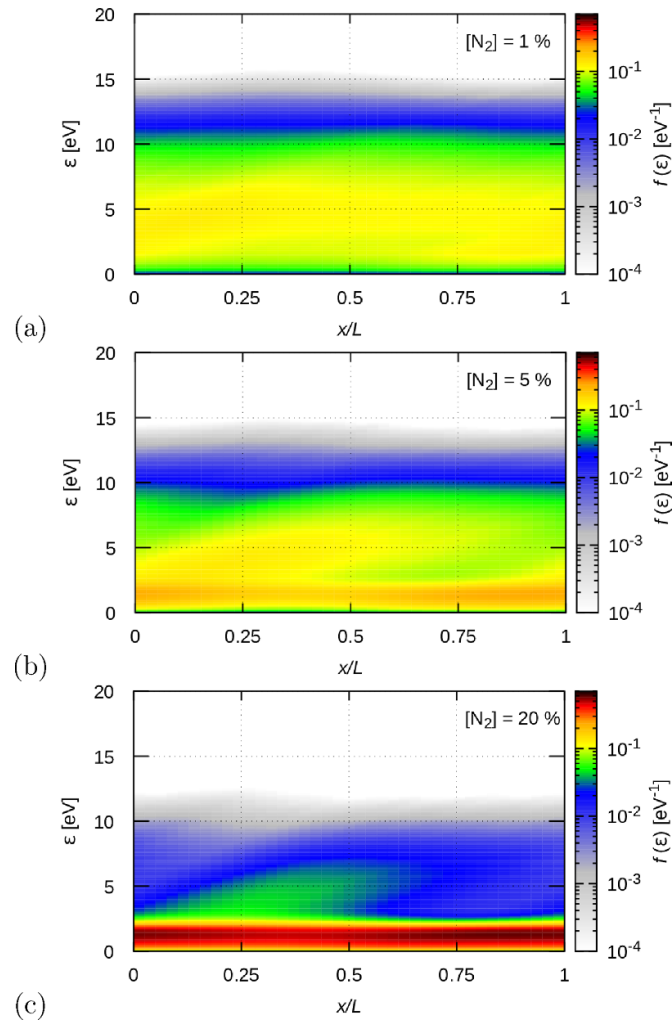
Figure 14. Spatial maps of the EEDF for $(E/N)_0 = 20$ Td and $M = 0.2$, and $L = 2.7$ cm, for N_2 concentrations of (a) 1%, (b) 5%, and (c) 20%.

Understanding the transport characteristics requires the analysis of the spatial variation of the electron energy distribution function (EEDF). We have computed this function for various parameter combinations and have found pronounced structures at the resonance condition where the potential drop over the simulation box is ≈ 13 V in pure Ar. The strongest resonance was found for $(E/N)_0 = 20$ Td. At lower reduced electric field, elastic collisions play a more prominent role in the electron energy balance, while at higher field more excitation channels are open due to the higher electron energy, and this adversely affects the synchronisation of the kinetics of individual electrons. The analysis of the rates of the inelastic collision processes at 20 Td showed that for these conditions only few levels of the Ar atom are preferentially excited.

Even small amounts of N_2 admixtures were found to lead to the vanishing of the structures in the EEDF due to the wider range of excitation energies of the N_2 molecule. Further directions of the present study include (a) the clarification of the combined effects of the modulated electric field and the Negative Differential Conductivity on the transport characteristics in the case of Ar–N_2 mixtures, (b) investigations of the transport properties in the presence of non-sinusoidal perturbation of the electric field strength, (c) inclusion of Coulomb collisions for an accurate prediction of the properties of the trapped part of the electron population in regions with reversed electric field, (d) the introduction of the self-consistent computation of the electric field distribution from the perturbed densities of the electrons via the Poisson equation in order to predict the range of existence of standing striations, and (e) extending the range of E/N to higher values, to observe the effects of appreciable ionisation on the characteristics of the electron transport.

J. Phys. D: Appl. Phys. **54** (2021) 135202

A Albert *et al*
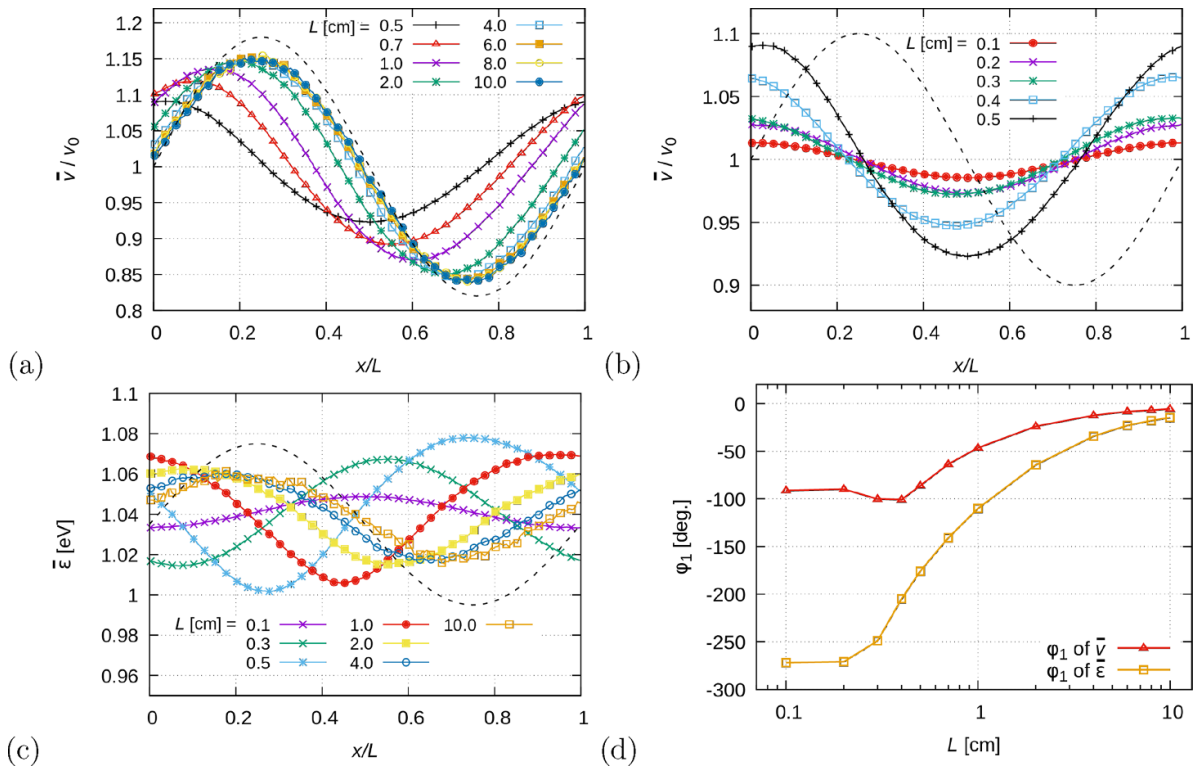
Figure 15. (a), (b) Normalized mean electron velocity in pure N_2 at $(E/N)_0 = 20$ Td and $M = 0.2$, for various values of L, given in the legends. (c) Profiles of the mean electron energy for the same conditions. The dashed black lines in each panel show the spatial variation of E/N, this curve is given without units. (d) Phase of first harmonic of $\bar{v}_1$ and $\bar{\varepsilon}_1$.
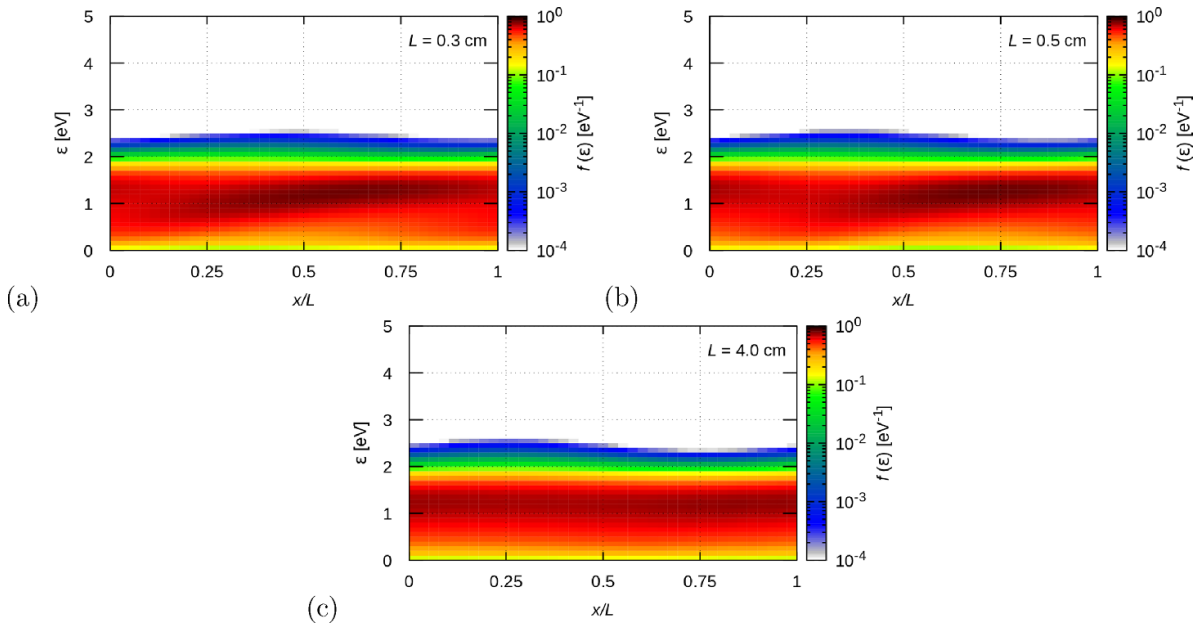
Figure 16. Spatial maps of the EEDF in pure N_2, for $(E/N)_0 = 20$ Td and $M = 0.2$, and various values of L.

J. Phys. D: Appl. Phys. **54** (2021) 135202

A Albert *et al*

ORCID iDs

A Albert https://orcid.org/0000-0002-7267-6056
D Bošnjaković https://orcid.org/0000-0002-2725-5287
S Dujko https://orcid.org/0000-0002-4544-9106
Z Donkó https://orcid.org/0000-0003-1369-6150

References

[1] Winkler R, Loffhagen D and Sigeneger F 2002 *Appl. Surf. Sci.* **192** 50
[2] Kumar K, Skullerud H R and Robson R E 1980 *Aust. J. Phys.* **33** 343
[3] Robson R E, White R D and Petrović Z L j 2005 *Rev. Mod. Phys.* **77** 1303
[4] Pitchford L C, Boeuf J-P, Segur P and Marode E 1990 *Non-Equilibrium Effects in Ion and Electron Transport* ed J W Gallagher (New York: Plenum)
[5] Tsendin L D 1995 *Plasma Sources Sci. Technol.* **4** 200
[6] Kudryavtsev A A, Morin A V and Tsendin L D 2008 *Tech. Phys.* **53** 1029
[7] Malović G, Strinić A, Živanov A, Marić D and Petrović Z 2003 *Plasma Sources Sci. Technol.* **12** S1
[8] Donkó Z 2011 *Plasma Sources Sci. Technol.* **20** 024001
[9] Franck J and Hertz G 1914 *Verh. Deut. Phys. Ges.* **16** 457
[10] Robson R E, Li B and White R D 2000 *J. Phys. B: At. Mol. Opt. Phys.* **33** 507
[11] Sigeneger F, Winkler R and Robson R E 2003 *Contrib. Plasma Phys.* **43** 178
[12] White R D, Robson R E, Nicoletopoulos P and Dujko S 2012 *Eur. Phys. J. D* **66** 117
[13] Robson R E, White R D and Hildebrandt M 2014 *Eur. Phys. J. D* **68** 188
[14] Loffhagen D, Winkler R and Donkó Z 2002 *Eur. Phys. J. Appl. Phys.* **18** 189
[15] Dujko S, White R D Petrović Z L 2008 *J. Phys.* D **41** 245205
[16] White R D, Robson R E, Dujko S, Nicoletopoulos P and Li B 2009 *J. Phys. D: Appl. Phys.* **42** 194001
[17] Donkó Z, Hartmann P, Korolov I, Jeges V, Bošnjaković V and Dujko S 2019 *Plasma Sources Sci. Technol.* **28** 095007
[18] Golubovsky Y B, Porokhova I A, Behnke J and Nekutchaev V O 1998 *J. Phys. D: Appl. Phys.* **31** 2447
[19] Golubovskii Y B, Maiorov V A, Porokhova I A and Behnke J 1999 *J. Phys. D: Appl. Phys.* **32** 1391
[20] Kolobov V I 2006 *J. Phys. D: Appl. Phys.* **39** R487
[21] Klarfeld B N 1952 *Sov. Phys. JETP* **22** 66
[22] Pekarek L and Krejčí V 1962 *Cechoslovackij Fiziceskij Zurnal* B **12** 450
[23] Sigeneger F, Sukhinin G I and Winkler R 2000 *Plasma Chem. Plasma Process.* **20** 87
[24] Sukhinin G I and Fedoseev A V 2006 *High Temp.* **44** 157
[25] Raizer Y P and Shneider M N 1997 *High Temp.* **35** 19
[26] Iza F, Yang S S, Kim H C and Lee J K 2005 *J. Appl. Phys.* **98** 043302
[27] Stittsworth J A and Wendt A E 1996 *IEEE Trans. Plasma Sci.* **24** 125
[28] Sigeneger F, Golubovskii Y B, Porokhova I A and Winkler R 1998 *Plasma Chem. Plasma Process.* **18** 153
[29] Sigeneger F and Winkler R 2000 *Plasma Chem. Plasma Process.* **20** 429
[30] Liu Y X, Schuengel E, Korolov I, Donkó Z, Wang Y N and Schulze J 2016 *Phys. Rev. Lett.* **116** 255002
[31] Arslanbekov R A and Kolobov V I 2019 *Phys. Plasmas* **26** 104501
[32] Kolobov V I, Arslanbekov R A, Levko D and Godyak V A 2020 *J. Phys. D: Appl. Phys.* **53** 25LT01
[33] Hartmann P, Rosenberg M, Juhasz Z, Matthews L S, Sanford D L, Vermillion K, Reyes J C and Hyde T W 2020 *Plasma Sources Sci. Technol.* **29** 115014
[34] Golubovskii Y B, Kolobov V I and Nekuchaev V O 2013 *Phys. Plasmas* **20** 101602
[35] Denpoh K 2012 *Japan. J. Appl. Phys.* **51** 106202
[36] Liu Y-X, Donkó Z, Korolov I, Schuengel E, Wang Y-N and Schulze J 2019 *Plasma Sources Sci. Technol.* **28** 075005
[37] Shvydky A A, Khudik V N, Nagorny V P and Theodosiou C E 2006 *IEEE Trans. Plasma Sci.* **34** 878
[38] Dyatko N A, Kochetov I V and Ochkin V N 2020 *Plasma Sources Sci. Technol.* **29** 125007
[39] Sato N and Tagashira H 1985 *J. Phys. D: Appl. Phys.* **18** 2451
[40] Boeuf J P and Marode E 1982 *J. Phys. D: Appl. Phys.* **15** 2169
[41] Fraser W and Mathieson E 1987 *Nucl. Instrum. Methods Phys. Res.* A **257** 339
[42] Rabie M and Franck C M 2016 *Comput. Phys. Commun.* **203** 268
[43] Renda M, Ciubotaru D A 2020 (arXiv:1901.08140v2) [physics.comp-ph]
[44] Hayashi M *Nagoya Institute of Technology Report* IPPJ-AM-19 (unpublished)
[45] Biagi Database Plasma Data Exchange Project LXCAT (available at: www.lxcat.net) (Accessed 23 July 2020)
[46] Petrović Z L, Crompton R W and Haddad G N 1984 *Aust. J. Phys.* **37** 23
[47] Dyatko N A, Kochetov I V and Napartovich A P 2014 *Plasma Sources Sci. Technol.* **23** 043001
[48] Hagelaar G J M and Pitchford L C 2005 *Plasma Sources Sci. Technol.* **14** 722
[49] Nicoletopoulos P, Robson R E and White R D 2012 *Phys. Rev.* E **85** 046404
[50] Sydorenko D, Smolyakov A, Kaganovich I and Raitses Y 2005 Kinetic simulation of effects of secondary electron emission on electron temperature in hall thrusters *Proc. 29th Annu. Int. Electric Propulsion Conf.* pp 2005–78
[51] Aleksandrov N L and Kochetov I V 1996 *J. Phys. D: Appl. Phys.* **29** 1476
[52] Loffhagen D, Sigeneger F and Winkler R 2004 *Eur. Phys. J. Appl. Phys.* **25** 45
[53] Boeuf J P and Pitchford L C 1995 *J. Phys. D Appl. Phys.* **28** 2083
[54] Kudryavtsev A A, Nisimov S U, Prokhorova E I and Slyshov A G 2011 *Tech. Phys. Lett.* **37** 838
[55] Weng Y and Kushner M J 1990 *Phys. Rev.* A **42** 6192
[56] Jovanović J V, Basurto E, Šašić O, Hernández-Ávila J L, Petrović Z L and De Urquijo J 2009 *J. Phys. D: Appl. Phys.* **42** 045202

PAPER • OPEN ACCESS

Electron transport parameters in CO_2: a comparison of two experimental systems and measured data

To cite this article: Máté Vass *et al* 2021 *J. Phys. D: Appl. Phys.* **54** 035202

View the article online for updates and enhancements.

Electron transport parameters in CO_2: a comparison of two experimental systems and measured data

Máté Vass[1,2] , **Eda Egüz**[3] , **Alise Chachereau**[3] , **Péter Hartmann**[1,4] , **Ihor Korolov**[2] , **Andreas Hösl**[3] , **Danko Bošnjaković**[5] , **Saša Dujko**[5] , **Zoltán Donkó**[1] and **Christian M Franck**[3]

[1] Institute for Solid State Physics and Optics, Wigner Research Centre for Physics, H-1121 Budapest, Konkoly-Thege Miklós str. 29-33, Hungary
[2] Department of Electrical Engineering and Information Science, Ruhr-University Bochum, D-44780, Bochum, Germany
[3] Power Systems and High Voltage Laboratories, ETH Zurich, Physikstr. 3, 8092 Zurich, Switzerland
[4] Center for Astrophysics, Space Physics and Engineering Research (CASPER), Baylor University, 100 Research Pkwy, Waco, TX, United States of America
[5] Institute of Physics, University of Belgrade, Pregrevica 118, 11080 Belgrade, Serbia

E-mail: vass.mate@wigner.hu

CrossMark

Abstract

Two experimental apparatuses used to obtain electron transport coefficients in gases are compared based on measurements in CO_2 over a wide range of E/N-values. The operation principles of the two experimental systems as well as their data acquisition methods are different. One operates under the time of flight (TOF) principle, where the transport coefficients are obtained by fitting the theoretical form of the electron density of a swarm in an unbounded region, $n(x,t)$, to the measured current at different values of the drift length, $I(L,t)$. The other experimental apparatus operates in the Pulsed Townsend (PT) mode, where the electron transport coefficients are obtained by fitting the spatial integral of $n(x,t)$ over the drift region to the measured, time-dependent current signal, $I(t)$. In both apparatuses, the measured E/N range was extended as much as possible to allow a large overlap for the comparison of the results. The bulk drift velocity, W, obtained by the two systems agrees well (within a few %) over a wide range of E/N values (100 Td $\leq E/N \leq$ 1000 Td). The agreement between the data sets for the longitudinal component of the bulk diffusion tensor, D_L, is less satisfactory, the TOF data show systematically higher values (by 10–50% depending on E/N) than the PT measurements. Significant differences are also found below 100 Td in case of the effective ionisation frequency, ν_{eff}, and the (steady state) Townsend ionisation coefficient, α_{eff}, where the TOF apparatus is unable to give accurate results. Our comparison justifies the correctness of the measured data over the range of agreement and also indicates the interval in E/N where the data obtained by each of the experimental systems can be taken to be reliable. The limits of the operating regimes of the two setups, stemming from the hardware and from the physical limits, are discussed.

1. Introduction

Transport coefficients of charged particles in gases, besides having paramount importance in swarm physics, serve as fundamental input parameters for fluid modelling of gas discharges. In addition, they can be used to check and adjust cross section sets of different collision processes relevant for gas discharge physics, as transport coefficients can accurately be computed from the cross sections [1]. In order to improve plasma technologies, a thorough understanding of the chemical and physical processes present in the plasma phase is required, for which transport coefficients can be of use. As the most mobile charged particles are electrons in the plasma, accurate measurements of electron transport coefficients are crucial.

The gas investigated in this work, CO_2, owing to its role in global warming, has been the subject of several research works, which mainly focus on its plasma-catalytic splitting into CO and O_2 [2–6], or its conversion into other valuable chemical compounds through e.g. a reaction with CH_4 (so-called dry reforming) [7–11]. Different types of plasma reactors have been applied for this purpose, e.g. dielectric barrier discharges (DBDs) [12–16], microwave plasmas [17–19], gliding arc [20–22] and spark discharges [23, 24]. The electron transport in CO_2 plays a key role in the optimization of non-equilibrium atmospheric pressure plasmas [25], in the modeling of production of oxygen in the atmosphere of Mars [26, 27] as well as in many studies of the CO_2 lasers [28] and particle detectors used in high energy physics [29].

The determination of transport coefficients has conventionally been based on *drift tube* measurements, where a low-density ensemble of electrons (an electron swarm) is created, which is subject to a homogeneous external electric field [30–32]. Based on their operation principles, we can distinguish between three major types of swarm experiments [33]:

- Time of flight (TOF) systems, where electron swarms are initiated by short pulses of an UV laser which hits a negatively biased electrode, thus emitting electrons through photoemission [31, 34, 35]. The system is equipped with a detector that collects 'arriving' charges and gives a signal that is proportional to the number of these particles. In our previous works [42, 43] it has been assumed that the detected signal is (under hydrodynamic conditions) proportional to the spatio-temporal distribution of the density of the electron swarm, $n(x,t)$ (see section 3 for definitions). From the functional form of $n(x,t)$, electron transport coefficients can be obtained through e.g. a fitting procedure.
- Pulsed Townsend (PT) systems [36–39], where the experimental realization is similar to that of a TOF system, but in this case the time-dependent displacement current generated by all the moving electrons within the whole

electrode gap is measured at fixed electrode separation, i.e. the measured current $I(t)$ is:

$$I(t) \propto \int_0^L n(x,t)\mathrm{d}x, \tag{1}$$

where L is the electrode separation. The measurement can be repeated with different electrode separations. This way the consistency of the results can be checked. In a PT system, essentially the same transport coefficients can be obtained as in case of a TOF experiment.

- Steady state Townsend (SST) systems, where, unlike the two other types above, a steady stream of electrons is emitted from the cathode. At sufficiently large distances from the cathode, the following assumption can be made:

$$n(x) \propto \mathrm{e}^{\alpha_{\mathrm{eff}}x}, \tag{2}$$

where α_{eff} is the effective ionization coefficient [40]. This transport coefficient can be determined by e.g. measuring the anode current at different gap distances. The other option under SST conditions would be the measurement of spatial profiles of emission that could be subsequently normalized at the anode to give spatially resolved net excitation rate. Such measurements in low current Townsend discharges allow a better understanding of various excitation mechanisms, including excitation by heavy particles and fast neutrals [41].

Assessing the accuracy of the measured coefficients is as important as the measured values themselves. Measurements obtained from a single experiment can only be evaluated with respect to their precision (which is related to the measurement scatter) but not with respect to their accuracy (i.e. how well the measurements represent the true physical values). An estimation of the measurement accuracy can only be done via a detailed comparison with other measurements or with simulations. Such comparisons require detailed knowledge of the experimental conditions and data acquisition procedures for measurements (respectively simulation settings and underlying assumptions for simulations), in order to identify the cause of possible differences.

In this work, a comparison of measurements of electron transport coefficients in CO_2 by two state-of-the-art experimental setups working under conceptually different principles and operating conditions, and using different data acquisition methods is presented. The transport coefficients investigated are the bulk drift velocity, W, the longitudinal component of the bulk diffusion tensor, D_{L}, the effective ionization frequency, ν_{eff}, and the effective ionization coefficient, α_{eff}. One

of these setups is a 'scanning' drift tube apparatus [30], operating under TOF conditions, where a given electrode separation is scanned over, i.e. one measurement consists of a series of measurements at gap distances between a given minimum and maximum value, thus enabling the determination of the whole spatio-temporal distribution of the electron number density, $n(x,t)$. The other experimental system [36, 37] works under PT conditions, where for a given point in the parameter space, (p,U,L), the displacement current from the electrons as well as the ions is measured. Here p is the pressure, U is the applied voltage and L is the electrode separation, which determine the reduced electric field (E/N) value. By integrating the known analytic formula for $n(x,t)$ (see section 2.2), the same transport coefficients can be determined as in case of the TOF system, thus enabling a direct comparison of two different techniques aiming to reach the same goal. To our knowledge, such a direct comparison has not yet been conducted for the experiments currently in active use. Thus, one of the main objectives of the present paper is to make comparisons between the two experimental systems using the measurements of electron transport coefficients in CO_2. This will allow us to assess the advantages and disadvantages of these two experimental systems, their accuracy and limits of applicability. The manuscript is structured as follows: In section 2 the experimental apparatuses and the related data acquisition methods are described in detail (in sections 2.1 and 2.2, respectively, for the TOF and PT setups). A comparison of the two approaches is given in section 2.3. The experimental results are presented in section 3 and discussed in section 4 and finally, conclusions are drawn.

2. Description and comparison of the experimental systems and data acquisition.

Below, in sections 2.1 and 2.2 we provide a detailed description of both experimental setups and the specific data acquisition methods used. In section 2.3 a comparison of the two techniques is given.

2.1. The time of flight experiment

2.1.1. Description of the experimental setup. TOF experiment is based on a 'scanning' drift tube apparatus, which has been presented in [30]. This apparatus has already been applied to measure transport coefficients of electrons in various gases: argon, synthetic air, methane, deuterium [42], carbon dioxide [43], acetylene (C_2H_2), ethylene (C_2H_4) and ethane (C_2H_6) [44]. The simplified scheme of the experimental apparatus is shown in figure 1.

The drift cell is situated in a stainless steel vacuum chamber. The chamber is evacuated by a turbomolecular pump coupled to a rotary pump to a pressure of $\approx 1 \times 10^{-5}$ Pa. The pressure of the gases used inside the chamber is measured by a capacitive gauge (Pfeiffer CMR 362). The experiments have been conducted with a continuous slow ($\sim$ sccm) flow of the gas. The pressure was varied as a function of E/N (between 300 Pa (at the lowest E/N) to 20 Pa (at the highest E/N)) in

order to optimize the measured current of the drift cell, while paying attention that the applied voltage remains below the breakdown threshold over the whole range of the electrode distances covered during the scanning process.

Ultraviolet light pulses of a frequency-quadrupled diode-pumped YAG laser enter the chamber with a pulse duration of 5 ns FWHM and a repetition rate of $\sim$3 kHz via a feed-through with a quartz window, traverse the grounded electrode via a hole with a diameter of 5 mm and reach the surface of a Mg disk of 5 mm diameter and 4 mm thickness, used as a photoemitter. The energy of a single pulse is 1.7 μJ (at $\lambda = 266$ nm). The Mg disk is embedded inside the cathode of the stainless steel drift cell, which is 105 mm in diameter. The detector facing the cathode at a distance L_1 consists of a grounded nickel mesh with $T = 88\%$ 'geometric' transmission and 45 lines/inch density (type MN17, manufactured by Precision Eforming LLC) and a stainless steel collector electrode that is positioned at $L_2 = L_1 + 1$ mm, i.e. 1 mm above the mesh.

Electrons generated by the laser pulses reaching the Mg disk move towards the collector under the influence of an accelerating DC voltage applied to the cathode by a BK Precision 9185B power supply. The voltage is adjusted according to the required fixed E/N value for the given experiment and the actual gap distance (L_1) during the scanning process. The current of the detector system is generated by the moving electrons within the mesh-collector gap. The collector current is amplified by a high speed current amplifier (type Femto HCA-400 M) connected to the collector, with a virtually grounded input, and is recorded by a digital oscilloscope (type Picoscope 6403B) with 0.8 ns time resolution. Data collection is triggered by a photodiode that senses the laser light pulses. Due to the low light pulse energy an averaging over typically 20 000 to 150 000 pulses is required. The experiment is fully controlled by a LabView software.

During the measurements, current traces are recorded for different values of the gap length (L_1). The mesh and the collector are moved together by a step motor connected to a micrometer screw mounted via a vacuum feedthrough to the vacuum chamber. The distance between the mesh and the cathode can be varied within a range of $L_1 = 7.8...58.3$ mm. Within this range 53 different gap distances are scanned over in the experiments reported here. The measurements have been carried out at a lab temperature of $T = 20 \pm 2$ °C.

Our apparatus performs the best at high E/N conditions. At low E/N we have observed low signal levels, which most likely originate from a decreasing 'escape factor' of the electrons from the cathode. It has been found [64], that at such conditions many of the electrons emitted from the cathode are backscattered and absorbed there after a few gas phase elastic collisions. This effect can significantly reduce the emission efficiency of the cathode. At higher E/N, where inelastic collisions also occur, these electrons cannot move back to the cathode and the 'escape factor' approaches a value of 1.

2.1.2. Data acquisition. The measured displacement current at the collector is proportional to the flux of the electrons
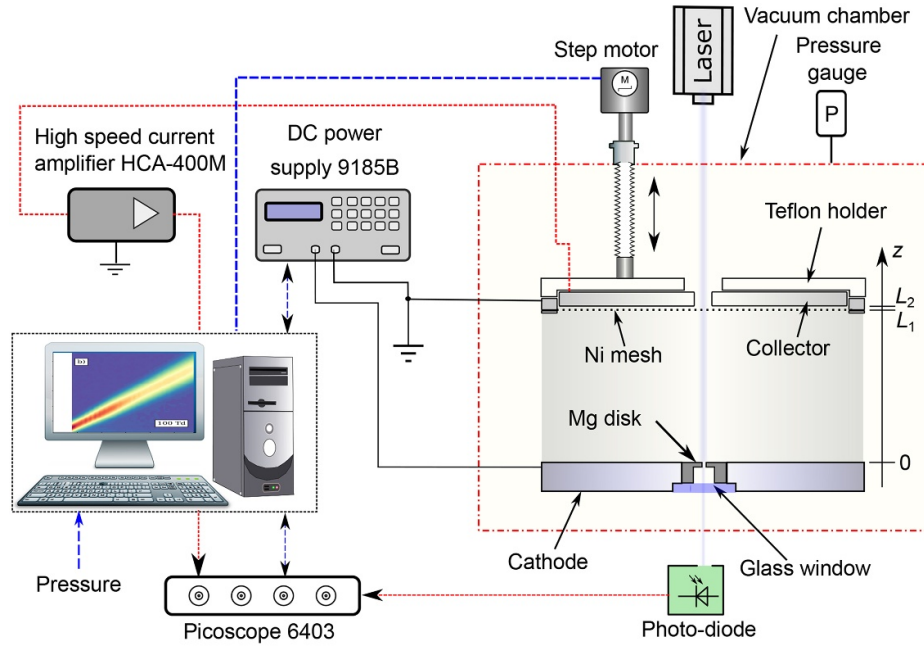
Figure 1. Schematic of the TOF system.

that enter the mesh-collector gap. Under hydrodynamic conditions, i.e. when electrons reach a stationary (local equilibrium) state where the (one particle) electron velocity distribution function, $f(\mathbf{v}, \mathbf{r}, t)$ has lost memory of its initial state and all space-time dependence is expressible through linear functionals of the electron number density, $n_e(\mathbf{r}, t)$, which means, that the macroscopic (transport) parameters of the swarm are space- and time-independent, the electron flux consists of two terms: the advective and diffusive component (assuming that higher spatial gradients of the electron density are negligible) [33]. The advective component is proportional to the electron density, where the proportionality factor is the flux drift velocity, and the diffusive component equals the flux diffusion tensor times the electron number density gradient [67].

Using Ramo's theorem [68, 69], it can be shown that for the experimental conditions considered in the present case, the contribution of the diffusive component to the current is negligible compared to the contribution of the advective component, except in the early stage of the swarm development when the spatial gradients of the electron number density are more significant. Therefore, we can assume, that the measured current is proportional to the electron number density, which, for a spatially infinite one dimensional (1D) system has the following analytic form [70]:

$$n_e(x, t) = \frac{n_0}{(4\pi D_{\mathrm{L}} t)^{1/2}} \exp\left[\nu_{\mathrm{eff}} t - \frac{(x - Wt)^2}{4 D_{\mathrm{L}} t} \right]. \quad (3)$$

This formula is the solution of the spatially one dimensional diffusion equation and describes a Gaussian pulse in infinite space drifting in the x-direction with bulk drift velocity, W, and diffusing with respect to the centre-of-mass with the longitudinal component of the bulk diffusion tensor, D_{L}.

Furthermore, n_0 is the electron number density at the initial point (i.e. $x = 0$, $t = 0$), and ν_{eff} is the effective ionization frequency (that is the difference of the ionization frequency and the attachment frequency). These transport coefficients, i.e. W, D_{L} and ν_{eff} are obtained by fitting equation (3) to the results of the measurements, the so-called 'swarm maps'. In the experiments we record current traces, i.e. the current signal generated by electrons reaching the collector at a given gap distance, averaged over many laser pulses. A swarm map is a collection of such current traces at different gap length values (see figure 2). From these transport coefficients the ionization coefficient, α_{eff}, can also be determined by applying the relation [67]:

$$\frac{1}{\alpha_{\mathrm{eff}}} = \frac{W}{2 \nu_{\mathrm{eff}}} + \frac{\nu_{\mathrm{eff}}}{|\nu_{\mathrm{eff}}|} \sqrt{\left(\frac{W}{2 \nu_{\mathrm{eff}}} \right)^2 - \frac{D_{\mathrm{L}}}{\nu_{\mathrm{eff}}}}. \quad (4)$$

The assumption that the measured signal is proportional to the electron number density (with the analytic form of (3)) is an approximation, because the detection sensitivity to the 'incoming' electrons i.e. those entering the mesh-collector gap was found to depend on the gas pressure and the collision cross sections, which both influence the mean free path of the electrons [71]. That is, a variation of the energy distribution function at different positions within the swarm (i.e. along the x-direction) may result in a distortion of the detected signal, which will then deviate from the analytical formula used to obtain the transport coefficients.

The deviation caused by this effect can be quantified by the simulation of the electrons motion in the experimental system, including the detector region. From such a simulation, one can derive the time-dependent response of the detector to the electron cloud at the same conditions as in the experiment (i.e. at the same pressure, E/N, and gap length L_1). When this
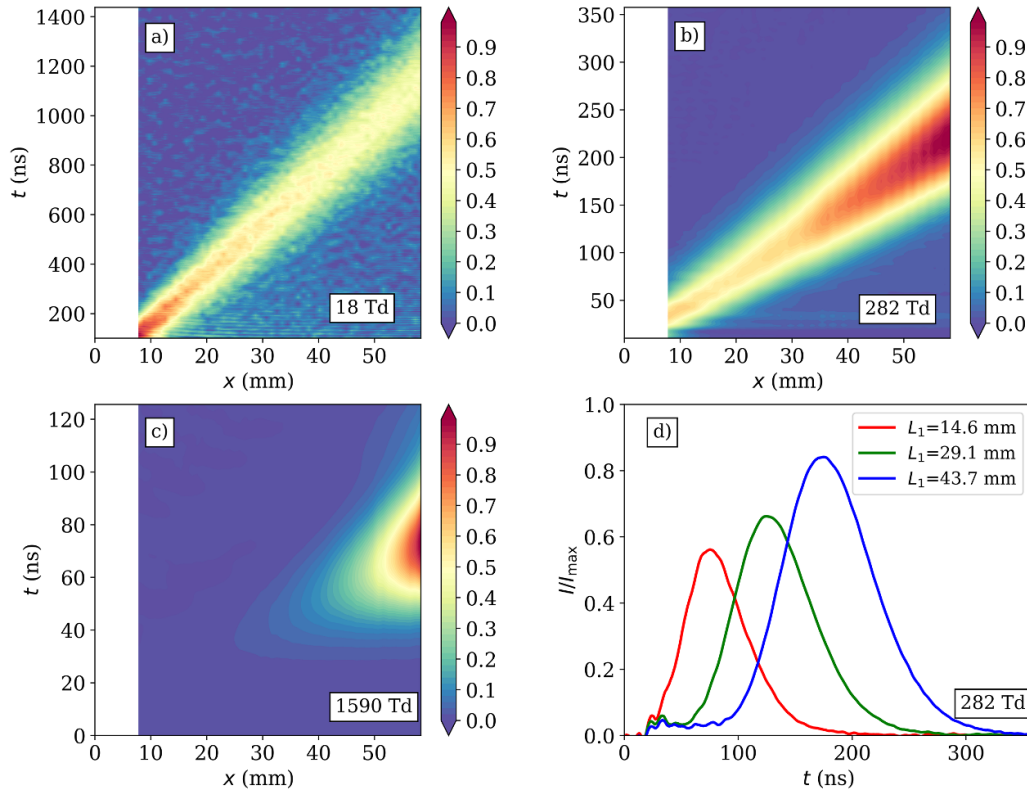
Figure 2. Measured and normalized swarm maps for different values of E/N in CO_2 (a)–(c), together with vertical cuts of (b) which are the measured current traces at the gap distances given in the legend (d).

procedure is accomplished for a sequence of gap length values, a simulated swarm map can be constructed. Applying the same fitting procedure as described above for the experimental data, a new set of transport coefficients can be calculated. Now, if some kind of 'reference' transport coefficients are known, the error created by the experimental method and related assumptions in the data analysis can readily be quantified. These 'reference' transport coefficients can be obtained from independent kinetic computations, based on either the solution of the Boltzmann equation or on Monte Carlo simulation, based on cross section set for the electrons' reactions in the given gas. For this purpose, we use the cross section set of Hayashi [45]. The result of the comparison of the transport coefficients obtained from the fitting of the simulated swarm maps and the 'reference' transport coefficients is a correction factor at the given p and E/N. Repeating the above procedure for all the experimental parameter settings yields corrections factors for all the experimental conditions. (We note that as the same cross section set is used in the system's simulation and in the computation of the 'reference' transport coefficients, any uncertainties in the cross sections vanish in first order.) Applying the correction factors to the experimental data yields 'Corrected' values for the measured transport coefficients which are expected to be free from the effects of the assumptions in the fitting procedure.

A low correction factor indicates that the fitting procedure using equation (3) is correct, whereas higher values indicate that this assumption cannot be made for the given conditions. Figure 3 shows the deviations between the simulation of the

experimental system and the kinetic swarm calculations. In case of the bulk drift velocity, W (figure 3(a)), the deviation is within 5% for the whole E/N range, and thus the determination of this transport coefficient can be taken to be reliable. The same can be stated about the effective ionization frequency, ν_{eff} and the effective ionization coefficient, α_{eff} (figure 3(c) and (d), respectively), except for E/N-values between 100 Td and 200 Td, where the deviation rapidly grows with decreasing E/N-values. The situation is worse for the longitudinal component of the bulk diffusion tensor, D_L (figure 3(b)). Here, the deviation ranges between $\approx -25\%$ to $\approx 20\%$. The reason for this is, that this transport coefficient is determined by the spread of the measured signal, which is more susceptible to a deviation from the assumed functional form of equation (3), as the electron energy is inhomogeneous within the swarm (electrons with higher energies tend to be in the front of the swarm, while those with lower energies tend to 'fall behind'), thus the detection sensitivity will not be uniform for the whole swarm.

The uncertainty of the measured data originates from (i) the finite precision of the components of the experimental system (e.g. pressure gauge, power supply, setting of the electrode gap, etc), (ii) slightly varying external conditions (fluctuations of the laser light intensity during the course of the scanning process (typically taking 10–100 min), the gas pressure, the temperature of the laboratory, etc) and (iii) the finite duration of the laser pulses and the finite noise level and response time of the measurement apparatus (amplifiers, oscilloscope, etc) [42]. Our estimation of these results in an uncertainty for the drift velocity that is below 5%, for the longitudinal component

of the diffusion tensor of $\approx 25\%$. For the effective ionization frequency, the uncertainty at high *E/N* is estimated to be in the order of $\approx 15\%$, which rapidly increases, when this coefficient decays orders of magnitude towards low *E/N* values. The errorbars shown with our experimental data express these values (only for some measurement points the uncertainty from the fitting procedure exceeds this value) which results in the slightly bigger errorbars for these cases.

2.2. The pulsed Townsend experiment

2.2.1. Description of the experimental setup. The PT experiment has already been described in detail in previous works [36, 37], and has been used to obtain electron and ion swarm parameters in many fluorinated gases and gas mixtures [46–59] as well as in Ar, N_2, CO_2, O_2, N_2O and mixtures of those [36, 37, 60–63].

The schematic layout of the experimental apparatus can be seen in figure 4. The electrodes are encapsulated in a 100 L stainless-steel vessel. The pressure inside the vessel is measured using the capacitive diaphragm gauges Pfeiffer CMR364, CMR371 and CMR372 which have full scale values of 100 Pa, 10 kPa and 100 kPa respectively, as well as a full range gauge PKR261. The lab temperature is regulated at 21 °C, and the temperature is measured on the external surface of the vessel with a T-type thermocouple.

When the turbo pump is running, the pressure in the vessel is about 1×10^{-5} Pa. Before the measurements, the pipes connecting the gas bottles are first evacuated through the vessel, and then abundantly flushed with the gas(es) under use. Then, the vessel is evacuated again and the gate valve is closed. The pressure in the vessel just before filling the gas is about 1×10^{-3} Pa. After filling, the valves are closed and the experiment is performed under fixed gas conditions.

The electrodes used for this experiment have a Rogowski profile, and have a total diameter of 16.5 cm. A photocathode of 2.5 cm diameter is mounted at the center of the cathode. The photocathode is made of quartz coated with two metallic layers: a 10 nm magnesium layer, topped with a 5 nm palladium layer. The photocathode is illuminated from the back with a UV laser of type FQSS 266–200 from Crylas, with a wavelength of 266 nm, a pulse duration of 1.5 ns FWHM, a pulse energy of 200 μJ and a repetition rate of 20 Hz, which releases electrons from the metallic layer. The laser beam is expanded ('BE' in figure 4) to cover about 4 cm^2 of the photocathode surface. The laser intensity is automatically reduced with a linear attenuator if needed to keep the total charge of the electron avalanche below 10 pC.

The emitted electrons move towards the grounded electrode under the influence of a negative DC voltage applied to the cathode using a Heinzinger PNChp power supply (either PNChp 1500 or PNChp 60 000, depending on the voltage required). The electrode spacing can be adjusted with a precision of ± 10 μm by moving the grounded electrode with a Newport UTSPPV6 stepper motor. The displacement current is measured at the grounded electrode using a transimpedance amplifier HCA-400 M-5 K-C and a voltage amplifier DHPVA-200 from Femto, and a RTO 1024 oscilloscope. A capacitor of

2 nF and a resistor of 1 MΩ are inserted between the power supply and the cathode, in order to make sure that the capacitive charging current in the circuit is negligible compared to the current induced to the electrodes by the motion of electrons and ions. The signals are averaged over approx. 200 measurements to increase the signal-to-noise ratio.

To perform a series of measurements, the change of voltage, electrode spacing and pressure is automated. For the automatic change of pressure, the gas is initially filled to the highest measuring pressure, then the pressure is automatically decreased step-wise by opening the valve to the rotary vane pump.

2.2.2. Data acquisition. In the PT system, the motion of the charge carriers (electrons and ions) present throughout the gap is sensed directly via the induced displacement current which flows in the outer circuit. Since electron and ion mobilities differ by orders of magnitude, the measured current is analyzed on two different timescales, nanoseconds and microseconds. Hydrodynamic conditions are assumed during the transit time of charged species. Assuming perfectly absorbing electrodes, time- and space-independent transport coefficients allow us to relate the measured displacement current to their total number via Ramo's theorem [68]:

$$I(t) = \sum_k q_0 \frac{w_k}{L} N_k(t) = \sum_k q_0 \frac{w_k}{L} \int_0^L n_k(x,t)dx, \quad (5)$$

where N_k is the number of particles of species k, drifting at constant flux velocity w_k between the electrodes of distance L [67]. In the evaluation method used in this paper, ion species are distinguished as two distinct positive and negative ion swarms with respective mobilities. On the electronic timescale, these can reasonably be assumed motionless. Hence, the temporal evolution of the positive and negative ion densities depends solely on the electron density and on the ionization or attachment event frequencies during the transit of electrons. The total current can then be expressed in terms of the electron component using equation (5) as:

$$I_{\text{tot}}(t) = I_e(t) + I_{\text{ion}}(t) = I_e(t) + \left(\nu_i \frac{w_p}{w_e} + \nu_a \frac{w_n}{w_e}\right) \int_0^t I_e(t')dt',$$
$$(6)$$

where ν_i, ν_a are the ionization and attachment frequencies and w_p, w_n and w_e are the positive and negative ion, and electron flux velocities, respectively. These are all unknown parameters at this point. However, it is possible to evaluate the constant in front of the integral by estimating a time T from the measurements at nanosecond timescale for which the electron current is zero, i.e. when all electrons have reached the anode. The electron current is separated by solving iteratively equation (6) starting with $I_e^{(0)}(t) = I_{\text{tot}}(t)$ until the sequence $I_e^{(j)}(t)$ converges:

$$I_e^{(j)}(t) = I_{\text{tot}}(t) - \left(\frac{I_{\text{tot}}(T)}{\int_0^T I_e^{(j-1)}(t')dt'}\right) \int_0^t I_e^{(j-1)}(t')dt', \quad (7)$$

where at time T, $I_{\text{tot}}(T) = I_{\text{ion}}(T)$.

J. Phys. D: Appl. Phys. **54** (2021) 035202

M Vass *et al*
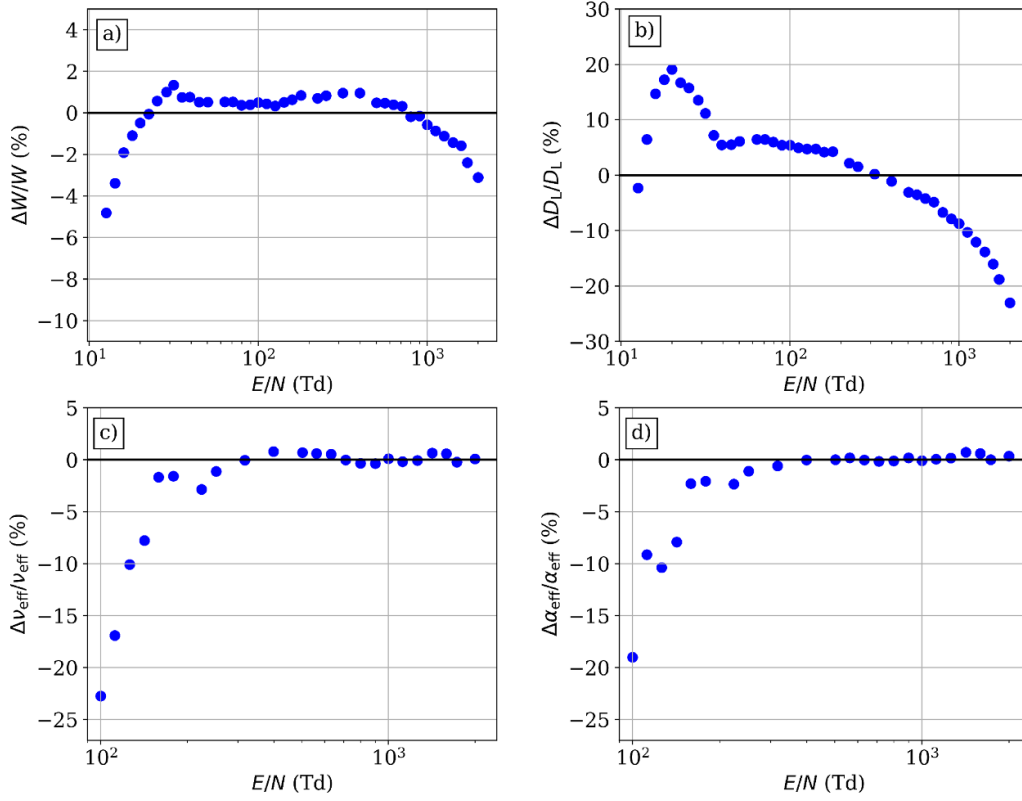
Figure 3. Deviations of the results between the swarm parameters obtained from the simulations of the experimental system (S) vs. the theoretical values (T), i.e. ($S - T$)/T for the bulk drift velocity (a), the longitudinal component of the diffusion tensor (b), the effective ionization frequency (c) and the effective ionization coefficient (d). Applying these correction factors to the experimental results (X_{exp}) leads to the set of 'Corrected' transport coefficients (X_{corr}) as $X_{corr} = \frac{X_{exp}}{1 + \frac{S-T}{T}} = \frac{T}{S} X_{exp}$.

Assuming that all electrons are emitted at $t = 0$ (i.e. no initial broadening of the electron cloud) the electron density is given by equation (3) and the electron current can be simply derived analytically as:

$$I_e(t) = \frac{q_0 N_e(0) w_e}{2\,L} \exp\left(\nu_{eff} t\right) \left(1 - \mathrm{erf}\left(\frac{W_e t - L}{\sqrt{4 D_L t}}\right)\right), \quad (8)$$

where the bulk drift velocity and longitudinal diffusion coefficients, W_e and D_L, as well as the effective ionization frequency $\nu_{eff} = \nu_i - \nu_a$ are obtained by fitting equation (8) to the extracted electron current waveforms of given E/N value. Strictly speaking, equation (8) is derived assuming the cathode is located at $-\infty$. An example of measured electron current in CO_2 at high E/N and its fit according to equation (8) is shown in figure 5(a).

The assumption of no initial broadening in equation (8) leads to an error (overestimation) when fitting the longitudinal diffusion coefficient ND_L. This error is negligible when the broadening of the electron swarm during the drift is much larger than the initial broadening σ_0, i.e. $\sqrt{2 D_L T_e} \gg \sigma_0$, where T_e is the electron transit time given by L/W_e. The condition $\sqrt{2 D_L T_e} \gg \sigma_0$ is fulfilled at sufficiently low pressure and sufficiently large electrode spacing. The amount by which ND_L is overestimated increases with increasing E/N because the drift time T_e decreases, and it also increases with increasing gas

pressure because D_L decreases. Consequently, the preferred values of ND_L are those obtained at the lowest available pressure. Figure 6(a) shows two electron currents measured in CO_2 at $E/N = 40$ Td, at two different pressures: 0.2 kPa and 60 kPa. It can be seen that the effect of the diffusion, i.e. the broadening of the signal, is much larger at 0.2 kPa than at 60 kPa. At 60 kPa, neglecting the initial broadening leads to a significant overestimation of the diffusion coefficient ND_L. Figure 6(b) shows the values of ND_L obtained at different pressures, and subject to an error because of neglecting the initial broadening. A clear increase of ND_L (and of its associated uncertainty) is visible with increasing pressure and with increasing E/N. Note that the error bars shown in figure 6(b) reflect the uncertainty on ND_L due to the fitting procedure and do not include the error due to neglecting the initial broadening.

In contrast to the diffusion coefficient ND_L, it is beneficial to measure the effective ionization coefficient ν_{eff} at the highest possible pressure, because the uncertainty of ν_{eff}/N is inversely proportional to the gas density N. In figure 6(a), the value of ν_{eff}/N can be read much more accurately at 60 kPa than at 0.2 kPa, where the negative slope of the current is barely visible. Therefore, the preferred values of ν_{eff}/N are those obtained at the highest available pressure.

Having extracted the electron transport coefficients, the positive and negative ion currents can be now derived

J. Phys. D: Appl. Phys. **54** (2021) 035202

M Vass *et al*
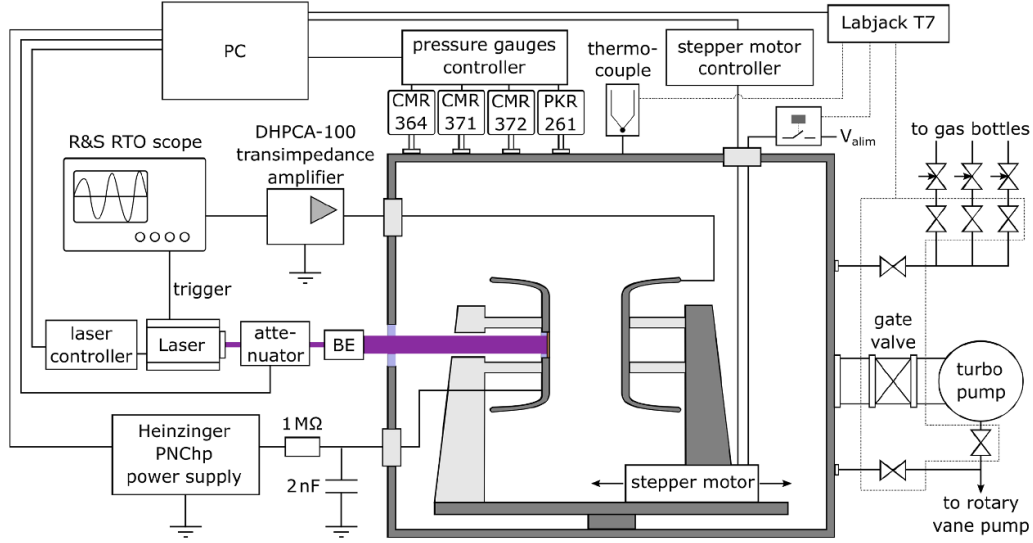
Figure 4. Schematic of the PT system.
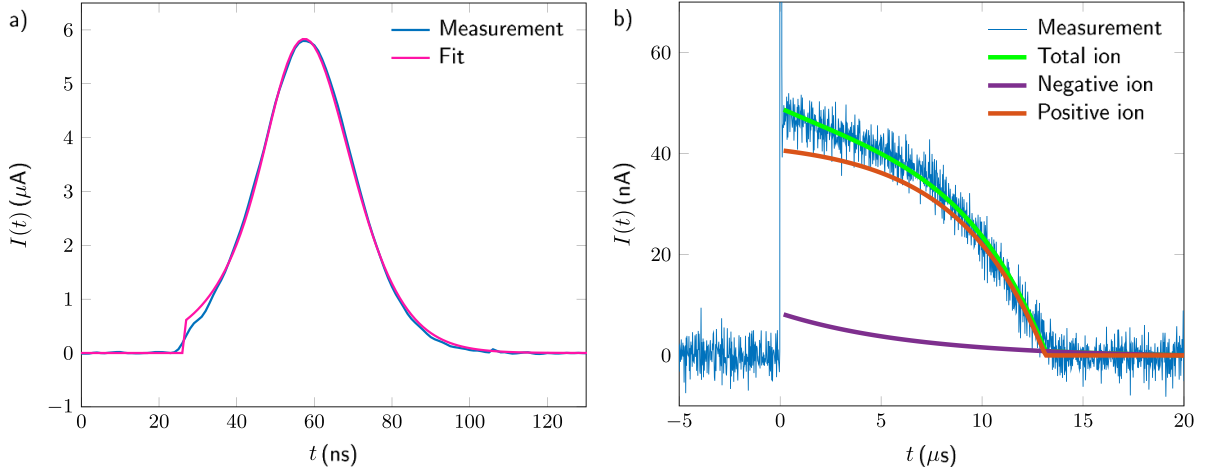
Figure 5. (a) Extracted electron current and fit according to equation (8). (b) Measured total current and calculated total, negative and positive ion components according to equation (9) in CO_2 at $E/N = 774$ Td, $p = 55$ Pa and electrode distance $L = 20$ mm.

for $t \geq T_e$:

$$I_p(t') = I_0 \frac{w_p}{w_e} \frac{\nu_i}{\nu_{eff}} \left(e^{\nu_{eff} T_e} - e^{\nu_{eff} \frac{T_e}{T_p} t'} \right) \quad \text{and}$$

$$I_n(t') = I_0 \frac{w_n}{w_e} \frac{\nu_a}{\nu_{eff}} \left(e^{\nu_{eff} T_e (1 - \frac{t'}{T_n})} - 1 \right), \quad (9)$$

where $t' = t - T_e$, $I_0 = \frac{q_0 N_e(0) w_e}{L}$ is the initial electron current and $T_n = L/W_n$ and $T_p = L/W_p$ the transit times of the negative and positive ion swarms. An example of calculated total, negative and positive ion currents is given in figure 5(b). The discussion of the ion transport properties is, however, not the topic of this work.

In the PT setup, the *E/N* values are set with an accuracy of $\pm 0.5\%$ over a wide range of pressures (0.01 Pa...100 kPa $\pm 0.15\%$), distances (11 mm...35 mm $\pm 10\,\mu$m) and voltages (7.5 V...60 kV $\pm 0.02\%$) taking also into account the uncertainty on the measured room temperature and the slight inhomogeneity of the applied electric field in between the electrodes (0.2%) [36]. In the evaluation of the effective ionization rate at a set of (U, L, p)-values, the main source of uncertainty is the noise on the signal. To increase the signal to noise ratio (SNR), the measurements are repeated a large number of times (200 to 400 repetitions for $20 \leq E/N \leq 1000$ Td and more than 1000 repetitions for $E/N \leq 20$ Td) and only the average signal is kept for the evaluation. In addition, the photocathodes are frequently renewed to maintain a number of initial electrons above 10^5. For the drift velocity and the longitudinal diffusion coefficient, an additional source of error is the limited bandwidth of the transimpedance and voltage amplifiers as well as the finite laser pulse length in the determination of the diffusion coefficient.

The high reproducibility of the measurements demonstrated in [36] allows a flexibility in choosing the appropriate range of operating conditions for which the uncertainty on the evaluated swarm parameters is the lowest as described above. To get an estimation on the accuracy of the measurement in

J. Phys. D: Appl. Phys. **54** (2021) 035202

M Vass *et al*
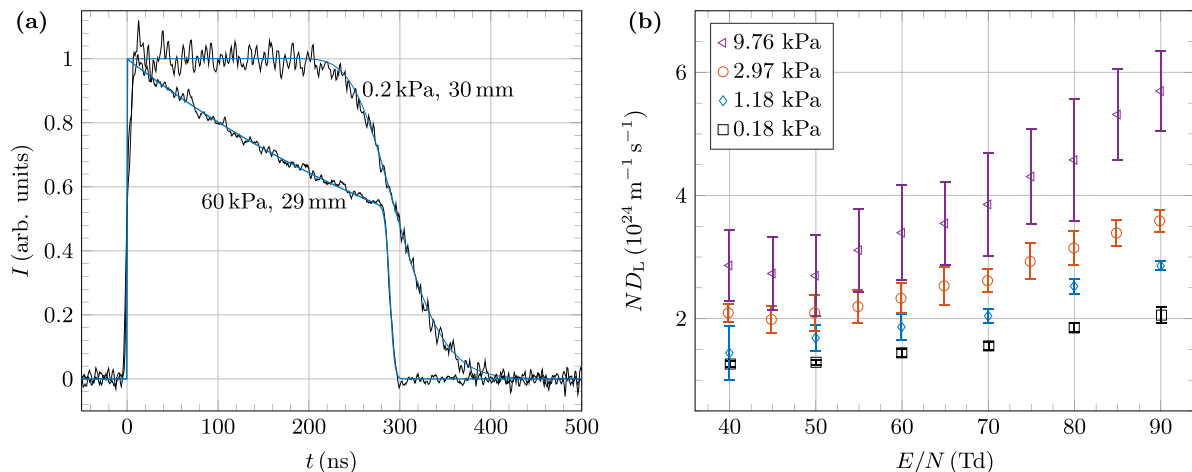
Figure 6. (a) Electron current in CO_2 at $E/N = 40$ Td, with an electrode spacing of about 30 mm, at two different pressures: 0.2 and 60 kPa. (b) Longitudinal electron diffusion coefficient derived from the measurements in CO_2 at different pressures (the vertical error bars reflect the uncertainty from the fitting procedure, they do not include the error due to neglecting the initial broadening of the swarm). According to the hydrodynamic approximation, the values of ND_L should be independent of pressure. Here, the values of ND_L are pressure-dependent, because neglecting the initial broadening of the swarm leads to overestimating ND_L by an amount increasing with pressure and with E/N. Therefore, the most reliable values are those obtained at the lowest pressure, here 0.18 kPa.

addition to the precision, measurements at a single E/N-value are repeated for a large set of (U, L, p)-values. The standard deviation which derives from this is included in the evaluation of the errorbars and is the largest contributor for $20 < E/N < 500$ Td.

2.3. Comparison of the approaches

Some key differences and limitations of the two experimental systems are highlighted in this section. Most of the time, these limitations can be prevented in the experiment itself or overcome by advanced signal analysis when they are detected and their origin is known. Because of different design goals, the two setups typically operate at different experimental conditions and with different hardware:

- **electrode diameter:** The electrode diameter should be sufficient to ensure that all electrons are collected, taking into account the transverse diffusion.
- **operating pressure**: A sufficiently low operating pressure enables measurements at elevated E/N values because the electron multiplication is limited and does not lead to electrical breakdown. In contrast, the benefit of a high operating pressure is to obtain more precise values for the reaction rate coefficients, and to observe the drift ions, additionally to that of the electrons. By analyzing the ion current, different reaction rate coefficients can be distinguished, not only the effective ionization rate coefficient. The TOF setup was primarily designed to operate at low pressure, from a few 10 Pa to a few 100 Pa, whereas the PT was designed to operate from 1 kPa to 100 kPa. A set of measurements in the PT setup typically includes different pressures, so that the rate coefficients of two and three-body processes can be distinguished. At low pressure, the PT technique is limited by the physical condition that swarm-equilibration should

be much faster than the drift time of electrons through the cell. The PT setup is limited at high pressure to 100 kPa because the experiment was not designed to have internal over-atmospheric pressure. Regarding the TOF system, the response time of the data acquisition electronics and the finite duration of the laser pulses sets the limit of operation at low pressures, while the vanishing signal level (as discussed in section 2) limits the operation at high pressures.

- **laser power**: The pulse energy influences the number of initial electrons in both setups. The benefit of a low pulse energy (smaller number of initial electrons) is that it is easier to avoid problems such as space charge effects, breakdown and excessive production of excited species. The benefit of high pulse energy is that less averaging (repetitions) are needed to measure the current signals. Additionally, a high number of initial electrons is required in case of gases and conditions when strong electron attachment is present. The TOF and PT setups operate at the same laser wavelength of 266 nm but with different pulse energy: 1.7 μJ per pulse for the TOF setup and adjustable from 2 to 200 μJ per pulse for the PT setup. The higher repetition rate in the TOF setup makes it easier to perform averaging over a higher number of pulses, which is necessary at the lower pulse energy of this system.
- **laser pulse length**: In both data acquisition methods the finite duration of the laser pulses is neglected. In reality, this finite duration (the time-dependent intensity during the pulse) extends the spatial size of the electron cloud, with respect to an 'ideal' cloud shape that belongs to an instantaneous emission of the electrons, of which the mathematical form (3) is assumed in the data analysis in both systems. The finite duration of laser pulses of 1.5 and 5 ns, respectively, for the PT and TOF setups, is however, short compared to the transport time scales that are typically in the order of $\sim$100–1000 ns (see figures 2 and 6). For the

TOF measurements, the possible effects of the broadening of the electron cloud has to be kept in mind at high *E/N* and low pressure conditions. For the PT setup, in turn, the effect of initial broadening is particularly noticeable in the evaluation of the diffusion coefficient at low electrode separation distance and higher pressure, as mentioned above in section 2.2.2.

Additionally, the two setups address differently the physical limitations of the measurements:

- **Non-hydrodynamic region**: A certain time/drift length is needed for the photoelectrons emitted from the cathode to reach the steady-state energy distribution. During this equilibration time / space, the transport parameters are not defined and there is no straightforward interpretation for the measured current. As such effects are not accounted for by the mathematical form of the spatio-temporal density distribution of the electron cloud used in the data acquisition for both systems, working under conditions that ensure a short equilibration time with respect to the transport time scale/short equilibration length with respect to the electrode gap is strongly preferred. In the swarm maps obtained from the TOF measurements non-equilibrium behavior can directly be observed [71] and excluded from the analysis. In the PT setup, in turn, this effect can neither be directly observed nor excluded. As the scanning TOF system has a minimum electrode gap defined by its construction the most sensitive region cannot be observed. Therefore, attention has to be paid in both experiments to avoid conditions with excessive equilibration time / length for the swarms. In general, non-equilibrium effects are most critical in atomic gases and at *E/N* values of typically few times 10 Td. In molecular gases the effect is less pronounced. Due to the pressure × length scaling, operation at high pressures is advantageous at low *E/N*, which favours the use of the PT system, which is more suited to work under such conditions.

- **Space charge effects**: In both setups, accumulation of space charges may distort the (otherwise) constant electric field over the electrode gap, thus it is to be avoided. The TOF setup operates with a lower number of initial electrons because of the low laser pulse energy and is thus less susceptible to this problem. In the PT setup, space charge effects are mitigated by illuminating a large area on the photocathode (4 cm^2), which lowers the electron density. Additionally, the total charge of the avalanches is actively regulated below 10 pC by attenuating the laser light between 1% and 100%. This 10 pC charge is an absolute maximum, and the vast majority of measurements have a much lower charge. This total charge corresponds to approximately 6×10^7 charged particles, which include not only electrons, but also anions and cations produced. Therefore, the number of electrons is significantly below Meek's criterion of 10^8 electrons for the avalanche to streamer transition [65]. Decreasing further the total charge is feasible, but a compromise is needed between avoiding space-charge effects and maintaining a sufficient SNR ratio [62].

- **Presence of excited species**: Both setups make efforts to limit the production and accumulation of excited molecules and dissociation products, which could affect the transport parameters by de facto changing the gas composition. The TOF experiment is pulsed at 3 kHz but a constant gas flow is maintained to avoid the accumulation of excited species. In contrast to this, the PT experiment uses no gas flow but operates with a slower repetition rate of 20 Hz.

- **Impact of ion collisional processes**: In the present study, both the TOF and PT analysis in CO_2 assume the presence of electron attachment and electron impact ionization only. Generally, this assumption should not be taken for granted. In some cases, ion collisional processes, such as an electron detachment from negative ions and ion conversion processes can significantly affect the measured current [62, 66]. The rates of ion collisional processes depend on the collision frequency for collisions between ions and neutral molecules, on the electric field strength and on the gas pressure. In conditions where these processes are significant, the numerical procedures used to analyse the current signals should be adapted to include their effects.

Additionally to all above-mentioned points, attention must be paid to unexpected measured current shapes in both experiments, as these could be indications of further limitations which were not identified, or operation outside the region of valid assumptions.

3. Results

In this section, results are presented for the transport coefficients (bulk drift velocity, longitudinal component of the bulk diffusion tensor, effective ionization rate coefficient and density reduced effective ionization coefficient) over a wide range of *E/N*-values: 8 Td $\leq$ *E/N* $\leq$ 2000 Td for *W*, 10 Td $\leq$ *E/N* $\leq$ 2000 Td for ND_L, 3 Td $\leq$ *E/N* $\leq$ 2000 Td for ν_{eff}/N and 80 Td $\leq$ *E/N* $\leq$ 2000 Td for α_{eff}/N. The data obtained by the two experimental systems are compared.

Figures 7 shows the bulk drift velocity, *W* for the PT experiment as well as for the TOF experiment along with the corrected values of the latter, whereby the correction method was carried out as described in section 2.1.2 (a), and their comparison to other experimental data (b). For the bulk drift velocity, this correction amounts to a few percents. The datasets from the two systems for the bulk drift velocity have very good agreement (within $\approx$5 %) over the whole overlapping *E/N* range.

For the PT system, each data point corresponds to the average over 2 to 8 (U, L, p)-values and the data set extends as low as 8 Td, below which the low SNR prevents a precise evaluation of the drift velocity, and as high as 1040 Td. The TOF-experiment provides high-precision data (within a few percents) at higher *E/N*-values (up to 2000 Td) and as low as 12 Td. Both methods give very precise results, i.e. they scatter within percents. As for the comparison with other experimental results, our data agrees very well with the works of the other authors listed above, except for Schlumbohm [74], who

J. Phys. D: Appl. Phys. **54** (2021) 035202

M Vass *et al*
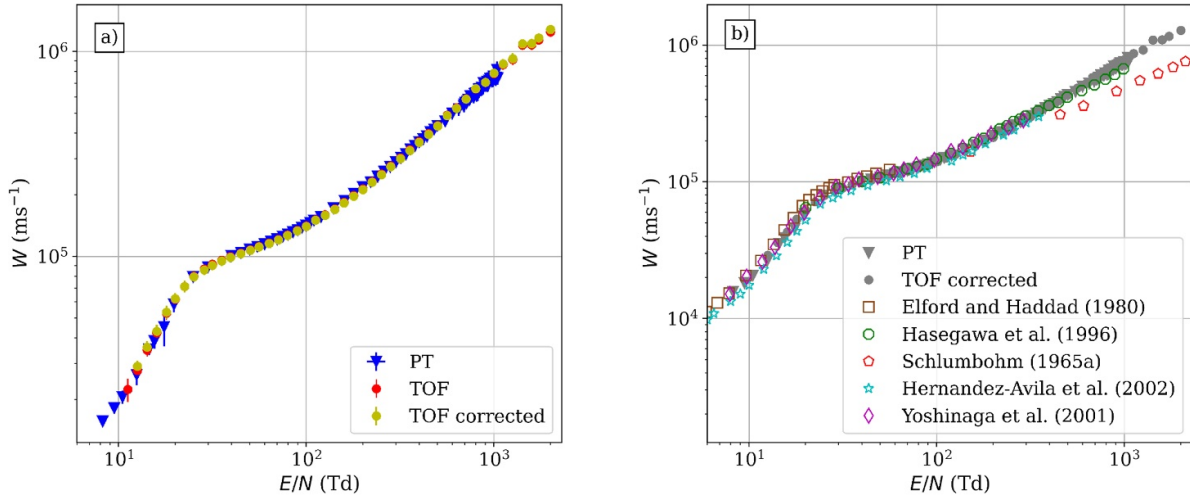
Figure 7. Comparison of the bulk drift velocity values (*W*) obtained by the two different experimental setups (a) and comparison of these values to other experimental data (b): Elford and Haddad [72], Hasegawa *et al* [73], Schlumbohm [74], Hernandez-Ávila *et al* [75], Yoshinaga *et al* [76]. For the determination procedure of the corrected experimental values in case of the TOF experiment in panel (a), see section 2.1.2. For most data points, error bars are smaller than the respective symbols.
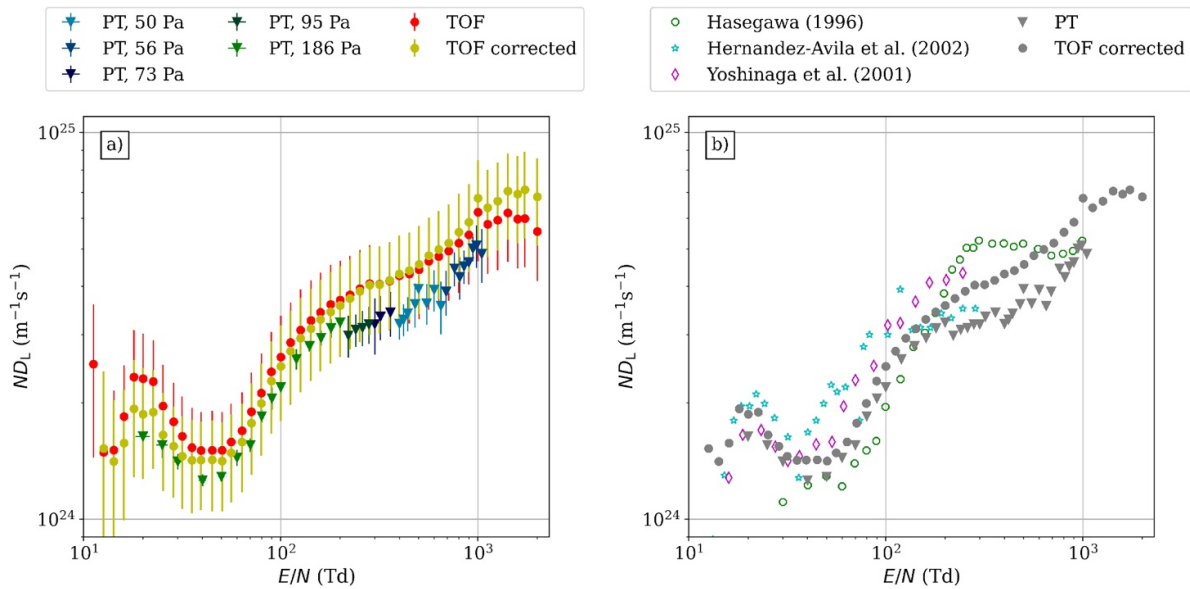
Figure 8. Comparison of the measured values of the longitudinal component of the bulk diffusion tensor (ND_L) obtained by the two experimental setups (a) and their comparison to other experimental data (b): Hasegawa *et al* [73], Hernandez-Ávila *et al* [75], Yoshinaga *et al* [76]. In the TOF experiment the pressure ranged between 20 Pa (at the highest *E/N*) to 300 Pa (at the lowest *E/N*). The operating pressures of the PT experiment are indicated in the legend.

also used a PT-method to obtain transport coefficients: in this case there is an increasing deviation with increasing *E/N*.

Figure 8 shows the longitudinal component of the bulk diffusion tensor, ND_L. In panel (a) the two systems show a generally good agreement as the error margin of both datasets overlap. Accordingly to section 2.2.2, for each *E/N*-value, the result obtained with the PT system in the lowest gas-pressure is kept and given here. The discrepancies between the sets of different pressures is clearly visible in figure 8 and the scatter of the results seems to be enhanced with increasing *E/N*. The TOF results have a high uncertainty over the measured

E/N range and increases significantly below 20 Td (as big as 100 % in some cases), therefore the determination of this transport coefficient is not reliable at such low *E/N* values in the TOF system. The TOF system has a wider range of measurements, i.e. its highest *E/N* value is 2000 Td . Between 10 Td and 1040 Td , the ND_L values obtained by the PT system are smaller than that of the TOF system, but the two datasets show a similar trend, in particular in the range between 20 Td and 200 Td. Considering other experimental data shown in figure 8(b), there is a reasonably good agreement between our datasets and previous measurements, especially at low and
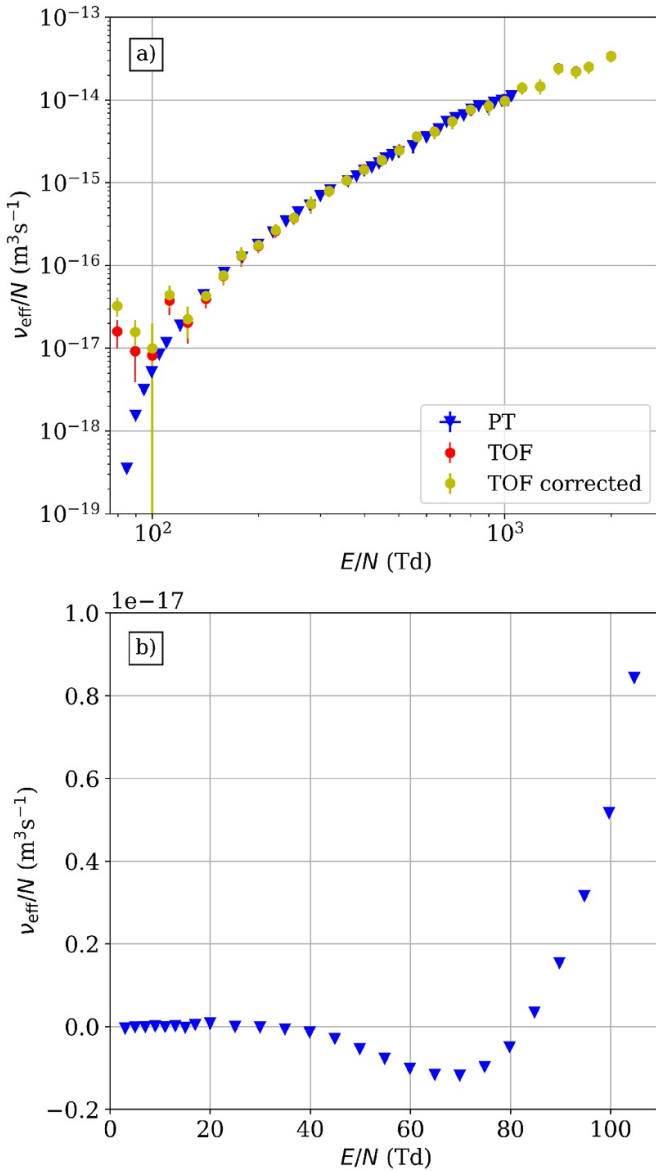
Figure 9. (a) Comparison of the effective ionization rate coefficient (ν_{eff}/N) obtained by the two experimental setups. (b) Effective ionization rate coefficient at low E/N values obtained from the PT experiment. Note the negative values that indicate the dominance of electron attachment over ionization.

intermediate (20 Td $\leq E/N \leq$ 200 Td) E/N-values. Furthermore, given the higher uncertainty of the TOF-system, the results of previous measurements are all within the uncertainty range of the TOF-system.

Figures 9 and 10 show the effective ionization rate coefficient, ν_{eff}/N, and the density reduced effective ionization coefficient, α_{eff}/N, respectively. As mentioned in section 2.2.2, the effective ionization rate coefficient obtained with the PT experiment at the highest gas pressure are shown here. The obtained results with the PT experiment have high precision over the whole E/N range, i.e. between 3 Td and 1040 Td. There is a good agreement between the two sets of data at intermediate and high E/N values, i.e. above 150 Td . Below 150

Td, the TOF system does not produce reliable results for the effective ionization rate coefficient due to the reduced SNR. As figure 9(b) reveals, electron attachment dominates ionization between $\sim$40 Td to $\sim$85 Td, as indicated by a negative ν_{eff} value. The strongest attachment occurs at around 70 Td and vanishes as $E/N \to 0$. Figure 10 (b) shows the comparison of the present measurements with available experimental data for α_{eff}/N. The datasets show very good agreement throughout the whole E/N-range, where data is available (100 Td $\leq E/N \leq$ 2000 Td).

3.1. Discussion

3.1.1. Bulk drift velocity and mobility.   Both setups derived the bulk drift velocity and electron mobility in CO_2 with a high precision. Furthermore, the excellent agreement of the results in the large overlapping region between 10 and 1000 Td confirms also the accuracy of the results. This implies that the physical assumptions underlying the analysis of both experiments are valid.

As an example, one of the physical limits of the PT setup is the non-equilibrium transport of electrons after their emission from the cathode. If the duration of the non equilibrium transport would not be negligible, the values of the bulk drift velocity would be affected. In contrast to this, the TOF experiment can exclude the non-equilibrium transport period from the analysis. The agreement of both results confirms the physical assumption of neglecting non-equilibrium transport under the present conditions in the PT setup.

3.1.2. Longitudinal component of the bulk diffusion tensor. In the PT system, the obtained values of the longitudinal component of the bulk diffusion tensor are subject to an error due to the underlying assumption of no initial broadening of the electron swarm. This error was minimized by selecting the measurements performed at the lowest pressure.

In the TOF system, the obtained values of longitudinal component of the bulk diffusion tensor have overall a large uncertainty. As discussed in section 2.1, the correction procedure of the TOF system yields a greater difference at high E/N values, as due to the higher energy of the electrons the electron swarm becomes more anisotropic and hence the detector sensitivity plays a major role. At low E/N values, the values of ND_L obtained in the TOF setup are subject to a larger uncertainty due to the reduced SNR. The reduced SNR affects the 'width' of the signal more than the position of the maximum value. Therefore, significant uncertainties result in case of the longitudinal component of the bulk diffusion tensor, which are not present in case of the bulk drift velocity.

Despite these issues in both experiments, a reasonable agreement of the results can be observed. It seems that in the case of the longitudinal component of the bulk diffusion tensor, the PT system yields slightly more accurate at low and intermediate values of the reduced electric field, whereas the
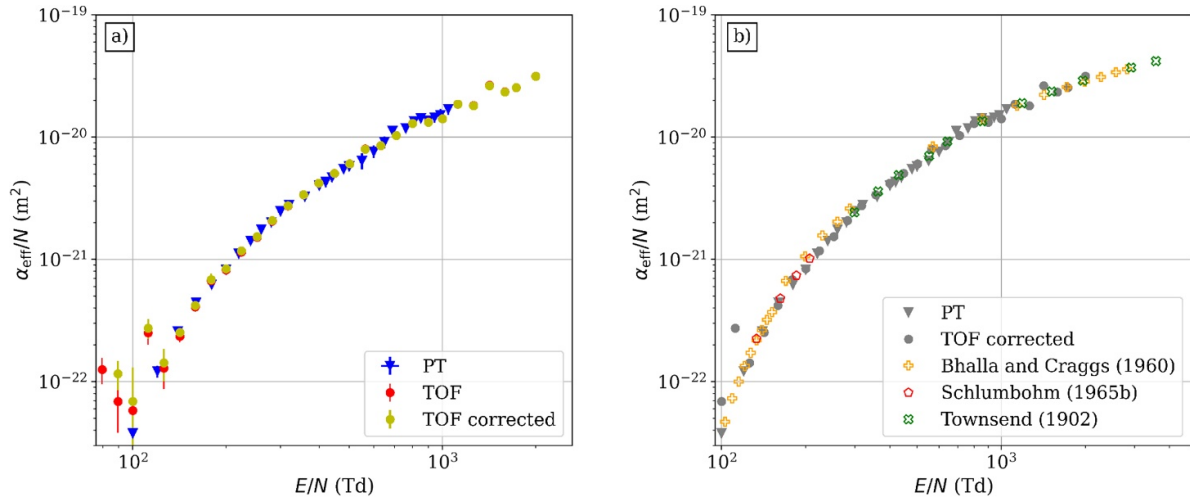
Figure 10. Comparison of the density reduced effective ionization coefficient values (α_{eff}/N) obtained by the two experimental setups (a) and their comparison to other experimental data (b): Bhalla and Craggs [77], Schlumbohm [78], and Townsend [79].

TOF system does the same at high values of *E/N*. In this sense, the two experimental setups complement each other.

3.1.3. Effective ionization rate coefficient and density reduced effective ionization coefficient. Above 150 Td , a good agreement is observed between the results of the two experiments, which confirms their accuracy. Below 150 Td the SNR in the TOF experiment is not sufficient to obtain reliable results for the effective ionization rate coefficient, and *a fortiori* for the density reduced effective ionization coefficient.

4. Conclusions

Electron rate and transport coefficients (bulk drift velocity, *W*, the longitudinal component of the bulk diffusion tensor, ND_{L}, effective ionization rate coefficient, ν_{eff}/N, and density reduced effective ionization coefficient, α_{eff}/N) have been measured in CO_2 by two independent experimental setups, which have been compared to each other and to previous independent measurements found in the literature. The experimental setups operate under the hydrodynamic conditions where one is a 'scanning' drift tube which belongs to a group of TOF experiments, whereas the other is a typical PT experiment. However, the data acquisition methods are different: in case of the TOF system, the whole spatio-temporal distribution of the density of an electron swarm for an unbound region, $n(x,t)$ (equation (3)) is fitted to the measured displacement current, whereas in the PT system its integral over the whole spatial domain of the drift tube is fitted to the measured time dependent displacement current. The TOF results undergo a correction procedure, where the sensitivity of the detector is taken into account by comparing Monte Carlo simulation results of the experimental setup and a spatially unbounded region [44]. Both experimental systems have already been used to obtain electron transport coefficients in different gases, which were compared to other, independently measured data.
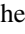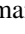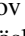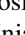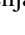
The results for the bulk drift velocity, *W*, showed almost perfect agreement (within $\approx$ 1–2%) over the whole reduced electric field (*E/N*) region, where both measurements have data (between 10 Td and 1000 Td). The TOF system has a wider range of reduced electric field where it can provide experimental data, up to 2000 Td. The comparison to previous measurements also showed a very good agreement except for Schlumbohm [74], where considerable deviation was observed at high *E/N*-values. The data obtained for the longitudinal component of the bulk diffusion tensor, ND_{L}, showed a generally good agreement, although the PT results are smaller than that of the TOF system over the whole *E/N* range. The PT and TOF setups both show a high repeatability of results. In the PT setup, to further test the accuracy of measurements, additional measurements are performed by varying pressure and distance as much a possible while keeping the same *E/N* ratio. The results differ more than the repeatability at a single condition would suggest, as was already observed in a previous work [36]. This shows that high repeatability is not sufficient to warranty high measurements accuracy. At low reduced electric field values the TOF system cannot produce accurate results, as due to the small SNR the 'width' of the signal cannot be properly detected and thus the fitting yields a high uncertainty. The comparison with other datasets yielded reasonably good agreement at low and intermediate *E/N*-values (between 20 Td and 200 Td). Regarding the effective ionization rate coefficient, ν_{eff}/N as well as the density reduced effective ionization coefficient, α_{eff}/N, the results above 100 Td agree within a few percents. Likewise, the agreement is very good between the present results and previous measurements. Below this threshold, the TOF system cannot produce reliable results, but it extends the *E/N* range in the direction of higher values, up to 2000 Td. Consequently, it can be stated, that the TOF system gives accurate results for a wide range of reduced electric field values, but at small values (below 10 Td for ND_{L} and 100 Td for ν_{eff}/N and α_{eff}/N), due to the small SNR, the data obtained are either not reliable

or have high uncertainties. For gases such as CO_2, which do not strongly attach electrons, the PT setup preferably operates below 1000 Td, whereas the TOF system's maximal value is 2000 Td. In the overlapping region, i.e. at intermediate E/N values the agreement of the data obtained by the two experimental systems indicate the correctness of the measured electron transport coefficients.

Acknowledgments

ORCID iDs

Máté Vass https://orcid.org/0000-0001-9865-4982
Eda Egüz https://orcid.org/0000-0001-6606-8102
Alise Chachereau https://orcid.org/0000-0003-1351-7669
Péter Hartmann https://orcid.org/0000-0003-3572-1310
Ihor Korolov https://orcid.org/0000-0003-2384-1243
Andreas Hösl https://orcid.org/0000-0001-8682-3750
Danko Bošnjaković https://orcid.org/0000-0002-2725-5287
Saša Dujko https://orcid.org/0000-0002-4544-9106
Zoltán Donkó https://orcid.org/0000-0003-1369-6150
Christian M Franck https://orcid.org/0000-0002-2201-7327

References

[1] Petrović Z L, Šuvakov M, Nikitović Ž, Dujko S and Šašić O *et al* 2007 *Plasma Sources Sci. Technol.* **16** S1
[2] Yu Q, Kong M, Liu T, Fei J and Zheng X *et al* 2012 *Plasma Chem. Plasma Process.* **32** 153–63
[3] Li R, Tang Q, Yin S and Sato T 2007 *J. Phys. D: Appl. Phys.* **40** 5187–91
[4] Li R, Tang Q, Yin S and Sato T 2007 *Appl. Phys. Lett.* **90** 131502
[5] Wang S, Zhang Y, Liu X and Wang X 2012 *Plasma Chem. Plasma Process.* **32** 979–89
[6] Fridman A 2008 *Plasma Chemistry* (New York: Cambridge University Press)
[7] Scarduelli C, Guella D, Ascenzi D and Tosi P 2011 *Plasma Processes Polym.* **8** 25–31
[8] De Bie C, Martens T, van Dijk J, Paulussen S and Verheyde B *et al* 2011 *Plasma Sources Sci. Technol.* **20** 024008
[9] Snoeckx R, Aerts R, Tu X and Bogaerts A 2013 *J. Phys. Chem. C* **117** 4957–70
[10] Fidalgo B, Dominguez A, Pis J and Menedez J 2008 *Int. J. Hydrogen Energy* **33** 4337–44
[11] Bo Z, Yan J, Li X, Chi Y and Cen K 2008 *Int. J. Hydrogen Energy* **33** 5545–53
[12] Bogaerts A, De Bie C, Snoeckx R and Kozák T 2017 *Plasma Processes Polym.* **14** 1600070
[13] Mei D, Zhu X, He Y, Yan J D and Tu X 2015 *Plasma Sources Sci. Technol* **24** 015011
[14] Ozkan A, Dufour T, Arnoult G, De Keyzer P and Bogaerts A *et al* 2015 *J. CO2 Util.* **9** 74
[15] Aerts R, Somers W and Bogaerts A 2015 *Chem. Sus. Chem.* **8** 702
[16] Ramakers M, Michielsen I, Aerts R, Meynen V and Bogaerts A 2015 *Plasma Process. Polym.* **12** 755
[17] Bongers W, Bouwmeester H, Wolf B, Peeters F and Welzel S *et al* 2017 *Plasma Processes Polym.* **14** 1600126
[18] Spencer L F and Gallimore A D 2013 *Plasma Sources Sci. Technol* **22** 015019
[19] Silva T, Britun N, Godfroid T and Snyders R 2014 *Plasma Sources Sci. Technol* **23** 025009
[20] Lee H and Sekiguchi H 2011 *J. Phys. D: Appl. Phys.* **44** 274008
[21] Tu X and Whitehead J C 2014 *Int. J. Hydrogen Energy* **39** 9658
[22] Liu J L, Park H W, Chung W J and Park D 2016 *Chem. Eng. J.* **285** 234–51
[23] Zhu B, Li X S, Shi C, Liu J L and Zhao T L *et al* 2012 *Int. J. Hydrogen Energy* **37** 4945
[24] Zhu B, Li X S, Liu J L, Zhu X and Zhu A M 2015 *Chem. Eng. J.* **264** 445
[25] Ruiz-Vargas G, Yousfi M and de Urquijo J 2010 *J. Phys. D: Appl. Phys.* **43** 455201
[26] Grofulović M, Alves L L and Guerra V 2016 *J. Phys. D: Appl. Phys.* **49** 395207
[27] Guerra V, Silva T, Ogloblina P, Grofulović M, Terraz L, da Silva M L, Pintassilgo C D, Alves L L and Guaitella O 2017 *Plasma Sources Sci. Technol.* **26** 11LT01
[28] Jawad E A and Jassim M K 2019 *Energy Procedia* **157** 117–27
[29] Attie D 2009 *Nucl. Instrum. Meth. Phys. Res.* A **598** 89–93
[30] Korolov I, Vass M, Bastykova N K and Donkó Z 2016 *Rev. Sci. Instrum.* **87** 063102
[31] Huxley L G H and Crompton R W 1974 *The Diffusion and Drift of Electrons in Gases* (New York: Wiley)
[32] Berghöfer T, Blümer J and Hörandel J R 2004 *Nucl. Instrum. Methods Phys.* A **525** 544
[33] Robson R E 1991 *Aust. J. Phys.* **44** 685
[34] Nakamura Y 1987 *J. Phys. D: Appl. Phys.* **20** 933–8
[35] Hasegawa H, Date H and Shimozuma M 2007 *J. Phys. D: Appl. Phys.* **40** 2495
[36] Haefliger P and Franck C M 2018 *Rev. Sci. Instrum.* **89** 023114
[37] Dahl D A, Teich T T and Franck C M 2012 *J. Phys. D: Appl. Phys.* **45** 485201
[38] Bekstein A, de Urquijo J, Ducasse O, Rodríguez-Luna J C and Juárez A M 2012 *J. Phys.: Conf. Series* vol 370 p 012006
[39] de Urquijo J, Arriaga C A, Cisneros C and Alvarez I 1999 *J. Phys. D: Appl. Phys.* **32** 41
[40] Tagashira H, Sakai Y and Sakamoto S 1977 *J. Phys. D: Appl. Phys.* **10** 1051
[41] Malović G, Strinić A, Zivanov S, Marić D and Petrović Z Lj 2003 *Plasma Sources Sci. Technol.* **12** S1
[42] Korolov I, Vass M and Donkó Z 2016 *J Phys. D: Appl. Phys.* **49** 415203
[43] Vass M, Korolov I, Loffhagen D, Pinhao N and Donkó Z 2017 *Plasma Sources Sci. Technol.* **26** 065007
[44] Pinhao N, Loffhagen D, Vass M, Hartmann P, Korolov I, Bošnjaković D, Dujko S and Donkó Z 2020 *Plasma Sources Sci. Technol.* **29** 045009
[45] Hayashi M 1990 Nonequilibrium Processes in Partially Ionized Gases *Electron Collision Cross Sections*

J. Phys. D: Appl. Phys. **54** (2021) 035202

M Vass *et al*

Determined From Beam and Swarm Data by Boltzmann Analysis (New York: Plenum) eds Capitelli M and Bardsley J N pp 333–40

[46] Hösl A, Pachin J, Egüz E, Chachereau A and Franck C M 2020 *IEEE Trans. Dielectr. Electr. Insul.* **27** 322–4

[47] Pachin J, Hösl A and Franck C M 2019 *J. Phs. D: Appl. Phys.* **52** 235204

[48] Hösl A, Chachereau A, Pachin J and Franck C M 2019 *J. Phys. D: Appl. Phys.* **52** 235201

[49] Egüz E A, Chachereau A, Hösl A and Franck C M 2019 *21st Int. Symp. on High Voltage Engineering* Springer, Cham pp 492–503

[50] Chachereau A, Hösl A and Franck C M 2018 *J. Phys. D: Appl. Phys.* **51** 335204

[51] Chachereau A and Franck C M 2018 *22nd Int. Conf. on Gas Discharges and Their Applications*

[52] Zawadzki M, Chachereau A, Kočišek J, Franck C M and Fedor J 2018 *J. Chem. Phys.* **149** 204305

[53] Hösl A, Pachin J, Chachereau A, Kornath A and Franck C M 2018 *J. Phys. D: Appl. Phys.* **52** 055203

[54] Chachereau A, Hösl A and Franck C M 2018 *J. Phys. D: Appl. Phys.* **51** 335204

[55] Chachereau A and Franck C M 2017 *20th Int. Symp. on High Voltage Engineering*

[56] Chachereau A and Franck C M 2017 *J. Phys. D: Appl. Phys.* **50** 445204

[57] Chachereau A and Franck C M 2016 *J. Phys. D: Appl. Phys.* **49** 375201

[58] Chachereau A, Fedor J, Janečková R, Kočišek J, Rabie M and Franck C M 2016 *Plasma Sources Sci. Technol.* **25** 045005

[59] Chachereau A and Franck C M 2015 *32nd Int. Conf. on Phenomena in Ionized Gases*

[60] Haefliger P and Franck C M 2019 *J. Phys. D: Appl. Phys.* **52** 025204

[61] Hösl A, Pachin J, Egüz E, Chachereau A and Franck C M 2019 *J. Phys. D: Appl. Phys.* **53** 135202

[62] Haefliger P, Hösl A and Franck C M 2018 *J. Phys. D: Appl. Phys.* **51** 355201

[63] Hösl A, Haefliger P and Franck C M 2017 *J. Phys. D: Appl. Phys.* **50** 485207

[64] Phelps A V and Petrovic Z L 1999 *Plasma Sources Sci. Technol.* **8** R21

[65] Meek J M 1940 *Phys. Rev.* **57** 722–8

[66] Wetzer J M and Wen C 1991 *J. Phys. D: Appl. Phys.* **24** 1964–73

[67] Blevin H A and Fletcher J 1984 *Aust. J. Phys.* **37** 593

[68] Ramo S 1939 *Proc. IRE* **27** 584

[69] Sirkis M D and Holonyak N J 1966 *Am. J. Phys.* **34** 943

[70] Kumar K, Skullerud H R and Robson R E 1980 *Aust. J. Phys.* **33** 343

[71] Donkó Z, Hartmann P, Korolov I, Jeges V, Bošnjaković D and Dujko S 2019 *Plasma Sources Sci. Technol.* **28** 095007

[72] Elford M T and Haddad G N 1980 *Aust. J. Phys* **33** 517–30

[73] Hasegawa H, Date H, Shimozuma M, Yoshida K and Tagashira H 1996 *J. Phys. D: Appl. Phys.* **29** 2664

[74] Schlumbohm H 1965 *Z. Phys.* **182** 317–27

[75] Hernández-Ávila J L, Basurto E and de Urquijo J 2002 *J. Phys. D: Appl. Phys.* **35** 2264–9

[76] Yoshinaga S-I, Nakamura Y and Hayashi M 2001 A measurement of temperature dependence of electron transport parameters in CO_2 *Proc. 25th ICPIG* vol 3 pp 285–6

[77] Bhalla M S and Craggs J D 1960 *Proc. Phys. Soc.* **76** 369

[78] Schlumbohm H 1965 *Z. Phys.* **184** 492–505

[79] Townsend J S 1902 *Philos. Mag.* **3** 557–76

Third-order transport coefficient tensor of charged-particle swarms in electric and magnetic fields

I. Simonović [1], D. Bošnjaković [1], Z. Lj. Petrović [2], P. Stokes [3], R. D. White,[3] and S. Dujko [1,*]

[1]*Institute of Physics, University of Belgrade, PO Box 68, 11080 Belgrade, Serbia*
[2]*Serbian Academy of Sciences and Arts, Knez Mihailova 35, 11001 Belgrade, Serbia*
[3]*College of Science and Engineering, James Cook University, 4810 Townsville, Australia*

Third-order transport coefficient tensor of charged-particle swarms in neutral gases in the presence of spatially uniform electric and magnetic fields is considered using a multiterm solution of Boltzmann's equation and Monte Carlo simulation technique. The structure of the third-order transport coefficient tensor and symmetries along its individual components in varying configurations of electric and magnetic fields are addressed using a group projector technique and through symmetry considerations of the Boltzmann equation. In addition, we focus upon the physical interpretation of the third-order transport coefficient tensor by considering the extended diffusion equation which incorporates the contribution of the third-order transport coefficients to the density profile of charged particles. Numerical calculations are carried out for electron and ion swarms for a range of model gases with the aim of establishing accurate benchmarks for third-order transport coefficients. The effects of ion to neutral-particle mass ratio are also examined. The errors of the two-term approximation for solving the Boltzmann equation and limitations of previous treatments of the high-order charged-particle transport properties are also highlighted.

I. INTRODUCTION

Studies of charged-particle swarms in neutral gases under the influence of electric and magnetic fields have applications in diverse areas of science and technology ranging from swarm experiments used to determine electron- and ion-neutral cross sections [1–5] to plasma processing technology [6–9], particle detectors used in high-energy physics [10,11], high-voltage technology [12], and positron physics [13,14]. These applications often require knowledge of swarm transport coefficients in the presence of the reduced electric and magnetic fields, E/n_0 and B/n_0, where E and B are the strengths of electric and magnetic fields, respectively, while n_0 is the neutral number density.

There is a large and growing literature dealing with the low-order transport coefficients, in which the variation of the reaction rate, drift velocity and diffusion tensor with E/n_0 (and B/n_0) for both the electrons and ions [15,16], and since recently even for positrons [14,17], are reported. In contrast, little is known about high-order transport coefficients, and limited data can be found in the literature, particularly for light charged particles such as electrons or positrons. The most obvious reason for this situation is the fact that the transport coefficients of higher-order have been difficult to measure, difficult to treat theoretically, and even more difficult to include in plasma models and thus were systematically ignored in the traditional interpretation of swarm experiments [1,3,4,16]. It was usually anticipated that swarm experiments are performed under conditions in which the

effects induced by transport coefficients of higher-order are negligible [18,19]. On the other hand, in the early 1970s, it was shown that some arrival-time spectra of ions in drift tubes significantly deviate from the ideal Gaussian pulses which are represented in terms of the lower-order transport coefficients only [20]. To our knowledge, there have been only a few attempts to measure the third-order transport coefficients, or to be more accurate to interpret the observed data in terms of the effects of higher order transport [21–24].

In spite of low interest in higher-order transport coefficients, it was pointed out by several specialists and research groups that the third-order transport coefficients for electrons are very sensitive to the rapid variations with the energy of the momentum transfer cross section as a function of the energy. For example, it was pointed out by Penetrante and Bardsley [18] almost 25 years ago that the third-order transport coefficients are at least as sensitive to the depth and position of the Ramsauer-Townsend minimum for elastic scattering of the electrons in noble gases as the lower-order transport coefficients, including the drift velocity and the characteristic energy. Along similar lines, it was pointed out by Vrhovac *et al.* [19] that the third-order transport coefficients would be very useful for a fine tuning of cross sections for inelastic collisions in the close vicinity of their thresholds. This implies that in principle one could use the higher-order transport coefficients as an additional input for enhancing the reliability of swarm-derived cross sections.

Early work on the higher-order transport coefficients of charged-particle swarms in electric fields has been presented by Whealton and Mason [25]. Using the analytical solution of Boltzmann's equation for the Maxwell model of interaction, they found that the third-order transport coefficient

tensor has seven nonzero elements of which three are independent. It was also shown that when the electric field is absent, all components of the third-order transport coefficient tensor vanish. Early studies of the third-order transport coefficients for ion swarms have been performed by Robson [26] and Larsen *et al.* [27] using Boltzmann's equation solutions.

In 1994, Penetrante and Bardsley [18] carried out the numerical solution of Boltzmann's equation for electrons in noble gases. Among many important points, they found that the third-order transport coefficients could be detected and resolved from the arrival time spectra of an electron swarm. A similar procedure for the determination of the transport coefficients of both the low and higher order was earlier proposed by Kondo and Tagashira [28]. Koutselos used molecular dynamics simulations and a three-temperature treatment of Boltzmann's equation with the aim of calculating the third-order transport coefficients for K^+ and Li^+ ions in noble gases [29–32].

Within the framework of the semiquantitative momentum transfer theory [2,33,34], Vrhovac *et al.* [19] have developed the method of calculations of the third-order transport coefficients for charged-particle swarms in the presence of an electric field only. The theory and the associated numerical code, were used to evaluate the third-order transport coefficients in noble gases, but only in the limit of the lower values of E/n_0 where electrons undergo elastic collisions only. The presented results were found to confirm the structure of the third-order transport coefficient tensor previously determined by Whealton and Mason [25].

Using the theory of arrival time spectra of an electron swarm initially developed by Kondo and Tagashira [28] and a Monte Carlo simulation technique, Kawaguchi and co-workers derived the relation between the longitudinal third-order transport coefficient and the α parameters (arrival-time spectra transport coefficients) [35,36]. Arrival-time spectra can be measured by a double-shutter drift tube clearly indicating that the longitudinal third-order transport coefficient can be obtained experimentally from the knowledge of the α parameters. Along similar lines, it was pointed out by Dujko *et al.* [37] that the conversion of hydrodynamic transport coefficients to those found in the steady-state Townsend experiment requires the knowledge of the third-order transport coefficients. Petrović and co-workers [38] have also used a Monte Carlo simulation technique to derive the longitudinal and transverse third-order transport coefficients in CH_4 over a broad range of the applied reduced electric fields. Among many important points, it was shown that the transverse third-order transport coefficient becomes negative in the same range of the applied electric fields where the negative differential conductivity occurs. The negativity of the third-order transport coefficients has also been observed for charged-particle transport in the presence of trapped (localized) states [39].

The signatures of the higher order transport processes have been observed in the numerical modeling of plasma discharges. For example, in the avalanche phase of the streamer development, the particle-in-cell Monte Carlo simulations have shown that a spatial profile of electrons may significantly deviate from an ideal Gaussian as predicted by fluid models based on the equation of continuity [40,41]. The clear signs

of high-order transport have been observed in the studies of the spatiotemporal development of the electron swarms [42,43]. The pronounced asymmetry in the spatial profiles of the electron swarm is particularly evident during the transient phase of relaxation, in the presence of strong nonconservative interactions [44,45], as well as for electron transport in noble gases with a Ramsauer-Townsend minimum under the influence of E/n_0's for which the mean electron energies are well below the first inelastic threshold. It is worth noting that a similar effect of nonconservative collisions is observed for positrons in gases where spatially dependent positronium formation skews the profile of the ensemble to the point that a Gaussian cannot be recognized and analyzed [46,47].

Furthermore, the transport coefficients of the third and higher orders are very often used to characterize fractional transport in a variety of situations, ranging from the trapping of charge carriers in local imperfections in semiconductors [48–51] to electron [52–54] and positronium [13,55,56] trapping in bubble states within liquids, and to transport in biological cells [57–60].

The above examples clearly show that a rigorous analysis of the third-order transport coefficients in the context of the contemporary kinetic theory of charged-particle swarms is a long overdue, and the present paper takes a few important steps in this direction. Besides being of intrinsic interest, we are also motivated by the following questions: What is the structure of the third-order transport coefficient tensor, and how can symmetries be identified in varying configurations of electric and magnetic fields? What is the physical interpretation of third-order transport coefficients, and what is their contribution to the spatial profile of the swarm in a typical time-of-flight experiment? Is this contribution more significant for light charged particles or for more massive ions? How does the magnetic field affect the third-order transport coefficients, and how large are the errors of the two-term approximation for solving the Boltzmann equation? In the present paper, we will try to address these issues.

This paper is organized as follows. In Sec. II we discuss the basic elements of the theory, the structure and physical interpretation of the third-order transport coefficient tensor, as well as our methods of calculations. In Sec. III we present results of calculations for a range of model gases. Where possible, the results of the Boltzmann equation analysis are compared with those calculated by the Monte Carlo method with the goal of establishing accurate benchmarks for third-order transport coefficients. As an example of our calculations in real gases, in Sec. III we discuss the behavior of the third-order transport coefficients for electron swarms in neon. Last, in Sec. IV we present our conclusions and future work recommendations.

II. THEORY: DEFINITIONS, SYMMETRIES, INTERPRETATIONS, AND METHODS OF CALCULATION

The main physical object of our study is a swarm of charged particles which moves through a background of neutral molecules in external electric and magnetic fields crossed at arbitrary angles. The density of charged particles is assumed to be sufficiently low so that the following properties apply: (1) charged-particle–charged-particle inter-

actions and space charge effects can be neglected, collisions of transported charged particles and excited or dissociated species are unlikely, (2) the motion of charged particles between collisions can be treated classically, and (3) the presence of charged particles does not perturb the background particles from thermal equilibrium.

All information on the drift, diffusion, and transport properties of higher order of charged particles is contained in the charged-particle phase-space distribution function $f(\boldsymbol{r}, \boldsymbol{c}, t)$, where $\boldsymbol{r}$ represents the spatial coordinate of a charged particle at time t, and $\boldsymbol{c}$ denotes its velocity. In the present work, the distribution function $f(\boldsymbol{r}, \boldsymbol{c}, t)$ is determined by solving Boltzmann's equation:

$$\frac{\partial f}{\partial t} + \boldsymbol{c} \cdot \frac{\partial f}{\partial \boldsymbol{r}} + \frac{q}{m}(\boldsymbol{E} + \boldsymbol{c} \times \boldsymbol{B}) \cdot \frac{\partial f}{\partial \boldsymbol{c}} = -J(f, f_0), \quad (1)$$

where q and m are the charge and mass of charged particles, respectively, while the electric and magnetic fields are assumed to be spatially homogeneous and of magnitudes E and B. In the present work we employ a coordinate system in which the z axis is defined by $\boldsymbol{E}$ while $\boldsymbol{B}$ lies in the y-z plane, making an angle ψ with respect to $\boldsymbol{E}$. The right-hand side of (1) denotes the linear charged-particle–neutral-particle collision operator, accounting for elastic and various types of inelastic collisions, including nonconservative collisions (the charged-particle number changing processes, such as ionization and attachment for electron swarms or positronium (Ps) formation and annihilation for positron swarms). The velocity distribution function of the background particles is denoted by f_0, and in the present study it is taken to be a stationary Maxwellian at fixed temperature. The explicit form of the collision operator can be found in Refs. [61,62].

A. Definition of the third-order transport coefficient tensor

The continuity of charged particles in the configuration space requires the following balance equation:

$$\frac{\partial n(\boldsymbol{r}, t)}{\partial t} + \boldsymbol{\nabla} \cdot \boldsymbol{\Gamma}(\boldsymbol{r}, t) = S(\boldsymbol{r}, t), \quad (2)$$

where

$$n(\boldsymbol{r}, t) = \int f(\boldsymbol{r}, \boldsymbol{c}, t) \, d\boldsymbol{c} \quad (3)$$

is the number density of charged particles while $\boldsymbol{\Gamma}(\boldsymbol{r}, t) = n\langle \boldsymbol{c} \rangle$ is the charged-particle flux given by

$$\Gamma(\mathbf{r}, t) = \int \mathbf{c} f(\mathbf{r}, \mathbf{c}, t) \, d\mathbf{c}. \quad (4)$$

The quantity $S(\boldsymbol{r}, t)$ is the production rate per unit volume per unit time arising from nonconservative processes. If the electron-impact ionization and electron attachment are the only nonconservative processes, then this property for electron swarms is given as

$$S(\mathbf{r}, t) = \int n_0 c [\sigma_i(\epsilon) - \sigma_a(\epsilon)] f(\mathbf{r}, \mathbf{c}, t) \, d\mathbf{c}, \quad (5)$$

where $\sigma_i(\epsilon)$ is the cross section for electron impact ionization while σ_a is the cross section for electron attachment. The equation of continuity (2) provides a direct link between experiment and theory, as in the majority of swarm experiments

the experimentally measurable quantities are usually charged-particle currents or charged-particle densities.

In the present work we follow the conventional definitions of transport coefficients and assume that the hydrodynamic conditions prevail, so that all space-time dependence is expressible through linear functionals of $n(\boldsymbol{r}, t)$. The hydrodynamic conditions are not satisfied near the boundaries of the system or in the vicinity of sources and/or sinks of charged particles, as well as under conditions in which electric and/or magnetic fields are not spatially homogeneous. The functional representation of the hydrodynamic approximation is the well-known density gradient expansion of the phase-space distribution function [63]:

$$f(\boldsymbol{r}, \boldsymbol{c}, t) = \sum_{k=0}^{\infty} \boldsymbol{f}^{(k)}(\boldsymbol{c}, t) \odot (-\nabla)^k n(\boldsymbol{r}, t), \quad (6)$$

where $\boldsymbol{f}^{(k)}(\boldsymbol{c}, t)$ are time-dependent tensors of rank k and $\odot$ denotes a k-fold scalar product. Performing equivalent representation of the flux $\boldsymbol{\Gamma}(\boldsymbol{r}, t)$ and source term $S(\boldsymbol{r}, t)$, we have

$$\boldsymbol{\Gamma}(\boldsymbol{r}, t) = \sum_{k=0}^{\infty} \boldsymbol{\Gamma}^{(k+1)}(t) \odot (-\nabla)^k n(\boldsymbol{r}, t), \quad (7)$$

$$S(\boldsymbol{r}, t) = \sum_{k=0}^{\infty} \boldsymbol{S}^{(k)}(t) \odot (-\nabla)^k n(\boldsymbol{r}, t), \quad (8)$$

where the superscripts (k) and $(k + 1)$ denote the ranks of the tensors. Equation (7) represents the flux-gradient relation and truncation of the expansion at $k = 2$ gives

$$\boldsymbol{\Gamma}(\boldsymbol{r}, t) = \boldsymbol{W} n(\boldsymbol{r}, t) - \boldsymbol{D} \odot \nabla n(\boldsymbol{r}, t) + \boldsymbol{Q} \odot (\nabla \otimes \nabla) n(\boldsymbol{r}, t), \quad (9)$$

where $\otimes$ is the tensor product, $\boldsymbol{W}$ and $\boldsymbol{D}$ are lower-order transport coefficients, the flux drift velocity and flux diffusion tensor, respectively, and $\boldsymbol{Q}$ defines the flux third-order transport coefficient tensor. The flux transport coefficients are given by

$$\mathbf{W} = \boldsymbol{\Gamma^{(1)}} = \int \mathbf{c} \boldsymbol{f}^{(1)}(\mathbf{c}, t) \, d\mathbf{c}, \quad (10)$$

$$\mathbf{D} = \boldsymbol{\Gamma^{(2)}} = \int \mathbf{c} \boldsymbol{f}^{(2)}(\mathbf{c}, t) \, d\mathbf{c}, \quad (11)$$

$$\mathbf{Q} = \boldsymbol{\Gamma^{(3)}} = \int \mathbf{c} \boldsymbol{f}^{(3)}(\mathbf{c}, t) \, d\mathbf{c}, \quad (12)$$

where $\boldsymbol{f}^{(1)}(\mathbf{c}, t)$, $\boldsymbol{f}^{(2)}(\mathbf{c}, t)$, and $\boldsymbol{f}^{(3)}(\mathbf{c}, t)$ are the expansion coefficients in the density-gradient expansion of the phase-space distribution function (6).

Substitution of expansions (7) and (8) into the continuity equation (2) yields the extended diffusion equation which incorporates the contribution of the third-order transport coefficient tensor,

$$\frac{\partial n(\boldsymbol{r}, t)}{\partial t} + \boldsymbol{W}^{(b)} \odot \nabla n(\boldsymbol{r}, t) - \boldsymbol{D}^{(b)} \odot (\nabla \otimes \nabla) n(\boldsymbol{r}, t)$$
$$+ \boldsymbol{Q}^{(b)} \odot (\nabla \otimes \nabla \otimes \nabla) n(\boldsymbol{r}, t) = -R_{\text{net}} n(\boldsymbol{r}, t), \quad (13)$$

where R_{net} is the net particle loss rate. For electron swarms, this quantity is given by

$$R_{\text{net}} = -S^{(0)} = -\iint n_0 c[\sigma_i(\epsilon) - \sigma_a(\epsilon)] f(\mathbf{r}, \mathbf{c}, t) \, d\mathbf{c} \, d\mathbf{r}.$$
(14)

$\mathbf{W}^{(b)}$ and $\boldsymbol{D}^{(b)}$ are the bulk drift velocity and bulk diffusion tensor, respectively, and $\boldsymbol{Q}^{(b)}$ is the bulk third-order transport coefficient tensor. The connection between the bulk and flux transport coefficients is given by

$$\mathbf{W}^{(b)} = \mathbf{W} + \mathbf{S}^{(1)}, \quad \mathbf{D}^{(b)} = \mathbf{D} + \mathbf{S}^{(2)}, \quad \mathbf{Q}^{(b)} = \mathbf{Q} + \mathbf{S}^{(3)},$$
(15)

where $\mathbf{S}^{(1)}$, $\mathbf{S}^{(2)}$, and $\mathbf{S}^{(3)}$ are the expansion coefficients in the hydrodynamic expansion of the source term (8).

The third-order transport coefficient tensor is referred to as the *skewness coefficient* by some authors [18], while other authors use the term *skewness* to denote just the diagonal component of this tensor along the direction of the electric field [19]. For brevity, in the rest of this work we will sometimes refer to the third-order transport coefficient tensor as the skewness tensor.

In the absence of nonconservative processes (or when the collision frequencies of these processes are independent of the energy) the bulk and the flux transport coefficients are equal [64]. In the presence of nonconservative collisions these two families of transport coefficients can vary quite substantially from each other. The physical interpretation, the origin of differences and the application of the bulk and flux low-order transport coefficients as well as their application in the modeling of plasma discharges have been thoroughly discussed and illustrated in our previous publications [6,16,41,62]. We defer a full discussion of the differences between the bulk and flux third-order tensor coefficients to a future publication.

In order to show the rank of the tensor explicitly, the third-order transport coefficient tensor in (9) can be rewritten

$$[\boldsymbol{Q} \odot (\nabla \otimes \nabla)n]_i \equiv \sum_{jk} Q_{ijk} \frac{\partial^2 n(\mathbf{r}, t)}{\partial x_j \partial x_k},$$
(16)

where the indices i, j, k each run over the space coordinates x, y, z. We note that there are 27 components in the tensor $\boldsymbol{Q}$ without considering any symmetry of the system under permutation operations. However, since the order of differentiation of n is irrelevant, some components of a tensor must be equal to each other. For example, for the magnetic-field-free case the maximal number of independent components is three, while when both the electric and magnetic fields are present and crossed at an arbitrary angle the maximal number of independent components is 18. It is clear that the structure of a tensor and symmetries along individual components depend on the field configuration.

B. Structure and symmetry considerations of the third-order transport coefficient tensor

One of the most important tasks in analysis of higher-order transport coefficients is to identify the symmetries along individual elements of the tensors. In this section we apply the group projector method [65] to determine the structure

of the skewness tensor. The group projector method is briefly discussed in Appendix A.

We first consider a magnetic-field-free case. The symmetry group of the system in the magnetic-field-free configuration is $C_{\infty V}$ (see Appendix A). This group has two connected components. The first component corresponds to rotations $R_z(\alpha)$ about the z axis through an arbitrary angle α. The second component corresponds to the composition of a rotation $R_z(\alpha)$ and a reflection in the symmetry plane σ_v. Polar vector (PV) representations of the group elements from the first and the second connected components are

$$D^{PV}(R_z(\alpha)) = \begin{pmatrix} \cos\alpha & -\sin\alpha & 0 \\ \sin\alpha & \cos\alpha & 0 \\ 0 & 0 & 1 \end{pmatrix},$$
(17)

$$D^{PV}(\sigma_v R_z(\alpha)) = \begin{pmatrix} \cos\alpha & -\sin\alpha & 0 \\ -\sin\alpha & -\cos\alpha & 0 \\ 0 & 0 & 1 \end{pmatrix},$$
(18)

where α is the angle of rotation around the z axis. Thus, for the magnetic-field-free case the following structure of the skewness tensor is derived:

$$Q_{xab} = \begin{pmatrix} 0 & 0 & Q_{xxz} \\ 0 & 0 & 0 \\ Q_{xxz} & 0 & 0 \end{pmatrix}, \quad Q_{yab} = \begin{pmatrix} 0 & 0 & 0 \\ 0 & 0 & Q_{xxz} \\ 0 & Q_{xxz} & 0 \end{pmatrix},$$

$$Q_{zab} = \begin{pmatrix} Q_{zxx} & 0 & 0 \\ 0 & Q_{zxx} & 0 \\ 0 & 0 & Q_{zzz} \end{pmatrix},$$
(19)

where $a, b \in \{x, y, z\}$. For the magnetic-field-free case the skewness tensor has seven nonzero elements and only three independent elements, including Q_{zzz}, Q_{zxx}, and Q_{xxz} [19,25,31,32]. Furthermore, the following symmetry properties along the individual elements of the tensor hold:

$$Q_{xxz} = Q_{xzx} = Q_{yyz} = Q_{yzy}, \quad Q_{zxx} = Q_{zyy}.$$
(20)

For parallel electric and magnetic fields the symmetry group of the system is C_{∞} (see Appendix A). This group has only a single component consisting of rotations $R_z(\alpha)$:

$$D^{PV}(R_z(\alpha)) = \begin{pmatrix} \cos\alpha & -\sin\alpha & 0 \\ \sin\alpha & \cos\alpha & 0 \\ 0 & 0 & 1 \end{pmatrix}.$$
(21)

In this case the structure of the skewness tensor is more complicated. For instance, the presence of the element Q_{xyz} is due to the explicit effects of the magnetic field on the trajectories of the charged particles. It is interesting to note that this component has exactly the opposite contribution to the third-order diffusive flux along the x and y directions. This is analogous to the D_{xy} component of the diffusion tensor. Likewise, the third-order flux along the magnetic field direction is the same as for the magnetic-field-free case. Thus, for parallel electric and magnetic fields the skewness tensor

has the following structure:

$$Q_{xab} = \begin{pmatrix} 0 & 0 & Q_{xxz} \\ 0 & 0 & Q_{xyz} \\ Q_{xxz} & Q_{xyz} & 0 \end{pmatrix},$$

$$Q_{yab} = \begin{pmatrix} 0 & 0 & -Q_{xyz} \\ 0 & 0 & Q_{xxz} \\ -Q_{xyz} & Q_{xxz} & 0 \end{pmatrix}, \qquad (22)$$

$$Q_{zab} = \begin{pmatrix} Q_{zxx} & 0 & 0 \\ 0 & Q_{zxx} & 0 \\ 0 & 0 & Q_{zzz} \end{pmatrix}.$$

For parallel electric and magnetic fields the skewness tensor has 11 nonzero elements and only four independent elements, including Q_{zzz}, Q_{zxx}, Q_{xxz}, and Q_{xyz}. Furthermore, the following symmetry properties along the individual elements of the tensor may be identified:

$$Q_{xxz} = Q_{xzx} = Q_{yyz} = Q_{yzy}, \quad Q_{zxx} = Q_{zyy},$$
$$Q_{xyz} = Q_{xzy} = -Q_{yxz} = -Q_{yzx}. \qquad (23)$$

For orthogonal electric and magnetic fields the symmetry group of the system is C_{1V}. This group has only two elements, the unity element e and a reflection in the symmetry plane σ_v, which is orthogonal to the direction of the magnetic field. The PV representations of these two elements are given by

$$D^{PV}(e) = \begin{pmatrix} 1 & 0 & 0 \\ 0 & 1 & 0 \\ 0 & 0 & 1 \end{pmatrix}, \quad D^{PV}(\sigma_v) = \begin{pmatrix} 1 & 0 & 0 \\ 0 & -1 & 0 \\ 0 & 0 & 1 \end{pmatrix}. \quad (24)$$

Thus, for orthogonal electric and magnetic fields the skewness tensor has the following structure:

$$Q_{xab} = \begin{pmatrix} Q_{xxx} & 0 & Q_{xxz} \\ 0 & Q_{xyy} & 0 \\ Q_{xxz} & 0 & Q_{xzz} \end{pmatrix},$$

$$Q_{yab} = \begin{pmatrix} 0 & Q_{yyx} & 0 \\ Q_{yyx} & 0 & Q_{yyz} \\ 0 & Q_{yyz} & 0 \end{pmatrix}, \qquad (25)$$

$$Q_{zab} = \begin{pmatrix} Q_{zxx} & 0 & Q_{zzx} \\ 0 & Q_{zyy} & 0 \\ Q_{zzx} & 0 & Q_{zzz} \end{pmatrix}.$$

We observe that for orthogonal fields the skewness tensor has 14 nonzero elements among which 10 are independent. The following symmetry properties along the individual elements of the tensor are clearly evident:

$$Q_{xxz} = Q_{xzx}, \quad Q_{yyz} = Q_{yzy}, \quad Q_{yyx} = Q_{yxy}, \quad Q_{zzx} = Q_{zxz}. \qquad (26)$$

When electric and magnetic fields are crossed at arbitrary angles, the symmetry group of the system is the trivial group, which has only the unity element, e.g.,

$$D^{PV}(e) = \begin{pmatrix} 1 & 0 & 0 \\ 0 & 1 & 0 \\ 0 & 0 & 1 \end{pmatrix}. \qquad (27)$$

For this general configuration, the skewness tensor is full, and it has 27 nonzero elements. However, there are only

18 independent components as the last two indices of the skewness tensor commute. Thus, the skewness tensor has the following structure:

$$Q_{xab} = \begin{pmatrix} Q_{xxx} & Q_{xxy} & Q_{xxz} \\ Q_{xxy} & Q_{xyy} & Q_{xyz} \\ Q_{xxz} & Q_{xyz} & Q_{xzz} \end{pmatrix},$$

$$Q_{yab} = \begin{pmatrix} Q_{yxx} & Q_{yyx} & Q_{yxz} \\ Q_{yyx} & Q_{yyy} & Q_{yyz} \\ Q_{yxz} & Q_{yyz} & Q_{yzz} \end{pmatrix}, \qquad (28)$$

$$Q_{zab} = \begin{pmatrix} Q_{zxx} & Q_{zxy} & Q_{zzx} \\ Q_{zxy} & Q_{zyy} & Q_{zzy} \\ Q_{zzx} & Q_{zzy} & Q_{zzz} \end{pmatrix}.$$

For this general configuration, one may identify the following symmetry properties along the individual elements:

$$Q_{xxy} = Q_{xyx}, \quad Q_{yyx} = Q_{yxy}, \quad Q_{zzx} = Q_{zxz},$$
$$Q_{xxz} = Q_{xzx}, \quad Q_{yyz} = Q_{yzy}, \quad Q_{zzy} = Q_{zyz}, \qquad (29)$$
$$Q_{xyz} = Q_{xzy}, \quad Q_{yzx} = Q_{yxz}, \quad Q_{zxy} = Q_{zyx}.$$

These symmetry arguments can be extended to any of the higher-order transport coefficients.

C. Physical interpretation of the third-order transport coefficients

In this section we discuss the physical meaning of the third-order transport coefficients. Let us assume that the contribution of the third-order transport coefficients to the density profile of charged particles is negligibly small. This reduces the extended diffusion equation (13) to the well-known form

$$\frac{\partial n(\boldsymbol{r}, t)}{\partial t} + \boldsymbol{W}^{(b)} \odot \nabla n(\boldsymbol{r}, t) - \boldsymbol{D}^{(b)} \odot (\nabla \otimes \nabla) n(\boldsymbol{r}, t)$$
$$= -R_{\text{net}} n(\boldsymbol{r}, t). \qquad (30)$$

Swarm experiments are traditionally analyzed by solving the the diffusion equation (30), which gives the density of charged particles throughout the bulk of medium. For example, in an idealized time-of-flight experiment, in which a pulse of N_0 particles is released from a plane source at $z = 0$ at time $t = 0$ into an unbounded medium, the initial and boundary conditions are

$$n(\mathbf{r}, 0) = N_0 \delta(\mathbf{r}),$$
$$n(\mathbf{r}, t) = 0 \ (\|\mathbf{r}\| \to \infty, \ t > 0), \qquad (31)$$

respectively, and the solution is

$$n^{(0)}(\boldsymbol{r}, t) = \frac{N_0 e^{-R_{\text{net}} t} e^{-\frac{(z - W^{(b)} t)^2}{4 D_L^{(b)} t} - \frac{x^2 + y^2}{4 D_T^{(b)} t}}}{(4\pi D_T^{(b)} t)\sqrt{4\pi D_L^{(b)} t}}, \qquad (32)$$

where $D_L^{(b)}$ and $D_T^{(b)}$ are the bulk longitudinal and bulk transverse diffusion coefficients, respectively, while x, y, and z are the Cartesian coordinates [62]. The solution (32) represents a Gaussian pulse, the peak of which drifts with the velocity $W^{(b)}$ and diffuses about the center of mass according to the diffusion coefficients $D_L^{(b)}$ and $D_T^{(b)}$. For brevity, in what follows

we omit explicit reference to the type of transport coefficients, e.g., the superscripting for all transport coefficients.

Assuming the above initial conditions (31), the extended diffusion equation (13), which incorporates the effects of the third-order transport coefficient tensor, cannot be solved analytically. Thus, we have applied the following procedure. First, the Fourier transform of the charged-particle density is expanded in terms of the longitudinal Q_L and transverse Q_T components of the third-order transport coefficient tensor. Using the inverse Fourier transformation of the expansion coefficients, we have derived the density of charged particles in which the corrections due to the third-order transport coefficients are included. In the first approximation, in which only the first-order corrections are assumed, the density of charged particles is given by

$$
n^{(1)}(\boldsymbol{r}, t) = \left[1 + Q_L \frac{t(z - Wt)^3 - 6D_L t^2(z - Wt)}{8(D_L t)^3} \right.
$$
$$
\left. + Q_T \frac{3t(z - Wt)(x^2 + y^2 - 4D_T t)}{8D_L t(D_T t)^2} \right] n^{(0)}(\boldsymbol{r}, t).
$$
$$(33)$$

The first-order correction along the longitudinal direction shown in Eq. (33) has been previously published by Penetrante and Bardsley [18]. This equation has a simpler form in relative coordinates that are defined as

$$
\chi_z = \frac{z - W^{(b)} t}{\sqrt{2D_L^{(b)} t}}, \quad \chi_x = \frac{x}{\sqrt{2D_T^{(b)} t}}, \quad \chi_y = \frac{y}{\sqrt{2D_T^{(b)} t}}. \quad (34)
$$

In these coordinates the approximate solution (32) may be written as

$$
n^{(1)}(\boldsymbol{r}, t) = n^{(0)}(\boldsymbol{r}, t) \left[1 + \frac{t Q_L^{(b)}}{\sigma_z^3} \chi_z (\chi_z^2 - 3) \right.
$$
$$
\left. + \frac{3t Q_T^{(b)}}{\sigma_x^2 \sigma_z} \chi_z (\chi_x^2 + \chi_y^2 - 2) \right]. \quad (35)
$$

It can be seen from Eq. (35) that the third-order transport coefficients describe elongation and compression of the number density of charged particles along different parts of the swarm. The detailed physical interpretation of the individual components of the third-order transport tensor is given in Appendix B.

D. Multiterm solutions of Boltzmann's equation

In this section we briefly describe the basic elements of a multiterm theory for solving the Boltzmann equation that has been used to calculate the components of the third-order transport coefficient tensor. The method is by now standard, and for details the reader is referred to our previous publications [66–68]. In brief, the dependence of the phase-space distribution function on the velocity coordinates is represented by its expansion in terms of spherical harmonics (angular dependence) and Sonine polynomials (speed dependence). Likewise, under hydrodynamic conditions a sufficient representation of the space dependence is an expansion in terms of the powers of the density gradient operator. After truncation and discretizing in time, the above expansions allow

a decomposition of the Boltzmann equation into a set of matrix equations in terms of the expansion coefficients which represent the moments of the distribution function. This set of matrix equations can be solved numerically by using the matrix inversion. Transport properties including mean energy, drift velocity, and components of the diffusion tensor can then be calculated directly from the moments of the phase-space distribution function.

In order to find the explicit expressions for the individual elements of the third-order transport coefficient tensor we use the definition of the spherical vector [69]:

$$
c_m^{[1]} = \sqrt{\frac{4\pi}{3}} c Y_m^{[1]}(\hat{\boldsymbol{c}}). \quad (36)
$$

The connection between Cartesian and spherical components of the velocity vector is given by

$$
c_x = \frac{i}{\sqrt{2}} \left(c_1^{[1]} - c_{-1}^{[1]} \right), \quad c_y = \frac{1}{\sqrt{2}} \left(c_1^{[1]} + c_{-1}^{[1]} \right),
$$
$$
c_z = -i c_0^{[1]}. \quad (37)
$$

Likewise, the flux of charged particles in irreducible tensor notation is given by

$$
\Gamma_m^{[1]} = n \langle c_m^{[1]} \rangle, \quad (38)
$$

while its connection with the Cartesian components is expressed by

$$
\Gamma_x = \frac{i}{\sqrt{2}} \left(\Gamma_1^{[1]} - \Gamma_{-1}^{[1]} \right), \Gamma_y = \frac{1}{\sqrt{2}} \left(\Gamma_1^{[1]} + \Gamma_{-1}^{[1]} \right), \quad (39)
$$
$$
\Gamma_z = -i \Gamma_0^{[1]}.
$$

Using the orthogonality relations for spherical harmonics and modified Sonine polynomials [61,69] and relation

$$
c^l = \left(\frac{\sqrt{2}}{\alpha} \right) \frac{R_{0l}(\alpha c)}{N_{0l}}, \quad (40)
$$

after some algebra we get the following expression for the flux of charged particles in the basis of Sonine polynomials:

$$
\Gamma_m^{(1)} = \frac{1}{\alpha} \sum_{s=0}^{\infty} \sum_{\lambda=0}^{s} \sum_{\mu=-\lambda}^{\lambda} F(01m|s\lambda\mu) G_\mu^{(s\lambda)} n(\boldsymbol{r}, t). \quad (41)
$$

Using the explicit expressions for the irreducible gradient tensor operator in the spherical form of the flux-gradient relation (41) [61], the relationship between the spherical quantities $\Gamma_m^{(1)}$ (where $m = -1, 0, 1$) and their Cartesian counterparts in (9) can be established. The explicit expressions for the individual elements of the flux third-order transport coefficient tensor in the absence of a magnetic field are given by

$$
Q_{xxz} = \frac{1}{\sqrt{2}\alpha} [\text{Im}(F(011|221; \alpha)) - \text{Im}(F(01-1|221; \alpha))],
$$
$$(42)$$

$$
Q_{zxx} = -\frac{1}{\alpha} \left[\frac{1}{\sqrt{3}} \text{Im}(F(010|200; \alpha)) + \frac{1}{\sqrt{6}} \text{Im}(F(010|220; \alpha)) \right]
$$
$$
+ \frac{1}{\alpha} \text{Im}(F(010|222; \alpha)), \quad (43)
$$

$$Q_{zzz} = \frac{1}{\alpha}\left[\sqrt{\frac{2}{3}}\,\mathrm{Im}(F(010|220;\alpha)) - \frac{1}{\sqrt{3}}\,\mathrm{Im}(F(010|200;\alpha))\right],$$

(44)

where $\mathrm{Re}(\cdot)$ and $\mathrm{Im}(\cdot)$, respectively, represent the real and imaginary parts of the moments. The explicit expressions for the individual elements of the flux skewness tensor in varying configurations of electric and magnetic fields are given in Appendix C. Expressions for the lower-order transport coefficients in terms of the moments of the distribution function can be found in our previous work [66–68,70].

E. Monte Carlo simulation method

The Monte Carlo simulation technique is used in this work as an independent tool to confirm the numerical accuracy and integrity of a multiterm solution of Boltzmann's equation. The Monte Carlo code applied in this work has been systematically tested for a range of model and real gases under both the hydrodynamic and nonhydrodynamic conditions in the presence of the electric and magnetic fields [67,68,71,72]. The subject of testing were the lower-order transport coefficients usually in the presence of nonconservative collisions. In the present work, we follow a large number of particles ($\sim 10^7$) moving in an infinite gas under the influence of spatially homogeneous electric and magnetic fields. Such a large number of charged particles is followed with the aim of reducing the statistical fluctuations of the output data required for the evaluation of the individual elements of the third-order transport coefficient tensor. The charged-particle trajectories between collisions are determined by solving the collisionless equation of motion of a charged particle. The position and velocity of each charged particle are updated after the time step Δt, which is obtained by solving the equation for collision probability. The numerical solution of this equation requires the extensive use of random numbers. The type of collision is also determined using random numbers as well as relative probabilities for individual collisional processes. The details of our Monte Carlo method are given in our several previous publications [67,71–73].

The third-order transport coefficients are determined after relaxation to the steady state. The flux third-order transport coefficient tensor is defined by

$$Q_{abc} = \frac{1}{3!}\left\langle \frac{d}{dt}\left(r_a^* r_b^* r_c^*\right)\right\rangle,$$

(45)

where (a, b, c) take values from the set $\{x, y, z\}$ while the angular brackets $\langle\rangle$ denote ensemble averages in phase space, and $\boldsymbol{r}^* = \boldsymbol{r} - \langle\boldsymbol{r}\rangle$.

It is important to note that although the third-order transport coefficient tensor has the three independent elements when the swarm is acted on solely by the electric field, we are able to identify only two independent elements in our Monte Carlo simulations. This follows from the fact that the expressions for sampling the third-order transport coefficients are derived from the generalized diffusion equation in which all tensor components are contracted with the corresponding partial derivatives of charged-particle density with respect to the coordinates. Thus, the expressions for evaluation the skewness coefficients represent the sum of all skewness tensor

components Q_{abc} which have the same combination of indices a, b, c where (a, b, c) take values from the set $\{x, y, z\}$. Therefore, the expressions for skewness coefficients in our Monte Carlo simulations are symmetric with respect to the permutation of any two indices. The analogy with the determination of the off-diagonal elements of the diffusion tensor is clearly evident. For example, for perpendicular electric and magnetic fields, we are not able to isolate and evaluate the individual off-diagonal elements of the diffusion tensor [67]. However, it is possible to determine the sum of the individual off-diagonal elements which is the well-known Hall diffusion coefficient. To calculate the individual elements of the third-order transport coefficient tensor and diffusion tensor, one must integrate the velocity over the corresponding hydrodynamic component of the distribution function in velocity space. This is beyond the scope of this work, and we defer this procedure to a future paper.

Due to inability to isolate the individual elements of the third-order transport coefficient tensor in our Monte Carlo simulations, we define the following third-order transport coefficients:

$$Q_{zzz} \equiv Q_L, \quad Q_{\pi(xxz)} \equiv Q_T,$$

(46)

where

$$Q_{\pi(xxz)} = \tfrac{1}{3}(Q_{xxz} + Q_{xzx} + Q_{zxx}),$$

(47)

and $\pi(abc)$ denote all possible permutations of (a, b, c).

The explicit form of the flux longitudinal and flux transverse third-order coefficients are calculated from

$$Q_L = \tfrac{1}{6}(3\langle z^2 c_z\rangle - 3\langle c_z\rangle\langle z^2\rangle - 6\langle z\rangle\langle zc_z\rangle + 6\langle z\rangle\langle z\rangle\langle c_z\rangle),$$

(48)

$$Q_T = \tfrac{1}{6}(\langle x^2 c_z\rangle + 2\langle zxc_x\rangle - \langle c_z\rangle\langle x^2\rangle - 2\langle z\rangle\langle xc_x\rangle),$$

(49)

where c_x, c_y, and c_z are velocity components. Explicit formulas for the elements of the flux third-order transport coefficient tensor which can be isolated and determined individually in our Monte Carlo simulations in various configurations of the electric and magnetic fields are given in the Appendix C.

III. RESULTS

A. Preliminaries

The aim of the present section is to highlight the general features of the third-order transport coefficients associated with the light charged-particle swarms in gases when both the electric and magnetic fields are present. Benchmark calculations are performed for a range of model gases, including the Maxwell (constant collision frequency) model, the hard-sphere model and the Reid ramp inelastic model. For the present study we consider conservative collisions only. We defer the investigation of the explicit effects of nonconservative collisions on the third-order transport coefficient tensor to a future study. The utility of model gases lies in the fact that through the use of simple analytically given cross sections we can isolate and elucidate physical processes which govern and control the specific behavior of a charged-particle swarm. This is particularly important for higher-order transport coefficients due to complexity of factors which contribute to, or influence, the corresponding tensors. However, the present theory and associated codes have been applied to a number of gases

and mixtures and preliminary results are available elsewhere [74–76]. Here we present some results for neon and compare them with the results of calculations that have been presented elsewhere. We employ the set of cross sections for electron scattering in neon developed by Hayashi [77] (see Fig. 2 in Ref. [78]).

In the Boltzmann equation analysis of the third-order transport coefficients the elastic collisions are treated using the original Boltzmann collision operator [79], while its semiclassical generalization is applied for inelastic processes [80]. All scattering is assumed isotropic and hence for elastic scattering we use the elastic momentum transfer cross section. Calculations are performed assuming that the internal states are governed by a Maxwell-Boltzmann distribution which essentially places all neutral particles in the ground state for systems considered. The thermal motion of background particles is carefully considered in both the Boltzmann equation analysis and Monte Carlo simulations [81].

The Monte Carlo results are presented with error bars. These error bars are required since the third-order transport coefficients are derived from the third-order monomials of coordinates and velocities which usually have high standard deviations. The statistical error of the third-order transport coefficients that are evaluated in our Monte Carlo simulations is estimated as the standard error. The standard error is equal to the standard deviation of the third-order transport coefficients divided by the square root of the number of electrons followed in the simulation. Thus, it is necessary to follow a large number of electrons (at least 10^7) in our Monte Carlo simulations in order to sufficiently reduce the standard error of the final results.

When the magnetic field is applied, the results and discussion are restricted to a crossed field configuration, although the theory and associated codes are valid for arbitrary field configurations. We use the unit of the Townsend (1 Td = 10^{-21} Vm^2) for the reduced electric field and the unit of the Huxley (1 Hx = 10^{-27} Tm^3) for the reduced magnetic field.

B. The Maxwell model

In this section we present benchmark results for the third-order transport coefficients assuming the Maxwell model of interaction. In this model the electrons undergo elastic collisions only and the collision frequency is independent of the energy. The details of the model used here are as follows:

$$\sigma_m(\epsilon) = A\epsilon^{-1/2} \text{ Å}^2 \quad \text{(elastic cross section)},$$

$$m_0 = 4 \text{ amu}, \quad m = 5.486 \times 10^{-4} \text{ amu}, \quad T_0 = 293 \text{ K}, \tag{50}$$

where ϵ is in eV, m is the electron mass and m_0 is the neutral mass. While the magnitude of potential for elastic scattering A in previous works was usually fixed to a single value of 6 [70,82,83], in the present work its value is varied in order to investigate the influence of elastic collisions on the third-order transport coefficients. We consider the reduced electric field range: 0.1–10 Td.

The results are obtained from the numerical solution of Boltzmann's equation and are presented in Table I. The three

TABLE I. Third-order transport coefficients for the Maxwell model. The results are presented as a function of the reduced electric field E/n_0 and the magnitude of potential for elastic scattering A.

A	E/n_0 (Td)	$n_0^2 Q_{xzx}$ (m^{-3} s^{-1})	$n_0^2 Q_{zxx}$ (m^{-3} s^{-1})	$n_0^2 Q_{zzz}$ (m^{-3} s^{-1})
1.0	0.1	5.2930×10^{45}	2.1761×10^{42}	1.0588×10^{46}
	1.0	4.3919×10^{48}	1.8055×10^{45}	8.7856×10^{48}
	10.0	4.3829×10^{51}	1.8017×10^{48}	8.7676×10^{51}
3.0	0.1	5.1740×10^{43}	2.1279×10^{40}	1.0351×10^{44}
	1.0	1.8373×10^{46}	7.5531×10^{42}	3.6754×10^{46}
	10.0	1.8039×10^{49}	7.4158×10^{45}	3.6087×10^{49}
6.0	0.1	4.7768×10^{42}	1.9648×10^{39}	9.5557×10^{42}
	1.0	6.0575×10^{44}	2.4903×10^{41}	1.2118×10^{45}
	10.0	5.6405×10^{47}	2.3187×10^{44}	1.1283×10^{48}
12.0	0.1	5.4425×10^{41}	2.2388×10^{38}	1.0888×10^{42}
	1.0	2.2880×10^{43}	9.4070×10^{39}	4.5769×10^{43}
	10.0	1.7665×10^{46}	7.2623×10^{42}	3.5340×10^{46}

independent elements of the third-order transport coefficient tensor are given as a function of the reduced electric field E/n_0 and the magnitude of potential for elastic scattering A. We observe that $n_0^2 Q_{xzx}$, $n_0^2 Q_{zxx}$, and $n_0^2 Q_{zzz}$ are positive and monotonically increasing functions of E/n_0. For brevity, in what follows we omit n_0^2, and $n_0^2 Q_{abc}$ will be written as Q_{abc}, where $a, b, c \in \{x, y, z\}$. In the logarithmic plot, the E/n_0 dependence of Q_{xzx}, Q_{zxx}, and Q_{zzz} is linear both for the higher values of E/n_0, where the diffusion deviates significantly from the thermal values, and for the lower values of E/n_0, where the diffusion is essentially thermal. However, the slope of these two linear dependencies is not the same. The slope is greater for those values of E/n_0 for which the diffusion is no longer thermal.

We observe that the Q_{zxx} is less than the remaining elements, Q_{xzx} and Q_{zzz} for all E/n_0 and A considered. The coefficient Q_{zxx} represents the difference in the flux of charged particles along the z direction between the center of the swarm and the transverse edges (see Appendix B). Since the collision frequency for the Maxwell model is independent of energy, the positive value of Q_{zxx} is a clear sign that the mobility of the electrons is greater at the transverse edges than at the center of the swarm, due to a parabolic increase of the mean energy along the transverse direction. This effect is very small and hence the coefficient Q_{zxx} is dominated by the coefficients Q_{xzx} and Q_{zzz}. This physical picture is no more valid for real gases in which the momentum transfer collision frequency is usually a complex function of the electron energy.

Comparing Q_{xzx} and Q_{zzz}, we observe that these two coefficients are of the same order of magnitude for all E/n_0 and A considered. In a certain way this is analogous to the behavior of the diffusion coefficients. For the Maxwell model the longitudinal and transverse diffusion coefficients are equal [82,83]. Likewise, the sum of the coefficients Q_{xzx} and Q_{xxz} which is proportional to the flux along the transverse direction, is equal to the coefficient Q_{zzz} which determines the corresponding flux along the field direction (note that the coefficient Q_{zxx} is negligible as compared to the coefficients Q_{xzx} and Q_{zzz}).
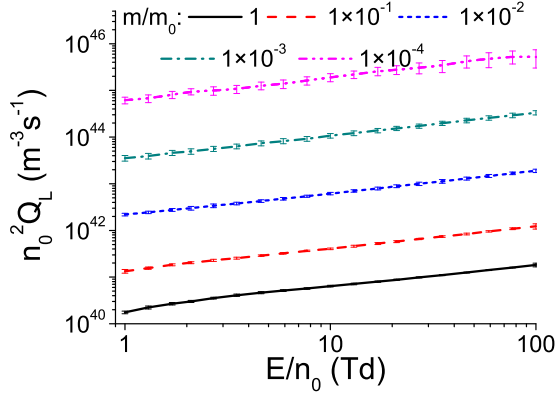
FIG. 1. Influence of the charged-particle to neutral-particle mass ratio on the variation of the longitudinal third-order transport coefficient $n_0^2 Q_L$ with E/n_0 for the hard sphere model. Calculations are performed using a Monte Carlo simulation technique.

C. Effects of the ion to neutral-particle mass ratio

In this section we explore the effects of the ion to neutral mass ratio on the variation of the third-order transport coefficients with E/n_0. Calculations are performed by a Monte Carlo simulation technique assuming the hard sphere model [84]. The details of the model are

$$\sigma_m(\epsilon) = 6 \text{ Å}^2 \quad \text{(elastic cross section)},$$
$$m_0 = 4 \text{ amu}, \quad T_0 = 293 \text{ K}. \quad (51)$$

We consider the mass ratio range 10^{-4}–1 and the reduced electric field range 1–100 Td.

In Fig. 1 we show the variation of the coefficient Q_L as a function of E/n_0 for various charged-particle to neutral-particle mass ratios, as indicated on the graph. For decreasing m/m_0 the energy transfer in elastic collisions is reduced, which in turn increases Q_L. In Monte Carlo simulations, the reduced energy transfer in elastic collisions for decreasing m/m_0 slows the relaxation of energy. As a consequence, Monte Carlo simulations require a large computation time while at the same time the statistical fluctuations deteriorate the accuracy of the output data. We see in the Fig. 1 that the error bars are increased for decreasing m/m_0.

For a fixed mass ratio we see that Q_L is increased monotonically with E/n_0. In this model, the elastic cross section is constant rendering collision frequency to be directly proportional to the square root of the charge particle energy. With the increase of E/n_0, the collision frequency also increases, but not enough to overcome the directed action of the force and the simultaneous increase of the mobility of charged particles (see Appendix B). As a consequence, Q_L rises with rising E/n_0. When it comes to Q_T, for the entire range of E/n_0 considered, it is found that $Q_T > 0$ (not shown here). This indicates that the absolute value of the sum of Q_{xxz} and Q_{xzx} is greater than the absolute value of the coefficient Q_{zxx}. In this model, $Q_{zxx} < 0$ since the collision frequency is directly proportional to the square root of charged-particle energy. The negative value of Q_{zxx} due to elastic collisions with a constant cross section has been observed for the Reid model gas at low
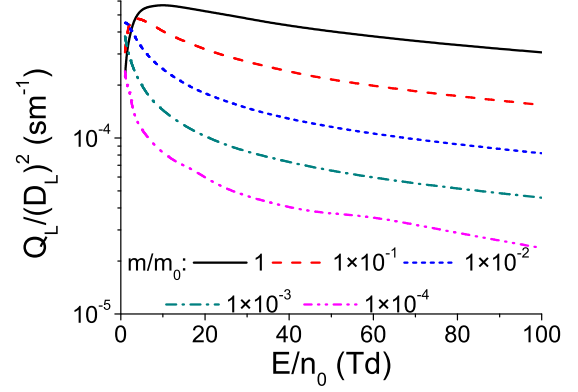
FIG. 2. Variation of the Q_L to D_L^2 ratio as a function of E/n_0 for the hard sphere model.

electric fields where the rate for inelastic collisions is negligible (see Sec. III D). Note that in our Monte Carlo simulations we are not able to evaluate the individual components Q_{xxz}, Q_{xzx} and Q_{zxx}, but only their sum [see Eq. (47)].

Figure 1 clearly illustrates that for decreasing m/m_0 the coefficients Q_L (and Q_T) are increased. It should be noted that for the hard sphere model the third-order transport coefficients scale with the factor $\frac{1}{\sqrt{m_0}}\left(\frac{m+m_0}{mA^2}\right)^{5/4}$ [19]. This raises an interesting question: does the spatial profile of the swarm deviate from a Gaussian distribution more for light charged particles, including electrons and/or positrons, or for more massive ions? In order to investigate this issue, in Figs. 2 and 3 we show the variation of the $\frac{1}{n_0}Q_L/D_L^3$ and Q_L/D_L^2 as a function of E/n_0, respectively, where D_L is the longitudinal diffusion coefficient. Recall that the asymmetric contribution to the spatial profile of the swarm along the field direction is represented by the two terms; the first term is proportional to Q_L/D_L^3, while the second one is proportional to Q_L/D_L^2 [see Eq. (33)]. We observe that both quantities $\frac{1}{n_0}Q_L/D_L^3$ and Q_L/D_L^2 are decreased with a decrease of m/m_0, which indicates that the contribution of the third-order transport coefficients to the spatial profile of the swarm becomes more significant for ions in comparison with electrons and/or positrons.
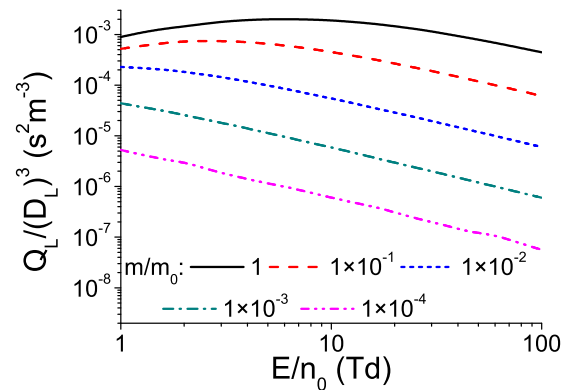
FIG. 3. Variation of the Q_L to D_L^3 ratio as a function of E/n_0 for the hard sphere model. Calculations are performed assuming the gas number density $n_0 = 3.54 \times 10^{22}$ m^{-3}.
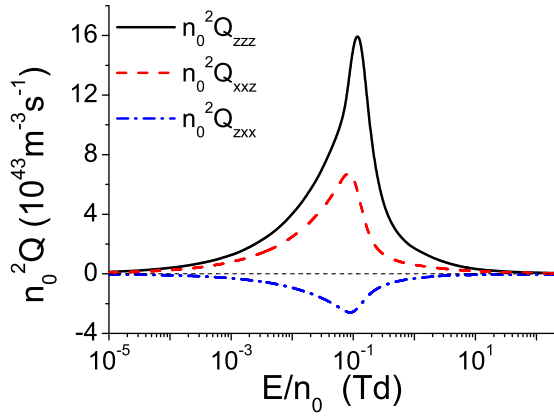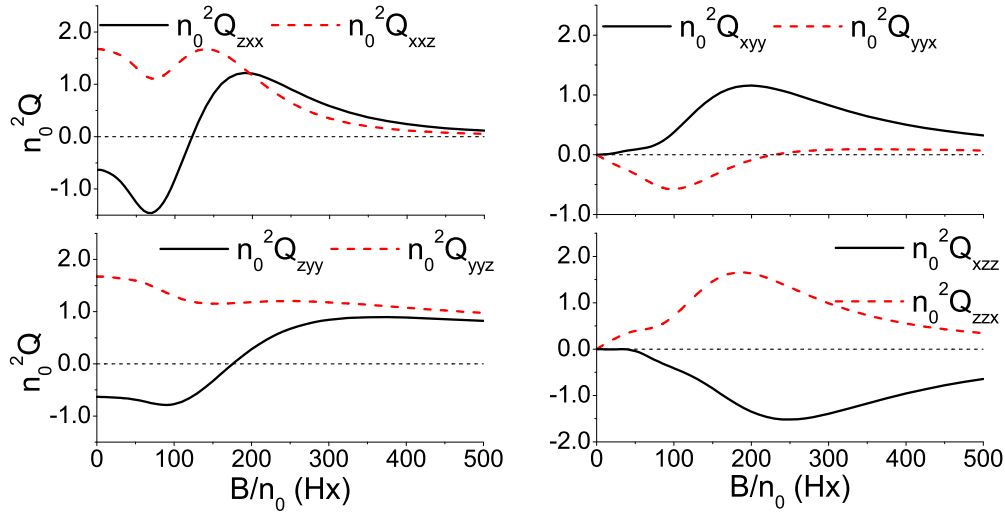
FIG. 4. Variation of the third-order transport coefficients with E/n_0 for the Reid ramp model. Calculations are performed via a multiterm theory for solving the Boltzmann equation.

D. The Reid ramp model

The Reid ramp inelastic model of interaction is given by [85]

$$\sigma_m(\epsilon) = 6 \text{ Å}^2 \quad \text{(elastic cross section)},$$

$$\sigma_{\text{inel}}(\epsilon) = \begin{cases} 10(\epsilon - 0.2) \text{ Å}^2, & \epsilon \geqslant 0.2 \text{ eV} \\ & \text{(inelastic cross section)}, \\ 0, & \epsilon < 0.2 \text{ eV} \end{cases}$$

$$m_0 = 4 \text{ amu},$$

$$T_0 = 0 \text{ K}, \tag{52}$$

where m_0 and T_0 represent the mass and temperature of the neutral gas particles while ϵ has the units of eV. Initially, this particular model was developed with the aim of testing the validity of the two-term approximation for solving the Boltzmann equation. Since the early work of Reid [85], the model has been used extensively as a benchmark for a variety of numerical techniques for solving the Boltzmann equation and Monte Carlo codes under steady-state [70–72,82,83] and time-dependent conditions [17,68]. In the present work we extend the model to consider the behavior of the individual elements of the third-order transport coefficient tensor in the presence of both electric and magnetic fields. Thus, the utility of the Reid ramp model in the present work is twofold: (1) it will enable us to determine the influence of an energy dependent collision frequency in addition to the influence of strong inelastic processes on the behavior of the third-order transport coefficients, and (2) it is a good test of the accuracy of the two-term approximation for solving Boltzmann's equation.

In Fig. 4 we show the variation of the coefficients Q_{zzz}, Q_{xxz}, and Q_{zxx} with the reduced electric field E/n_0. Over the range of E/n_0 considered, we see that Q_{zzz} and Q_{xxz} are positive while Q_{zxx} is negative. Such behavior of the third-order transport coefficients can be attributed to the fact that for the Reid ramp model the total collision frequency is a monotonically increasing function of the electron energy. Due to the increase of the total collision frequency over the entire range of E/n_0, Q_{zxx} is negative (see Appendix B). However, this increase is not significant enough to render Q_{zzz} and Q_{xxz} negative. In any case, the absolute values of

the third-order transport coefficients are increasing functions of E/n_0 until reaching the particular value of E/n_0 value for which the inelastic collisions begin to play a significant role. In this case, their direct effect is to enhance collisions and thereby reduce diffusion which in turn reduces the third-order transport coefficients. In the limit of the highest E/n_0, the third-order transport coefficients are significantly reduced and approach zero values.

In Figs. 5 and 6 we show the comparison between the Boltzmann equation and Monte Carlo results of Q_L and Q_T, respectively. The comparison is presented only for relatively higher values of E/n_0 where both Q_L and Q_T are monotonically decreasing functions of E/n_0. In the limit of lower values of E/n_0, the relaxation of energy is a very slow process and Monte Carlo simulations require large computation time. The results from the Monte Carlo simulations are consistent and agree very well with those predicted by the Boltzmann equation analysis, validating the theoretical method for solving the Boltzmann equation and numerical integrity of both methods of calculations.

In Fig. 7 the percentage differences in the third-order transport coefficients for the Reid ramp model, calculated using the two-term and the fully converged multiterm solutions

FIG. 5. Comparison between the multiterm Boltzmann equation results for longitudinal third-order transport coefficient and those calculated with a Monte Carlo simulation technique.
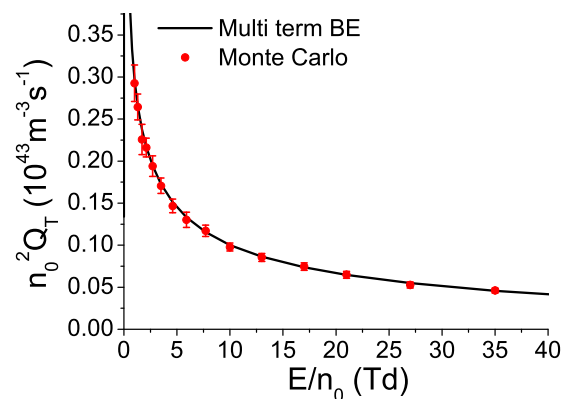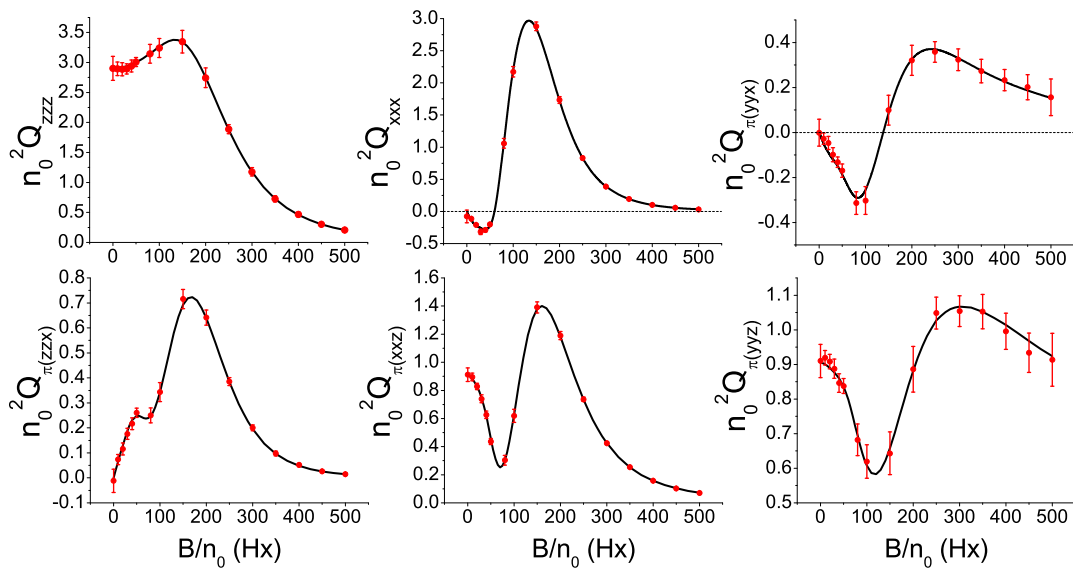

FIG. 6. Comparison between the multiterm Boltzmann equation results for transverse third-order transport coefficient and those calculated with a Monte Carlo simulation technique.
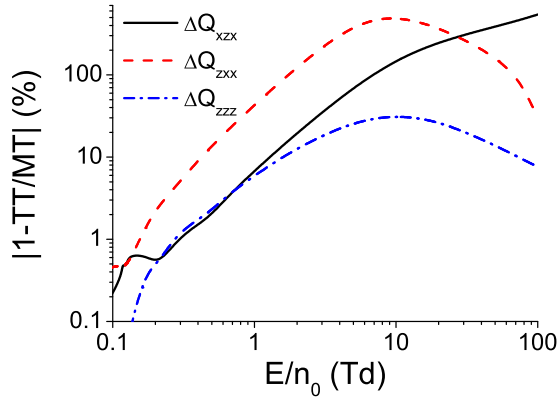
FIG. 7. Percentage difference between the two-term (TT) and multiterm (MT) results for the third-order transport coefficients for the Reid ramp model.

FIG. 8. Variation of $n_0^2 Q_{zzz}$ and $n_0^2 Q_{xxx}$ with B/n_0 for the Reid ramp model. Calculations are performed by a multiterm theory for solving the Boltzmann equation in a crossed field configuration. The reduced electric field E/n_0 is set to 12 Td.

of Boltzmann's equation, are shown. We see that maximum errors in the two-term approximation, for Q_{zzz} and Q_{zxx}, occur at about 10 Td where the mean energy of the electrons is close to the threshold of a cross section for inelastic collisions. On the other hand, the discrepancy between the two-term and multiterm solutions of Boltzmann's equation for Q_{xxz} increases with E/n_0 monotonically over the range of E/n_0 considered in this work. For the lower values of E/n_0, the coefficient Q_{zxx} appears to be the most sensitive with respect to the number of spherical harmonics used for solving Boltzmann's equation while for the higher values of E/n_0 the most sensitive coefficient is Q_{xzx}. We observe that the errors between the two-term and converged multiterm results can be as high as 500%. The presence of inelastic collisions produces asymmetry in velocity space which makes the two-term approximation inadequate for the analysis of the third-order transport coefficients. It is also important to note that the differences between the two-term approximation and multiterm solution of Boltzmann's equation for third-order transport coefficients are much higher than those for the lower-order transport coefficients, e.g., for the drift velocity and diffusion coefficients. This suggests that the third-order transport coefficients are more sensitive with respect to the way of solving the Boltzmann equation. Thus, it seems that the use of a multiterm theory for solving the Boltzmann equation is mandatory in the presence of inelastic collisions when it comes to calculations of the third-order transport coefficients.

In Fig. 8 we show the variation of the coefficients Q_{xxx} and Q_{zzz} as a function of B/n_0 at $E/n_0 = 12$ Td. As already discussed, Q_{zzz} describes the deviation from the Gaussian along the z axis (see Appendix B). For perpendicular electric and magnetic fields, Q_{xxx} is a measure of the deviation from the Gaussian along the $E \times B$ direction. For B/n_0 greater than approximately 150 Hx, we observe that both Q_{xxx} and Q_{zzz} monotonically decrease with increasing B/n_0. This is a clear indication of the magnetic-field-controlled regime in which the cyclotron frequency dominates the collision frequency and the electrons are held by the magnetic field lines. For B/n_0 less than approximately 150 Hx, the behavior of Q_{xxx} and Q_{zzz} is less intuitive. For these values of B/n_0 the collision
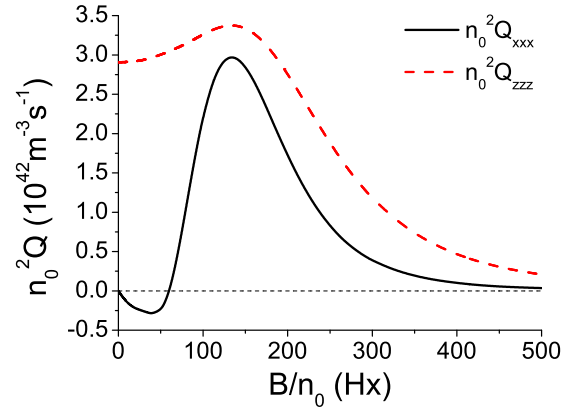
frequency is generally higher than the cyclotron frequency, but on average, an increasing magnetic field acts to increase the fraction of the orbit completed between collisions. As a consequence, the collision frequency begins to fall down with increasing B/n_0 and Q_{zzz} raises.

The behavior of Q_{xxx} for the lower values B/n_0 is particularly interesting. Initially, in the limit of the lowest B/n_0, Q_{xxx} is negative due to the Lorentz force and spatial variation of the energy (and hence spatial variation of the collision frequency), which on average induces the spatial variation of the average velocity of the electrons along the negative direction of the x axis. In this B/n_0 region, the negative sign of Q_{xxx} corresponds to an elongation of the swarm in the direction of the x component of the drift velocity (along the negative x axis in this field configuration). This is analogous to the elongation of the swarm described by the Q_{zzz} element along the z component of the drift velocity (the qE direction). With a further increase of B/n_0 the influence of collisions becomes more and more significant which in turn leads to the compressing or spreading of the swarm along the negative or positive direction of the x axis. Due to these effects Q_{xxx} becomes positive and increases with increasing B/n_0.

In Fig. 9 we show the remaining components of the third-order transport coefficient tensor as a function of B/n_0 for perpendicular electric and magnetic fields. For the higher values of B/n_0 all components decrease with an increasing B/n_0 as more and more electrons are held in their orbits by the magnetic field. For the lower values of B/n_0, however, the behavior of the third-order transport coefficients is complex due to many individual factors which simultaneously influence the third-order coefficient tensor. These individual factors include the thermal anisotropy (the chaotic motion of charged particles is different along different directions), magnetic anisotropy (the orientation of charged-particle orbits is controlled by the magnetic field), and spatial variations of the average velocity and average energy along the longitudinal and transverse directions. However, comparing the magnetic-field-free case and crossed electric and magnetic fields the interpretation of the third-order transport coefficients is similar (see Appendix B). For example, the coefficient Q_{zyy} describes

FIG. 9. Variation of the third-order transport coefficients with the repeated indices for the Reid ramp model. Calculations are performed via a multiterm theory for solving the Boltzmann equation in a crossed field configuration. The reduced electric field E/n_0 is set to 12 Td. The components of the $n_0^2 Q$ tensor are given in units of 10^{42} m^{-3}s^{-1}.

the differences in the longitudinal spreading in the central part of the swarm and along its transverse edges in the y direction. Likewise, the coefficient Q_{yyz} reflects the differences in the transverse spreading at the front of the swarm (along the direction given by the positive z) and at the trailing edge of the swarm (along the direction given by the negative z). The similar interpretation may be given for the remaining third-order transport coefficients shown in Fig. 9.

In Fig. 10 we show the comparison between the individual components of the third-order transport coefficient tensor, which could be identified in our Monte Carlo simulations, and the corresponding results, which are obtained from the numerical solution of the Boltzmann equation. The two sets

of results agree very well, even over the range of E/n_0 where the values of the coefficients are negative. We see that the error bars are not identical for different third-order transport coefficients. This indicates that the statistical fluctuations of the individual dynamical variables required for the evaluation of the third-order transport coefficients are not the same. Nevertheless, we see that the results obtained from the numerical solution of the Boltzmann equation are in very good agreement with those predicted by Monte Carlo simulations. This validates the theory and numerical scheme for solving the Boltzmann equation and Monte Carlo method when both the electric and magnetic fields are present and crossed at the right angle.

FIG. 10. Comparison between the multiterm Boltzmann equation results (full line) for various third-order transport coefficients and those calculated by a Monte Carlo simulation technique (symbols with error bars) in a crossed field configuration. The reduced electric field E/n_0 is set to 12 Td. The components of the $n_0^2 Q$ tensor are given in units of 10^{42} m^{-3}s^{-1}.
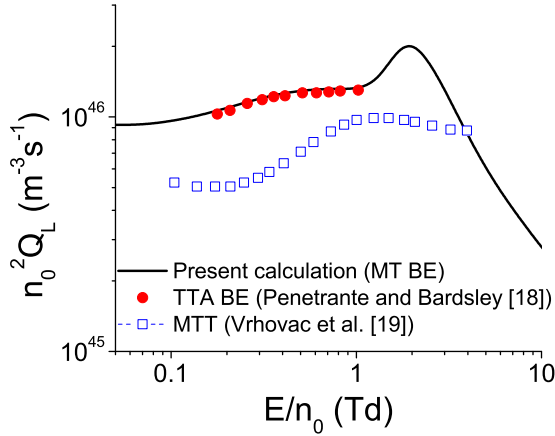
FIG. 11. Variation of the longitudinal third-order transport coefficient $n_0^2 Q_L$ with E/n_0 for electrons in neon. Our multiterm Boltzmann equation results (MT BE) are compared with those obtained by two-term approximation for solving the Boltzmann equation (TTA BE) [18] and momentum transfer theory (MTT) [19].

E. Third-order transport coefficients for electrons in neon

As an example of our calculations in real gases, in Fig. 11 we display the variation of the Q_L with E/n_0 for electrons in neon. The results obtained from the multiterm solution of the Boltzmann equation are compared with those predicted by the two-term approximation [18] and momentum transfer theory (MTT) [19]. The agreement between our multiterm results and those obtained by the two-term approximation is very good. This is a clear sign that there is no significant difference between the cross sections for elastic collisions of the electrons in neon used in the present multiterm calculations and in the previous two-term calculations performed by Penetrante and Bardsley [18]. The additional factor which favors the good agreement is the minimal influence of inelastic collisions. If inelastic collisions would play a more important role, then undoubtedly the differences between the multiterm and two-term results would be much higher. In any case, no calculations of Q_L were made by Penetrante and Bardsley for the higher values of E/n_0. On the other hand, the discrepancy between our results and those predicted by the momentum transfer theory (MTT) is clearly evident. This can be attributed to the fact that the momentum transfer theory assumes a very simple energy distribution function based on an effective mean energy. MTT produces reasonable results for the lowest-order transport coefficients such as drift velocity and even diffusion but it is expected to fail for ionization which depends on the high energy tail and also for higher-order transport coefficients that are very sensitive on the cross sections and correspondingly on the distribution function at all energies. Limitations of the MTT have been discussed many times [2,16,33,34,66].

In Fig. 12 we show the variation of the individual elements of the third-order transport coefficient tensor as a function of E/n_0 for electrons in neon. The same generic features of the third-order transport coefficients observed previously for the Reid ramp model are clearly evident. Both Q_{zzz} and Q_{xxz} are positive while the coefficient Q_{zxx} is negative over the range of E/n_0 considered. The total collision frequency
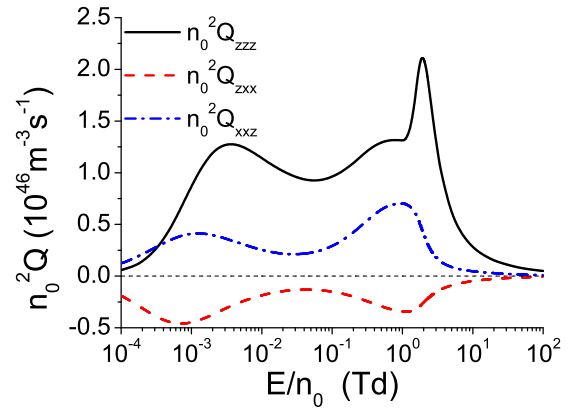
FIG. 12. Variation of the third-order transport coefficients with E/n_0 for electrons in neon. Calculations are performed using a multiterm approach for solving the Boltzmann equation.

increases with the increase of E/n_0, but not sufficiently fast to induced negative values of Q_{zzz} and Q_{xxz} (see Appendix B). The oscillatory behavior in the profiles of Q_{zzz}, Q_{xxz} and Q_{zzz} occurs for E/n_0 approximately less than 1 Td reflecting the energy variation of the cross section for elastic collisions. For E/n_0 approximately greater than 1 Td, inelastic collisions begin to play a significant role. As for the Reid ramp model, it appears that significant inelastic processes are required to suppress the longitudinal and transverse third-order transport coefficients.

IV. CONCLUSION

In this paper we have discussed the third-order transport coefficient tensor of charged-particle swarms moving in an infinite neutral gas under the influence of spatially homogeneous electric and magnetic fields. The third-order transport coefficient tensor is defined in terms of the extended flux gradient relation and the extended diffusion equation. The group projector method is then used for identifying the structure of the tensor and symmetries along its individual elements when both the electric and magnetic fields are present. For an electric-field-only situation, we have found that the third-order transport coefficient tensor has seven nonzero and only three independent elements. For parallel electric and magnetic fields, rotational invariance implies the third-order transport coefficient tensor has 11 nonzero and four independent elements, while for orthogonal electric and magnetic fields the tensor has 14 nonzero and 10 independent elements. Finally, when electric and magnetic fields are crossed at an arbitrary angle, it is found that the third-order transport coefficient tensor has 27 nonzero elements among which 18 are independent. The proposed methodology based on the group projector method and symmetry considerations of the Boltzmann equation can be applied to any of the transport coefficient of an arbitrary tensorial rank.

The second important issue addressed in the present work is the physical interpretation of the third-order transport coefficients. In order to resolve this issue, we have expanded the Fourier transform of the number charged-particle density in terms of the longitudinal and transverse third-order transport

coefficients. Using the inverse Fourier transformation of the expansion coefficients, we have derived the expression for the number density of charged particles in which the effects of third-order transport coefficients are explicitly included. It is found that deviations of the Gaussian distribution along the specific directions are directly related with the sign of the individual third-order transport coefficients.

Explicit expressions for the third-order transport coefficients in terms of the moments of the distribution function and in the absence of nonconservative collisions are derived in the framework of a multiterm theory for solving the Boltzmann equation. Using the symmetry properties of the moments, we have analyzed the structure of the third-order transport coefficient tensor. We have also developed the Monte Carlo method in which the third-order transport coefficients are defined in terms of the moments of charged-particle density in configuration space. It is found that only two independent components of the third-order transport coefficient tensor can be identified, as all tensor components are contracted with the corresponding spatial partial derivatives of charged-particle density. Thus, care must be taken when comparing the Monte Carlo results with those obtained by other theories.

Numerical calculations are performed using a multiterm solution of the Boltzmann equation for a range of model gases, including the Maxwell, hard sphere, and Reid ramp models. The results obtained are in very good agreement with those predicted by the Monte Carlo method when possible, over the range of the applied electric and magnetic fields. An important observation is that the contribution of the third-order transport coefficients to the spatial profile of the swarm becomes more pronounced for increasing the charged-particle to neutral-particle mass ratio. In this work we have also displayed and emphasized the need for a multiterm solution technique of Boltzmann's equation. It is found that the discrepancy between the two-term and fully converged multiterm results are much higher for the third-order transport coefficients than those for the lower order transport coefficients, e.g., drift velocity and diffusion coefficients. The theory and associated computer codes in the present work are equally valid for real gases. The third-order transport coefficients are calculated for electrons in neon and the results of calculations are compared with those evaluated by the two-term approximation for solving the Boltzmann equation and momentum transfer theory. Comparison with previous theories have shown surprisingly good agreement with the two-term solution of the Boltzmann equation and a significant disagreement with the momentum transfer theory.

The duality of transport coefficients, e.g., the existence of two different families of transport coefficients, the bulk and the flux, is well known in the presence of nonconservative collisions. Third-order transport coefficients are expected to be more sensitive to the explicit influence of nonconservative collisions. In order to investigate the effects of nonconservative collisions on the third-order transport coefficients one must go to third-order in the density gradient expansion to account for such effects. This remains the focus of our future investigation. Likewise, the remaining step to be taken, is to apply the theory and mathematical machinery developed in this work to investigate the correlation between the third-order transport coefficients and those of lower order, e.g., the

drift and diffusion coefficients [19]. Additional issues which should be considered are the effects of anisotropic scattering and the behavior of the third-order transport coefficients in time-dependent electric and magnetic fields. Finally, it would be very challenging to model strong nonequilibrium systems such as streamer discharges by suitable coupling of the extended diffusion equation which incorporates the third-order transport coefficients for both the electrons and ions, and Poisson's equation for the space charge electric field calculation.

The theory presented here covers the structure, symmetries, and method of calculation of the third-order transport coefficients and the advantages that it may bring should it be applied. In this paper, we focus on physics of ionized gases (swarms and low-temperature collisional plasmas), but approach may be extended to other physical systems if one accounts for the dominant physical interactions and expected symmetries. One such example where these results may be applied directly is modeling of positron thermalization in gas filled traps [86,87] or thermalization of positrons in gases [88–90].

APPENDIX A: THE GROUP PROJECTOR METHOD

The structure of tensorial transport coefficients can be determined by employing group theory, since their structure reflects the symmetry of the system. The studied system consists of a swarm of charged particles, neutral background gas particles and the applied electric and magnetic fields. The symmetry group of a system is the group of all transformations under which the system is invariant [91–93]. The symmetry groups of the electric and magnetic fields are $C_{\infty V}$ and $C_{\infty h}$ respectively, since the electric field is a polar vector, and the magnetic field is an axial vector. These are the symmetry groups of an immobile cone and of a rotating cylinder, respectively [91]. If both electric and magnetic fields are present in the system, the symmetry group of the field configuration is determined by the angle between the fields. The symmetry group of the parallel fields configuration is C_{∞}. This is the symmetry group of a rotating cone [91]. Orthogonal field configuration has the symmetry group C_{1v}. The symmetry group of the general field configuration is the trivial group C_1. Background gas is invariant under all transformations from the orthogonal group $O(3)$. This is the symmetry group of a sphere. Therefore, the symmetry group of the field configuration is also the symmetry group of the entire system.

The structure of a tensor can be determined from its invariance, under operations from the symmetry group of the system. The action of a group G on vectors, from a vector space H, is represented by a group homomorphism from G to the general linear group on H, $GL(H)$ [92,93]. Polar

vectors, such as drift velocity, are transformed by the polar vector representation of the symmetry group of the system $D^{pv}(G)$. This representation is reducible [65,93] and, for finite and compact groups, it decomposes into the irreducible components $D^{(\mu)}(G)$ as

$$D^{pv}(G) = \oplus_{\mu=1}^{r} a_\mu D^{(\mu)}(G). \tag{A1}$$

Here a_μ is the number of times the irreducible representation $D^{(\mu)}(G)$ appears in the decomposition of $D^{pv}(G)$, and r is the number of inequivalent irreducible representations of the group G. In addition, for decomposable representations there exists a symmetry-adapted basis [65,93], which satisfies the condition

$$D^{pv}(G)|\mu t_\mu m\rangle = \sum_{n=1}^{|\mu|} D_{nm}^{(\mu)}(G)|\mu t_\mu n\rangle. \tag{A2}$$

This implies that for every irreducible representation $D^{(\mu)}(G)$ from (A1) there will be a subspace in H which transforms by $D^{(\mu)}(G)$ [65,93]. A very important representation, which exists for every group G, is the trivial irreducible representation A_0. This representation is defined as $D^{(A_0)}(g) = 1, \forall g \in G$. This representation is irreducible, since it is one dimensional.

It can be seen from (A2) that a vector is invariant under the action of $D^{(pv)}(G)$ if it belongs to the subspace of the trivial irreducible representation. This invariant subspace can be found by employing group projectors. In the case of the trivial representation, the group projector is simply

$$P^{(A_0)}(D^{pv}, G) = \frac{1}{|G|} \sum_{g \in G} D^{pv}(g) \tag{A3}$$

for finite groups, where $|G|$ is the order of the group G [65]. For one-parameter Lie groups the group projector for A_0 is

$$P^{(A_0)}(D^{pv}, G) = \sum_R \int D^{pv}(R) \, dR. \tag{A4}$$

Here the summation goes over distinct connected components, and integration is taken over the range of the group parameter [93]. Any vector, from the invariant subspace of $D^{pv}(G)$, including the drift velocity, is a linear combination of the eigenvectors of the projection operator $P^{(A_0)}(D^{pv}, G)$.

Diffusion tensor is a linear operator which maps the local density gradient vector $\nabla n(\mathbf{r}, t)$ onto the diffusive flux vector. Therefore diffusion tensor belongs to the range of the projector $P^{(A_0)}(D^{pv \otimes 2}, G)$ where $D^{pv \otimes 2}(G)$ represents $D^{pv} \otimes D^{pv}(G) = D^{pv}(G) \otimes D^{pv}(G)$. Similarly the skewness tensor maps the tensor square of the gradient vector, which acts upon the local density $\nabla \otimes \nabla n(\mathbf{r}, t)$, onto the vector of the third-order diffusive flux. Thus the skewness tensor belongs to the range of the projection operator $P^{(A_0)}(D^{pv} \otimes [D^{pv}]^2, G)$, where $[D^{pv}]^2$ represents the symmetrized tensor square of the polar vector representation. This symmetrization is a result of the commutativity of the gradient operators.

Strictly speaking, the action of the group on operators, such as diffusion tensor and skewness tensor, is represented by employing superoperators [94]. They are defined as $\widehat{\widehat{D}}(g)\hat{A} = D^{pv}(g)\hat{A}D^{pv}(g^{-1})$. Therefore, the most straightforward application of group theory would require the use of group superoperators. However, this is not necessary, since every

second rank basis operator $|i\rangle \otimes \langle j|$ acting on a vector space H is uniquely paired with a basis vector $|i\rangle \otimes |j\rangle$ from the vector space $H \otimes H$. The same applies for the basis operators of the third rank $|i\rangle \otimes [\langle j| \otimes \langle k|]$ and basis vectors $|i\rangle \otimes [|j\rangle \otimes |k\rangle]$ from the vector space $H \otimes [H \otimes H]$. Here square brackets represent symmetrization of the tensor product. Thus, the group projector method can be applied for representations $D^{pv}(G) \otimes D^{pv}(G)$ and $D^{pv} \otimes [D^{pv}]^2$ in the corresponding vector spaces. Then eigenvectors of the group projectors can be mapped into the corresponding basis tensors. Therefore diffusion tensor and skewness tensor are linear combinations of the basis tensors, which are obtained from eigenvectors of the projection operators $P^{(A_0)}(D^{pv} \otimes D^{pv}, G)$ and $P^{(A_0)}(D^{pv} \otimes [D^{pv}]^2, G)$, respectively. Moreover, it is not necessary to use $D^{pv} \otimes [D^{pv}]^2$ for determining the structure of the skewness tensor. One can instead use $D^{pv} \otimes D^{pv} \otimes D^{pv}$ and symmetrize the resulting tensors by the last two indices.

APPENDIX B: PHYSICAL INTERPRETATION OF THE INDIVIDUAL COMPONENTS OF THE THIRD-ORDER TRANSPORT COEFFICIENT TENSOR AND ANALYSIS OF THEIR SIGN

Using the flux gradient relation (7), the fluxes of charged particles induced exclusively by the third-order transport coefficient tensor are given by

$$\Gamma_{Q,z} = Q_{zzz} \frac{\partial^2 n(\mathbf{r}, t)}{\partial z^2} + Q_{zxx} \left[\frac{\partial^2 n(\mathbf{r}, t)}{\partial x^2} + \frac{\partial^2 n(\mathbf{r}, t)}{\partial y^2} \right],$$

$$\Gamma_{Q,x} = 2Q_{xxz} \frac{\partial^2 n(\mathbf{r}, t)}{\partial x \partial z}, \tag{B1}$$

where Q_{zzz}, Q_{zxx}, and Q_{xxz} are independent components of the third-order transport coefficient tensor (see Sec. II B). The leading term in the expansion of the density of charged particles (33) is of key importance in considering the sign of the derivative of the charged-particle density. Therefore, in what follows we consider only this term in the analysis of the fluxes of charged particles (B1). The second-order derivatives of the Gaussian (32) are given by

$$\frac{\partial^2 n^{(0)}(\mathbf{r}, t)}{(\partial z)^2} = \left(z^2 - \sigma_z^2 \right) \frac{n^{(0)}(\mathbf{r}, t)}{\sigma_z^4}, \tag{B2}$$

$$\frac{\partial^2 n^{(0)}(\mathbf{r}, t)}{(\partial x)^2} = \left(x^2 - \sigma_x^2 \right) \frac{n^{(0)}(\mathbf{r}, t)}{\sigma_x^4}, \tag{B3}$$

$$\frac{\partial^2 n^{(0)}(\mathbf{r}, t)}{(\partial x \partial z)} = xz \frac{n^{(0)}(\mathbf{r}, t)}{\sigma_x^2 \sigma_z^2}, \tag{B4}$$

where

$$\sigma_x^2 = 2D_T t, \quad \sigma_z^2 = 2D_L t. \tag{B5}$$

For simplicity, the above derivatives correspond to the coordinate system whose origin is placed at the center of the Gaussian distribution. Thus, the term $z - Wt$ is replaced by the term z in (B2) and (B4).

In order to visualize these second-order derivatives in the most efficient way for arbitrarily values of σ_z, we introduce the set of new coordinates $x/\sigma_x = \chi_x$, $y/\sigma_y = \chi_y$, and $z/\sigma_z = \chi_z$.
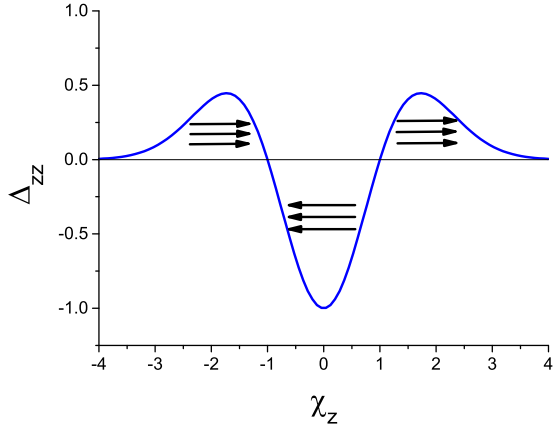
FIG. 13. The normalized derivative Δ_{zz} of the density of charged particles as a function of the relative coordinate χ_z. The arrows denote the direction of motion represented by Q_{zzz} if this component is positive. The field force is oriented along the positive χ_z direction.

Using the new coordinates, Eqs. (B2)–(B4) become

$$\frac{\partial^2 n^{(0)}}{\partial \chi_z^2} = (\chi_z^2 - 1)n^{(0)}, \tag{B6}$$

$$\frac{\partial^2 n^{(0)}}{\partial \chi_x^2} = (\chi_x^2 - 1)n^{(0)}, \tag{B7}$$

$$\frac{\partial^2 n^{(0)}}{\partial \chi_x \partial \chi_z} = \chi_x \chi_z n^{(0)}, \tag{B8}$$

where

$$n^{(0)}(\boldsymbol{\chi}, t) = C_\chi \exp\left[-\tfrac{1}{2}(\chi_z^2 + \chi_x^2 + \chi_y^2)\right] \tag{B9}$$

and

$$C_\chi = \frac{N_0 e^{-R_{\text{net}}t}}{(2\pi)^{3/2}\sigma_x^2 \sigma_z}. \tag{B10}$$

By combining equations (B6)–(B10) the normalized second-order derivatives of the density of charged particles can be written as follows:

$$\Delta_{zz} \equiv \frac{1}{C_\chi}\frac{\partial^2 n^{(0)}}{\partial \chi_z^2} = (\chi_z^2 - 1)e^{-\frac{1}{2}(\chi_z^2 + \chi_x^2 + \chi_y^2)}, \tag{B11}$$

$$\Delta_{xx} \equiv \frac{1}{C_\chi}\frac{\partial^2 n^{(0)}}{\partial \chi_x^2} = (\chi_x^2 - 1)e^{-\frac{1}{2}(\chi_z^2 + \chi_x^2 + \chi_y^2)}, \tag{B12}$$

$$\Delta_{xz} \equiv \frac{1}{C_\chi}\frac{\partial^2 n^{(0)}}{\partial \chi_x \partial \chi_z} = \chi_x \chi_z e^{-\frac{1}{2}(\chi_z^2 + \chi_x^2 + \chi_y^2)}. \tag{B13}$$

In Fig. 13 we show the quantity Δ_{zz} as a function of χ_z. We see that the representing curve is symmetric with respect to the origin in which it has a minimum. If Q_{zzz} is positive the direction of motion represented by this component depends on the sign of Δ_{zz} in the following way. When Δ_{zz} is positive, the motion described by Q_{zzz} is also directed along the positive z axis, which is indicated by arrows that are oriented to the right. Conversely, when Δ_{zz} is negative, the motion described by Q_{zzz} is directed along the negative z axis, which is indicated in this case by arrows that are oriented to the left. Therefore, when $Q_{zzz} > 0$ the leading edge of the Gaussian is elongated while the training edge is compressed to a certain extent. It is
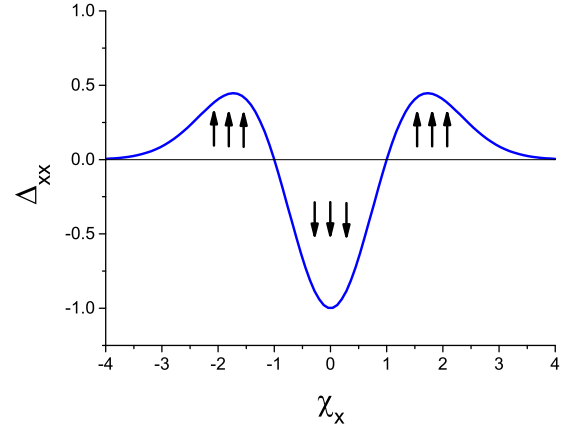
FIG. 14. The normalized derivative Δ_{xx} of the density of charged particles as a function of the relative coordinate χ_x. The arrows denote the direction of motion represented by Q_{zxx} if this component is positive: the arrows directed upwards (downwards) represent motion in the positive (negative) z direction.

clear that when $Q_{zzz} < 0$, then the opposite situation holds: the leading edge of the Gaussian is compressed while the trailing edge is elongated.

Figure 14 shows the graph of the function Δ_{xx}. This function is identical to the one illustrated in Fig. 13. When Q_{zxx} is positive, the motion described by Q_{zxx} is directed along the positive z axis at the swarm edges, which is indicated by arrows that are oriented upwards. However, the motion represented by Q_{zxx} at the swarm center is directed along the negative z axis in this case, which is indicated by arrows that are oriented downwards. Likewise, if Q_{zxx} is negative, then the motion described by Q_{zxx} is directed along the negative z axis at the edges of the swarm, and along the positive z axis at the swarm center.

In Fig. 15 we show the contour plot of the function Δ_{xz} as a function of χ_x and χ_z. This function is positive in the first and
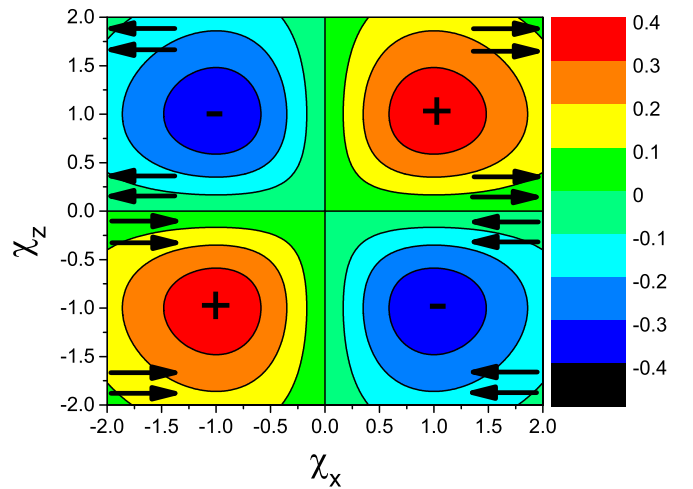
FIG. 15. The normalized derivative Δ_{xz} of the density of charged particles as a function of the relative coordinates χ_x and χ_z. The arrows denote the direction of motion represented by Q_{xxz} if this component is positive.

third quadrant and negative in the second and fourth quadrant. If Q_{xxz} is positive the direction of motion represented by this component depends on the sign of Δ_{xz} in the following way. When Δ_{xz} is positive the motion described by Q_{xxz} is directed along the positive x axis which is indicated by arrows that are oriented to the right. Conversely, when Δ_{xz} is negative the motion described by Q_{xxz} is directed along the negative x axis which is indicated by arrows that are oriented to the left. It is clear that when $Q_{xxz} < 0$ the direction of motion represented by this component is reversed. It should be noted that the joint contribution of Q_{zxx} and Q_{xxz} leads to a pear-shaped Gaussian distribution.

In what follows we investigate the effects of the gas pressure on the third-order transport coefficients. Using the set of new coordinates χ_x, χ_y and χ_z, the number density of charged particles given by Eq. (33) can be written as

$$n^{(1)}(\boldsymbol{r}, t) = n^{(0)}(\boldsymbol{r}, t) \left[1 + \frac{tQ_L}{\sigma_z^3} \chi_z (\chi_z^2 - 3) \right.$$
$$\left. + \frac{3tQ_T}{\sigma_x^2 \sigma_z} \chi_z (\chi_x^2 + \chi_y^2 - 2) \right]. \quad \text{(B14)}$$

From Eq. (B14) we see that the contribution of the third-order transport coefficients to the spatial profile of the swarm is reduced with increasing number density of the neutral particles n_0. This is due to the fact that Q_L and Q_T scale as $1/n_0^2$ while σ_x and σ_z scale as $1/\sqrt{n_0}$ with the variation of n_0. From this, it follows that the terms tQ_L/σ_z^3 and $3tQ_T/\sigma_x^2\sigma_z$ scale as $1/\sqrt{n_0}$ with with the variation of n_0. In addition, from Eq. (B14) we can also see that the influence of the third-order transport coefficients on the spatial profile of charged particles is reduced as $1/\sqrt{t}$ with increasing t due to the time dependence of the terms tQ_L/σ_z^3 and $3tQ_T/\sigma_x^2\sigma_z$. Thus, from the scalings of the third-order transport coefficients and associated properties it can be concluded that their experimental determination would be the most efficient at low pressures. On the other hand, measurements at low pressures in drift tubes require optimal gaps and volumes in order to reach the conditions where hydrodynamic approximation is applicable (negligible length or relaxation distances as compared to the overall gap). Special care should be taken in order to avoid kinetic phenomena [16] such as diffusion cooling [95,96] and other issues associated with an inability of the swarm to be fully relaxed due to a small number of collisions of charged particles and neutral gas particles. In any case, the experimental determination of third-order transport coefficients requires large gas volumes and low pressures. Similar findings have been reported in Ref. [18].

In studies of third-order transport coefficients tensor we often find it necessary to refer to the sign of the third-order transport coefficients to explain certain phenomena. Let us assume that the swarm of charged particles is acted on solely by an electric field. The following elementary considerations apply.

The motion of charged particles represented by the longitudinal component Q_{zzz} produces differences in the spreading of the density profile between the front and trailing edges of the swarm. When $Q_{zzz} > 0$, the front edge of the density profile is elongated, while the trailing edge is compressed. The opposite situation holds when $Q_{zzz} < 0$: the front edge of the swarm is compressed while the trailing edge of the profile is elongated.

Charged particles at the front of the swarm have higher energies on average, than those at the back of the swarm, as they are accelerated through the larger potential difference. If the collision frequency is independent of energy, the spread of charged particles along the field direction is induced by the action of the force and by the chaotic motion of particles. If the collision frequency is a decreasing function of the charged-particle energy, the friction due to collisions along the field direction is also decreased contributing additionally in the spreading of the density profile. When collision frequency increases with the particle energy, however, the friction will be enhanced along the field direction which in turn reduces the spreading of the density profile. Thus, the longitudinal component Q_{zzz} is positive whenever the growth of collision frequency and associated energy losses in collisions are not able to affect the spreading of charged particles due to the electric field force and chaotic motion of charged particles. This is exactly what happens in most cases considered in our calculations.

The motion of a swarm represented by Q_{xzx} produces differences in the transverse spreading of the density profile. When $Q_{xzx} > 0$, the density profile is expanded along the transverse direction at the front of the swarm while at the back of the swarm the profile is compressed. When $Q_{xzx} < 0$, the density profile is compressed along the transverse direction at the front and extended at the trailing edge of the swarm.

The electric force does not act along the transverse direction. This suggests that the spreading of the density profile is entirely controlled by the chaotic motion of charged particles. If the collision frequency decreases with energy, this will further enhance the transverse spread at the front of the swarm as collisions between charged particles and background gas molecules are less frequent. If the collision frequency increases with energy, the reverse situation occurs. In this case it is the high energy electrons, which predominantly exist at the front of the swarm, have more collisions than those at the back of the swarm. This results in a greater resistance to the transverse spreading at the front of the swarm. Thus, the transverse component Q_{xzx} is positive under conditions in which the growth of the collision frequency and energy losses in collisions are not intensive enough to exceed the higher average speed of charged particles at the front of the swarm.

The off-diagonal component Q_{zxx} describes the differences in the longitudinal spreading in the central part of the swarm and along its transverse edges. If $Q_{zxx} > 0$, the longitudinal spreading is faster at the transverse edges than in the central part of the swarm. Conversely, if $Q_{zxx} < 0$, the reverse situation occurs: the longitudinal spreading is more pronounced in the central part of the swarm than at the edges. The parabolic rise in mean energy along the transverse direction favors the faster longitudinal spreading at the transverse edges of the swarm. The parabolic rise in mean energy is due to the fact that the most energetic electrons quickly cross the distance between the swarm's center and its edges, if the increase of the collision frequency is not large enough to compensate for the high speed of energetic electrons. If the collision frequency is independent of energy, this is the only contribution to the difference in the rate of longitudinal expansion along

TABLE II. Symmetry properties of the individual components of the skewness tensor. The transformation represents A (parity), B (rotation of π about the z axis), C (parity and rotation of π about the y axis), and D (parity and rotation of π about the x axis).

	Transformation			
Tensor component	$E \to -E, B \to B$	$E \to E, B \to (-B_y, B_z)$	$E \to E, B \to (B_y, -B_z)$	$E \to E, B \to -B$
Q_{xxz}, Q_{xzx}	$-Q_{xxz}, -Q_{xzx}$	Q_{xxz}, Q_{xzx}	Q_{xxz}, Q_{xzx}	Q_{xxz}, Q_{xzx}
Q_{yyz}, Q_{yzy}	$-Q_{yyz}, -Q_{yzy}$	Q_{yyz}, Q_{yzy}	Q_{yyz}, Q_{yzy}	Q_{yyz}, Q_{yzy}
Q_{zxx}	$-Q_{zxx}$	Q_{zxx}	Q_{zxx}	Q_{zxx}
Q_{zyy}	$-Q_{zyy}$	Q_{zyy}	Q_{zyy}	Q_{zyy}
Q_{zzz}	$-Q_{zzz}$	Q_{zzz}	Q_{zzz}	Q_{zzz}
Q_{xxx}	$-Q_{xxx}$	$-Q_{xxx}$	Q_{xxx}	$-Q_{xxx}$
Q_{xyy}	$-Q_{xyy}$	$-Q_{xyy}$	Q_{xyy}	$-Q_{xyy}$
Q_{xzz}	$-Q_{xzz}$	$-Q_{xzz}$	Q_{xzz}	$-Q_{xyy}$
Q_{yxy}, Q_{yyx}	$-Q_{yxy}, -Q_{yyx}$	$-Q_{yxy}, -Q_{yyx}$	Q_{yxy}, Q_{yyx}	$-Q_{yxy}, -Q_{yyx}$
Q_{zxz}, Q_{zzx}	$-Q_{zxz}, -Q_{zzx}$	$-Q_{zxz}, -Q_{zzx}$	Q_{zxz}, Q_{zzx}	$-Q_{zxz}, -Q_{zzx}$
Q_{xyz}, Q_{xzy}	$-Q_{xyz}, -Q_{xzy}$	Q_{xyz}, Q_{xzy}	$-Q_{xyz}, -Q_{xzy}$	$-Q_{xyz}, -Q_{xzy}$
Q_{yxz}, Q_{yzx}	$-Q_{yxz}, -Q_{yzx}$	Q_{yxz}, Q_{yzx}	$-Q_{yxz}, -Q_{yzx}$	$-Q_{yxz}, -Q_{yzx}$
Q_{zxy}, Q_{zyx}	$-Q_{zxy}, -Q_{zyx}$	Q_{zxy}, Q_{zyx}	$-Q_{zxy}, -Q_{zyx}$	$-Q_{zxy}, -Q_{zyx}$
Q_{xxy}, Q_{xyx}	$-Q_{xxy}, -Q_{xyx}$	$-Q_{xxy}, -Q_{xyx}$	$-Q_{xxy}, -Q_{xyx}$	Q_{xxy}, Q_{xyx}
Q_{yxx}	$-Q_{yxx}$	$-Q_{yxx}$	$-Q_{yxx}$	Q_{yxx}
Q_{yyy}	$-Q_{yyy}$	$-Q_{yyy}$	$-Q_{yyy}$	Q_{yyy}
Q_{yzz}	$-Q_{yzz}$	$-Q_{yzz}$	$-Q_{yzz}$	Q_{yzz}
Q_{zyz}, Q_{zzy}	$-Q_{zyz}, -Q_{zzy}$	$-Q_{zyz}, -Q_{zzy}$	$-Q_{zyz}, -Q_{zzy}$	Q_{zyz}, Q_{zzy}

the transverse direction. If the collision frequency decreases with energy, this is an additional factor which contributes to the rapid longitudinal spread at the transverse edges of the swarm. If the collision frequency increases with energy, this contributes to greater resistance to longitudinal expansion at the transverse edges than in the center of the swarm. For a constant collision frequency, Q_{zxx} component is positive, but much less in comparison to Q_{zzz} and Q_{xzx}. If the collision frequency decreases with energy, this component is positive and greater in magnitude than in the previous case. If the collision frequency increases with energy and Q_{xzx} is positive then the Q_{zxx} component is negative. This could be

expected, since the particles at the transverse edges have a slightly higher energy, and thus higher collision frequency. Such behavior of Q_{zxx} has been observed in the case of electron swarms in most atomic and molecular gases. If the collision frequency increases with energy and Q_{xzx} is negative then Q_{zxx} is positive. A possible explanation for this effect is that when Q_{xzx} is negative the energy of the electrons at the transverse edges of the swarm is, on average, less than in the center of the swarm. The high-energy electrons undergo more and more collisions for increasing electron energy which in turn prevent them from reaching the transverse edges of the swarm.

APPENDIX C: EXPRESSIONS FOR THE INDIVIDUAL ELEMENTS OF THE THIRD-ORDER TRANSPORT COEFFICIENT TENSOR IN THE BOLTZMANN EQUATION ANALYSIS AND MONTE CARLO SIMULATIONS

Using symmetry properties of the moments $F(\nu lm|s\lambda\mu)$ discussed in Ref. [70], the corresponding symmetry properties of the individual elements of the third-order transport coefficient tensor are detailed in Table II. The structure of the tensor may be determined by applying the symmetries in Table II in combination with the additional physical arguments that concern fluxes of charged particles induced by magnetic field. These arguments are necessary to identify the zero elements as well as those elements of the tensor which are equal between each other for a given configuration of the fields. The similar procedure has been applied for the vectorial and tensorial transport coefficients of the lower order [70].

In this Appendix we present the explicit expressions for the individual elements of the flux third-order transport coefficient tensor. These expressions have been derived by considering the flux-gradient relation in the spherical form (41) and explicit expressions for the irreducible gradient tensor operator [33]. In the following expressions α is omitted from the argument of F for brevity.

For parallel electric and magnetic fields, the individual elements of the flux tensor are given by

$$Q_{xxz} = \frac{1}{\sqrt{2}\alpha}[\text{Im}(F(011|221)) - \text{Im}(F(01-1|221))], \tag{C1}$$

$$Q_{xyz} = \frac{1}{\sqrt{2}\alpha}[\text{Re}(F(01-1|221)) - \text{Re}(F(011|221))], \tag{C2}$$

$$Q_{zxx} = -\frac{1}{\alpha}\left[\frac{1}{\sqrt{3}}\text{Im}(F(010|200)) + \frac{1}{\sqrt{6}}\text{Im}(F(010|220))\right] + \frac{1}{\alpha}\text{Im}(F(010|222)), \tag{C3}$$

$$Q_{zzz} = \frac{1}{\alpha}\left[\sqrt{\frac{2}{3}}\text{Im}(F(010|220)) - \frac{1}{\sqrt{3}}\text{Im}(F(010|200))\right]. \tag{C4}$$

For perpendicular electric and magnetic fields, the individual elements of the flux tensor are given by

$$Q_{xxx} = \frac{\sqrt{2}}{\alpha}\left[\frac{1}{\sqrt{3}}\text{Im}(F(011|200)) + \frac{1}{\sqrt{6}}\text{Im}(F(011|220))\right] + \frac{1}{\sqrt{2}\alpha}[-\text{Im}(F(011|222)) + \text{Im}(F(01-1|222))], \tag{C5}$$

$$Q_{xyy} = \frac{\sqrt{2}}{\alpha}\left[\frac{1}{\sqrt{3}}\text{Im}(F(011|200)) + \frac{1}{\sqrt{6}}\text{Im}(F(011|220))\right] + \frac{1}{\sqrt{2}\alpha}[\text{Im}(F(011|222)) - \text{Im}(F(01-1|222))], \tag{C6}$$

$$Q_{xzz} = \frac{\sqrt{2}}{\alpha}\left[\frac{1}{\sqrt{3}}\text{Im}(F(011|200)) - \sqrt{\frac{2}{3}}\text{Im}(F(011|220))\right], \tag{C7}$$

$$Q_{xxz} = \frac{1}{\sqrt{2}\alpha(t)}[\text{Im}(F(011|221)) - \text{Im}(F(01-1|221))], \tag{C8}$$

$$Q_{yxy} = -\frac{1}{\sqrt{2}\alpha}[\text{Im}(F(011|222)) + \text{Im}(F(01-1|222))], \tag{C9}$$

$$Q_{yyz} = \frac{1}{\sqrt{2}\alpha}[\text{Im}(F(011|221)) + \text{Im}(F(01-1|221))], \tag{C10}$$

$$Q_{zxz} = -\frac{1}{\alpha}\text{Im}(F(010|221)), \tag{C11}$$

$$Q_{zxx} = -\frac{1}{\alpha}\left[\frac{1}{\sqrt{3}}\text{Im}(F(010|200)) + \frac{1}{\sqrt{6}}\text{Im}(F(010|220))\right] + \frac{1}{\alpha}\text{Im}(F(010|222)), \tag{C12}$$

$$Q_{zyy} = -\frac{1}{\alpha}\left[\frac{1}{\sqrt{3}}\text{Im}(F(010|200)) + \frac{1}{\sqrt{6}}\text{Im}(F(010|220))\right] - \frac{1}{\alpha}\text{Im}(F(010|222)), \tag{C13}$$

$$Q_{zzz} = \frac{1}{\alpha}\left[\sqrt{\frac{2}{3}}\text{Im}(F(010|220)) - \frac{1}{\sqrt{3}}\text{Im}(F(010|200))\right]. \tag{C14}$$

When electric and magnetic fields are crossed at an arbitrary angle, the individual elements of the flux tensor are given by

$$Q_{xxy} = \frac{1}{\sqrt{2}\alpha}[\text{Re}(F(011|222)) - \text{Re}(F(01-1|222))], \tag{C15}$$

$$Q_{yxx} = \frac{\sqrt{2}}{\alpha}\left[\frac{1}{\sqrt{3}}\text{Re}(F(011|200)) + \frac{1}{\sqrt{6}}\text{Re}(F(011|220))\right] + \frac{1}{\sqrt{2}\alpha}[-\text{Re}(F(011|222)) - \text{Re}(F(01-1|222))], \tag{C16}$$

$$Q_{yyy} = \frac{\sqrt{2}}{\alpha}\left[\frac{1}{\sqrt{3}}\text{Re}(F(011|200)) + \frac{1}{\sqrt{6}}\text{Re}(F(011|220))\right] + \frac{1}{\sqrt{2}\alpha}[\text{Re}(F(011|222)) + \text{Re}(F(01-1|222))], \tag{C17}$$

$$Q_{yzz} = \frac{\sqrt{2}}{\alpha}\left[\frac{1}{\sqrt{3}}\text{Re}(F(011|200)) - \sqrt{\frac{2}{3}}\text{Re}(F(011|220))\right], \tag{C18}$$

$$Q_{zxy} = -\frac{1}{\alpha}\text{Re}(F(010|222)), \tag{C19}$$

$$Q_{zyz} = \frac{1}{\alpha}\text{Re}(F(010|221)), \tag{C20}$$

$$Q_{xyz} = \frac{1}{\sqrt{2}\alpha}[\text{Re}(F(01-1|221)) - \text{Re}(F(011|221))], \tag{C21}$$

$$Q_{yxz} = \frac{1}{\sqrt{2}\alpha}[\text{Re}(F(011|221)) + \text{Re}(F(01-1|221))]. \tag{C22}$$

The elements of the third-order transport coefficients that are independent in a crossed field configuration, are also independent when the electric and magnetic fields cross at an arbitrary angle. Thus, the corresponding expressions in the Boltzmann equation analysis are identical.

In what follows, we present the explicit expressions for the flux components of the third-order transport coefficient tensor that might be identified and computed in our Monte Carlo simulations.

For parallel electric and magnetic fields, the explicit expressions of the flux longitudinal and flux transverse third-order transport coefficients are given by Eqs. (48) and (49), respectively. We are not able to isolate the additional elements of the tensor in the Monte Carlo method used in the present work. As already discussed in this Appendix, the coefficients Q_{xxz}, Q_{xyz}, Q_{zxx}, and $Q_L \equiv Q_{zzz}$ could be identified and computed using Boltzmann equation solutions.

For perpendicular electric and magnetic fields, we are able to identify six components of the third-order transport coefficient tensor in our Monte Carlo simulations. The tensor components are

$$Q_L \equiv Q_{zzz}, \quad Q_{E \times B} \equiv Q_{xxx} \tag{C23}$$

and

$$Q_{\pi(xxz)} \equiv \tfrac{1}{3}(Q_{xxz} + Q_{xzx} + Q_{zxx}), \tag{C24}$$

$$Q_{\pi(yyx)} \equiv \tfrac{1}{3}(Q_{yyx} + Q_{yxy} + Q_{xyy}) \tag{C25}$$

$$Q_{\pi(yyz)} \equiv \tfrac{1}{3}(Q_{yyz} + Q_{yzy} + Q_{zyy}), \tag{C26}$$

$$Q_{\pi(zzx)} \equiv \tfrac{1}{3}(Q_{zzx} + Q_{zxz} + Q_{xzz}), \tag{C27}$$

where the cross product $\boldsymbol{E} \times \boldsymbol{B}$ defines the x axis while $\pi(abc)$ denotes all possible permutations of (a, b, c). The explicit expressions of the flux tensor components are given by

$$Q_{zzz} = \tfrac{1}{6}(3\langle z^2 c_z \rangle - 3\langle c_z \rangle \langle z^2 \rangle - 6\langle z \rangle \langle zc_z \rangle + 6\langle z \rangle \langle z \rangle \langle c_z \rangle), \tag{C28}$$

$$Q_{xxx} = \tfrac{1}{6}(3\langle x^2 c_x \rangle - 3\langle c_x \rangle \langle x^2 \rangle - 6\langle x \rangle \langle xc_x \rangle + 6\langle x \rangle \langle x \rangle \langle c_x \rangle), \tag{C29}$$

$$Q_{xzz} = \tfrac{1}{6}(\langle z^2 c_x \rangle + 2\langle zxc_z \rangle - 2\langle c_z \rangle \langle zx \rangle - \langle c_x \rangle \langle z^2 \rangle - 2\langle z \rangle \langle xc_z \rangle - 2\langle z \rangle \langle zc_x \rangle - 2\langle x \rangle \langle zc_z \rangle + 2\langle c_x \rangle \langle z \rangle \langle z \rangle + 4\langle x \rangle \langle z \rangle \langle c_z \rangle), \tag{C30}$$

$$Q_{zxx} = \tfrac{1}{6}(\langle x^2 c_z \rangle + 2\langle xzc_x \rangle - 2\langle c_x \rangle \langle xz \rangle - \langle c_z \rangle \langle x^2 \rangle - 2\langle x \rangle \langle zc_x \rangle - 2\langle x \rangle \langle xc_z \rangle - 2\langle z \rangle \langle xc_x \rangle + 2\langle c_z \rangle \langle x \rangle \langle x \rangle + 4\langle z \rangle \langle x \rangle \langle c_x \rangle), \tag{C31}$$

$$Q_{zyy} = \tfrac{1}{6}(\langle y^2 c_z \rangle + 2\langle yzc_y \rangle - \langle c_z \rangle \langle y^2 \rangle - 2\langle z \rangle \langle yc_y \rangle), \tag{C32}$$

$$Q_{xyy} = \tfrac{1}{6}(\langle y^2 c_x \rangle + 2\langle yxc_y \rangle - \langle c_x \rangle \langle y^2 \rangle - 2\langle x \rangle \langle yc_y \rangle). \tag{C33}$$

For the most general case when electric and magnetic fields are crossed at an arbitrary angle, we are able to identify 10 components of the third-order transport coefficient tensor in our Monte Carlo simulation code. They include six components already defined for perpendicular electric and magnetic fields and four additional coefficients, including

$$Q_{E \times (E \times B)} \equiv Q_{yyy}, \tag{C34}$$

where the cross product $\boldsymbol{E} \times (\boldsymbol{E} \times \boldsymbol{B})$ defines the y axis, and

$$Q_{\pi(xxy)} \equiv \tfrac{1}{3}(Q_{xxy} + Q_{xyx} + Q_{yxx}), \tag{C35}$$

$$Q_{\pi(zzy)} \equiv \tfrac{1}{3}(Q_{zzy} + Q_{zyz} + Q_{yzz}), \tag{C36}$$

$$Q_{\pi(xyz)} \equiv \tfrac{1}{6}(Q_{xyz} + Q_{yzx} + Q_{zxy} + Q_{xzy} + Q_{yxz} + Q_{zyx}). \tag{C37}$$

The remaining explicit expressions for the flux components of the third-order transport coefficient tensor are given by

$$Q_{yyy} = \tfrac{1}{6}(3\langle y^2 c_y \rangle - 3\langle c_y \rangle \langle y^2 \rangle - 6\langle y \rangle \langle yc_y \rangle + 6\langle y \rangle \langle y \rangle \langle c_y \rangle), \tag{C38}$$

$$Q_{xyz} = \tfrac{1}{6}(\langle yzc_x \rangle + \langle xzc_y \rangle + \langle xyc_z \rangle - \langle c_x \rangle \langle yz \rangle - \langle x \rangle \langle zc_y \rangle - \langle x \rangle \langle yc_z \rangle - \langle c_y \rangle \langle xz \rangle - \langle y \rangle \langle zc_x \rangle - \langle y \rangle \langle xc_z \rangle - \langle c_z \rangle \langle xy \rangle$$
$$- \langle z \rangle \langle yc_x \rangle - \langle z \rangle \langle xc_y \rangle + 2\langle c_x \rangle \langle y \rangle \langle z \rangle + 2\langle c_y \rangle \langle x \rangle \langle z \rangle + 2\langle c_z \rangle \langle y \rangle \langle x \rangle), \tag{C39}$$

$$Q_{yxx} = \tfrac{1}{6}(\langle x^2 c_y \rangle + 2\langle yxc_x \rangle - 2\langle c_x \rangle \langle yx \rangle - \langle c_y \rangle \langle x^2 \rangle - 2\langle x \rangle \langle yc_x \rangle - 2\langle x \rangle \langle xc_y \rangle - 2\langle y \rangle \langle xc_x \rangle + 2\langle c_y \rangle \langle x \rangle \langle x \rangle + 4\langle y \rangle \langle x \rangle \langle c_x \rangle), \tag{C40}$$

$$Q_{yzz} = \tfrac{1}{6}(\langle z^2 c_y \rangle + 2\langle yzc_z \rangle - 2\langle c_z \rangle \langle yz \rangle - \langle c_y \rangle \langle z^2 \rangle - 2\langle z \rangle \langle yc_z \rangle - 2\langle z \rangle \langle zc_y \rangle - 2\langle y \rangle \langle zc_z \rangle + 2\langle c_y \rangle \langle z \rangle \langle z \rangle + 4\langle y \rangle \langle z \rangle \langle c_z \rangle), \tag{C41}$$

$$Q_{zyy} = \tfrac{1}{6}(\langle y^2 c_z \rangle + 2\langle yzc_y \rangle - 2\langle c_y \rangle \langle yz \rangle - \langle c_z \rangle \langle y^2 \rangle - 2\langle y \rangle \langle zc_y \rangle - 2\langle y \rangle \langle yc_z \rangle - 2\langle z \rangle \langle yc_y \rangle + 2\langle c_z \rangle \langle y \rangle \langle y \rangle + 4\langle z \rangle \langle y \rangle \langle c_y \rangle), \tag{C42}$$

$$Q_{xyy} = \tfrac{1}{6}(\langle y^2 c_x \rangle + 2\langle yxc_y \rangle - 2\langle c_y \rangle \langle yx \rangle - \langle c_x \rangle \langle y^2 \rangle - 2\langle y \rangle \langle xc_y \rangle - 2\langle y \rangle \langle yc_x \rangle - 2\langle x \rangle \langle yc_y \rangle + 2\langle c_x \rangle \langle y \rangle \langle y \rangle + 4\langle x \rangle \langle y \rangle \langle c_y \rangle). \tag{C43}$$

[1] L. G. H. Huxley and R. W. Crompton, *The Diffusion and Drift of Electrons in Gases* (Wiley, London, 1974).

[2] E. A. Mason and E. W. McDaniel, *Transport Properties of Ions in Gases* (Wiley, New York, 1988).

[3] R. W. Crompton, Adv. At. Mol. Opt. Phys. **32**, 97 (1994).

[4] Z. Lj. Petrović, M. Šuvakov, Ž. Nikitović, S. Dujko, O. Šašić, J. Jovanović, G. Malović, and V. Stojanović, Plasma Sources Sci. Technol. **16**, S1 (2007).

[5] R. D. White, D. Cocks, G. Boyle, M. Casey, N. Garland, D. Konovalov, B. Philippa, P. Stokes, J. de Urquijo, O. Gonzales-Magana, R. P. McEachran, S. J. Buckman, M. J. Brunger, G. Garcia, S. Dujko, and Z. Lj. Petrović, Plasma Sources Sci. Technol. **27**, 053001 (2018).

[6] T. Makabe and Z. Lj. Petrović, *Plasma Electronics: Applications in Microelectronic Device Fabrication* (CRC Press, New York, 2014).

[7] M. A. Lieberman and A. J. Lichtenberg, *Principles of Plasma Discharges and Materials Processing* (Wiley Interscience, Hoboken, NJ, 2005).

[8] L. L. Alves, A. Bogaerts, V. Guerra, and M. M. Turner, Plasma Sources Sci. Technol. **27**, 023002 (2018).

[9] I. Adamovich, S. D. Baalrud, A. Bogaerts, P. J. Bruggeman, M. Cappelli, V. Colombo, U. Czarnetzki, U. Ebert, J. G. Eden, P. Favia, D. B. Graves, S. Hamaguchi, G. Hieftje, M. Hori, I. D. Kaganovich, U. Kortshagen, M. J. Kushner, N. J. Mason, S. Mazouffre, S. Mededovic Thagard, H. R. Metelmann, A. Mizuno, E. Moreau, A. B. Murphy, B. A. Niemira, G. S. Oehrlein, Z. Lj. Petrovic, L. C. Pitchford, Y. K. Pu, S. Rauf, O. Sakai, S. Samukawa, S. Starikovskaia, J. Tennyson, K. Terashima, M. M. Turner, M. C. M. Van De Sanden, and A. Vardelle, J. Phys. D: Appl. Phys. **50**, 323001 (2017).

[10] L. Rolandi, W. Riegler, and W. Blum, *Particle Detection with Drift Chambers* (Springer, Berlin, 2008).

[11] D. Bošnjaković, Z. Lj. Petrović, R. D. White, and S. Dujko, J. Phys. D: Appl. Phys. **47**, 435203 (2014).

[12] D. Xiao, *Gas Discharge and Gas Insulation* (Springer, Heidelberg, 2016).

[13] M. Charlton and J. W. Humberston, *Positron Physics* (Cambridge University Press, Cambridge, 2001).

[14] Z. Lj. Petrović, A. Banković, S. Dujko, S. Marjanović, G. Malović, J. P. Sullivan, and S. Buckman, in *Eighth International Conference on Atomic and Molecular Data and Their Applications: ICAMDATA-2012*, edited by J. D. Gillaspy, W. L. Wiese, and Y. A. Podpaly, AIP Conf. Proc. No. 1545 (AIP, New York, 2013).

[15] L. C. Pitchford *et al.*, Plasma Process. Polym. **14**, 1600098 (2016).

[16] Z. Lj. Petrović, S. Dujko, D. Marić, G. Malović, Ž. Nikitović, O. Šašić, J. Jovanović, V. Stojanović, and M. Radmilović-Rađenović, J. Phys. D: Appl. Phys. **42**, 194002 (2009).

[17] R. D. White, S. Dujko, R. E. Robson, Z. Lj. Petrović, and R. P. McEachran, Plasma Sources Sci. Techol. **19**, 034001 (2010).

[18] B. M. Penetrante and J. N. Bardsley, in *Non-equilibrium Effects in Ion and Electron Transport*, edited by J. W. Gallagher, D. F. Hudson, E. E. Kunhardt, and R. J. Van Brunt (Plenum, New York, 1990), p. 49.

[19] S. B. Vrhovac, Z. Lj. Petrović, L. A. Viehland, and T. S. Santhanam, J. Chem. Phys. **110**, 2423 (1999).

[20] J. H. Schummers, G. M. Thomson, D. R. James, I. R. Gatland, and E. W. McDaniel, Phys. Rev. A **7**, 683 (1973).

[21] S. R. Hunter, Ph.D. thesis, Flinders University, Adelaide, Australia (1977).

[22] H. A. Blevin, J. Fletcher, and S. R. Hunter, J. Phys. D: Appl. Phys. **9**, 471 (1976).

[23] H. A. Blevin, J. Fletcher, and S. R. Hunter, Aust. J. Phys. **31**, 299 (1978).

[24] C. A. Denman and L. A. Schlie, in *Non-equilibrium Effects in Ion and Electron Transport*, Proceedings of the 6th International Swarm Seminar, Glen Cove, NY, edited by J. W. Gallagher *et al.* (Springer, New York, 1989), p. 359.

[25] J. H. Whealton and E. A. Mason, Ann. Phys. **84**, 8 (1974).

[26] R. Robson, Aust. J. Phys. **28**, 523 (1975).

[27] P. H. Larsen, H. R. Skullerud, T. H. Lovaas, and T. Stefansson, J. Phys. B: At. Mol. Opt. Phys. **21**, 2519 (1988).

[28] K. Kondo and H. Tagashira, J. Phys. D: Appl. Phys. **23**, 1175 (1990).

[29] A. D. Koutselos, J. Chem. Phys. **104**, 8442 (1996).

[30] A. D. Koutselos, J. Chem. Phys. **106**, 7117 (1997).

[31] A. D. Koutselos, Chem. Phys. **270**, 165 (2001).

[32] A. D. Koutselos, Chem. Phys. **315**, 193 (2005).

[33] R. E. Robson, J. Chem. Phys. **85**, 4486 (1986).

[34] S. B. Vrhovac and Z. Lj. Petrović, Phys. Rev. E **53**, 4012 (1996).

[35] S. Kawaguchi, K. Takahashi, and K. Satoh, Plasma Sources Sci. Technol. **27**, 085006 (2018).

[36] S. Kawaguchi, K. Takahashi, and K. Satoh, in *Proceedings of the 22nd International Conference on Gas Discharges and Their Applications, Novi Sad, Serbia*, edited by Z. Lj. Petrović, N. Puač, S. Dujko, and N. Škoro (Serbian Academy of Sciences and Arts, Belgrade, 2018), p. 531.

[37] S. Dujko, R. D. White, and Z. Lj. Petrović, J. Phys. D: Appl. Phys. **41**, 245205 (2008).

[38] Z. Lj. Petrović, I. Simonović, S. Marjanović, D. Bošnjaković, D. Marić, G. Malović, and S. Dujko, Plasma Phys. Control. Fusion **59**, 014026 (2017).

[39] P. W. Stokes, I. Simonović, B. Philippa, D. Cocks, S. Dujko, and R. D. White, Sci. Rep. **8**, 2226 (2018).

[40] C. Li, W. J. M. Brok, U. Ebert, and J. J. A. M. van der Mullen, J. Appl. Phys. **101**, 123305 (2007)

[41] A. H. Markosyan, S. Dujko, and U. Ebert, J. Phys. D: Appl. Phys. **46**, 475203 (2013).

[42] Z. M. Raspopović, S. Dujko, R. D. White, and Z. Lj. Petrović, IEEE Trans. Plasma. Sci. **39**, 2566 (2011).

[43] S. Dujko, Z. M. Raspopović, R. D. White, T. Makabe, and Z. Lj. Petrović, Eur. Phys. J. D **68**, 166 (2014).

[44] M. Šuvakov, Z. Ristivojević, Z. Lj. Petrović, S. Dujko, Z. M. Raspopović, N. A. Dyatko, and A. P. Napartovich, IEEE Trans. Plasma Sci. **33**, 532 (2005).

[45] J. Mirić, D. Bošnjaković, I. Simonović, Z. Lj. Petrović, and S. Dujko, Plasma Sources Sci. Technol. **25**, 065010 (2006).

[46] M. Šuvakov, Z. Lj. Petrović, J. P. Marler, S. J. Buckman, R. E. Robson, and G. Malović, New J. Phys. **10**, 053034 (2008).

[47] A. Banković, S. Dujko, R. D. White, S. J. Buckman, and Z. Lj. Petrović, Nucl. Instrum. Meth. Phys. Res. B **279**, 92 (2011).

[48] R. T. Sibatov and V. V. Uchaikin, Semiconductors **41**, 335 (2007).

[49] M. Schubert, E. Preis, J. C. Blakesley, P. Pingel, U. Scherf, and D. Neher, Phys. Rev. B **87**, 024203 (2013).

[50] H. Krüsemann, A. Godec, and R. Metzler, Phys. Rev. E **89**, 040101(R) (2014).

[51] H. Krüsemann, R. Schwarzl, and R. Metzler, Transp. Porous Media **115**, 327 (2016).

[52] A. Mauracher, M. Daxner, J. Postler, S. E. Huber, P. Denifl, P. Scheier, and J. P. Toennies, J. Phys. Chem. Lett. **5**, 2444 (2014).

[53] A. F. Borghesani and M. Santini, Phys. Rev. E **65**, 056403 (2002).

[54] Y. Sakai, W. F. Schmidt, and A. Khrapak, Chem. Phys. **164**, 139 (1992).

[55] S. V. Stepanov, V. M. Byakov, D. S. Zvezhinskiy, G. Duplâtre, R. R. Nurmukhametov, and P. S. Stepanov, Adv. Phys. Chem. **2012**, 431962 (2012).

[56] S. V. Stepanov, V. M. Byakov, B. N. Ganguly, D. Gangopadhyay, T. Mukherjee, and B. Dutta-Roy, Physica B: Condens. Matter **322**, 68 (2002).

[57] K. Norregaard, R. Metzler, C. M. Ritter, K. Berg-Sørensen, and L. B. Oddershede, Chem. Rev. **117**, 4342 (2017).

[58] M. Schwarzl, A. Godec, and R. Metzler, Sci. Rep. **7**, 3878 (2017).

[59] F. Höfling and T. Franosch, Rep. Prog. Phys. **76**, 046602 (2013).

[60] M. Magdziarz, A. Weron, K. Burnecki, and J. Klafter, Phys. Rev. Lett. **103**, 180602 (2009).

[61] K. F. Ness and R. E. Robson, Phys. Rev. A **34**, 2185 (1986)

[62] R. Robson, R. White, and M. Hildebrandt, *Fundamentals of Charged Particle Transport in Gases and Condensed Matter* (CRC Press, Boca Raton, FL, 2018).

[63] K. Kumar, H. R. Skullerud, and R. E. Robson, Aust. J. Phys. **33**, 343 (1980).

[64] S. Dujko, R. D. White, Z. M. Raspopović, and Z. Lj. Petrović, Nucl. Instrum. Meth. Phys. Res. B **279**, 84 (2012).

[65] M. Damnjanović and I. Milošević, J. Phys. A: Math. Gen. **28**, 1669 (1995).

[66] R. D. White, R. E. Robson, S. Dujko, P. Nicoletopoulos, and B. Li, J. Phys. D: Appl. Phys. **42**, 194001 (2009).

[67] S. Dujko, R. D. White, Z. Lj. Petrović, and R. E. Robson, Phys. Rev. E **81**, 046403 (2010).

[68] S. Dujko, R. D. White, Z. Lj. Petrović, and R. E. Robson, Plasma Sources Sci. Technol. **20**, 024013 (2011).

[69] R. E. Robson and K. F. Ness, Phys. Rev. A **33**, 2068 (1986).

[70] R. D. White, K. F. Ness, R. E. Robson, and B. Li, Phys. Rev. E **60**, 2231 (1999).

[71] Z. M. Raspopović, S. Sakadžić, S. Bzenić, and Z. Lj. Petrović, IEEE Trans. Plasma Sci. **27**, 1241 (1999).

[72] Z. Lj. Petrović, Z. M. Raspopović, S. Dujko, and T. Makabe, Appl. Surf. Sci. **192**, 1 (2002).

[73] S. Dujko, Z. M. Raspopović, and Z. Lj. Petrović, J. Phys. D: Appl. Phys. **38**, 2952 (2005).

[74] I. Simonović, Z. Lj. Petrović, and S. Dujko, in *Proceedings of the 27th Symposium on Physics of Ionized Gases—SPIG 2014, Belgrade, Serbia*, edited by D. Marić, A. R. Milosavljević, and Z. Mijatović, Contributed Papers and Abstracts of Invited Lectures, Topical Invited Lectures. Progress Reports and Workshop Lectures (Institute of Physics, Belgrade & Klett izdavacka kuca d.o.o., Belgrade, 2014), pp. 138–141.

[75] I. Simonović, Z. Lj. Petrović, R. D. White, D. Bošnjaković, and S. Dujko, in *Proceedings of the 22nd International Conference on Gas Discharges and Their Applications—GD 2018, Novi Sad, Serbia*, edited by Z. Lj. Petrović, N. Puač, S. Dujko, and N. Škoro (Serbian Academy of Sciences and Arts, Belgrade, 2018), pp. 551–554.

[76] I. Simonović, Z. Lj. Petrović, R. D. White, D. Bošnjaković, and S. Dujko, in *Proceedings of the 29th Symposium on Physics of Ionized Gases—SPIG 2018, Belgrade, Serbia*, edited by G. Poparić, B. Obradović, D. Borka, and M. Rajković, Contributed Papers and Abstracts of Invited Lectures, Topical Invited Lectures. Progress Reports and Workshop Lectures, (Vinča Institute of Nuclear Sciences, University of Belgrade, Belgrade, 2018), pp. 67–70.

[77] M. Hayashi (private commutation, 2000).

[78] R. D. White, R. E. Robson, P. Nicoletopoulos, and S. Dujko, Eur. Phys. J. D **66**, 117 (2012).

[79] L. Boltzmann, Wein. Ber. **66**, 275 (1872).

[80] C. S. Wang-Chang, G. E. Uhlenbeck, and J. DeBoer, in *Studies in Statistical Mechanics*, edited by J. DeBoer and G. E. Uhlenbeck (Wiley, New York, 1964), Vol. 2, p. 241.

[81] Z. Ristivojević and Z. Lj. Petrović, Plasma Sources Sci. Technol. **21**, 035001 (2012).

[82] K. F. Ness, J. Phys. D: Appl. Phys. **27**, 1848 (1994).

[83] R. D. White, M. J. Brennan, and K. F. Ness, J. Phys. D: Appl. Phys. **30**, 810 (1997).

[84] R. D. White, R. E. Robson, and K. F. Ness, Comput. Phys. Commun. **142**, 349 (2001).

[85] I. D. Reid, Aust. J. Phys. **32**, 231 (1979).

[86] S. Marjanović, A. Banković, D. Cassidy, B. Cooper, A. Deller, S. Dujko, and Z. Lj. Petrović, J. Phys. B: At. Mol. Opt. Phys. **49**, 215001 (2016).

[87] S. Marjanović and Z. Lj. Petrović, Plasma Sources Sci. Technol. **26**, 024003 (2017).

[88] S. Marjanović, M. Šuvakov, A. Banković, M. Savić, G. Malović, S. J. Buckman, and Z. Lj. Petrović, IEEE Trans. Plasma Sci. **39**, 2614 (2011).

[89] Z. Lj. Petrović, S. Marjanović, S. Dujko, A. Banković, G. Malović, S. Buckman, G. Garcia, R. White, and M. Brunger, Appl. Radiat. Isotop. **83**, 148 (2014).

[90] M. R. Natisin, J. R. Danielson, and C. M. Surko, J. Phys. B: At. Mol. Opt. Phys. **47**, 225209 (2014).

[91] L. M. Blinov, *Structure and Properties of Liquid Crystals* (Springer, New York, 2011).

[92] W. K. Tung, *Group Theory in Physics* (World Scientific, Singapore, 1984).

[93] A. O. Barut and R. Raczka, *Theory of Group Representations and Applications* (Polish Scientific Publishers, Warsaw, 1980).

[94] F. P. Temme and B. C. Sanctuary, J. Magn. Reson. **69**, 1 (1986).

[95] R. E. Robson, Phys. Rev. A **13**, 1536 (1976).

[96] R. E. Robson, Phys. Rev. E **61**, 848 (2000).

PAPER

Non-equilibrium of charged particles in swarms and plasmas—from binary collisions to plasma effects

View the article online for updates and enhancements.

Non-equilibrium of charged particles in swarms and plasmas—from binary collisions to plasma effects

Z Lj Petrović[1,2]**, I Simonović, S Marjanović**[1]**, D Bošnjaković**[1]**, D Marić**[1]**, G Malović**[1] **and S Dujko**[1]

[1] Institute of Physics, University of Belgrade, POB 68, 11080 Zemun, Belgrade, Serbia
[2] Serbian Academy of Sciences and Arts, 11001 Belgrade, Serbia

E-mail: zoran@ipb.ac.rs

Abstract

In this article we show three quite different examples of low-temperature plasmas, where one can follow the connection of the elementary binary processes (occurring at the nanoscopic scale) to the macroscopic discharge behavior and to its application. The first example is on the nature of the higher-order transport coefficient (second-order diffusion or skewness); how it may be used to improve the modelling of plasmas and also on how it may be used to discern details of the relevant cross sections. A prerequisite for such modeling and use of transport data is that the hydrodynamic approximation is applicable. In the second example, we show the actual development of avalanches in a resistive plate chamber particle detector by conducting kinetic modelling (although it may also be achieved by using swarm data). The current and deposited charge waveforms may be predicted accurately showing temporal resolution, which allows us to optimize detectors by adjusting the gas mixture composition and external fields. Here kinetic modeling is necessary to establish high accuracy and the details of the physics that supports fluid models that allows us to follow the transition to streamers. Finally, we show an example of positron traps filled with gas that, for all practical purposes, are a weakly ionized gas akin to swarms, and may be modelled in that fashion. However, low pressures dictate the need to apply full kinetic modelling and use the energy distribution function to explain the kinetics of the system. In this way, it is possible to confirm a well established phenomenology, but in a manner that allows precise quantitative comparisons and description, and thus open doors to a possible optimization.

Keywords: charged particle swarms, non-equilibrium plasma, skewness, resistive plate chambers, positron traps, Monte Carlo simulations, Boltzmann equation

(Some figures may appear in colour only in the online journal)

1. Introduction

The idea of thermodynamic equilibrium (TE) is one of the most widely used ideas in the foundations of plasma physics. Not only is TE used as a background gas, but it is also used as the plasma itself, and, further, TE is implicitly incorporated in most theories through application of the Maxwell Boltzmann distribution function. On the other hand, the idea of local thermodynamic equilibrium (LTE) in principle means that TE is not maintained, and that energy converted into the effective temperature is being used as a fitting parameter, but also that all the principles of TE still apply for the adjusted (local) temperature. It is often overlooked that TE implies that each process is balanced by its inverse process. It is difficult to envisage just exactly how this condition could be met under circumstances where most of the energy that is fed into the non-equilibrium, low-temperature discharges comes from an external electric field. The notion

of non-equilibrium is implemented very well in a wide range of plasma models, starting from fluid models and hybrid models, all the way to fully kinetic codes such as particle-in-cell (PIC) modelling.

At end of a field of ionized gases, opposite to the fully developed plasma, at the lowest space charge densities, electrons are accelerated (gain energy) from the external electric field and dissipate in collisions with the background gas. This realm is known as a swarm (swarm physics), and is often described by simple swarm models. We shall try to illustrate how and where one may employ concepts developed in low-temperature plasmas for problems that are not traditional non-equilibrium plasmas such as positrons in gases and gas-filled traps, gas breakdown and particle detectors.

The three selected examples are: the use and properties of higher-order transport coefficients (skewness) and how they may be implemented to close the system of equations for modeling of atmospheric plasmas; modeling of resistive plate chamber (RPC) particle detectors with a focus on the development of avalanches, and prediction of the current and deposited charge; and, finally, modeling of a generic representation of the three stage gas-filled positron trap, where the same models as for electrons may be employed in a full kinetic description to calculate the temporal development of the energy distribution function, and, through that, to describe how and when individual elementary processes affect the performance of the trap.

This is a review article as it covers three different topics that will (or have been) be presented in detail elsewhere. Yet the majority of the results will be developed in this paper. Necessarily, as it is a broad review, some finer points will be omitted in pursuit of the bigger picture, however, all will be covered elsewhere and the relevant literature is cited.

2. Higher-order transport and plasma modeling

The fluid equations often employed in plasma modeling are a part of an infinite chain, and whenever the chain is broken one needs a higher-order equation and related quantities to close the system of equations (Dujko *et al* 2013). That is why a closing of the equations is forced, sometimes labeled as ansatz, although the closure is not quite arbitrary. It is often based on some principles or simplifying arguments (Robson *et al* 2005) involving higher-order equations and related transport coefficients. Robson *et al* (2005) claimed that some serious errors have been incorporated into fluid equations that are commonly used in plasma modeling, and suggested benchmarks to test plasma models.

Equations (1) and (2) shown below, are the flux gradient equation and generalized diffusion equation, respectively, truncated at the contribution of the third order transport coefficients (also known as skewness). The terms, including $\widehat{Q}^{(F)}$ and $\widehat{Q}^{(B)}$ are terms that represent the contribution of the skewness tensor:

$$\vec{\Gamma}(\vec{r},t) = \vec{W}^{(F)}n(\vec{r},t) - \widehat{D}^{(F)} \cdot \nabla n(\vec{r},t) + \widehat{Q}^{(F)} : (\nabla \otimes \nabla)n(\vec{r},t) + \dots$$
$$(1)$$

$$\frac{\partial n(\vec{r},t)}{\partial t} + \vec{W}^{(B)} \cdot \nabla n(\vec{r},t) - \widehat{D}^{(B)}$$
$$: (\nabla \otimes \nabla)n(\vec{r},t) + \widehat{Q}^{(B)} \vdots (\nabla \otimes \nabla \otimes \nabla)n(\vec{r},t) + \dots$$
$$= Rn(\vec{r},t) \qquad (2)$$

where $\vec{\Gamma}(\vec{r},t)$, $n(\vec{r},t)$, $\vec{W}^{(F)}$, $\widehat{D}^{(F)}$, $\widehat{Q}^{(F)}$, $\vec{W}^{(B)}$, $\widehat{D}^{(B)}$, $\widehat{Q}^{(B)}$, R are the flux of charged particles, charged particle number density, flux drift velocity, flux diffusion tensor, flux skewness tensor, bulk drift velocity, bulk diffusion tensor, bulk skewness tensor and rate for reactions, respectively. If equations (1) and/or (2) are coupled to the Poisson equation for an electric field then the system of corresponding differential equations might be closed in the so-called local field approximation. This means that all transport properties are functions of the local electric field. The skewness tensor has been systematically ignored in previous fluid models of plasma discharges, although its contribution may be significant for discharges operating at high electric fields, and in particular for discharges in which the ion dynamics play an important role.

As for experimental determination of the higher-order diffusion of electrons, there have been some attempts, but those were mostly regarded as unsuccessful due to the end effects (Denman and Schlie 1990). In other words, those experiments may have failed to comply with both the requirements for negligible non-hydrodynamic regions and for lower pressures. An estimate was made that reliable skweness experiments would have to be up to 10 m long with pressures that are at least ten times smaller than those in standard swarm experiments. It seems that the only reliable yet very weak result was observed for H$_2$ in time of flight (TOF) emission experiments of Blevin *et al* (1976, 1978), as described in the PhD thesis by Hunter (1977). This is because the measurement was made away from the electrodes, thus providing a hydrodynamic environment.

At the same time some calculations were performed based on the available cross sections either by using a Monte Carlo simulation (MCS) and two term solutions of the Boltzmann equation (BE) (Penetrante and Bardsley 1990) or by using the momentum transfer theory (Vrhovac *et al* 1999). Whealton and Mason (1974) were the first to determine the correct structure of the skewness tensor in the magnetic field free case. For ions there have been more general studies and in particular theoretical studies. Koutselos gave a different prediction of the structure and symmetry of the tensor (Koutselos 1997) but those results were challenged (corrected) by Vrhovac *et al* (1999), who confirmed the structure of the skewness tensor previously determined by Whealton and Mason. Subsequently Koutselos confirmed the structure of the skewness tensor obtained by previous authors (Koutselos 2001).

Finally, having in mind the need for data in fluid modeling and the poor likelihood of experimental studies in the near future, a systematic study has been completed by Simonović *et al* (2016) dealing with the symmetry by using the group projector method (Barut and Raczka 1980, Tung 1984), multi-term Boltzmann equation solutions and MCS results in general terms. It should be noted that the third-order transport coefficients are often called skewness, but in principle it is the term that was to be applied only for the longitudinal diagonal
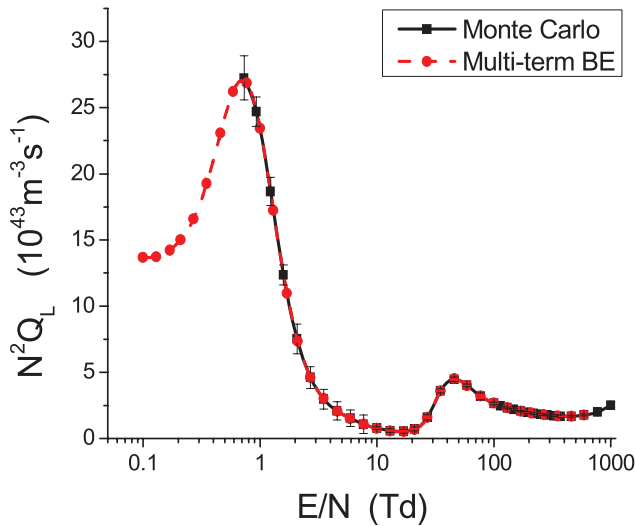
Figure 1. The longitudinal component of the skewness tensor calculated for electrons in methane.

Figure 2. The transverse component of the skewness tensor calculated for electrons in methane.

term, which defines most directly the (departure from the) shape of the moving Gaussian. We will, however, use the term skewness for the entire tensor and all its terms.

The structure of the skewness tensor is the following (Whealton and Mason 1974, Vrhovac *et al* 1999, Koutselos 2001, Simonović *et al* 2016):

$$Q_{xab} = \begin{pmatrix} 0 & 0 & Q_{xxz} \\ 0 & 0 & 0 \\ Q_{xxz} & 0 & 0 \end{pmatrix}, \quad Q_{yab} = \begin{pmatrix} 0 & 0 & 0 \\ 0 & 0 & Q_{xxz} \\ 0 & Q_{xxz} & 0 \end{pmatrix}$$

$$Q_{zab} = \begin{pmatrix} Q_{zxx} & 0 & 0 \\ 0 & Q_{zxx} & 0 \\ 0 & 0 & Q_{zzz} \end{pmatrix},$$

where $a, b \in \{x, y, z\}$ and Q_{abc} are the independent, non-zero terms in the tensor (although some of them may be identical if they are established for different permutations of the same derivatives). The components of the tensor may be grouped as longitudinal $Q_L = Q_{zzz}$ and transverse $Q_T = \frac{1}{3}(Q_{zxx} + Q_{xxz} + Q_{xzx})$.

In this paper, we present results for skewness of electron swarms in methane. Methane is known for producing negative differential conductivity (NDC) and in this work we will demonstrate the unusual variation of the longitudinal and transverse components of the skewness tensor for *E/N* (electric field over the gas number density) regions in which NDC occurs. NDC is characterized by a decrease in the drift velocity despite an increase in the magnitude of the applied reduced electric field. Cross sections for electron scattering in methane are taken from Šašić *et al* (2004). For the purpose of this calculation we assumed a cold gas approximation: $T = 0$ K, which is justified as we covered mostly the *E/N* range where mean energies are considerably higher than the thermal energy. The initial number of electrons in the simulations was 10^7 and those were followed for sufficient time to achieve full equilibration with the applied field before sampling was applied. Sampling in an MCS is performed either
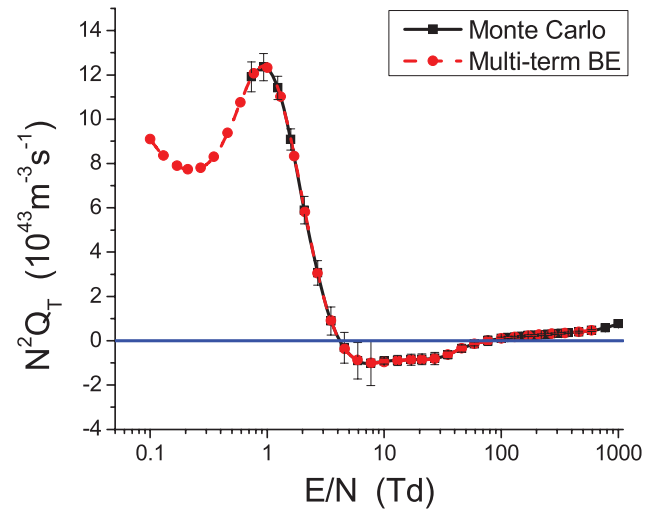
for the flux (velocity space) $Q_{abc}^{(f)} = \frac{1}{3!}\left\langle \frac{d}{dt}(r_a^* r_b^* r_c^*) \right\rangle$ or for the bulk (real space) $Q_{abc}^{(b)} = \frac{1}{3!}\frac{d}{dt}\langle r_a^* r_b^* r_c^* \rangle$ components (Simonović *et al* 2016) where $r_a^* = r_a - \langle r_a \rangle$.

Uncertainties are established as the root mean square deviations. Statistical fluctuations in MCSs are more pronounced for skewness than for the lower-order transport coefficients. Thus, it is very important to present statistical uncertainties (errors) associated with the results. In addition to Monte Carlo results, the skewness tensor is calculated from the multi-term Boltzmann equation solution. The explicit formulas for skewness tensor elements in terms of moments of the distribution function will be given in a forthcoming paper (Simonović *et al* 2016).

In figures 1 and 2 we show the variation of the longitudinal and transverse skewness tensor components with *E/N* for electrons in CH_4, respectively. In figure 3 we show the variation of independent components of the skewness tensor with *E/N*. The independent components of the skewness tensor have been calculated from a multi-term solution of the Boltzmann equation.

The first observation that is very important is that the multi-term Boltzmann equation results agree very well with those obtained in MCSs. This is an important cross check and it means that the techniques to calculate the skewness are internally consistent, although two very different approaches are implemented (having said that we assume that the solution to the Boltzmann equation and the MC are both well established and tested (Dujko *et al* 2010)).

We see that Q_T becomes negative in the same range of *E/N* where NDC occurs. At the same time Q_L remains positive. Q_{zxx} and the sum of Q_{xxz} and Q_{xzx} are negative in different regions of *E/N*.

Comparing the second- and third-order longitudinal transport coefficients we noticed that if diffusion decreases with increasing *E/N* then the skewness also decreases, but even faster (figures 4 and 5). When it comes to the effect of the cross sections (or inversely to the ability to determine the cross sections from the transport data) it seems that skewness has a
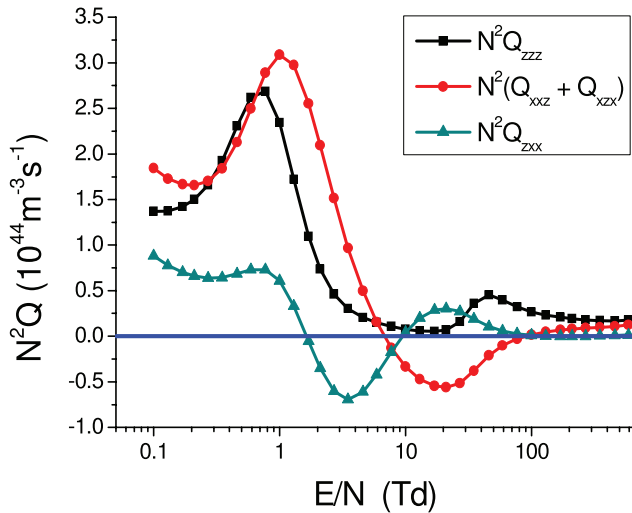
Figure 3. All independent components of the skewness tensor calculated for electrons in methane.
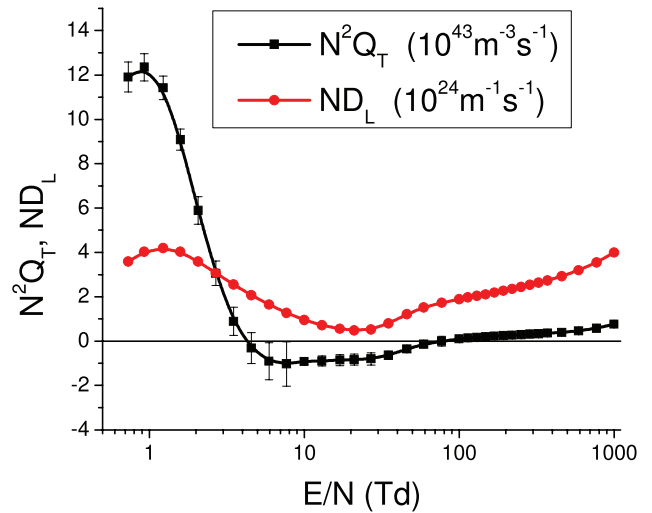
Figure 5. Comparison between longitudinal diffusion and transverse skewness for electrons in methane (the scale for the two different transport coefficients are provided in the legend).
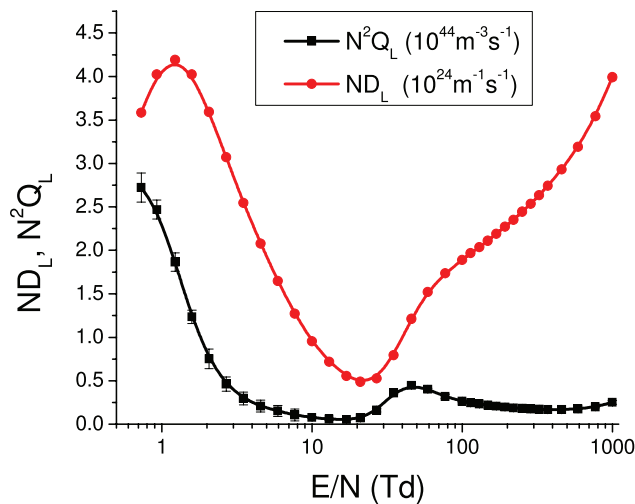
Figure 4. Comparison between longitudinal diffusion and skewness for electrons in methane (the scale for the two different transport coefficients are provided in the legend).

Figure 6. Off-diagonal components of skewness compared to the drift velocity for electrons in methane (the scale for the two different transport coefficients are provided in the legend).

more pronounced structure, and thus is more useful in fixing the shape and absolute values of the cross sections. If the diffusion increases, then we are able to distinguish between the two scenarios: if diffusion increases as a concave function, then the skewness decreases, while if the diffusion increases as a convex (or linear) function then the skewness increases.

We have observed that the transverse skewness is also in a good, if not better, correlation with the longitudinal diffusion (figure 5). This is a good example that illustrates that the skewness tensor represents directional motion.

Different transverse components have different *E/N* profiles. Q_{zxx} follows the behavior of the drift velocity while the remaining components change their trends of behavior near the end of the NDC region (figure 6). For different gases we have seen different trends and a clear correlation was not found (Simonović *et al* 2016).

Furthermore, but without illustrating it with special figures, the explicit effect of non-conservative collisions (ionization in this case) has been observed. However, in many cases the

agreement between multi-term BE results and those obtained in MCSs is better than what would be expected based on the estimated errors. At the same time it turned out that discrepancies between a two-term and multi-term (MCS) results may be quite large, ranging up to a factor of 10.

Possible measurements of higher-order transport coefficients seem possible and also profitable for the sake of determining the cross sections. Nevertheless the difficulties and possible uncertainties may outweigh the benefits. Thus, calculation of the data seems like an optimum choice for application in higher-order plasma models. The behavior of higher-order transport coefficients provides an insight into the effect of individual cross sections (their shape and magnitude), and their features such as the Ramsauer Townsend effect or resonances on the overall plasma behavior. The transport coefficients as an intermediate step give a guidance, especially when they develop special features (kinetic effects
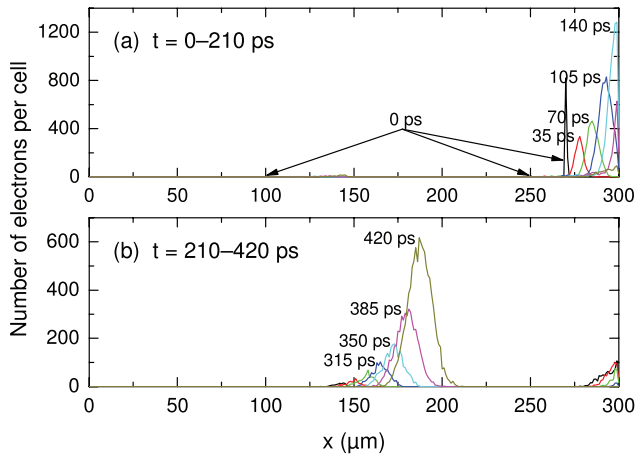
Figure 7. The spatio-temporal development of electron avalanches ((a) and (b)) in an RPC device. The number of electrons per cell (1 cell = 1 μm) is shown where the cells (1 cell = 1 μm) are along the discharge axis *x*. The cathode corresponds to $x = 0$ while the anode corresponds to $x = 300$ μm.
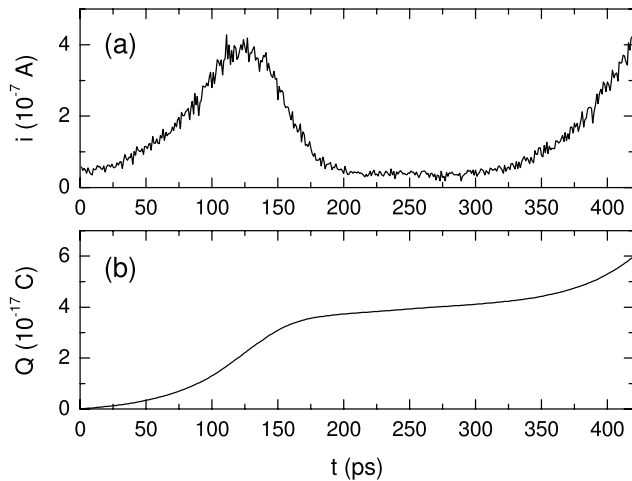
Figure 8. The time development of (a) electron induced current and (b) induced charge in the RPC device.

(Petrović *et al* 2009)) that may also be easily implemented in the determination of the cross sections.

3. Avalanches in resistive plate chambers

The next example of the connection of the elementary processes to plasma behavior through intermediate swarm-like phenomenology modeling will be modeling of RPC detectors. These devices are used for timing and triggering purposes in many high-energy physics experiments at CERN and elsewhere (The ATLAS Collaboration 2008, Santonico 2012). RPCs may be both used for spatial and temporal detection while providing large signal amplifications. They are usually operated in avalanche (swarm) or plasma (streamer) regimes depending on the required amplification and performance characteristics. Numerous models have been developed to predict RPC performance and modes of operation (Lippmann *et al* 2004, Moshaii *et al* 2012). We have studied systematically the swarm data (Bošnjaković *et al* 2014a) and then the
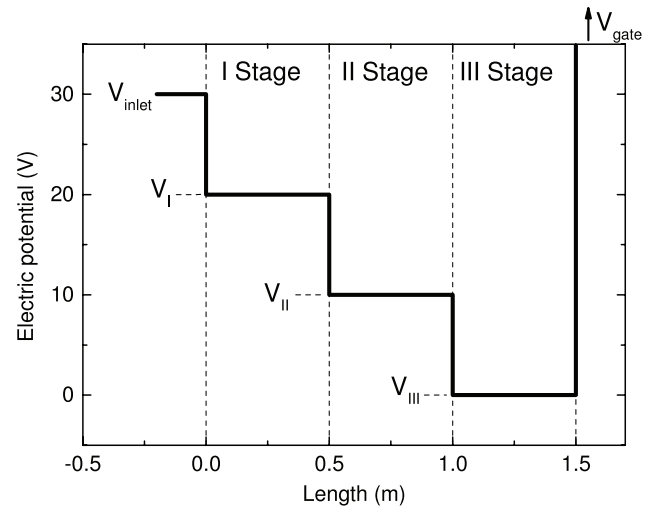
Figure 9. Schematic drawing of a generic Surko trap consisting of three equal potential drops. The composition of the background gas, its pressure and geometry are given in table 1.

Table 1. Parameters for simulation of a generic positron Surko trap.

Parameters	Stage I	Stage II	Stage III
Radius (mm)	5	20	20
Length (m)	0.5	0.5	0.5
Pressure (Torr)	10^{-3}	10^{-4}	10^{-5}
Background gas	N_2	N_2	$N_2^{0.5} + CF_4^{0.5}$
Magnetic field (G)	530	530	530
Voltage (V)	20	10	0
The initial parameters			
Potential of the entrance electrode (V)		30	
Potential of the source (V)		0.1	
Width (FWHM) of the initial energy distribution (eV)		1.5	

model of RPCs (Bošnjaković *et al* 2014b) where RPC efficiency and timing resolution have been predicted by MCS without any adjustable parameters, and were found to agree with experiment very well. Here we show some of the data not presented in Bošnjaković *et al* (2014b), which focuses on avalanche development and furthermore the induced current and charge.

Calculations of the development of the Townsend avalanche have been performed for a timing RPC gas mixture of $C_2H_2F_4$:i-C_4H_{10}:SF_6 = 85:5:10 with realistic chamber geometry (gas gap = 0.3 mm) at $E/N = 421$ Td. We show in figure 7 the development of an avalanche in the gap with three initial clusters of charges (first generation secondary electrons indicated by arrows at 0 ps) formed by an incoming high-energy particle. The first cluster (from the left) has one electron, the second has nine and the third has 983 initial electrons. The distribution over a small group of cells has been randomly selected according to well-established distributions. At the beginning, the initial condition shapes the profile of the ensemble, but eventually a Gaussian is formed that drifts under the influence of an electric field and diffuses due to numerous collisions.
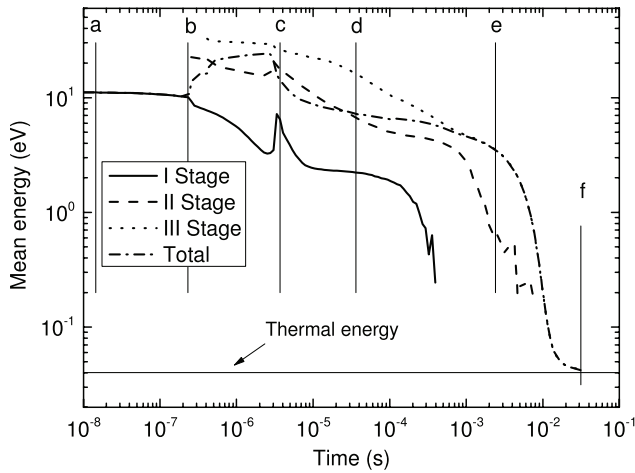
Figure 10. The mean energy of the positron ensemble (swarm) as a function of time. Averages for each stage and for the entire volume (total) are provided. The energy distribution function is plotted in figure 11 for the times marked by the points (a)–(f) in this figure.

We will first follow the development of the cluster closest to the anode (at 270 μm), as indicated by spatial electron profiles at different times in figure 7(a). The largest initial group, which is also the closest to the anode, develops the fastest: from the initial very sharp profile it quickly establishes a Gaussian shape that also very quickly gets absorbed by the anode. The second peak (from the right) is quick to follow but it is very small and cannot be observed clearly due to interference from the first pulse. In figure 7(b), we show the development of the first cluster (at 100 μm) for longer times. This cluster is the furthest from the anode and it takes the most time to reach the anode, again as a well developed moving Gaussian. It develops, however, a well-separated and defined current pulse (unlike the second cluster of charged particles). The induced current and the corresponding induced charge are shown in figure 8.

The predictions in figure 8, extended to provide important information on the temporal resolution, may be used to optimize the device by changing gas composition, field and geometry, and also may be extended to allow for the formation of the plasma in later stages when a streamer discharge may be generated at atmospheric pressure (Bošnjaković *et al* 2016). Trial and error development of such devices is simply too costly to allow for an empirical learning curve. Nevertheless, one could argue that it could be possible to develop a model based on a standard swarm description of a moving Gaussian with drift and diffusion plus the benefit of multiplication through ionization. All of these processes have their swarm coefficients. However, the very short times of the formation of the initial cluster, it being inhomogeneous and a very nonlinear growth with a possible separation of faster and slower electrons, dictate the need to perform an MCS in order to achieve the required accuracy. Thus, this example allows for the use of transport coefficients, but is better accomplished by full kinetic modeling. Transport coefficients are better taken advantage of in fluid modeling of the possibly developing streamer (Bošnjaković *et al* 2016). In any case, the ionized gas and the developing plasma channel are both represented very

accurately (qualitatively and quantitatively). Here we have used kinetic swarm modeling, although using transport coefficients may also be an option, albeit a less accurate option.

4. Gas-filled positron (and electron) traps

While it is often assumed that keeping the antimatter away from the matter is a way of preserving it longer, the introduction of background gas to the vacuum magnetic field trap led to the birth of the so-called Penning Malmberg Surko traps (often known simply as Surko traps). These devices take advantage of the very narrow region of energies, where in nitrogen electronic excitation can compete and even overpower the otherwise dominant (for almost all other gases and inelastic processes) positronium (Ps) formation (Murphy and Surko 1992, Cassidy *et al* 2006, Clarke *et al* 2006, Sullivan *et al* 2008, Marjanovic *et al* 2011, Danielson *et al* 2015). To be fair, the principles of the trap have been worked out in great detail, but mostly based on beam-like considerations (Murphy and Surko 1992, Charlton and Humberston 2000). However the device consists of a charge being released in a gas in the presence of electric and magnetic fields, and thus it is an ionized gas that is exactly described by a swarm model until the space charge effects begin to play a significant role, and then it is best described by a plasma model (again with a significant reference to collisions and transport). Thus, for quantitative representation and accurate modeling of traps, a swarm-like model is required and recently two such models were used to explain the salient features of Surko traps (Marjanović *et al* 2011, Petrović *et al* 2014, Natisin *et al* 2015). An explanation and quantitative comparisons will be the subject of a specialized publication (Marjanović and Petrović 2016). Here we only focus on the development of the energy distribution function, which is the primary medium connecting the large-scale behavior of the trap with microscopic binary collisions.

As pressures used in the gas-filled traps are very low, and the mean free paths become comparable to the dimensions of the trap, one may be assured that the description at the level of transport coefficients and fluid models would fail. This example thus requires a full kinetic level of description.

The generic (model) trap consists of three stages, each with a 10 V potential drop and each of the same length (figure 9). The properties, the pressures and other features are listed in table 1. A standard, well-tested (for electron benchmarks—Lucas and Saelee 1975, Reid 1979, Ness and Robson 1986, Raspopović *et al* 1999) Monte Carlo code has been used here. Realistic geometry was included along with the boundary conditions (potentials, energy distributions and losses). Special care was given to the testing of the modeling of trajectories in magnetic fields (Raspopović *et al* 1999 Dujko *et al* 2005).

First results are shown in figure 10 where we plot mean energies as a function of time in three separate stages (chambers) and also averaged for the entire volume. The energy steps provided by the potential drops are observable for the mean energies in stages II and III. The overall increase in energy is also observed in the total volume average. The initial plateau of the mean energy is extended mainly due to
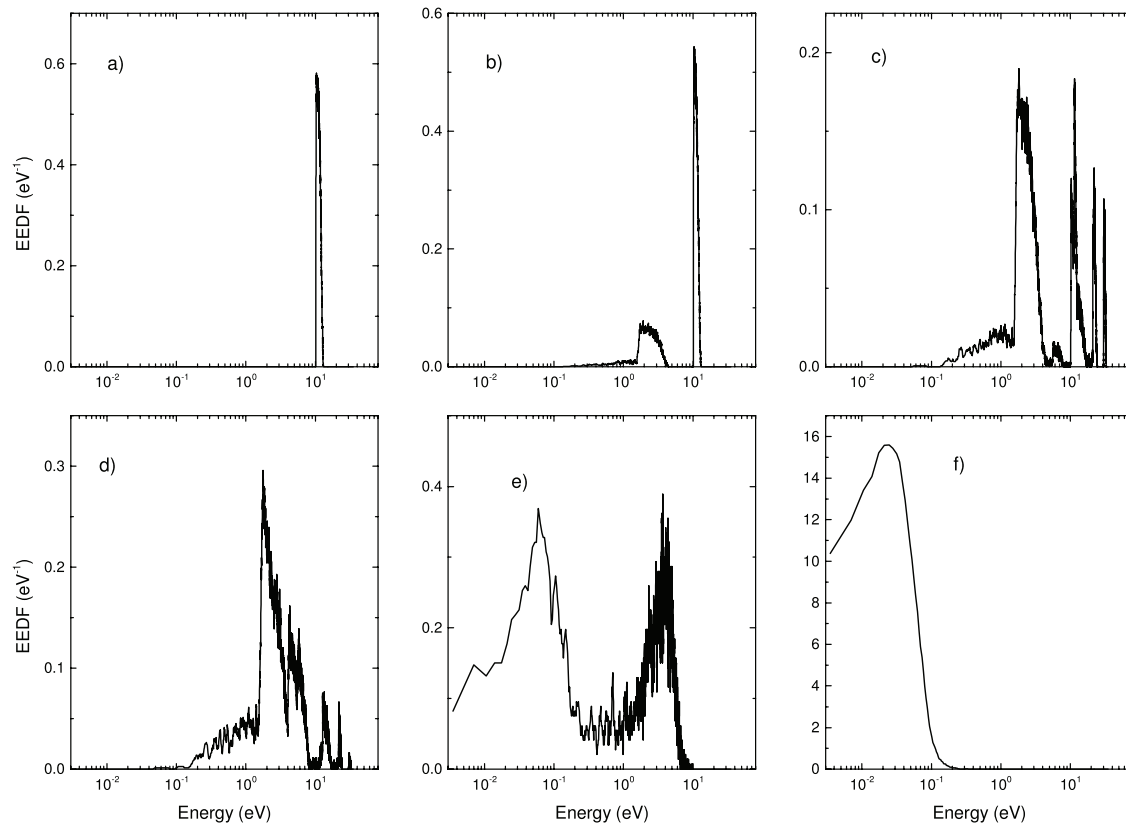
Figure 11. Positron kinetic energy distribution of the entire swarm sampled at different times (indicated in figure 10). Calculations were performed for the Surko trap as shown in figure 9 with the conditions listed in table 1.

the logarithmic nature of the plot. Following another plateau due to inelastic energy losses, the mean energy falls to the thermal value for the final thermalization.

The voltage drop in the initial stage is used to accelerate the positrons coming from the moderator into the energy range where electronic excitation of nitrogen is as efficient as Ps formation. Thus the initial distribution in figure 11 is a mono-energetic beam at 10 eV. Upon development of the group of positrons that have lost energy in excitation (figure 11(b)), positrons leave the stage I and pass into stages II and III so the two new peaks develop at 20 eV and 30 eV (figure 11(c)). The positrons that have collided form a group peaking at around 2 eV. During the next period two processes are obvious. The first is the quenching of the initial beams into the group, peaking at around 2 eV but extending up to 7 eV, where Ps formation removes the particles. The second is the process that uses vibrational excitation of CF_4 and thermalizes the 2 eV group into a low-energy group peaking at around 0.07 eV (figures 11(d) and (e)). It is interesting to see that the peak at around 2 eV is the first to disappear, leaving a group at around 5 eV to thermalize more slowly. At this point the low-energy positrons are also mainly localized in the third stage.

The final stage is characterized by two processes, the disappearance of the higher-energy group at around 5 eV and the gradual thermalization of the low-energy group at around 70 meV towards the thermal energy (*f*) of around 40 meV. At that point a quasi-thermal Maxwellian is developed. The transition appears to be rapid but, by the virtue of a logarithmic plot, it is the longest transition in the process of thermalization and

involves bouncing between the potential boundaries of the third stage many times. At the same time one should see that the properties of the trap are adjusted so that in the first bounce across the three stages most particles suffer electronic excitation/ Ps formation collisions and either disappear or are trapped.

The simulation provides many different properties of the positron ensemble (swarm) but the point of this paper is to show a direct connection between binary collision processes and the macroscopic behavior. Using the energy distribution one can easily see the dominant processes and predict which aspects of the processes are promoted by the clever design of the Surko trap. It may also be used to optimize its characteristics (Marjanović *et al* 2016). Nevertheless, the principles of the trap were properly understood from the initial concepts but in this case we have detailed representation of the energy distribution, allowing accurate quantitative comparisons. For example, one may now adjust the details of the cross section in order to fit the measured properties (such as sampled mean energy that may be somewhat skewed by the sampling process). In that respect the measured observables from the trap may play a role in the swarm data that need to be fitted in order to tune the cross sections so that the number, momentum and energy balances may be preserved. As analysis of the positron swarm data led to a number of complex kinetic effects (Banković *et al* 2009, 2012) it would be interesting to see whether similar effects may be observed or even affect the operation of the traps.

These results are akin to the well-established initial equilibration for electrons in gases (Dujko *et al* 2014) with

temporal and spatial Holst Oosterhuis luminous layers (Hayashi 1982, Fletcher 1985) that are strongly related to the well-known Frank Hertz experiment (White *et al* 2012, Robson 2014). In addition, it must be noted that even if we were to start simulation with a Maxwellian distribution and try to follow the thermalization, due to the sharp energy dependence of the processes non-Maxwellian distribution function, it would develop immediately making it necessary to employ a full kinetic treatment. While fluid equations will not work well under the circumstances, and while transport coefficients may be difficult to define and even more difficult to implement in modeling, kinetic (Monte Carlo) modeling is still a typical swarm-like model that needs to be employed. Once we fill the trap with sufficient charge to allow for plasma effects, then we may need to add-in true plasma modeling based on fluid equations and on the calculation of the effective fields.

5. Conclusion

In this review we address three recent examples on how swarm based modeling may connect the microscopic binary processes to the macroscopic behavior of ionized gases, even plasmas. The necessary prerequisite for this approach to be effective is that the systems belong to the so-called collisional plasmas (also known as the non-equilibrium or low-temperature plasmas). The examples are chosen to reveal three different aspects of swarm modeling: (a) that based on transport coefficients and fluid models and how they may be improved, (b) a system that may be described by both fluid models and simulations where simulations are used here to verify the more basic modeling, while the fluid modeling is allowing us to extend predictions further to plasma conditions, and, finally, (c) for the situation where full kinetic modeling is required. Thus, these examples should be viewed as confirmation of the validity and usefulness of the swarm models that are often overlooked by plasma modelers. Swarm models are sometimes regarded as a limit that is unrealistic and useful only to describe well-designed experiments that provide swarm data. One subscribing to that view would then need to reply to why the use of swarm data and also swarm data based fluid equations is so successful. In fact, we believe that often an 'overkill' is performed by using plasma models to describe inherently swarm-like conditions. One such example is the popular modeling of breakdown by PIC of hybrid codes. If done properly, it is all fine, although less transparent due to a more complex nature of the codes. However, at the same time such complexity does not allow us to add special tests or sampling that may reveal more insight into the pertinent physical processes. Examples may include details of the energy distribution function, adjusting boundary conditions to include detailed representation of surface processes and observation and inclusion of the kinetic phenomena.

In doing modeling of low-temperature plasmas that may need to go both more towards the swarm-like and plasma conditions we would strongly recommend that all the plasma codes need to be verified against swarm benchmarks and include sampling of relevant data. It all may become more and more difficult as one develops codes for inhomogeneous systems with complex geometry, but in the limit of a simple geometry and simple swarm conditions all swarm benchmarks should be satisfied to the highest of accuracy.

This article may be viewed as an extension of an article that has been recently submitted for a special issue on plasma modeling covering physical situations where swarm type models are valid and useful and accurate. There is no overlap of the two papers, although a common idea of the need to present the usefulness of the swarm model is obvious. The focus here is more on how elementary processes are producing an intermediate realm of phenomenology (swarm models and properties) that then clearly point at the macroscopic behavior. Be it sprite propagation or positron traps these connections not only reveal relevant physics, but also provide a means to tailor applications based on elementary processes and low-temperature plasmas.

References

Banković A, Dujko S, White R D, Marler J P, Buckman S J, Marjanović S, Malović G, Garcia G and Petrović Z Lj 2012 *New J. Phys.* **14** 035003

Banković A, Petrović Z Lj, Robson R E, Marler J P, Dujko S and Malović G 2009 *Nucl. Instrum. Methods Phys. Res.* B **267** 350–3

Barut A O and Raczka R 1980 *Theory of Group Representations and Applications* (Warszawa, PWN: Polish Scientific Publishers)

Blevin H A, Fletcher J and Hunter S R 1976 *J. Phys. D: Appl. Phys.* **9** 471

Blevin H A, Fletcher J and Hunter S R 1978 *Aust. J. Phys* **31** 299

Bošnjaković D, Petrović Z Lj and Dujko S 2014b *J. Instrum.* **9** P09012

Bošnjaković D, Petrović Z Lj and Dujko S 2016 *J. Phys. D: Appl. Phys.* **49** 405201

Bošnjaković D, Petrović Z Lj, White R D and Dujko S 2014a *J. Phys. D: Appl. Phys.* **47** 435203

Cassidy D B, Deng S H M, Greaves R G and Mills A P 2006 *Rev. Sci. Instrum.* **77** 073106

Charlton M and Humberston J 2000 *Positron Physics* (New York: Cambridge University)

Clarke J, van der Werf D P, Griffiths B, Beddows D C S, Charlton M, Telle H H and Watkeys P R 2006 *Rev. Sci. Instrum.* **77** 063302

Danielson J R, Dubin D H E, Greaves R G and Surko C M 2015 *Rev. Mod. Phys.* **87** 247–306

Denman C A and Schlie L A 1990 Nonequilibrium effects in ion and electron transport *Proc. of the 6th Int. Swarm Seminar (Glen Cove, NY, 1989)* ed J W Gallagher *et al* (New York: Springer)

Dujko S, Markosyan A H, White R D and Ebert U 2013 *J. Phys. D: Appl. Phys.* **46** 475202

Dujko S, Raspopović Z M and Petrović Z Lj 2005 *J. Phys. D: Appl. Phys.* **38** 2952–66

Dujko S, Raspopović Z M, White R D, Makabe T and Petrović Z Lj 2014 *Eur. Phys. J.* D **68** 166

Dujko S, White R D, Petrović Z Lj and Robson R E 2010 *Phys. Rev.* E **81** 046403

Fletcher J 1985 *J. Phys. D: Appl. Phys.* **18** 221–8

Hayashi M 1982 *J. Phys. D: Appl. Phys.* **15** 1411–8

Hunter S R 1977 *PhD Thesis* Flinders University, Adelaide, Australia unpublished

Koutselos A D 1997 *J. Chem. Phys.* **106** 7117–23

Koutselos A D 2001 *Chem. Phys.* **270** 165–175

Lippmann C and Riegler W 2004 *Nucl. Instrum. Methods Phys. Res.* A **533** 11–5

Lucas J and Saelee H T 1975 *J. Phys. D: Appl. Phys.* **8** 640–50

Marjanović S, Banković A, Cassidy D, Cooper B, Deller A, Dujko S and Petrović Z Lj 2016 *J. Phys. B: At. Mol. Opt. Phys.* **49** 215001

Marjanovic S, Šuvakov M, Bankovic A, Savic M, Malovic G, Buckman S J and Petrovic Z Lj 2011 *IEEE Trans. Plasma Sci.* **39** 2614–5

Marjanović S and Petrović Z Lj 2016 *Plasma Sources Sci. Technol.* submitted

Moshaii A, Khosravi Khorashad L, Eskandari M and Hosseini S 2012 *Nucl. Instrum. Methods Phys. Res.* A **661** S168–71

Murphy T J and Surko C M 1992 *Phys. Rev.* A **46** 5696–705

Natisin M R, Danielson J R and Surko C M 2015 *Phys. Plasmas* **22** 033501

Ness K F, Robson R E 1986 *Transp. Theor. Stat. Phys.* **14** 257–90

Penetrante B M and Bardsley J N 1990 *Nonequilibrium Effects in Ion and Electron Transport* ed J W Gallagher *et al* pp 49–66 (New York: Plenum)

Petrović Z Lj, Dujko S, Marić D, Malović G, Nikitović Ž, Šašić O, Jovanović J, Stojanović V and Radmilović-Rađenović M 2009 *J. Phys. D: Appl. Phys.* **42** 194002

Petrović Z Lj *et al* 2014 *J. Phys.: Conf. Ser.* **488** 012047

Raspopović Z M, Sakadžić S, Bzenić S and Petrović Z Lj 1999 *IEEE Trans. Plasma Sci.* **27** 1241–8

Reid I D 1979 *Aust. J. Phys.* **32** 231–54

Robson R E, White R D and Hildebrandt M 2014 *Euro. Phys J.* D **68** 188

Robson R E, White R D and Petrović Z Lj 2005 *Rev. Mod. Phys.* **77** 1303

Santonico R 2012 *Nucl. Instrum. Methods Phys. Res.* A **661** S2–5

Simonović I *et al* 2016 unpublished

Šašić O, Malović G, Strinić A, Nikitović Ž and Petrović Z Lj 2004 *New J. Phys.* **6** 74–85

Sullivan J P, Jones A, Caradonna P, Makochekanwa C and Buckman S J 2008 *Rev. Sci. Instrum.* **79** 113105

Whealton J H and Mason E A 1974 *Ann. Phys.* **84** 8–38

White R D, Robson R E, Nicoletopoulos P and Dujko S 2012 *Eur. Phys. J.* D **66** 117

The ATLAS Collaboration 2008 *J. Instrum.* **3** S08003

Tung W-K 1984 *Group Theory in Physics* (Singapore: World Scientific Publishing)

Vrhovac S B, Petrović Z Lj, Viehland L A and Santhanam T S 1999 *J. Chem. Phys.* **110** 2423–30

Regular Article

Third-order transport coefficient tensor of electron swarms in noble gases[⋆]

Ilija Simonović[1], Danko Bošnjaković[1], Zoran Lj. Petrović[2], Ronald D. White[3], and Saša Dujko[1,a]

[1] Institute of Physics, University of Belgrade, P.O. Box 68, 11080 Belgrade, Serbia
[2] Serbian Academy of Sciences and Arts, Knez Mihailova 35, 11001 Belgrade, Serbia
[3] College of Science and Engineering, James Cook University, 4810 Townsville, Australia

Abstract. In this work we extend a multi term solution of the Boltzmann equation for electrons in neutral gases to consider the third-order transport coefficient tensor. Calculations of the third-order transport coefficients have been carried out for electrons in noble gases, including helium (He), neon (Ne), argon (Ar), krypton (Kr) and xenon (Xe) as a function of the reduced electric field, E/n_0 (where E is the electric field while n_0 is the gas number density). Three fundamental issues are considered: (i) the correlation between the longitudinal component of the third-order transport tensor and the longitudinal component of the diffusion tensor, (ii) the influence of the third-order transport coefficients on the spatial profile of electron swarm, and (iii) the errors associated with the two term approximation for calculating the third-order transport coefficients for electron swarms in noble gases. It is found that a very strong correlation exists between the longitudinal components of the third-order transport coefficient tensor and diffusion tensor for the higher values of E/n_0. The effects of the third-order transport coefficients on the spatial profile of electron swarms are the most pronounced for noble gases with the Ramsauer-Townsend minimum in the cross sections for elastic scattering. The largest errors of two term approximation are observed in the off-diagonal elements of the third-order transport coefficient tensor in Ar, Kr and Xe for the higher values of E/n_0.

1 Introduction

The investigation of charged particle transport in neutral gases has a wide range of applications, ranging from the modeling of swarm experiments [1–5] and modeling of low-temperature plasmas [6,7], to high-voltage technology [8] and modeling of particle detectors used in high-energy physics [9,10]. While there is a rich amount of data concerning the lower-order transport coefficients, including the drift velocity, diffusion coefficients and rate coefficients, for both electrons and ions, [11,12] and recently for positrons [13,14], the third-order transport coefficients are still largely unexplored as they are difficult to measure, and difficult to investigate theoretically.

The third-order transport coefficient tensor is required for the conversion of hydrodynamic transport coefficients into transport data that are measured in the arrival time

spectra [15,16] and the steady-state Townsend experiments [4]. In addition, the third-order transport coefficients are needed for the representation of the spatial distribution of the swarm under conditions where this distribution deviates from the ideal Gaussian. Moreover, the third-order transport coefficients would be very useful in the swarm procedure for determining the sets of cross sections for the scattering of electrons and/or ions with neutral particles, if these transport coefficients were both calculated and measured with sufficient accuracy [17,18].

The third-order transport coefficients have been investigated by several authors. Whealton and Mason have determined the structure of the third-order transport tensor for an electric field only situation, and have calculated third-order transport coefficients for electrons assuming the constant collision frequency model gas [19]. Penentrante and Bardsley calculated the third-order transport coefficients for electrons in He, Ne and Ar by using the Monte Carlo simulations and a two term approximation for solving the Boltzmann equation [17]. Vrhovac and co-workers investigated the third-order transport tensor for electrons in He, Ne and Ar by employing the momentum transfer theory [18]. Koutselos studied the third-order transport coefficients of ions in atomic gases by using the molecular

dynamics simulations and a three-temperature method for solving Boltzmann's equation [21–24]. The equality of the higher-order transport coefficients between an electron swarm developing from multiple electron sources and another originating from a single electron source was investigated by Sugawara and Sakai [25]. The third-order transport coefficients for electrons in methane (CH_4) and sulfur hexafluoride (SF_6) have been recently investigated by Kawaguchi and co-workers via Monte Carlo simulations [16]. They have also derived the relation between the longitudinal third-order transport coefficient and the alpha-parameters, by using the theory of arrival time spectra of an electron swarm initially developed by Kondo and Tagashira [15]. Petrović and co-workers also recently investigated the third-order transport coefficient tensor for electrons in CH_4 by using Monte Carlo simulations and the multi term method for solving the Boltzmann equation [26]. Finally, Stokes and co-workers have studied the third-order transport coefficients for localized and delocalized charged-particle transport [27].

In this work we extend the multi term solution of Boltzmann's equation with the aim of investigating behavior of third-order transport coefficients in noble gases. As noble gases have simpler cross section sets than molecular gases, they are a good starting point for studying the third-order transport coefficients. Moreover, it is interesting to investigate the influence of the Ramsauer-Townsend minimum on the third-order transport tensor for electrons in Ar, Kr and Xe, as it can be expected that a rapid variation of the cross section for elastic collisions in these gases will leave a distinguishable signature on the profiles of the third-order transport coefficients. Moreover, if the components of the third-order transport tensor have very high values for electrons in Ar, Kr and Xe at low electric fields, due to the presence of the Ramsauer-Townsend minimum, they could also have a significant influence on the spatial profile of a swarm of electrons under these conditions.

The paper is organized as follows. In Section 2.1 we present the basic elements of the theory and definition of the third-order transport tensor. In Section 2.2 we describe the multi term method for solving the Boltzmann equation used in the present work where special emphasis is placed on the relating the third-order transport coefficients and the moments of the distribution function. In Section 3.1 we describe the cross sections used as an input to solve Boltzmann's equation and the conditions of our calculations. In Section 3.2 we analyze the E/n_0-dependence of mean energy for electrons in He, Ar, Kr and Xe. In Section 3.3 we investigate the variation of the third-order transport coefficients with E/n_0 for electrons in four noble gases. In Section 3.4 we study correlation between the longitudinal component of the third-order transport tensor and the longitudinal component of the diffusion tensor for electrons in He, Ne, Ar, Kr and Xe. In Section 3.5 we consider the influence of the third-order transport coefficients on the spatial profile of the swarm for electrons in these five gases. Finally, in Section 3.6 we discuss the errors associated with the two term approximation for solving the Boltzmann equation in the framework of calculations of the third-order transport coefficients for electrons in noble gases. Our conclusions are summarized in Section 4.

2 Theory: definitions and methods of calculation

2.1 Definition of the third-order transport coefficient tensor

In the present work, we consider a swarm of electrons which moves in an infinite and homogeneous background gas under the influence of a constant and uniform electric field. The z axis of the system is oriented along the direction of the electric field. The number density of electrons is very low and hence, the space charge effects and collisions between electrons are considered to be negligible. The background gas is regarded to be in a thermodynamic equilibrium at a temperature T_0, and the effect of the swarm on the state of the background gas can be neglected. The swarm of electrons is represented by the phase space distribution function $f(\mathbf{r}, \mathbf{c}, t)$, which is a function of position $\mathbf{r}$, velocity $\mathbf{c}$ and time t.

The continuity of the swarm in the configuration space is expressed by the following equation

$$\frac{\partial n(\mathbf{r}, t)}{\partial t} + \nabla \cdot \mathbf{\Gamma}(\mathbf{r}, t) = S(\mathbf{r}, t), \qquad (1)$$

where $n(\mathbf{r}, t)$ is the number density of electrons, while $\mathbf{\Gamma}(\mathbf{r}, t)$ and $S(\mathbf{r}, t)$ are the flux of electrons and the source term, respectively. The number density of electrons can be expressed in terms of the phase space distribution function $f(\mathbf{r}, \mathbf{c}, t)$ as

$$n(\mathbf{r}, t) = \int f(\mathbf{r}, \mathbf{c}, t) \, \mathrm{d}\mathbf{c}, \qquad (2)$$

where integration is performed over the entire velocity space.

When the swarm is located far from boundaries of the system, and far from sources and sinks of charged particles, and when the applied electric field is spatially uniform, the swarm can enter the hydrodynamic regime [2,28]. In the hydrodynamic regime all space-time dependence of the phase space distribution function may be expressed in terms of functionals of the number density $n(\mathbf{r}, t)$. Under the hydrodynamic conditions, the phase space distribution function can be represented by the following expression

$$f(\mathbf{r}, \mathbf{c}, t) = \sum_{k=0}^{\infty} \mathbf{f}^{(k)}(\mathbf{c}, t) \odot (-\nabla)^k n(\mathbf{r}, t), \qquad (3)$$

where $\mathbf{f}^{(k)}(\mathbf{c}, t)$ are time-dependent tensors of rank k and $\odot$ denotes a k-fold scalar product. This expression is known as the density gradient expansion of the phase space distribution function [28]. If the background electric field is static, the tensors $\mathbf{f}^{(k)}(\mathbf{c}, t)$ are independent of time, after the swarm has relaxed to a stationary state. In the hydrodynamic regime, the flux of

velocity of charged particles is defined by the flux gradient relation

$$\mathbf{\Gamma}\left(\mathbf{r}, t\right) = \sum_{k=0}^{\infty} \mathbf{\Gamma}^{(k+1)} \odot \left(-\nabla\right)^k n\left(\mathbf{r}, t\right), \qquad (4)$$

where the superscripts (k) denote the order of the density gradient, while $(k+1)$ denote the ranks of the tensors $\mathbf{\Gamma}^{(k+1)}$. These tensors represent the flux transport coefficients [29]. By truncating the flux gradient relation at $k = 2$, the following equation is obtained

$$\mathbf{\Gamma}\left(\mathbf{r}, t\right) = \mathbf{W}^{(\mathbf{f})} n\left(\mathbf{r}, t\right) - \mathbf{D}^{(\mathbf{f})} \odot \nabla n\left(\mathbf{r}, t\right)$$
$$+ \mathbf{Q}^{(\mathbf{f})} \odot \left(\nabla \otimes \nabla\right) n\left(\mathbf{r}, t\right), \qquad (5)$$

where $\otimes$ is the tensor product, $\mathbf{W}^{(\mathbf{f})}$ and $\mathbf{D}^{(\mathbf{f})}$ are the flux drift velocity and the flux diffusion tensor, respectively, while $\mathbf{Q}^{(\mathbf{f})}$ defines the flux third-order transport coefficient tensor.

For an electric field only configuration, the third-order transport coefficient tensor has seven non-zero elements of which three are independent [19]. The independent components of the third-order transport tensor are $Q_{xxz}^{(f)}$, $Q_{zxx}^{(f)}$ and $Q_{zzz}^{(f)}$. Other non-zero components are related to the independent components by the following symmetry relations [19]:

$$Q_{xzx}^{(f)} = Q_{xxz}^{(f)} = Q_{yyz}^{(f)} = Q_{yzy}^{(f)}, \qquad (6)$$

$$Q_{zyy}^{(f)} = Q_{zxx}^{(f)}. \qquad (7)$$

The longitudinal and transverse third-order transport coefficients are defined as:

$$Q_L^{(f)} = Q_{zzz}^{(f)}, \ Q_T^{(f)} = \frac{1}{3}(Q_{xxz}^{(f)} + Q_{xzx}^{(f)} + Q_{zxx}^{(f)}). \qquad (8)$$

The hydrodynamic expansion of the source term is given by [28]

$$S\left(\mathbf{r}, t\right) = \sum_{k=0}^{\infty} \mathbf{S}^{(k)} \odot \left(-\nabla\right)^k n\left(\mathbf{r}, t\right), \qquad (9)$$

where the superscripts (k) denote the rank of tensors $S^{(k)}$ [29]. By substituting equations (5) and (9) into (1) the generalized diffusion equation, which is truncated at third-order gradients, is obtained. This equation can be written as

$$\frac{\partial n\left(\mathbf{r}, t\right)}{\partial t} + \mathbf{W}^{(b)} \odot \nabla n\left(\mathbf{r}, t\right) - \mathbf{D}^{(b)} \odot \left(\nabla \otimes \nabla\right) n\left(\mathbf{r}, t\right)$$
$$+ \mathbf{Q}^{(b)} \odot \left(\nabla \otimes \nabla \otimes \nabla\right) n\left(\mathbf{r}, t\right) = R_{\mathrm{prod}} n\left(\mathbf{r}, t\right), \qquad (10)$$

where R_{prod} is the net particle production-rate, $\mathbf{W}^{(b)}$ and $\mathbf{D}^{(b)}$ are the bulk drift velocity and bulk diffusion tensor, respectively, and $\mathbf{Q}^{(b)}$ is the bulk third-order transport coefficient tensor. Bulk transport coefficients are related to the corresponding flux transport coefficients as [2,11,29]

$$\mathbf{W}^{(\mathbf{b})} = \mathbf{W}^{(\mathbf{f})} + \mathbf{S}^{(\mathbf{1})}, \qquad (11)$$

$$\mathbf{D}^{(\mathbf{b})} = \mathbf{D}^{(\mathbf{f})} + \mathbf{S}^{(\mathbf{2})}, \qquad (12)$$

$$\mathbf{Q}^{(\mathbf{b})} = \mathbf{Q}^{(\mathbf{f})} + \mathbf{S}^{(\mathbf{3})}. \qquad (13)$$

Equation (10) cannot be solved analytically, even for the set of simple boundary conditions found in an idealized time-of-flight experiment [2]. However, this equation can be solved approximately if the Fourier transform of the solution is expanded in a Taylor series in terms of components of the third-order transport coefficient tensor [20]. The approximate solution up to the first-order can be written as [20]

$$n^{(1)}\left(\mathbf{r}, t\right) = n^{(0)}\left(\mathbf{r}, t\right)$$
$$\times \left[1 + Q_L^{(b)} \frac{t\left(z - W^{(b)}t\right)^3 - 6D_L^{(b)}t^2\left(z - W^{(b)}t\right)}{8\left(D_L^{(b)}t\right)^3}\right.$$
$$\left. + Q_T^{(b)} \frac{3t\left(z - W^{(b)}t\right)\left(x^2 + y^2 - 4D_T^{(b)}t\right)}{8D_L^{(b)}t\left(D_T^{(b)}t\right)^2}\right], \quad (14)$$

where $n^{(0)}(\mathbf{r}, t)$ is the solution of the diffusion equation, which has the form [2]

$$n^{(0)}(\mathbf{r}, t) = \frac{N_0 e^{R_{\mathrm{prod}}t} e^{-\frac{\left(z - W^{(b)}t\right)^2}{4D_L^{(b)}t} - \frac{x^2 + y^2}{4D_T^{(b)}t}}}{\left(4\pi D_T^{(b)}t\right)\sqrt{4\pi D_L^{(b)}t}}, \qquad (15)$$

while N_0, $W^{(b)}$, $D_L^{(b)}$, $D_T^{(b)}$, $Q_L^{(b)}$ and $Q_T^{(b)}$ are the initial number of particles, bulk drift velocity, bulk longitudinal diffusion, bulk transverse diffusion, and bulk values of longitudinal and transverse third-order transport coefficients, respectively. Expression (14) has a simpler form in the relative coordinates that are defined as [20]

$$\chi_z = \frac{z - W^{(b)}t}{\sqrt{2D_L^{(b)}t}}, \ \chi_x = \frac{x}{\sqrt{2D_T^{(b)}t}}, \ \chi_y = \frac{y}{\sqrt{2D_T^{(b)}t}}. \quad (16)$$

In these coordinates the approximate solution (14) is given by

$$n^{(1)}(\mathbf{r}, t) = n^{(0)}(\mathbf{r}, t)$$
$$\times \left(1 + \frac{tQ_L^{(b)}}{\sigma_z^3}\chi_z(\chi_z^2 - 3) + \frac{3tQ_T^{(b)}}{\sigma_x^2\sigma_z}\chi_z(\chi_x^2 + \chi_y^2 - 2)\right), \qquad (17)$$

where $\sigma_z = \sqrt{2D_L^{(b)}t}$ and $\sigma_x = \sigma_y = \sqrt{2D_T^{(b)}t}$. From this expression it can be seen that the contribution of the third-order transport coefficient tensor to the spatial profile of the swarm is proportional to $Q_L^{(b)}/(t^{1/2}(D_L^{(b)})^{3/2})$ and $Q_T^{(b)}/(t^{1/2}\sqrt{D_L^{(b)}D_T^{(b)}})$ [20].

2.2 Multi term solutions of Boltzmann's equation

The evolution of the phase space distribution function is given by the Boltzmann equation. In the case of a swarm of electrons, which are moving in an infinite and homogeneous background gas, the Boltzmann equation can be written as

$$\frac{\partial f}{\partial t} + \mathbf{c} \cdot \frac{\partial f}{\partial \mathbf{r}} + \frac{e}{m}\left(\mathbf{E} + \mathbf{c} \times \mathbf{B}\right) \cdot \frac{\partial f}{\partial \mathbf{c}} = -J\left(f, f_0\right), \quad (18)$$

where e and m are the charge and mass of electrons, $\mathbf{E}$ and $\mathbf{B}$ are the electric and magnetic fields, and $J(f, f_0)$ is the collision operator. The Boltzmann equation is an integro-differential equation, which cannot be solved analytically in the case of electrons in real gases [2,6]. We employ the moment method where the phase space distribution function is expanded in terms of Burnett functions [28,30,31,33]:

$$\Phi_m^{[\nu l]}(\alpha \mathbf{c}) = N_{\nu l}\left(\frac{\alpha c}{\sqrt{2}}\right)^l S_{l+1/2}^{(\nu)}\left(\frac{\alpha^2 c^2}{2}\right) Y_m^{[l]}(\hat{\mathbf{c}})$$
$$= R_{\nu l}(\alpha c) Y_m^{[l]}(\hat{\mathbf{c}}), \qquad (19)$$

where $Y_m^{[l]}$ is a spherical harmonic, while $S_{l+1/2}^{(\nu)}$ is a Sonine polynomial, α is a parameter and $\hat{\mathbf{c}}$ is a unit vector in velocity space [30,32]. The constant $N_{\nu l}$ is given by

$$N_{\nu l}^2 = \frac{2\pi^{3/2}\nu!}{\Gamma(\nu + l + 3/2)}, \qquad (20)$$

where $\Gamma(\nu + l + 3/2)$ is the gamma function, while

$$R_{\nu l}(\alpha c) = N_{\nu l}\left(\frac{\alpha c}{\sqrt{2}}\right)^l S_{l+1/2}^{(\nu)}(\alpha^2 c^2/2), \qquad (21)$$

determines the radial part of the Burnett function. The Burnett functions satisfy the orthogonality relations [30]:

$$\int \omega(\alpha, c)\Phi_m^{(\nu l)}(\alpha \mathbf{c})\Phi_{m'}^{[\nu' l']}(\alpha \mathbf{c})\mathrm{d}\mathbf{c} = \delta_{\nu'\nu}\delta_{l'l}\delta_{m'm}, \qquad (22)$$

where

$$\omega(\alpha, c) = \left(\frac{\alpha^2}{2\pi}\right)^{3/2} e^{-\alpha^2 c^2/2}, \qquad (23)$$

is the weighting function [30]. Orthogonality of the Burnett functions is due to orthogonality of the spherical harmonics and Sonine polynomials. The phase space distribution function can be expanded as

$$f(\mathbf{r}, \mathbf{c}, t) = \omega(\alpha, c)\sum_{\nu=0}^{\infty}\sum_{l=0}^{\infty}\sum_{m=-l}^{l}\mathbf{f}_m^{(\nu l)}(\alpha, \mathbf{r}, t)\Phi_m^{[\nu l]}(\alpha \mathbf{c}), \qquad (24)$$

where $\mathbf{f}_m^{(\nu l)}(\alpha, \mathbf{r}, t)$ are the expansion coefficients which depend on the coordinates in the configuration space $\mathbf{r}$ and time t [30,32].

In the hydrodynamic regime the phase space distribution function can be expanded in terms of powers of the density gradient operator as [30,33–35]

$$f(\mathbf{r}, \mathbf{c}, t) = \omega(\alpha, c)\sum_{s=0}^{\infty}\sum_{\lambda=0}^{s}\sum_{\mu=-\lambda}^{\lambda}\sum_{\nu=0}^{\infty}\sum_{l=0}^{\infty}\sum_{m=-l}^{l}$$
$$F(\nu lm|s\lambda\mu; \alpha, t)R_{\nu l}(\alpha, c)Y_m^{[l]}(\hat{\mathbf{c}})G_\mu^{(s\lambda)}n(\mathbf{r}, t), \qquad (25)$$

where $F(\nu lm|s\lambda\mu; \alpha, t)$ are the moments of the phase space distribution function, while $G_\mu^{(s\lambda)}$ is the spherical form of the density gradient operator [30].

When the Boltzmann equation is multiplied by an arbitrary moment $F(\nu lm|s\lambda\mu; \alpha, t)$ and integrated over the entire velocity space, an infinite hierarchy of matrix equations in terms of moments $F(\nu lm|s\lambda\mu; \alpha, t)$ is obtained [31,33–35]. This hierarchy is truncated at a finite number of spherical harmonics $l = l_{\max}$, and a finite number of Sonine polynomials $\nu = \nu_{\max}$. The values of these numbers are determined by the criterion for convergence. The resulting system of equations is then solved numerically by using the matrix inversion. In our calculations, values of $l_{\max} = 4$ were sometimes required, when the phase space distribution function substantially deviates from an isotropy in the velocity space. Likewise, values of $\nu_{\max} = 80$ were required when the distribution function was far away from a thermal Maxwellian at the basis temperature T_b. The basis temperature is a parameter which is used to optimize the convergence.

The explicit expressions for determining the flux transport coefficients in terms of moments of the phase space distribution function can be obtained by expanding the flux of velocity of the charged particles $\mathbf{\Gamma}(\mathbf{r}, t)$ in terms of these moments and by recognizing terms which are contracted with the corresponding partial derivative of the number density $n(\mathbf{r}, t)$ [33–35]. The expansion of $\mathbf{\Gamma}(\mathbf{r}, t)$ in terms of $F(\nu lm|s\lambda\mu; \alpha, t)$ is given by

$$\Gamma_m^{[1]}(\mathbf{r}, t) = \int c_m^{[1]} f(\mathbf{r}, \mathbf{c}, t)\mathrm{d}\mathbf{c}$$
$$= \int c_m^{[1]}\omega(\alpha, c)\sum_{s=0}^{\infty}\sum_{\lambda=0}^{s}\sum_{\mu=-\lambda}^{\lambda}\sum_{\nu=0}^{\infty}\sum_{l=0}^{\infty}\sum_{m'=-l}^{l}$$
$$F(\nu lm'|s\lambda\mu; \alpha, t)R_{\nu l}(\alpha, c)Y_{m'}^{[l]}(\hat{\mathbf{c}})G_\mu^{(s\lambda)}n(\mathbf{r}, t)\mathrm{d}\mathbf{c}, \qquad (26)$$

where $\Gamma_m^{[1]}(\mathbf{r}, t)$ is the flux of velocity of charged particles $\mathbf{\Gamma}(\mathbf{r}, t)$ written in the spherical form [30]. Cartesian components of a vector whose spherical form is given by

$$c_m^{(1)} = \sqrt{\frac{4\pi}{3}}cY_m^{[1]}(\hat{\mathbf{c}}), \qquad (27)$$

are given by the expressions [30]

$$c_x = \frac{i}{\sqrt{2}}\left(c_1^{[1]} - c_{-1}^{[1]}\right), \qquad (28)$$

$$c_y = \frac{1}{\sqrt{2}}\left(c_1^{[1]} + c_{-1}^{[1]}\right), \qquad (29)$$

$$c_z = -ic_0^{[1]}. \qquad (30)$$

The components of the third-order transport coefficient tensor for an electric field only configuration are given by

$$Q_{xxz}^{(f)} = \frac{1}{\sqrt{2}\alpha}\left(\mathrm{Im}\{F(011|221)\} - \mathrm{Im}\{F(01-1|221)\}\right), \qquad (31)$$

$$Q_{zxx}^{(f)} = -\frac{1}{\alpha}\left(\frac{1}{\sqrt{3}}\mathrm{Im}\{F(010|200)\} + \frac{1}{\sqrt{6}}\mathrm{Im}\{F(010|220)\}\right)$$
$$+ \frac{1}{\alpha}\mathrm{Im}\{F(010|222)\}, \qquad (32)$$

and

$$Q_{zzz}^{(f)} = \frac{1}{\alpha}\left(\sqrt{\frac{2}{3}}\text{Im}\{F(010|220)\} - \frac{1}{\sqrt{3}}\text{Im}\{F(010|200)\}\right),$$

(33)

where Re{} and Im{} refer to the real and imaginary parts of the moments $F(\nu lm|s\lambda\mu; \alpha, t)$, respectively [20]. The explicit expressions for the lower order transport coefficients in terms of moments of the phase space distribution function can be found in [33–35]. For brevity, in the following sections the superscript (f) in the flux third-order transport coefficients (and in the flux diffusion coefficients) will be omitted.

3 Results and discussion

3.1 Preliminaries

In this work we calculate the third-order transport coefficients for electrons in noble gases. Calculations are performed in the E/n_0 range between 10^{-4} Td and 100 Td $(1\,\text{Td} = 10^{-21}\,\text{Vm}^2)$. The temperature of the background gas T_0 is 293 K and thermal motion of background atoms is taken into account. All background atoms are assumed to be in the ground state. All electron scattering is considered to be isotropic. Elastic collisions are represented by the elastic momentum transfer cross section, while the inelastic collisions are represented by the total inelastic cross sections. For electrons in He we use the set of cross sections which has been detailed by Šašić *et al.* [36] while for electrons in Ne we use the set of cross sections, initially developed by Hayashi [37]. Likewise, for electron scattering in Ar and Xe we use the cross section sets developed by Hayashi [38,39]. For electrons in Kr we use the cross section set from a publicly available Monte Carlo code MAGBOLTZ [40].

3.2 Mean energy

In the following section we often find it necessary to refer to the mean energy of the electron swarm to understand and explain certain trends of the behavior of the third-order transport coefficients. Thus, in Figure 1 we show the mean energies of electrons in He, Ar, Kr and Xe as a function of E/n_0. Comparing the profiles of mean energy in He and the remaining three gases, we observe that the mean energy of electrons in He is different not only quantitatively, but also qualitatively. Specifically, there are four distinct regions of transport as E/n_0 increases for electrons in He and five distinct regions of transport in the case of Ar, Kr and Xe. First, for electrons in all considered gases, there is an initial plateau region where the mean energy is thermal. In the second distinct region of transport for electrons in He, the mean energy rises with an approximately constant slope in the log-log plot. The slope of mean energy is significantly lower in the third region, due to the influence of inelastic collisions. Finally, the slope is again increased in the fourth region. This
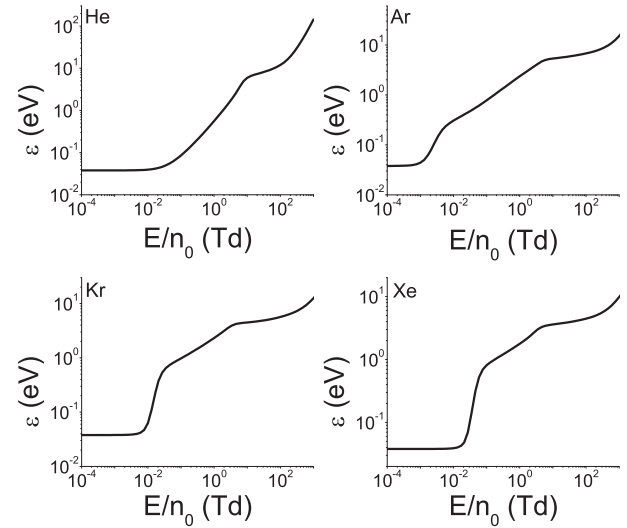
Fig. 1. Variation of the mean energy with E/n_0 for electron swarms in He, Ar, Kr and Xe.

increase can be attributed to a greater fraction of electrons being in the energy range where the collision frequency for all scattering processes reduces with increasing energy. For electrons in Ar, Kr and Xe, the rise of mean energy with increasing E/n_0 is very steep in the second distinct region of transport. A large fraction of electrons is thus in the energy range where elastic momentum transfer cross section is a monotonically decreasing function of energy, due to the presence of the Ramsauer-Townsend minimum. However, the slope of the mean energy is lower in the third region, in which high energy electrons are in the energy range where the elastic momentum transfer cross section is rising sharply. The slope of mean energy is further reduced in the fourth region where electrons can undergo inelastic collisions. Finally, this slope increases in the fifth distinct region of transport, in which the profile of mean energy changes from a power-law-like behavior to the more exponential-like increase. In this field region, the most energetic electrons are in the energy range where the collision frequency for all scattering processes is being reduced with increasing energy.

3.3 Variation of the third-order transport coefficients with E/n_0

3.3.1 Brief analysis

In Figure 2 we show the variation of the individual components of the third-order transport coefficient tensor with E/n_0 for electrons in He. We observe that $n_0^2 Q_{xxz}$ and $n_0^2 Q_{zzz}$ components are positive over the range of E/n_0 considered in the present work. However, the $n_0^2 Q_{zxx}$ component is negative until approximately 10 Td and positive at higher E/n_0. The absolute values of all individual components of the third-order transport tensor increase with increasing E/n_0 in the sub-excitation field region, which corresponds to the first two characteristic regions of the mean energy (see Fig. 1). This can be attributed
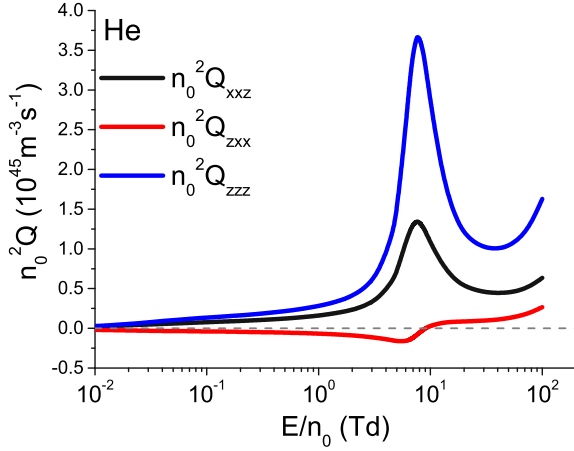
Fig. 2. Variation of $n_0^2Q_{xxz}$, $n_0^2Q_{zxx}$ and $n_0^2Q_{zzz}$ components of the third-order transport coefficient tensor with E/n_0 for electrons in He.

Fig. 4. Variation of $n_0^2Q_{xxz}$, $n_0^2Q_{zxx}$ and $n_0^2Q_{zzz}$ components of the third-order transport coefficient tensor with E/n_0 for electrons in Kr.

Fig. 3. Variation of $n_0^2Q_{xxz}$, $n_0^2Q_{zxx}$ and $n_0^2Q_{zzz}$ components of the third-order transport coefficient tensor with E/n_0 for electrons in Ar.
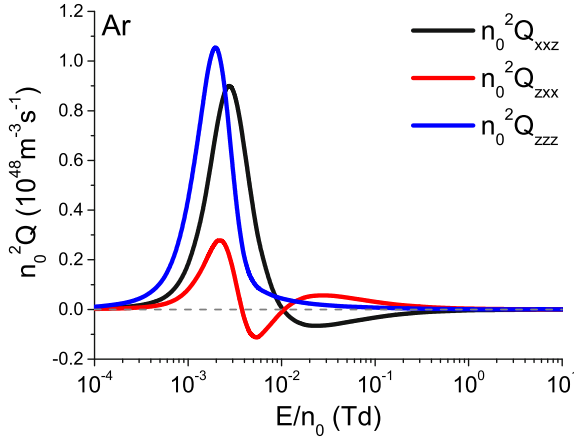
Fig. 5. Variation of $n_0^2Q_{xxz}$, $n_0^2Q_{zxx}$ and $n_0^2Q_{zzz}$ components of the third-order transport coefficient tensor with E/n_0 for electrons in Xe.

to a slow rise of elastic momentum transfer cross section in the energy range up to about 2 eV, as well as to its reduction at higher energies. However, the absolute values of all individual components of the third-order transport tensor are reduced for the higher values of E/n_0, where the high energy electrons can undergo many inelastic collisions. This field region roughly corresponds to the third characteristic region of the mean energy. Finally, all three components are increasing functions of E/n_0 in the limit of the highest fields considered in this work, where the collision frequency of the high energy electrons decreases with increasing electron energy.

In Figures 3–5 we show the variation of the individual components of the third-order transport coefficient tensor with E/n_0 for electrons in Ar, Kr and Xe, respectively. It can be seen that in these gases all components of the third-order transport tensor are rapidly rising functions of E/n_0 in the limit of the lowest fields, where most of the electrons are in the energy range in which the elastic momentum transfer cross section is reduced with the increase of
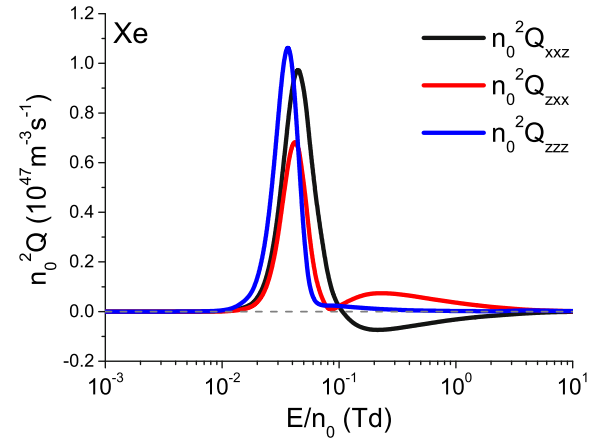
energy, due to the presence of the Ramsauer-Townsend minimum. This field region corresponds to the first characteristic region of the mean energy, as well as to the first half of the second characteristic region of the mean energy, shown in Figure 1. However, all three components of the third-order transport tensor are rapidly decreasing functions of E/n_0 at higher fields, where the most energetic electrons are in the energy range in which the elastic momentum transfer cross section has a steep rise with an increase of energy. This field region corresponds to the second half of the second characteristic region of the mean energy. In the remaining field region considered in this work, $n_0^2Q_{zxx}$ and $n_0^2Q_{zzz}$ components exhibit a local minimum and a local maximum, while the $n_0^2Q_{xxz}$ component has a single local minimum only. The positions of these local maximums and local minimums correspond to those values of E/n_0 where the ratio between the mean energy and the position of the Ramsauer-Townsend minimum or the threshold of the first electronic excitation have similar values. For instance, the $n_0^2Q_{xxz}$ component becomes negative at the reduced electric field where the

mean energy is higher than the position of the Ramsauer-Townsend minimum by a factor that has values in the range between 1.3 and 1.4 for all three gases. Likewise, this component reaches the local minimum at approximately the same field where the $n_0^2 Q_{zxx}$ component reaches the second local maximum, and the mean energy is about 1.75 times higher than the energy of the Ramsauer-Townsend minimum at the position of these local extremes in all three gases. Moreover, the $n_0^2 Q_{zzz}$ component reaches the second local maximum at the value of the reduced electric field where the mean energy of electrons is about 2.5 times lower than the threshold of the first electronic excitation for all three gases (see Fig. 8). At the highest fields, where the most energetic electrons may undergo many inelastic collisions with the background atoms, the absolute values of all components of the third-order transport tensor are reduced with increasing E/n_0. This field region roughly corresponds to the fourth and the fifth characteristic regions of the mean energy in Ar, Kr and Xe. In the following subsubsection the E/n_0-profiles of the individual components of the third-order transport coefficient tensor for electrons in He, Ar, Kr and Xe are analyzed in a greater detail.

3.3.2 Comprehensive analysis

For electrons in He, the absolute values of all three components of the third-order transport tensor are monotonically increasing functions of E/n_0, but only in the limit of low electric fields. Specifically, $n_0^2 Q_{xxz}$ and $n_0^2 Q_{zzz}$ components rise in the field region below around 8 Td, where the mean energy of electrons is lower than 5 eV. Likewise, the absolute value of $n_0^2 Q_{zxx}$ increases up to approximately 5.9 Td, where the mean energy is around 3.6 eV. In the field region, where the absolute values of all three components are being increased with increasing E/n_0 most of the electrons undergo elastic collisions only. Moreover, the elastic momentum transfer cross section is gradually rising in the energy range between approximately 10^{-2} eV and 2 eV, while it is being reduced at higher energies. For this reason, resistance to diffusive motion that is caused by collisions of electrons with the background atoms is not very intensive in the field region up to approximately 5.9 Td. This in turn induces an increase of the absolute values of all three components of the third-order transport coefficient tensor in this range of E/n_0. However, at higher fields the most energetic electrons can undergo inelastic collisions with the background atoms, as the threshold for the first electronic excitation in helium is around 19.82 eV. This leads to a rapid decrease of $n_0^2 Q_{xxz}$ and $n_0^2 Q_{zzz}$ components in the field range between approximately 8 Td and 40 Td. Likewise, the increased resistance to the spreading of the swarm due to inelastic collisions leads to a rapid decrease of the absolute value of the $n_0^2 Q_{zxx}$ component in the field range between approximately 5.9 Td and 8 Td, and to a gradual increase of this component up to around 40 Td. For the higher values of E/n_0, all three components of the third-order transport coefficient tensor rise with increasing E/n_0. Over this range of E/n_0, the collision frequency of the most energetic electrons decreases

with increasing E/n_0 which in turn enhances the third-order transport coefficients.

For electrons in Ar, Kr and Xe, all components of the third-order transport tensor are initially, rapidly increased with increasing E/n_0 for the lower values of E/n_0, as a large fraction of electrons is in the energy range where the elastic momentum transfer cross section markedly decreases with increasing energy, due to the presence of the Ramsauer-Townsend minimum in the cross sections for elastic scattering. These components reach local maximums in the E/n_0 region where the mean energy is lower than the position of the Ramsauer-Townsend minimum by a factor which is approximately between 2 and 3 in case of Ar, and approximately between 2 and 4 in case of Kr and Xe. Thus, all components of the third-order transport tensor start to decrease with an increase of E/n_0 in the E/n_0 region where the collision frequencies of the most energetic electrons increase with the rising energy of electrons.

The $n_0^2 Q_{zxx}$ component is the first to reach a local minimum in all three gases. However, the behavior of this component is somewhat different in the case of Ar, as compared to Kr and Xe. Specifically, this component becomes negative for electrons in Ar, while it remains positive over the entire considered range of E/n_0 for electrons in Kr and Xe. For electrons in Ar, the $n_0^2 Q_{zxx}$ component becomes negative at the value of E/n_0 where the mean energy is around 1.4 times lower than the position of the Ramsauer-Townsend minimum. The same component reaches a local minimum at the value of E/n_0 where the mean energy of the swarm is approximately equal to the energy position of the Ramsauer-Townsend minimum. However, in case of Kr and Xe this component reaches a local minimum at the value E/n_0 where the mean energy is around 1.25 times higher than the energy position of the Ramsauer-Townsend minimum. The $n_0^2 Q_{zxx}$ component becomes positive in Ar at approximately the same field, where the $n_0^2 Q_{xxz}$ component becomes negative. The $n_0^2 Q_{xxz}$ component starts to be negative at the value of E/n_0 where the mean energy is higher than the position of the Ramsauer-Townsend minimum by a factor of around 1.3 in case of Ar and Xe, and by a factor of approximately 1.4 in case of Kr. The sign of the $n_0^2 Q_{xxz}$ component remains unaltered until the end of the considered E/n_0 range for Ar, Kr and Xe. The $n_0^2 Q_{zxx}$ component reaches the second local maximum at approximately the same E/n_0 where the $n_0^2 Q_{xxz}$ component reaches the local minimum. The position of these local extremes for $n_0^2 Q_{xxz}$ and $n_0^2 Q_{zxx}$ components is at the value of E/n_0 where the mean energy is about 1.75 times higher than the position of the Ramsauer-Townsend minimum for electrons in all three gases. For the higher values of E/n_0, the absolute values of $n_0^2 Q_{xxz}$ and $n_0^2 Q_{zxx}$ are being reduced with increasing E/n_0 until the end of the considered field range.

The $n_0^2 Q_{zzz}$ component reaches a local minimum at the value of E/n_0 where the electrons with energies that are between approximately 2 and 3 times higher than mean energy, are in the energy range where the elastic momentum transfer cross section for electrons in Ar, Kr and Xe, is reduced (see Fig. 8) with increasing energy. For the higher E/n_0 values, the $n_0^2 Q_{zzz}$ component rises with

increasing E/n_0. This component reaches a local maximum at the value of E/n_0 where the electrons with energies that are about 2.5 times higher than the mean energy can undergo inelastic collisions with the background atoms. The absolute values of all three components of the third-order transport coefficient tensor are reduced with increasing E/n_0 at higher fields until reaching the end of the considered E/n_0 range.

At the qualitative level, the E/n_0-profiles of each component of the third-order transport coefficient tensor are very similar for electrons in Ar, Kr and Xe. Specifically, these components reach local maximums and local minimums at the values of E/n_0 at which the ratios between the mean energy and the position of the Ramsauer-Townsend minimum and/or the threshold for the first electronic excitation have very similar values. However, there is a significant difference in the profile of $n_0^2 Q_{zxx}$ component for electrons in Ar, when compared to the corresponding profiles in Kr and Xe, as this component becomes negative in Ar. The absence of negative values of $n_0^2 Q_{zxx}$ for electrons in Kr and Xe might be attributed to a steeper rise of the elastic momentum transfer cross section with an increasing energy, after the Ramsauer-Townsend minimum, in these two gases. As discussed recently by Simonović et al. [20] when the collision frequency is rising with increasing electron energy, one of the off-diagonal components of the third-order transport tensor ($n_0^2 Q_{zxx}$ and $n_0^2 Q_{xxz}$) is often negative. If the rise of the collision frequency with energy is not too steep, $n_0^2 Q_{zxx}$ component is usually negative (and $n_0^2 Q_{xxz}$ is positive). However, $n_0^2 Q_{xxz}$ component is negative (and $n_0^2 Q_{zxx}$ is positive) when the rise of the collision frequency with increasing electron energy is very steep.

3.4 Correlation between the longitudinal components of the skewness and diffusion tensors

Another issue that is highly relevant for understanding higher-order transport coefficients is the correlation between higher-order and lower-order transport coefficients. In this work we investigate the correlation between the longitudinal component of the third-order transport tensor and the longitudinal component of the diffusion tensor of electrons in noble gases. Recently, this correlation has been investigated for electrons in CH$_4$ [26]. It has been shown that whenever D_{zz} decreases, then Q_{zzz} is reduced markedly, and whenever D_{zz} increases in a decelerating way, Q_{zzz} also decreases, but less intensively. The Q_{zzz} was found to increase only when D_{zz} increases in an accelerating manner. It can be expected that this correlation is absent at the lowest E/n_0, as $n_0^2 Q_{zzz}$ represents an asymmetric correction to diffusive motion and it vanishes in the limit of the lowest fields, unlike diffusion coefficients which have non-zero thermal values. For this reason $n_0^2 Q_{zzz}$ is expected to rise with increasing E/n_0 at the lowest fields, regardless of the field dependence of $n_0 D_{zz}$. The value of E/n_0 at which the correlation between the profiles of field dependence of $n_0^2 Q_{zzz}$ and $n_0 D_{zz}$ occurs is different for various gases.
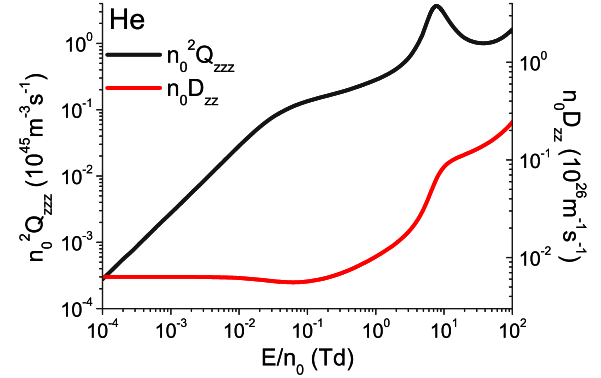
Fig. 6. The correlation of the longitudinal component of the third-order transport tensor $n_0^2 Q_{zzz}$ and the longitudinal component of the diffusion tenzor $n_0 D_{zz}$ for electrons in He.

The correlation between the profiles of $n_0^2 Q_{zzz}$ and $n_0 D_{zz}$ for electrons in He and Ne is shown in Figures 6 and 7, respectively. For electrons in He, $n_0^2 Q_{zzz}$ and $n_0 D_{zz}$ rise with increasing E/n_0 in the E/n_0 region between approximately $5.9 \cdot 10^{-2}$ Td and 7.5 Td. This increase is the most intensive for E/n_0 between around 2.1 Td and 7.7 Td. However, between approximately 7.7 Td and 35 Td, the rise of $n_0 D_{zz}$ with increasing E/n_0 slows down, and $n_0 D_{zz}$ becomes a concave function of E/n_0 in the log-log plot. In this E/n_0 region, $n_0^2 Q_{zzz}$ is reduced with increasing E/n_0. For E/n_0 between approximately 35 Td and 100 Td, the slope of $n_0 D_{zz}$ rises with E/n_0 and $n_0 D_{zz}$ becomes a convex function of E/n_0 in the log-log plot. As a consequence, in this E/n_0 region, $n_0^2 Q_{zzz}$ rises monotonically with increasing E/n_0.

For electrons in Ne, $n_0^2 Q_{zzz}$ and $n_0 D_{zz}$ decrease with increasing E/n_0 between approximately $3.5 \cdot 10^{-3}$ Td and $3.5 \cdot 10^{-2}$, and $n_0^2 Q_{zzz}$ continues to decrease up to about $5.9 \cdot 10^{-2}$ Td. For the reduced electric fields higher than approximately $5.9 \cdot 10^{-2}$ Td, both $n_0^2 Q_{zzz}$ and $n_0 D_{zz}$ rise with increasing field up to around 1.9 Td. This rise is especially rapid for E/n_0 between approximately 1 Td and 1.9 Td. At higher fields, $n_0 D_{zz}$ becomes a concave function of E/n_0 in the log-log plot, and it slowly decreases with increasing field for E/n_0 between approximately 5.9 Td and 30 Td, while it saturates at higher fields. In the E/n_0 region between approximately 1.9 Td and 100 Td, $n_0^2 Q_{zzz}$ decreases monotonically with increasing E/n_0.

The correlation between the profiles of $n_0^2 Q_{zzz}$ and $n_0 D_{zz}$ for electrons in Ar, Kr and Xe is shown in Figure 8. As can be seen, there is a very strong correlation between the profiles of $n_0^2 Q_{zzz}$ and $n_0 D_{zz}$ for all three gases. It can also be seen that the profiles of $n_0^2 Q_{zzz}$ and $n_0 D_{zz}$ in each of these gases are very similar. At the lowest E/n_0 $n_0^2 Q_{zzz}$ and $n_0 D_{zz}$ rise with increasing E/n_0 in all three cases, as most of the electrons are in the energy range in which the elastic momentum transfer cross section decreases rapidly with increasing electron energy. The $n_0^2 Q_{zzz}$ component reaches a local maximum at around $2.1 \cdot 10^{-3}$ Td, $1.4 \cdot 10^{-2}$ Td and $3.7 \cdot 10^{-2}$ Td for electrons in Ar, Kr, and Xe, respectively, while $n_0 D_{zz}$ reaches a local maximum at approximately $2.7 \cdot 10^{-3}$ Td, $1.7 \cdot 10^{-2}$ Td and $4.6 \cdot 10^{-2}$ Td,
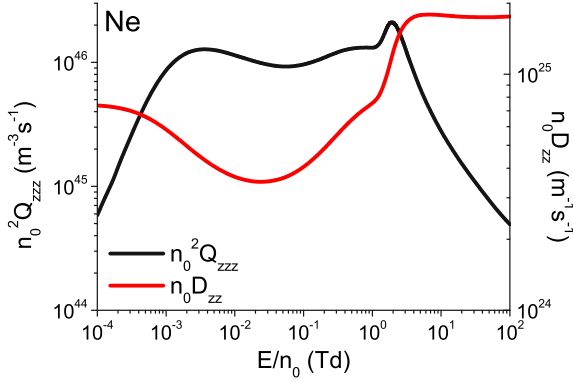
Fig. 7. The correlation of the longitudinal component of the third-order transport tensor $n_0^2 Q_{zzz}$ and the longitudinal component of the diffusion tenzor $n_0 D_{zz}$ for electrons in Ne.

for electrons in Ar, Kr and Xe, respectively. In all three gases $n_0 D_{zz}$ reaches a local maximum at a somewhat higher E/n_0 as compared to $n_0^2 Q_{zzz}$. After the local maximum, $n_0^2 Q_{zzz}$ and $n_0 D_{zz}$ are decreased markedly with increasing E/n_0, up to around $5.9 \cdot 10^{-3}$ Td, $2.9 \cdot 10^{-2}$ Td and $7.7 \cdot 10^{-2}$ Td for electrons in Ar, Kr and Xe, respectively. For the higher values of E/n_0, these two quantities continue to decrease until reaching approximately 2.7 Td for electrons in Ar, and until reaching approximately 2.1 Td for electrons in Kr and Xe. However, the rate of decreasing of both $n_0^2 Q_{zzz}$ and $n_0 D_{zz}$ is less intensive in this field region as compared to the lower fields. At higher fields, $n_0^2 Q_{zzz}$ and $n_0 D_{zz}$ rise with increasing E/n_0 in a narrow field range. The $n_0^2 Q_{zzz}$ component reaches the second local maximum at around 5.9 Td, 4.1 Td and 4.2 Td for electrons in Ar, Kr and Xe, respectively. After the second local maximum, the $n_0^2 Q_{zzz}$ component decreases monotonically with increasing E/n_0 for the remaining E/n_0 in all three gases. In the field region around the second local maximum of $n_0^2 Q_{zzz}$, the slope of $n_0 D_{zz}$ is significantly reduced with increasing E/n_0 up to about 13 Td for all three gases. At higher fields, $n_0 D_{zz}$ is saturated with increasing E/n_0.

In Figures 6–8 we observe a strong correlation between the profiles of $n_0^2 Q_{zzz}$ and $n_0 D_{zz}$ for electrons in noble gases. Specifically, at relatively high enough fields $n_0^2 Q_{zzz}$ decreases with increasing E/n_0 whenever $n_0 D_{zz}$ is a decreasing function of E/n_0, or when it increases as a concave function of E/n_0 in the log-log plot. The $n_0^2 Q_{zzz}$ increases only at the lowest fields, and in those regions of E/n_0 where $n_0 D_{zz}$ raises with increasing field as a convex (or possibly linear) function in the log-log plot. The correlation between $n_0^2 Q_{zzz}$ and $n_0 D_{zz}$ can be understood on an intuitive level. The third-order transport tensor represents an asymmetric deviation of the total diffusive motion, from the motion which is represented by the diffusion tensor. Thus, the third-order transport tensor describes a small correction to total diffusion. For this reason, the motion which is represented by the third-order transport tensor 'carries' a much smaller amount of energy and momentum than the motion which is described by the diffusion tensor. As a consequence, this transport
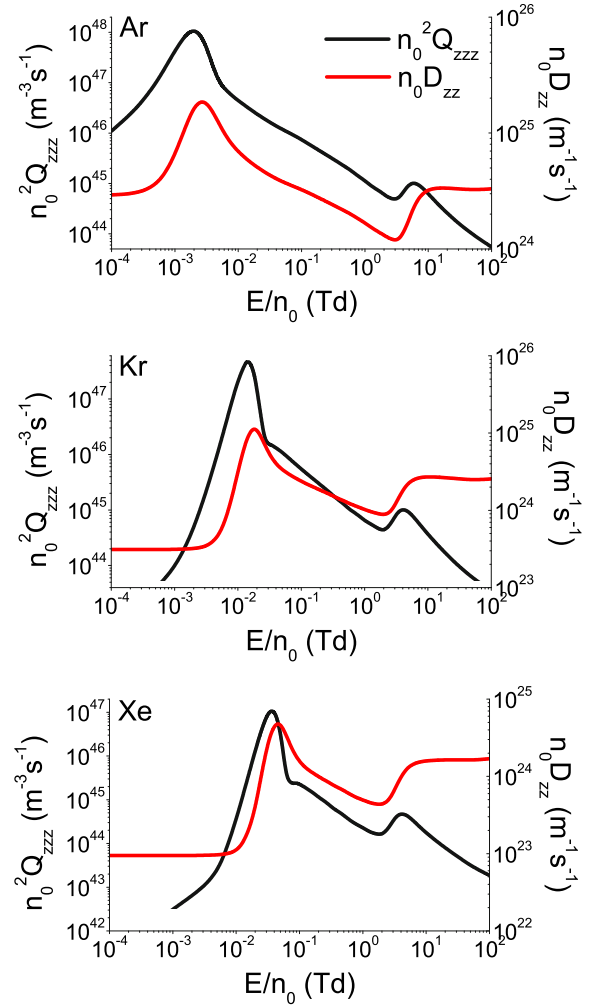
Fig. 8. The correlation of the longitudinal component of the third-order transport tensor $n_0^2 Q_{zzz}$ and the longitudinal component of the diffusion tenzor $n_0 D_{zz}$ for electrons in Ar, Kr and Xe.

property is much more sensitive with respect to the collisions between the electrons and the background atoms. This leads to a reduction of the $n_0^2 Q_{zzz}$ component with increasing E/n_0 (at high enough fields) whenever the resistance to diffusive motion due to collisions is intensive enough to cause a decrease of $n_0 D_{zz}$ or even a decelerated rise with increasing E/n_0. The correlation of the longitudinal component of the third-order transport tensor and the longitudinal component of the diffusion tensor is important for two reasons. Firstly, it enables an easier understanding of the E/n_0-dependence of the third-order transport coefficients in comparison to the direct analysis from the cross sections and from the variation of the mean energy with E/n_0, which might be sometimes difficult. Secondly, the correlation between $n_0^2 Q_{zzz}$ and $n_0 D_{zz}$ shows that the third-order transport coefficients are more sensitive with respect to the energy dependence of the cross sections than the diffusion coefficients. This suggests that the third-order transport coefficients would be very useful in swarm procedure for determining and
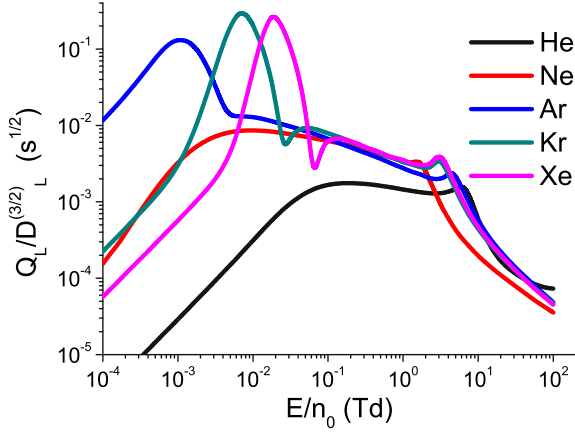
Fig. 9. The values of ratio $Q_L/(D_L)^{3/2}$ for electron swarms in He, Ne, Ar, Kr and Xe as functions of the reduced electric field E/n_0. Calculations have been performed assuming the gas number density of 3.54×10^{22} m^{-3}.

normalizing the cross section sets, if they were both calculated and measured with a sufficient accuracy.

3.5 Effects of the third-order transport coefficients on the spatial profile of the swarm

In this work, we also investigate the influence of the third-order transport coefficients on the spatial profiles of the swarm of electrons in noble gases. As was shown in [27], the components of the third-order transport tensor represent an asymmetric deviation of the spatial profile of the swarm of charged particles from an ideal Gaussian, which represents the solution of the diffusion equation. Specifically, the longitudinal component of the third-order transport tensor describes longitudinal elongation or compressing of the swarm along the longitudinal direction, while the off-diagonal components describe transverse elongation or compressing of the swarm along the longitudinal direction. It can be seen from equation (17) that the contribution of the third-order transport coefficients to the spatial profile of the swarm is proportional to $Q_L/(t^{1/2}(D_L)^{3/2})$ and $Q_T/(t^{1/2}\sqrt{D_L}D_T)$.

In Figure 9 we show the ratio $Q_L/(D_L)^{3/2}$ for electrons in noble gases as a function of E/n_0. It should be emphasized that in Figure 9 we show the ratio where the flux values of Q_L and D_L are assumed, although the influence of the third-order transport coefficients on the spatial profile of the swarm is proportional to the corresponding ratio of the bulk values of Q_L and D_L. The reason for this is a much better accuracy of our multi term results when compared to our Monte Carlo results, and our current inability to obtain the bulk values from our multi term code. However, the difference between the flux and the bulk values of the longitudinal components of the third-order transport coefficient tensor is within statistical uncertainty of Monte Carlo simulations up to about 21 Td in He and Ne, and up to 100 Td in Ar, Kr and Xe. Moreover, we are principally interested in the field dependence of this ratio for E/n_0 less than 10 Td, due to the presence of local maximums

and local minimums in this particular field range. For this reason, we investigate the field dependence of the ratio $Q_L/(D_L)^{3/2}$ assuming the flux values of Q_L and D_L.

We may observe in Figure 9 that the ratio $Q_L/(D_L)^{3/2}$ increases monotonically with increasing E/n_0 in the limit of the lowest E/n_0 (below 10^{-3} Td). For the higher values of E/n_0 (higher than 10 Td) we see that this property decreases monotonically with increasing E/n_0 for electrons in all considered gases. At intermediate fields, however, this ratio reaches several local maximums and local minimums. Specifically, this ratio has only a single local maximum for electrons in Ne, at around 0.01 Td[1]. For electrons in He and Ar, this ratio has two local maximums and one local minimum. In the case of He these local maximums are at about 0.21 Td and 5.9 Td, and both of these maximums are of a similar magnitude. However, in the case of Ar, the first local maximum at around 10^{-3} Td is much higher than the other local maximum at about 4.6 Td. This difference is caused by the presence of the Ramsauer-Townsend minimum in the elastic cross section of Ar. The local minimum is shallow, and it is at around 2.7 Td in both gases. For electrons in Kr and Xe, the investigated ratio has three local maximums and two local minimums. The first local maximum occurs at about $7 \cdot 10^{-3}$ Td and $1.9 \cdot 10^{-2}$ Td for electrons in Kr and Xe, respectively, and is quite high in both gases, due to the presence of Ramsauer-Townsend minimum in the cross sections for elastic scattering. This maximum is followed by a local minimum at about $2.7 \cdot 10^{-2}$ Td for electrons in Kr and at around $6.8 \cdot 10^{-2}$ Td for electrons in Xe. The second local maximum of this ratio is at around 0.046 Td and 0.13 Td for electrons in Kr and Xe, respectively. The last local minimum is at about 2.1 Td, and it is quite shallow in both Kr and Xe. The third local maximum is at about 2.7 Td in both gases. In the case of electrons in Ar, Kr and Xe the value of E/n_0 at which $Q_L/(D_L)^{3/2}$ reaches the first local maximum is about 2 times lower than the value of E/n_0 where Q_L reaches the first local maximum. This is expected, on a qualitative level, as $Q_L/(D_L)^{3/2}$ reaches the first local maximum after D_L starts rising with increasing E/n_0, but before reaching the first peak.

The ratio $Q_L/(D_L)^{3/2}$ has the highest values for Ar, Kr and Xe near the position of the first local maximum. Thus, the contribution of the third-order transport coefficients to the spatial profile of the swarm is the most pronounced exactly for these conditions. However, it must be emphasized that the approximate expression (17) has been derived under an assumption that transport coefficients are constant in time, from the initial time ($t = 0$). As this condition is satisfied only after relaxation of the swarm to the stationary state, the expression (17) is not applicable to the early stages of swarm development

---

[1] There is an additional local maximum of this ratio at around 1.5 Td for electrons in neon, that is preceded by a local minimum at around 1.2 Td. However, both of these local extremes are very shallow. Specifically, the difference between the value of this ratio at these two local extremes is about 4 %. For this reason, the authors are not certain if these two local extremes would appear if a different cross section set is used, due to the sensitivity of both Q_L and D_L to the energy dependence of the cross sections for elementary scattering processes.
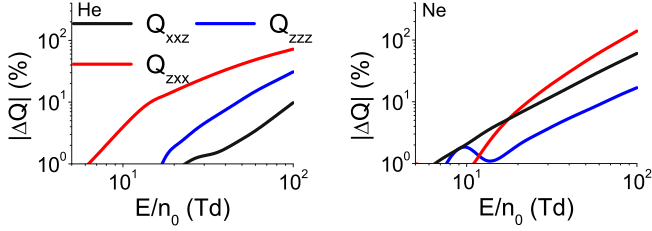
Fig. 10. The absolute value of the percentage difference between the two term and fully converged, multi term results, for the third-order transport coefficients of electrons in He and Ne.

(small values of t). In addition, this expression has been derived by using the Taylor expansion in terms of the components of the third-order transport tensor. For this reason, the expression (17) is applicable only when the ratios $Q_L/(t^{1/2}(D_L)^{3/2})$ and $Q_T/(t^{1/2}\sqrt{D_L}D_T)$ are not too large.

3.6 Comparison of the two term and fully converged multi term results

In Figure 10 we show the absolute value of the percentage difference between the two term and fully converged, multi term results, for the third-order transport coefficients of electrons in He and Ne. The absolute value of the percentage difference between the two sets of results for electrons in Ar, Kr and Xe is shown in Figure 11. The absolute value of the percentage difference ΔQ_{abc} is calculated as

$$|\Delta Q_{abc}| = \left|1 - \frac{Q_{abc}^{(TT)}}{Q_{abc}^{(MT)}}\right| \qquad (34)$$

where the superscripts TT and MT refer to two term and multi term results, respectively.

We see that the two sets of results agree very well in the limit of the lowest E/n_0, where electrons undergo elastic collisions only. Specifically, the deviation between the results that are determined by these two methods is very low, up to approximately 8 Td, 17 Td, 0.2 Td, 0.35 Td, and 1.3 Td for electrons in He, Ne, Ar, Kr and Xe, respectively. The disagreement between these two methods for the off-diagonal components increases continuously with increasing E/n_0 until the end of the range of the considered E/n_0. Moreover, the deviation of multi term results for $n^2 Q_{xxz}$ and $n^2 Q_{zxx}$ from the corresponding two term results is much higher for electrons in Ar, Kr and Xe, as compared to the case of He and Ne. However, the behavior of the percentage difference between these two sets of results is somewhat different for the longitudinal component. While the disagreement between these two methods for the longitudinal component in He and Ne increases with increasing E/n_0, these methods, surprisingly, remain in a very good agreement for electrons in Ar, Kr and Xe, over the entire range of E/n_0 considered in this work. The percentage difference for the longitudinal component reaches values up to 30% and 17% for electrons in He
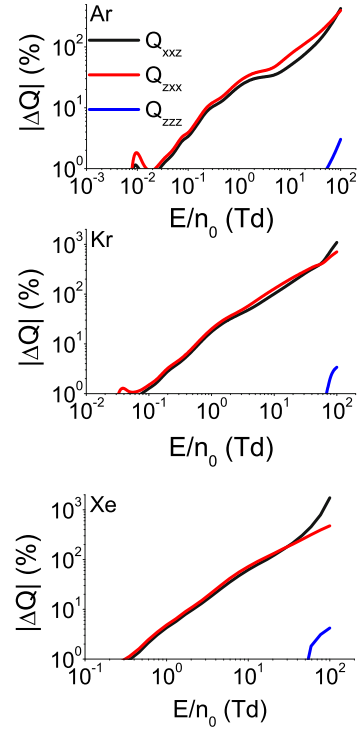
Fig. 11. The absolute value of the percentage difference between the two term and fully converged, multi term results, for the third-order transport coefficients of electrons in Ar, Kr and Xe.

and Ne, respectively, while it remains lower than 5% for electrons in Ar, Kr and Xe. We expect that the deviations between the two term and multi term results are much greater for the higher values of E/n_0. It should also be noted that the errors of the two term approximation are significantly lower for the lower-order transport coefficients, over the same region of E/n_0. Therefore, higher order transport coefficients appear more sensitive to anisotropy in the velocity distribution function.

4 Conclusion

In this work we have extended a multi term solution of the Boltzmann equation, initially developed for evaluating the lower-order transport coefficients, to investigate the third-order transport coefficients of electrons in noble gases. For electrons in helium, we have observed that the Q_{zxx} component is negative for the lower values of E/n_0. In this field region, the collision frequency for elastic scattering of a large fraction of electrons is an increasing function of the electron energy. However, for electrons in argon, krypton, and xenon all three components of the third-order transport tensor are positive in the limit of the lower fields considered in this work, as the collision frequency of the low-energy electrons decreases with increasing energy. For higher fields, the Q_{xxz} component is negative in argon, krypton and xenon over a wide range of E/n_0. In addition, for electrons in argon, the Q_{zxx} component is also negative, but over a narrower field range. For

electrons in helium in the sub-excitation field region, the absolute values of all three components of the third-order transport tensor are increasing functions of E/n_0. On the other hand, for electrons in argon, krypton and xenon, all components are significantly reduced over the range of E/n_0 where the energy of high-energy electrons exceeds the position of the Ramsauer-Townsend minimum.

One of the fundamental topics considered in this work is the existence of the correlation between the longitudinal component of the third-order transport tensor $n_0^2 Q_{zzz}$ and the longitudinal component of the diffusion tensor $n_0 D_{zz}$. We have observed that at high enough fields whenever $n_0 D_{zz}$ decreases or increases as a concave function of E/n_0 (in the log-log plot) $n_0^2 Q_{zzz}$ is being reduced. We have also observed that $n_0^2 Q_{zzz}$ increases when $n_0 D_{zz}$ increases as a convex function of E/n_0 (in the log-log plot). However, this correlation is absent in the limit of the lowest E/n_0, as the third-order transport coefficients vanish in the low-field limit, unlike diffusion which has non-zero thermal values. This behavior of $n_0^2 Q_{zzz}$ can be attributed to a greater sensitivity of the third-order transport coefficients with respect to the energy dependence of cross sections for elementary scattering processes.

Another highly relevant topic that has been investigated in this work is the influence of the third-order transport coefficients on the spatial profiles of the swarm in noble gases. It has been shown that this influence is the most pronounced for electrons in Ar, Kr and Xe, at low E/n_0, due to the presence of the Ramsauer-Townsend minimum. Specifically, the ratio $Q_L/(D_L)^{3/2}$ that describes the contribution of the longitudinal component of the third-order transport tensor to the spatial profile of the swarm reaches the first local maximum at about 10^{-3} Td, $7 \cdot 10^{-3}$ Td, and $1.9 \cdot 10^{-2}$ Td for electrons in Ar, Kr and Xe, respectively. Around these values of E/n_0 the effects of the longitudinal component of the third-order transport coefficient tensor on the spatial profile of the electron swarm are the most significant.

Finally, we investigated the deviation of the two term approximation from the fully converged multi term results for the third-order transport coefficients. We have found that the two term approximation is applicable at the lowest fields, where electrons undergo elastic collisions only. However, the two term approximation deviates from the multi term results for higher fields, where electrons may undergo inelastic collisions also with the background atoms. The difference between the two sets of results is especially pronounced for the off-diagonal components of the third-order transport tensor. This difference is much higher for electrons in Ar, Kr and Xe than for electrons in He and Ne. Conversely, the difference between the two sets of results for the longitudinal component is much larger in He and Ne than in Ar, Kr and Xe. This difference is up to about 30% and 17% for electrons in He and Ne, respectively. Surprisingly, the two term approximation is in an excellent agreement with the multi term results for the longitudinal component in the case of Ar, Kr and Xe. The difference between the results that are obtained by using these two methods is not higher than approximatelly 5% in the case of the longitudinal component of the third-order transport tensor for electrons in Ar, Kr and Xe.

Author contribution statement

All the authors have been involved in the research and in the preparation of the manuscript. All the authors have read and approved the final manuscript.

Publisher's Note The EPJ Publishers remain neutral with regard to jurisdictional claims in published maps and institutional affiliations.

References

1. L.G.H. Huxley, R.W. Crompton, *The Diffusion and Drift of Electrons in Gases* (Wiley, London, 1974)
2. R. Robson, R. White, M. Hildebrandt, *Fundamentals of Charged Particle Transport in Gases and Condensed Matter* (CRC Press, Boca Raton, 2018)
3. Z.Lj. Petrović, M. Šuvakov, Ž. Nikitović, S. Dujko, O. Šašić, J. Jovanović, G. Malović, V. Stojanović, Plasma Sources Sci. Technol. **16**, S1 (2007)
4. S. Dujko, R.D. White, Z.Lj. Petrović, J. Phys. D: Appl. Phys. **41**, 245205 (2008)
5. Z. Donko, P. Hartman, I. Korolov, V. Jeges, D. Bošnjaković, S. Dujko, Plasma Sources Sci. Technol. **28**, 095007 (2019)
6. T. Makabe, Z.Lj. Petrović, *Plasma Electronics: Applications in Microelectronic Device Fabrication* (CRC Press, 2014)
7. M.A. Lieberman, A.J. Lichtenberg, *Principles of Plasma Discharges and Materials Processing*, 2nd edn. (Wiley, 2005)
8. D. Xiao, *Gas Discharge and Gas Insulation* (Springer, Heidelberg, 2016)
9. L. Rolandi, W. Riegler, W. Blum, *Particle Detection with Drift Chambers* (Springer, Berlin, 2008)
10. D. Bošnjaković, Z.Lj. Petrović, R.D. White, S. Dujko, J. Phys. D: Appl. Phys. **47**, 435203 (2014)
11. Z.Lj. Petrović, S. Dujko, D. Marić, G. Malović, Ž. Nikitović, O. Šašić, J. Jovanović, V. Stojanović, M. Radmilović Rađenović, J. Phys. D: Appl. Phys. **42**, 194002 (2009)
12. L.C. Pitchford et al., Plasma Process. Polym. **14**, 1600098 (2016)
13. A. Banković, S. Dujko, S. Marjanović, R.D. White, Z.Lj. Petrović, Eur. Phys. J. D **68**, 127 (2014)
14. A. Banković, S. Dujko, R.D. White, S.J. Buckman, Z.Lj. Petrović, Eur. Phys. J. D **66**, 174 (2012)
15. K. Kondo, H. Tagashira, J. Phys. D: Appl. Phys. **23**, 1175 (1990)
16. S. Kawaguchi, K. Takahashi, K. Satoh, Plasma Sources Sci. Technol. **27**, 085006 (2018)
17. B.M. Penetrante, J.N. Bardsley, in *Non-equilibrium Effects in Ion and Electron Transport*, edited by J.W. Gallagher, D.F. Hudson, E.E. Kunhardt, R.J. Van Brunt (Plenum, New York, 1990), p. 49

18. S.B. Vrhovac, Z.Lj. Petrović, L.A. Viehland, T.S. Santhanam, J. Chem. Phys. **110**, 2423 (1999)
19. J.H. Whealton, E.A. Mason, Ann. Phys. **84**, 8 (1974)
20. I. Simonović, D. Bošnjaković, Z.Lj. Petrović, P. Stokes, R.D. White, S. Dujko, Phys. Rev. E **101**, 023203 (2020)
21. A.D. Koutselos, J. Chem. Phys. **104**, 8442 (1996)
22. A.D. Koutselos, J. Chem. Phys. **106**, 7117 (1997)
23. A.D. Koutselos, Chem. Phys. **270**, 165 (2001)
24. A.D. Koutselos, Chem. Phys. **315**, 193 (2005)
25. H. Sugawara, Y. Sakai, Jpn. J. Appl. Phys. **45**, 5189 (2006)
26. Z.Lj. Petrović, I. Simonović, S. Marjanović, D. Bošnjaković, D. Marić, G. Malović, S. Dujko, Plasma Phys. Controlled Fusion **59**, 014026 (2017)
27. P.W. Stokes, I. Simonović, B. Philippa, D. Cocks, S. Dujko, R.D. White, Sci. Rep. **8**, 2226 (2018)
28. K. Kumar, H.R Skullerud, R.E. Robson, Aust. J. Phys. **33**, 343 (1980)
29. R.E. Robson, Aust. J. Phys. **44**, 685 (1991)
30. R.E. Robson, K.F. Ness, Phys. Rev. A **33**, 2068 (1986)
31. K.F. Ness, R.E. Robson, Phys. Rev. A **34**, 2185 (1986)
32. K. Kumar, Phys. Rep. **112**, 319 (1984)
33. R.D. White, R.E. Robson, S. Dujko, P. Nicoletopoulos, B. Li, J. Phys. D: Appl. Phys. **42**, 194001 (2009)
34. S. Dujko, R.D. White, Z.Lj. Petrović, R.E. Robson, Phys. Rev. E **81**, 046403 (2010)
35. S. Dujko, R.D. White, Z.Lj. Petrović, R.E. Robson, Plasma Sources Sci. Technol. **20**, 024013 (2011)
36. O. Šašić, J. Jovanović, Z.Lj. Petrović, J. de Urquijo, J.R. Castrejón-Pita, J.L. Hernández-Ávila, E. Basurto, Phys. Rev. E **71**, 046408 (2005)
37. R.D. White, R.E. Robson, P. Nicoletopoulos, S. Dujko, Eur. Phys. J. D **66**, 117 (2012)
38. M. Hayashi, *Bibliography of Electron and Photon Cross Sections With Atoms and Molecules Published in the 20th Century Argon Report, NIFS-DATA-72* (National Institute for Fusion Science of Japan, Tokyo, Japan, 2003)
39. M. Hayashi, *Bibliography of Electron and Photon Cross sections with Atoms and Molecules Published in the 20th Century Xenon, NIFS-DATA-79* (National Institute for Fusion Science of Japan, Tokyo, Japan, 2003)
40. Biagi-v7.1 database, www.lxcat.net (accessed 19 April 2013)

SAPP XXII

22nd Symposium on Application of Plasma Processes
and
11th EU-Japan Joint Symposium on Plasma Processing

Book of Contributed Papers

Štrbské Pleso, Slovakia
18-24 January, 2019

Edited by V. Medvecká, J. Országh, P. Papp, Š. Matejčík

HIDEN ANALYTICAL

ELEVATE

Local Organizers

Department of Experimental Physics
Faculty of Mathematics, Physics and Informatics
Comenius University in Bratislava
Mlynská dolina F2
842 48 Bratislava, Slovakia
URL: http://www.fmph.uniba.sk/
Tel.: +421 2 602 95 686
Fax: +421 2 654 29 980

Society for plasma research and applications
Faculty of Mathematics, Physics and Informatics
Comenius University Bratislava
Mlynská dolina F2
842 48 Bratislava, Slovakia
URL: https://spvap.eu/
E-mail: spvap@neon.dpp.fmph.uniba.sk
Tel.: +421 2 602 95 686

Local Organizing Committee

Štefan Matejčík (chair)
František Krčma
Peter Papp
Juraj Országh
Veronika Medvecká
Ladislav Moravský

International Scientific Committee

22nd Symposium on Application of Plasma Processes

Prof. J. Benedikt	Christian-Albrechts-University, Kiel, Germany
Dr. R. Brandenburg	INP, Greifswald, Germany
Dr. Z. Donkó	Hungarian Academy of Sciences, Budapest, Hungary
Dr. T. Field	Queen's University, Belfast, United Kingdom
Prof. S. Hamaguchi	Osaka University, Japan
Prof. F. Krčma	Brno University of Technology, Brno, Czech Republic
Prof. N. Mason	University of Kent, United Kingdom
Prof. Š. Matejčík	Comenius University in Bratislava, Slovakia
Prof. J. Pawlat	University of Technology, Lublin, Poland
Prof. M. Radmilović-Radjenović	Institute of Physics, Belgrade, Serbia
Prof. P. Scheier	Leopold-Franzens University, Innsbruck, Austria

11th EU-Japan Joint Symposium on Plasma Processing

Prof. S. Hamaguchi	Osaka University, Japan
Prof. N. Mason	University of Kent, United Kingdom
Prof. Z. Petrović	Institute of Physics, Belgrade, Serbia

Reading Committee

Prof. Š. Matejčík	Comenius University in Bratislava, Slovakia
Prof. F. Krčma	Brno University of Technology, Brno, Czech Republic
Prof. N. Mason	University of Kent, United Kingdom
Dr. P. Papp	Comenius University in Bratislava, Slovakia
Dr. J. Országh	Comenius University in Bratislava, Slovakia
Dr. V. Medvecká	Comenius University in Bratislava, Slovakia

Conference Topics

1. **Electrical discharges and other plasma sources**

2. **Elementary processes and plasma chemical reactions**

3. **Plasma-surface interactions**

4. **Plasma treatment of polymer and biological materials**

5. **Nanometer-scaled plasma technology**

6. **Ion mobility spectrometry**

Table of Content

POSTER PRESENTATIONS

NON-EQUILIBRIUM TRANSPORT OF ELECTRONS IN GASES AND LIQUIDS AND ITS APPLICATIONS IN MODELING OF PARTICLE DETECTORS

S. Dujko[1], D. Bošnjaković[1], I. Simonović[1], Z.Lj. Petrović[1,2] and R.D. White[3]

[1]*Institute of Physics, University of Belgrade, Pregrevica 118, 11080 Belgrade, Serbia*
[2]*Serbian Academy of Sciences and Arts, Knez Mihailova 35, 11001 Belgrade, Serbia*
[3]*College of Science and Engineering, James Cook University, 4811 Towsville, Australia*
E-mail: sasa.dujko@ipb.ac.rs

In this work we explore the connections between transport theory of charged particle swarms and modelling of particle detectors used in high-energy physics. In particular, we discuss the physics of resistive plate chambers (RPCs), including the electron transport and propagation of streamers in the gas filled gaps and signal induction in the electrodes. Electron transport coefficients are calculated in a variety of RPC gas mixtures as a function of the reduced electric field, using a Boltzmann equation analysis and Monte Carlo simulations. A 1.5D fluid model with photoionization is developed to investigate how the nature of transport data affects the calculated signals in various RPCs used in high-energy physics experiments at CERN. Electron transport and propagation of streamers are also considered in liquid rare gases. Solutions of Boltzmann's equation and Monte Carlo method for electrons in dilute neutral gases, are extended and generalized to consider the transport processes of electrons in liquid non-polar gases by accounting for the coherent and other liquid scattering effects.

1. Introduction

Studies of charged particle transport processes in gases and liquids in combined electric and magnetic fields are of vital interest in the modelling of non-equilibrium plasmas [1], particle detectors in high-energy physics [2], and numerous other applications. Further optimization and understanding of such applications is dependent on an accurate knowledge of the cross sections for charged particle scattering, transport coefficients and the physical processes involved. In particular, the advanced technology associated with detection of high-energy particles using various types of gaseous and liquid detectors demands the most accurate modelling of charged particle transport. Over the last two decades, there has been a lot of progress in the understanding of charged particle transport in combined electric and magnetic fields [3,4], but this has not always been taken advantage of by physicists working in high-energy physics.

One of the main goals of the present work is to discuss how to bridge the gap between the modelling of particle detectors in high-energy physics and the swarm-plasma nexus that has been thoroughly investigated in our recent reviews [3-5]. We discuss how to adopt the well know techniques in plasma physics, including the numerical solution of Boltzmann's equation [4,5], Monte Carlo simulation technique [6,7] and fluid equation based models [4,8,9], to model the particle detectors in high-energy physics. Indeed, there is a considerable overlap between the two fields and in this work we present the methodology, quantitative and qualitative procedures for modelling of gaseous and liquid detectors of high-energy particles.

2. Modeling of resistive plate chambers

In the first part of this work we discuss the transport of electrons in gases, propagation of streamers and signal induction in resistive plate chambers (RPCs). RPCs are gaseous detectors often used for timing and triggering purposes in many high-energy physics experiments [10-12]. RPCs consist of a single or multiple gas filled gaps between the electrodes of high volume resistivity, such as glass or bakelite, which are used for the suppression of destructive higher current discharges. Despite the simple construction, modeling of RPCs is not a simple task due to many physical processes occurring on different time scales, including primary ionization, charge transport and multiplication, electrode relaxation and signal formation. After passing through the detector, a high energy charged particle

(muon, charged pion and/or kaon, etc.) makes clusters of electrons in the gas, which are drifting towards the anode and multiplied in the process of ionization. Electrons move in a homogeneous electric field which is provided by the high voltage that is applied to the parallel plate electrodes. Depending on the applied electric field strength, geometry and gas mixture, RPCs can be operated in an avalanche or streamer mode. Typical gas mixtures used in RPCs are composed of tetrafluoroethane ($C_2H_2F_4$), iso-butane (iso-C_4H_{10}) and sulfur hexafluoride (SF_6). Each of these gas components has a specific purpose: $C_2H_2F_4$ is a weak electronegative gas with a high primary ionization efficiency while iso-C_4H_{10} is a UV-quencher gas. SF_6, on the other hand, is a strongly electronegative gas, often used in avalanche mode to suppress and control the development of streamers.

The first building block in the modeling of RPCs is the analysis of cross sections for electron scattering in $C_2H_2F_4$, iso-C_4H_{10} and SF_6. In this work, we propose a complete and consistent set of cross sections for electron scattering in $C_2H_2F_4$ [13], while for iso-C_4H_{10} and SF_6 we use the sets of cross sections found in the literature [14,15]. The set of cross sections for C_2H_2F4 is validated through a series of comparisons between swarm data calculated using a multi term theory for solving the Boltzmann equation and Monte Carlo simulations, and the measurements under the pulsed Townsend conditions. Other sets of cross sections for electron scattering in $C_2H_2F_4$ were also used as input in our numerical codes with the aim of testing their completeness, consistency and accuracy. The calculated swarm parameters are compared with measurements in order to assess the quality of the cross sections in providing data for modeling.
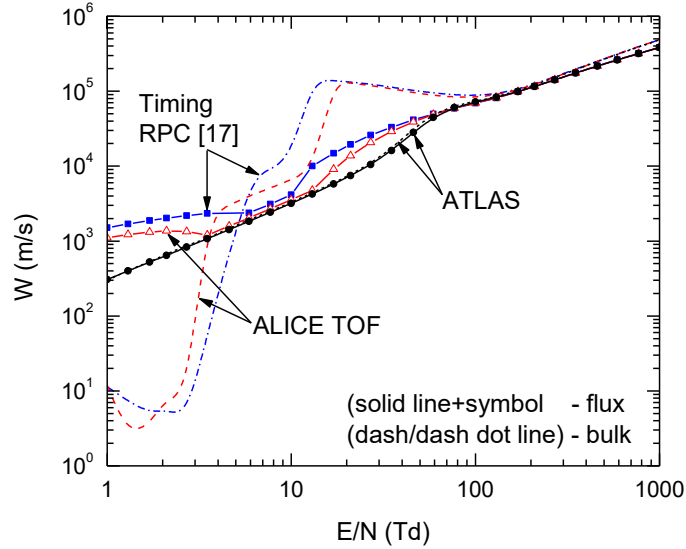

Figure 1. Bulk and flux drift velocities as a function of E/N for gas mixtures used in ATLAS triggering RPC, ALICE timing RPC and timing RPC [17].

In addition to pure gases, we investigate electron transport in various $C_2H_2F_4$/iso-C_4H_{10}/SF_6 mixtures used in RPCs in the ALICE, CMS and ATLAS experiment using a multi term theory for solving the Boltzmann equation and Monte Carlo simulation technique [16]. The duality of transport coefficients, e.g., the existence of two different families of transport coefficients, the bulk and the flux, in the presence of non-conservative collisions, is investigated. A multitude of interesting and atypical kinetic phenomena, induced by the explicit effects of non-conservative collisions, is observed. Perhaps the most striking phenomenon is the occurrence of negative differential conductivity (NDC) in the bulk drift velocity with no indication of any NDC for the flux component in the ALICE timing RPC system. Figure 1 displays the variation of the bulk and flux drift velocities with the reduced electric field for ATLAS triggering RPC (94.7% $C_2H_2F_4$+5% iso-C_4H_{10}+0.3% SF_6), ALICE timing RPC (90% $C_2H_2F_4$+5% iso-C_4H_{10}+5%SF_6) and timing RPC (85% $C_2H_2F_4$+5% iso-C_4H_{10}+10%SF_6) [17]. We systematically study the origin and mechanisms for such phenomena as well as the possible physical implications which arise from their explicit inclusion into models of RPCs.

The Boltzmann equation analysis and Monte Carlo simulations are performed assuming the hydrodynamic conditions and motion of electrons in an infinite gas. The more realistic RPC simulations with implementing gas gap boundaries and primary ionization models have been performed using a Monte Carlo simulation technique with the aim of obtaining the performance characteristics of a timing RPC [18,19]. Timing resolutions and efficiencies are calculated for a specific timing RPC with a 0.3mm gas gap and gas mixture of 85% $C_2H_2F_4$ + 5% iso-C_4H_{10} + 10% SF_6.

In this work we also present our 1.5D fluid model with photoionization to investigate the transition from an electron avalanche into a streamer, propagation of streamers and signal induction in the system of electrodes [20]. In particular, we investigate how the duality of transport coefficients affects the calculated signals of the ATLAS triggering RPC and ALICE timing RPC used at CERN, and also a timing RPC [17] with high SF_6 content. Calculations are performed using the classical fluid model in which both the bulk and flux transport data are used as an input. In addition, we present a new approach in fluid modelling of RPCs based on the equation of continuity and density gradient expansion of the source term. The model requires knowledge of the coefficients in the density gradient expansion of the source term as a function of the reduced electric field. We apply the Monte Carlo method for the determination of these coefficients using the cross sections for electron scattering as a set of input data.
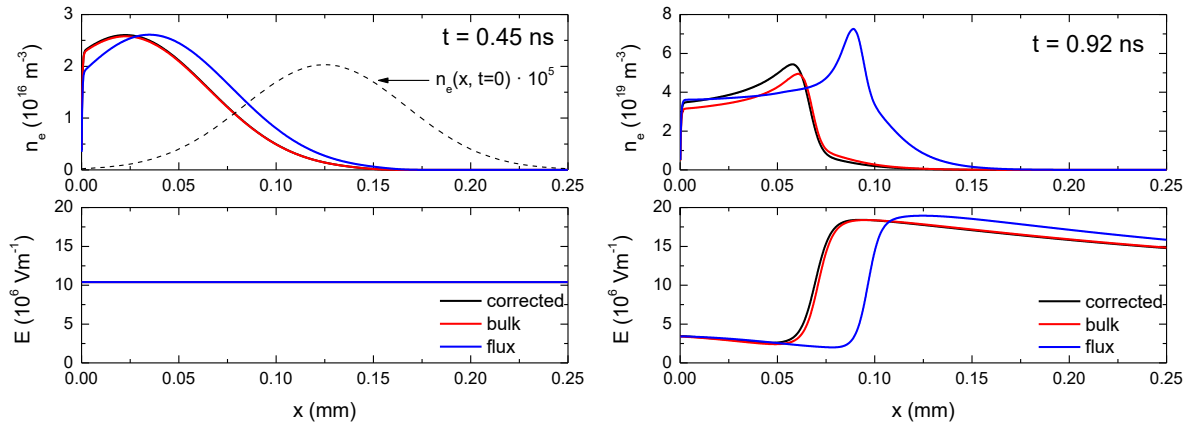
Figure 2. Electron number density and electric field along the gas gap of ALICE timing RPC at t = 0.45 ns during avalanche development (left panel), and t = 0.92 ns during positive streamer formation (right panel). The external electric field is set to 10.4 MV/m and pressure is 1 atm. Calculations are made using a corrected fluid model and classical fluid model with flux and bulk transport data as an input [20].

As an illustrative example of our fluid simulations of RPCs, in figure 2 we show the development of an electron avalanche and its transition into a positive streamer. On the left panel we show the electron number density and electric field at time instant t = 0.45 ns during avalanche development in ALICE timing RPC. We observe that there are no space charge effects and the profiles obtained using corrected model match very well with those obtained using classical model with bulk data. Comparing avalanches with bulk and flux data, we see that the avalanche with the flux data is slower. This might be expected, since the bulk drift velocity is greater than the flux drift velocity for a given electric field. During the avalanche phase, the induced current grows exponentially with time. However, the exponential rise gradually stops due to both space charge effects and electron absorption at the anode. At about t = 0.92 ns, the positive streamers starts to develop (see the right panel in figure 2) and the current rises again while the streamer progress towards the cathode. Since the positive streamer move against the electron drift direction, it requires a source of electrons ahead of the streamer to support the ionization process. This is the reason why photoionization should be included in the modelling. The positive streamer stops at about 1 ns and starts to diminish while the induced current slowly drops to zero. The differences between the profiles shown in the streamer stage are clearly evident. These differences follow from the differences between the bulk and flux drift velocities as well as due to representation of the source term employed in these models.

3. Electron transport and negative streamers in liquid rare gases

In the second part of this work we investigate electron transport, transition from an electron avalanche into a negative streamer, and propagation of negative streamers in liquid rare gases. Liquid rare gases, particularly liquid argon and liquid xenon, are very good detecting media, due to their unique physical properties [21]. The high density and high atomic numbers make them very efficient in stopping penetration radiation, while a significant abundance of many isotopes with different values of nuclear spin enables the study of both spin dependent and spin independent interactions.

In this work we extend and generalize the Monte Carlo method, initially developed for dilute neutral gases, to consider the transport processes of electrons in liquids by accounting for the coherent and other liquid scattering effects [22]. The extended code is tested through a series of benchmark calculations for the Percus-Yevick model. Values and general trends of the mean energy, drift velocity, diffusion tensor and ionization coefficient are calculated for liquid rare gases and compared to the available measurements. The comparison is also made between the liquid and gas phase results. Calculated transport coefficients are then used as an input in fluid simulations of negative streamers, which are realized in both 1D and 1.5D setups. In particular, we investigate how various scenarios of representing the inelastic energy losses in liquid rare gases affect both electron transport and propagation of streamers. We consider three different cases where: (1) the energy losses to electronic excitations are neglected, (2) certain particular excitations are taken into account, and finally (3) all electronic excitations are included. These individual cases are discussed in light of the available spectroscopy and photoconductivity experiments in liquid rare gases [22].
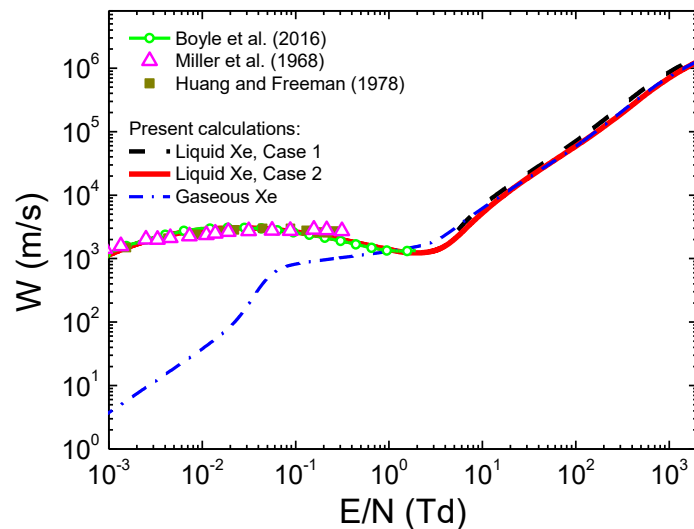
Figure 3. Comparison of the measured drift velocities in liquid xenon (Miler et al. (1968) [23] and Huang and Freeman (1978) [24] with our theoretical calculations. The theoretically calculated drift velocities in liquid xenon, include the Boltzmann equation results of Boyle et al. (2016) [25] and the present calculations obtained in Monte Carlo simulations. The bulk drift velocity of electrons in gaseous xenon is also shown in this figure for comparison [22].

In figure 3 we show the variation of the bulk drift velocity with E/N for electrons in liquid xenon. Our Monte Carlo calculations over a wide range of E/N are compared with those obtained from the numerical solution of Boltzmann's equation for the lower values of E/N, as well as with the available measurements. The Boltzmann equation results for gaseous xenon are also included in figure 3. We consider the following two cases for representing the inelastic energy losses: (1) no electronic excitations, and (2) all electronic excitations are included. The cross sections detailed in [22,25] are used in the present study. We observe that for the lower values of E/N (lower than approximately 1

Td), the drift velocity in the liquid phase significantly exceeds the drift velocity in the gas phase. This is a clear sign of the significant reduction of the rate of momentum transfer of the lower energy electrons occurring in liquids. This reduction follows from the modification of the scattering potential and the coherent scattering effects. As a consequence, the electric field accelerates electrons more efficiently in liquid xenon than in the gas phase. For the higher values of electric fields, however, this effect is reduced, as the scattering of a high energy electron on a xenon atom is significantly less perturbed by the surrounding liquid. Thus, we see that the drift velocity decreases between approximately 0.02 and 2 Td. The reduction of the drift velocity with increasing E/N is the well known phenomenon of negative differential conductivity (NDC). In the gas phase, NDC is caused by inelastic and/or non-conservative collisions, but in liquid xenon this is structure induced phenomenon. We observe that our values of the drift velocity are close to those predicted in the experiments of Miler et al. [23] and Huang and Freeman [24]. However, as we can see NDC is not observed in the experiments.
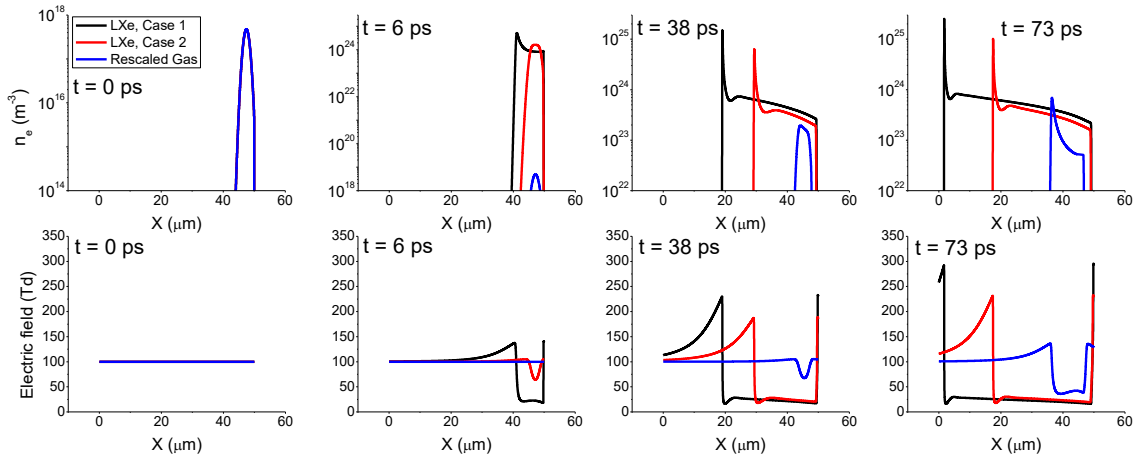
Figure 4. The formation and propagation of negative streamers in liquid xenon for E/N=100 Td, The presented results are determined by assuming the following two cases for representing the inelastic energy losses: (1) no electronic excitations (Case 1), and (2) all electronic excitations are included (Case 2). Streamers propagate from the right to the left.

In figure 4 we show the formation and propagation of a negative streamer in liquid xenon. In the same figure we include the simulation in which the transport data for electrons in the gas phase are scaled to liquid density (Rescaled gas). The initial condition for both electrons and positive ions is a Gaussian, which is positioned near the cathode [22]. In liquid xenon, positive charge carriers are holes, with a mobility that is several orders of magnitude less than the electron mobility. Thus, the positive holes are assumed to be stationary, on the time scales relevant for this study.

Comparing streamers in gases and liquids, we observe that the transition from an electron avalanche and formation of a negative streamer occur much faster in liquid xenon. We also observe that the formation and propagation of a streamer are reduced by including the inelastic energy losses in the model (Case 2). The number density of electrons in both the streamer head and the streamer interior is also reduced. Other streamer features in liquid xenon are similar as those in the gas phase. We see that the electron number density has a sharp peak in the streamer head where the electric field is significantly enhanced by the space charge effects. In the streamer interior, however, the number density of electrons is reduced. The reason is twofold: (1) As electric field decreases, the contribution of ionization is less pronounced, and (2) the recombination of electrons and positive holes is enhanced.

4. References

[1] Makabe T and Petrović Z Lj 2014 *Plasma Electronics: Applications in Microelectronic Device Fabrication* (New York: CRC Press).

[2] Rolandi L, Riegler W and Blum W 2008 *Particle Detection with Drift Chambers* (Berlin: Springer).

[3] Petrović et al. 2009 *J. Phys. D: Appl. Phys.* **42** 194002.

[4] White R D, Robson R E, Dujko S, Nicoletopoulos P and Li B 2009 *J. Phys. D: Appl. Phys.* **42** 194001.

[5] Dujko S, White R D, Petrović Z Lj and Robson R E 2011 *Plasma Source Sci. Technol.* **20** 024013.

[6] Dujko S, White R D and Petrović Z Lj 2008 *J. Phys. D: Appl. Phys.* **41** 245205.

[7] Dujko S, Raspopović Z M and Z.Lj. Petrović 2005 *J. Phys. D: Appl. Phys.* **38** 2952.

[8] Boyle G J, White R D, Robson R E, Dujko S and Petrović Z Lj 2012 New J. Phys. **14** 045011.

[9] Dujko S, Markosyan A H, White R D and Ebert U 2013 *J. Phys. D: Appl. Phys.* **46** 475202.

[10] The ALICE Collaboration 2008 *J. Instrum.* **3** S08002.

[11] The ATLAS Collaboration 2008 *J. Instrum.* **3** S08003.

[12] The CMC Collaboration 2008 *J. Instrum.* **3** S08004.

[13] Šašić O, Dupljanin S, de Urquijo J and Petrović Z Lj 2013 *J. Phys. D: Appl. Phys.* **46** 325201.

[14] Itoh H, Matsumura T, Satoh K, Date H, Nakao Y and Tagashira H 1993 *J. Phys. D: Appl. Phys.* **26** 1975.

[15] Biagi S, MAGBOLTZ – Program to compute electron transport parameters in gases, v.2, CERN.

[16] Bošnjaković D, Petrović Z Lj White R D and Dujko S 2014 *J. Phys. D.* **47** 435203.

[17] Lopes L, Fonte P and Mangiarotti A 2012 *Nucl. Instrum. Methods A* **661** S194.

[18] Bošnjaković D, Petrović Z Lj and Dujko S 2014 *J. Intrum.* **9** P09012.

[19] Petrović Z Lj, Simonović I, Marjanović S, Bošnjaković D, Marić D, Malović G and Dujko S 2017 *Plasma Phys. Control. Fusion* **59** 014026.

[20] Bošnjaković D, Petrović Z Lj and Dujko S 2016 *J. Phys. D: Appl. Phys.* **49** 405201.

[21] Aprile E and Doke T 2010 *Rev. Mod. Phys.* **82** 2053.

[22] Simonović I, Garland N A, Bošnjaković D, Petrović Z Lj, White R D and Dujko S, accepted manuscript in Plasma Sources Sci. Technol, doi: https://doi.org/10.1088/1361-6595/aaf968

[23] Miller L S, Howe S, and Spear W E 1968 *Phys. Rev.* **166** 871.

[24] Huang S S and Freeman G R 1978 *J. Chem. Phys.* **47** 1355.

[25] Boyle G J, McEachran R P, Cocks D G, Brunger M J, Buckman S J, Dujko S and White R D 2016 *J. Phys. D: Appl. Phys.* **49** 355201

PROCEEDINGS OF
THE XXII$^{\text{ND}}$ INTERNATIONAL
CONFERENCE ON GAS DISCHARGES
AND THEIR APPLICATIONS

- VOLUME 2 -

2$^{\text{nd}}$ - 7$^{\text{th}}$ September 2018

Novi Sad, SERBIA

Serbian Academy of Sciences and Arts

&

Institute of Physics, University of Belgrade

Editors: Prof. Zoran Lj. Petrović

Dr. Nevena Puač

Dr. Saša Dujko

Dr. Nikola Škoro

INVITED PROGRESS REPORTS

WS1. Swarm Physics and Gaseous Dielectrics: Future Challenges in Theory and Practice

WS2. Advanced Plasma Technologies in medicine, biotechnology and agriculture

WS3. Modeling of plasma-materials interactions

FLUID MODELING OF RESISTIVE PLATE CHAMBERS

D. BOŠNJAKOVIĆ[1]*, Z. LJ. PETROVIĆ[1,2], S. DUJKO[1]

[1] Institute of Physics, University of Belgrade, Pregrevica 118, Belgrade, 11080, Serbia
[2] Serbian Academy of Sciences and Arts, Knez Mihailova 35, Belgrade, 11001, Serbia
*dbosnjak@ipb.ac.rs

ABSTRACT

We discuss how models based on fluid equations can be applied to investigate the underlying physics of Resistive Plate Chambers (RPCs) — particle detectors used for timing and triggering purposes in many high energy physics experiments. In addition to the classical first-order fluid model, we present a new model based on density gradient expansion. Both models are numerically implemented in a 1.5-dimensional scenario and are utilized for studying of streamer and signal development in two RPC configurations used at CERN.

1. INTRODUCTION

Owing to their good efficiency, excellent timing resolution and low cost, Resistive Plate Chambers (RPCs) became widely used particle detectors for large area timing and triggering purposes in high energy physics experiments [1, 2]. They consist of one or many gas gaps sandwiched between the electrodes of high volume resistivity such as glass or bakelite. RPCs also found their way into other areas such medical imaging, cosmic ray physics and geophysics [3].

Many approaches were used in simulation and modeling of RPCs. Stochastic methods, e.g. microscopic Monte Carlo simulation [4], are useful for calculating the RPC performance characteristics such as timing resolution and efficiency. However, these models are often computationally demanding and cannot include all relevant physical processes. On the other hand, numerical models based on fluid equations [5, 6] can only provide the mean values of RPC signals but they are frequently used for studying various physical phenomena in RPC operation, in a computationally efficient manner. However, these were based on

classical fluid model where the diffusion flux was often neglected and the duality of transport data used as input was systematically ignored. Namely, in particle detector community, there seems to be a lack of awareness of the two types of transport data named 'flux' and 'bulk' [7]. The two may differ considerably when non-conservative collisions such as attachment and ionization are present [8].

In this work, we employ fluid models to investigate streamer and signal development in two RPC configurations used in ALICE and ATLAS experiments at CERN. Particular emphasis is placed on sensitivity of the simulated signals with respect to the duality of transport data used as input. In addition, we present a new approach in fluid modeling of RPCs which is based on density gradient expansion.

2. THEORETICAL METHODS

In order to investigate the development of streamers and signals in RPCs, we use a 1.5-dimensional classical fluid model based on balance equations for the number densities of electrons and ions with the local field approximation [5]. For comparison, the classical model is used with either flux or bulk transport data as input. In addition, we have developed a new 'corrected' fluid model based on hydrodynamic approximation which assumes that the electron distribution function can be expanded in terms of gradients of the electron number density [9]. This assumption is strictly valid for weak gradients in absence of sources or sinks of electrons. Under these conditions, the continuity equation for electrons in one-dimensional scenario can be written as

$$\frac{\partial n_e}{\partial t} = \frac{\partial}{\partial x}\left(W_F\,\mathrm{sgn}(E)\,n_e + D_{L,F}\,\frac{\partial n_e}{\partial x}\right) \\ + S_i - S_a + S_{ph}\,, \quad (1)$$

where the electric field $\mathbf{E}$ is oriented along the x-axis while W_{F}, $D_{\mathrm{L,F}}$ and S_{ph} denote flux drift velocity, flux longitudinal diffusion and source term due to photoionization, respectively. The drift velocity W_{F} is defined as positive and $\mathrm{sgn}(E)$ is the sign (signum) function. Using hydrodynamic approximation, the source terms due to ionization (S_{i}) and attachment (S_{a}) are also expanded as

$$S_m = S_m^{(0)} n_{\mathrm{e}} + S_m^{(1)} \mathrm{sgn}(E) \frac{\partial n_{\mathrm{e}}}{\partial x}$$
$$+ S_{\mathrm{L},m}^{(2)} \frac{\partial^2 n_{\mathrm{e}}}{\partial x^2} \quad (m = \mathrm{i}, \mathrm{a}) . \tag{2}$$

The ions can be considered as immobile on the timescale of fast electron signal. Therefore, the balance equations for number densities of positive (n_{p}) and negative ions (n_{n}) are written as

$$\frac{\partial n_{\mathrm{p}}}{\partial t} = S_{\mathrm{i}} + S_{\mathrm{ph}} \quad \text{and} \quad \frac{\partial n_{\mathrm{n}}}{\partial t} = S_{\mathrm{a}} . \tag{3}$$

We assume that the charge is contained inside a cylinder, with radius R_0 along the x axis, and distributed uniformly in the radial direction. For this case, the expression for electric field along the x axis is given in [5, 10]. Source term due to photoionization is calculated as in [5, 11] and assumes that the photon production rate is proportional to the ionization rate.

Equations (1) and (3) are solved numerically imposing homogeneous Dirichlet boundary conditions at the gas gap boundaries. The numerical scheme uses second-order central finite differences for discretization of spatial derivatives and classical fourth-order Runge–Kutta 4 scheme for integration in time. Finally, the induced current is calculated using Ramo's theorem [5, 12]

$$i(t) = e_0 \, \pi R_0^2 \, \frac{E_{\mathrm{w}}}{V_{\mathrm{w}}} \int_0^d n_{\mathrm{e}}(x,t)$$
$$\cdot W_{\mathrm{F}}(|E(x,t)|) \, \mathrm{sgn}(E(x,t)) \, \mathrm{d}x , \tag{4}$$

where $E_{\mathrm{w}}/V_{\mathrm{w}}$ is the weighting field and d is the gas gap length.

3. RESULTS AND DISCUSSION

Both 'corrected' fluid model described in previous section and classical model (with either bulk or flux transport data) are used to study the streamer development and signal formation in ATLAS triggering RPC [1] and ALICE timing RPC [2].
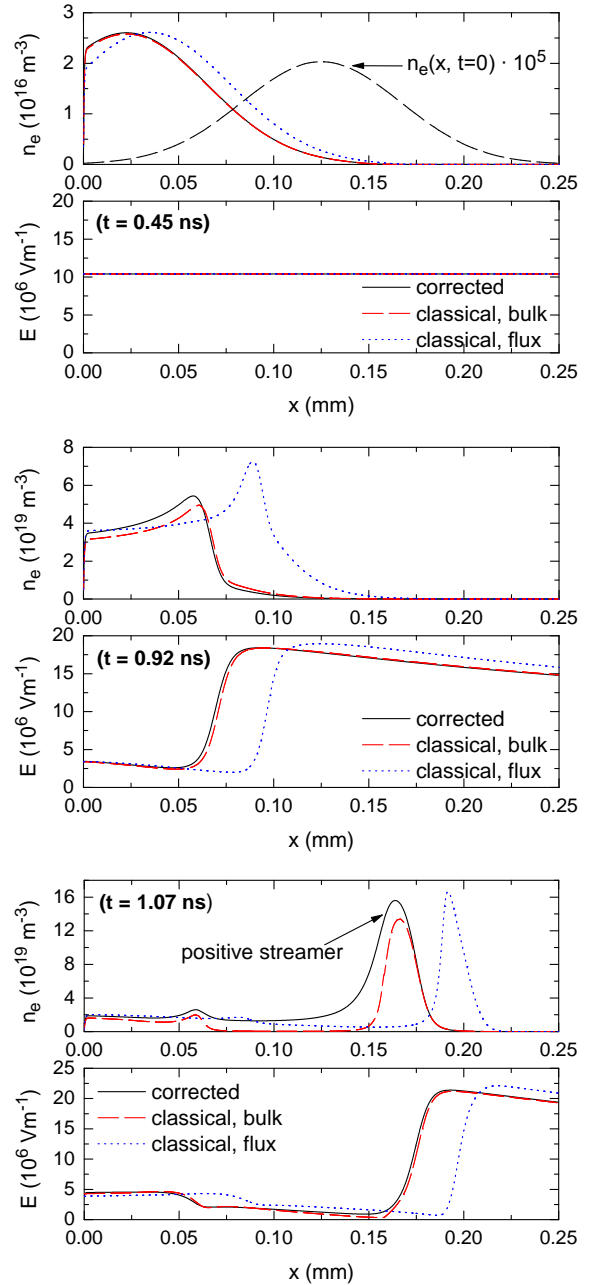

Fig. 1: *Electron number density and electric field along the gas gap of ALICE timing RPC at $t = 0.45$ ns during avalanche development (top), $t = 0.92$ ns during positive streamer formation (middle) and $t = 1.07$ ns during positive streamer propagation (bottom). The external electric field is set to 10.4 MV/m. Calculations are made using corrected fluid model and classical fluid model with flux and bulk transport data as input.*

For example, ALICE timing RPC uses five 0.25 mm gas gaps with a gas mixture of 90% $C_2H_2F_4$ + 5% iso-C_4H_{10} + 5% SF_6. The transport data and source term expansion coefficients are calculated by our Monte Carlo code [13] using the cross section set for electron scattering in $C_2H_2F_4$ developed by our group [14], cross sections for iso-C_4H_{10} taken from MAGBOLTZ 7.1 code (developed by S. Biagi [15]), and cross sections for SF_6 taken from Itoh et al. [16].
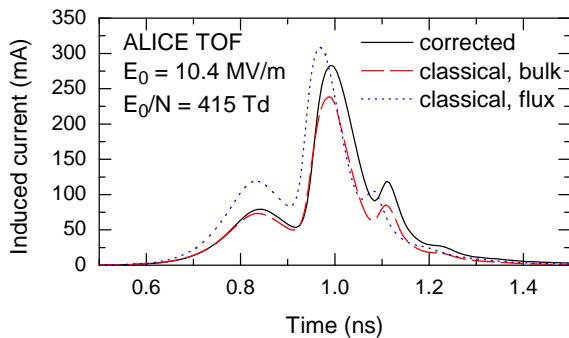
Fig. 2: *Induced current in ALICE timing RPC calculated using corrected fluid model and classical fluid model with flux and bulk transport data as input. The external electric field is set to 10.4 MV/m.*
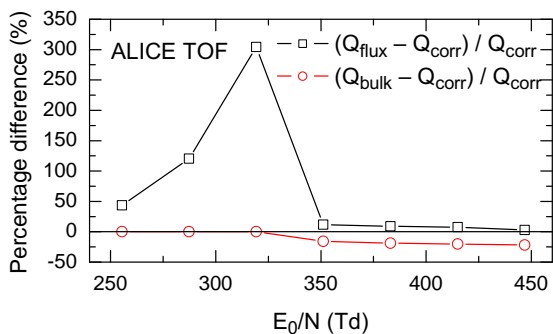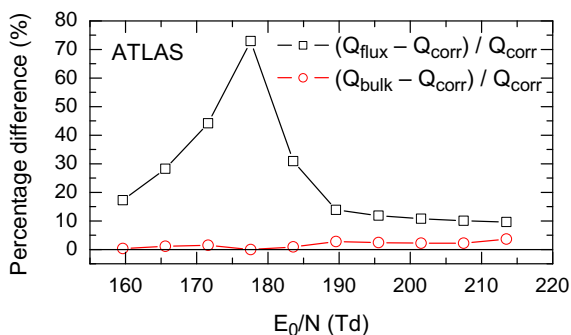

Fig. 3: *Percentage difference between the induced charges calculated using classical fluid model with either flux (Q_{flux}) or bulk (Q_{bulk}) transport data, and corrected fluid model (Q_{corr}). Results are obtained over a range of applied electric fields for ATLAS triggering RPC (top) and ALICE timing RPC (bottom).*

We assume that the initial electron distribution at $t = 0$ is a Gaussian representing 6 primary electrons. Fig. 1 (top) shows the electron number density and electric field at time instant $t = 0.45$ ns during avalanche development in ALICE timing RPC. At this moment, there are no space charge effects and the profiles obtained using corrected model match with those obtained using classical model with bulk data. During the avalanche phase, the induced current grows exponentially with time (Fig. 2). Afterwards, the exponential rise gradually stops due to both space charge effects and electron absorption at the anode. At about 0.92 ns,

the positive streamer starts to develop (Fig. 1, middle) and the current rises again while the streamer progresses towards the cathode (Fig. 2). The positive streamer stops at about 1 ns (Fig. 1, bottom) and starts to diminish while the induced current slowly drops to zero (Fig. 2). In the streamer stage, there is an obvious difference between the profiles and induced currents for the three modeling scenarios. The difference is even more pronounced if we consider the induced charge over a range of applied electric field strengths (Fig. 3). The induced charge is defined as an integral of the induced current. The difference between the induced charge calculated using classical model with flux data and the one calculated using corrected model reaches a maximum of 70% for ATLAS RPC (Fig. 3, top) and about 300% for ALICE timing RPC (Fig. 3, bottom). These discrepancies arise mainly due to different drift velocities and representation of the source term employed in fluid models.

REFERENCES

[1] The ATLAS Collaboration, J. Instrum. 3, S08003 (2008)

[2] The ALICE Collaboration, J. Instrum. 3, S08002 (2008)

[3] R. Santonico, Nucl. Instrum. Meth. A 661, S2 (2012)

[4] D. Bošnjaković, Z. Lj. Petrović and S. Dujko, J. Instrum. 9, P09012 (2014)

[5] D. Bošnjaković, Z. Lj. Petrović and S. Dujko, J. Phys. D: Appl. Phys. 49, 405201 (2016)

[6] A. Moshaii et al., Nucl. Instrum. Meth. A 661, S168 (2012)

[7] R. E. Robson, Aust. J. Phys. 44, 685 (1991)

[8] D. Bošnjaković, Z. Lj. Petrović, R. D. White and S. Dujko, J. Phys. D: Appl. Phys. 47, 435203 (2014)

[9] K. Kumar, H. R. Skullerud and R. E. Robson, Aust. J. Phys. 33, 343 (1980)

[10] A. J. Davies, C. J. Evans and F. L. Jones, Proc. R. Soc. A Math. Phys. Eng. Sci. 281, 164 (1964)

[11] L. E. Kline, J. Appl. Phys. 45, 2046 (1974)

[12] S. Ramo, Proc. I.R.E. 27, 584 (1939)

[13] Z. M. Raspopović et al., IEEE Trans. Plasma Sci. 39, 2566 (2011)

[14] O. Šašić et al., unpublished

[15] S. Biagi, Nucl. Instrum. Meth. A 421, 234 (1999)

[16] H. Itoh et al., J. Phys. D: Appl. Phys. 26, 1975 (1993)

Electron transport and propagation of negative streamers in liquid-phase xenon

Saša Dujko
Institute of Physics
University of Belgrade
Belgrade, Serbia
sasa.dujko@ipb.ac.rs

Ilija Simonović
Institute of Physics
University of Belgrade
Belgrade, Serbia
ilija.simonovic@ipb.ac.rs

Danko Bošnjaković
Institute of Physics
University of Belgrade
Belgrade, Serbia
dbosnjak@ipb.ac.rs

Zoran Lj. Petrović
Institute of Physics
University of Belgrade and Serbian
Academy of Sciences and Arts
Belgrade, Serbia
zoran@ipb.ac.rs

Ronald White
College of Science and Engineering,
James Cook University
Townsville, QLD, Australia
ronald.white@jcu.edu.au

Abstract—The Monte Carlo method, initially developed for charged particle swarms in neutral dilute gases, is extended and generalized to investigate the transport processes of electrons in liquid-phase noble gases by accounting for the coherent and other liquid scattering effects. Electron transport coefficients, including the electron mobility, diffusion coefficients and ionization coefficient, are calculated as a function of the reduced electric field in liquid-phase xenon. Calculated transport coefficients are then used as an input in the classical fluid model to investigate the dynamics of negative streamers. Using the language of the contemporary kinetic theory of plasma discharges, in the present work among many important points, we investigate how various representations of inelastic energy losses in inelastic scattering events affect the electron transport and the macroscopic streamer properties.

Keywords—Monte Carlo, liquid noble gases, transport coefficients, streamers, fluid models

I. INTRODUCTION

Understanding of the behavior of free electrons under the influence of electric field in liquids is of interest in both fundamental physics and in numerous technological applications. Those applications include the interdisciplinary field of plasma medicine [1], liquid dielectrics [2], plasma-water purification [3] and liquid particle detectors [4]. In particular, liquid-phase noble gases are used in the technology of the time-projection chambers, which are designed for detection of cosmic radiation and neutrinos [4], as well as in the search for dark matter particles [4]. Further optimization of such applications requires an accurate understanding of electron transport coefficients, streamer properties and the physical processes involved.

In our previous studies, we investigated the elastic scattering of electrons from liquid-phase argon [5] and liquid-phase xenon [6]. Electron transport coefficients were calculated in the sub-excitation energy region, e.g., for those values of the reduced electric fields, E/n_0, (where E is the electric field strength and n_0 is the neutral atom density) for which the mean energies are well below the first inelastic threshold. More recently, we have investigated the way in which electron transport coefficients are influenced by various representations of the inelastic energy losses in liquid-phase xenon with the special emphasis on the explicit effects of ionization (or interband transition having in mind that the electrons are quasi-free particles in liquid xenon) [7].

We have also discussed the fluid modeling methods with the aim of understanding electron transport and streamer propagation across the gas-liquid interfacial regions [8]. In this paper, as a part of our ongoing investigations of electron transport in liquid-phase noble gases in an electric field, we study the transition from an electron avalanche into a negative streamer ionization front and its propagation in liquid xenon. Calculations are performed using a fluid model in local field approximation. Using the electron scattering cross sections for both gas and liquid xenon, transport coefficients of electrons are calculated in Monte Carlo simulations to serve as input data for a fluid model used in this study.

We begin this study by briefly reviewing the basic elements of the fluid theory used to simulate negative streamers in liquid xenon in section 2. In section 3.A, we present the electron transport coefficients as a function of the reduced electric field. In the same section, we briefly discuss the cross sections for electron scattering in liquid xenon and the basic elements of the Monte Carlo method used for calculating electron transport coefficients. The development of negative streamers without formation of expanding gaseous filaments is discussed in section 3.B. In section 4 we present our conclusions and recommendations for future work.

II. THEORETICAL METHOD

Simulations of negative streamers in liquid xenon are performed by using the classical fluid model. In this model the electron flux is obtained by assuming a steady-state of the momentum balance equation, and that the electron energy of the field-directed motion is much greater than the thermal contribution [9]. The generalized one-dimensional continuity equation for the electron number density is

$$\frac{\partial n_e(x,t)}{\partial t} = \frac{\partial}{\partial x}\left(D_L \frac{\partial n_e(x,t)}{\partial x} + \mu_e n_e(x,t)E\operatorname{sgn}(E)\right) + \left(\nu_i - \beta n_p(x,t)n_e(x,t)\right), \quad (1)$$

where $n_e(x,t)$ and $n_p(x,t)$ are the number densities of electrons and positive holes, respectively, which are functions of the coordinate x and time t. In this equation D_L and μ_e are the longitudinal diffusion coefficient and the electron mobility, respectively, E is the electric field,

oriented along the x-axis, while ν_i and β are the ionization rate and the recombination coefficient, respectively.

In addition to the electron continuity equation (1), the time evolution of the number density of positive holes is described by the number balance equation

$$\frac{\partial n_p(x,t)}{\partial t} = \left(\nu_i - \beta n_p(x,t)\right) n_e(x,t) , \qquad (2)$$

where transport of positive holes has been neglected over the transient time scales considered in this study, owing to the significantly reduced mobility and diffusion of positive holes in liquid xenon [10].

The model is realized in a 1.5 dimensional (1.5D) setup. Thus, the total electric field in the system is evaluated as the sum of the uniform external electric field and the electric field due to space charge:

$$E(x,t) = E_0 + \frac{e}{2\epsilon_0\epsilon_r} \int_0^l \left(\text{sgn}(x - x') - \frac{x-x'}{\sqrt{(x-x')^2+R_0^2}} \right) \left(n_p - n_e(x',t) \right) dx' , \qquad (3)$$

where E_0 is the external electric field, e is the elementary charge, ϵ_0 and ϵ_r are the vacuum permittivity and the relative permittivity, respectively, and l is the length of the system. In this model, the space charge is contained inside cylinder with radius R_0 and the charge density varies along the axial direction only.

The recombination coefficient is given by the scaled Debye formula

$$\beta = \xi\beta_D = \xi \frac{4\pi e\mu_e}{\epsilon_0\epsilon_r} , \qquad (4)$$

where β_D is the Debye recombination coefficient and ξ is the scaling factor which is taken to be 0.1 [11].

The above fluid equations are closed, assuming the local field approximation. According to this approximation the input terms, including μ_e, D_L, ν_i and β are assumed to be functions of the local instantaneous electric field. In the numerical implementation of our fluid model, the spatial discretization is performed by using the second order central finite difference, while the fourth order Runge–Kutta method is used for the integration in time.

III. RESULTS AND DISCUSSION

A. Transport coefficients of electrons in liquid xenon

In case of electrons, the transport data needed for the solution of fluid equations (1) and (2) are μ_e, D_L, and ν_i. These electron transport data are calculated by using the Monte Carlo method. The Monte Carlo method, initially developed for charged particle swarms in neutral dilute gases [12], has been recently extended and generalized by including three effective scattering processes, which give a good representation of the coherent scattering of low energy electrons in non-polar liquids [7]. The validity of our Monte Carlo method has been tested by calculating the transport properties of electrons in the Percus Yevick model liquid. It was found that our results are in an excellent agreement with those calculated by Tattersall et al [13].

In order to account for excitations in liquid xenon, the set of inelastic atomic excitation cross sections of the Hayashi database was modified to form a set of excitation cross sections for intermediate excitons in liquid state. For example, the intermediate $n = 1 \left[\Gamma\left(\frac{3}{2}\right)\right]$ and $n' = 1 \left[\Gamma\left(\frac{1}{2}\right)\right]$

excitons have been observed at 8.2 eV and 9.45 eV, respectively [14]. The former has parentage in the excited atomic $6s'[3/2]_1$ state, while the latter has parentage in the $6s'[1/2]_1$ state. As these intermediate excitons have a unique parentage, via the isolated atom's excited states, we thus approximate the cross sections for intermediate exciton excitations by cross sections of the corresponding atomic excitations. Likewise, the cross section for interband transitions is approximated by the cross section of the electron impact ionization, from the Hayashi's cross section set. However, the cross section is shifted by 2.1 eV, so that the threshold of the ioization is 9.22 eV in liquid xenon. This value corresponds to the $\Gamma\left(\frac{3}{2}\right)$ band gap in liquid xenon, which is the energy difference between the uppermost valence and the bottom of the conduction band. For simplicity, in the rest of this work the interband transition and the inelastic collisions will be referred to as ionization and excitations, respectively. For more details on the band structure and cross sections for electron scattering in liquid xenon, the reader is referred to [7].

In the present calculations, we cover a range of reduced electric fields between 10^{-3} and 10^3 Td (1 Td = 10^{-21} Vm^2). The number density of xenon atoms is 1.4×10^{28} m^{-3}, while the temperature of the background liquid is 163 K. In our simulations, we usually follow 10^6 electrons except in the limit of the lowest values of E/n_0. Due to numerous elastic collisions in which only a fraction of the initial electron energy is transferred to a heavy xenon atom, the efficiency of energy transfer is very low in the limit of the lowest E/n_0. As a consequence, the relaxation of energy is very slow and requires a large computation time. In order to optimize the simulation speed, the simulations were usually begun with 10^4 electrons and after the relaxation to the steady state the electron swarm scaled up to 10^6 electrons. The details of this procedure are given elsewhere [7].

In Fig. 1 we show the dependence of the electron mobility on E/n_0. It should be noted that the density normalized mobility $n_0\mu$ and density normalized diffusion coefficients n_0D_L and n_0D_T shown in Fig. 2, are not independent of the neutral atom density [15]. These transport coefficients are given as a function of E/n_0, so that any linear dependence on density (as occurs in the dilute-gas limit) has been removed. Thus, we have a true comparison of the gas and liquid phases.

Calculations are performed assuming the following two scenarios: (*i*) no electronic excitations (case 1), and (*ii*) all electronic excitations from the gas-phase are included (case 2). Both the bulk and flux mobility components are shown. The bulk transport coefficients, are associated with the swarm's centre of mass transport and spread about its centre of mass. In Monte Carlo simulations, the bulk transport coefficients may be determined from the rate of changes of the appropriate averages of the positions of the electrons in the configuration space. The flux transport coefficients should be interpreted in terms of averages over the ensemble in velocity space. For example, the flux mobility is associated with the average velocity of the ensemble in the swarm. In liquid and gas xenon, these two sets of transport coefficients are equal in the absence of ionization.

For comparison, the theoretical [6,7] and experimental values [16] of mobility are displayed at the same figure, along with the mobility in gaseous xenon.
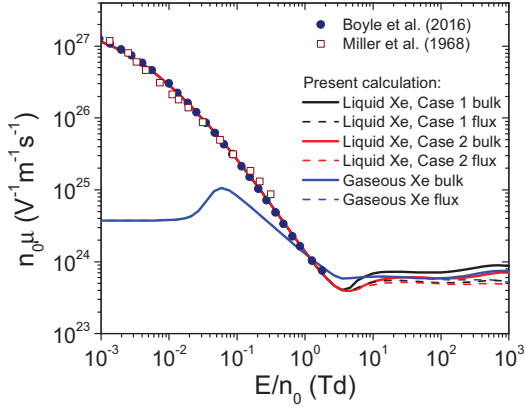
Fig 1. Variation of the electron mobility with E/n_0. Our Monte Carlo results, for liquid and gaseous xenon, are compared with the measurements (Miller et al. (1986)) and theoretical calculations (Boyle et al. (2016)). It should be noted that all three dashed lines for the flux properties emerge from the solid lines of the same colour above 10 Td.
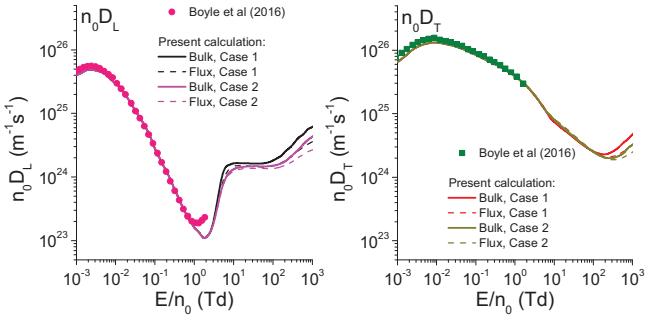

Fig. 2. Variation of the longitudinal (left panel) and transverse diffusion coefficients with E/n_0. Our Monte Carlo results are compared with the theoretical calculations (Boyle et al. (2016)).

The agreement between our Monte Carlo results and those obtained from a multi term solution of the Boltzmann equation is excellent.

For the lower values of E/n_0 we observe that the electron mobility in the liquid phase exceeds the mobility in the gas phase by more than two orders of magnitude. This is a clear sign of the reduction of the rate of momentum transfer of the lower energy electrons in liquid xenon. The lowering of the rate of momentum transfer follows from the modification of the scattering potential and the coherent scattering effects. Due to these liquid scattering effects, the electric field accelerates electrons more efficiently in liquid xenon than in gaseous xenon, which in turn leads to a significant enhancement of the electron mobility as compared to the gas xenon.

In Fig. 2 we show the variation of the longitudinal and the transverse diffusion coefficient as a function of E/n_0. The agreement between our Monte Carlo results and those evaluated from the solution of Boltzmann's equation for the lower values of E/n_0 is very good. For the higher values of E/n_0, we observe that the diffusion coefficients are reduced with an increase of the number of excitations used in the modeling. Due to the explicit effects of ionization, the bulk values of both $n_0 D_L$ and $n_0 D_T$ are greater than the corresponding flux values.

In Fig. 3 we show the variation of the ionization rate coefficient with E/n_0. We observe that the ionization rate is monotonically increasing function of E/n_0 for both the liquid- and gas-phase xenon. We also observe that the ionization rate is increased by reducing the number of
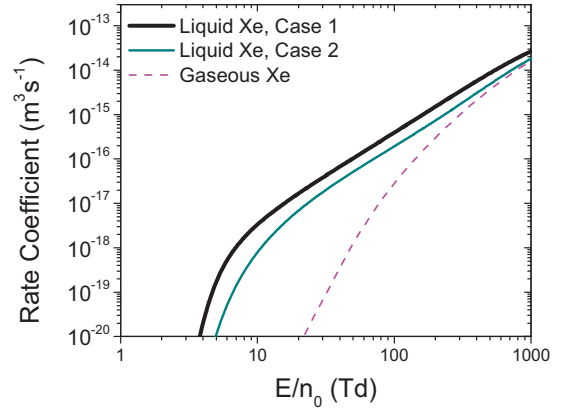

Fig. 3. Variation of the ionization rate coefficient with E/n_0. Calculations in gaseous xenon are compared with those in liquid xenon.

excitations. Likewise, the ionization coefficient in liquid xenon is significantly greater than the ionization coefficient in gaseous xenon. This can be expected due to the reduction of the threshold for ionization in the liquid phase. In addition, electrons can lose a significant amount of energy in a wide range of inelastic scattering processes at energies lower than the threshold energy for ionization in gaseous xenon. Likewise, there is a far lower number of inelastic scattering processes with thresholds which are lower than the threshold for ionization in the liquid phase compared to the gas phase.

B. Negative streamer fronts in liquid xenon

In Fig. 4 we show the formation and propagation of a negative streamer under the influence of the externally applied electric field of 77 Td. The initial Gaussian is positioned in the close vicinity of the cathode. The electric field is oriented to the right, so the negative fronts propagate to the left. The initial densities of electrons and positive holes are equal reflecting the macroscopic neutrality of a plasma. In addition, these densities are selected in such way that the space charge effects are negligible. The values of l and R_0 are set to 5×10^{-5} m and 1×10^{-5} m, respectively. The particular value of R_0 is chosen as an educated guess taking into account the width of the initial distribution and the spreading due to transverse diffusion. The length of the system l is determined by the requirement that the streamer velocity relaxes to a stationary value. The simulation in the gaseous xenon employs transport data for electrons for the gas phase scaled to the liquid density. We employ the bulk transport coefficients as an input in fluid simulations of negative streamer fronts in both the liquid and gas phases.

In the absence of gas filaments and trapping of electrons in the density fluctuations, the general features of the streamer profiles in the liquid xenon are the same as those of the streamers in gases [7]. We observe that the streamer front caries an overshoot of electrons, generating a thin space charge layer that screens the electric field in the streamer interior behind the front. In this screened interior region, the density of charge is not constant. The electron number density and the positive hole density are further reduced due to the recombination of electrons and positive holes. A similar decrease in the electron number density in the streamer interior and behind the front, is observed for streamers in electronegative gases, where electron attachment consumes the lower energy electrons. We observe that the streamer formation as well as streamer
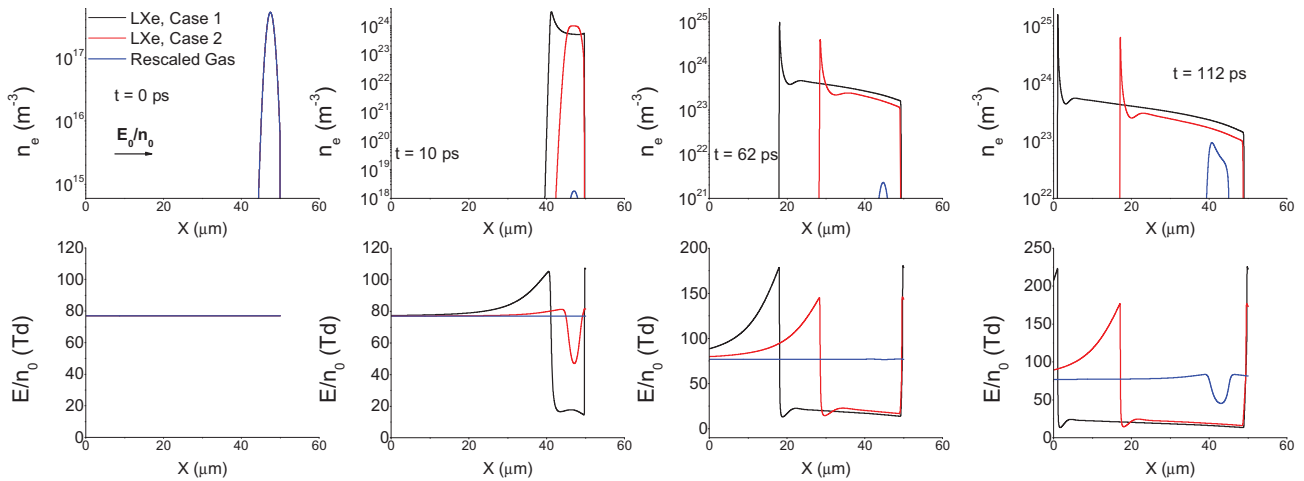
Fig. 4. The formation and propagation of a negative streamer in liquid xenon for E/n_0 = 77 Td. Here n_e refers to the electron number density while E/n_0 refers to the reduced resultant electric field.

propagation are greatly influenced by the number of excitations in the model. For example, the streamer velocity and the electron number density in the streamer interior are increased by reducing the number of excitationsIt can also be observed that the transition from an electron avalanche into a streamer is much slower in the case of the rescaled gas than in the liquid phase.

IV. CONCLUSION

Using a Monte Carlo simulation technique and 1.5 dimensional classical fluid model, we have investigated the influence of inelastic energy losses on both the transport properties of electrons and dynamics of negative streamers in liquid xenon. The cross sections for inelastic scattering and interband transitions of electrons in liquid xenon are approximated by using the cross sections for electron scattering on an isolated xenon atom. The *ab initio* cross section for elastic scattering in liquid xenon is taken and adopted in order to include the effects of coherent scattering and atomic potential screening which are critical for low-energy electron scattering. Calculations in the liquid phase are augmented by those in the gas phase. It is found that, above approximately 1 Td there is a significant difference between the values of transport properties determined by employing different representations of the inelastic energy losses. The electron mobility and diffusion coefficients, as well as the ionization rate coefficient are reduced with increasing number of excitations in the model. Likewise, it is found that the streamer properties, including the streamer velocity, the ionization degree in the streamer interior and the distribution of electric field strongly depend on the number of excitations which are included in the model.

The present work will be extended in a near future by investigating the propagation of positive and negative streamers in a point-to-plane geometry. We will also consider the influence of density fluctuations and gas filaments, as well as trapping of electrons in these structures, on both the electron transport and the streamer dynamics.

REFERENCES

[1] M. G. Kong, G. Kroesen, G. Morfill, T. Nosenko, T. Shimizu, J. van Dijk and J. L. Zimmermann, "Plasma medicine: an introductory review," New J. Phys. vol. 11, 115012, 2009.

[2] V. Y. Ushakov, V. F. Klimkin and S. M. Korobeynikov, "Impulse Breakdown of Liquids," (Berlin: Springer), 2007.

[3] B. Jiang, J. Zheng, S. Qiu, M. Wu, Q. Zhang, Z. Yan and Q. Xue, "Review on electrical discharge plasma technology for wastewater remediation," Chem. Eng. J. vol. 236, 348, 2014.

[4] E. Aprile and T. Doke, "Liquid xenon detectors for particle physics and astrophysics, " Rev. Mod. Phys. vol. 82, 2053, 2010.

[5] G. J. Boyle, R. P. McEachran, D. G. Cocks and R. D. White, "Electron scattering and transport in liquid argon, " J. Chem. Phys. vol. 142, 154507, 2015.

[6] G. J. Boyle, R. P. McEachran, D. G. Cocks, M. J. Brunger, S. J. Buckman, S. Dujko and R. D. White, "*Ab initio* electron scattering cross-sections and transport in liquid xenon, " J. Phys. D: Appl. Phys. vol. 49, 355201, 2016.

[7] I. Simonović, N. A. Garland , D. Bošnjaković , Z. Lj. Petrović, R. D. White and S. Dujko, "Electron transport and negative streamers in liquid xenon, " Plasma Sources Sci. Technol. vol. 18, 015006, 2019.

[8] N. A. Garland, I. Simonović, G. J. Boyle, D. G. Cocks, S. Dujko and R. D. White, "Electron swarm and streamer transport across the gas–liquid interface: a comparative fluid model study, " Plasma Sources Sci. Technol. vol. 27, 105004, 2018.

[9] S. Dujko, A. H. Markosyan, R. D. White and U. Ebert, "High-order fluid model for streamer discharges: I. Derivation of model and transport data," J. Phys. D: Appl. Phys. vol. 46, 475202, 2013

[10] O. Hilt and W. F. Schmidt, "Positive hole mobility in liquid xenon, " Chem. Phys. vol. 183, 147, 1994.

[11] N. Y. Babaeva and G. V. Naidis, "Modeling of positive streamers in liquid argon, " Tech. Phys. Lett. vol. 25, 91, 1999.

[12] S. Dujko, Z. M. Raspopović and Z. Lj. Petrović, "Monte Carlo studies of electron transport in crossed electric and magnetic fields in CF_4, " J. Phys. D: Appl. Phys. vol. 38, 2952, 2005.

[13] W. J. Tattersall, D. G. Cocks, G. J. Boyle, S. J. Buckman and R. D. White, "Monte Carlo study of coherent scattering effects of low-energy charged particle transport in Percus-Yevick liquids, " Phys. Rev. E vol. 91, 043304, 2015.

[14] P. Laporte, J. L. Subtil, U. Asaf, I. T. Steinberger and S. Wind, "Intermediate and Wannier Excitons in Fluid Xenon, " Phys. Rev. Lett. vol. 45, 2138, 1980.

[15] Y. Sakai, "Quasifree electron transport under electric field in nonpolar simple-structured condensed matters," J. Phys. D: Appl. Phys. vol. 40, R441, 2007.

[16] L. S. Miller, S. Howe and W. E. Spear, "Charge Transport in Solid and Liquid Ar, Kr, and Xe, " Phys. Rev. vol. 166, 871, 1968.

Electron transport coefficients and negative streamer dynamics in CF$_3$I-SF$_6$ mixtures

Saša Dujko
Institute of Physics
University of Belgrade
Belgrade, Serbia
sasa.dujko@ipb.ac.rs

Jasmina Atić
Institute of Physics
University of Belgrade
Belgrade, Serbia
jasmina.atic@ipb.ac.rs

Danko Bošnjaković
Institute of Physics
University of Belgrade
Belgrade, Serbia
dbosnjak@ipb.ac.rs

Zoran Lj. Petrović
Institute of Physics
University of Belgrade and Serbian
Academy of Sciences and Arts
Belgrade, Serbia
zoran@ipb.ac.rs

Jaime de Urquijo
Instituto de Ciencias Físicas,
Universidad Nacional Autónoma de
México
Cuernavaca, Morelos, Mexico
mistenisrojos@gmail.com

Abstract—**A multi term theory for solving the Boltzmann equation and a Monte Carlo simulation technique are used to calculate electron transport coefficients in the mixtures of CF$_3$I and SF$_6$ as a function of the applied electric field. The calculated transport coefficients are then used as an input in the fluid equation based models to investigate the transition from an electron avalanche into a streamer and streamer propagation. Electron transport coefficients are also calculated in radio-frequency electric and magnetic fields crossed at arbitrary phases and angles. A multitude of kinetic phenomena induced by the synergism of the magnetic field and electron attachment is observed and discussed using physical arguments.**

Keywords—Boltzmann equation, Monte Carlo, transport coefficients, streamers, electron attachment, ionization

I. INTRODUCTION

Studies of electron transport processes in strongly attaching gases in electric and magnetic fields have many important applications. These applications range from the modelling of magnetically-assisted low-pressure collision dominated plasma discharges to the modelling of gaseous particle detectors in high-energy physics and to the development of a new generation of gaseous dielectrics in high-voltage technology. In the present work, we are investigating the electron transport and the streamer propagation in the mixtures of strongly attaching gases trifluoroiodomethane (CF$_3$I) and sulfur hexafluoride (SF$_6$). In high-voltage technology, strongly attaching gases and their mixtures with other appropriate gases such as N$_2$ and/or CO$_2$ are used with the aim of controlling and preventing the electrical breakdown in electric power systems. The most important gaseous dielectric in high voltage technology nowadays is SF$_6$. SF$_6$ is a strongly attaching gas, with a high dielectric strength, and a breakdown voltage nearly three times higher than that of air at atmospheric pressure. However, in electrical discharges, SF$_6$ creates highly toxic and corrosive compounds such as S$_2$F$_{10}$ and SOF$_2$. In addition, SF$_6$ has an extremely high global warming potential (23900 times higher than that of CO$_2$) and an extremely long atmospheric lifetime (3200 years) [1]. These facts have moved physicists and engineers into finding possible substitutes of SF$_6$. One of the most promising candidates is CF$_3$I. CF$_3$I is also a strongly attaching gas, but with much higher dielectric strength than SF$_6$. The global warming potential of CF$_3$I is much less than that of SF$_6$ (approximately 0.4 times that of CO$_2$), and its lifetime in the atmosphere is very short (1.8 days). Using these facts as motivational factors, we have undertaken a program to understand electron interactions with CF$_3$I as well as the basic properties of electron transport and streamer propagation in pure CF$_3$I and its mixtures with SF$_6$.

In the present investigations, we have calculated electron transport coefficients in various mixtures of CF$_3$I and SF$_6$ subjected to an external static electric field. Our results are based on a numerical multi term solution of the Boltzmann equation [2,3], which is solved for values of E/N ranging from approximately 50 to 10 000 Td (1 Td = 10^{-21} Vm^2). For the lower values of E/N, due to poor convergence of transport coefficients we have applied the Monte Carlo method. The Monte Carlo code has been recently optimized and specified to consider the transport processes of electrons in strongly attaching gases [4]. The poor convergence of transport coefficients is a consequence of predominant removal of the lower energy electrons due to a strong electron attachment, which in turn shifts the bulk of the distribution function towards a higher energy. Under these conditions, the moment method for solving the Boltzmann equation used in the present work usually fails, as it requires a prohibitive number of basis functions for resolving the energy dependence of the distribution function.

Calculations have also been performed in the case of alternating current (ac) electric and magnetic fields. We investigate the way in which the transport coefficients and other swarm properties are influenced by the field frequency, electric and magnetic field strengths, and the phase difference between the fields under conditions in which the electron transport is greatly affected by electron attachment. The time-dependent behavior of electron swarms in varying configurations of electric and magnetic fields is particularly important for the modeling of magnetically controlled/assisted radio-frequency plasma discharges [3]. In addition, the time-dependent studies are useful for a future development of sensors for detection of electromagnetic waves induced in gas-insulated high-voltage switchgear (GIS) by partial discharges.

Finally, the calculated transport coefficients in a direct current (dc) electric field are used as an input in the fluid-equation based models with the aim of investigating the transition from an electron avalanche into a streamer and

streamer propagation. Among many important points, in the present work we discuss how streamer properties, including the electron density, electric field and streamer velocity are affected by introducing CF_3I into SF_6.

II. THEORETICAL METHOD

The behavior of electron swarms in neutral gases under the influence of electric and magnetic fields is described by the phase-space distribution function $f(\boldsymbol{r}, \boldsymbol{c}, t)$, representing the solution of the Boltzmann equation

$$\frac{\partial f}{\partial t} + \boldsymbol{c} \cdot \frac{\partial f}{\partial \boldsymbol{r}} + \frac{e}{m}(\boldsymbol{E} + \boldsymbol{c} \times \boldsymbol{B}) \cdot \frac{\partial f}{\partial \boldsymbol{c}} = -J(f, f_0), \quad (1)$$

where $\boldsymbol{r}$, and $\boldsymbol{c}$ denote the position and velocity coordinates respectively, while e and m are the charge and the mass of the swarm particle and t is the time. The right-hand side $J(f, f_0)$ denotes the linear electron-neutral molecule collision operator, accounting for elastic, inelastic and non-conservative collisions. The electric and magnetic fields are assumed to be spatially-homogeneous and in the general case time-dependent.

The methods and techniques for solving the Boltzmann equation are by now standard and the reader is referred to our previous works [3,4]. Nevertheless, we highlight some important steps of our methodology for solving the Boltzmann equation:

1) No assumptions on symmetries in velocity space are made, and the directional dependence of $f(\boldsymbol{r}, \boldsymbol{c}, t)$ in velocity space is represented in terms of a spherical harmonic expansion:

$$f(\boldsymbol{r}, \boldsymbol{c}, t) = \sum_{l=0}^{\infty} \sum_{m=-l}^{l} f(\boldsymbol{r}, \boldsymbol{c}, t) Y_m^{[l]}(\hat{\boldsymbol{c}}), \quad (2)$$

where $Y_m^{[l]}(\hat{\boldsymbol{c}})$ are spherical harmonics, and $\hat{\boldsymbol{c}}$ represents the angles of $\boldsymbol{c}$. In contrast to the frequently used two-term approximation which forms the basis of the classical theory of electron transport in gases, our method is a truly multi-term approach. The differences between the two-term approximation and our multi-term approach for solving the Boltzmann equation will be illustrated for electron transport in CF_3I in the next section.

2) Under hydrodynamic conditions (far away from the boundaries, sources and sinks of electrons) a sufficient representation of the space dependence is an expansion of $f(\boldsymbol{r}, \boldsymbol{c}, t)$ in terms of the powers of the density gradient operator:

$$f(\boldsymbol{r}, \boldsymbol{c}, t) = \sum_{k=0}^{\infty} f^{(k)}(\boldsymbol{c}, t) \odot (-\nabla)^k n(\boldsymbol{r}, t), \quad (3)$$

where $f^{(k)}(\boldsymbol{c}, t)$ are time-dependent tensors of rank k while $\odot$ denotes a k-fold scalar product.

3) The energy dependence of $f(\boldsymbol{r}, \boldsymbol{c}, t)$ is represented by an expansion about a variety of Maxwellians at an arbitrary temperature in terms of Sonine polynomials.

The combination of spherical harmonics and Sonine polynomials yields the well-known Burnett functions. Using the appropriate orthogonality relations of the Burnett functions, the Boltzmann equation is converted into a hierarchy of doubly and infinite coupled inhomogeneous matrix equations for the time-dependent moments. The finite truncation of the Burnett functions, permits a solution of this hierarchy by direct numerical inversion. These equations are solved numerically and both families of

transport coefficients, the bulk and the flux, including other transport properties, are expressed in terms of moments of the distribution function [2,3].

In addition to Boltzmann's equation, in the present work we apply a Monte Carlo simulation technique. Our standard MC code has been recently extended to consider the spatially inhomogeneous electron swarms in strongly attaching gases by implementing the rescaling procedures [4]. The so-called discrete and continuous rescaling procedures are developed and benchmarked in the aim of simulating electron transport under conditions of extensive losses of seed electrons due to a strong electron attachment. In this work, Monte Carlo method is employed as a tool to confirm the numerical accuracy and integrity of a multi-term theory for solving the Boltzmann equation. However, whenever the convergence of transport coefficients was poor in the Boltzmann equation analysis, then MC results are in turn included in the plots.

Transition from an avalanche into a streamer, and propagation of streamers have been considered by the fluid equation based models. We employ the so-called classical fluid model in which the equation of continuity is combined with the drift-diffusion approximation. The resulting equation is coupled with the Poisson equation for the space charge electric field calculations. The resulting system of partial differential equations is solved numerically assuming the local field approximation [5,6].

III. RESULTS AND DISCUSSION

A. Cross sections and inputs

The development of the complete cross-section set of electron scattering in CF_3I has been detailed in recent studies [4,7], and is based largely on the original set proposed by Kimura and Nakamura [8]. The accuracy and the completeness of the initial set developed by Kimura and Nakamura was improved by applying the standard swarm procedure using the measurements of transport coefficients in the mixtures of CF_3I with Ar and CO_2 under the pulsed-Townsend (PT) conditions. Cross sections for electron scattering in SF_6 are taken from Itoh et al. [9]. In the present investigation, we consider the density-reduced electric field range from 1 to 10^4 Td. The background gas mixture temperature is fixed at 293 K. In the domain time-dependent studies, we cover a range of magnetic field amplitudes between 0 and 10^4 Hx (1 Hx = 10^{-27} Tm^{-3}).
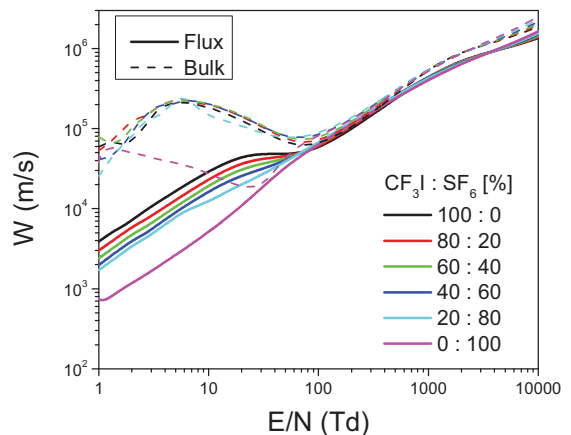

Fig. 1. Variation of the flux and bulk drift velocities with E/N for various CF_3I-SF_6 mixtures.

B. Transport coefficients in the mixtures of CF_3I and SF_6

In Fig. 1 we show the variation of the flux and bulk drift velocities with E/N for various CF_3I-SF_6 mixtures. We observe that over the entire range of E/N the flux drift velocity is a monotonically increasing function of E/N, while the bulk drift velocity in pure CF_3I and SF_6, as well as in their mixtures, exhibits a pronounced negative differential conductivity (NDC). NDC is characterized by a decrease in the bulk drift velocity despite an increase in the magnitude of the applied electric field. In the case of strongly attaching gases such as CF_3I and SF_6, NDC is induced by the combined effects of attachment heating and inelastic cooling of the swarm. In addition, due to attachment heating and explicit effects of ionization, the bulk drift velocity dominates the flux component over the entire range of E/N considered in this work.

In Fig. 2 we show the variation of the ionization and attachment rate coefficients with E/N for various mixtures. As expected, the ionization rate coefficient is a monotonically increasing function of E/N and becomes significant at the higher values of E/N when sufficient electrons have enough energy, to cause ionization. We observe that the ionization rate is less sensitive with respect to the composition of the gas mixture at higher values of E/N. The behavior of the attachment rate coefficient is more complex, but generally it tends to decrease with increasing E/N.
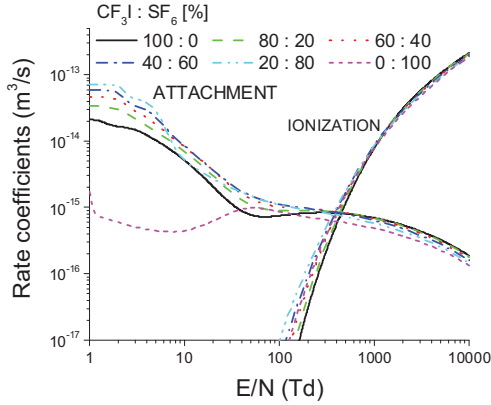

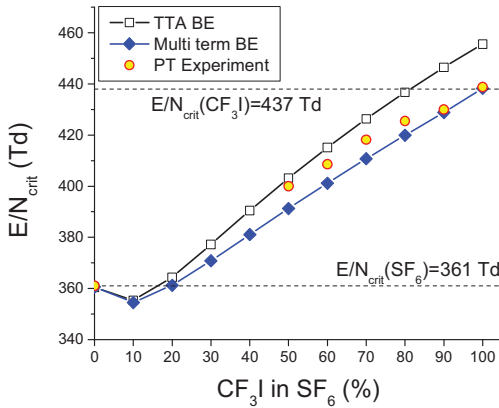Fig. 2. Variation of the attachment and ionization rate coefficients with E/N for various CF_3I-SF_6 mixtures.

Fig. 3. Variation of the critical field strength as a function of the CF_3I content in the CF_3I-SF_6 mixture. Results obtained by the two-term approximation (TTA) and multi-term approach for solving the Boltzmann equation are compared with the measurements under the PT conditions.
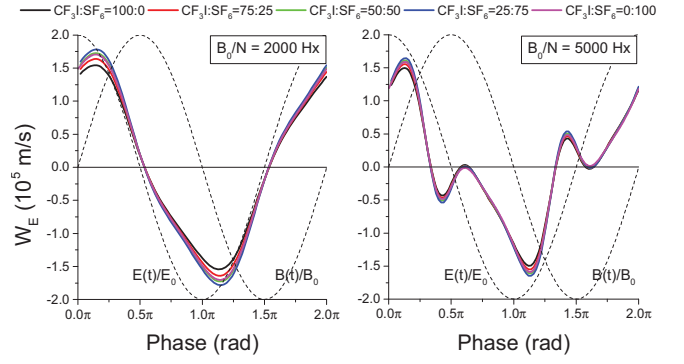

Fig. 4. Temporal profiles of the flux drift velocity for various CF_3I-SF_6 mixtures. The electric field amplitude is 350 Td and the field frequency is 1000 MHz.

In Fig. 3 we show the variation of the critical electric field (or limited electric field) as a function of the per cent content of CF_3I in the mixture. The critical electric field is a value of E/N for which rate coefficients of electron attachment and ionization are equal. This property is of great importance not only in studies of low-current dc discharges and streamers, but may also be useful for studies of some rf discharges. The results obtained by solving the Boltzmann equation are compared with the measurements under the PT conditions. Our multi term results and measurements agree very well for the pure gases. We observe that the TTA significantly overestimates the measurements and multi-term results for pure CF_3I.

C. Transport coefficients in radio-frequency electric and magnetic fields

In Fig. 4 we show the temporal profiles of the longitudinal flux drift velocity for various CF_3I-SF_6 mixtures. Calculations are performed in a crossed field configuration while the phase difference between the electric and magnetic fields is set to $\pi/2$ rad. The magnetic field amplitudes are 2000 Hx (left panel) and 5000 Hx (right panel). We observe that the profiles are asymmetric and phase-delay of the W_E curves relative to the electric field is clearly evident due to temporal non-locality [4]. The maximum values of W_E are dependent on the gas composition. The time-averaged power absorbed by the swarm (or plasma or any active medium) is given by:

$$\langle p_{abs} \rangle = \frac{1}{T} \int_0^T -eN_0 \boldsymbol{W}(t) \cdot \boldsymbol{E}(t) dt , \qquad (4)$$

where N_0 is the number of electrons in the swarm, $T=2\pi/\omega$ is the period, $\boldsymbol{W}$ is the time-dependent average velocity and $\boldsymbol{E}$ is the time-dependent electric field. From Eq. (4), it is clear that the phase difference between the drift velocity and electric field controls the power absorption: (i) when the drift velocity $\boldsymbol{W}$ and electric field $\boldsymbol{E}$ have the same sign, the instantaneous power is positive, and (ii) when the drift velocity $\boldsymbol{W}$ and electric field $\boldsymbol{E}$ have the opposite sign, then the instantaneous power is negative. This suggests that when the power is positive the electric field pumps the energy into the system while when the power is negative the energy is transferred from an active medium to the external circuit.

In Fig. 5 we show the variation of the cycle-averaged power as a function of the magnetic field amplitude for various CF_3I-SF_6 mixtures. We observe that the absorbed power depends on the gas composition. One of the most striking phenomena is the presence of periodic structures in

the profile of the absorbed power. Comparing CF_3I and SF_6, these structures are more pronounced for CF_3I. For dc electric and magnetic fields the absorbed power is always a monotonically decreasing function of the applied magnetic field, while in this case we may observe a multitude of peaks in the B_0/N-profiles of this property. This is a clear sign of the resonant absorption of energy from the rf electric and magnetic fields. We see that these effects are more pronounced for the lower values of B_0/N, where on the average the electrons only complete partial orbits between collisions.

D. Transition from an electron avalanche into a negative streamer its propagation in the CF_3I-SF_6 mixtures

In Figs. 6 (a) and (b) we show the temporal evolution of the electric field and electron density, respectively for various CF_3I-SF_6 mixtures. Calculations are performed in a 1-dimensional setup. The initial Gaussian grows due to the ionization and then charge separation occurs due to the drift of positive ions in the opposite direction. As a consequence, the initial homogeneous electric field is disturbed and the field in the ionized region becomes more and more screened. Due to space charge effects the electric field drops off to the level in which ionization stops and only attachment occurs. As a consequence, the electron density in the streamer channel is significantly reduced. By mixing CF_3I with SF_6, the streamers become slower and the screening of the externally applied electric field is less pronounced.
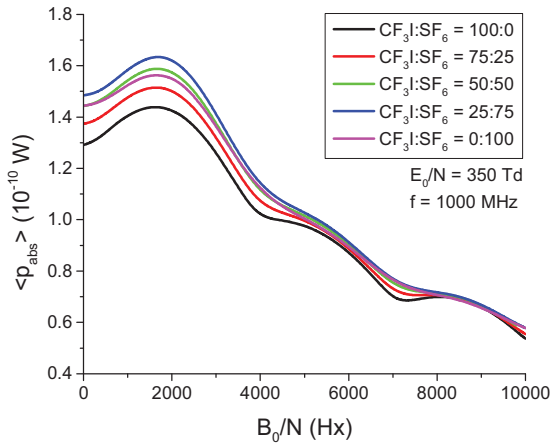

Fig. 5. Variation of the cycle-averaged power of electrons for various CF3I-SF6 mixtures. The electric field amplitude is 350 Td and the field frequency is 1000 MHz.

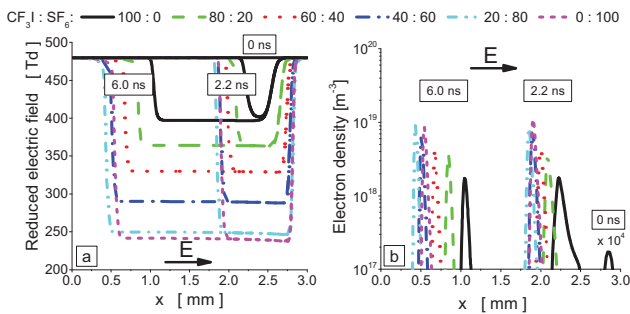
Fig. 6. Temporal evolution of the electric field (a) and electron density (b) in a planar front in various CF_3I-SF_6 mixtures. The externally applied electric field is 480 Td and streamers move from the right to the left.

IV. CONCLUSION

In this paper, we have used a multi term theory for solving the Boltzmann equation and a Monte Carlo simulation technique to investigate electron transport in the mixtures of CF_3I and SF_6. From the point of view of a possible application of CF_3I and its mixtures with SF_6 as gaseous dielectrics, we have calculated the drift velocity, rate coefficients for electron attachment and ionization and critical electric field. The previous studies [10] are extended by considering the duality of transport coefficients, e.g. the existence of two different families of transport coefficients, the bulk and the flux. Comparing the bulk and flux drift velocities, it is found that the bulk component shows a very strong NDC and behaves in a qualitatively different fashion. Calculations in dc electric fields are augmented by those in rf electric and magnetic fields. We have paid a particular attention to the power absorption of the swarm. Due to a complex interplay of the effects induced by temporal non-locality, magnetic field and cyclotron resonance, we have observed a multitude of peaks in the B_0/N profiles of the absorbed power. Finally, using the classical fluid model we have simulated the transition from an electron avalanche into a negative streamer. It is shown that streamers in the mixtures with a higher content of CF_3I are slower, the electron density is reduced and the electric field in the streamer interior is enhanced. Thus, by mixing CF_3I with SF_6, the insulation characteristics of the mixtures are considerably improved.

REFERENCES

[1] J. de Urquijo, "Is CF_3I a good gaseous dielectric? A comparative swarm study of CF_3I and SF_6," J. Phys. Conf. Series, vol. 86, 012008, 2007.

[2] S. Dujko, R.D. White, Z.Lj. Petrović and R.E. Robson, "Benchmark calculations of nonconservative charged-particle swarms in dc electric and magnetic fields crossed at arbitrary angles," Phys. Rev. E. vol. 81, 046403, 2010.

[3] S. Dujko, R.D. White, Z.Lj. Petrović and R.E. Robson, "A multi-term solution of the non-conservative Boltzmann equation for the analysis of temporal and spatial non-local effects in charged-particle swarms in electric and magnetic fields," Plasma Sources Sci. Technol. vol. 20, 024013, 2011.

[4] J. Mirić, D. Bošnjaković, I. Simonović, Z.Lj. Petrović, "Electron swarm properties under the influence of a very strong attachment in SF_6 and CF_3I obtained by Monte Carlo rescaling procedures," Plasma Sources Sci. Technol. vol. 25, 065010, 2016.

[5] C. Li, W.J.M.Brok, U.Ebert nd J.J.A. van der Mullen,R. Nicole, "Deviations from the local field approximation in negative streamer heads," J. Appl. Phys. vol. 101, 123305,2007.

[6] D. Bošnjaković, Z.Lj. Petrović and S. Dujko, "Fluid modeling of resistive plate chambers: impact of transport data on development of streamers and induced signals," J. Phys. D: Appl. Phys. vol. 49, 405201,2016.

[7] J. Atić et al. "Scattering cross sections and electron transport in CF_3I," unpublished.

[8] M. Kimura and Y. Nakamura, "Electron swarm parameters in CF_3I and a set of electron collision cross sections for the CF_3I molecule," J. Phys. D: Appl. Phys. vol. 43, 145202, 2010.

[9] H. Itoh ,T. Matsumura, K. Satoh K, H. Date, Y. Nakano and H. Tagashira, "Electron transport coefficients in SF_6," J. Phys. D: Appl. Phys. vl. 26, 1975, 1993.

[10] J. de Urquijo, A. Mitrani, G.R. Vargaz E. Baurto, "Limited field strength and electron swarm coefficients of the CF_3I-SF gas mixtures," J. Phys. D: Appl. Phys. vol. 44, 342001, 2011.

IPB

Институт за физику у Београду

на основу одлуке Жирија о додељивању Годишње награде додељује:

СТУДЕНТСКУ НАГРАДУ
ИНСТИТУТА ЗА ФИЗИКУ ЗА 2017. ГОДИНУ

др Данку Бошњаковићу

за докторску тезу под називом *"Моделовање гасних детектора честица високих енергија применом технике електронских ројева"*.

др Марија Радмиловић Рађеновић
председница
Научног већа

Београд
11. мај 2017.

др Александар Богојевић
директор
Института за физику

50

Journal of Physics series

On the 50th anniversary of
Journal of Physics D: Applied Physics

This is to certify that the article:

Fluid modeling of resistive plate chambers: impact of transport data on
development of streamers and induced signals

by D Bošnjaković, Z Lj Petrović and S Dujko

has been selected by the Editorial Board of
Journal of Physics D: Applied Physics for inclusion in the exclusive
'Highlights of 2016' collection, and were chosen on the basis of
novelty, scientific impact and broadness of appeal

Tom Miller
Executive Editor
Journal of Physics D: Applied Physics

IOP Publishing | science first

Committee

Executive management committee:

Dr. J.E. Jones, Chair
Prof. G.R. Jones
Prof. J.W. Spencer
Prof. K Hidaka
Dr. A.B. Murphy
Prof. D. Hong
Dr. P. Robin-Jouan

International scientific committee:

Dr. J.-M. Bauchire, France
Dr. J.-P. Borra, France
Prof. Yann Cressault, France
Prof. M. Farzaneh, Canada
Prof. C.M. Franck, Switzerland
Prof. A. Haddad, UK
Prof. K. Hidaka, Japan
Prof. D. Hong, France
Prof. G.R. Jones, UK
Dr. J.E. Jones, UK
Dr. A.B. Murphy, Australia
Prof. Z. Lj. Petrović, Serbia
Prof. G.J. Pietsch, Germany
Prof. V. Rakov, USA
Prof. Ph. Robin-Jouan, France
Prof. A. Robledo-Martinez, Mexico
Prof. Kohki Satoh, Japan
Dr. M. Seeger, Switzerland
Prof. J.W. Spencer, UK
Dr. S. Stangherlin, Switzerland
Dr. T. Teich, Switzerland
Dr. Igor Timoshkin, UK
Prof. J. -Y. Trepanier, Canada
Prof. K.-D. Weltmann, Germany
Prof. Y. Wu, China
Dr. J. D. Yan, UK
Dr. J. L. Walsh, UK

Local organizing committee:

Prof. Zoran Lj. Petrović, Chair
Dr. Nevena Puač, Co-Chair
Dr. Saša Dujko, Co-Chair
Dr. Nikola Škoro, Secretary
Dr. Danko Bošnjaković
Kosta Spasić
Prof. Bratislav Obradović
Dr. Dragana Marić
Dr. Gordana Malović
Jelena Sivoš
Marija Puač
Dejan Maletić
Nenad Selaković
Jasmina Atić
Ilija Simonović
Vladan Simić

Contact

Organisers

Sponsors

‹ ›

Institute of Physics Belgrade

POSMOL 2019

XX International Workshop on Low-Energy Positron and Positronium Physics
XXI International Symposium on Electron-Molecule Collisions and Swarms
18 - 20 JULY 2019
Belgrade, Serbia

SPONSORS

MINISTRY OF EDUCATION, SCIENCE
AND TECHNOLOGICAL DEVELOPMENT

EPJ.org

EUROPEAN PHYSICAL JOURNAL D

Committees

Local Organising Committee

- Zoran Lj. Petrović (SASA, IPB) *Chair*
- Bratislav Marinković (IPB) *Co-Chair*
- Saša Dujko (IPB) *Co-Chair*
- Sanja Tošić (IPB) *Secretary*
- Dragana Marić (IPB) *Conference Manager*
- Gordana Malović (IPB)
- Danko Bošnjaković (IPB)
- Andrej Bunjac (IPB)
- Jelena Sivoš (IPB)
- Marija Puač (IPB)
- Ilija Simonović (IPB)
- Vladan Simić (IPB)
- Nenad Selaković (IPB)
- Dejan Maletić (IPB)
- Kosta Spasić (IPB)
- Olivera Jovanović (IPB)
- Anđelija Petrović (IPB)
- Goran Poparić (FP)
- Biljana Grozdanić (SASA)
- Aleksandra Hreljac (SASA)

Positron International Advisory Committee

- David Cassidy (University College London), *Chair*
- Gustavo Garcia (Consejo Superior de Investigaciones Científicas)
- Michael Bromley (University of Queensland)
- Marcio Varella (Universidade de São Paulo)
- Masanori Tachikawa (Yokohama City University)
- Roberto Brusa (Università di Trento)
- James Danielson (University of California, San Diego)
- Laszlo Liszkay (University of Paris, Saclay)

Electron International Advisory Committee

- Michael J. Brunger (Flinders University), *Chair*
- Ilya I. Fabrikant (University of Nebraska, Lincoln)
- Roman Čurik (J. Heyrovsky Institute of Physical Chemistry)
- Roma da Costa (Universidade Federal do Espirito Santo)
- Paulo Limao-Vieira (Universidade Nova de Lisboa)
- Dragana Maric (Institute of Physics Belgrade)
- Sylwia Ptasinska (University of Notre Dame)
- Petra Swiderek (University of Bremen)
- Hajime Tanuma (Tokyo Metropolitan University)
- Ronald D. White (James Cook University)

ORGANIZERS

Subject	**[JINST] Thank you for your report for JINST_035P_0814**
From	Yi Wang <yiwang@mail.tsinghua.edu.cn>
To	Danko Bosnjakovic <dbosnjak@ipb.ac.rs>
Cc	JINST Editorial Office <jinst-eo@jinst.sissa.it>
Date	2015-01-16 01:57

```
JINST_035P_0814 [RPC2014]
Authors: Roberto Iuppa
Title: Potential of RPCs in cosmic ray experiments for the next decade

Dear Danko Bosnjakovic,

I wish to thank you for reviewing JINST_035P_0814.
Your help is very much appreciated.


Sincerely yours,
Yi Wang
JINST Editor
```

Subject	**Thank you for reviewing for J. Phys. D: Appl. Phys. - JPhysD-110660**
From	Journal of Physics D: Applied Physics <onbehalfof+jphysd+iop.org@manuscriptcentral.com>
Sender	<onbehalfof+jphysd+iop.org@manuscriptcentral.com>
To	<dbosnjak@ipb.ac.rs>
Reply-To	<jphysd@iop.org>
Date	2016-10-27 01:00

Dear Mr Bosnjakovic,

Re: "Measurement of ion and electron drift velocity and electronic attachment in air for ionization chambers" by Boissonnat, Guillaume; Fontbonne, Jean; Colin, Jean; Remadi, Aurélien; Salvador, Samuel
Article reference: JPhysD-110660

Thank you for your report on this Paper, which is being considered by Journal of Physics D: Applied Physics.

We appreciate the time and effort that you have spent reviewing this manuscript and we are very grateful for your assistance.

We hope that we will be able to call upon you again to review future manuscripts.

Yours sincerely

On behalf of the IOP peer-review team:
Giorgio Margaritondo - Editor-in-Chief
Tom Miller - Executive Editor
Dean Williams - Editor
Lucy Evans, Johnathan Keen, Eden Brent-Jones and Freddie White - Associate Editors
Elin Morris, Sarah Poulter and Lorna Wroe - Editorial Assistants
jphysd@iop.org

IOP Publishing
Temple Circus, Temple Way, Bristol
BS1 6HG, UK

www.iopscience.org/jphysd

Impact Factor: 2.772

Letter reference: ESPSNS05

Exploring ultra low global warming potential gases for insulation in high-voltage technology: Experiments and modelling

- EGWIn -

Natural sciences and mathematics

Institute of Physics, Belgrade – IPB

Dr Saša Dujko

Abstract. In the present project, we propose a research program to investigate dielectric properties of ultra low global warming potential (GWP) gases, as possible candidates for replacement of SF_6 for insulation of power equipment in high voltage technology. The project brings together junior and well-experienced members of the Laboratory for non-equilibrium processes and plasma applications that is one of the Centres of excellence at the Institute of Physics Belgrade on a joint mission related to fundamental experimental and theoretical investigations of charged-particle swarms and electrical discharges in ultra low GWP gases. The experimental program includes the contemporary measurements of breakdown data in a low-pressure Townsend direct-current (DC) discharge. Using a novel method for the detection of the radio-frequency (RF) breakdown that is based on the combined balanced capacitive-bridge technique and ICCD imaging, the measurements in DC electric fields, will be extended and generalized to RF electric fields. Using experimentally measured and theoretically calculated electron transport and rate coefficients, in the framework of the swarm method of deriving cross sections, we will develop complete, self-consistent and accurate sets of cross sections for electron scattering in ultra low GWP gases. Calculations and modelling will be performed using state-of-the-art computer codes based on the Boltzmann equation and the Monte Carlo method. Electron transport and rate coefficients and associated insulation properties will be investigated for a range of pure ultra low GWP gases and their mixtures with the industry relevant gases such as N_2, CO_2 and SF_6 in varying configurations of electric and magnetic fields. A versatile multi-scale modelling platform consisting of 2D classical fluid model with the non-local description of ionization and 2.5D Particle-in-cell/Monte Carlo Collision model will be developed to study the inception, propagation and branching of positive and negative streamers in ultra low GWP gases. The proposed research program will initiate innovations in HV technology, which in turn will enable applications of a new class of eco-friendly gases for insulation of power equipment, better situating our Centre of Excellence in this emerging area of international research.

Total requested budget: 300. 000 EUR

Work package number	5	Work package title	PIC/MCC and Fluid simulations of streamers
Lead SRO's acronym	IPB		
WP Coordinator - team member's ID	P4		
Team members` IDs	PI, P2, P3, P6, P7		

Objectives: Development of a multi-scale modelling platform consisting of multi-dimensional Particle-in-cell/Monte Carlo (PIC/MC) model and classical fluid model with the non-local description of ionization to investigate inception, propagation and branching of both positive and negative streamers in ultra low GWP gases.

Description of work: Sub-activity 5.1: PIC-MCC: Implementation of Velocity Verlet scheme for particle motion. Implementation of null-collision method for sampling of time until the next collision (PI, P3, P6); **Sub-activity 5.2:** PIC-MCC: Implementation of the Poisson equation solver based on iterative geometric multigrid method. Implementation of an adaptive grid refinement technique (PI, P3, P6); **Sub-activity 5.3:** PIC-MCC: Implementation of particle management techniques in order to optimize the number of particles in a simulation. Implementation of photoionization models for simulating positive streamers. Implementation of parallel processing using OpenMP/MPI (PI, P2, P3, P6); **Sub-activity 5.4:** PIC-MCC: Simulation of positive and negative streamers in 2.5D with cylindrical symmetry (PI, P3, P6, P7); **Sub-activity 5.5:** Fluid model: Implementation of classical fluid model with improved non-local description of ionization. Coupling transport equations and the Poisson solver (PI, P3, P6); **Sub-activity 5.6:** Fluid model: Implementation of 2D adaptive grid refinement technique. Implementation of photoionization models for simulating positive streamers. Implementation of parallel processing using OpenMP/MPI (PI, P2, P3, P6); **Sub-activity 5.7:** Fluid model: Simulation of positive and negative streamers in various 2D geometries (PI, P3, P6, P7); **Sub-activity 5.8:** Fluid model: Application of deep learning approach as an alternative to the Poisson equation solver (PI, P2, P3, P6). **Sub-activity 5.9:** Verification and testing of the implemented methods/algorithms for each sub-activity. Benchmarking and comparing to previously published results, when appropriate (PI, P3, P6, P7).

Deliverables of the work package: D5.1: Modified and optimized Monte Carlo code as a basis for a versatile 2.5D PIC/MCC streamer code. (M3); **D5.2:** Poisson equation solver based on iterative geometric multigrid method. (M15) **D5.3:** 2.5D PIC/MCC code for simulation of streamers with cylindrical symmetry (M21); **D5.4:** Results of PIC/MCC simulations (evolution of streamers for a given distribution of initial ionization), including electron and ion densities, field distribution, streamer radius and velocity, for streamers in ultra low GWP gases (M36). **D5.5:** 2D classical fluid code with the non-local description of the source term (M24) **D5.6:** Results of fluid simulations and comparison between PIC/MCC and fluid results M36.

Work package number	6	Work package title	Breakdown studies in RF electric fields
Lead SRO's acronym	IPB		
WP Coordinator - team member's ID	P1		
Team members` IDs	P3, P5, P8, P9		

Objectives: To develop a novel technique of breakdown detection in high frequency fields based on the balanced capacitive bridge. To measure breakdown voltages in RF electric fields in ultra low GWP gases.

Description of work:Sub-activity 6.1: The technique itself needs to be "fine-tuned", to meet the requirements of the project. Some of the challenges are in increasing the achievable voltages (at the moment, the experiment can provide voltages up to 600-700 V), expected in strongly attaching gases, while other are in achieving full control in low-current regimes of the discharge (P1, P3,P5, P8, P9); **Sub-activity 6.2:** Test measurements to validate results on "well known" gases (argon, synthetic air) (P1,P5, P8, P9); **Sub-activity 6.3:** Breakdown measurements in ultra low GWP gases (P5, P8, P9); **Sub-activity 6.4:** Analysis of measured data, comparisons to DC measurements (P1, P3, P5, P8 P9).

Deliverables of the work package: D6.1: Results and database of measurements of RF breakdown voltage in Ar and synthetic air (M22); **D6.2:** Database containing breakdown voltages in low-pressure RF discharges initiated and sustained by RF electric fields in ultra low GWP gases. (M36).

Table 3.2c: Major Deliverables

Deliverable ID	Deliverable name	WP No	Month of delivery
D1.1	Reference set of DC breakdown data, including breakdown voltages, field strengths, ionization coefficients, secondary electron yields	1	18
D2.1	Monte Carlo computer code for modelling the pulsed-Townsend experiment	2	6
D2.4	Database containing complete and self-consistent sets of cross sections for electron scattering in HFO1234ze , C5-PFK and C4-PFN and transport and rate coefficients in their mixtures with Ar and N_2	2	18
D3.1	Database of electron transport and rate coefficients for electrons and insulation properties of pure HFO1234ze, C5-PFK and C4-PFN and their mixtures with Ar, N_2, CO_2 and SF_6	3	24
D4.1	Database of electron transport and rate coefficients and critical magnetic fields for HFO1234ze, C5-PFK and C4-PFN and their mixtures with Ar, N_2, CO_2 and SF_6 in DC electric and magnetic fields	4	24
D4.2	Database of electron transport and rate coefficients for HFO1234ze, C5-PFK and C4-PFN and their mixtures with Ar, N_2, CO_2 and SF_6 in RF electric and magnetic fields	4	36
D5.1	Results of PIC/MCC simulations (evolution of streamers for a given distribution of initial ionization), including electron and ion densities, field distribution, streamer radius and velocity, for streamers in ultra low GWP gases.	5	36
D5.2	Results of fluid simulations and comparison between PIC/MCC and fluid results.	5	36
D6.2	Database containing breakdown voltages in low-pressure RF discharges initiated and sustained by RF electric fields in ultra low GWP gases.	6	36

Table 3.2.d: Milestones

Milestone ID	Milestone name	Means of verification	WP No	Due month
M1.1	Adaptation, adjustment and fine tunning of the experimental set-up to achieve stable operation of a discharge in ultra low GWP gases.	Recordings of Paschen curves and emission profiles in stable Townsend regime.	1	4
M2.1	Solving diffusion equation assuming various boundary conditions and implementation of the corresponding solutions into the MC code, along with testing and benchmarking.	Current signal fitting and extraction of transport coefficients for gases with known values for transport coefficients.	2	3
M2.2	Constructing initial sets of cross sections for ultra low GWP gases based on existing data for similar molecules and critical evaluation of scattering and transport data found in the literature.	Calculation of partial cross sections by Quantemol –N code and implementation of the available partial cross sections for ultra low GWP gases that are available in the literature.	2	13